Academic Press is an imprint of Elsevier
Linacre House, Jordan Hill, Oxford OX2 8DP, UK
32 Jamestown Road, London NW1 7BY, UK
Radarweg 29, PO Box 211, 1000 AE Amsterdam, The Netherlands
225 Wyman Street, Waltham, MA 02451, USA
525 B Street, Suite 1900, San Diego, CA 92101-4495, USA

First edition 2011

British Library Cataloguing in Publication Data
A catalogue record for this book is available from the British Library

Library of Congress Cataloging-in-Publication Data
A catalog record for this book is available from the Library of Congress

ISBN: 978-0-08-097072-1
ISSN: 0066-4103

Printed and bound in Great Britain
11 12 13 14 10 9 8 7 6 5 4 3 2 1

CONTRIBUTORS

Sabine Bouguet-Bonnet
Méthodologie RMN (CRM2; UMR 7036, UHP-CNRS), Faculté des Sciences et Techniques, B.P. 239, Vandœuvre-lès-Nancy (cedex), France

Daniel Canet
Méthodologie RMN (CRM2; UMR 7036, UHP-CNRS), Faculté des Sciences et Techniques, B.P. 239, Vandœuvre-lès-Nancy (cedex), France

Sara Cozzolino
Agricultural Research Council—Research Centre for Plant Soil System, Instrumental Centre of Tor Mancina, S.P. Pascolarese—Strada della Neve Km 1, Monterotondo, Rome, Italy

Julien Furrer
Department für Chemie und Biochemie, Universität Bern, Freiestrasse 3, Bern, Switzerland

Sébastien Leclerc
LEMTA (UMR 7563, Nancy-Université-CNRS), B.P. 160, Vandoeuvre-lès-Nancy (cedex), France

Gary E. Martin
Merck Research Laboratories, Discovery and Preclinical Sciences, Global Chemistry—Structure Elucidation Group, Summit, New Jersey, 07901, USA

Z. Rozwadowski
Department of Inorganic and Analytical Chemistry, West Pomeranian University of Technology, Szczecin, Al. Piastów 42, 70-065 Szczecin, Poland

Hazime Saitô
Department of Life Science, Himeji Institute of Technology, University of Hyogo, Koto 3-chome, Kamigori, Hyogo, Japan

Paolo Sequi
Agricultural Research Council—Research Centre for Plant Soil System, Instrumental Centre of Tor Mancina, S.P. Pascolarese—Strada della Neve Km 1, Monterotondo, Rome, Italy

Kazuyuki Takeda
Division of Chemistry, Graduate School of Science, Kyoto University, Kyoto, Japan

Massimiliano Valentini
Agricultural Research Council—Research Centre for Plant Soil System, Instrumental Centre of Tor Mancina, S.P. Pascolarese—Strada della Neve Km 1, Monterotondo, Rome, Italy

Mehdi Yemloul
Méthodologie RMN (CRM2; UMR 7036, UHP-CNRS), Faculté des Sciences et Techniques, B.P. 239, Vandœuvre-lès-Nancy (cedex), France

PREFACE

Volume 74 of *Annual Reports on NMR* contains reviews of advances in several of the most prominent areas of molecular science where NMR plays a key role. The volume commences with an account on 'NMR Studies on Structurally or Dynamically Heterogeneous Systems: Dynamic Aspects of Hydrogels, Protein Fibrils and Membrane Proteins' by H. Saitô; this represents a career long interest in NMR by the author. Following this is a review of 'Carbon-13 Heteronuclear Longitudinal Spin Relaxation for Geometrical (and Stereochemical) Determinations in Small or Medium Size Molecules' by D. Canet, S. Bouguet-Bonnet, S. Leclerc and M. Yemloul; Z. Rozwadowski covers 'NMR Studies of Optically Active Schiff Bases'; S. Cozzolino, P. Sequi and M. Valentini report on 'Probing Interactions Between Small Molecules and Polymers by Means of NMR Spectroscopy'; 'Using 1,1- and 1,n-ADEQUATE 2D NMR Data in Structure Elucidation Protocols' is the topic chosen by G. E. Martin; J. Furrer reports on 'Recent Developments in HMBC Studies'; finally K. Takeda covers 'Highly Customised NMR Systems Using an Open-Resource, Home-Built Spectrometer'.

My sincere thanks goes to all of these reporters for the diligence with which they have prepared and presented their timely and interesting contributions.

G. A. Webb
Royal Society of Chemistry
Burlington House
London, UK

CHAPTER 1

NMR Studies on Structurally or Dynamically Heterogeneous Systems: Dynamic Aspects of Hydrogels, Protein Fibrils and Membrane Proteins

Hazime Saitô*

Contents

1. Introduction 5
2. Dynamic Parameters for Characterization of Heterogeneous Systems Available From Solution and Solid-state NMR 8
   - 2.1. Longitudinal or transverse relaxation times 8
   - 2.2. Chemical exchange 15
   - 2.3. Time domain NMR measurements 16
3. Structurally Heterogeneous Systems: Network Structures and Dynamics of Hydrogels 19
   - 3.1. Synthetic polymer gels 19
   - 3.2. Polysaccharide gels 28
   - 3.3. Fibrillation and amyloid proteins 34
4. Dynamically Heterogeneous Systems: Membrane Proteins 44
   - 4.1. Retinal proteins 45
   - 4.2. Membrane proteins other than retinal proteins 74
5. Concluding Remarks 79

Acknowledgements 81

References 81

Department of Life Science, Himeji Institute of Technology, University of Hyogo, Koto 3-chome, Kamigori, Hyogo, Japan
* Address correspondence to 203, 3-15-21 Sumiyoshi-honmachi, Higashinada-ku, Kobe, Japan 658-0051

Annual Reports on NMR Spectroscopy, Volume 74
ISSN 0066-4103, DOI: 10.1016/B978-0-08-097072-1.00001-7

Abstract There are a variety of macromolecular systems exhibiting structural and dynamic heterogeneity, in which expected NMR signals are not always fully visible by a single set of NMR measurements. The former includes hydrogels of synthetic polymers, polysaccharides, and aggregated proteins, the latter of which can be further converted to amyloids or prions. They are very important as materials for biomedical or industrial applications, a variety of biological functions including host-defence systems, components of biological tissues, or key substances leading to several serious diseases. In addition, membrane proteins are typical dynamically heterogeneous systems which give rise to suppressed peaks depending upon local protein dynamics. In particular, it is emphasized that the presence of such suppressed peaks affords an invaluable means to determine their dynamic information.

In this chapter, we first briefly review several parameters to be able to analyse their dynamic features. Then, we discuss two types of heterogeneous systems in more detail: structurally and/or dynamically heterogeneous systems. NMR studies on synthetic and polysaccharide gels and protein fibrils are reviewed with emphasis on revealing their secondary structures and dynamic aspects. Dynamic aspects of membrane proteins are also discussed in relation to their biological function. It turned out that the combined use of a solution (and or solution-like) state and a solid-state NMR technique are essential to be able to fully observe signals from portions of different mobility. We emphasize that recording spectra based on dipolar decoupled (or the direct detection) magic angle spinning (DDMAS) approach is essential to be able to reveal the more flexible portions of these systems, because the conventional solid-state NMR, using cross-polarization magic angle spinning (CPMAS) alone, is not sufficient for detecting signals from the solid-like portions.

Key Words: Structurally and/or dynamically heterogeneous systems, Hydrogels, Protein fibrils, Membrane proteins, Dynamic aspects

ABBREVIATIONS

ABC	ATP-binding cassette
AS	α-Synuclein
bO	Bacterio-opsin
bR	Bacteriorhodopsin
CODEX	Centerband-only detection of exchange
CP	Cytoplasmic

CPMAS	Cross-polarization magic angle spinning
CPMG	Curr-Purcell-Meiboom-Gill
CSA	Chemical shift anisotropy
CT	Calcitonin
cyt b_5	Cytochrome b_5
cyt P450	Cytochrome P450
DCC	Dipolar coupling constant
DCE	Dipolar correlation effect
DDMAS	Dipolar decoupled (or direct detection) magic angle spinning
DGK	Diacylglycerol kinase
DIPSHIFT	Dipolar chemical shift separation
DMPC	Dimyristoylphosphatidylcholine
DPC	Dodecylphosphocholine
DP_n	Numerical average degree of polymerization
DPPC	Dipalmitoylphosphatidylcholine
DQ	Double quantum
EC	Extracellular
EmrE	*Escherichia coli* multidrug resistant transporter
EPR	Electron paramagnetic resonance
FCR	Field cycling relaxometry
FID	Free induction decay
fp RFDR	Finite pulse radio-frequency driven recoupling
FTIR	Fourier transform infrared
GPR	Green proteorhodopsin
hCT	Human calcitonin
HET-s	The prion protein of *P. anserine*
HIMSELF	Heteronuclear isotropic mixing leading to spin exchange via the local field
HR	Halorhodopsin
HRMAS	High-resolution magic angle spinning
HtrII	Cognate transducer of sensory rhodopsin II
IAPP	Islet amyloid polypeptide
IP_3	D-myo-inositol 1,4,5-trisphosphate
LAL	Hoseshoe crab amebocyte lysate
LGCP	Lee-Goldburg CP
MAS	Magic angle spinning
MBA	*N,N′*-methylenebisacrylamide
MBP	Myelin basic protein
MMA	Methylmethacrylate
MQ	Multiple quanturm
NPCs	Nuclear pore complexes
PAP	Prostatic acid phosphatase

PDMAA	Poly(*N*,*N*-dimethylacrylamide)
PDMS	Poly(dimethylsiloxane)
PDSD	Proton-driven spin diffusion
PFGSE	Pulsed field gradient spin-echo
PH	Pleckstrin homology
PHEMA	Poly(hydroxyethylmethacrylate)
PHFs	Paired helical filaments
*p*HtrII	Cognate transducer of *pharaonis* sensory rhodopsin II
PIP_2	Phosphatidylinositol 4,5-bisphosphate
PISEMA	Polarization inversion spin exchange at the magic angle
PLB or PLN	Phospholamban
PLC-δ1	Phospholipase C-δ1
PM	Purple membrane
PMEA	Poly(2-methoxyethyl acrylate)
PNVP	Poly(*N*-vinylpyrrolidone)
*p*pR	Pharaonis phoborhodopsin
PR	Proteorhodosin
pR	phoborhodopsin
PrP^c	Prion protein
PS	Polystyrene
PTHFA	Poly(tetrahydrofurfuryl acrylate)
PVA	Poly(vinyl alcohol)
REDOR	Rotational echo double resonance
Refocused INEPT or RINEPT	Refocused insensitive nuclei enhanced by polarization transfer
SBR	Styrene-butadiene rubbers
SERCA	Sarco(endo)plasmic reticulum Ca-ATPase
SEVI	Semen-derived enhancer of viral infection
SLF	Separated local field
SR	Sarcoplasmic reticulum
sR	Sensory rhodopsin
SRI	Suppressed or recovered intensities
TAT	Thrombin–antithrombin III complex
TM	Transmembrane
TROSY	Transverse relaxation-optimized spectroscopy
TTR	Transthyretin
UVRR	Ultraviolet resonance Raman
WISE	Wide-line separation
WT	Wild type

1. INTRODUCTION

It is usually expected that a given NMR signal is proportional to the number of nuclei contributing to that line, so long as the instrumental conditions such as pulse width, repetition time, contact time, etc., are carefully optimized. To achieve unambiguous spectral interpretation, therefore, one starts spectral analysis by counting a possible number of nuclei contributing to such given signals, as far as they are presumably fully visible. It is true, however, that this premise is not always fulfilled for a variety of extremely large supramolecular systems, including swollen gels, biological tissues, large fibrillar or membrane proteins, because several signals from such regions could be either broadened or suppressed depending upon the experimental conditions utilized.

Swollen gels formed by chemically or physically cross-linked synthetic polymers or naturally occurring biopolymers are structurally heterogeneous, exhibiting no flow together with a solid-like appearance.[1–8] They can be also naturally characterized as dynamically heterogeneous systems, because they arise from an assembly of various dynamically different portions which being fluctuating with correlation times on a very broad timescale: liquid-like portions undergoing very fast fluctuation motions, solid-like portions consisting of aggregated or cross-linked region, and portions undergoing fluctuation motions with intermediate frequencies between them. Further, biological tissues, collagen fibres, amyloid and prion fibrils, and membrane proteins can be recognized as dynamically heterogeneous systems: they consist of various portions whose dynamic states differ substantially, depending upon their locations at the structured areas whose motions are substantially limited or unstructured and terminal areas undergoing very flexible motions by mutual interaction with surrounding solvent molecules.

Distinguishing spectral feature between flexible and rigid portions is straightforward for a variety of hydrogels,[9–17] membrane proteins embedded in fluid lipid bilayers, etc.,[16,18–25] by recording both ^{13}C (or ^{15}N) dipolar decoupling magic angle spinning (DDMAS) and cross-polarization magic angle spinning (CPMAS) NMR spectra, respectively, as demonstrated in Figure 1, together with simplified illustrations for the curves of isotropic reorientation of the spin–lattice (T_1^C) and spin–spin relaxation times (T_2^C), and spin–lattice relaxation times in the rotating frame ($T_{1\rho}^H$). Careful comparative evaluation of the peak intensities from *both* liquid-like and solid-like portions is therefore essential in order to *locate* such portions and *evaluate* their local dynamic parameters.

^{13}C (or ^{15}N) NMR signals recorded by both CPMAS and DDMAS NMR, however, could be broadened or suppressed, when fluctuation motions with intermediate frequencies of 10^4–10^5 Hz interfere with

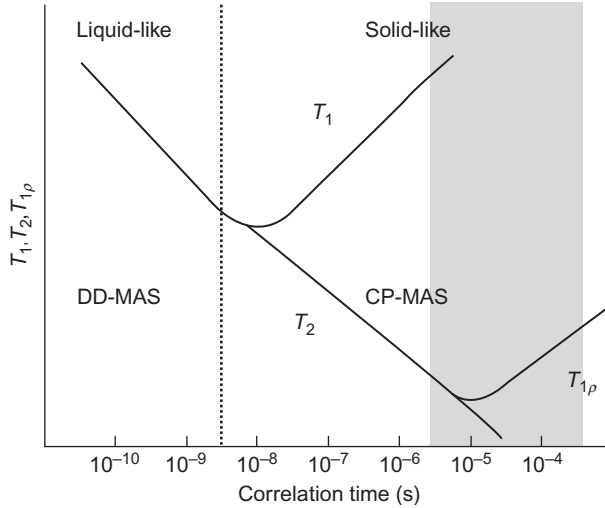

Figure 1 Schematic representation of the ^{13}C (or ^{15}N) spin–lattice relaxation times (T_1), spin–spin relaxation (T_2), and ^{1}H spin–lattice relaxation time in the rotating frame ($T_{1\rho}$) for the liquid-like and solid-like domains, as a function of the correlation times of local motions. ^{13}C (or ^{15}N) NMR signals from the solid-like domains undergoing incoherent fluctuation motions with the correlation times of 10^{-4}–10^{-5} s (indicated by the grey colour) could be lost due to failure of attempted peak-narrowing due to interference of frequency with proton decoupling or magic angle spinning.

frequencies of either proton decoupling or magic angle spinning (MAS) (shaded portion in Figure 1), leading to the failure of achieving high-resolution NMR signals because of ineffective MAS or proton decoupling experiments, respectively.[26,27] Accordingly, the T_2^C curve, which is otherwise monotonously decreased with increased correlation time as shown in Figure 1, is modified to yield the curves with their two minima due to interference of fluctuation frequencies with frequency of proton decoupling [$(T_2^C)^{dd}$] or MAS [$(T_2^C)^{CS}$],[28] as will be discussed in the next section (Figure 2). The observations of the resulting suppressed or recovered intensities (SRI), around these respective T_2^C minima as recorded by *both* CPMAS and DDMAS experiments, turn out to be a very effective means to identify such motions at certain functional groups or residues in swollen gels or membrane proteins, as compared with the data without suppressed or recovered peaks in the absence of such motions.[29,30]

Even though, structure and dynamics are most important to characterize hydrogels, protein fibrils, and membrane proteins, they cannot be simultaneously determined. We emphasize here the importance of the dynamic aspect mainly available from NMR measurements at ambient temperature, even though structural data can be obtained more easily at lower temperatures under suppressed dynamics.

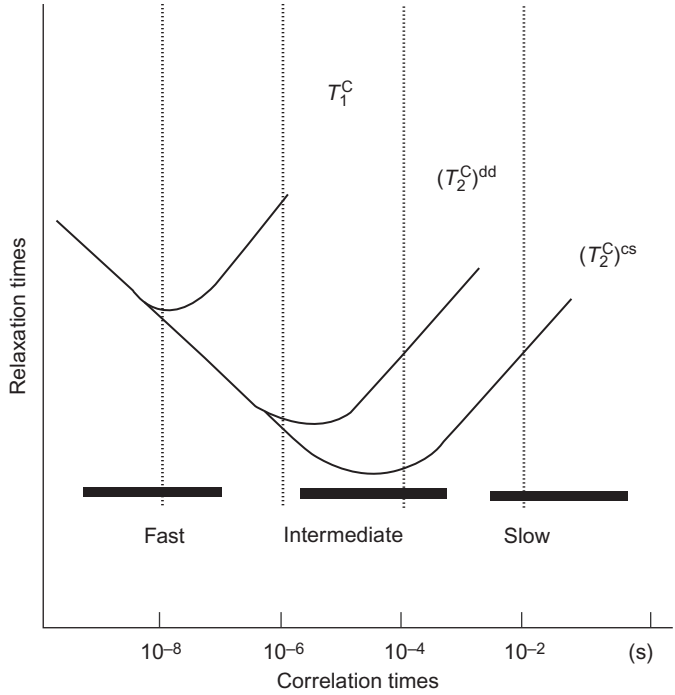

Figure 2 Schematic representation of carbon spin–lattice relaxation time, T_1^C, and spin–spin relaxation time under CPMAS or DDMAS condition, T_2^C, as a function of correlation times.

In what follows, we emphasize that NMR characterization of both liquid-like and solid-like domains with fast and intermediate frequency motions, respectively, proves to be a very important means for a variety of hydrogels to be able to reveal their network structures and gelation mechanism as well. There remain also flexible portions which play an important role during the course of the fibrillation process even in amyloid and prion proteins (PrP^cs), even if the three-dimensional (3D) structure of the rigid, solid-like portion which constitutes core portions of a variety of protein fibrils is obviously more important. In the case of membrane proteins, however, the presence of both high and intermediate frequency motions also is important in view of their biological functions, because they consist of hydrophilic N- or C-terminal groups as well as interhelical loops which are exposed to the aqueous phase and hydrophobic portions which are surrounded by lipid molecules within the membrane. The 3D structure is indeed missing from an X-ray picture in the former and it is obviously very difficult to obtain such information. It is therefore very important to gain insight into their biological significance

based on the dynamic as well structural data partly available from a careful analysis of the NMR data. In fact, we emphasize here that the presence of such flexible or slowly fluctuating areas have their own significance and dynamic information with various time-scales is very important for this purpose.

2. DYNAMIC PARAMETERS FOR CHARACTERIZATION OF HETEROGENEOUS SYSTEMS AVAILABLE FROM SOLUTION AND SOLID-STATE NMR

Dynamic parameters for heterogeneous systems have been explored in the liquid, liquid like, solid like, and solid states, based on analyses of the longitudinal or transverse relaxation times, chemical exchange based on line-shape analysis and separated local field (SLF), time domain ^{1}H NMR, etc., as summarized in Figure 3. It is therefore possible to utilize these most appropriate dynamic parameters, to explore the dynamic features of our concern, depending upon the systems we study.

2.1. Longitudinal or transverse relaxation times

^{13}C (or ^{15}N) spin–lattice relaxation times (T_1^C), spin–spin relaxation times (T_2^C) and nuclear Overhauser enhancement (NOE; η) are generally given by[31–34]

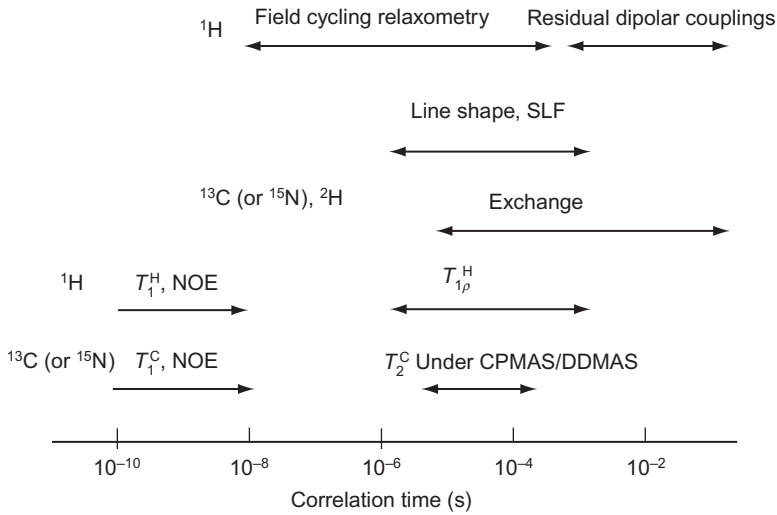

Figure 3 Time scale of motions detected by a variety of NMR measurements including relaxation parameters, and analyses of line shape, SLF and exchanges.

$$1/T_1^{\mathrm{C}} = (1/10)\gamma_{\mathrm{C}}^2\gamma_{\mathrm{H}}^2\hbar^2\Sigma_i r_i^{-6}[J(\omega_{\mathrm{H}} - \omega_{\mathrm{C}}) + 3J(\omega_{\mathrm{C}}) + 6J(\omega_{\mathrm{H}} + \omega_{\mathrm{C}})], \quad (1)$$

$$1/T_2^{\mathrm{C}} = (1/20)\gamma_{\mathrm{C}}^2\gamma_{\mathrm{H}}^2\hbar^2\Sigma_i r_i^{-6}[4\tau + J(\omega_{\mathrm{H}} - \omega_{\mathrm{C}}) + 3J(\omega_{\mathrm{C}}) + 6J(\omega_{\mathrm{H}}) + 6J(\omega_{\mathrm{H}} + \omega_{\mathrm{C}})], \quad (2)$$

$$\eta = 1 + (\gamma_{\mathrm{H}}/\gamma_{\mathrm{C}})[6J(\omega_{\mathrm{H}} + \omega_{\mathrm{C}}) - 6J(\omega_{\mathrm{H}} - \omega_{\mathrm{C}})]/[J(\omega_{\mathrm{H}} - \omega_{\mathrm{C}}) + 3J(\omega_{\mathrm{C}}) + 6J(\omega_{\mathrm{H}} + \omega_{\mathrm{C}})]. \quad (3)$$

where γ_{C} and γ_{H} are gyromagnetic ratios for carbon and proton nuclei, respectively; $\hbar$ is Planck's constant divided by 2π; r_i is the distance between the ^{13}C nucleus i and neighbouring proton; ω_{C} and ω_{H} are resonance frequencies for carbon and proton, respectively. The spectral density functions $J(\omega_i)$ are the Fourier transforms of the autocorrelation functions of the second-order spherical harmonics.

2.1.1. Liquid-like portion: Fast fluctuation motions

In the case of extreme narrowing in which fast isotropic molecular motions dominate as in the solution state, the spectral density is written by a single correlation time,

$$J(\omega) = \tau_{\mathrm{R}}/\left(1 + \omega^2\tau_{\mathrm{R}}^2\right), \quad (4)$$

where τ_{R} is the rotational correlation time. In such a case where $\omega\tau_{\mathrm{R}} \ll 1$, Equations (1) and (2) are shown by

$$1/T_1^{\mathrm{C}} = 1/T_2^{\mathrm{C}} = N\gamma_{\mathrm{C}}^2\gamma_{\mathrm{H}}^2\hbar^2 r_i^{-6}\tau_{\mathrm{R}}, \quad (5)$$

where N is the number of attached proton(s). The NOE factor is 2.988 and -3.93 for ^{13}C and ^{15}N, respectively, for the extreme narrowing condition. Obviously, both $T_1{}^{\mathrm{C}}$ and $T_2{}^{\mathrm{C}}$ are good indicators of the high-frequency motions characterized by shorter rotational correlation times as encountered in the solution state. It is expected, for instance, that a prolonged τ_{R} value for a structured form such as an α-helical chain caused by helix–coil transition of polypeptides results in reduced $T_1{}^{\mathrm{C}}$ and NOE values, in view of the location of the correlation times at the high temperature side of the $T_1{}^{\mathrm{C}}$ minimum.[35–37]

For highly viscous polymers in solution or swollen gels, however, it has been demonstrated that the description of the $T_1{}^{\mathrm{C}}$, $T_2{}^{\mathrm{C}}$, and NOE data by a single correlation time is insufficient, because of marked discrepancies evident among the correlation times based on these respective data. Indeed, it has been shown that various slow motions resulting from entanglements of chains can be treated by the superposition of simple isotropic motions with long-correlation times leading to shortened $T_2{}^{\mathrm{C}}$ values.

Therefore, Schaefer proposed a data analysis based on a log-χ^2 distribution of the correlation times instead of the single correlation time[33,38]:

$$F_p(s) = (ps)^{p-1}\mathrm{e}^{-ps}p/\Gamma(p) \tag{6}$$

with

$$s = \log_b(1 + (b-1)\tau/\bar{\tau}), \tag{7}$$

where $F_p(s)$ is the probability density function of the correlation time τ and $\Gamma(p)$ is the gamma function which normalizes $F_p(s)$ to unity. Here, p is used to describe the width of the distribution of the correlation times. As p becomes larger, the distribution becomes narrower. The logarithmic time scale b is usually taken as 1000. Thus, one obtains an approximately self-consistent analysis of these data, because $T_2{}^{\mathrm{C}}$ is more strongly affected by the long-correlation time or low-frequency end of the distributions in the long tail of the log-χ^2 function. This treatment was successfully utilized for the interpretation of the relaxation times of *cis*-polyisoprene[33,38] and elastin and cartilage.[39,40]

2.1.2. Solid-like portion: Intermediate frequency motions

It is expected that the maximum ^{13}C CPMAS NMR intensity (S) of any molecular system is available from samples of static or nearly static states (I_{a}) which is usually achieved in the crystalline or frozen state, if the contact time is appropriately chosen, as shown in Figure 4. In the nearly static region at low temperatures, however, the peak intensities could be modified as the dotted lines I_{a}', if persistent molecular motions are presented as in the glassy state. The expected CPMAS peak-intensity is gradually decreased with increased fluctuation frequencies to a certain area (III_{a}) as in the liquid-like portion. In contrast, the maximum ^{13}C intensity (S) of DDMAS NMR spectra is concomitantly achieved at a temperature above the glass transition or a liquid-like portion under the condition of the repetition time being $t \gg T_1{}^{\mathrm{C}}$. Here, the observed peak intensity $I(t)$ is related to the ratio $t/T_1{}^{\mathrm{C}}$,[41]

$$I(t) = I(\infty)\left[1 - \exp\left(-t/T_1^{\mathrm{C}}\right)\right], \tag{8}$$

where t and T_1 show the pulse repetition and ^{13}C spin–lattice relaxation times, respectively, and $I(\infty)$ is the peak intensity at $t \gg T_1{}^{\mathrm{C}}$. Therefore, the presence of intermediate fluctuation motions with frequencies of the order of 10^4–10^5 Hz, if any, can be conveniently identified by observation of a broadened line width ($1/\pi T_2{}^{\mathrm{C}}$) or suppressed peak intensities arising from the respective $T_2{}^{\mathrm{C}}$ minima by both CPMAS and DDMAS NMR experiments (Figures 2 and 4).[26–28] Indeed, this is caused by interference of incoherent frequencies from random fluctuation motions with coherent

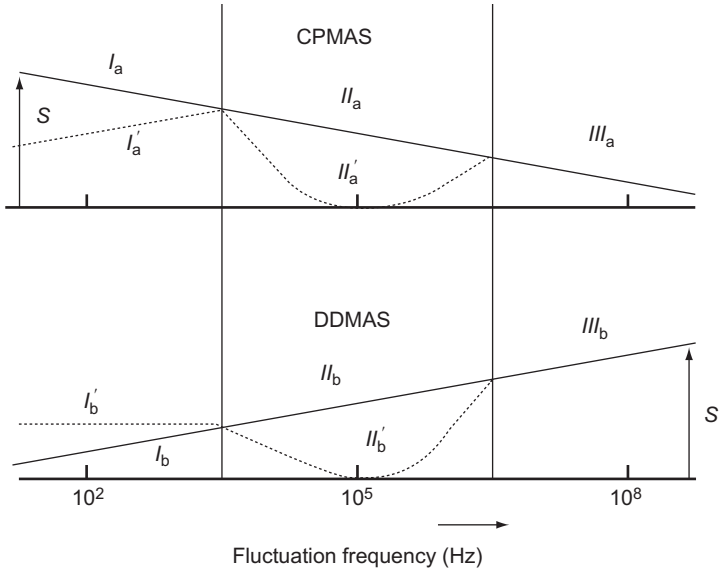

Figure 4 Expected SRI plots for ^{13}C CPMAS (top) and DDMAS (bottom) NMR peak intensities (solid lines) against fluctuation frequency (Hz). The fluctuation frequencies were divided into the following three regions, static (I_a or I_b), slow (II_a or II_b), and high frequency (III_a or III_b) regions. The maximum intensities are given by *S*. In the presence of slow fluctuation motions, the peak intensities can be modified as the dotted lines (II_a' or II_b'). In the nearly static region, the peak intensities could be changed into the dotted lines I_a' or I_b', depending upon efficiency of cross-polarization or T_1 values. From Ref. 29.

frequencies of proton decoupling ($\sim 10^5$Hz) or MAS ($\sim 10^4$ Hz),[26–28] as pointed out already.

Resulting ^{13}C NMR line width $1/\pi T_2{}^C$ caused by such motions can be dominantly determined by the following second or third terms, instead of the first static component,[28]

$$1/T_2^C = \left(1/T_2^C\right)^S + \left(1/T_2^C\right)^{dd} + \left(1/T_2^C\right)^{CS}, \tag{9}$$

where $(1/T_2{}^C)^S$ is the transverse component due to static C–H dipolar interactions, and $(1/T_2{}^C)^{dd}$ and $(1/T_2{}^C)^{CS}$ are the transverse components due to the fluctuation of dipolar and chemical shift interactions in the presence of internal fluctuation motions, respectively. The latter two terms are given as a function of the correlation time τ_c by, [26,27]

$$\left(1/T_2^C\right)^{dd} = \Sigma\left(4\gamma_C^2\gamma_H^2\hbar^2/15r^6\right)I(I+1)\left(\tau_c/\left(1+\omega_H^2\tau_c^2\right)\right), \tag{10}$$

$$\left(1/T_2^{\mathrm{C}}\right)^{\mathrm{CS}} = \left(\omega_{\mathrm{C}}^2\delta^2\eta^2/45\right)\left(\tau_{\mathrm{c}}/\left(1+4\omega_{\mathrm{r}}^2\tau_{\mathrm{c}}^2\right)+2\tau_{\mathrm{c}}/\left(1+\omega_{\mathrm{r}}^2\tau_{\mathrm{c}}^2\right)\right). \quad (11)$$

Here, ω_{r} is the rate of spinner rotation. I is the proton spin number, δ is the chemical shift anisotropy (CSA) and η is the asymmetric parameter of the CSA tensor. Thus, the line broadening occurs when an incoherent fluctuation frequency is very close to the coherent amplitude of proton decoupling ω_{H} ($\sim 10^5$ Hz; Equation (3)) or the MAS frequency ω_{r} ($\sim 10^4$ Hz; Equation (4)) as seen in the respective $T_2{}^{\mathrm{C}}$ minima (Figure 2) instead of the monotonously decreased values without such interference in Figure 1.

Thus, the expected peak intensities can be modified from the solid lines (II_{a} and II_{b}) to the dotted lines (II_{a}' or II_{b}'), due to a failure of the attempted peak narrowing to achieve high-resolution NMR (Figure 4). It is appropriate to plot the observed peak intensities against the fluctuation frequency as in Figure 1, in order to locate a portion undergoing such a possible intermediate fluctuation in molecules as viewed from the $T_2{}^{\mathrm{C}}$ minimum. The experimentally feasible, ^{13}C suppressed or recovered intensity (SRI) plots for both CPMAS and DDMAS spectra are conveniently available from plots against temperature,[29] pH[30], etc., which are closely related to the fluctuation frequency, depending upon the individual situation. In the former, the suppression temperature T_{s}, at which the peak intensity is most suppressed, can be conveniently utilized as a parameter to define the polymer dynamics of specific sites with the fluctuation frequencies of 10^5 Hz (protonated) or 10^4 Hz (unprotonated) carbons caused by interference with frequencies of the proton decoupling or MAS, respectively.

The application of this approach will be described in more detail in Sections 3.1.1 and 4.1.1 to clarify the presence and its significance of the fluctuation motions with intermediate frequencies for a variety of swollen gels and membrane proteins. Here, we illustrate how the backbone dynamics of small peptides containing Gly-Gly residues in the solid can be analyzed by the ^{13}C $T_2{}^{\mathrm{C}}$ obtained under proton decoupling.[28] A possibility of a two-site jump motion model about the $C_\alpha C_{\alpha'}$ carbons from the connecting two peptide units was revealed by observation of the temperature-dependent ^{15}N line-shape analysis of the Gly[^{15}N]Gly moiety with reference to that of the simulated spectra. The observed displacement of the principal values of the ^{15}N CSA tensor was interpreted by taking account of librational motions with small amplitudes. The correlation time of the librational motions of the peptide plane is estimated as 2.3×10^{-4} s at ambient temperature by analyzing the ^{13}C $T_2{}^{\mathrm{C}}$ values in the presence of a ^{1}H-decoupling field of 50 kHz.

The frequency scale detected by ^{13}C-resolved ^{1}H spin–lattice relaxation time in the rotating frame $T_1\rho^{\mathrm{H}}$ evaluated from the ^{13}C CPMAS spectra[42] is similar to that of the ^{13}C $T_2{}^{\mathrm{C}}$ values and line-shape analysis[16] for ^{13}C (or ^{15}N) or ^{2}H nuclei, as illustrated in Figure 3. It is demonstrated

that the β-bend structure of Leu-enkephalin turns out to be very flexible as compared with other crystalline forms taking the β-sheet form, as judged by rather long $T_1\rho^H$ values in which the spin diffusion process otherwise dominant is not effective due to the presence of the rapid backbone motions as detected by $T_1{}^C$ values.[43] It is also shown that prolonged $T_1\rho^H$ values for the side-chain aliphatic protons (~25 ms) in bovine cytochrome c oxidase crystals may be considered as a measure of the intermediate frequency motions at the interface of protein/detergent interactions as compared with those (~3 ms) of lysozyme crystal.[44] In the latter, almost identical values are obtained among protons at different sites, because they are averaged over the ensemble of protons due to strong dipolar coupling between protons and give rise to efficient spin diffusion.[45]

2.1.3. Restricted group rotations caused by either short interatomic contact or strong interactions

Naturally, very long $T_1{}^C$ values are expected for solids as viewed from the expected correlation time at the low temperature side of the $T_1{}^C$ minimum (0.1–0.2 s) as shown in Figure 1. Indeed, their values turns out to be the order of 10–30 s for carbon sites in the absence of internal fluctuations as in polysaccharides such as (1 → 3)-β-D-glucan and (1 → 3)-β-D-xylan,[46–48] fibrous proteins such as collagen[49] and silk fibroin,[50] free and metal-complexed ionophores,[51] or in some instances up to 1000 s as in crystalline polyethylene.[52]

Even in such solid states, it is shown that the correlation time of the rotational motion of the methyl group in a molecule like L-alanine satisfies the condition of the extreme narrowing $\omega^2\tau_c{}^2 \ll 1$.[53] The experimentally obtained ^{13}C $T_1{}^C$ values agree well with the calculated ones, showing that the CH_3 group rotation provides the main source of the relaxation in solid alanine, while the $NH_3{}^+$ group motion plays an important role for the relaxation in glycine and serine. Therefore, it is very important to take into account such methyl rotation ($T_1{}^C < 0.5$ s) for spin relaxation of a variety of molecular systems as major relaxation sources, even if the rest of the molecule is static without any motions.

Nevertheless, it is noted in some methyl signals of free or metal-complexed ionophores, tetranactin or nonactin (Figure 5A), that the methyl $T_1{}^C$ could be appreciably prolonged when C_3 rotation of methyl groups is hindered due to a short contact of the methyl groups with other groups in a crystalline lattice.[51] Indeed, the $T_1{}^C$ values of four C-11 and two C-10 carbons of uncomplexed tetranactin, involved in pairs of short interatomic contacts revealed by X-ray diffraction data,[54] are prolonged to 6.6 and 3.7 s, respectively (Figure 5B). In the K^+-complexed tetranactin, this type of short contact is restricted to the C-11 carbons: C(27)–C(28) = 3.80 Å, C(28)–C(77) = 3.813 Å according to the numbering system

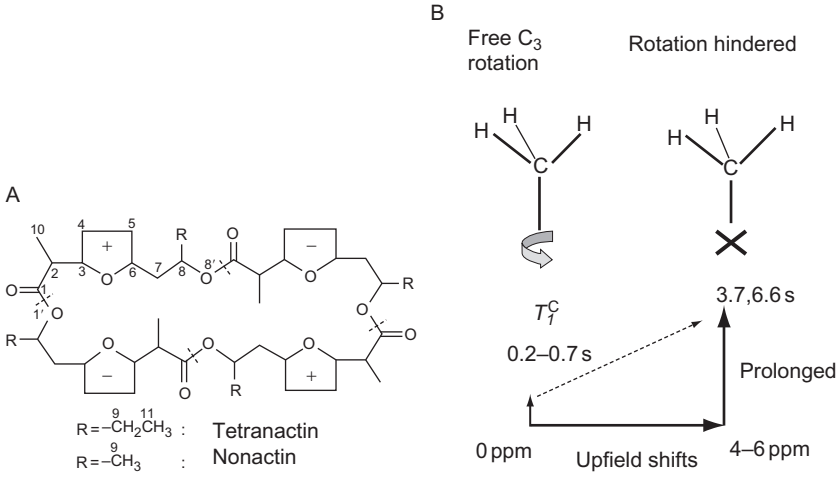

Figure 5 (A) Chemical structures of tetranactin and nonactin, (B) The effect of hindered CH_3 rotation by short contact with other groups to the prolonged methyl T_1^C and chemical shift changes.

of the original work.[55] Consistent with this prediction, the $T_1{}^C$ value of the C-10 methyl group is not so prolonged (1.4 s), whereas that of the C-11 methyl group is slightly increased (2.4 s). Moreover, the methyl groups of uncomplexed nonactin are involved in several types of short intermolecular contacts,[56] although the corresponding $T_1{}^C$ value is at most 1.4 s, probably owing to the presence of puckering motions of the tetrahydrofuran ring and the fluctuation of the macrocyclic ring in the solid state (with a time-scale of 10^{-8} s). It should be noted that the $T_1{}^C$ value of the C-10 and C-11 or C-9 methyl groups for tetranactin or nonactin, respectively, are usually very short such as 0.2–0.7 s in the absence of such a short contact. Notably, the presence of such a short contact results in the maximum upfield displacements of the C-10 peaks (as compared with those in chloroform solution) as 6 and 4 ppm for uncomplexed tetranactin and nonactin, respectively (Figure 5B). Similar upfield displacements of peaks due to short interatomic contact are also noted for the two methyl carbons at L- and D-positions in oligomers of α-aminoisobutyric acids $[(Aib)_n]$ by as much as 6 ppm.[57]

In a similar manner, it is found that the C-6 ^{13}C T_1 value (6.3 s) of the anhydrous paramylon [a linear (1 → 3)-β-D-glucan, to be discussed in more detail in Section 3.2] becomes one order of magnitude longer than that of the hydrated one (0.61 s),[47] probably because the hydroxymethyl group in the former ceases to rotate, owing to strong interatomic interactions including hydrogen bonding.[58]

In any case, it is worthwhile to point out that the observation of such unusually prolonged ^{13}C T_1 values or displacement of the ^{13}C chemical shifts can be utilized as a characteristic means to be able to locate a possible site for the presence of restricted or ceased group rotations for either methyl or hydroxymethyl groups caused by short interatomic contact or strong interactions.

2.2. Chemical exchange

In the solid, dynamics occurring within the kHz frequency scale can be examined by line-shape analysis of ^{2}H or ^{13}C (or ^{15}N) NMR spectra by respective quadrupolar and CSA interactions, isotropic peaks[16,59–62] or dipolar couplings based on dipolar chemical shift correlation experiments.[63–65] In the former, tyrosine or phenylalanine dynamics of Leu-enkephalin are examined at frequencies of 10^3–10^4 Hz by ^{2}H NMR of deuterated samples and at 1.3×10^2 Hz by ^{13}C CPMAS, respectively.[60–62] In the latter, dipolar interactions between the ^{1}H–^{1}H and ^{1}H–^{13}C (or ^{1}H–^{15}N) pairs are determined by a 2D-MAS SLF technique such as wide-line separation (WISE)[63] and dipolar chemical shift separation (DIPSHIFT)[64,65] or Lee-Goldburg CP (LGCP) NMR,[66] respectively. In the WISE experiment, the ^{1}H wide-line spectrum of the blend polymers consists of a rather featureless superposition of components with different dipolar widths which can be separated in the second frequency dimension and related to structural units according to their ^{13}C chemical shifts.[63]

In the DIPSHIFT experiment, the dipolar interaction in a constant time fashion evolves maximally over the one-rotor period and the resulting time domain data are fitted to yield the coupling strengths of ^{1}H–^{13}C (or ^{1}H–^{15}N) dipolar coupling along C–H (or N–H) bond vector.[64,65] A motionally reduced dipolar coupling strength is observed if any sort of segmental motion occurs at the site where the dipolar coupling strength is measured. The segmental motion can be characterized by an order parameter (S) that contains amplitude information and correlation times. The order parameter S is calculated according to

$$S = \bar{\delta}/\delta \tag{12}$$

$\bar{\delta}$ is the magnitude of the motionally averaged dipolar coupling and δ is the full dipolar coupling without motional averaging. Sub-microsecond dynamics of soluble and membrane-bound colicin Ia channel-forming domain were further analyzed to obtain information on their motional amplitudes, based on the order parameters thus obtained.[65] In the Lee-Goldburg CP (LGCP) under MAS experiment in which ^{1}H–^{1}H homonuclear dipolar interaction is effectively suppressed, the heteronuclear

dipolar coupling can be directly measured by observation of a Pake pattern without the outer two ''shoulders''.[66]

Much slower tyrosine dynamics, however, with a rate constant of up to 1.3×10^2 s^{-1} was determined for Tyr-NH_2[61] by utilizing 1D and 2D exchange experiments (Figure 3).[67,68] In fact, the range of correlation times accessible in exchange experiments under either static or MAS conditions covers approximately 500 μs (5×10^{-4} s) to 20 s, although the most specific information about slow motions with correlation times of ms to s are available in organic molecules.[69] Among a variety of multi-dimensional exchange experiments so far performed,[69]characterization of slow segmental dynamics in solids has been developed by the centerband-only detection of exchange (CODEX) NMR experiment which employs recoupling of the CSA under MAS before and after a long mixing time during which molecular reorientations may occur.[70,71] By an analysis of the difference tensor of the chemical shifts before and after the mixing time, the dependence on the reorientation angle is obtained analytically for uniaxial interactions, and a relation to 2D exchange NMR patterns has been established. Here, a pure-exchange CODEX spectrum is obtained by subtracting the CODEX spectrum of a reference spectrum obtained simply by interchanging the mixing time t_m and Δ, to remove the often dominant signal of the immobile site.[70] Large-amplitude motions of $COOCH_3$ side groups on a ~50-ms time scale at 300 K are easily observed by CODEX in amorphous PMMA. Estimates of the motional amplitudes can be obtained as demonstrated for dimethyl sulfone (DMS).

2.3. Time domain NMR measurements

2.3.1. ^{1}H field cycling relaxometry (FCR) and residual dipolar couplings

Revealing chain dynamics of cross-linked elastomers or swollen gels with various time-scales is also feasible by analysis of time domain ^{1}H NMR measurements, although more detailed structural data are unavailable from unresolved ^{1}H resonances. The covered proton frequency range for the frequency dispersion spin–lattice relaxation time T_1 by the aid of the FCR technique is less than 10^3 Hz to more than 10^8 Hz.[72,73] The T_1 dispersion to different cross-link densities of styrene-butadiene rubbers (SBR) exhibits only insignificant differences down to a few kHz. In the low-frequency range a power-law behaviour of $T_1 \propto \omega^{\alpha}$ is observed with an exponent ranging from 0.2 to 0.24 depending on the cross-link density.[74] Instead, it is also shown that the relaxation times decrease sharply with increasing cross-link density for isoprene and butadiene rubber.[75] Here, the cross-links defined as the inverse of the number of segments N between the nearest neighbour cross-links is proportional to P_s, that is, $P_s \propto 1/N$.

Chain motion in the cross-linked system is not isotropic but anisotropic, leading to a nonzero average of residual ^{1}H dipolar couplings that have been preaveraged over the fast dynamic process.[76] The frequency range covered in relation to the residual dipolar interaction is less than 10^4 Hz.[74] The effect of the dipolar couplings has been obtained by a combination of solid echo and free induction decay (FID) decays,[76] stimulated echo,[77] and ^{1}H transverse relaxation obtained in a solid and spin echo.[78] A related sequence that directly visualizes the dipolar couplings and suppresses Zeeman effects was also developed.[79] Chain dynamics in a series of natural rubbers with different cross-link densities was studied using the dipolar correlation effect (DCE) on the stimulated echo.[80] Attenuation curves of the dipolar-correlation quotient, that is, the quotient of the stimulated and primary echo amplitudes, were fitted using analytical expressions.[74,80] The mean-squared fluctuation of the dipolar coupling constant (DCC), $\langle \delta\Omega_d^2 \rangle$, and correlation times were determined. In dry samples, values of $\langle \delta\Omega_d^2 \rangle$ were shown to scale with the number of segments between cross-links (N) as $N^{-1.3 \pm 0.2}$. The DCE of dry and swollen rubber is thus suggested as a method for the determination of cross-link densities,[80] as a useful tool for routine application using a low-magnetic field instrument.[81] Investigations of the segmental order and chain dynamics in polymer networks using mixed magic-Hahn echo decay can be accurately performed because of simultaneous refocusing of the residual multispin dipolar interactions as well as linear interactions.[82] Based on dipolar-correlation functions the ^{1}H residual second van Vleck moment, correlation times, and parameters of the correlation time distribution were determined for a series of natural rubber samples with different cross-link densities.

Alternatively, proton double quantum (DQ) NMR, based on a combined DQ excitation and a reconversion block of the pulse sequence, has been utilized to gain direct access to residual DCCs for cross-linked systems.[69,83–89] For this purpose, double-quantum buildup curves are obtained with use of a well-defined double-quantum Hamiltonian along with a specific normalization approach. Residual interactions are directly proportional to a dynamic order parameter S_b of the polymer backbone,[87]

$$S_b = (D_{res}/D_{stat})(1/P_2(\cos\bar{\alpha})) = 3r^2/5N \tag{13}$$

and can be calculated from the residual DCC, D_{res}, by comparison with its static component, D_{stat}. $\bar{\alpha}$ is the average orientation of the internuclear coupling vector with respect to the segmental orientation. S_b is related to r, the normalized deviation of the end-to-end vector from its average and to N, the number of statistical chain segments between the constraints. The τ_{DQ} is the effective evolution time. The resulting DQ buildup curve can then be analyzed with a monomer-specific buildup function,

$$I_{n\mathrm{DQ}} = 0.5\left(1 - \exp\left\{-31.91(D_{\mathrm{res}}/2\pi)^2\tau_{\mathrm{DQ}}{}^2\right\}\right). \quad (14)$$

here given for poy(dimethylsiloxane) (PDMS). $D_{\mathrm{res}}/2\pi$ and τ_{DQ} are in kHz and ms, respectively. The experimental result of the DQ buildup curves for sample net0 of poly(dimethylsiloxane) (PDMS) is seen to undergo no appreciable change in spite of measured temperature variations (Figure 6A).[86] This represents a very strong argument for the validity of

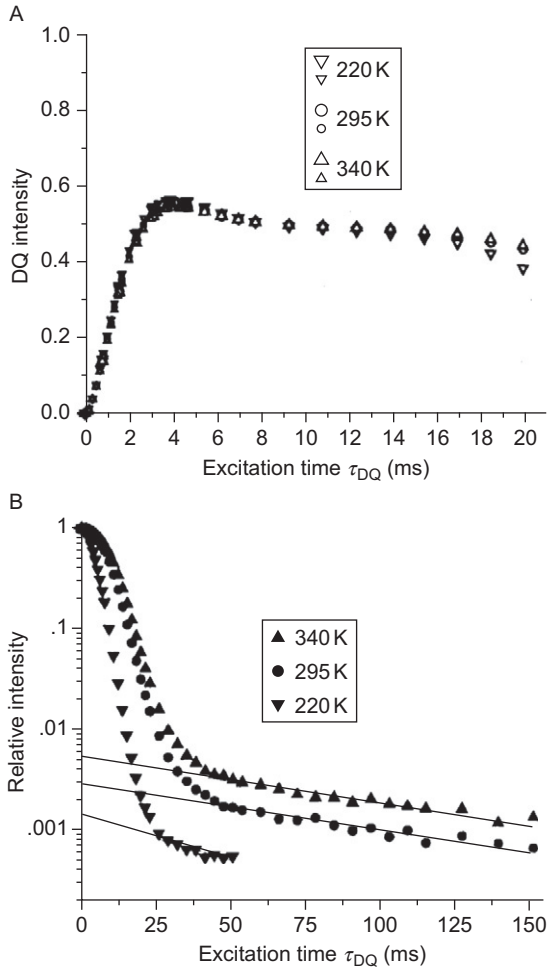

Figure 6 (A) Experimental normalized DQ buildup for sample net0 at three different temperatures. The small and large symbols denote $t_c = 0.2$ and 0.8 ms, respectively. (B) Corresponding sum intensity decay curves plotted on a semilogarithmic scale. From Ref. 86 with permission.

the separation-of-time-scale (or fast motion) approximation. On the contrary, the slow exponential tail of the intensity decay curves (Figure 6B) is ascribed to signal contributions which are not subject to orientational constraints, that is they lack residual DCCs and behave as liquid like.

2.3.2. Diffusometry

Diffusometry based on ^{1}H pulsed field gradient spin-echo (PFGSE) NMR provides a rich source of information about interactions of water or probe molecules, sizes in cavities and spatial inhomogeneity in the cross-linked hydrogels.[17,90–92] The method to determine the self-diffusion constant D is based on the attenuation of a spin echo arising from diffusion dephasing under the influence of a steady applied field gradient. The attenuation is given by

$$A(\delta)/A(0) = -\exp\left[\gamma^2 G^2 D\delta^2(\Delta - \delta/3)\right], \tag{15}$$

where $A(\delta)$ and $A(0)$ are echo signal intensities at $t = 2\tau$ with and without the magnetic field gradient pulse being of the length δ, respectively. τ is the pulse interval, γ the gyromagnetic ratio of the proton, G the field gradient strength, and Δ the gradient pulse interval. The diffusion constant of HDO (D_{HDO}) contained in a poly(*N*,*N*-dimethylacrylamide) (PDMAA) gel is determined at 303-K by varying the degree of swelling

$$Q = M_{\mathrm{swollen}}/M_{\mathrm{dry}}, \tag{16}$$

where M_{swollen} and M_{dry} stand for the weight of swollen and dry state, respectively, as shown in Figure 7.[93] It is seen that D_{HDO} increases as Q is increased, and is almost independent of M_{W} for PEG contained in the gel. The D_{HDO} value in the large-Q region asymptotically approaches that of HDO in neat D_2O. This behaviour is reasonably explained by the modified free volume theory. Further D_{HDO} in poly(*N*-isopropylacrylamide) gel with a constant degree of swelling in going from 20 to 45 °C decreases transitionally at about 32 °C, which corresponds to the phase transition temperature.[94]

3. STRUCTURALLY HETEROGENEOUS SYSTEMS: NETWORK STRUCTURES AND DYNAMICS OF HYDROGELS

3.1. Synthetic polymer gels

3.1.1. Biocompatible hydrogels

In relation to the characterization of network structure and dynamics in swollen gels, it seems to be very important to have a prior knowledge of under what conditions the expected ^{13}C NMR signals are visible from

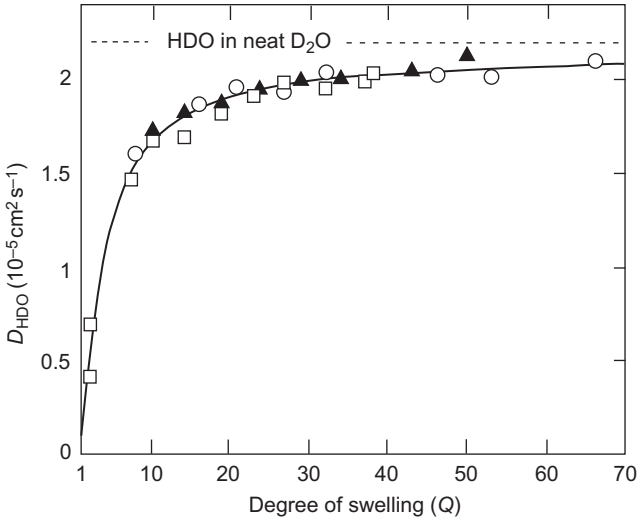

Figure 7 Dependence of the diffusion coefficient of water molecule (D_{H2O}) on the degree of swelling (Q) in a PDMAA gel containing PEG with $M_w = 4250$ (□), 10,890 (▲), and 20,000 (○) at 303 K. From Ref. 93 with permission.

swollen molecular chains in liquid-like domains or the rigid cross-linked portion either by solution or solid-state NMR, respectively. This is because all of the carbons in such systems do not always contribute to high-resolution solution or solid-state ^{13}C NMR signals, since a sizable amount of peak-area is suppressed due to the presence of immobilized segments such as cross-links or an accompanied crystallite.[33,95,96]

To answer this question, Yokota et al.[97] recorded the 25.05 MHz solution ^{13}C NMR spectra of chemically cross-linked synthetic polymers in which the extent of the cross-links is varied by adjusting the amount of cross-linking agent. The ^{13}C NMR signals of the cross-linked poly (*N*-vinylpyrrolidone) (PNVP) swollen by water are considerably broadened as compared with those of PNVP solution together with an increasing proportion of the cross-linking as demonstrated in Figure 8A. Only about 55 and 35 mol% of the polymer chains contribute to the observed ^{13}C NMR signals of the hydrogels, containing 0.1% (water content 90%) and 1 mol% cross-linking (75% water content), respectively. The cause of the line broadening is obviously interpreted in terms of the restriction of chain mobility due to the presence of cross-links and entanglement of polymer chains especially in the vicinity of cross-links, since the line broadening is remarkable in samples of higher cross-linking such as 5% (water content 53%) (Figure 8A(d)).

For a firm resilient opaque gel (water content 46%, 0.1 mol% of cross-linking) of a blend-type copolymer consisting of NVP and MMA (1:1 in

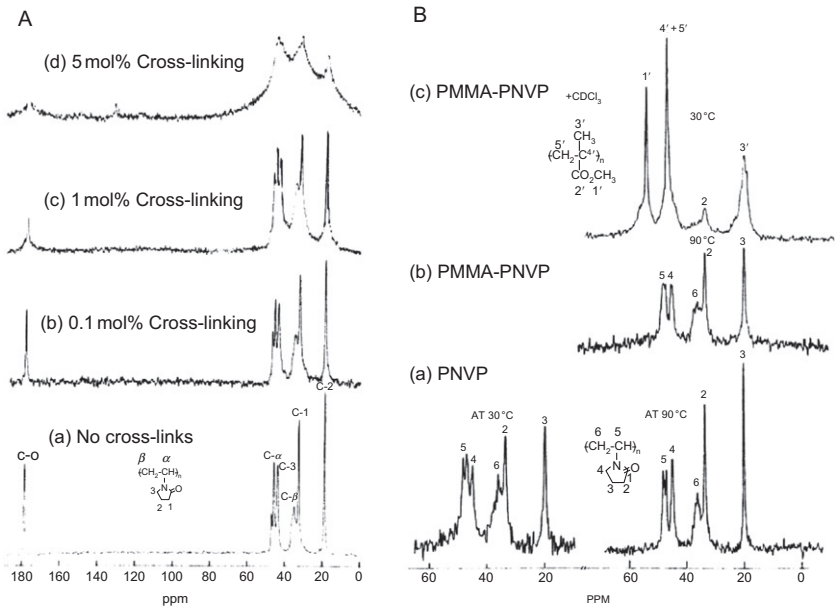

Figure 8 (A) 25.05 MHz ^{13}C NMR spectra of hydrogels with various degrees of cross-linkings (b–d) and aqueous solution of PVP (a) at 30 °C. (B) ^{13}C NMR spectra of PVP gel of water content 90% and a blend-type copolymer of MMA and NVP at 30 °C. (a) PVP gel, (b) hydrogel of copolymer of MMA and NVP (1:1 in weight), and (c) gel of (b) swollen by mixture of $CDCl_3$ and water. From Ref. 97 with permission.

weight ratio), the expected peaks arising from the hydrophobic methylmethacrylate (MMA) component are completely lost in its ^{13}C NMR spectrum as shown in Figure 8B(b). Thus, the observed peaks are identical to those of the PVP component. However, it is found that the ^{13}C NMR spectrum of the MMA component is made visible by swelling by organic solvents such as chloroform (Figure 8B(c)) or dimethyl sulfoxide (DMSO) (spectrum not shown). These results indicate that only the hydrophilic NVP component can be swollen by water, while the hydrophobic MMA can be swollen by chloroform (in the mixture of chloroform and water) or DMSO which are good diluents for the hydrophobic segment. The observation of such differential swelling strongly suggests that NVP and MMA constitute separate domains in this gel. In the gel of poly(hydroxyethylmethacrylate) (PHEMA) in the absence of a cross-linking agent for preparation of this gel, a remarkable temperature dependence of the ^{13}C line width up to ~600 MHz is noted as a result of chain entanglement. It is also emphasized that the line widths of hydrogels such as PNVP or blend-type copolymers are appreciably increased (the T_2's being decreased) in accordance with increased cross-links or a decrease of the water content.

Nevertheless, the T_1 and NOE values are found to be unchanged from the solution to the gel of water content 75% and 53%. As discussed already in Section 2.1, it is very difficult to analyse such relaxation parameters in terms of a single correlation time. The calculated correlation times are found to give consistent values among those obtained from the T_1, T_2, and NOE values with the width parameter of $p = 18$ (PVP solution) and $p = 16$ (PVP gel) and $b = 1000$. As the degree of cross-linking is increased, a discrepancy in the correlation times still occurs (a factor of 3 at 75%) but is much improved by this treatment.

Much interest has been paid to develop a variety of hydrogels as biocompatible materials used for contact lens, drug delivery systems, surface-coating materials for medically used devices, etc.[98] Tanaka et al. demonstrated that the poly(2-methoxyethyl acrylate) (PMEA)[99] surface exhibits excellent blood compatibility among poly(acrylate)s including [poly(2-hydroxyethyl methacrylate) (PHEMA), and poly(tetrahydrofurfuryl acrylate) (PTHFA)] (see Figure 9, for their chemical structures and numbering).[29] In order to gain insight into the characteristic ^{13}C NMR features of their liquid-like and solid-like domains, it is preferable to record both the ^{13}C DDMAS and CPMAS NMR of any swollen gels.

Temperature-dependent ^{13}C CPMAS and DDMAS NMR spectra of PMEA hydrogels containing 7% water were recorded at temperatures between -80 and 37 °C, as shown in Figure 10.[29] The maximum peak intensities are available from the CPMAS and DDMAS spectra recorded at the lowest (-80 °C) and highest temperatures (37 °C), respectively. As a typical SRI plot, the individual peak intensities for hydrogels of PMEA and PHEMA, available from the DDMAS (Figure 11A and B, respectively)

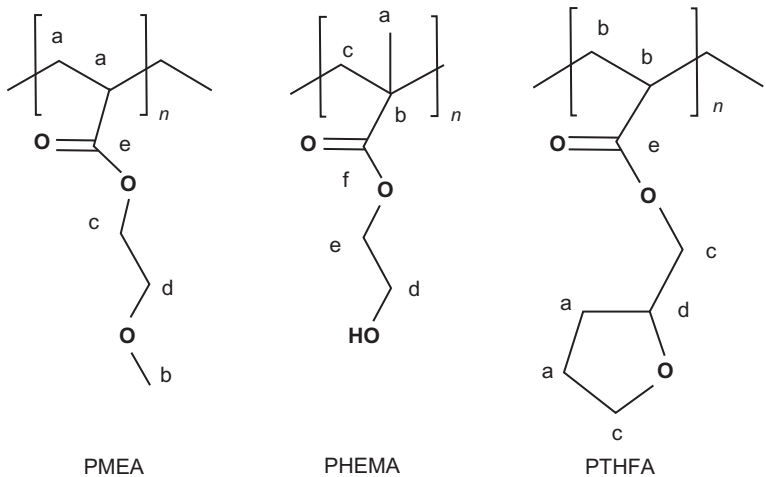

Figure 9 Chemical structures of poly(acrylate)s and numberings of carbons.

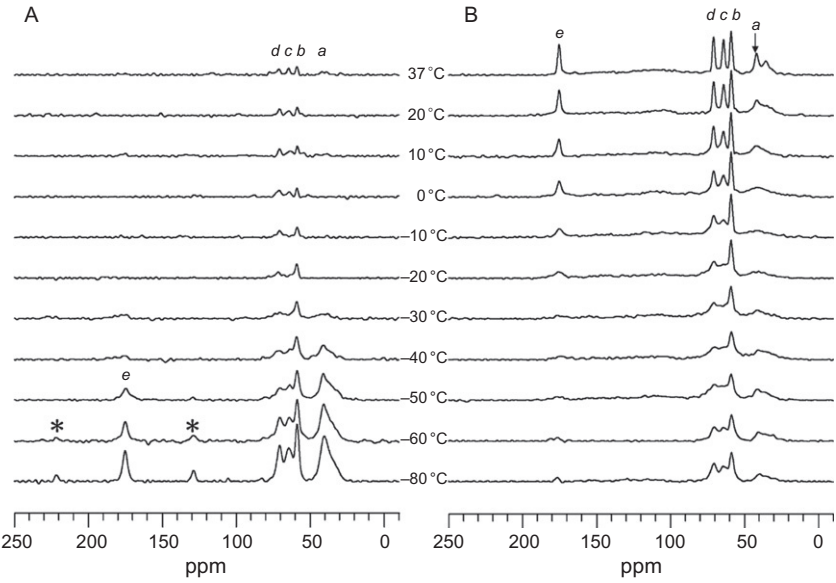

Figure 10 ^{13}C CPMAS (A) and DDMAS (B) NMR spectra of PMEA gel containing 7 wt% water, recorded at various temperatures. Note the peak intensity *a* (arrows) in the DDMAS NMR spectra is more evident at higher temperatures. From Ref. 29 with permission.

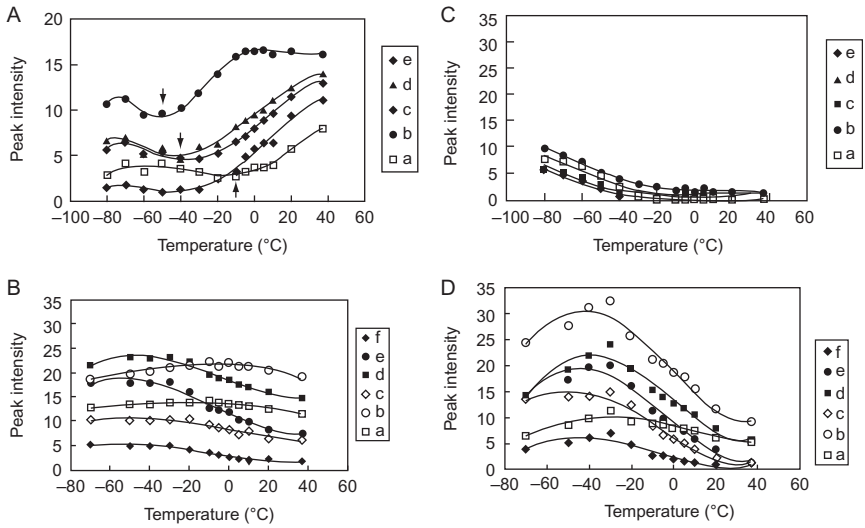

Figure 11 The SRI plots of the ^{13}C DDMAS NMR spectra of (A) PMEA (containing 7 wt% water), (B) PHEMA gels (containing 40 wt% water), CPMAS NMR spectra of (C) PMEA, and (D) PHEMA gels against temperature. Suppression temperatures T_S at which respective peaks are most reduced are shown by the arrows. From Ref. 29 with permission.

and CPMAS (Figure 11C and D, respectively) spectra, were plot against temperatures. It is noteworthy that several T_2^C minima are evident as viewed from the temperature-dispersion of the peak intensities, instead of the frequency dependence corresponding to Equation (10), as indicated by the arrows in the SRI plots. It is noted that the suppression temperature T_s at which their respective peaks are most suppressed can be characterized as the critical temperature at which fluctuation motions with frequencies of the order of 10^5 Hz occur. Such temperatures differ substantially among signals from various sites, as summarized in Table 1. Unfortunately, such T_s changes in the SRI plot of the PMEA gel as observed by DDMAS NMR are less pronounced in the similar plots from CPMAS NMR spectra (Figure 11C), because underlying changes may be masked by the differential cross-polarization rate at lower temperature together with their extremely suppressed intensities caused by fast isotropic motions at ambient temperature.

The intensity minima for PHEMA gel are evident at ambient temperature, as viewed from its SRI plots as recorded by the DDMAS spectrum, as shown in Figure 11B. This means that the T_s's of PHEMA gel are at ambient temperature. This is because the network of PHEMA (containing ~40 wt% of water) gel is firmly held together by mutual association of both backbone and side chains through hydrophobic or hydrogen bonding interactions, as viewed from their suppression temperatures T_s being almost identical and close, at ambient temperature, to those of variety of carbons (Table 1). In contrast, the network of PMEA gel (containing 7 wt% of water) might be formed by association of the backbone only as viewed

TABLE 1 The suppressed temperature T_s at which ^{13}C NMR peak intensities are most suppressed in the presence of slow motions (°C)

	PMEA		PTHFA	PHEMA
	Dry	Containing 7% D_2O	Containing 9% D_2O	Containing 40% D_2O
Backbone	7	−10	30	≥37
$COO\underline{C}H_2CH_2$ (or —OH)[a]	−12	−30	0	≈37
or $COOCH_2$furfuryl[b]				
$COOCH_2\underline{C}H_2$ (or —OH)[a]	−20	−40		≈37
$COOCH_2\underline{C}H_2O\underline{C}H_3$ (or OH)[a]	−30	−50	−10	≥37
or $COOCH_2$furfuryl[c]				
$\underline{C}OOCH_2CH_2OCH_3$ (or —OH)[a]	−20	−40		≥37

[a] PHEMA.
[b] PTHFA.
[c] From peak *d*.

from their differential suppression temperatures. The suppressed temperatures T_s's of the side chain in PTHFA gel (9 wt% of water) are again much lower than those of the backbone, and are located between those of PMEA and PHEMA (Table 1). It is also interesting to note that the flexibility of the gel networks (PMEA > PTHFA > PHEMA), as viewed from their suppression temperatures T_s (PMEA < PTHFA < PHEMA), is well related to a characteristic parameter for their biocompatibility such as the production of thrombin–antithrombin III complex (TAT) as a marker of activation of the coagulation system.

So far, it is not easy to locate signals from the cross-links of chemically cross-linked gels, except for unswollen crystallites region which behave as additional cross-links in the above mentioned blend-type copolymer consisting of hydrophilic NVP and hydrophobic MMA components. In addition, only a lower amount of cross-linking is sufficient for gelation.[97] In the case of physically cross-linked gels of synthetic polymers such as poly(acrylate)s, the distinction of signals from such cross-links and solid-like portions is extremely difficult, since there appears to be no chemical shift change between them due to taking randomly coiled polymer chains.[29]

3.1.2. PVA and MMA gels

Kobayashi et al. recorded the ^{13}C CPMAS NMR spectra of poly(vinyl alcohol) (PVA) gel with different polymer concentration, prepared by repeating a freeze-thaw cycle (frozen at −20 °C for 20 h, and then melted and sustained at 25 °C for 4 h) from its aqueous solution without any cross-linking agent as illustrated in Figure 12.[100,101] The triply split sharp CH signals arising from the liquid-like portion are assigned from their stereo-selective aspect to the mm, mr, and rr triads from high frequency. The peaks I, II and III which are dominant for the gels of higher PVA concentrations are assigned to the CH carbons involved in two intra- or intermolecular hydrogen bonds, one hydrogen bond, and no hydrogen bond, respectively, in the hydrogen bond networks of the cross-linked structure. The spectrum for the sample *D* is very similar to that of solid PVA, except that the intensity of the peak III in the former is somewhat larger than that in the latter. It was also shown that the ^{13}C T_1^C values for the triads and CH_2 (0.16–0.37 s) are shorter than those (5.2–7.8 s) for peaks II, III and CH_2 carbons in the cross-linked region formed by inter- and intramolecular hydrogen bonds.[102] The ^{13}C T_1^C values for the immobile components in the PVA gel are very close to those for the non-crystalline components of solid PVA.

By application of proton multiple quantum (MQ) NMR experiments, information about the segmental order parameter, which is directly related to the restrictions on chain motion (cross-links) formed upon gelation of PVA, is obtained.[103]The quantitative study of rigid phase

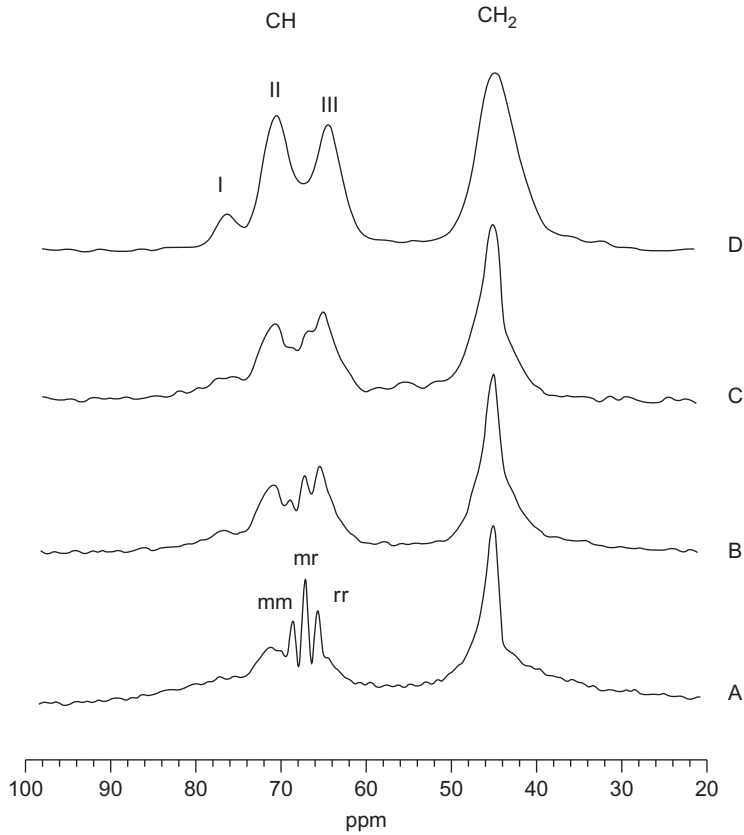

Figure 12 ^{13}C CPMAS NMR spectra for the PVA gels with different polymer concentrations. The polymer concentrations are (A) 9.1, (B) 11.8, (C) 13.8, and (D) 35% (wt/wt%), respectively. From Ref. 100 with permission.

with a specific refocusing pulse sequence shows that it is composed of a primary crystalline polymer phase (~5%), which constitutes the main support of the network structure and determines the mesh size, and a secondary population of more imperfect crystallites, which increase the number of elastic chain segments in the polymer gel. Ageing or imposition of additional freeze/thaw cycles of PVA hydrogels augments the level of crystallinity and transforms the as-formed liquid-like microstructure, characterized by the electrom microscope by arounded ~30 nm pores, into a fibrillar network.[104] It is also shown that an increase in the number of freeze/thaw cycle induces an increase in the degree of crystallinity in the polymer-rich phase together with an increase in the storage modulus.[105]

The ^{13}C T_1 values of the liquid-like portion from PMMA gel, prepared by cross-linking with *N*,*N*′-methylenebisacrylamide (MBA), are shown to vary with the mole ratio of MBAA to MAA.[106] The diffusion coefficient D_{H2O} in PMMA gel is shown[107] to increase with $Q^{1/3}$, where Q is the degree of swelling as defined in Equation (16). Q is also rewritten as $(\rho_{swollen}/M_{dry})\ r^3$, if $\rho_{swollen}$ is the density of swollen polymer gel of a cube with the length of an edge being r. Thus,

$$r = \left(M_{dry}/\rho_{swollen}\right)^{1/3} Q^{1/3}. \tag{17}$$

The diffusion coefficient (D) of *tert*-butyloxycarbonyl-L-phenylalanine (Boc-Phe) was determined in a Merrifield network of polystyrene (PS) gels used as a solid phase reaction field.[108] When probe molecules have multicomponents in diffusion on the measurement time scale, the total echo attenuation is given by a superposition of contributions from the individual components:

$$A(\delta)/A(0) = -\Sigma_i\, p_i \exp\left[\gamma^2 G^2 D_i \delta^2 (\Delta - \delta/3)\right], \tag{18}$$

where D_i is the self-diffusion coefficient of the ith component, p_i the fractional proton number of the ith component and $\Sigma_i p_i = 1$. Definition of γ, G, and δ is the same as that in Equation (15). It is found that the fraction of slow diffusion component depends on the diffusion time Δ which is related to the diffusion distance. Diffusional behaviours of probe PSs with $M_w = 4$, 19, 29, and 400 K and chloroform as solvent are observed in the same PMMA gel matrix with the diffusing time varied ($4 - 500$ ms).[109] The diffusion of the solvent and the smallest PS with $M_w = 4$ K proved to be of a single mode for sufficiently small size of the probes compared with the network mesh (1.5 nm). The other PS molecules that should be larger than or comparable to the mesh size shows a multimode diffusional behaviour, which was analyzed as a dual mode diffusion composed of a fast component and a slow one. Thus, those larger PS molecules are suitable to ''probe'' the inhomogeneity for the mesh size distribution of the network. It was shown that for the open network structure the region size is scaled to be of the order of micrometers at least, while the mesh size of the dense region is to be larger than 1.5 nm and must be considerably smaller than 30 nm. A series of inhomogeneities are introduced to PMMA gels in the presence of various amounts of PS ($M_w = 400{,}000$).[110] The pulsed-field-gradient stimulated-echo ^1H NMR measurements are performed for the PMMA gel samples with variable diffusion time Δ, which permits the investigation of the PMMA gel network structure on the basis of the diffusional behaviour of the large probe molecule (PS) and a small probe molecule (unreacted monomer) in PMMA gels. It is shown that the PS diffusion consists of

two diffusion components, while it changes to a single mode with increasing PS concentration. These results were ascribed to the course of the phase separation resulting from development of ''open'' network structure induced by the PS probe molecule in the gelation batch.

3.2. Polysaccharide gels

3.2.1. Linear and branched (1 → 3)-β-D-glucans

(1 → 3)-β-D-glucans are widely distributed in plants, especially among the algae and fungi, where they have storage, structural or protective roles.[111] Their physical properties differ substantially among their primary structures of either linear or branched (with 1 → 6 linkages) ones and molecular weights. In particular, curdlan, a linear exocellular (1 → 3)-β-D-glucan of high-molecular weight (with, numerical average degree of polymerization, $DP_n = 250$) from *Alcaligenes faecalis*, forms an elastic gel when its aqueous suspension is heated to a temperature above 54 °C,[9–13,112] whereas many branched glucans from cell wall of fungi, such as lentinan from *Lentinus edodes*, schizophyllan from *Schizophyllum commune*, etc., formed soft or brittle gels.[9–13] It is tempting to judge that these two types of gels arise solely from the triple helical structures, because the triple helical structure is the most stable form in (1 → 3)-β-D-glucan in view of fibre X-ray diffraction data of annealed, crystalline preparation of curdlan.[113] There remains, however, a question why the above mentioned physical properties are so different between the linear and branched glucans.

The 25.05-MHz solution ^{13}C NMR spectrum of the liquid-like domain of resilient curdlan gel (Figure 13A) differs substantially from that of the soluble, low molecular fragment with $DP_n = 13$, taking a random coil form (Figure 13B), as viewed from their relative peak intensities, line widths, and peak positions.[114,115] The C-3 or C-6 peak intensities of curdlan in aqueous suspension rose abruptly at a temperature between 46 and 50 °C, concomitantly with acquired chain dynamics by swelling (Figure 13C), but diminish together with further heating beyond 50 °C as a result of shrinkage of the gel by expelling water molecules (syneresis).[9] The obviously displaced C-1 and C-3 peaks at the glycosidic linkages are due to a conformational transition arising from gelation, namely the change from single chain to *single* helical chains present in the liquid-like domain of the gel as viewed from the conformation-dependent ^{13}C chemical shifts.[116] The changes in the T_1^C's and NOE's, however, turn out to be not sensitive to such temperature-changes, NaOH or DP_n-dependent helix–coil transition, although the substantial changes in the line widths were noted (Figure 13A and B).[114] Accompanied changes in the correlation times of the segmental motion, from the helix (gel) (30–40 ns, with $p = 26$ and $b = 1000$ from Equations (6) and (7), based on log-χ^2 distribution) to

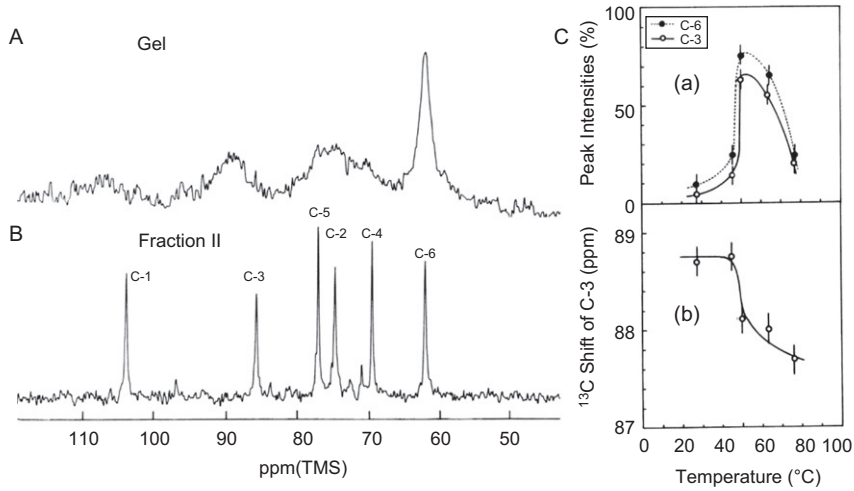

Figure 13 ^{13}C NMR spectra of (A) soluble oligomer and (B) resilient gel of curdlan. From Ref. 112 with permission. (C) (a) A plot of the intensity changes of C-6 and C-3 signals (%) in curdlan against temperature with reference to those obtained in the presence of 0.3 M NaOH. (b) a plot the C-3 ^{13}C chemical shift against temperature. From Ref. 9.

coil (4.3–2.2 ns), are unexpectedly small. Molecular-weight dependence of the helical conformation for curdlan and its hydrolyzates was also analyzed to gain insight into at what chain length is the helical conformation adopted and subsequently junction zones formed.[115] It is found that a physically cross-linked structure appears in a sample of $\overline{DP_n} = 49$, in which the primary molecules adopt the single helix conformation. Comparison of the peak intensities versus $\overline{DP_n}$ show that an infinite network, corresponding to the gel formation, might occur at $\overline{DP_n} \sim 300$.

It is noted that the 75.46-MHz ^{13}C CPMAS NMR spectra of the solid-like domain of curdlan gel (Figure 14A(d)) turn out to be the same as those of the above mentioned liquid-like domains recorded by DDMAS NMR, except for the presence of a minor shoulder peak indicated by the arrow (Figure 14 A(b and c)) and curdlan hydrate in the solid state (Figure 14 A (a); recorded by CPMAS NMR).[117] This finding shows that no conformational change accompanies the gelation of (high-molecular weight) curdlan from the starting hydrate powders to the resilient gel (the single helix form). In contrast, solution ^{13}C NMR spectra are completely suppressed when brittle gels of the branched (1 → 3)-β-D-glucan, such as lentin, are examined.[118,119] This is because the gel networks of the branched glucans are composed mainly of the triple helical chains immediately converted from the single helix to the triple helix forms during the course of gelation

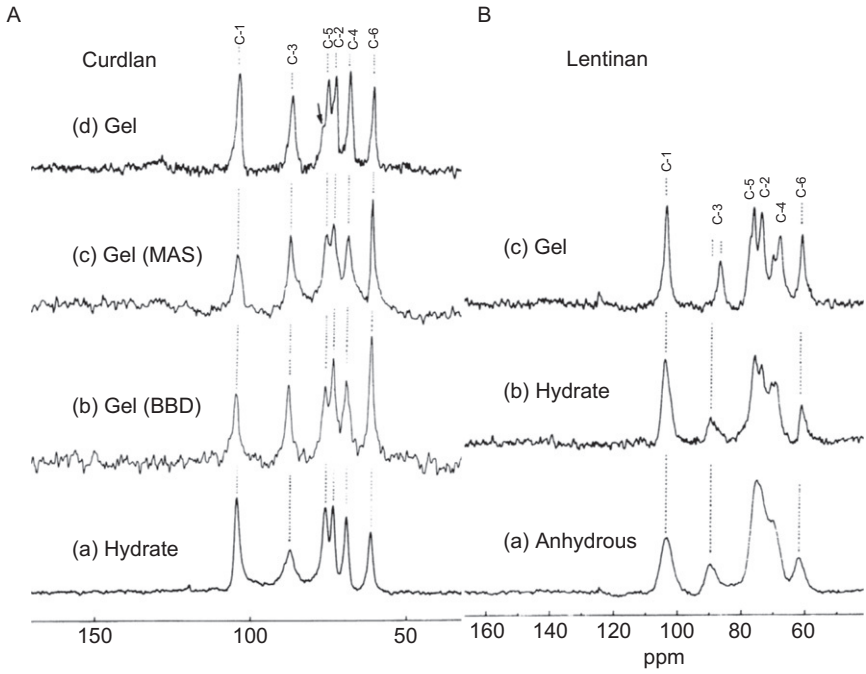

Figure 14 (A) ^{13}C NMR spectra of curdlan hydrate (a) and gel (b–d) recorded by different type of experiments: (a and d) by CPMAS, (b) by broad-band decoupling (BBD), and (c) by MAS experiment. (B) ^{13}C CPMAS NMR spectra of lentinan at anhydrous (a), hydrate (b), and gel (c). From Ref. 117 with permission.

as viewed from the displaced C-3 chemical shifts between the gel (c) and anhydrous (a) or hydrated samples (b) (Figure 14B).[117]

Such conformational elucidation is straightforward when the individual ^{13}C NMR signals are compared with those of possible polymorphs (Figure 15).[47,120] The reference spectrum of the single chain form is readily available from the anhydrous powder preparation either spray-dried or lyophilized from DMSO solution. Subsequent hydration, by placing it in a desiccator at relative humidity at 95% overnight, results in conversion to either the triple helix (route A) or the single helix (route B) for the branched or linear glucans, respectively as illustrated in Figure 16. This distinction obviously arises from how easily the individual polymer chains can be hydrated: the linear glucan is very hydrophobic and not sufficiently hydrated until its aqueous suspension is heated to a temperature above 150 °C and slowly cooled (route C).[120] Such an annealed preparation alone yields a highly crystalline sample giving rise to an X-ray diffraction pattern of the triple helix conformation.[113] The branched

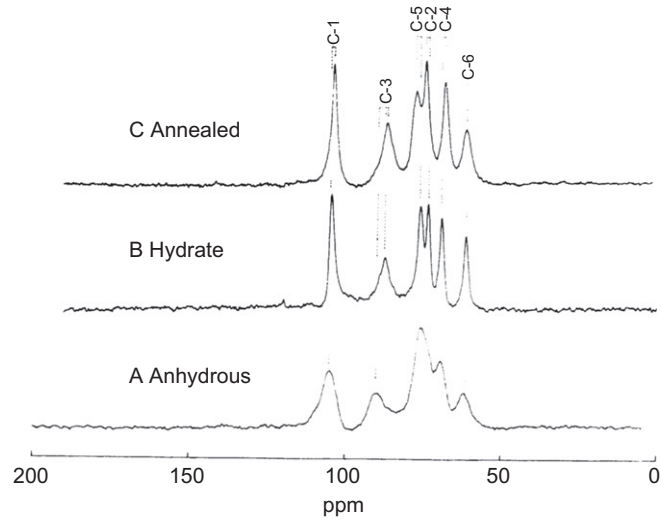

Figure 15 75.46 MHz ^{13}C CPMAS NMR spectra of curdlan in the solid state. (A) anhydrous, (B) hydrate, (C) annealed at 180 °C followed by slow cooling. From Ref. 120 with permission.

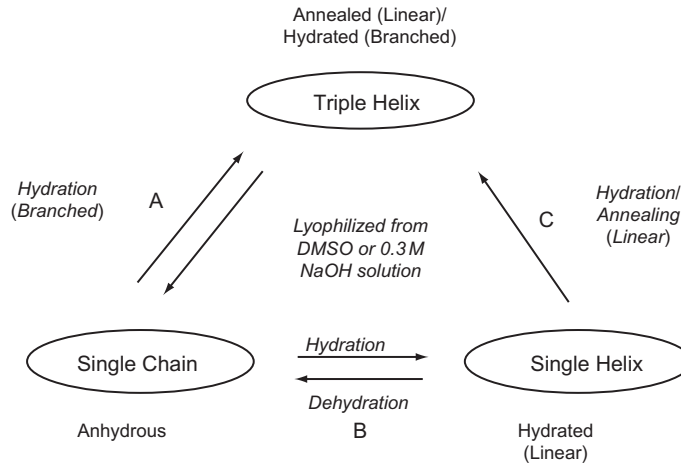

Figure 16 Conversion diagram for (1 → 3)-β-D-glucans by a variety of physical treatments (based on Refs. 48 and 119).

glucans can be readily hydrated when they are exposed to an aqueous environment (route A). Further, it should be noted that the triple helical curdlan is formed *with the expense of a thermal depolymerization* of the chain from $DP_n = 3890$ to 106, by heating at 180 °C for 10 min.[121] A similar conversion diagram is obtained for (1 → 3)-β-D-xylan,[48] but the corresponding pathway from the single helix to the triple helix (route C)

is not achieved, probably because (1 → 3)-β-D-xylan can be more hydrophobic than curdlan in the absence of the hydroxmethyl group at C-5 on the side chain.

Accordingly, the network structure and gelation mechanism turns out to be completely different between the linear and branched (1 → 3)-β-D-glucans.[9–13,114,117–121] The network structure of the elastic curdlan gel is highly heterogeneous and mainly arises from the single helical chain, irrespective of the liquid-like (A), intermediate solid-like (B) and solid-like (C) portions, as schematically depicted in Figure 17, left.[117] These single helical chains are primarily held together by the triple helical junction zone (less than 10%) and by subsequently hydrophobic association of the single helical chain to yield additional cross-links (crystallite) together with syneresis caused by heating at a higher temperature (high-set gel). On the contrary, the brittle gel network of the branched glucans is formed by partial hydrophobic association of the readily formed triple helical chains by hydration, as schematically depicted in Figure 17, right. This finding is consistent with the effects of several biological responses of (1 → 3)-β-D-glucans, such as antitumor activity, activation of the coagulation system of hoseshoe crab amebocyte lysate (LAL),[122] and endo (1 → 3)-β-D-glucanase, which are mainly initiated by recognition of the single helical conformations rather than the triple helical chains.

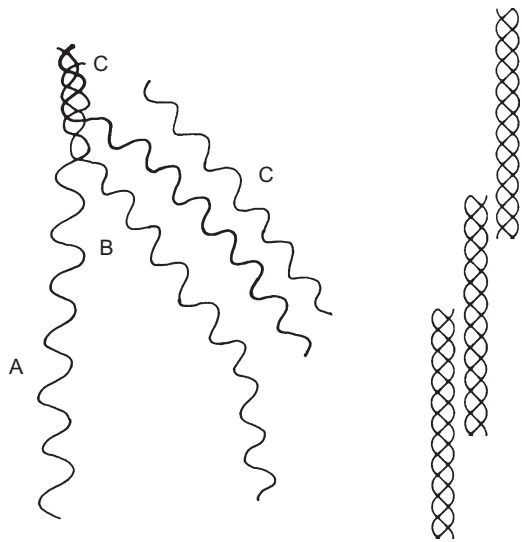

Figure 17 Schematic representation of heterogeneous portions of curdlan hydrogel (left): (A) liquid-like portion, (B) portion of intermediate mobility, and (C) triple-helical cross-links in the solid-like portion and crystallites as additional cross-links, and branched glucans (triple helical chains) (right). From Ref. 117 with permission.

3.2.2. Amylose, agarose and carrageenan gels

Amylose gel contains two types of ^{13}C NMR signals: the signals from the liquid-like domain are identical to those found in aqueous solution and the B-type signals from the solid-like domain arise from motionally restricted regions as recorded by the CPMAS NMR method.[123] Retrogradation of starch gel is shown to be accompanied by a conformational change from random coil to the B-form, because the corresponding peak intensities of the retrograded samples as recorded by CPMAS NMR spectra, after standing them three days in a refrigerator, are significantly increased.[12] It appears that the ''B-form'' structure thus obtained by hydration is a *single* helical structure[124] as viewed from the ^{13}C NMR spectra together with the conversion procedure.[125] This ''B-form'' is of course not the same as the most recent X-ray structure of the left-handed, parallel double stranded helix.[126]

Intense ^{13}C NMR signals are visible from the liquid-like domain of agarose gel as recorded by the DDMAS method, while the intense ^{13}C NMR signals are also visible from the solid-like domain recorded by the CPMAS NMR experiment.[12] This finding indicates that the network structure of agarose gel consists mainly of the single helical chain, instead of the well-documented multiple helical chains. Indeed, the current view of the flexible network structure for agarose gel is obviously in contrast to the well documented picture of a rigid network structure consisting of double helical chains.[127] Further, the flexibility of the molecular chains in the polysaccharides, described here, decreases in the following order: starch > agarose ~ curdlan > branched (1 → 3)-β-D-glucans.

For a brittle gel sample (5% w/v) of κ-carrageenan as received, there appears to be no ^{13}C NMR signals from the flexible portions taking a random coil conformation as recorded by the DDMAS NMR technique, although intense signals from the solid-like domain are readily available from the CPMAS method.[15] ^{13}C NMR signals from the liquid-like domain, however, are available by the DDMAS NMR method for the resilient gel of κ-carrageenan in the absence of cations other than Na^+ ion, prepared by treatment with Dowex 50W-XB ion exchange resin, followed by addition of NaOH at pH 7.0. Inevitably, the ^{13}C NMR signals from the solid-like domain recorded by CPMAS NMR turn out to be less intense. In particular, the ^{13}C NMR peaks at the two lowermost regions of the liquid-like domain at 104.5 and 96.6 ppm (C-1 peaks of (1 → 3)-linked β-D-galactosyl and (1 → 4)-linked 3,6-anhydro-α-L-galactosyl residues, respectively) recorded by DDMAS NMR are significantly displaced downfield as compared with those recorded by CPMAS NMR and also the corresponding peaks in the solid state. This may be caused either by a smaller proportion of the cross-linked regions of the associated single helices or double helical junction zones, if any, or suppressed ^{13}C NMR

signals by interference of the motional frequency with the frequency of proton decoupling or MAS. In any case, the possibility should be always taken into account that a substantial amount of signal intensity could be lost in the swollen gel samples when polysaccharide backbone undergoes fluctuation motions with the time-scale as mentioned in Figure 2.

3.3. Fibrillation and amyloid proteins

3.3.1. Connective tissues, collagen and hydrogels of nuclear pore proteins

The data of reconstituted fibrils of chick calvaria collagen enriched at the glycine C_α and C′ positions by dipolar decoupled ^{13}C NMR spectra are consistent with a model in which collagen molecules reorient about the long axis of the helix with a rotational diffusion constant (R_1) of $\sim 10^7$ s^{-1}.[128] The powder line width of [1-^{13}C]Gly-labelled collagen, $\Delta = \delta_{zz} - \delta_{xx}$ at 22 °C for the uncross-linked reconstituted collagen fibril is 108 ppm, whereas the maximum value of delta (140 ppm) is observed for the cross-linked and mineralized collagen fibrils in rat calvaria.[129] The line shapes are analyzed using a dynamic model in which azimuthal orientation of the collagen backbone is assumed to fluctuate as a consequence of reorientation about the helix axis. Fluctuations in the azimuthal orientation are smaller in the cross-linked tendon and demineralized calvaria collagen fibres than in the reconstituted collagen fibres.[130]

Monomeric collagen molecules are soluble in aqueous solution at $3.5 \leq \text{pH} \leq 7.4$ and low ionic strength at temperatures in the range from freezing to a maximum of ~20 °C. At a temperature greater than this, aggregates and fibrils begin to form.[131] In spite of tightly held triple helical chains, it is demonstrated that ^{13}C spin–lattice relaxation times T_1^C of both C_β and C_γ carbons of Pro and Hyp residues in hydrated collagen fibrils are substantially reduced compared with those of some crystalline peptides, indicating the presence of fast ring puckering motions in these residues.[132] The fast and slow dynamics of collagen fibrils at various hydration levels were examined by ^{13}C CPMAS experiements.[133,134] Fast motions with correlation times much shorter than 40 μs were detected by dipolar couplings measured by the DIPSHIFT experiment,[135] and by the CSA values of the carbon sites in collagen. These motionally averaged anisotropic interactions provide a measure of the amplitudes of the segmental motions as described by a segmental order parameter. The data reveal that increasing hydration has a much stronger effect on the amplitude of the molecular processes than increasing temperature. Slow motions with correlation times of the order of milliseconds are also detected for hydrated collagen. In particular, the CODEX experiment[70] shows that the Hyp residues in the hydrated state have an appreciable level of mobility in the millisecond range.[133]

Recently, time-resolved dehydration-induced structural changes in an intact bovine cortical bone were studied by solid-state ^{13}C NMR spectroscopy, in order to clarify the underlying structural mechanism at the atomic level as to how dehydration affects the mechanical properties by decreasing its strength and toughness.[136] The experiment revealed the slow denaturation of collagen due to dehydration while the *trans*-Xaa-Pro conformation in collagen remained unchanged. These results suggest that glycosaminoglycans in the collagen fibre and mineral interface may chelate with a Ca^{2+} ion present on the surface of the mineral through sulphate or carboxylate groups. To prove this view, Ramamoorthy et al. recorded the ^{43}Ca MAS NMR spectra of bovine cortical bone with reference to those of hydroxyapatite and carbonated apatite.[137] They found the presence of protein-bound and free calcium sites which is in agreement with a model developed from the X-ray crystal structure of the protein, on the basis of 2D triple quantum ^{43}Ca MAS spectra.

Nuclear pore complexes (NPCs) are large protein complexes that cross the nuclear envelope, which is the double membrane surrounding the eukaryotic cell nucleus. NPCs permit the rapid passage of cargoes bound to nuclear transport receptors, but otherwise suppress nucleocytoplasmic fluxes of inert macromolecules $\geq$30 kDa.[138] To explain this selectivity, a sieve structure of the permeability barrier has been proposed that is created through reversible cross-linking between Phe and Gly (FG)-rich nucleoporin repeats. Indeed, the phenylalanine-mediated inter-repeat interactions cross-link FG repeat domains into elastic and reversible hydrogels. Using solid-state NMR spectroscopy, two types of integrated interactions, namely, transient hydrophobic interactions between Phe and methyl side chains as well as intermolecular β-sheets between the Asn-rich spacer regions are identified.[139] They appear to be essential for gelation, because mutant FG repeat domains lacking hydrophobic residues fail to form hydrogels. These data suggest a fully unexpected cellular function of such interchain β-structures in maintaining the permeability barrier of nuclear pores.

3.3.2. Fibrillized amyloid and PrP^cs

The failure of proteins to fold into their functional forms can occasionally lead to ''misfolding'' or ''conformational'' diseases.[140] Many of these diseases are associated with the formation of amyloid protein, an insoluble material that is deposited as fibrils or plaques in different tissues and organs of the body. They include amyloid Aβ protein as the major constituent of the plaques in Alzheimer patients, PrP^c associated with neurodegenerative diseases, α-synuclein (AS) associated with Parkinson's diseases, transthyretin (TTR) as a homotetrameric protein that is involved in the transport of thyroid hormones and retinol in human serum. In particular, the Aβ protein is a peptide of 39–43 amino acids that is the

main constituent of amyloid plaques in the brains of patients of Alzheimer's disease. A structural model for Aβ (1–40) protofilaments was derived by energy minimization with constraints of chemical shifts and interatomic distances determined by finite pulse radio-frequency driven recoupling (fp RFDR) from solid-state NMR data.[141–144] In this model, each molecule contains two β-strand (residues 12–24 and 30–40) that form separate parallel β-sheets in a double-layered cross-β motif. Two such cross-β units comprise the protofilament, which is then a four layered structure (Figure 18).[142] Here, approximately the first 10 residues of the structurally disordered form were distinguished from the ordered segments by observation of their increased line widths (>3 ppm) as compared with the ordered one (≤ 2 ppm) in the lyophilized fibrils. The fully hydrated amyloid sample may exhibit the missing signals for disordered segments that undergo large-amplitude motions when hydrated, as demonstrated for TTR (105–115) and AS.[145–148]

The 140-residue protein AS is able to form amyloid fibrils and as such is the main component of protein inclusions involved in Parkinson's disease. Full-length $^{13}C/^{15}N$-labelled AS fibrils and AS reverse-labelled for two of the most abundant amino acids, K and V, were examined by homonuclear and heteronuclear 2D and 3D NMR.[147] Two different types of fibrils display chemical shift differences of up to 13 ppm in the ^{15}N dimension and up to 5 ppm for the backbone and side-chain ^{13}C chemical shifts. Selection of regions with different mobility indicates the existence of monomers in the sample and allows the identification of mobile segments of the protein within the fibril in the presence of monomeric protein. At least 35 C-terminal residues are mobile and lack a defined secondary structure, whereas the N terminus is rigid starting from residue 22. In addition, temperature-dependent sensitivity enhancement is also noted for the AS fibrils due to both the CP efficiency and motional interference with proton decoupling.[148]

Prions are infectious proteins capable of self-replicating their conformation and are best known as the agent of diseases such as scrapie in sheep,[149] bovine spongiform encephalopathy in cattle[150] and a new variant of Creutzfeldt-Jakob disease in human.[151] It has been demonstrated that amyloid fibrils of recombinant PrP^cs from yeast, *Podospora anserina* and mammals can induce prion phenotypes in the corresponding hosts. HET-s (the PrP^c of *P. anserina*), contains a carboxy-terminal prion domain comprising residues 218–289.[152–155] Early studies showed that highly flexible residues are identified for the protein fragment HET-s (218–289) which gives rise to well-resolved ^{13}C, ^{15}N, and ^{1}H NMR resonances arising from portions taking a random coil conformation under high-resolution magic angle spinning (HRMAS) conditions.[152] The four β-strands are constituted by two pseudo repeat sequences, each forming a β-strand-turn-β-strand motif as the sequence specific secondary structure

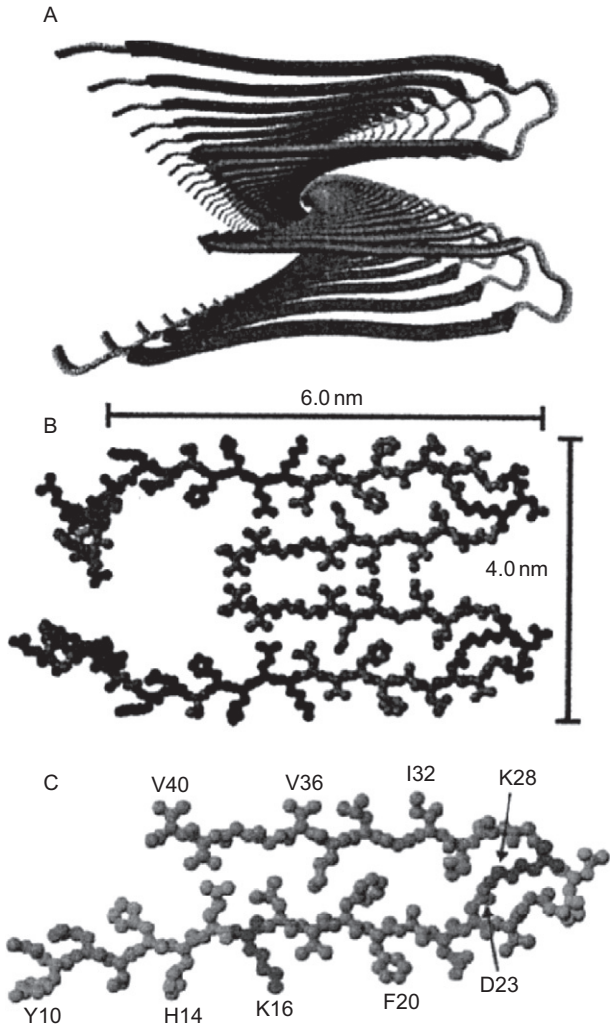

Figure 18 Structural model for Aβ (1–40) protofilaments, derived by energy minimization with constraints based on solid-state NMR data. (a) Ribbon representation of residues 8–40, viewed down the long axis of the protofilament. (b) Atomic representation of residues 1–40. From Ref. 141.

elements.[153] The ^{1}H–^{1}H and ^{13}C–^{13}C internuclear distance restraints were derived for HET-s (218–289)[154] from ^{13}C-detected proton–spin diffusion [carbon–proton–proton–carbon] (CHHC) and nitrogen–proton–proton–carbon (NHHC) experiments[156,157] and from proton-driven spin diffusion (PDSD),[158] respectively. On the basis of 134 intra- and intermolecular experimental distance restrains thus obtained, Wasmer et al. found that

HET-s (218–289) forms a left-handed β-solenoid, with each molecule forming two helical windings, a compact hydrophobic core, at least 23 hydrogen bonds, three salt bridges, and two asparagine ladders.[154] Further, solid-state NMR spectra of full-length HET-s proteins[155] were compared with those of isolated C-terminal prion domain fibrils[154] and the crystalline N-terminal globular domain HET-s (1–227), exhibiting a predominantly α-helical fold. It is shown that the highly ordered structure of the isolated prion domain HET-s (218–289) is conserved in the context of the full-length fibrils investigated. However, the globular domain loses much of its tertiary structure while partly retaining its secondary structure, thus exhibiting behaviour reminiscent of a molten globule (Figure 19). Flexible residues that may constitute the linker connecting the two domains are detected using refocused INEPT or RINEPT (refocused insensitive nuclei enhanced by polarization transfer)[159] spectroscopy under MAS conditions.

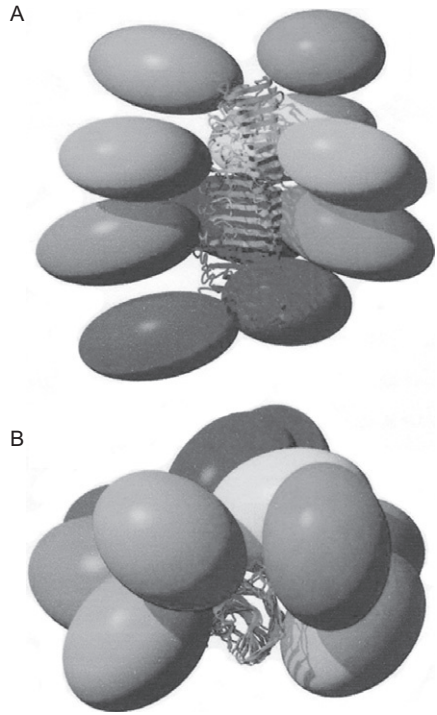

Figure 19 Structural model of full-length HET-s. (A) Side view and (B) top view of 10 HET-s molecules within a HET-s amyloid fibril. Ellipsoids represent the N-terminal domains (residues 1–217) whose structure is not precisely known in this context. From Ref. 155 with permission.

3.3.3. Fibrillation process

It appears that amyloid formation involves unordered or at least partly unfolded precursors.[160–162] Thus, it is worthwhile to examine the fibrillation process in detail to determine the conditions such as pH, concentration, temperature, etc., whereby amyloid precursors tend to aggregate to form fibrils. Calcitonin (CT) is a peptide hormone consisting of 32 amino-acid residues and contains an intrachain disulfide bridge between Cys1 and Cys7 and a proline amide at the C-terminus. CT is employed as a useful drug for various bone disorders such as Paget's disease and osteoporsis. Human calcitonin (hCT), however, has a tendency to associate to form fibril precipitate in aqueous solution. This fibril is the same type as amyloid fibril, and hence has been studied as a model of amyloid fibril formation.

The conformational transition of hCT during fibrillation in acidic and neutral conditions has been studied by both ^{13}C DDMAS and CPMAS NMR spectra of selectively ^{13}C-labelled hCTs.[163–166] When hCT is dissolved in 15 mM acetic acid solution, it becomes a turbid, viscous hydrogel in 2–3 days. Variation of the ^{13}C NMR signal intensities for the monomer and fibril states of [1-^{13}C]Phe22-, [3-^{13}C]Ala31-labelled hCT can be observed separately in the same sample as illustrated in Figure 20[163], because the DDMAS and CPMAS NMR signals correspond to the monomer and fibril states of hCT, respectively. The signal intensities of the ^{13}C DDMAS spectra decrease gradually with elapsed time (Figure 20; left), while those of the ^{13}C CPMAS pectra increase after the delay time as the solution turns viscous to form the gel (Figure 20; right). The changes of the peak intensities in the DDMAS and CPMAS spectra (Figures 20 and 21A)[166] show a two-step reaction process: for the case of [1-^{13}C]Gly10-hCT, the first and second step may occur at ~60 and 60–118 h, respectively. The chained changes in the DDMAS and CPMAS spectra and the presence of the lag time suggest that this hCT fibrillation process could be explained by a two-step autocatalytic reaction mechanism, in which the first reaction is a homogeneous nucleation step and the second one is a heterogeneous fibrillation process to elongate and to mature the fibrils.

Here, the components of hCT molecules observed by the DDMAS and CPMAS experiments are defined as A and B forms, respectively. For early stages, it is proposed[163] that a formation of micelles corresponding to the α-helical bundle is reversibly formed from the monomers with the same aggregation number n_0 (A_{n0}),

$$n_0 A(\text{monomers}) \leftrightarrow A_{n_0}(\text{micelle}). \tag{19}$$

The first reaction step is given by

$$A_{n_0} \xrightarrow{k_1} B_{n_0}, \tag{20}$$

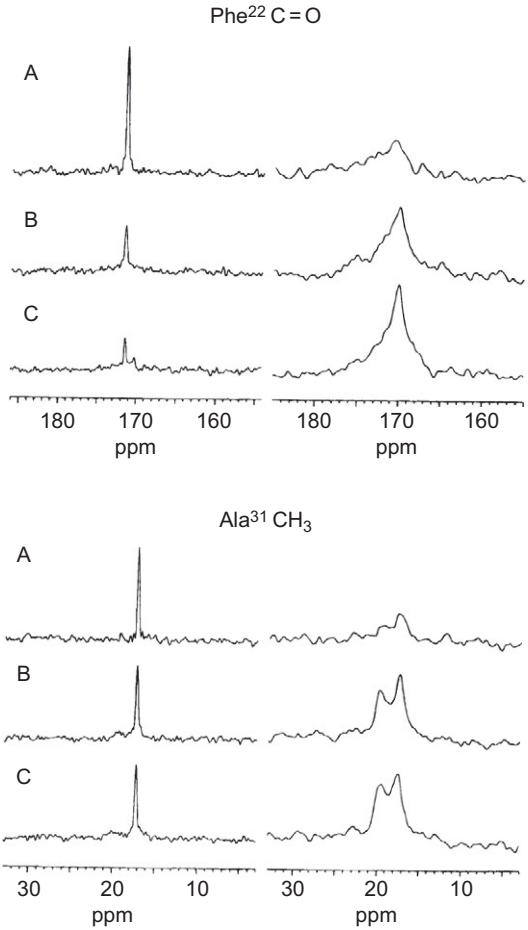

Figure 20 Time course of ^{13}C DDMAS (left panel) and CPMAS (right panel) of [1-^{13}C] Phe22, [3-^{13}C]Ala-labelled hCT dissolved in 0.015M acetic acid solution at the concentration of 80 mg/mL. pH of the solution was 3.3. Acquisition was started after 6 h from dissolution by accumulating 1000 scans for DDMAS and 2000 scans for CPMAS experiments: (A) 12 h, (B) 26.4 h, and (C) 179.2 h after dissolution. From Ref. 163 with permission.

where k_1 is the rate constant of the reaction Equation (20) and B_{n0} is the nucleus of fibril consisting of n_0 number of hCT. If f is defined as the fraction of the B-form (fibril) in the system, the kinetic equation of the reaction Equation (20) can be given by

$$(\mathrm{d}f/\mathrm{d}t)_1 = k_1(1-f). \tag{21}$$

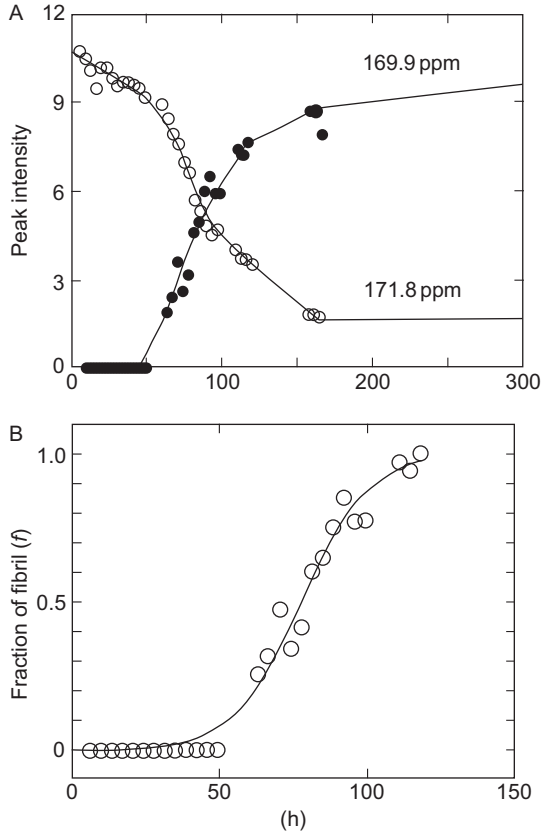

Figure 21 A plot of [1-^{13}C]Gly10 peak heights in ^{13}C DDMAS (open circle) and CPMAS (closed circle) of hCT (pH 3.3, 90 mg/mL) against elapsed time (A). The time of dissolution was taken as 0. Acquisition was started 6 h after dissolution. The intensity of the CPMAS signal was normalized as that observed at 119 h after dissolution as unity (B). The line in (B) shows the best fit to Equation (21) representing the two-step reaction mechanism. From Ref. 163 with permission.

The second autocatalytic fibrillation process can be given by

$$A + B_n \xrightarrow{k_2} B_{n+1}, \tag{22}$$

where k_2 is the rate constant of the reaction Equation (22). The differential equation for the reaction Equation (22) is

$$(\mathrm{d}f/\mathrm{d}t)_2 = k_2 af(1-f) \tag{23}$$

by using $[B] = n_0[B_{n_0}] + (n_0+1)[B_{n_0+1}] + \cdots + n[B_n] + \cdots = af$. The overall kinetic equation can be expressed as

$$(df/dt) = (df/dt)_1 + (df/dt)_2 = k_1(1-f) + k_2af(1-f). \quad (24)$$

This differential equation can be integrated to give

$$f = \rho\{\exp[(1+\rho)kt] - 1\}/\{1 + \rho\exp[(1+\rho)kt]\}, \quad (25)$$

under the boundary condition of $t = 0$ and $f = 0$, where $k = k_2a$, and ρ represents the dimensionless value to describe the ratio of k_1 to k. The fraction of fibril in Figure 21B is obtained by analysis of the fibrillation process based on Equation (25). The most striking feature in the kinetic analysis at pH 3.3 is the rate constant for the first step, k_1 values, are three to five and one to three orders of magnitude smaller than those of the second step, k_2 and ak_2 (effective rate constant) values, respectively, for the two labelled samples. These results suggest that the first homogeneous nucleation process is much slower than the second heterogeneous fibrillation process. It is also noted that the k_2 values are similar for the samples, whereas the k_1 values are quite different and sensitive to salt concentration or to a small amount of impurity, etc.

A fibrillation process derived by the kinetic analysis as well as the conformational transition is illustrated in Figure 22.[163] At pH 3.3, a local α-helical structure (depicted by a box in Figure 22A, with the positive (+) charge at NH_3, Lys18 and His20) is present around Gly10, whereas a random coil is dominant for Phe22, Ala26, and Ala31 in the monomer as viewed from their ^{13}C chemical shifts with reference to those of the conformation-dependent ^{13}C chemical shifts.[16,18,19,22,116] Fibrillation proceeds together with the local conformational changes to β-sheet forms around Gly10 and Phe22, on the basis of the ^{13}C chemical shift data (Figure 20D). The random coil components still remain in the fibril around the Ala26 and Ala31 residues in addition to the converted β-sheet. The fibril at pH 7.5, however, forms a local β-sheet at the centre region from the initial α-helix (with +charge at NH_3 and Lys18 and −charge at Asp15) and exhibits a random coil at the C-terminus region, reflecting that the fibril structure is substantially changed under a particular pH condition. This difference is caused by the changes in molecular interactions among the charged side chains such as Asp15, Lys18, and His20. The electrostatic interaction of the positive and negatively charged side chains between the hCT molecules may assemble the hCT in an antiparallel way at pH 7.5, where the positively charged side chains associate in both parallel and antiparallel ways at pH 3.3 (Figure 22).

Contributing to the etiology of Alzheimer's disease is the tau protein, which dissociates from microtubules and aggregates into intracellular protein deposits arising from paired helical filaments (PHFs).[162,167] Based on strong spin exchange and pyrene excimer formation of core residues, it is shown that individual tau proteins form single molecule layers along the fibre axis that perfectly stack on top of each other by

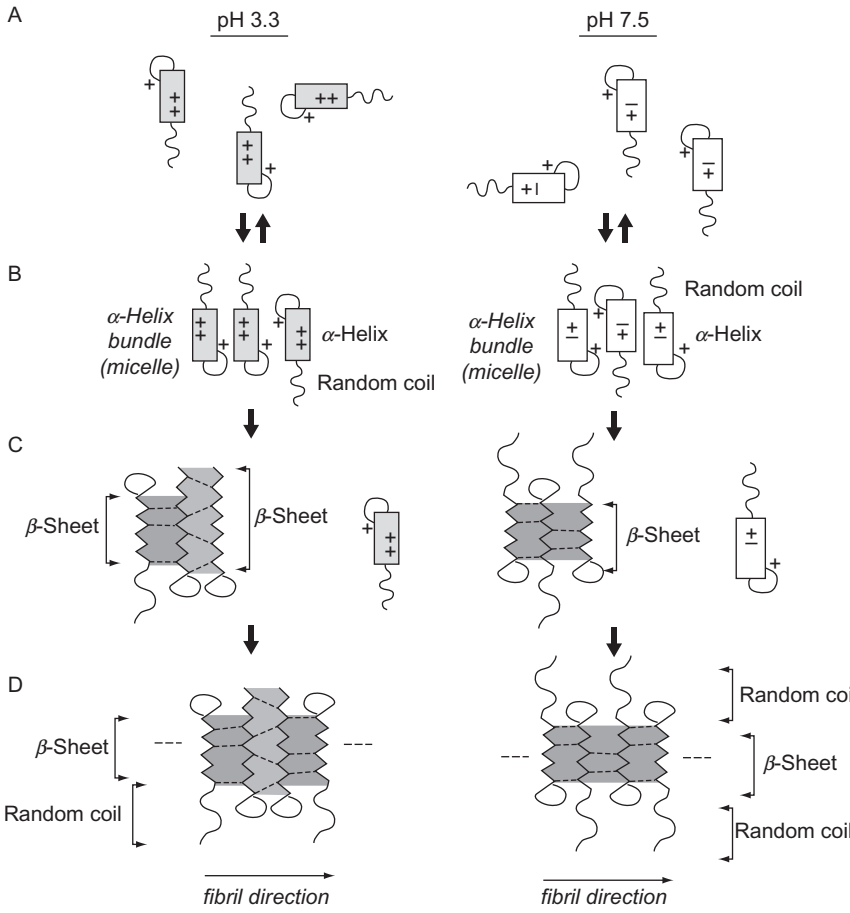

Figure 22 Schematic representation of proposed models for the fibril formation in the cases of pH 3.3 and 7.5. (A) hCT monomers in solution; (B) a homogeneous association to form the α-helical bundle (micelle); (C) a homogeneous nucleation process to form the β-sheet and heterogeneous association process; (D) a heterogeneous fibrillation process to grow a large fibril. α-helix, antiparallel β-sheet, and parallel β-sheet forms are shown by a box, drawn by dark grey and grey, respectively. From Ref. 163 with permission.

in-register, parallel alignment of β-strands.[168] The N-terminal tau 2–19 peptide undergoes gelation, syneresis, and aggregation over a period of years. These changes may be approximated on a shorter time scale by agitation and partial dehydration.[169] The anomalously enhanced (229 nm) ultraviolet resonance Raman (UVRR) imide II band reveals a common structural feature for gels of nondehydrated tau 2–19 and collagen I. The Fourier transform infrared (FTIR) amide I band shows that the

antiparallel β-sheet structure increases with syneresis in the aged, dehydrated tau 2–19 hydrogel.

Human amylin, or islet amyloid polypeptide (hIAPP), is a 37-residue peptide hormone which forms both intracellular and extracellular (EC) amyloid deposits in the pancreas of most type II diabetic subjects. The core of the structure in the SDS micelle is an α-helix that runs from about residues 5–28.[170,171] Although the basic structural unit in the fibrils in amylin striated ribbons, which we call the protofilament, contains four layers of parallel β-sheets, formed by two symmetric layers of amylin molecules.[172]A distortion or kink near residues 18–22 introduces pliancy in the angle between the N- and C-terminal segments of the α-helix. Under conditions mimicking the immature secretory granule (37 °C, pH 6), amylin forms amyloid aggregates more rapidly than its processing intermediates, and more rapidly than its reduced counterparts. Indeed, fibre formation by hIAPP is markedly accelerated by lipid bilyers despite adopting an α-helical state on the membrane.[173] In spite of forming transient α-helical structures, however, rat IAPP does not progress further to form amyloid fibrils.[172] To understand the nature of this intermediate state and the difference in toxicity between human and rat versions of IAPP, Nanga et al. solved the high-resolution structure of rat IAPP in the membrane-mimicking detergent micelles.[174] A comparison to the detergent-bound structures of other IAPP variants indicates that the N-terminal region may play a crucial role in the self-association and toxicity of IAPP by controlling access to the putative dimerization interface on the hydrophobic face of the amphipathic helix.

A peptide fragment prostatic acid phosphatase [PAP (248–286)], isolated from the seminal fluid that dramatically enhances HIV infectivity by up to 4–5 order of magnitude, appears to enhance HIV infection by forming amyloid fibres known as semen-derived enhancer of viral infection (SEVI).[175] PAP (248–286) is most disordered when bound to the surface of SDS micelles. Two regions of nascent structure (an α-helix from V262-H270 and a dynamic $\alpha/3_{10}$ helix from S279-L283) match the prediction of highly amyloidogenic sequences and may serve as nuclei for aggregation and amyloid fibril formation.

4. DYNAMICALLY HETEROGENEOUS SYSTEMS: MEMBRANE PROTEINS

Structural as well as dynamical studies of membrane proteins, constituting an estimated 30% of all proteins, are very important in view of their crucial biological importance. These membrane proteins are obviously dynamically heterogeneous systems, even though they are structurally homogeneous without any cross-links or aggregation so far discussed.

Indeed, hydrophilic N- or C-terminal ends and loop domains of these membrane proteins exposed to aqueous phases are able to undergo rapid or intermediate motional fluctuations, respectively, as shown in the 3D pictures of transmembrane (TM) moieties of bacteriorhodopsin (bR) as a typical membrane protein in the purple membrane (PM) of *Halobacterium salinarum*.[176–178] Structural information about protein surfaces, including the interhelical loops and N- and C-terminal ends, is completely missing from X-ray data. It is also conceivable that such pictures should be further modified, when membrane proteins in biologically active states are not always present as oligomers such as dimer or trimer as in 2D or 3D crystals but as monomers in lipid bilayers.

4.1. Retinal proteins

4.1.1. Bacteriorhodopsin

BR from *H. salinarum* is a light-driven proton pump, which is triggered by the photoisomerization of retinal covalently linked to its Lys216. It consists of a single polypeptide of 248 amino-acid residues, including seven α-helical TM chains A–G and interconnecting loops, as schematically illustrated in Figure 23. BR is one of the most intensively studied membrane proteins. A variety of experimental techniques have shown it to be

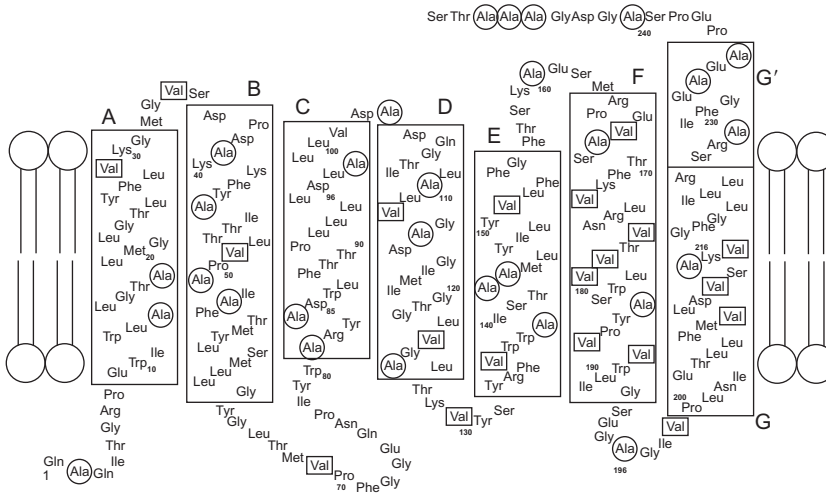

Figure 23 Amino-acid sequence of bR by taking into account the secondary structure revealed by X-ray diffraction studies. All Ala and Val residues labelled by [^{13}C]Ala and [1-^{13}C]Val are indicated by the circles and boxes, respectively. A–G denotes the seven transmembrane α-helical segments revealed by X-ray diffraction and G′ denotes the α-helical segments as revealed by NMR measurements.

an excellent model for the very important 7TM, G-protein coupled receptors (GPCR's).The most simple and effective approach is to analyse *both* the ^{13}C CPMAS and DDMAS NMR spectra of ^{13}C- or ^{15}N-labelled bR of *H. sarinurum* by site-directed (or amino-acid specific) enrichment,[16,18,20–25] as in the cases of hydrogels in structurally heterogeneous systems.

4.1.1.1. Assignment of ^{13}C NMR peaks An appropriate isotope labelling or enrichment either by ^{13}C or ^{15}N nuclei through biosynthesis is essential for an NMR study on the structure and dynamics of membrane proteins to achieve enhanced sensitivity and selectivity of their labelled signals from crowded background signals. Site-directed (or amino-acid specific) enrichment has proved to be one of the simplest and valuable approaches, in which one of the unlabelled amino-acid residues is replaced by a selectively ^{13}C-labelled amino acid such as [3-^{13}C]Ala, [1-^{13}C]Ala, Val, etc., or their combination in the growth TS medium for bR from *H. salinarum* or M9 medium for a variety of membrane proteins expressed from *E. coli*.[16]

The ^{13}C NMR spectra of a naturally occurring 2D crystalline preparation of [3-^{13}C]Ala-labelled bR from PM, as an illustrative example, are recorded by DDMAS (A) and CPMAS (B) NMR spectra as shown in Figure 24A and B, respectively.[16,23,179–182] Twelve ^{13}C NMR signals, including five single carbon signals, are well resolved in the CPMAS NMR spectra (Figure 24B) among 29 Ala residues (see Figure 23). Site-specific assignment of these twelve carbons signals is performed by locating the missing ^{13}C NMR signal of a site-directed mutant which lacks the amino-acid residue under consideration with respect to the corresponding peaks of the wild type (WT). It is essential that no major conformational changes occur during the site-directed mutagenesis under consideration. In addition, Tuzi et al. introduced Mn^{2+}-induced spectral editing to simplify crowded spectra by suppression of peaks from the residues located within 8.7 Å from the surface by accelerated transverse relaxation.[182] The assigned ^{13}C NMR signals of [3-^{13}C]Ala-bR thus obtained are indicated on the top of the individual peaks in Figure 24A and B, together with their revealed local conformations, on the basis of the conformation-dependent ^{13}C chemical shifts.[16,18,19,22,25,116,181–184] Here, the conformations for the α-helical Ala C_β signals designated as the α_I and α_{II} peaks are referred to the peak positions of $(Ala)_n$ in the solid and hexafluoroisopropanol (HFIP) solution, respectively.[22–25] The former and latter correspond to Ala C_β signals from the ordinary right-handed α-helices and those undergoing time-averaged fluctuations, respectively. In membrane proteins, it is important to distinguish the [3-^{13}C]Ala and [1-^{13}C]Val, Gly, Pro and Ala peaks of the TM α-helices from those of the interhelical loops as hinges connecting two TM α-helices, instead of the most common peaks from the β-sheets, as shown in Figure 25.[25] The α-helical Ala C_β peaks always resonate at higher field peak-position than

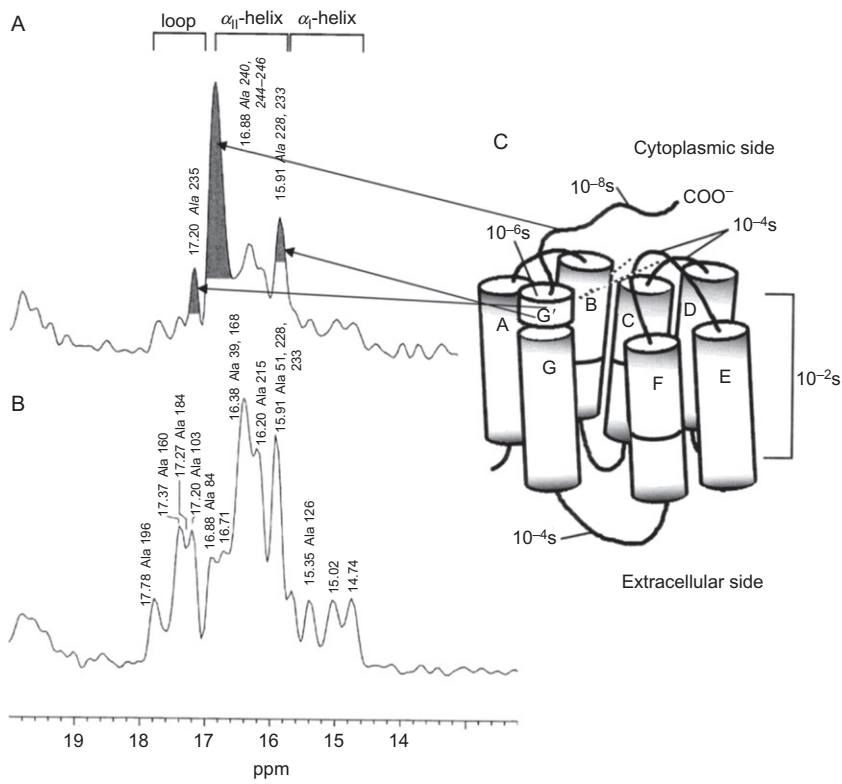

Figure 24 (A) ^{13}C DDMAS and (B) CPMAS NMR spectra of [3-^{13}C]Ala-labelled bR from PM. The intense three peaks indicated by the grey in the top trace are ascribed to three Ala residues in the α-helix (helix G′ in this figure) protruding from the cytoplasmic membrane surface and four Ala residue in the C-terminal. (C) Schematic representation of the dynamic structure of bR in 2D crystal. The interfacial and kinked portions are illustrated by the shade and belts, respectively. From Refs. 22 and 179 with permission.

those of the random coil peak at 16.88 ppm as demonstrated for [3-^{13}C]Ala-labelled bR, while those of the loops are resonate at a lower field (Figure 25A). In some instances, the Ala C_β ^{13}C NMR peaks from the α-helices resonate exactly at the peak of the random coil form. The most effective means, in such a case, to distinguish the peak of the α-helix which is accidentally superimposed upon the same position as that of the random coil form is to check whether any anisotropic dipolar interaction, essential for the cross-polarization (CP) remains or does not. CP is effective in the former while this effect is completely averaged out in the latter.

In the DDMAS NMR spectrum of [3-^{13}C]Ala-bR, the three emerging intense peaks marked by the grey (Figure 24A) are ascribable to the three Ala residues in the cytoplasmic (CP) α-helix at the membrane surface

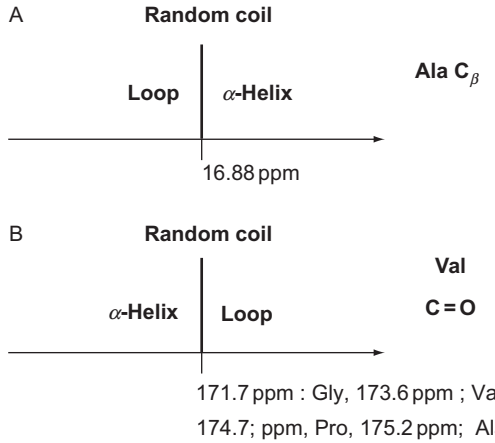

Figure 25 Schematic representation of the distinction of ^{13}C chemical shifts between the α-helix and loops for Ala C_β (A) and Val C=O (B) carbons of bR. The random coil peaks for both are located at the boundary between the ^{13}C NMR peaks of the α-helix and loops. From Ref. 25 with permission.

(helix G′ in Figure 23) and the additional four Ala residues (beyond the helix G′) at the C-terminal end taking the random coil conformation (see the three arrows pointing to the structural model (C). Of course, these residues cannot be located by either cryo-electron micrograph or X-ray diffraction studies.[176–178] The remaining background peaks from the TM α-helices are naturally the same as those of the CPMAS experiments in view of their shorter ^{13}C $T_1{}^C$ values of the order of 0.5 s.[18]

Further, the ^{13}C NMR spectra of [1-^{13}C]Val-labelled bR as recorded by CPMAS (A) and DDMAS (B) methods are also well resolved (Figure 26),[185–188] as compared with those of [1-^{13}C]Ala-bR (Figure 27).[179] The peak-assignment indicated above the individual peaks of the former was performed on the basis of the site-directed mutagenesis[185–187] and rotational echo double resonance (REDOR) filter experiments on [1-^{13}C]Val-, [^{15}N]Pro-labelled bR.[188] Therefore, the ^{13}C NMR signals from the more mobile loops, with shortened spin–lattice relaxation times in the order of 1 s as compared with the TM α-helices (10–15 s),[185] are readily distinguishable by the DDMAS spectrum of [1-^{13}C]Val-bR. The peaks A (V34; A–B loop), B (V69; B–C loop and 130; D–E loop), and C (V101; C–D loop, and V199; F–G loop) exhibit shorter T1 values than the those of TM α-helix C. These results indicate that the [1-^{13}C]Val-labelled TM α-helical peaks resonate at lower field than the random coil peak at 173.6 ppm, while those of the loops resonate at higher field than the random coil peak (Figure 25B). Obviously, these [1-^{13}C]Val-peaks from the loop regions are very useful for revealing the surface dynamics as well as their secondary and tertiary structures as a whole.

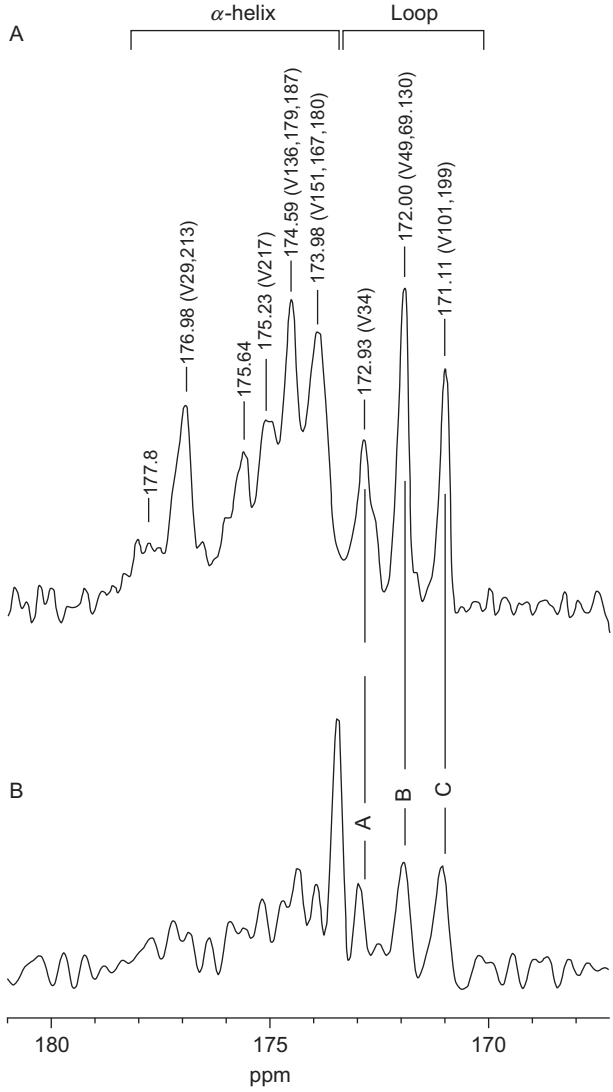

Figure 26 ^{13}C CPMAS (A) and DDMAS (B) NMR spectra of [1-^{13}C]Val-labelled bR from PM. From Ref. 19. The assigned peaks is based on the data of site-directed mutagenesis[185–187] and REDOR filter experiment.[188]

Surprisingly, the ^{13}C CPMAS NMR signals from [1-^{13}C]Ala-labelled bR are very broad[179](Figure 27, left panel) compared with those of [1-^{13}C] Val- and [3-^{13}C]Ala-bR (Figures 24B and 26A), even though the ^{13}C DDMAS NMR spectrum gives rise to very sharp signals (Figure 27, right panel). This is caused by the presence of broadened or suppressed

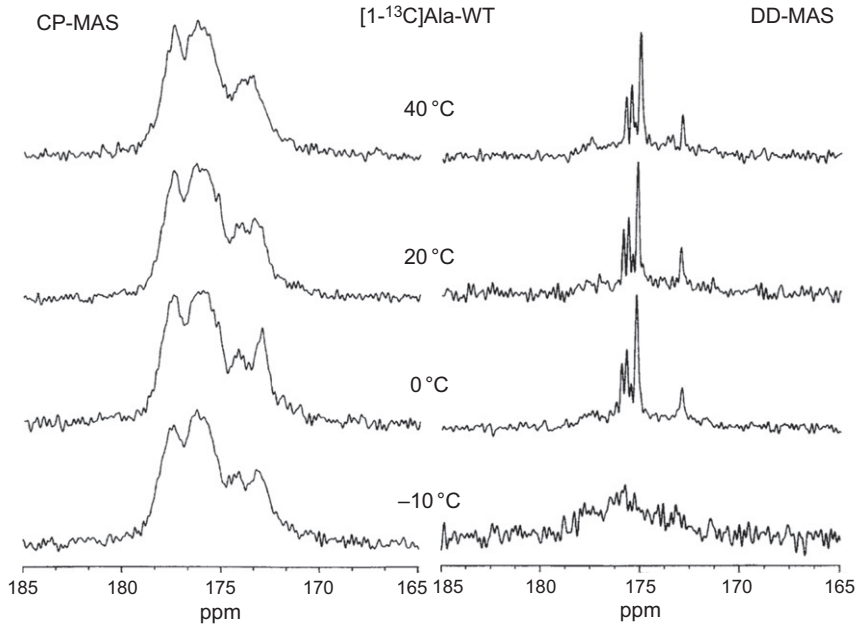

Figure 27 ^{13}C CPMAS (left) and DDMAS (right) of [1-^{13}C]Ala-labelled bR from PM recorded at various temperatures between −10 and 40 °C. From Ref. 179 with permission.

^{13}C signals from [1-^{13}C]Ala-labelled residues near at the membrane surface caused by an interference of the fluctuation frequency with the MAS frequency (10^4 Hz). Indeed, the expected ^{13}C NMR signals of [1-^{13}C] Ala103, 160 and 196 from the loops which should resonate at higher field than 175.2 ppm (Figure 25B) are completely absent,[179] consistent also with that no spectral change is observed among the WT and A196G and A103C mutants. Instead, the sharp signals appearing in this region are ascribed to the CP α-helix and random coiled C-terminal end protruding from the membrane surface, consistent with the data of [3-^{13}C]Ala-bR.[189] Further, it is noted that the ^{13}C NMR signals of the TM α-helices near the CP surface disappear completely when the temperature is lowered to −10° C,[179] because the lowered fluctuation frequency at this temperature interferes with the frequency of the MAS, leading to suppressed peaks based on the argument described in Section 2.1.2. Undoubtedly, such suppressed peaks both from the loops and TM α-helices result in the broadened and featureless ^{13}C CPMAS NMR signals. In addition, it should be pointed out here that such suppressed peaks are found for the ^{13}C NMR signals of [1-^{13}C] Leu-, Phe- and -Trp-bR with the side chains shown as C_α–$C_\beta H_2$(X)-: the observed intensities are much lower than the predicted relative amounts

in the membrane surface.[186] Instead, full peak intensities are noted for [1-^{13}C]Val-, Ile-bR with the side chains expressed as C_α–$C_\beta(X)(Y)$.

The assignment of the ^{13}C NMR peaks of Pro 50, 91, and 186 from [1-^{13}C]Pro-labelled bR is performed with reference to those of P50G, P91G, and P186A mutants, to reveal the dynamic features of the Pro residues located at the possible kinked portions in the inner part of the TM α-helices, as demonstrated in Figure 28A, top trace.[190,191] For this purpose, selection of these three peaks was made among seven resolved peaks by use of Mn^{2+} induced suppression of peaks from residues located near the surface due to accelerated spin–spin relaxation times, as shown in Figure 28A, middle and bottom traces.

4.1.1.2. Dynamic picture of bR from PM in 2D crystal A dynamic picture of bR in the 2D crystal thus obtained turns out to be highly heterogeneous: the correlation times of which vary substantially from 10^{-2} to $<10^{-8}$ s depending upon the portions such as the TM and CP α-helices, loops, and N- or C-terminal ends (Figure 24C). Here, the above mentioned CP

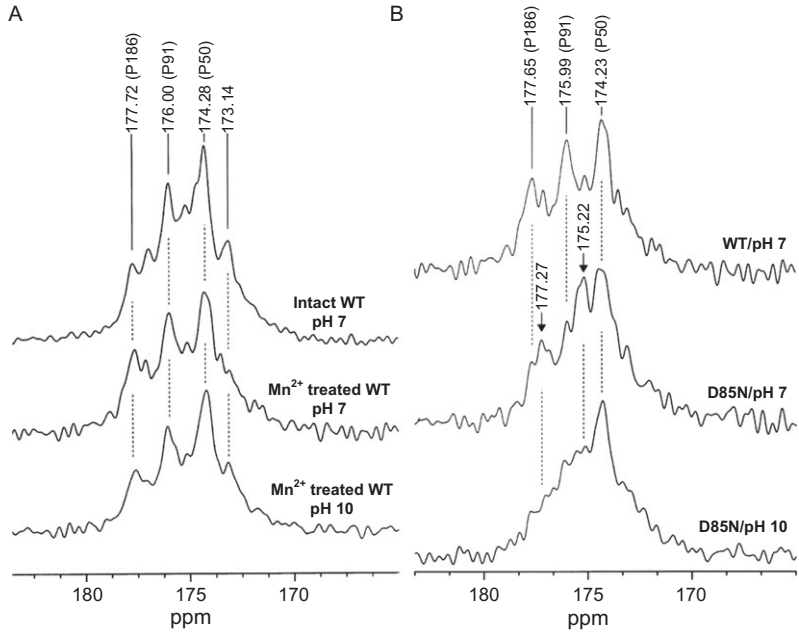

Figure 28 ^{13}C CPMAS NMR spectra of (A) [1-^{13}C]Pro-labelled WT-bR at pH 7 (top), and the same preparation in the presence of 40 μM Mn^{2+} at pH 7 (middle) and pH 10 (bottom), respectively, and (B) [1-^{13}C]Pro-labelled WT-bR and D85N mutant in the presence of 40 μM Mn^2: WT-bR at pH 7 (top), D85N at pH 7 (middle) and D85N at pH 10 (bottom). From Refs. 190 and 191 with permission.

α-helix is also identified on the basis of the ^{13}C chemical shifts of [1-^{13}C] and [2-^{13}C]Ala labelled.[189] These ^{13}C chemical shifts of the α-helices and loops vary also with a variety of environmental factors such as temperature, lipid composition, pH, cations, surface electric charges, etc.[16,22,179,192,193] Further, the observed peak intensities vary with the type of [^{13}C]amino-acid residues at the loop regions as pointed out already: therefore, choice of [3-^{13}C]Ala and [1-^{13}C]Val labelling is most preferable, whereas the choice of [1-^{13}C]Ala, -Phe, -Trp is not always preferable for this purpose.

It is noted, however, that the ^{13}C chemical shift of Ala184 from [3-^{13}C] Ala-bR occurs at an unexpectedly lower field region (17.27 ppm) corresponding to the loop domains, in spite of its location at the TM α-helix as revealed by the X-ray diffraction method at low temperatures (see Figure 24B). This anomaly is caused by adopting an altered conformation and dynamics from that of the TM α-helix F in the lipid bilayer *at ambient temperature* which can be detected by the ^{13}C NMR spectra alone.[179] This is caused by the presence of a kinked structure at Pro 186 where the intrahelical hydrogen bond between Trp 182 and Pro 186 is absent. In fact, this possibility is confirmed by comparison of the ^{13}C NMR spectra of WT with those of P186L mutant of [3-^{13}C]Ala-, [1-^{13}C]Val-labelled TM peptide F (164−194) recorded both in dimyristoylphosphatidylcholine (DMPC) bilayer and solid at ambient temperatures: the ^{13}C NMR signal of [3-^{13}C] Ala184-labelled fragment F (164–194) of WT appears at 17.4 ppm ascribable to an Ala residue from the loop region in DMPC bilayer, while its corresponding peak from the TM peptide F of P186L mutant occurs at the normal α-helical peak-position at 15.8 ppm in the solid. In addition, it is shown that the ^{13}C chemical shift of [1-^{13}C]Val 187 from WT peptide F occurs at 172.0 ppm, far from the peak-position of the α-helix region in the DMPC bilayer, while the corresponding peak of the peptide F from P186L mutant is at the normal α-helical peak-position. Further, the anomaly in the peak-position of [3-^{13}C]Ala-labelled Ala235 is seen at 17.20 ppm for the loop region in spite of its location at the CP α-helix, and is caused by the well-known effect due to the presence of Ala-Pro sequence.[194,195] Therefore, it is cautioned that there might be a possibility that the ^{13}C NMR peak from a residue near to a kinked structure or X-Pro occurs at such an anomalous position with reference to conformation-dependent ^{13}C chemical shifts or any data base available from solution NMR.

The estimated correlation times for the loop domains of the order of 10^{-4} s are obtained for the suppressed peaks in the [1-^{13}C]amino-acid-labelled bR, including Gly, Ala, and Leu residues as shown in Figure 24C. The loop dynamics can be also examined by measurements of the ^{13}C–^{1}H dipolar couplings by DIPSHIFT experiment in which fluctuations of the C_α–C_β vector result in additional motional averaging as order parameters, in addition to the rotation of Ala methyl groups which scales the dipolar

coupling to 1/3 of the rigid limit value.[196] Typical order parameters thus obtained for mobile sites in bR are between 0.25 and 0.29. They arise from Ala103 of the C–D loop, Ala235 at the end of the CP α-helix protruding from the membrane surface, and Ala196 of the F–G loop, in addition to Ala228 and 233 of the CP α-helix and Ala51 from the TM α-helix B. The order parameter for Ala160 from the expectantly more flexible E–F loop, however, is unavailable because of the suppressed peak found under high-field NMR conditions.

The above mentioned cytoplsamic α-helix G′(Figure 23) and interhelical loops of bR are not always present independently but are organized to form the CP surface structures by their mutual interactions and cation binding.[192,193] They also interact closely with each other, through formation of salt bridges or metal-mediated linkages, as demonstrated by the significant NMR spectral changes in the presence of these metal ions. Indeed, either complete removal of cations or lowering the bulk pH to 1.2 results in a prominent colour change from purple to blue and the resulting ^{13}C NMR spectral change, in which all the ^{13}C NMR peaks from the loop regions are completely suppressed as a result of acquired motional freedom by one order of magnitude to the order of 10^{-5} s.[180] Truncation of the cytoplsamic α-helix by a proteinase or mutation at the CP loops results in similar changes in the ^{13}C NMR spectra to indicate the modified surface structures.[192] Temperature change also induces additional changes in the surface structures as demonstrated in the plots of the ^{13}C chemical shifts of [3-^{13}C]Ala-labelled A160G bR versus temperatures as shown in Figure 29.[192] All of these peaks, except for the E and F peaks, are displaced upfield when temperature is lowered from 40 to −10 °C. Such upfield shifts upon a decrease in temperature are most prominent for the CP α-helix (0.43 ppm) and is interpreted in terms of the reduced thermal fluctuation at lower temperatures, because the downfield displacements of such an α-helix peak upon raising temperature is due to conformational fluctuation in the region. It is also interesting to note that such a spectral change for the CP α-helix is coupled with that of Ala103 as encountered for the A160G mutant.

Further, it was demonstrated that the surface structure of the M-like state differs from that of the ground state as viewed from the ^{13}C NMR spectra.[193] At ambient temperature, the surface structure of WT is formed from the CP α-helix G′ and the C–D and E–F loops and probably the A–B loop, at the expense of the stability of the CP α-helix itself through salt bridges from charged residues as viewed from the suppressed ^{13}C NMR signals concerned. Thus, preventing unnecessary fluctuation of these helices for efficient proton uptake during the photocycle. On the contrary, the CP α-helix G′ does not take such a tilted structure when the surface structure is disrupted at low temperature or an M-like state like that of D85N. This view is consistent with a previously published paper on the

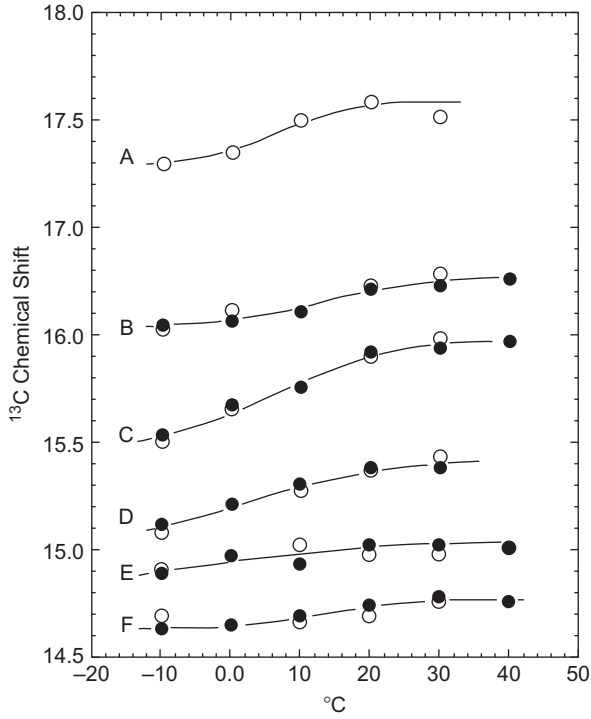

Figure 29 ^{13}C chemical shifts of several peaks from wild type (closed circles) and A160G mutant (open circles) against temperature. (A) Ala103 (C–D loop), (B) Ala39 (helix B), 168 (helix F), (C) Ala228, 233 (C-terminal α-helix), D–F (transmembrane α-helices). From Ref. 192 with permission.

''proton binding cluster'' consisting of Asp104, Glu166 and Glu234.[197] In addition, it is shown that glutamic acid residues at the extracelluar (EC) surface can be served as determinants for the conformation and dynamics of bR.[198] Replacement of Glu-9 or Glu-74 and Glu-194/204 at the EC surface by glutamine(s) induces significant dynamic changes in the CP and EC surface structure as viewed from the suppressed ^{13}C NMR signals of the CP α-helix, CP and EC loops, in [3-^{13}C]Ala- and [1-^{13}C]Val-labelled proteins. Additional conformational changes in the TM α-helices are induced as modified retinal-protein interactions for multiple mutants involving the E194Q/E204Q pair in the proton releasing cluster. In particular, significant dynamic changes are induced for the triple (E9Q/E194Q/E204Q) or quadruple mutants (E9Q/E74Q/E194Q/E204Q), as shown by the suppressed [1-^{13}C]Val-V199/101 peak at the F–G loop and broadening of the remaining ^{13}C NMR peaks in [1-^{13}C]Val-labelled proteins. These changes are due to acquired global fluctuation motions of the

order of 10^{-4}–10^{-5} s as a result of a disorganized trimeric form. Accordingly, these Glu residues at the EC surface are shown to play an important role in maintaining the native secondary structure of bR in the PM.

Bacterio-opsin (bO) is produced either from removal of retinal by bleaching bR with hydroxylamine or from a retinal-deficient E1001 bR strain. In order to gain insight into the correct folding of bR by retinal, ^{13}C NMR spectra of [3-^{13}C]Ala, [1-^{13}C]Val-labelled bR and bO were examined.[199] It is found that distinct dynamics changes are especially induced at the E–F and F–G loops and some TM helices, in the absence of retinal which plays an essential role for the correct protein folding, as viewed from the ^{13}C CPMAS NMR spectral change between[3-^{13}C]Ala-bO and -bR. A possible involvement of the B–C loops as viewed from the ^{13}C NMR spectrum of [1-^{13}C]Val-bO is not straightforward in the early work[199] due to the incorrect assignment of the peak at 172.0 ppm for bR which was recently revised[200] as shown in Figure 26. Kawamura et al. showed that the participation of the B–C loop is essential for the correct folding of bR on the basis of their regeneration studies of [^{15}N]Pro-, [1-^{13}C]Val-labelled bO and -E1001 bR.[200] The ^{15}N (A) and ^{13}C (B) NMR spectra (Figure 30) shows that regeneration from bO or E1001 bR to bR by addition of retinal results in the incorrect or partially incorrect folding for bO and E1001 bR, respectively, as viewed from the substantially suppressed ^{15}N Pro 70 signal at 122.3 ppm and the ^{13}C Val 69 signal at 172.0 ppm as well as broadening of the remaining peaks. This finding indicates that the B–C loop may not always fold correctly in the regenerated bR, which leads to different properties in the regenerated bR compared to those of WT-bR.

The first proton transfer of bR occurs from the protonated Schiff base of retinal to the anionic Asp85 at the central part of the protein in the L–M states. Global conformational changes of the protein backbone occur in the M and/or N intermediates with a deprotonated and a protonated Schiff base, respectively. Kamikubo et al.[201] showed on the basis of a low-resolution X-ray diffraction study that characteristic conformational changes of the M intermediate occur at helices F and G. Therefore, D85N and D85N/D96N mutants at alkaline pH, with the unprotonated Schiff base, can be conveniently used as an excellent model system to achieve an M-like state at ambient temperature without photo-illumination. Intermediate-frequency dynamics (with a frequency of 10^4–10^5 Hz) accompanied by this process can be revealed by examination of the suppressed or recovered intensities of [3-^{13}C]Ala-, [1-^{13}C]Val-, and [1-^{13}C]Pro-labelled D85N and D85N/D96N which are located at the helices B, C, and G and accompanied loops, together with role of kinked structure.[191,202] In particular, it is noteworthy that the Pro 91 and Pro 186 ^{13}C NMR peaks of D85N mutant are displaced upfield by 0.77 and 0.38 ppm, respectively, as compared with those of WT at pH 7 and suppressed

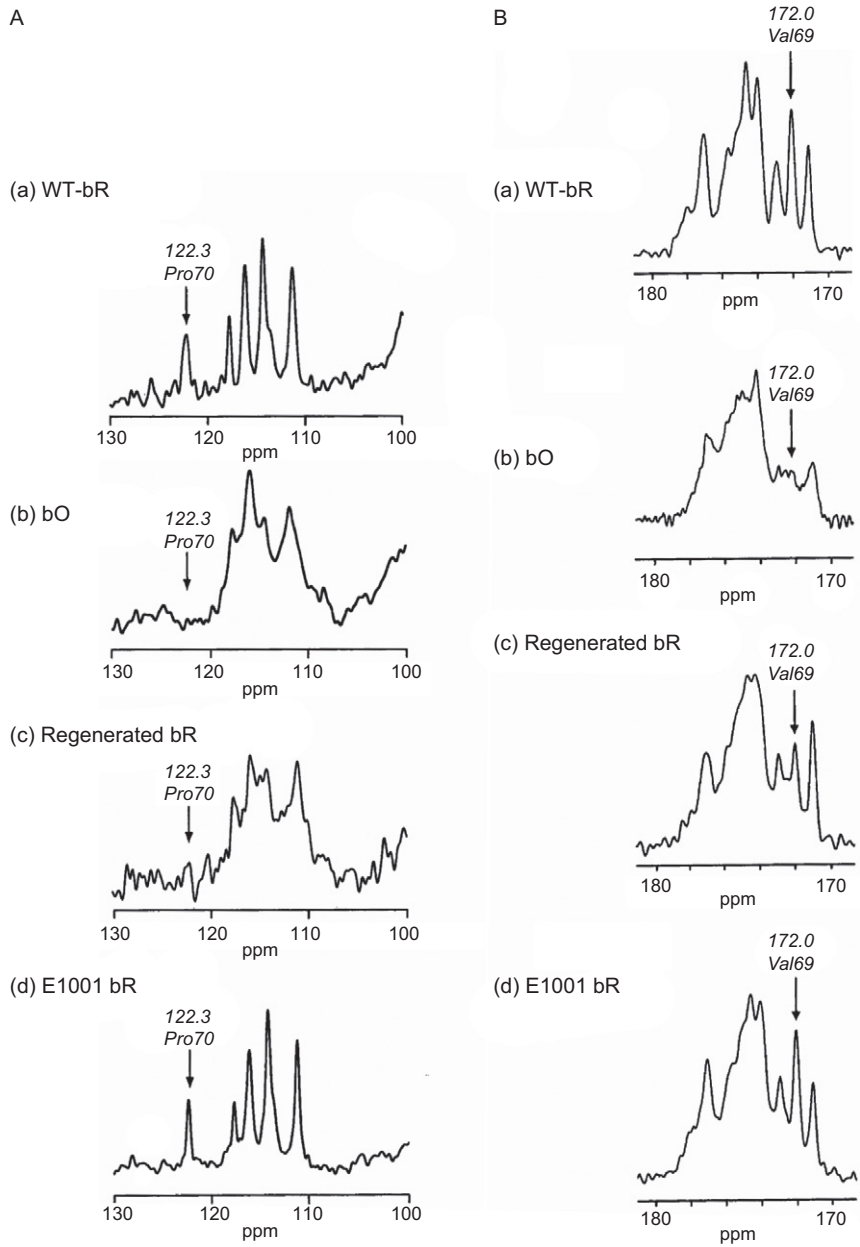

Figure 30 (A) ^{15}N CPMAS NMR spectra of [^{15}N]Pro-labelled WT-bR (a), bO (b), regenerated bR (c) and E1001 bR (d) at 293 K. The arrows indicate the peak positions at Pro 70. (B) ^{13}C CPMAS NMR spectra of [1-^{13}C]Val-labelled WT-bR (a), bO (b), regenerated bR (c) E1001 bR (d) at 293 K. The arrows indicate the peak positions at Val 69. From Ref. 200 with permission.

at the M-like state at pH 10, although the Pro 50 peak remains unchanged between WT and D85N (Figure 28B).

This problem was recently clarified further[30] by examination of the ^{13}C NMR spectra of [1-^{13}C]Val-labelled WT and D85N mutants in which key signals located at the loops are completed or confirmed.[186,188] Global dynamic changes of the D85N backbone at neutral pH, caused by neutralization of the anionic D85, are evaluated by the decreased peak intensities in the displaced [1-^{13}C]Val signals from the B–C and D–E loops with fluctuation frequencies of the order of 10^4 Hz. In addition, a closer look at the ^{13}C NMR spectra of [1-^{13}C]Val-D85N recorded at various pH (Figure 31) shows that several peak intensities are suppressed at pH 10 corresponding to the M-like state due to interference of a resulting fluctuation frequency with the MAS frequency [Equation (11)], whereas several peaks are concomitantly recovered due to escape from the interference. A plot of the suppressed or recovered intensities (SRI) versus pH, instead of frequency as shown in Figure 32, is very convenient to clarify such dynamics based on the argument given in Section 2.1.2. This is expected from the fact that the fluctuation frequency can be increased together with pH which causes such a conformational change. A similar plot of SRI versus temperature proved to be also a very useful tool to clarify the chain dynamics of poly(acrylate)s with correlation times of the order of 10^{-5} s in Section 3.1.1.[29] The accelerated dynamic changes of D85N in the M-like state, by deprotonation of the Schiff base at alkaline pH, cause an accelerated fluctuation frequency which interferes with the frequency of MAS or escape from such interference, as viewed from the intensities changes in the V34, 69, and 130 from the loops and V49, 213, and 17 from the TM α-helices, together with the changes in the [3-^{13}C]Ala160 and 196 and [1-^{13}C] Pro 91 and 186 peaks, shown as the shaded areas in Figure 33. The intensity change in V101 and 199 are also noted for D85N/D96N. Distinguishing fluctuation frequencies as those which are higher and lower than 10^4 Hz is now possible, instead of a simple description of the data around 10^4 Hz available from one-point data analysis previously reported.

4.1.1.3. Dynamics of bR in disrupted or partially disorganized 2D lattice In 2D crystalline preparation, trimeric units of bR are hexagonally packed to form PM as shown on the right hand panel of Figure 34. It is anticipated, therefore, that the above mentioned dynamic picture is readily altered when 2D crystals are partially disorganized or disrupted by failure of either a proper formation of the trimeric structure or lattice assembly leading to the hexagonal crystal. This is because selective interaction between bR and certain endogenous lipid molecules as well as protein–protein interactions is essential for the lattice assembly.[203,204] In order to examine the effect of 2D lattice formation on backbone dynamics, the ^{13}C NMR spectra of [3-^{13}C]Ala-, [1-^{13}C]Val-labelled W80L and W12L, in

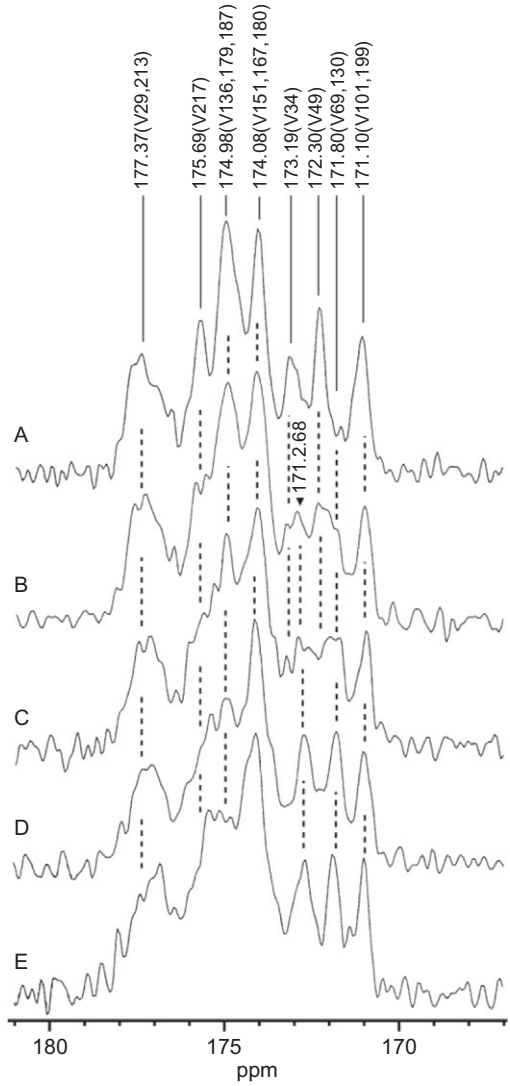

Figure 31 100.6 MHz ^{13}C CPMAS NMR spectra of [1-^{13}C]Val-labelled D85N mutant at various pH values: pH 6 (A), 8 (B), 9 (C), 10 (D), and 11 (E). From Ref. 30. The assignment of peaks is based on newly performed[186] and corrected ones[188].

which side chains of these two Trp residues are oriented outward from the TM α-helices at the interface for lipid–protein interaction, and bO from E1001, in which the helix–helix interactions are modified due to a lack of retinal were examined.[205] The trimeric structure is preserved for W12L, but disrupted for W80L mutant as viewed from their bilobed CD

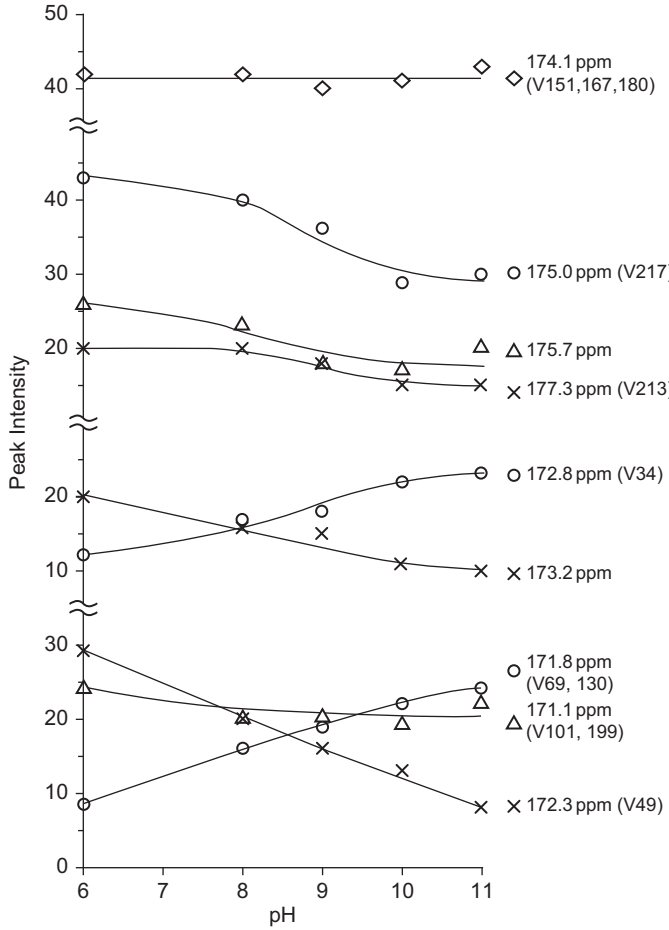

Figure 32 SRI plots for D85N mutant against pH. The peak intensities are either increased or decreased together with the increased pH, depending upon the respective peaks, except for the peak V151, 167, 180 whose intensity was unchanged. From Ref. 30 with permission.

spectra. The presence of a disrupted or disorganized 2D lattice for [3-^{13}C] Ala-labelled W12L and W80L and bO is readily visualized by an increased relative proportion of surrounding lipids per protein, together with their broadened ^{13}C NMR signals. The ^{13}C CPMAS NMR spectra of [1-^{13}C]Ala- and Val-labelled mutants, however, are almost completely suppressed due to the presence of backbone fluctuations with a time scale of 10^{-4} s interfering with the MAS frequency.

Such a trimeric structure is almost completely disrupted but present as a monomer for regenerated bR in lipid bilayer of the liquid crystalline phase (Figure 34A and B). As demonstrated in Figure 34B, the ^{13}C NMR

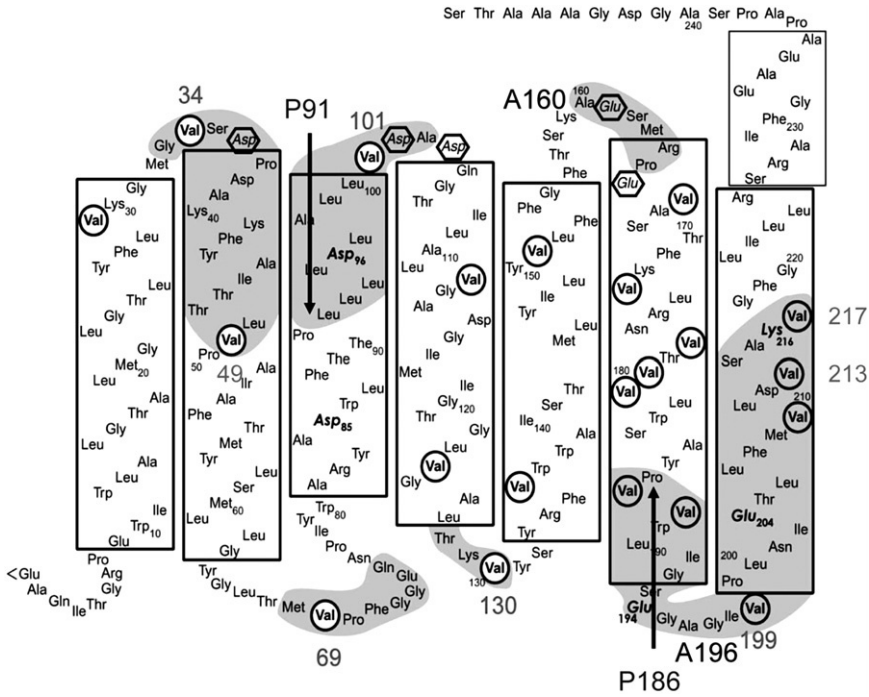

Figure 33 Portions undergoing intermediate-fluctuations with frequency of 10^4–10^5 Hz in the M-like state of D85N are shaded. Residue numbers without alphabets are from Val, and Pro and Ala residues are indicated by the numbers initiated by the *P* and *A*, respectively (see Ref. 30).

signals are partially visible for monomeric [3-^{13}C]Ala-bR in the egg PC bilayer at ambient temperatures, because several ^{13}C NMR signals from the loops and TM α-helices are suppressed as compared with those of [3-^{13}C]Ala-bR from PM.[206] In addition, the ^{13}C CPMAS NMR spectrum of the regenerated [1-^{13}C]Val-bR in DMPC bilayer at 40 °C (Figure 35A) is much broadened as compared with that of PM.[186] This happens when monomeric bR reconstituted into egg PC, DMPC or dipalmitoylphosphatidylcholine (DPPC) bilayers undergoes conformational fluctuations with frequencies of the order of 10^4–10^5 Hz at ambient temperature, this frequency interferes with the frequencies of the MAS or proton decoupling. The ^{13}C NMR signals of regenerated [1-^{13}C]Val-bR, however, are almost fully recovered in gel phase lipids of DMPC or DPPC bilayers at around 0 °C as judged by the methylene peak-position of fatty acyl chains of the lipid at 32 ppm (Figure 35D). This finding is interpreted in terms of aggregation to the trimeric form of bR in the DMPC or DPPC bilayers leading to a 2D-hexagonal array at low temperature, because endogenous

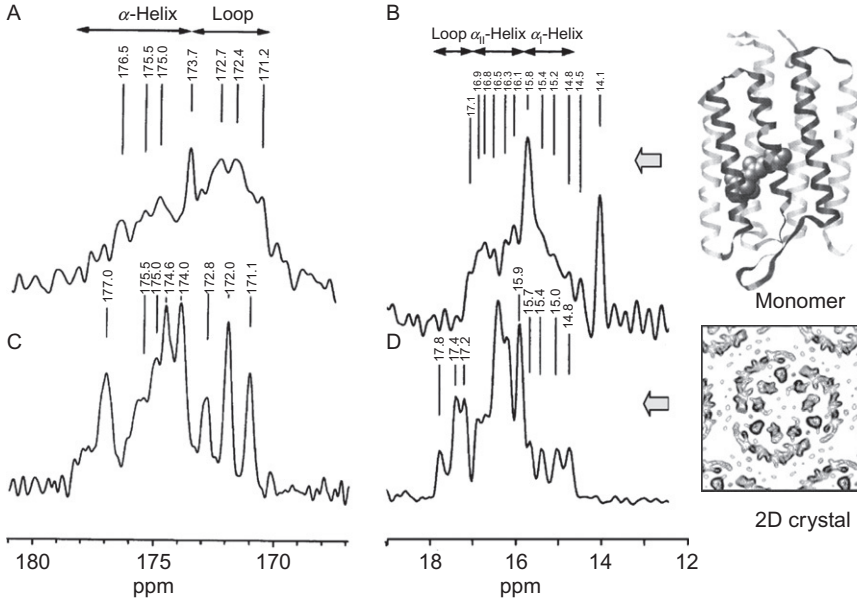

Figure 34 ^{13}C CPMAS NMR spectra of [1-^{13}C]Val- and [3-^{13}C]Ala-labelled bR reconstituted in egg PC bilayer (A and B) and those from PM (C and D). From Ref. 206 with permission.

lipids from halobacteria are accompanied with bR prepared from halobacteria, resulting in favourable backbone dynamics for the ^{13}C NMR observation. It is therefore concluded that [3-^{13}C]Ala- and [1-^{13}C]Val-bR reconstituted in egg PC, DMPC or DPPC bilayers at ambient temperature, or [3-^{13}C]Ala-bR at low temperature gave rise to well-resolved ^{13}C NMR signals as far as the endogeneous lipids are present, although they are not always completely the same as those of the 2D hexagonal lattice from PM.

These findings indicate that the dynamic structures of bR are greatly modified with and without intact trimeric form leading to hexagonal packing. In the latter, correlation times of the TM α-helices are substantially shortened from 10^{-2} in the 2D crystal to 10^{-4} s in the monomer, as schematically shown in Figure 36. Further, the correlation times of the CP and EC loops decrease one order of magnitude from 10^{-4} to 10^{-5} s. In this connection, it is surprising to note that the ^{13}C NMR spectra of the [3-^{13}C]Ala-labelled D85N mutant of bR reconstituted in egg PC or DMPC bilayers are very similar to those of [3-^{13}C]Ala-labelled bR in lipid bilayers, in spite of the presence of a globular conformational and dynamic change in the former as found in 2D crystalline preparations.[207] Fortunately, the ^{13}C NMR spectral feature of [3-^{13}C]Ala- and [1-^{13}C]Val-labelled bR and D85N is recovered to yield the characteristic features of the 2D crystalline form in gel-forming lipids at lowered temperatures.

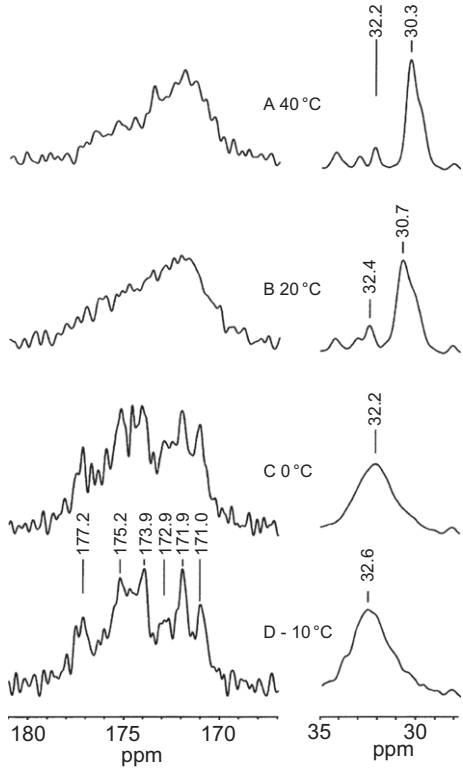

Figure 35 ^{13}C CPMAS NMR spectra of [1-^{13}C]Val- and [3-^{13}C]Ala-labelled bR reconstituted in DMPC bilayer (1:50 mole ratio) at various temperatures from 40 (A) to −10 °C (D). The methylene peak-position of the fatty acyl chain of the lipid at 32 and 30 ppm is a good indicator of the gel and liquid-crystalline phase, respectively. From Ref. 206 with permission.

The ^{15}N spectral peaks of fully hydrated [^{15}N]Gly-bR, obtained via cross-polarization, are suppressed at 293 K due to interference with the proton decoupling frequency, and also because of short values of T_2 in the loops.[208] The motion of the TM α-helices in bR is strongly affected by the freezing of excess water at low temperatures. It is shown that motions in the 10-μs correlation regime may be functionally important for the photocycle of bR, and protein–lipid interactions are motionally coupled in this dynamic regime.

4.1.2. Sensory rhodopsin (sR) and proteorhodopsin

4.1.2.1. Sensory rhodopsin Halobacteria contain a family of four retinal proteins, bR, halorhodopsin (hR), sensory rhodopsin I (sR I), and phoborhodopsin (pR or sensory rhodopsin II, sR II), which carry two distinct functions through common photochemical reactions. In particular, bR

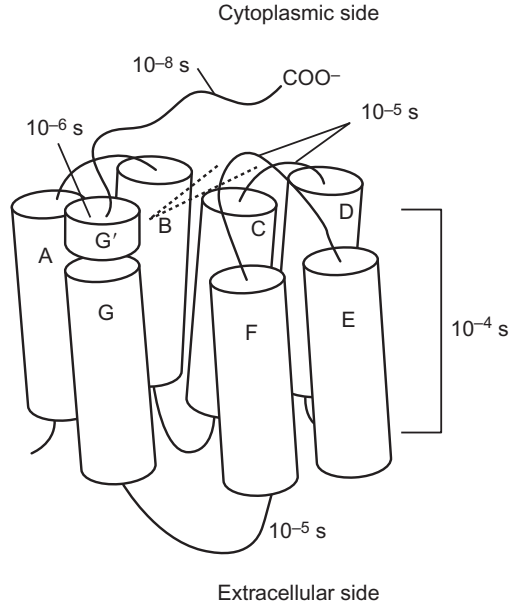

Figure 36 Schematic representation of dynamic picture of bR in monomer. See the correlation times for the cytoplasmic and extracellular loops and transmembrane α-helices are significantly shortened as compared with those in 2D crystal as shown in Figure 24.

and hR are light-driven pumps used to transport proton and chloride, respectively,[209] while the two sRs are photoreceptors active for positive and negative pthototaxis, respectively.[210,211] The ^{13}C CPMAS and DDMAS NMR spectra of [3-^{13}C]Ala, [1-^{13}C]Val-labelled *pharaonis* phobor-hodopsin (*p*pR or sR II) in egg PC bilayer were compared with those of bR from PM, as demonstrated in Figure 37.[212] Seven ^{13}C NMR signals from the TM α-helices are resolved for [3-^{13}C]Ala-*p*pR at almost the same positions as those of bR, except for the suppressed peaks in the loop regions in spite of the presence of at least three Ala residues. The motional frequency of the loop regions in *p*pR is estimated as 10^5 Hz from the suppressed peaks of the loops of [3-^{13}C]Ala-*p*pR, similar to the case of bR in egg PC bilayer.[206] The ^{13}C NMR signals from the loops, however, are visible from [1-^{13}C]Val-*p*pR but the peak positions of the TM α-helices are not always the same for *p*pR and bR. It is also found that the conformation and dynamics of *p*pR are appreciably altered by complex formation with a cognate truncated transducer *p*Htr II (1–159). In particular, the CP α-helix protruding from the membrane surface, also present in this system, is involved in complex formation and the subsequent fluctuation frequency is reduced by one order of magnitude.

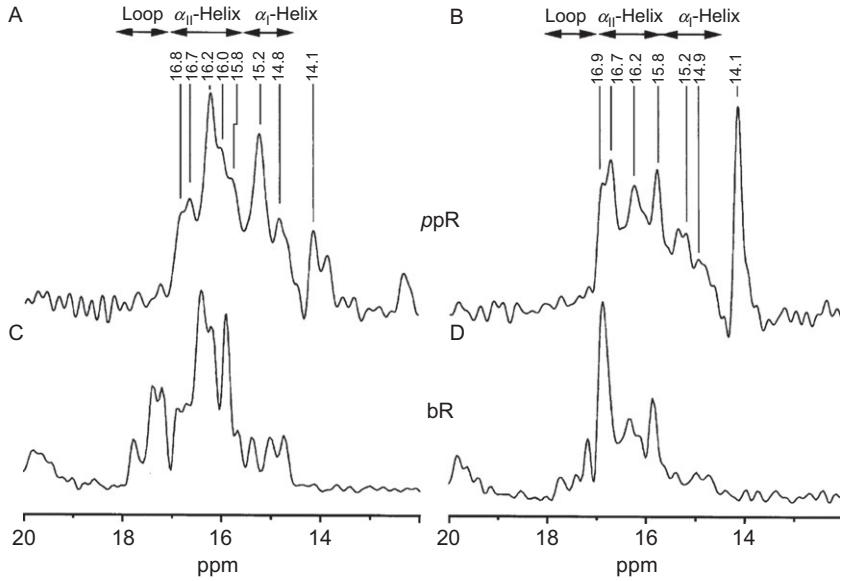

Figure 37 ^{13}C CPMAS (left) and DDMAS (right) NMR spectra of [3-^{13}C]Ala-labelled *p*pR (a), (b) in egg PC bilayer as compared with those of [3-^{13}C]Ala-labelled bR (c), (d) from PM. From Ref. 212 with permission.

It appears that the cognate transducer *pharaonis* transducer *p*HtrII (1–159) consists of two TM α-helices with the C-terminal residue protruding from the CP membrane surface, as manifested from the ^{13}C DDMAS NMR spectra of the [3-^{13}C]Ala-labelled transducer [*p*HtrII (1–159)] in the presence and absence of *p*pR in egg PC bilayer (Figure 38A and B, respectively).[213] The intense, low-field α_{II}-helical peaks of *p*HtrII (1–159) at 16.6 and 16.3 ppm, which are not visible by ^{13}C CPMAS NMR (spectrum not shown), are ascribed to the [3-^{13}C]Ala residues taking α-helices protruding from the membrane surface, with reference to the conformation-dependent displacement of Ala C_β peaks.[16,18,19,22,25,116,181–184] Further, it is noted that the α-helical peaks of *p*HtrII (1–159) are not always fully visible in the absence of *p*pR (Figure 38B), because their increased fluctuation frequency in the absence of *p*pR is close to the proton decoupling frequency (10^5 Hz) thus resulting in suppressed peaks.[213] The high-field envelope peaks at 15.5 ppm, however, are ascribed to Ala residues in the TM α-helices, with reference to the data of the conformation-dependent displacement of peaks. It appears that there are two kinds of spectral changes at both the CP and TM α-helices, as shown in the temperature-dependent spectral change (Figure 38C): the former peaks are suppressed at lower temperatures, while the latter peaks are suppressed at higher

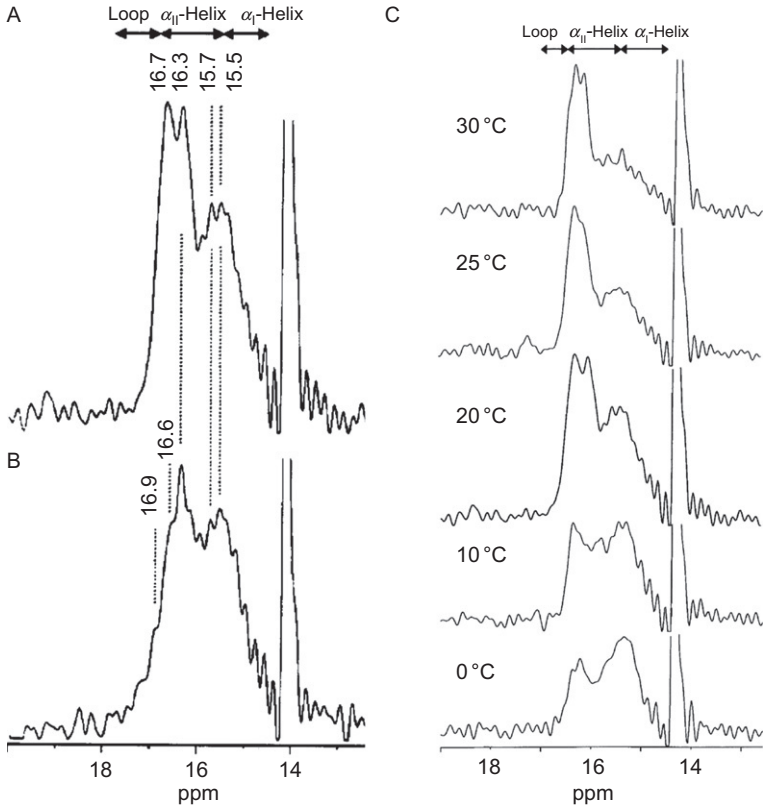

Figure 38 ^{13}C DDMAS NMR spectra of [3-^{13}C]Ala-labelled transducer *p*HtrII (1–159) (A) in the presence and (B) absence of *p*pR in egg PC bilayer. (C) Temperature-dependent spectral change of ^{13}C DDMAS NMR of [3-^{13}C]Ala-labelled transducer *p*HtrII (1–159) in the presence of *p*pR. From Ref. 213 with permission.

temperatures due to the differential fluctuation frequencies which interfere with the proton decoupling frequency, depending upon their locations inside or outside of the bilayers.

The assignment of the peaks of *p*pR to Ala149 (helix E) and 221 (C-terminal stem; CP α-helix) are marked by grey and 228 and 234–238 (C-terminal tip) was made by comparison of the peak intensities of the [3-^{13}C]Ala-labelled *p*pR with those of A149S, A149V mutants or truncated *p*pR (1–220), as shown in Figures 39–41 (see Figure 42 for its amino-acid sequences).[214,215] The CP surface structure described already for bR[192,193] is also present in *p*pR. In order to gain insight into its possible role in *p*pR, ^{13}C DDMAS and CPMAS NMR spectra of [3-^{13}C]Ala-labelled *p*pR, A149S and A149V, and their complexes with the cognate transducer *p*HtrII

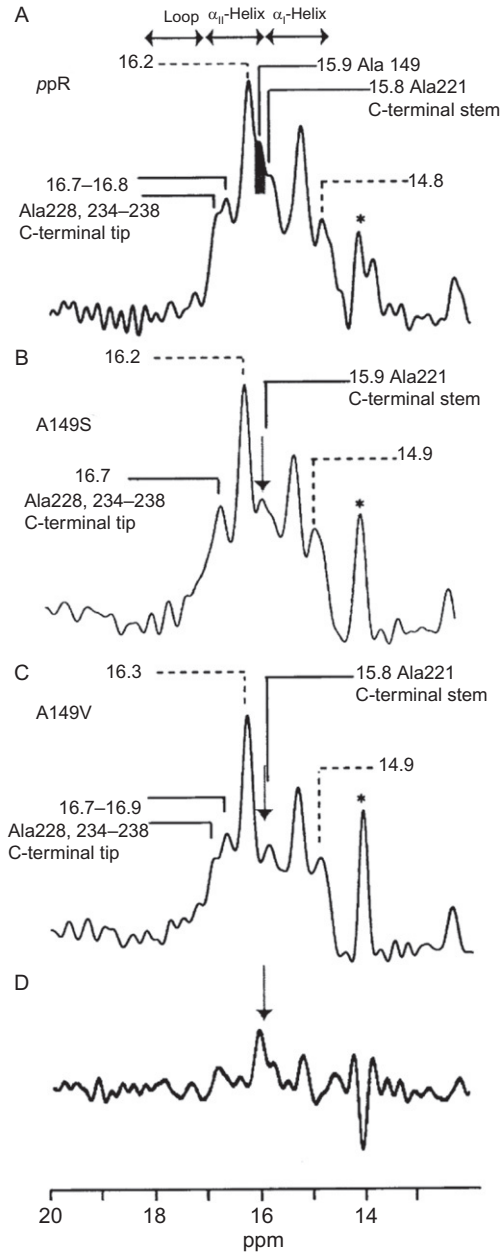

Figure 39 ^{13}C CPMAS NMR spectra of [3-^{13}C]Ala-labelled *pp*R (a), A149S (b) and A149V (c) reconstituted in egg PC bilayer. ^{13}CNMR signal at 15.9 ppm corresponding to Ala149 in ppR is shown by the grey (a) and arrows (b, c, and d). The resonance peak at 14.1 ppm is ascribed to methyl carbon peak of egg PC as shown as asterisk. Difference spectrum between (a) and (c) is shown in (d). From Ref. 214 with permission.

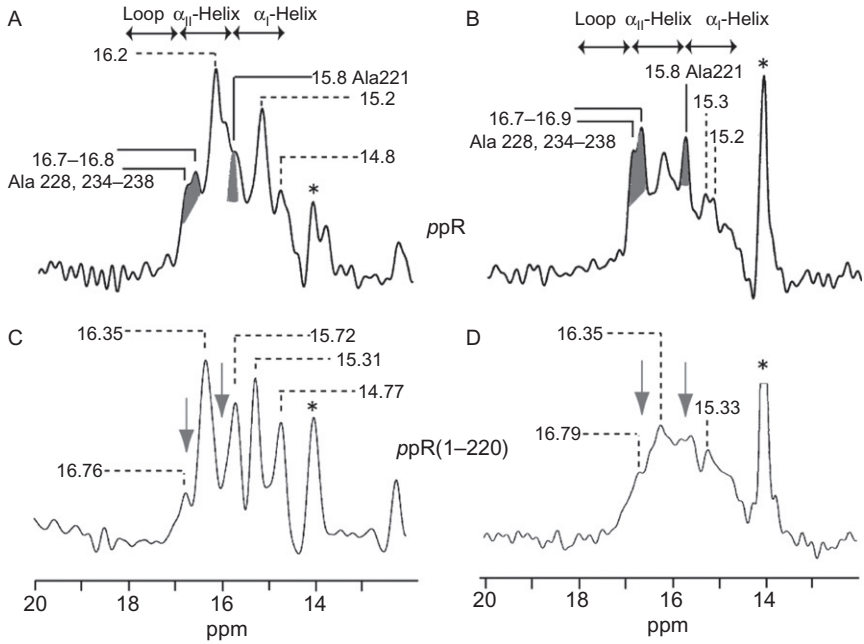

Figure 40 ^{13}C CPMAS (left) and DDMAS (right) NMR spectra of [3-^{13}C]Ala-*p*pR alone (a and b) and truncated ppR (1–220) (c and d) reconstituted in egg PC bilayer, respectively. ^{13}C NMR signals from the C-terminal region in *p*pR are shown in the grey (a and b) and arrows (c and d). The resonance peak at 14.1 ppm is ascribed to the methyl carbon peak of egg PC as shown by the asterisk. From Ref. 215 with permission.

(1–159) were examined with emphasis on revealing their structures and the stability of the 2:2 complex.[215] It turns out that the ^{13}C DDMAS NMR peak intensities of the C-terminal α-helix from [3-^{13}C]Ala-*p*pR and A149V mutant are substantially reduced when they are complexed with those of the cognate transducer *p*HtrII (1–159) (Figure 41A, B and E, F), whereas those of [3-^{13}C]Ala-A149S are almost unchanged (Figure 41C and D). Such a change is less sensitive as observed by ^{13}C CPMAS NMR spectra, however. This is obviously caused by an underlying characteristic dynamic change, leading to reduced fluctuation frequency in the surface structure including the C-terminal stem and tip portion of the α-helix and the E–F loop of *p*pR, which interfere with the proton decoupling frequency (10^5 Hz). This finding suggests that a mutual interaction between the two types of α-helices, the C-terminal (cytoplasmic) α-helix of *p*pR and CP α-helix of *p*HtrII (1–159) (TM2) is responsible for the stabilization of the complex as viewed from the surface structure. Indeed, the C-terminal α-helix of *p*pR is located at a very important site and is thus able to interact

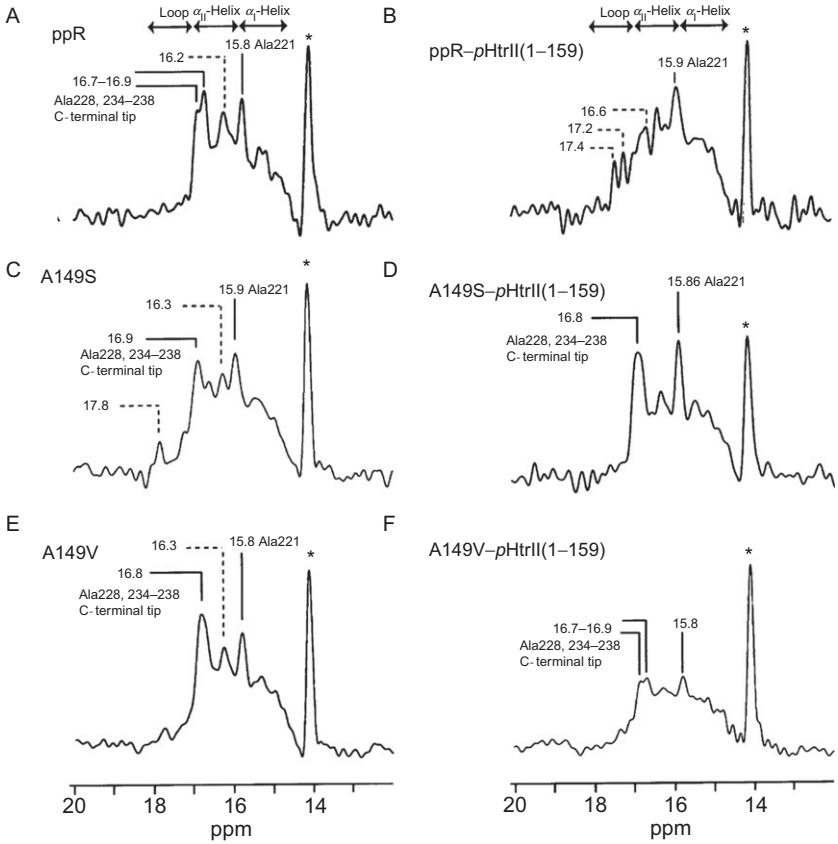

Figure 41 ^{13}C DDMAS NMR spectra of uncomplexed [3-^{13}C]Ala-labelled *p*pR (a), A149S (c) and A149V (e) (left panel) and those complexed with *p*HtrII (1–159) (right panel). And those of *p*pR (b), A149S (d), and A149V (f) complexed with *p*Htrl I(1–159) reconstituted in egg PC bilayer (right panel). From Ref. 214 with permission.

with the CP α-helix of *p*HtrII (1–159). This means that an altered surface structure of A149S results in a destabilized complex as viewed from the ^{13}C NMR spectrum of the surface areas, probably because of a modified conformation at the corner of the helix E in addition to a change of hydropathy. It is, therefore, concluded that the surface structure of *p*pR, including the C-terminal α-helix and the E–F loops, is directly involved in the stabilization of the complex through the conformational stability of the helix E, as manifested from the ^{13}C NMR spectra of A160G and A160V of bR mutants (corresponding to Ala149 in ppR),[192,193] by taking into account of the well-known structural homology between *p*pR and bR. It is, therefore, suggested that the dynamics of the membrane surface

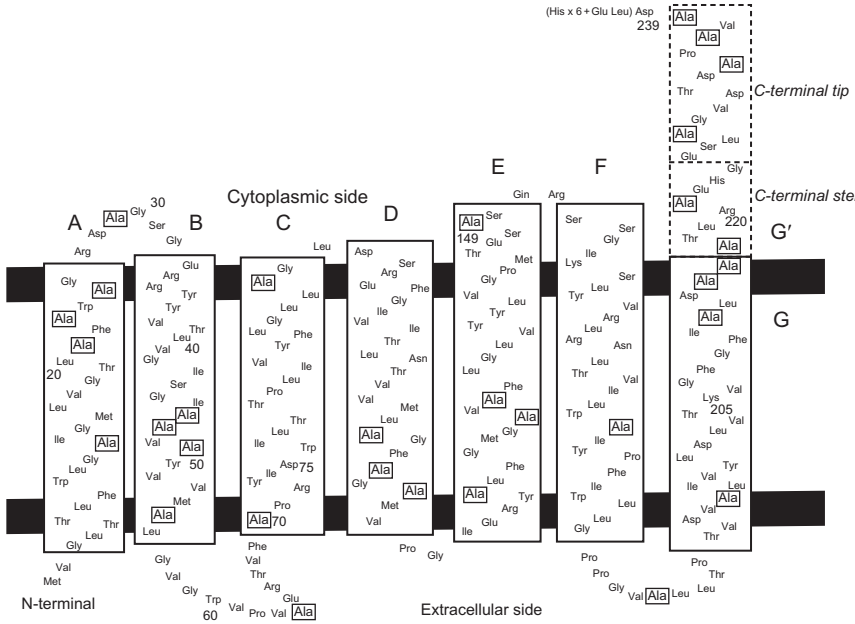

Figure 42 A schematic representation of the secondary structures in *p*pR based on crystallographic structures reported by H. Luecke et al. (ppR: PDB code 1JGJ) and V. I. Gordeliy et al. (*p*pR-*p*HtrII [1–114]: PDB code 1H2S). The surface areas of the lipid bilayer are represented by grey bands. [3-^{13}C]Ala residues are marked with squares. From Ref. 214.

residues, including the E–F loop in the CP side in *p*pR, are strongly correlated with the manner of mutual interaction with *p*HtrII and its resulting biological function in relation to the signal relay.

Assuming that the break of the hydrogen bonding between the C and G helices is a trigger of the phototaxis signal, the D75N mutant of *p*pR was used as a ''quasi''-activated receptor.[215] Clear dynamic changes of the C-terminal tip portion of the receptor (10^4–10^5 Hz) are observed when the receptor bound to the transducer and the complex changes to the ''quasi''-signalling state. This can be named as a ''switch model'' as shown in Figure 43: the CP α-helix in the transducer interacts with the C-terminal helices of the receptor, leading to the activation of the receptor, based on the ^{13}C NMR observation of [3-^{13}C]Ala- and [1-^{13}C]Val-labelled preparations. The interaction site at the linker switches to the linker region of the paired transducer. This formation of a paired transducer may further relay the signals to the phosphorylation cascade. Indeed, the local fluctuation frequency at the C-terminal tip (Table 2) as viewed from the suppressed [3-^{13}C]Ala-labelled ^{13}C NMR peak intensities, recorded by

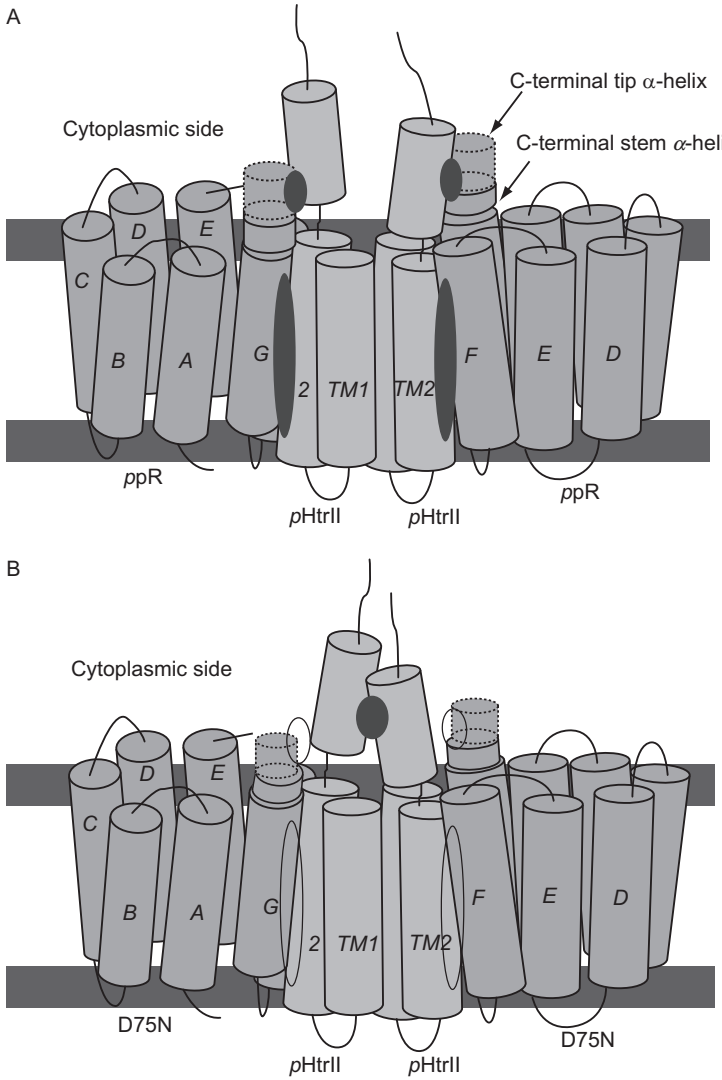

Figure 43 Schematic representation of the manner of interaction of the C-terminal α-helical tip region in *p*pR (a) and D75N (b) with the transmembrane and cytoplasmic α-helices of *p*HtrII(1–159). The helix–helix interaction between the cytoplasmic α-helices is also presented. Elliptical grey areas and open areas show the enhanced and weakened interaction parts, respectively. From Ref. 215 with permission.

DDMAS (Figure 44), is appreciably decreased when *p*pR is bound to *p*HtrII (Figure 44D), while it is increased when D75N which mimics the signalling state is bound to *p*HtrII (Figure 44F). This signal change may be

TABLE 2 Estimated fluctuation changes in the transmembrane and cytoplasmic α-helices for a variety of membrane proteins and their complexes (Hz)[a]

		Retinal proteins			Transducer		
			C-terminal α-helix				
		Transmembrane α-helix	Stem	Tip	Transmembrane α-helix	Cytoplasmic α-helix	Reference
bR	2D crystal	10^2	10^6	10^8			205
bR	Monomer	10^4–10^5	10^6	10^8			206
D85N	Monomer	10^4					207
*p*pR	Monomer	10^4	10^6	10^8			212
*p*pR*/*p*HtrII	2:2 Complex	10^4–10^5	10^6	10^4–10^5			215
*p*pR/*p*HtrII*	2:2 Complex				10^4	$>10^6$	213
D75N*/*p*HtrII	2:2 Complex	10^4–10^5	10^6	10^6			215
D75N/*p*HtrII*	2:2 Complex				10^5	10^5	215

Asterisked proteins are ^{13}C labelled either by [3-^{13}C]Ala or [1-^{13}C]Val.

[a] This is based on the following observations: 10^8 Hz, ^{13}C CPMAS NMR signals are completely suppressed; 10^6 Hz, based on ^{13}C T_2 data; 10^5 Hz, ^{13}C NMR signals of [3-^{13}C]Ala-labelled proteins are preferentially suppressed; 10^4–10^5 Hz, ^{13}C NMR signals of both [3-^{13}C]Ala- and [1-^{13}C]Val-labelled proteins are partially suppressed; 10^4 Hz, ^{13}C NMR signals of [1-^{13}C]Val-labelled proteins are preferentially suppressed.

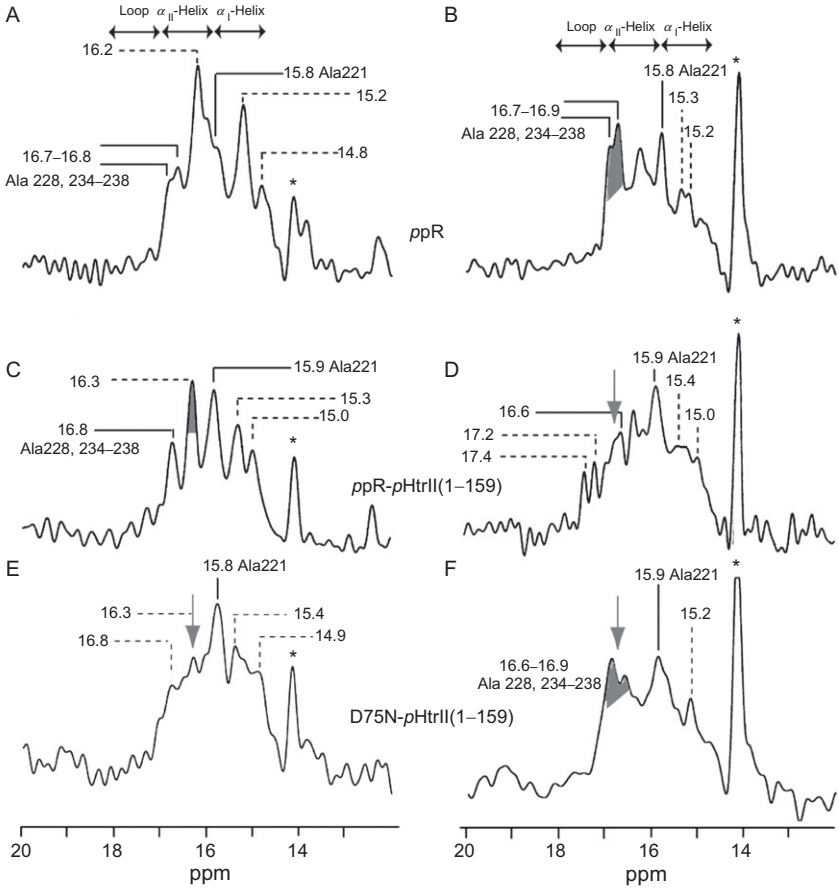

Figure 44 ^{13}C CPMAS (left) and DDMAS (right) NMR spectra of uncomplexed [3-^{13}C]Ala-labelled *p*pR (a and b), *p*pR-*p*HtrII (1–159) (c and d) and D75N-*p*HtrII (1–159) (e and f) reconstituted in egg PC bilayer, respectively. ^{13}C NMR signals from the C-terminal region of *p*pR, *p*pR to *p*pR-*p*HtrII(1–159) and D75N-*p*HtrII (1–159) are shown in the grey (b and f) and arrows (d and f). The resonance peak at 14.1 ppm is the methyl peak of egg PC as shown by the asterisk. From. Ref. 215 with permission.

considered together with the larger dissociation constant of the complex between *p*HtrII and M-like state of *p*pR. The fluctuation frequency of the CP portion of *p*HtrII (Table 2) is lowered when *p*pR is replaced by D75N in the complex with *p*HtrII and the interaction between *p*HtrII (1–159) and *p*pR in the TM region is weakened at the activated receptor (Figure 44A). Then, it is more likely that the helices of the transducer proximate to the membrane, the linker region of *p*HtrII (1–159), interact with each other within the dimer (Figure 44B), which greatly reduces the fluctuation due

to the increase in apparent molecular mass. The association of the linker region of two *p*HtrII transducers is consistent with an earlier observation that the interaction of the E–F loop of *p*pR with *p*HtrII decreases in the light-activated state.

Multi-dimensional ^{13}C NMR spectra were recorded for proteoliposome of uniformly ^{13}C, ^{15}N-labelled *p*pR with the exception of the four dominant residue types (Val, Leu, Phe, and Tyr), which occur in natural abundance U [^{13}C, ^{15}N (V, L, F, Y)]N*p*sRII and its complex with cognate transducer of sensory rhodopsin II (HtrII).[216,217] In total, the resonances are assigned for 98 amino acids, that is, 73% of the sequentially assignable receptor residues mainly at the TMe α-helices.[216] This approach is also extended to the system of the sRII-*p*HtrII complex[217] which turns out to be complementary to the works mainly concerned with the surface structures described above.[212–214] Recently, the structural determination of *p*sRII solubilized in diheptanoylphosphatidylcholine (DHPC) was performed with a backbone r.m.s. deviation of 0.48 Å, based on ^{13}C- or ^{15}N-resolved NOE distance information, supplemented by dihedral angles and hydrogen bonds in the α-helical regions, although the remaining 20 residues of the C-terminal parts are highly flexible and unstructured.[218] The resulting NMR structure agrees well with the previously determined X-ray structures. In these data, however, no indication is given about the presence of the C-terminal α-helix protruding from the bilayer surface as described above. The multi-dimensional NMR approach is further applited to a single lipid-reconstituted, uniformly ^{13}C,^{15}N-labelled sample of sRII from *Anabaena* sp. PCC 7120 (ASR).[219] Backbone and side-chain resonances for approximately 85% of the TM region and for many residues in the loop regions are assigned. H/D exchange experiments reveal the solvent-exposed surface of the protein, which is asymmetrically positioned in the bilayer.

4.1.2.2. Proteorhodopsin Proteorhodopsins are typical retinal-binding light-driven proton pumps of heptahelical architecture they are widely distributed in marine and freshwater bacteria. Green proteorhodopsin (GPR) in a lipid-bound state gives well-resolved multi-dimensional solid-state NMR spectra in samples with different patterns of reverse labeling.[220,221] 3D and 4D sequential chemical shifts are assigned through experiments conducted on a uniformly ^{13}C-, ^{15}N-labelled sample.[220,221] These experiments provide the assignments of 153 residues, with a particularly high density in the TM regions (∼74% of residues). Experimental evidence of mobility is shown for proteorhodopsin in the lipid environment at the protein's termini and of the A–B, C–D and F–G loops, the latter being possibly coupled to the GPR ion-transporting function. A 2D-crystal formation with hexagonal protein packing is observed under a very wide range of conditions, indicating that proteorhodosin (PR) might be also closely packed under native conditions.[222] A low-resolution X-ray

2D projection map reveals a ring-shaped oligomeric assembly of PR. The protein state is analyzed by ^{15}N MAS NMR data on Lys-, Trp- and Met-labelled samples. The chemical shift of the protonated Schiff base is almost identical to those of non-crystalline preparations. 2D crystal formation with hexagonal protein packing is observed under a very wide range of conditions indicating that PR might be also closely packed under native conditions.[223]

4.2. Membrane proteins other than retinal proteins

4.2.1. Multidrug transporters

EmrE (*Escherichia coli* multidrug resistant transporter) is a prototypical example of a small multidrug transporter which removes positively charged aromatic drugs like ethidium, tetraphenylphosphonium or methyl viologen from the cell. It comprises four TM segments and has a molecular weight of about 10 kDa. A 1D ^{13}C CPMAS and 2D PDSD[159] as well as one pulse excitation and refocused INEPT spectra were recorded for u-[^{13}C–^{15}N] EmrE.[224] The sensitivity gains by a factor of 2–2.5 at a temperature of -60 °C as compared with that at 0 °C due to the high mobility of EmrE. The signals recorded via ^{1}H excitation by INEPT for magnetic transfer to ^{13}C or direct excitation are ascribed to the C-terminus of the protein. It is speculated that the increased ^{15}N (and to some extent also ^{13}C) line width is at least partially due to the larger residual dynamics of the protein in the lipid bilayer. The molecular dynamics of another type of the multidrug transporter, the 64-kDa ATP-binding cassette (ABC) multidrug efflux pump LmrA from *Lactococcus lactis*, was studied by the line-shape analysis of ^{2}H solid-state NMR of [^{2}H]Ala-labelled protein within lipid membranes (see Figure 3 for the timescale concerned).[225] The minimal functional unit in the LmrA transporter is the homodimer: each of the monomers is comprised of six TM regions in the amino-terminal hydrophobic domain, followed by a large hydrophilic domain with an ATP-binding site. A comparison of static ^{2}H NMR spectra of full-length LmrA in the resting state and its isolated TM domain reveals a high mobility for the nucleotide binding domains. Their motional freedom is restricted upon ATP binding as seen for LmrA in the complex with AMP-PNP, a nonhydrolyzable ATP analogue. LmrA returns to full motional flexibility in the posthydrolysis, vanadate-trapped state. These experiments provide insight into the molecular dynamics of a full-length ABC transporter during the catalytic cycle.

4.2.2. Membrane enzymes

Diacylglycerol kinase (DGK) from *E. coli* is a small 121 amino-acid, integral membrane protein which catalyses the conversion of diacylglycerol and MgATP to phosphatic acid and MgADP. DGK is homotrimeric,

each monomeric component contains three TM helices. In ^{13}C NMR measurements of [3-^{13}C]Ala-, [1-^{13}C]Val-labelled DGK embedded in 1-palmitoyl-2-oleoyl-*sn*-glycero-3-phosphocholine (POPC) or DPPC bilayers, it is found that the ^{13}C NMR spectra are broadened to yield rather featureless peaks at physiological temperatures, both in DM solution or lipid bilayers at the liquid crystalline phase, due to interference of the motional frequencies of DGK with frequencies of MAS or proton decoupling of 10^4 or 10^5 Hz, respectively.[226] In gel phase lipids, however, up to six distinct ^{13}C NMR peaks are well-resolved due to lowered fluctuation frequencies ($<10^5$ Hz) for the TM region, the amphipathic α-helices and loops. While DGK can be tightly packed in gel phase lipids, it becomes more mobile in the liquid crystalline phase. It appears that acquisition of intermediate frequency backbone motions in the liquid phase, on the microsecond to millisecond time scale, may facilitate the efficient enzymatic activity of DGK. Comparison of ^{15}N-leucine- and ^{13}C uniformly or selectively and extensively (SE)-labelled DGK between proteoliposome and nano-crystalline preparations, however, show that the crystalline samples produce better-resolved spectra than the proteoliposomes.[227] This finding indicates that NMR experiments carried out under physiological conditions are crucially important for understanding the properties of the enzyme in relation to its biological activity. It was also demonstrated that the identification of lipids bound to such membrane-protein crystals is feasible by examination of the ^{31}P MAS NMR. Nevertheless, it seems to be also important to clarify how the dynamic features of this protein are modified by this sort of crystallization. Assignments of peaks for DGK, which is found to be almost exclusively on helical protein in detergent micelles, were made using transverse relaxation-optimized spectroscopy (TROSY)[228]-based pulse sequences.[229]

In *E. coli*, the formation of disulfide bonds in the periplasm is catalysed by DsbB, a 20-kDa integral membrane enzyme comprising of four TM helices and two periplasmic loops to one of which DsbA binds, using the oxidizing power of membrane-embedded quinones. Functionally relevant changes induced by these substrates are revealed by solution NMR measurement[230] in detergent micelles and X-ray diffraction studies.[231]It is further demonstrated that ^{13}C and ^{15}N chemical shift assignments for the majority of the residues in the TM helices are achieved for MAS NMR measurements on a uniformly ^{13}C, ^{15}N-labelled DsbB pellet consisting of contaminating protein and lipid.[232]

4.2.3. Phospholamban

Phospholamban (PLB or PLN) is a single-pass, 52-residue integral membrane protein that regulates myocardial contractility by direct physical interaction with sarco(endo)plasmic reticulum Ca-ATPase (SERCA), a 110-kDa enzyme that maintains calcium homeostasis in the sarcoplasmic

reticulum (SR). PLN assembles spontaneously into a 30-kDa pentamer in the membrane of heart muscle cells.[233] Four structural domains of the ''L-shaped'' monomeric PLN mutant, in which the three TM cysteins have been replaced by A36, F41, and A46 (AFA-PLN) in dodecylphosphocholine (DPC), are identified on the basis of backbone dynamics on the *ps–ns* timescale using $^{1}H/^{15}N$ heteronuclear spectroscopy. These are domain Ia (residues 1–16), the loop (residues 17–22), domain Ib (residues 23–30), and domain II (31–52: TM helix).[234–236] A Curr-Purcell-Meiboom-Gill (CPMG)-based relaxation analysis,[237] used to determine the two-site exchange rate, shows the presence of slow dynamics on the *μs–ms* timescale in domain Ia, the loop, and domain Ib, whereas domain II is more motionally restricted. NMR and electron paramagnetic resonance (EPR) data have demonstrated a dynamic (*μs*-to-*ms*) equilibrium between two conformational states in the CP domain of PLN.[236] These results support the hypothesis that SERCA attracts the CP domain of PLN away from the lipid surface, shifting the pre-existing equilibrium of PLN conformers toward a structure that is poised to interact with the regulatory target. It is also shown, by a polarization inversion spin exchange at the magic angle (PISEMA) experiment in the oriented lipid bilayer, that the CP domain of PLN is helical and makes an angle of $93^\circ \pm 6^\circ$ with respect to the bilayer normal.[238] A through-bond (^{1}H, ^{13}C) transfer based on a refocused INEPT experiment,[159] which selects proton signals with long T_2 relaxation times and hence probes mobile protein segments, shows that a CP domain of [^{13}C,^{15}N]-labelled PLN exhibits a high degree of structural disorder.[239]

In the unphosphorylated PLN pentamer, solution NMR data show that the unusual bellflower-like assembly is held together by leucine/isoleucine zipper motifs along the membrane-spanning helices.[240] The structure reveals a channel-forming architecture that could allow passage of small ions. Alternatively, the CP domain of PLN is stabilized through its association with the phospholipid bilayer surface as studied by ^{31}P and ^{2}H NMR of lipids.[241,242] Solid-state ^{15}N studies on selectively [^{15}N-amide]-labelled PLN embedded inside a mechanically oriented phospholipids support a pinwheel geometry, This contracts with the bellflower structure in micelles and indicates that the orientation of the CP domain of WT-PLN is similar to that reported for the monomeric AFA mutant.[243]

Structural properties of both AFA-PLN and WT-PLN bound to SERCA1a after reconstitution in a functional lipid bilayer environment were examined by ^{13}C solid-state NMR.[241] Chemical-shift assignments in all domains of AFA-PLN provide direct evidence for the presence of two terminal α-helices connected by a linker region of reduced structural order that differs from previous findings on free PLN. A combination of the spectroscopic data with biophysical and biochemical data using flexible protein–protein docking simulations provides a structural basis for understanding the interaction between PLN and SERCa1a.[244] Using a

hybrid of solid and solution NMR restraints, together with molecular dynamics simulations in an explicit lipid environment, it is shown that the N-terminal amphipathic helical domain Ia (1-16) of monomeric PLN rests on the surface of the lipid membrane with the hydrophobic face of domain Ia embedded in the membrane interior.[245]

4.2.4. Integral monotopic and peripheral membrane proteins

4.2.4.1. Integral monotopic membrane proteins Cytochrome P450s (cyt P450s) are a super family of microsomal heamoproteins used for the oxidation of organic substances present as integral monotopic (single TM) membrane proteins.[246] Solid-state NMR is a potentially very useful approach to study such a membrane-bound enzyme in which effective mutual interactions occur with their redox partners cyt P450 reductase (P450R) or cytochrome b_5 (cyto b_5).[247,248] Their truncated forms or bacterial cytosol proteins have been utilized to elucidate their 3D structures by X-ray diffraction or solution NMR measurements. Ramamoorthy and coworkers attempted to explore this problem based on ^{15}N MAS and static experiments on uniformly ^{15}N-labelled holo-cyt b_5 in macroscopically oriented DMPC/DHPC bicelles.[248–251] It is demonstrated that the signals appearing between 100 and 130 ppm originates from the less-rigid residues in the soluble domain as confirmed by a RINEPT experiment,[159] while the signals in the 40–90 ppm region as recorded by a CP experiment are ascribed to the TM helical region. For the latter, ^{15}N heteronuclear isotropic mixing leading to spin exchange via the local field (HIMSELF) experiment for uniformly ^{15}N-labelled cyt b_5.[252] This gives rise to better resolution than the conventional PISEMA,[253] and allows the correlation of the ^{15}N–H dipolar coupling with the ^{15}N chemical shift. Subsequent spectral simulation shows that the tilt of the TM α-helix from the bilayer normal is 13°.

4.2.4.2. Peripheral membrane proteins Peripheral membrane proteins are not integrated but bound to a surface of a biological membrane and are only temporarily associated. The pleckstrin homology (PH) domain of phospholipase C-δ1 (PLC-δ1) is localized at the surface of the plasma membrane via the stereo-selective affinity for the head group of phosphatidylinositol 4,5-bisphosphate (PIP_2) (Figure 45A).[254] This arrangement enables PLC-δ1 to hydrolyze PIP_2 thereby generating the second messengers D-myo-inositol 1,4,5-trisphosphate (IP_3) (Figure 45A) and diacylglycerol which are required for Ca^{2+} mobilization and activation of protein kinase C, respectively. Therefore, structural information about the [3-^{13}C] Ala-labelled PLC-δ1(1–140) PH domain which is most extensively studied as a peripheral membrane protein was examined through its high affinity specific interaction with PIP_2 at the lipid bilayer surface by ^{13}C NMR.[255–258] It is demonstrated that four and five resolved ^{13}C NMR

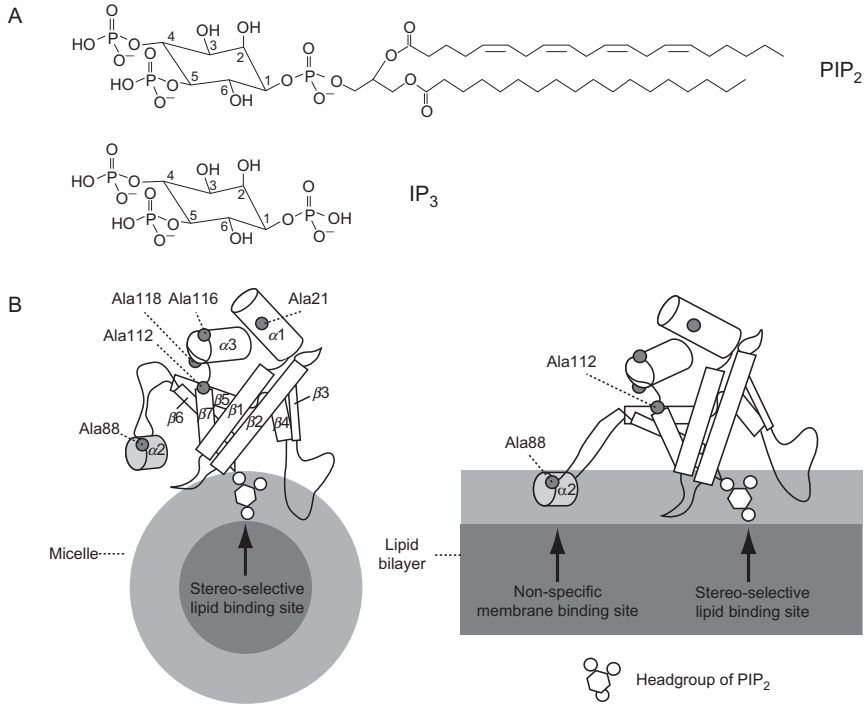

Figure 45 A. Chemical structures of PIP_2 and IP_3. B. Schematic representation of the PLC-δ1 PH domain bound to PIP_2 embedded in micelle (left) and lipid bilayer (right). The micelle and the lipid bilayer are indicated by shaded circle and rectangle, respectively. Hydrophobic inner-layer and interface region between water and the hydrophobic inner layer are coloured deep and pale grey, respectively. Inositol head groups of PIP_2 are represented by hexagons flanked with three circles indicating phosphate groups. Schematic models of the PH domain are constructed based on the X-ray structure of the PLC-δ1 PH domain-IP_3 complex (1MAI). The β-sheets, α-helices and loops are indicated by rectangles, cylinders and solid lines. The α2-helix is highlighted with shade. Alanine residues are indicated by a shaded circles. From Ref. 255 with permission.

signals, as recorded by DDMAS and CPMAS NMR spectra, respectively, are utilized as conformational probes of the present protein system.[255,256] Tuzi et al. found changes in local conformations due to the membrane location, in the vicinity of β5/β6 loop containing Ala88 and the C-terminus of the β7 strand containing Ala112 of this protein, based on their characteristic displacements of [3-^{13}C]Ala-chemical shifts. It is also found that underlying conformational changes of this protein originate from a hydrophobic interaction between the amphipathic α-helix located in the β5/β6 loop and the hydrophobic layer of the membrane through a *non-specific membrane binding site* (Figure 45B, right). Such local conformation,

however, is lost at the surface of PC/phosphatidylserine (PS)/PIP_2, and becomes identical to that of solution structure of the PH domain bound to IP_3. This is because the effect of PS is caused by electrostatic interactions between the protein and PS.[257] Further, it is interesting to note what happens to such *non-specific membrane binding sites* when the PLC-δ1(1–140) PH domain is embedded in detergent micelles of DPC or DM with increased curvature of the water-hydrophobic layer.[255] It turns out that membrane-penetration of the amphipathic α2-helix of the PH domain, which assists the membrane-association of the PH domain dominated by the PIP_2 specific lipid binding site, is not possible in these detergent micelles (Figure 45B, left).[255] This finding is based on the fact that the presence of split and displaced peaks of Ala88 and 112, respectively, in detergents indicates their conformations to be close to those in the PH domain complex with IP_3 as encountered in solution. This means that utilization of the detergent system is not always sufficient to mimic the bilayer system as viewed from its curvature. The cooperative membrane binding mechanism thus obtained, consisting of a stereo-selective lipid binding site and non-specific membrane binding site, is consistent with the previous proposal for a variety of proteins relating to signal transductions.

Myelin basic protein (MBP) is also a peripheral membrane protein that is essential for maintaining the structural integrity of the multilamellar myelin sheath of the central nervous system. A combination of solution and solid-state NMR approaches was utilized on 18.5 kDa [^{13}C,^{15}N]-labelled MBP reconstituted with lipids based on INEPT and high-power decoupling yields spectra for the mobile fragments.[259] To partially circumvent the problem of short transverse relaxation, 3D constant-time correlation experiments (NCOCX, NCACX, CONCACX, and CAN(CO)CX) are able to provide interresidue and intraresidue backbone correlations. These experiments result in partial spectral assignments for mobile fragments of the protein. The mobile fragments are exposed to solvent and are likely to be located outside the lipid bilayer, or in its hydrophilic portion.

5. CONCLUDING REMARKS

We have emphasized here that the dynamic aspects of NMR studies are crucially important for structurally or dynamically heterogeneous systems such as synthetic or natural hydrogels, protein fibrils and membrane proteins. This is in order to characterize their unique chemical, physical and biological properties in terms of a variety of fluctuation frequencies, including high ($>10^8$ Hz) or intermediate (10^4–10^5 Hz) frequency fluctuations. It turns out that the presence of the high-frequency motions, which are readily evaluated by comparative CPMAS and DDMAS studies, is

characteristic of fully hydrated hydrogels of both synthetic or polysaccharide gels. However, a less significant contribution of such motions seems to be related to the formation of a rather brittle type of gel. Protein hydrogels have also proved to be present either at an initial stage of fibrillation or together with several fibrils of amyloid or PrP^cs. In particular, the intermediate frequencies are readily estimated, if any, by the SRI plots against temperature or pH, rather than fluctuation frequency. These fluctuation frequency motions, on the other hand, turn out to be very important in connection with the development of biocompatible materials and for exhibiting the biological functions of several membrane proteins such as photochemical reaction, enzymatic activity, signal transduction, transporter, etc.

It is emphasized that revealing the dynamics as well as the structure (or conformation) based on several types of spin-relaxation times is undoubtedly a unique and indispensable means, only available from NMR techniques at ambient temperature of physiological significance. Usually, the structure data themselves are available also from X-ray diffraction studies in a more refined manner. Indeed, better structural data can be obtained at lower temperature by preventing the unnecessary molecular fluctuations, which are major subjects in this chapter, since structural data can be seriously deteriorated for domains where dynamics are predominant even in the 2D or 3D crystalline state or proteoliposome at ambient temperature. It should be also taken into account that the solubilization of membrane proteins in detergents is an alternative means to study structure in solution NMR. However, it is not always able faithfully to mimick the biomembrane environment, because the interface structure is not always the same between the bilayer and detergent system. This typically occurs in the case of PLC-δ1(1–140) described in Section 4.2.4 and other types of peptide systems.

We have mainly discussed the dynamic aspects of hydrogels, protein fibrils, and membrane proteins by detecting signals from the portions undergoing high or intermediate fluctuation motions by the DDMAS NMR approach. Recently, the refocused INEPT MAS technique has been utilized to detect ^{13}C (or ^{15}N) NMR signals from the above mentioned rather flexible portions. These two approaches are not always e able to detect identical signals. The DDMAS NMR method is able to detect signals from the boarder, between liquid-like and solid-like, portions (Figure 1) in which signals are also broadened by dipolar–dipolar interactions. The INEPT MAS approach, however, selects ^{13}C (or ^{15}N) NMR signals by through-bond magnetization transfer from isotropic ^{1}H NMR signals rather than the above mentioned whole portions. It is anticipated, therefore, that ^{13}C NMR signals of the CP or C-terminal α-helix of bR, ppR, or transducer protruding from the membrane surface might be missed by the refocused INEPT experiment.

ACKNOWLEDGEMENTS

The author thanks Drs. Akira Naito, Izuru Kawamura (Yokohama National University), Satoru Tuzi, Satoru Yamaguchi, Atushi Kira (Himeji Institute of Technology/University of Hyogo), Miya Ishijima-Kamihira (Tohoku University), Yuko Miwa (Toray Research Center, Inc.), Katsuyuki Nishimura, and Michikazu Tanio (Institute for Molecular Science) for their stimulating discussions and help.

REFERENCES

1. K. Dušek (ed.), Polymer networks, *Adv. Polym. Sci.*, 1982, **44,** pp. 1–158.
2. A. H. Clark and S. B. Rose-Murphy, Structural and mechanical property of biopolymer gels. *Adv. Polym. Sci.*, 1987, **83,** 57–192.
3. V. J. Morris, *in*: Functional Properties of Food Macromolecules, J. R. Mitchell and D. A. Ledward (eds.), Elsevier, London, 1986, pp. 121–170.
4. Y. Osada, K. Kajiwara, T. Fushimi, O. Irasa, Y. Hirokawa, T. Matsunaga, T. Shimomura, L. Wang, and H. Ishida (eds.) *In* Gels Handbook, Elsevier, 2001.
5. J. D. Ferry, *Viscoelastic Properties of Polymers*. Wiley, New York, 1980.
6. J. M. Guenet, *Thermoreversible Gelation of Polymers and Biopolymers*. Academic Press, 1992.
7. K. Te Nijenhuis (ed.), Thermoreversible Networks: Viscoelastic Properties and Structure of Gels, *Adv. Polym. Sci.*, 1997, **130,** p. 267.
8. J. Patrick, A. Fairclough and A. I. Norman, *Annu. Rep. Prog. Chem. Sect. C*, 2003, **99,** 243–276.
9. H. Saitô, *ACS Symp. Ser.*, 1981, **150,** 125–147.
10. H. Saitô, *ACS Symp. Ser.*, 1992, **489,** 296–310.
11. H. Saitô, *Annu. Rep. NMR Spectrosc.*, 1995, **31,** 157–170.
12. H. Saitô, H. Shimizu, T. Sakagami, S. Tuzi and A. Naito, *in*: Magnetic Resonance in Food Science, P. S. Belton, I. Delgadillo, A. M. Gil, and G. A. Webb (eds.) Royal Society of Chemistry, London, 1995, pp. 257–271.
13. H. Saitô, *in*: Encyclopedia of Nuclear Magnetic Resonance, D. M. Grant and R. K. Harris (eds.), Wiley, 1996, pp. 3740–3745.
14. H. Saitô, S. Tuzi and A. Naito, *in*: Solid State NMR for Polymers, I. Ando and T. Asakura (eds.), Elsevier, 1998, pp. 891–921.
15. H. Saitô, *in*: Polysaccharides: Structural Diversity and Functional Versatility, S. Dumitru (ed.), 2nd edn., Marcel Dekker, New York, 2005, pp. 253–266.
16. H. Saitô, I. Ando and A. Naito, *Solid State NMR Spectroscopy for Biopolymers, Principles and Application*. Springer, Dordrecht, 2006.
17. K. Kamiguchi, S. Kuroki, Y. Yamane, M. Satoh and I. Ando, *Annu. Rep. NMR Spectrosc.*, 2010, **70,** 159–202.
18. H. Saitô, S. Tuzi, S. Yamaguchi, M. Tanio and A. Naito, *Biochim. Biophys. Acta*, 2000, **1460,** 39–48.
19. H. Saitô, S. Tuzi, M. Tanio and A. Naito, *Annu. Rep. NMR Spectrosc.*, 2002, **47,** 39–108.
20. H. Saitô, S. Yamaguchi, H. Okuda, A. Shiraishi and S. Tuzi, *Solid State Nucl. Magn. Reson.*, 2004, **25,** 5–14.
21. H. Saitô, *Chem. Phys. Lipids*, 2004, **132,** 101–112.
22. H. Saitô, *Annu. Rep. NMR Spectrosc.*, 2006, **57,** 99–175.
23. H. Saitô, *in*: Modern Magnetic Resonance, G. A. Webb (ed.), 2006, pp. 283–289.
24. H. Saitô, Y. Kawase, A. Kira, K. Yamamoto, M. Tanio, S. Yamaguchi, S. Tuzi and A. Naito, *Photchem. Photobiol.*, 2007, **83,** 253–262.
25. H. Saitô and A. Naito, *Biochim. Biophys. Acta*, 2007, **1768,** 3145–3161.

26. D. Suwelack, W. P. Rothwell and J. S. Waugh, *J. Chem. Phys.*, 1980, **73,** 2559–2569.
27. W. P. Rothwell and J. S. Waugh, *J. Chem. Phys.*, 1981, **75,** 2721–2732.
28. A. Naito, A. Fukutani, M. Uitdehaag, S. Tuzi and H. Saitô, *J. Mol. Struct.*, 1998, **441,** 231–241.
29. Y. Miwa, H. Ishida, H. Saitô, M. Tanaka and A. Mochizuki, *Polymer*, 2009, **50,** 6091–6099.
30. H. Saitô, A. Kira, T. Arakawa, M. Tanio, S. Tuzi and A. Naito, *Biochim. Biophys. Acta*, 2010, **1798,** 167–176.
31. A. Allerhand, D. Doddrell and R. Komoroski, *J. Chem. Phys.*, 1971, **55,** 189.
32. J. Schaefer and D. F. S. Natusch, *Macromolecules*, 1972, **5,** 416–427.
33. J. Schaefer, *in*: Topics in Carbon-13 NMR Specroscopy, G. C. Levy (ed.), 1974, Vol. 1, A Wiley-Interscience Publication, pp. 149–208.
34. R. A. Komoroski, *in*: High Resolution NMR Spectroscopy of Synthetic Polymers in Bulk, R. A. Komoroski (ed.), VCH, 1986, pp. 121–155.
35. A. Allerhand and E. Oldfield, *Biochemistry*, 1973, **12,** 3428–3433.
36. H. Saitô and I. C. P. Smith, *Arch. Biochem. Biophys.*, 1973, **158,** 154–163.
37. H. Saitô, T. Ohki, M. Kodama and C. Nagata, *Biopolymers*, 1978, **17,** 2587–2599.
38. J. Schaefer, *Macromolecules*, 1973, **6,** 882–888.
39. J. R. Lyerla and D. A. Torchia, *Biochemistry*, 1975, **14,** 5175–5183.
40. D. A. Torchia, M. A. Hasson and V. C. Hascall, *J. Biol. Chem.*, 1977, **252,** 3617–3625.
41. E. D. Becker, *High Resolution NMR, Theory and Chemical Applications*. 3rd edn., Academic Press, 2000.
42. M. Mehring, *High Resolution NMR Spectroscopy in Solids*. Springer Verlag, New York, 1983.
43. M. Kamihira, A. Naito, K. Nishimura, S. Tuzi and H. Saitô, *J. Phys. Chem.*, 1998, **B102,** 2826–2834.
44. S. Tuzi, K. Shinzawa-Itoh, T. Erata, A. Naito, S. Yoshikawa and H. Saitô, *Eur. J. Biochem.*, 1992, **208,** 713–720.
45. E. O. Stejskal, J. Schaefer, M. D. Sefcik and R. A. McKay, *Macromolecules*, 1981, **14,** 275–279.
46. H. Saitô, R. Tabeta, M. Yokoi and T. Erata, *Bull. Chem. Soc. Jpn.*, 1987, **60,** 4259–4266.
47. H. Saitô, M. Yokoi and Y. Yoshioka, *Macromolecules*, 1989, **22,** 3892–3898.
48. H. Saitô, J. Yamada, Y. Yoshioka, Y. Shibata and T. Erata, *Biopolymers*, 1991, **31,** 933–940.
49. H. Saitô and M. Yokoi, *J. Biochem.*, 1992, **111,** 376–382.
50. H. Saitô, M. Ishida, M. Yokoi and T. Asakura, *Macromolecules*, 1990, **23,** 83–88.
51. H. Saitô, R. Tabeta and M. Yokoi, *Magn. Reson. Chem.*, 1988, **26,** 775–786.
52. D. E. Axelson, *in*: High Resolution NMR Spectroscopy of Synthetic Polymers in Bulk, R. A. Komoroski (ed.), VCH, 1986, pp. 157–245.
53. A. Naito, S. Ganapathy, K. Akasaka and C. A. McDowell, *J. Magn. Reson.*, 1983, **54,** 226–235.
54. Y. Nawata, T. Sakamaki and Y. Iitaka, *Acta Crystallogr. Sect.*, 1974, **B30,** 1047–1053.
55. T. Sakamaki, Y. Iitaka and Y. Nawata, *Acta Crystallogr. Sect.*, 1976, **B32,** 768–774.
56. M. Dobler, *Helv. Chim. Acta*, 1972, **55,** 1371–1384.
57. H. Saitô, R. Tabeta, F. Formaggio, M. Crisma and C. Toniolo, *Biopolymers*, 1988, **27,** 1607–1617.
58. Y. Deslandes, R. H. Marchessault and A. Sarko, *Macromolecules*, 1980, **13,** 1466–1471.
59. H. Saitô, I. Ando and A. Ramamoorthy, *Prog. Nucl. Magn. Reson. Spectrosc.*, 2010, **57,** 181–228.
60. D. M. Rice, R. J. Wittebort, R. G. Griffin, E. Meirovich, E. R. Stimson, Y. C. Meinwald, J. H. Freed and H. A. Scheraga, *J. Am. Chem. Soc.*, 1981, **103,** 7707–7710.
61. A. Naito, M. Kamihira, S. Tuzi and H. Saitô, *J. Phys. Chem.*, 1995, **99,** 12041–12046.
62. M. Kamihira, A. Naito, S. Tuzi and H. Saitô, *J. Phys. Chem.*, 1999, **A103,** 3356–3363.
63. K. Schmidt-Rohr, J. Clauss and H. W. Spiess, *Macromolecules*, 1992, **25,** 3273–3277.

64. M. G. Munowitz, R. G. Griffin, G. Bodenhausen and T. H. Huang, *J. Am. Chem. Soc.*, 1981, **103,** 2529–2533.
65. D. Huster, L. Xiao and M. Hong, *Biochemistry*, 2001, **40,** 7662–7674.
66. M. Hong, X. Yao, K. Jakes and D. Huster, *J. Phys. Chem.*, 2002, **B106,** 7355–7364.
67. S. Macura, Y. Huang, D. Suter and R. R. Ernst, *J. Magn. Reson.*, 1981, **43,** 259.
68. C. Connor, A. Naito, K. Takegoshi and C. A. McDowell, *Chem. Phys. Lett.*, 1985, **113,** 123–128.
69. K. Schmidt-Rohr and H. W. Spiess, *Multidimensional Solid State NMR and Polymers*. Academic Press, London, 1994.
70. E. R. deAzevedo, W. G. Hu, T. J. Bonagamba and K. Schmidt-Rohr, *J. Am. Chem. Soc.*, 1999, **121,** 8411–8412.
71. E. R. deAzevedo, W. G. Hu, T. J. Bonagamba and K. Schmidt-Rohr, *J. Chem. Phys.*, 2000, **112,** 8988–9001.
72. N. Fatkullin and R. Kimmich, *J. Chem. Phys.*, 1994, **101,** 822–832.
73. R. Kimmich and E. Anoardo, *Prog. Nucl. Magn. Reson. Spectrosc.*, 2004, **44,** 257–320.
74. E. Fischer, F. Grinberg, R. Kimmich and S. Hafner, *J. Chem. Phys.*, 1998, **109,** 846–854.
75. S. Stapf, S. Kariyo and B. Blümich, *in*: Modern Magnetic Resonance, G. A. Webb (ed.), Springer, 2006, pp. 1435–1441.
76. J. P. Cohen-Addad, *J. Chem. Phys.*, 1974, **60,** 2440–2453.
77. R. Kimmich, E. Fischer, P. Callaghan and N. Fatkullin, *J. Magn. Reson.*, 1995, **117,** 53–61.
78. P. Sotta, C. Fülber, D. E. Demco, B. Blümich and H. W. Spiess, *Macromolecules*, 1996, **29,** 6222–6230.
79. P. T. Callaghan and E. T. Samulski, *Macromolecules*, 1997, **30,** 113–122.
80. F. Grinberg, M. Garbarczyk and W. Kuhn, *J. Chem. Phys.*, 1999, **111,** 11222–11231.
81. M. Garbarczyk, F. Grinberg, N. Nestle and W. Kuhn, *J. Polym. Sci. B Polym. Phys.*, 2001, **39,** 2207–2216.
82. F. Fechete, D. E. Demco and B. Blümich, *J. Chem. Phys.*, 2003, **118,** 2411–2421.
83. J. Baum and A. Pines, *J. Am. Chem. Soc.*, 1986, **108,** 7447–7454.
84. R. Graf, D. E. Demco, S. Hafner and H. W. Spiess, *Solid State Nucl. Magn. Reson.*, 1998, **12,** 139–152.
85. M. Schneider, L. Gasper, D. E. Demco and B. Blümich, *J. Chem. Phys.*, 1999, **111,** 402–415.
86. K. Saalwächter, P. Ziegler, O. Spykerelle, B. Haidar, A. Vidal and J. U. Sommer, *J. Chem. Phys.*, 2003, **119,** 3468–3482.
87. K. Saalwächter, *J. Am. Chem. Soc.*, 2003, **125,** 14684–14685.
88. K. Saalwächter, *Macromolecules*, 2006, **39,** 3291–3303.
89. K. Saalwächter, *Prog. Nucl. Magn. Reson. Spectrosc.*, 2007, **51,** 1–35.
90. E. O. Stejskal and J. E. Tanner, *J. Chem. Phys.*, 1965, **42,** 288–292.
91. Y. Yamane and S. Kim, *in*: Modern Magnetic Resonance, G. A. Webb (ed.), Springer, 2006, pp. 119–123.
92. J. Götz and R. Hinrichs, *in*: Modern Magnetic Resonance, G. A. Webb (ed.), Springer, 2006, pp. 1691–1697.
93. S. Matsukawa and I. Ando, *Macromolecules*, 1996, **29,** 7136–7140.
94. N. Tanaka, S. Matsukawa, H. Kurosu and I. Ando, *Polymer*, 1998, **39,** 4703–4706.
95. M. W. Duch and D. M. Grant, *Macromolecules*, 1970, **3,** 165–174.
96. R. A. Komoroski, J. Maxfield and L. Mandelkern, *Macromolecules*, 1977, **10,** 545–549.
97. K. Yokota, A. Abe, S. Hosaka, I. Sakai and H. Saitô, *Macromolecules*, 1978, **11,** 95–100.
98. N. A. Peppas, J. Z. Hilt, A. Khademhosseini and R. Langer, *Adv. Mater.*, 2006, **18,** 1345–1360.
99. M. Tanaka, T. Motomura, M. Kawada, T. Anzai, Y. Kasori, T. Shiroya K. Shimura, *et al.*, *Biomaterials*, 2002, **21,** 1471–1481.
100. M. Kobayashi, I. Ando, T. Ishii and S. Amiya, *Macromolecules*, 1995, **28,** 6677–6679.

101. H. Yasunaga, M. Kobayashi and S. Matsukawa, *in*: Solid State NMR of Polymers, Studies in Physical and Theoretical Chemistry, I. Ando and T. Asakura (eds.), 1998, Vol. 84, Elsevier, pp. 737–769, Chapter 20.
102. M. Kobayashi, I. Ando, T. Ishii and S. Amiya, *J. Mol. Struct.*, 1998, **440,** 155–164.
103. J. L. Valentín, D. López, R. Hernández, C. Mijangos and K. Saalwächter, *Macromolecules*, 2009, **42,** 263–272.
104. P. J. Willcox, D. W. Howie, Jr., K. Schmidt-Rohr, D. A. Hoagland, S. P. Gido, S. Pudjijanto, L. W. Kleiner and S. Venkatraman, *J. Polym. Sci. B Polym. Phys.*, 1999, **37,** 3438–3454.
105. R. Ricciardi, F. Auriemma, C. De Rosa and F. Lauprêtre, *Macromolecules*, 2004, **37,** 1921–1927.
106. H. Yasunaga and I. Ando, *J. Mol. Struct.*, 1993, **301,** 129–136.
107. H. Yasunaga and I. Ando, *Polym. Gels Netw.*, 1993, **1,** 83–92.
108. Y. Yamane, M. Kobayashi, H. Kimura, S. Kuroki and I. Ando, *Polymer*, 2002, **43,** 1767–1772.
109. K. Kamiguchi, S. Kuroki, M. Sato and I. Ando, *Macromolecules*, 2008, **41,** 1318–1322.
110. K. Kamiguchi, S. Kuroki, M. Satoh and I. Ando, *Macromolecules*, 2009, **42,** 231–235.
111. B. A. Stone and A. E. Clarke, *Chemistry and Biology of (1 → 3)-β-Glucans*. La Trobe Unversity Press, 1992.
112. T. Harada, *ACS Symp. Ser.*, 1977, **45,** 265.
113. C. T. Chuah, A. Sarko, Y. Deslandes and R. H. Marchessault, *Macromolecules*, 1983, **16,** 1375–1382.
114. H. Saitô, T. Ohki and T. Sasaki, *Biochemistry*, 1977, **16,** 908–914.
115. H. Saitô, E. Miyata and T. Sasaki, *Macromolecules*, 1978, **11,** 1244–1251.
116. H. Saitô, *Magn. Reson. Chem.*, 1986, **24,** 835–852.
117. H. Saitô, Y. Yoshioka, M. Yokoi and J. Yamada, *Biopolymers*, 1990, **29,** 1689–1698.
118. H. Saitô, T. Ohki, N. Takasuka and T. Sasaki, *Carbohydr. Res.*, 1977, **58,** 293–305.
119. H. Saitô, T. Ohki and T. Sasaki, *Carbohydr. Res.*, 1979, **74,** 227–240.
120. H. Saitô, M. Yokoi and Y. Yoshioka, *Macromolecules*, 1989, **22,** 3892–3898.
121. J. Aketagawa, S. Tanaka, H. Tamura, Y. Shibata and H. Saitô, *J. Biochem. (Tokyo)*, 1993, **113,** 683–686.
122. H. Saitô, Y. Yoshioka, N. Uehara, J. Aketagawa, S. Tanaka and Y. Shibata, *Carbohydr. Res.*, 1991, **217,** 181–190.
123. M. J. Gidley, *Macromolecules*, 1989, **22,** 351–358.
124. F. R. Senti and F. R. Witnauer, *J. Am. Chem. Soc.*, 1948, **70,** 1438–1444.
125. H. Saitô, J. Yamada, T. Yukumoto, H. Yajima and R. Endo, *Bull. Chem. Soc. Jpn.*, 1991, **64,** 3528–3537.
126. Y. Takahashi, T. Kumano and S. Nishikawa, *Macromolecules*, 2004, **37,** 6827–6832.
127. S. Arnott, A. Fulmer, W. E. Scott, I. C. M. Dea, R. Moorhouse and D. A. Rees, *J. Mol. Biol.*, 1974, **90,** 269–272.
128. D. A. Torchia and D. L. VanderHart, *J. Mol. Biol.*, 1976, **104,** 315–321.
129. S. K. Sarkar, C. E. Sullivan and D. A. Torchia, *J. Biol. Chem.*, 1983, **258,** 9762–9767.
130. S. K. Sarkar, C. E. Sullivan and D. A. Torchia, *Biochemistry*, 1985, **24,** 2348–2354.
131. A. Veis and K. Payne, *in*: Collagen, M. E. Nimi (ed.), 1988, vol 1, CRC Press, pp. 113–137.
132. H. Saitô and M. Yokoi, *J. Biochem. (Tokyo)*, 1992, **111,** 376–382.
133. D. Reichert, O. Pascui, E. R. De Azevedo, T. J. Bonagamba, K. Arnold and D. Huster, *Magn. Reson. Chem.*, 2004, **42,** 276–284.
134. D. Huster, *Annu. Rep. NMR Spectrosc.*, 2008, **64,** 127–159.
135. M. Hong, J. D. Gross and R. G. Griffin, *J. Phys. Chem.*, 1997, **101,** 5869–5874.
136. P. Zhu, J. Xu, N. Sahar, M. D. Morris, D. H. Kohn and A. Ramamoorthy, *J. Am. Chem. Soc.*, 2009, **131,** 17064–17065.

137. J. Xu, P. Zhu, Z. Gan, N. Sahar, N. Tecklenburg, M. D. Morris, D. H. Kohn and A. Ramamoorthy, *J. Am. Chem. Soc.*, 2010, **132,** 11504–11509.
138. S. Frey, R. P. Richter and D. Görlich, *Science*, 2006, **314,** 815–817.
139. C. Ader, S. Frey, W. Maas, H. B. Schmidt, D. Görlich and M. Baldus, *Proc. Natl. Acad. Sci. USA*, 2010, **107,** 6281–6285.
140. H. Schwalbe and J. Wirmer, *in*: Modern Magnetic Resonance, G. A. Webb (ed.), 2006, pp. 1369–1373.
141. A. T. Petkova, Y. Ishii, J. J. Balbach, O. N. Antzutkin, R. D. Leapman, F. Delaglio and R. Tycko, *Proc. Natl. Acad. Sci. USA*, 2002, **99,** 16742–16747.
142. R. Tycko, *Biochemistry*, 2003, **42,** 3151–3159.
143. R. Tycko, *Curr. Opin. Struct. Biol.*, 2004, **14,** 96–103.
144. R. Tycko, *Q. Rev. Biophys.*, 2006, **39,** 1–55.
145. C. P. Jaroniec, C. E. MacPhee, N. S. Astrof, C. M. Dobson and R. G. Griffin, *Proc. Natl. Acad. Sci. USA*, 2002, **99,** 16748–16753.
146. C. P. Jaroniec, C. E. MacPhee, V. S. Bajaj, M. T. McMahon, C. M. Dobson and R. G. Griffin, *Proc. Natl. Acad. Sci. USA*, 2004, **101,** 711–716.
147. H. Heise, W. Hoyer, S. Becker, O. C. Andronesi, D. Riedel and M. Baldus, *Proc. Natl. Acad. Sci. USA*, 2005, **102,** 15871–15876.
148. K. D. Kloepper, D. H. Zhou, Y. Li, K. A. Winter, J. M. George and C. M. Rienstra, *J. Biomol. NMR*, 2007, **39,** 197–211.
149. S. B. Prusiner, *Science*, 1982, **216,** 136–144.
150. G. A. Wells, A. C. Scott, C. T. Johnson, R. F. Gunning, R. D. Hancock, M. Jeffrey, M. Dawson and R. Bradley, *Vet. Rec.*, 1987, **121,** 419–420.
151. R. G. Will, J. W. Ironside, M. Zeidler, K. Estibeiro, S. N. Cousens, P. G. Smith, A. Alperovitch, S. Poser, M. Pocchiari and A. Hofman, *Lancet*, 1996, **347,** 921–925.
152. A. B. Siemer, A. A. Arnold, C. Ritter, T. Westfeld, M. Ernst, R. Riek and B. H. Meier, *J. Am. Chem. Soc.*, 2006, **128,** 13224–13228.
153. C. Ritter, M. L. Maddelein, A. B. Siemer, T. Lührs, M. Ernst, B. H. Meier, S. Saupe and R. Riek, *Nature*, 2005, **435,** 844–848.
154. C. Wasmer, A. Lange, H. Van Melckebeke, A. B. Siemer, R. Riek and B. H. Meier, *Science*, 2008, **319,** 1523–1526.
155. C. Wasmer, A. Schütz, A. Loquet, C. Buhtz, J. Greenwald, R. Riek, A. Böckmann and B. H. Meier, *J. Mol. Biol.*, 2009, **394,** 119–127.
156. A. Lange, S. Luca and M. Baldus, *J. Am. Chem. Soc.*, 2002, **124,** 9704–9705.
157. A. Lange, S. Becker, K. Seidel, K. Giller, O. Pongs and M. Baldus, *Angew. Chem. Int. Ed. Engl.*, 2005, **44,** 2089–2092.
158. N. M. Szeverenyi, M. J. Sullivan and G. E. Maciel, *J. Magn. Reson.*, 1982, **47,** 462.
159. D. P. Burum and R. R. Ernst, *J. Magn. Reson.*, 1980, **39,** 163–168.
160. C. M. Dobson, *Trends Biochem. Sci.*, 1999, **24,** 329–332.
161. J. K. Kelly, *Curr. Opin. Struc. Biol.*, 1998, **8,** 101–106.
162. P. Tompa, *FEBS J.*, 2009, **276,** 5406–5415.
163. M. Kamihira, A. Naito, S. Tuzi, A. Y. Nosaka and H. Saitô, *Protein Sci.*, 2000, **9,** 867–877.
164. A. Naito, M. Kamihira, R. Inoue and H. Saitô, *Magn. Reson. Chem.*, 2004, **42,** 247–257.
165. M. Kamihira, Y. Ohsiro, S. Tuzi, A. Y. Nosaka, H. Saitô and A. Naito, *J. Biol. Sci.*, 2003, **278,** 2859–2865.
166. M. Kamihira, H. Saitô and A. Naito, *in*: Modern Magnetic Resonance, G. A. Webb (ed.), 2006, pp. 7–13.
167. K. Iqbal and I. G.- Iqbal, *J. Cell. Mol. Med.*, 2008, **12,** 38–55.
168. M. Margittai and R. Langen, *Proc. Natl. Acad. Sci. USA*, 2004, **101,** 10278–10283.
169. L. J. Juszczak, *J. Biol. Chem.*, 2004, **279,** 7395–7404.
170. S. M. Patil, S. Xu, S. R. Sheftic and A. Alexandrescu, *J. Biol. Chem.*, 2009, **284,** 11982–11991.

171. I. T. Yonemoto, G. A. Kroon, H. Jane Dyson, W. E. Balch and J. W. Kelly, *Biochemistry*, 2008, **47,** 9900–9910.
172. S. Luca, W.-M. Yau, R. Leapman and R. Tycko, *Biochemistry*, 2007, **47,** 13505–13522.
173. J. D. Knight, J. A. Hebda and A. D. Mranker, *Biochemistry*, 2006, **45,** 9496–9508.
174. R. P. R. Nanga, J. R. Brender, J. Xu, K. Hartman, V. Subramanian and A. Ramamoorthy, *J. Am. Chem. Soc.*, 2009, **131,** 8252–8261.
175. R. P. R. Nanga, J. R. Brender, S. Vivekanandan, N. Popovych and A. Ramamoorthy, *J. Am. Chem. Soc.*, 2009, **131,** 17972–17979.
176. N. Grigorieff, T. A. Ceska, K. H. Downing, J. M. Baldwin and R. Henderson, *J. Mol. Biol.*, 1996, **259,** 393–421.
177. E. Pebay-Peyroula, G. Rummel, J. P. Rosenbusch and E. M. Landau, *Science*, 1997, **277,** 1676–1681.
178. H. Luecke, H. T. Richter and J. K. Lanyi, *Science*, 1998, **280,** 1934–1937.
179. H. Saitô, S. Yamaguchi, H. Okuda, A. Shiraishi and S. Tuzi, *Solid State Nucl. Magn. Reson.*, 2004, **25,** 5–14.
180. S. Tuzi, S. Yamaguchi, M. Tanio, H. Konishi, S. Inoue, A. Naito, R. Needleman, J. K. Lanyi and H. Saitô, *Biophys. J.*, 1999, **76,** 1523–1531.
181. H. Saitô, Y. Kawase, A. Kira, K. Yamamoto, M. Tanio, S. Yamaguchi, S. Tuzi and A. Naito, *Photochem. Photobiol.*, 2007, **83,** 253–262.
182. S. Tuzi, J. Hasegawa, R. Kawaminami, A. Naito and H. Saitô, *Biophys. J.*, 2001, **81,** 425–434.
183. S. Kimura, A. Naito and H. Saitô, *Biopolymers*, 2001, **58,** 78–88.
184. H. Saitô and I. Ando, *Annu. Rep. NMR Spectrosc.*, 1989, **21,** 209–290.
185. M. Tanio, S. Inoue, K. Yokota, T. Seki, S. Tuzi, R. Needleman, J. K. Lanyi, A. Naito and H. Saitô, *Biophys. J.*, 1999, **77,** 431–442.
186. H. Saitô, J. Mikami, S. Yamaguchi, M. Tanio, A. Kira, T. Arakawa, K. Yamamoto and S. Tuzi, *Magn. Reson. Chem.*, 2004, **42,** 218–230.
187. H. Saitô, R. Kawaminami, M. Tanio, T. Arakawa, S. Yamaguchi and S. Tuzi, *Spectroscopy*, 2002, **16,** 107–120.
188. I. Kawamura, M. Ohmine, J. Tanabe, S. Tuzi, H. Saitô and A. Naito, *Biochim. Biophys. Acta*, 2007, **1768,** 3090–3097.
189. S. Yamaguchi, S. Tuzi, K. Yonebayashi, A. Naito, R. Needleman, J. K. Lanyi and H. Saitô, *J. Biochem. (Tokyo)*, 2001, **129,** 373–382.
190. S. Tuzi, A. Naito and H. Saitô, *J. Mol. Struct.*, 2003, **654,** 205–214.
191. A. Kira, M. Tanio, S. Tuzi and H. Saitô, *Eur. Biophys. J.*, 2004, **33,** 580–588.
192. S. Yamaguchi, K. Yonebayashi, H. Konishi, S. Tuzi, A. Naito, J. K. Lanyi, R. Needleman and H. Saitô, *Eur. J. Biochem.*, 2001, **268,** 2218–2228.
193. K. Yonebayashi, S. Yamaguchi, S. Tuzi and H. Saitô, *Eur. Biophys. J.*, 2003, **32,** 1–11.
194. D. A. Torchia and J. R. Lyerla, *Biopolymers*, 1974, **13,** 97–114.
195. D. S. Wishart, C. G. Bigam, A. Holm, R. S. Hodges and B. D. Sykes, *J. Biomol. NMR*, 1995, **5,** 67–81.
196. P. Barré, S. Yamaguchi, H. Saitô and D. Huster, *Eur. Biophys. J.*, 2003, **32,** 578–584.
197. S. Checover, Y. Maranz, E. Nachliel, M. Gutaman, M. Pfeifer, J. Titor, D. Oesterhelt and N. A. Dencher, *Biochemistry*, 2001, **40,** 4281–4292.
198. H. Saitô, S. Yamaguchi, K. Ogawa, S. Tuzi, M. Márquez, C. Sanz and E. Padrós, *Biophys. J.*, 2004, **86,** 1673–1681.
199. S. Yamaguchi, S. Tuzi, M. Tanio, A. Naito, J. K. Lanyi, R. Needleman and H. Saitô, *J. Biochem. (Tokyo)*, 2000, **127,** 861–869.
200. I. Kawamura, J. Tanabe, M. Ohmine, S. Yamaguchi, S. Tuzi and A. Naito, *Photochem. Photobiol.*, 2009, **85,** 624–630.
201. H. Kamikubo, T. Oka, Y. Imamoto, F. Tokunaga, J. K. Lanyi and M. Kataoka, *Biochemistry*, 1997, **36,** 12282–12287.
202. Y. Kawase, M. Tanio, A. Kira, S. Yamaguchi, S. Tuzi, A. Naito, M. Kataoka, J. K. Lanyi, R. Needleman and H. Saitô, *Biochemistry*, 2000, **39,** 14472–14480.

203. B. Sternberg, C. L'Hostis, C. A. Whiteway and A. Watts, *Biochim. Biophys. Acta*, 1992, **1108,** 21–30.
204. M. K. Krebs and T. A. Isenbarger, *Biochim. Biophys. Acta*, 2000, **1460,** 15–26.
205. H. Saitô, T. Tsuchida, K. Ogawa, T. Arakawa, S. Yamaguchi and S. Tuzi, *Biochim. Biophys. Acta*, 2002, **1565,** 97–106.
206. H. Saitô, K. Yamamoto, S. Tuzi and S. Yamaguchi, *Biochim. Biophys. Acta*, 2003, **1616,** 127–135.
207. K. Yamamoto, S. Tuzi, H. Saitô, I. Kawamura and A. Naito, *Biochim. Biophys. Acta*, 2006, **1758,** 181–189.
208. M. Kamihira and A. Watts, *Biochemistry*, 2006, **45,** 4304–4313.
209. J. K. Lanyi, *J. Struct. Biol.*, 1999, **124,** 164–178.
210. W. D. Hoff, K. W. Jung and J. L. Spudich, *Annu. Rev. Biophys. Biomol. Struct.*, 1997, **26,** 223–258.
211. R. Seidel, B. Scharf, M. Gautel, K. Kleine, D. Oesterhelt and M. Engelhard, *Proc. Natl. Acad. Sci. USA*, 1995, **92,** 3036–3040.
212. T. Arakawa, K. Shimono, S. Yamaguchi, S. Tuzi, Y. Sudo, N. Kamo and H. Saitô, *FEBS Lett.*, 2003, **536,** 237–240.
213. S. Yamaguchi, K. Shimono, Y. Sudo, S. Tuzi, A. Naito and N. Kamo, *Biophys. J.*, 2004, **86,** 3131–3140.
214. I. Kawamura, Y. Ikeda, Y. Sudo, M. Iwamoto, K. Shimono, S. Yamaguchi, S. Tuzi, H. Saitô, N. Kamo and A. Naito, *Photochem. Photobiol.*, 2007, **83,** 339–345.
215. I. Kawamura, H. Yoshida, Y. Ikeda, S. Yamaguchi, S. Tuzi, H. Saitô, N. Kamo and A. Naito, *Photochem. Photobiol.*, 2008, **84,** 921–930.
216. M. Etzkorn, S. Martell, O. C. Andronesi, K. Seidel, M. Engelhard and M. Baldus, *Angew. Chem. Int. Ed. Engl.*, 2007, **46,** 459–462.
217. M. Etzkorn, K. Seidel, L. Li, S. Martell, M. Geyer, M. Engelhard and M. Baldus, *Structure*, 2010, **18,** 293–300.
218. A. Gautier, H. R. Mott, M. J. Bostock, J. P. Kirkpatrick and D. Nietlispach, *Nat. Struct. Mol. Biol.*, 2010, **17,** 768–774.
219. L. Shi, I. Kawamura, Jung Kwang-Hwan, L. S. Brown and V. Ladizhansky, *Angew. Chem. Int. Ed. Engl.*, 2010, **49,** 1–5.
220. L. Shi, E. M. R. Lake, M. A. M. Ahmed, L. S. Brown and V. Ladizhansky, *Biochim. Biophys. Acta*, 2009, **1788,** 2563–2574.
221. L. Shi, M. A. M. Ahmed, W. Zhang, G. Whited, L. S. Brown and V. Ladizhansky, *J. Mol. Biol.*, 2009, **386,** 1078–1093.
222. S. Shastri, J. Vonck, N. Pfeger, W. Haase, W. Kuehlbrandt and C. Glaubitz, *Biochim. Biophys. Acta*, 2007, **1768,** 3012–3019.
223. N. Pfleger, A. C. Wörner, J. Yang, S. Shastri, U. A. Helllmich, L. Aslimovska, M. S. M. Marier and C. Glaubitz, *Biochim. Biophys. Acta*, 2009, **1787,** 697–705.
224. V. Agarwal, U. Fink, S. Schuldiner and B. Reif, *Biochim. Biophys. Acta*, 2007, **1768,** 3036–3043.
225. A. Siarheyeva, J. J. Lopez, I. Lehner, U. A. Hellmich, H. W. van Veen and C. Glaubitz, *Biochemistry*, 2007, **46,** 3075–3083.
226. S. Yamaguchi, S. Tuzi, J. U. Bowie and H. Saitô, *Biochim. Biophys. Acta*, 2004, **1698,** 97–105.
227. M. Lorch, S. Faham, C. Kaiser, I. Weber, A. J. Mason, J. U. Bowie and C. Glaubitz, *Chembiochem*, 2005, **6,** 1693–1700.
228. K. Pervushin, R. Riek, G. Wider and K. Wuthrich, *Proc. Natl. Acad. Sci. USA*, 1997, **94,** 12366–12371.
229. K. Oxenoid, H. J. Kim, J. Jacob, F. D. Sönnichsen and C. R. Sanders, *J. Am. Chem. Soc.*, 2004, **126,** 5048–5049.

230. Y. Zhou, T. Cierpicki, R. H. Flores Jimenez, S. M. Lukasik, J. F. Ellena, D. S. Cafiso, H. Kadokura, J. Beckwith and J. H. Bushweller, *Mol. Cell*, 2008, **31,** 896–908.
231. K. Inaba, S. Murakami, A. Nakagawa, H. Iida, M. Kinjo, K. Ito and M. Suzuki, *EMBO J.*, 2009, **28,** 779–791.
232. Y. Li, D. H. Berthold, R. B. Gennis and C. D. Rienstra, *Protein Sci.*, 2008, **17,** 199–204.
233. D. H. MacLennan and E. G. Kranias, *Nat. Rev. Mol. Cell Biol.*, 2003, **4,** 566–577.
234. J. Zamoon, A. Mascioni, D. D. Thomas and G. Veglia, *Biophys. J.*, 2003, **85,** 2589–2598.
235. E. E. Metcalfe, J. Zamoon, D. D. Thomas and G. Veglia, *Biophys. J.*, 2004, **87,** 1205–1214.
236. J. Zamoon, F. Nitu, C. Karim, D. D. Thomas and G. Veglia, *Proc. Natl. Acad. Sci. USA*, 2005, **102,** 4747–4752.
237. Z. Luz and S. Meiboom, *J. Chem. Phys.*, 1963, **39,** 366–370.
238. N. J. Traaseth, J. J. Buffy, J. Zamoon and G. Veglia, *Biochemistry*, 2006, **45,** 13827–13834.
239. O. C. Andronesi, S. Becker, K. Seidel, H. Heise, H. S. Young and M. Baldus, *J. Am. Chem. Soc.*, 2005, **127,** 12965–12974.
240. K. Oxenoid and J. J. Chou, *Proc. Natl. Acad. Sci. USA*, 2005, **102,** 10870–10875.
241. J. C. Clayton, E. Hughes and D. A. Middleton, *Biochemistry*, 2005, **44,** 17016–17026.
242. S. Abu-Baker and G. A. Lorigan, *Biochemistry*, 2006, **45,** 13312–13322.
243. S. Abu-Baker, J. X. Lu, S. Chu, K. K. Shetty, P. L. Gor'kov and G. A. Lorigan, *Protein Sci.*, 2007, **16,** 2345–2349.
244. K. Seidel, O. C. Andronesi, J. Krebs, C. Griesinger, H. S. Young, S. Becker and M. Baldus, *Biochemistry*, 2008, **47,** 4369–4376.
245. N. J. Traaseth, L. Shi, R. Verardi, D. G. Mullen, G. Barany and G. Veglia, *Proc. Natl. Acad. Sci. USA*, 2009, **106,** 10165–10170.
246. P. R. Ortiz de Montellano, *Cytochrome P450: Structure, Mechanism, and Biochemistry*. Kluwer Academic/Plenum Publishers, New York, 2005.
247. S.-C. Im and L. Waskell, *Arch. Biochem. Biophy.*, 2011, **507,** 144–153.
248. U. H. N. Dürr, L. Waskell and A. Ramamoorthy, *Biochim. Biophys. Acta*, 2007, 3235–3259.
249. U. H. N. Dürr, K. Yamamoto, S. C. Im, L. Waskell and A. Ramamoorthy, *J. Am. Chem. Soc.*, 2007, **129,** 6670–6671.
250. J. Xu, U. H. N. Dürr, S. C. Im, Z. Gan, L. Waskell and A. Ramamoorthy, *Angew. Chem. Int. Ed. Engl.*, 2008, **47,** 7864–7867.
251. R. Soong, P. E. S. Smith, J. Xu, K. Yamamoto, S.-C. Im, L. Waskell and A. Ramamoorthy, *J. Am. Chem. Soc.*, 2010, **132,** 5779–5788.
252. S. V. Dvinskikh, K. Yamamoto and A. Ramamoorthy, *J. Am. Chem. Soc.*, 2006, **128,** 6326–6327.
253. C. H. Wu, A. Ramamoorthy and S. J. Opella, *J. Magn. Reson. A*, 1994, **109,** 270.
254. P. Várnai, X. Lin, S. Bong Lee, G. Tuymetova, T. Bondeva, A. Spät, S. G. Rhee, G. Hajnóczky and T. Balla, *J. Biol. Chem.*, 2002, **277,** 27412–27422.
255. N. Uekama, T. Aoki, T. Maruoka, S. Kurisu, A. Hatakeyama, S. Yamaguchi, M. Okada, H. Yagisawa, K. Nishimura and S. Tuzi, *Biochim. Biophys. Acta*, 2009, **1788,** 2575–2583.
256. S. Tuzi, N. Uekama, M. Okada, S. Yamaguchi, H. Saitô and H. Yagisawa, *J. Biol. Chem.*, 2003, **278,** 28019–28025.
257. S. Tuzi, N. Uekama, M. Okada and H. Yagisawa, *in*: Modern Magnetic Resonance, G. A. Webb (ed.), Springer, 2006, pp. 295–299.
258. N. Uekama, T. Sugita, M. Okada, H. Yagisawa and S. Tuzi, *FEBS J.*, 2007, **274,** 177–187.
259. L. Zhong, V. V. Bamm, M. A. M. Ahmed, G. Harauz and V. Ladizhansky, *Biochim. Biophys. Acta*, 2007, **1768,** 3193–3205.

CHAPTER 2

Carbon-13 Heteronuclear Longitudinal Spin Relaxation for Geometrical (and Stereochemical) Determinations in Small or Medium Size Molecules

Daniel Canet,[*,1] **Sabine Bouguet-Bonnet,**[*] **Sébastien Leclerc,**[†] and **Mehdi Yemloul**[*]

Contents

1. Introduction 90
2. Overview of Longitudinal Nuclear Spin Relaxation 92
   - 2.1. Dipolar interaction 93
   - 2.2. Chemical shift anisotropy 94
3. Cross-Relaxation (and Cross-Correlation): Solomon Equations 96
   - 3.1. Simple Solomon equations 96
   - 3.2. Longitudinal spin order: Extended Solomon equations 99
4. Spectral Densities 101
   - 4.1. Isotropic tumbling of a rigid molecule 102
   - 4.2. Anisotropic tumbling of a rigid molecule 103
   - 4.3. Local motions: The model free approach 105
5. Experimental Procedures 106
   - 5.1. Measurement of ^{13}C longitudinal relaxation time 107
   - 5.2. Measurement of the NOE factor 108

* Méthodologie RMN (CRM2; UMR 7036, UHP-CNRS), Faculté des Sciences et Techniques, B.P. 239, Vandœuvre-lès-Nancy (cedex), France
† LEMTA (UMR 7563, Nancy-Université-CNRS), B.P. 160, Vandoeuvre-lès-Nancy (cedex), France
[1] Corresponding author: Daniel.Canet@crm2.uhp-nancy.fr

Annual Reports on NMR Spectroscopy, Volume 74
ISSN 0066-4103, DOI: 10.1016/B978-0-08-097072-1.00002-9

5.3. The HOESY (Heteronuclear Overhauser Effect Spectroscopy) experiment 110
6. Examples 114
6.1. Stereo and conformational studies 114
6.2. Geometrical determinations 117
7. Conclusion 121
Acknowledgement 121
References 122

Abstract

Owing to an extremely abundant literature making use of spin relaxation for structural studies, this review is limited to carbon-13 spectroscopy, to small or medium size molecules, to stereochemical and preferably geometrical determinations. The parameter of choice is evidently the Nuclear Overhauser effect (NOE) because it depends exclusively on the dipolar interaction mechanism, thus on $1/r^6$, where r is the distance between the two interacting spins. However, it depends also on the dynamical features of the system under investigation which must be characterized prior to any attempt for obtaining geometrical or stereochemical information. Therefore, this review is devoted not only to $^1H–^{13}C$ NOE but, more generally, to ^{13}C longitudinal relaxation. After comprehensive theoretical developments, experimental methods presently available will be presented. The latter include the usual gated decoupling experiment and pulse experiments of the HOESY (Heteronuclear Overhauser Effect SpectroscopY) family. These pulse experiments, which imply carbon-13 observation, can be one-dimensional, selective one-dimensional or two-dimensional. The emphasis will be put on the interpretation which is different according to the occurrence or not of extreme narrowing conditions. Along with a literature survey, some selected examples will be presented in detail in order to illustrate the potentiality of the method.

Key Words: Carbon-13 spin relaxation, T_1 Measurements, Nuclear Overhauser effect, Rotation-diffusion tensor, HOESY experiments

1. INTRODUCTION

Spin relaxation in NMR is known to provide information about the dynamics of molecular entities and possibly about molecular geometry or electron distribution. Generally, dynamical information is obtained if the tensor of the relevant relaxation mechanism is known from independent determinations. Conversely, if parameters describing the dynamics of the considered molecule have been deduced beforehand, geometrical parameters may be derived. Only in particular situations, one can hope to access both types of parameters (dynamical and geometrical). For

instance, this can occur when relaxation parameters become frequency dependent (i.e. dependent on the static magnetic field value at which measurements are performed). This method, sometimes dubbed ''relaxometry'', may yield, independently of the relaxation mechanism details, a so-called ''spectral density mapping'' which contains the major dynamical features of the considered molecule. In turn, when inserted in the theoretical expression of a given relaxation rate (the inverse of the corresponding relaxation time), it can provide some geometrical parameters.

The dipolar interaction (or, in other terms, the interaction between the magnetic moments associated with two nuclear spins) is the relaxation mechanism of choice when one attempts to access inter-atomic distances (and sometimes bond angles). As it will be explained later, this mechanism brings a contribution to relaxation rates proportional to $1/r^6$, where r is the distance between the two interacting spins. The problem is that the two usual relaxation times depend on other relaxation mechanisms and that it is not always easy to separate the dipolar contribution. Let us recall that the two usual relaxation times include T_1, the longitudinal or spin–lattice relaxation time, which refers to the recovery of the longitudinal nuclear magnetization component (the component along the static magnetic field direction) and T_2, the transverse or spin–spin relaxation time, which refers to the decay of nuclear magnetization components perpendicular to B_0, the static magnetic field. T_1 and T_2 are involved in Bloch equations[1] which predict a mono-exponential evolution of the nuclear magnetization components. It turns out that, when two spins ½, A and B, are coupled by dipolar interactions, their *longitudinal* relaxation is no longer mono-exponential. The longitudinal components of their magnetizations (or rather their polarizations) are coupled by a cross-relaxation rate denoted by σ_{AB} which depends *solely* on their *mutual dipolar interaction*. Hence, the interest brought to this parameter from which arises the so-called nuclear Overhauser effect[2] (NOE) from Overhauser who discovered that polarization of an electron spin could be partly transferred to a nuclear spin through a cross-relaxation rate. Note that we are interested here in mutual transfers from one nuclear spin to another nuclear spin. Of course, there is an enormous literature about proton–proton NOE, especially through the NOESY[3] (Nuclear Overhauser Effect SpectroscopY) two-dimensional experiment. The latter is routinely used for determining distance correlations in all types of molecules, noticeably in macromolecules of biological interest (proteins, nucleic acids,...), these correlations being invaluable in view of determining, for instance, the tertiary structure of proteins. In the present review, we shall limit ourselves to ^{13}C–^{1}H NOE and more especially to the exploitation of cross-relaxation rates in view of geometrical (or stereochemical) determinations. This means that we also disregard the classical use of the heteronuclear NOE factor which enables us to evaluate the amount of non-dipolar contributions to the

longitudinal relaxation rates.[4] For achieving such an objective, a firm theoretical background is required. It will be provided in Section 2 by a brief overview of longitudinal nuclear spin relaxation and, in Section 3, by the presentation of Solomon equations which constitute the basis of NOE studies. We shall also see in this section that, besides cross-relaxation rates, cross-correlation rates, which couple polarizations and longitudinal order, can be accounted for in extended Solomon equations. In Section 4, we shall concentrate on spectral densities which represent the dynamical part of cross-relaxation or cross-correlation rates and which must be considered carefully if geometrical or stereochemical information has to be derived from cross-relaxation or cross-correlation rates. Sections 3 and 4 represent actually a sort of manual for interpreting heteronuclear (intra-molecular) proton–carbon-13 relaxation data. Experimental procedures for measuring ^{13}C–^{1}H cross-relaxation or cross-correlation rates will be presented in Section 5, while some selected examples will be detailed in Section 6 along with a survey of literature on the subject of the present review.

2. OVERVIEW OF LONGITUDINAL NUCLEAR SPIN RELAXATION[5,6]

At thermal equilibrium, the nuclear magnetization M_0 lies along the B_0 direction, generally denoted as z. When nuclear magnetization has been taken out from its equilibrium state (with the help of a radio-frequency field), its longitudinal component M_z tends to recover toward M_0. As for any physical system, this is a relaxation phenomenon which should originate from a perturbation comparable to the radio-frequency field which has been responsible for the non-equilibrium situation. The latter is time dependent and perfectly coherent. Moreover, it acts at a well defined frequency. Conversely, a given nuclear spin is subjected within the sample to randomly fluctuating magnetic fields arising from other spins or from whatever interaction that the considered spin could experience. These randomly fluctuating fields $b(t)$ could play the same role as radio-frequency field, but in a reverse way, in order to restore the longitudinal magnetization toward its equilibrium value. These random fields are effectively time dependent with a zero mean value: $\overline{b(t)} = 0$ (actually, the bar denotes an ensemble average). They should also present some degree of coherence which can be evaluated by the so-called correlation function $\overline{b(t)b(0)}$. This can be seen from the following *a contrario* argument: if the random field at time t is independent of the random field at time zero, one has $\overline{b(t)b(0)} = \overline{b(t)}\,\overline{b(0)} = 0$. Thus the correlation function is the key to the efficiency of a given relaxation mechanism. It remains to determine at which frequencies this correlation function is active. This

feature is deduced from the Fourier transform of the correlation function. This latter quantity is called *spectral density* and can be expressed as

$$J(\omega) \propto \int_{-\infty}^{+\infty} \overline{b(t)b(0)} e^{-i\omega t} dt. \quad (1)$$

As we shall see, all relaxation rates are expressed as linear combinations of spectral densities. We shall retain the two relaxation mechanisms which are involved in the present study: the dipolar interaction and the so-called chemical shift anisotropy (csa) which can be important for carbon-13 relaxation. We shall disregard all other mechanisms because it is very likely that they will not affect carbon-13 relaxation. Let us denote by R_1 the inverse of T_1. R_1 governs the recovery of the longitudinal component of polarization, I_z, and, of course, the usual nuclear magnetization which is simply the nuclear polarization times the gyromagnetic constant λ. The relevant evolution equation is one of the famous Bloch equations,[1] valid, in principle, for a single spin but which, in many cases, can be used as a first approximation.

$$\frac{dI_z}{dt} = -R_1(I_z - I_{eq}). \quad (2)$$

2.1. Dipolar interaction

The classical interaction energy of two magnetic dipoles oriented along the direction of the static magnetic field (Figure 1) is given by

$$E_d = \frac{\mu_A \mu_B}{r_{AB}^3}(3\cos^2\theta - 1). \quad (3)$$

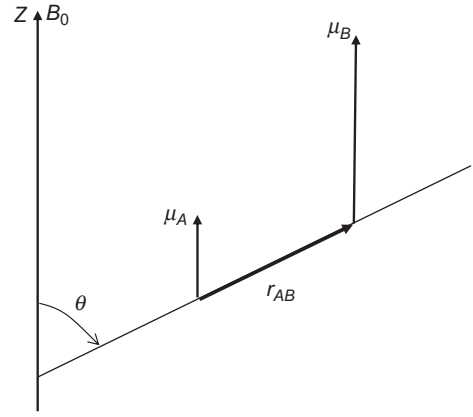

Figure 1 Magnetic dipoles associated with nuclear spins in the presence of B_0.

As a consequence, the local field acting on μ_A is of the form

$$b(t) \propto \frac{\mu_B}{r_{AB}^3}[3\cos^2\theta(t) - 1], \tag{4}$$

since the time dependence arises from the angle θ and is related to the molecular reorientation (molecular tumbling and possibly internal motions). As a matter of fact, the problem must be treated by quantum mechanics so as to introduce the proper spin operators and, doing so, we obtain the following spectral density actually involved in relaxation rates

$$\begin{aligned} &J_{\mathrm{d}}(\omega) = \frac{K_{\mathrm{d}}}{r_{AB}^6}\widetilde{J}(\omega), \\ &\text{where } \widetilde{J}(\omega) = \frac{5}{4}\int_{-\infty}^{+\infty} \overline{[3\cos^2\theta(t) - 1][3\cos^2\theta(0) - 1]}\mathrm{e}^{-\mathrm{i}\omega t}\mathrm{d}t. \end{aligned} \tag{5}$$

In Equation (5), $\widetilde{J}(\omega)$ is independent of the relaxation mechanism and the constant K_{d} is given by

$$K_{\mathrm{d}} = (1/20)(\mu_0/4\pi)^2(\gamma_A\gamma_B\hbar)^2 \tag{6}$$

μ_0 is the vacuum permeability, γ_A and γ_B the gyromagnetic constants, $\hbar$ the Planck constant divided by 2π. If A stands for a carbon-13 and B for a proton, K_{d} is equal to 1.8 10^9 provided that, in Equations (4) and (5), r is expressed in Å.

In Equation (5), we can first notice (i) the factor $1/r^6$ which makes the spectral density very sensitive to the interatomic distance, and (ii) the dynamical part which is the Fourier transform of a correlation function involving the Legendre polynomial. We shall denote this Fourier transform by $J(\omega)$ (we shall dub this quantity ''normalized spectral density''). For calculating the relevant longitudinal relaxation rate, one has to take into account the transition probabilities in the energy diagram of a two-spin system. In the expression below, the first term corresponds to the double quantum (DQ) transition, the second term to single quantum (1Q) transitions and the third term to the zero quantum (ZQ) transition.

$$R_{1,\mathrm{d}}^A = (K_{\mathrm{d}}/r_{AB}^6)[6\widetilde{J}_{\mathrm{d}}(\omega_A + \omega_B) + 3\widetilde{J}_{\mathrm{d}}(\omega_A) + \widetilde{J}_{\mathrm{d}}(\omega_A - \omega_B)]. \tag{7}$$

2.2. Chemical shift anisotropy

This mechanism arises from the asymmetry of the shielding tensor. Let us recall that the chemical shift in NMR has its origin in the screening (shielding) of the static magnetic field B_0 by the electronic distribution at

the level of the considered nucleus. This effect proceeds in fact from a tensorial quantity and the screening coefficient which defines the chemical shift in the liquid phase is just one third of the (Cartesian) tensor trace. Now, as far as relaxation is concerned, we have to consider the whole tensor and, more precisely, the system of its principal *molecular* axes (x, y, z) in which the tensor is diagonal. Let us denote by Z the direction of B_0.

The static magnetic field sensed by the considered nucleus is given by $B_0(1 - \sigma_{ZZ})$, where σ_{ZZ} is the shielding for a given molecular orientation (Figure 2). Of course, σ_{ZZ} which is defined in the *laboratory* frame must be expressed as a function of the shielding tensor in a *molecular* frame where it is diagonal (the principal axis system). Since the latter rotates with respect to the laboratory frame, it is conceivable that the shielding effect can constitute a relaxation mechanism. For simplicity we shall assume a shielding tensor of axial symmetry (Figure 2). σ_{ZZ} can be expressed as

$$\sigma_{ZZ} = \frac{\sigma}{3} + \frac{\Delta\sigma}{3}(3\cos^2\theta - 1), \tag{8}$$

where we have introduced the isotropic shielding coefficient (responsible for the chemical shift in liquid phase, hence the appellation ''isotropic chemical shift'')

$$\sigma = \sigma_{//} + 2\sigma_{\perp} \tag{9}$$

and the anisotropy of the shielding tensor (usually called ''chemical shift anisotropy'')

$$\Delta\sigma = \sigma_{//} - \sigma_{\perp}. \tag{10}$$

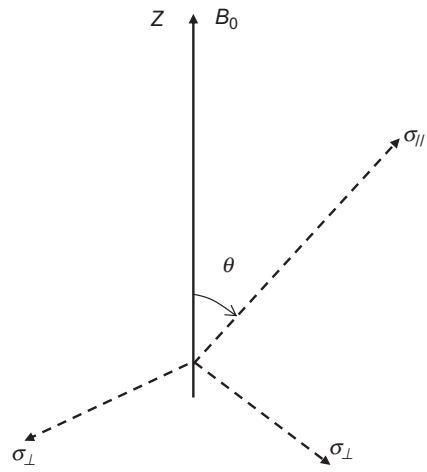

Figure 2 Principal axis system of a shielding tensor assumed to be of axial symmetry.

The time dependence result evidently from the angle θ and, considering from a quantum mechanical point of view the interaction between a magnetic moment and the static magnetic field B_0 (Zeeman term), we can invoke a local field of the form

$$b(t) \propto B_0 \Delta\sigma[3\cos^2\theta(t) - 1]. \tag{11}$$

Thus, the relevant spectral density, here equal to the longitudinal relaxation rate, is given by

$$J_{\mathrm{csa}}(\omega) = R_{1,\mathrm{csa}} = (1/15)(\gamma B_0)^2(\Delta\sigma)^2\widetilde{J}_{\mathrm{csa}}(\omega), \tag{12}$$

$\widetilde{J}(\omega)$ refers to the motion of the tensor symmetry axis. An immediate consequence of Equation (12) is the proportionality of the csa contribution to the square of the static magnetic field value, meaning that it can be safely neglected, in the case of carbon-13, up to 4.7 T (proton resonance frequency of 200 MHz). Another important feature of csa relaxation is its dependence with respect to the anisotropy $\Delta\sigma$ (expressed here in ppm), which is weak for aliphatic carbons but of the order of 150–200 ppm for ethylenic, aromatic or carbonyl carbons.

In the general case, when the shielding tensor is not of axial symmetry, in place of its diagonal elements σ_{xx}, σ_{yy} and σ_{zz} with $|\sigma_{zz}| \geq |\sigma_{yy}| \geq |\sigma_{xx}|$, the following parameters are generally used: $\sigma_{\mathrm{iso}} = (\sigma_{xx} + \sigma_{yy} + \sigma_{zz})/3$, $\Delta\sigma = \sigma_{zz} - (\sigma_{xx} + \sigma_{yy})/2$ and the asymmetry parameter $\eta = (\sigma_{xx} - \sigma_{yy})/\sigma_{zz} = (3/2)(\sigma_{xx} - \sigma_{yy})/\Delta\sigma$. The second form of η arises from the fact that, as far as relaxation is concerned, the shielding tensor can be defined with respect to any time-independent reference (which therefore will not act as a relaxation mechanism). σ_{iso} is such a reference and will be taken as zero, hence the second form of η. Now, if the molecular re-orientational motion is isotropic, Equation (12) is transformed into

$$R_{1,\mathrm{csa}} = (1/15)(\gamma B_0)^2(1 + \eta^2/3)(\Delta\sigma)^2\widetilde{J}_{\mathrm{csa}}(\omega). \tag{13}$$

3. CROSS-RELAXATION (AND CROSS-CORRELATION): SOLOMON EQUATIONS

3.1. Simple Solomon equations[7]

Whenever the system is no longer constituted by single non-interacting spins, the simple Bloch Equation (2) must be completed by additional coupling terms. Let us consider the dipolar interaction between two spins

½ A and B. This interaction is responsible for a bi-exponential evolution of their polarization which is accounted for by two simultaneous differential equations called Solomon equations

$$\begin{aligned}\frac{\mathrm{d}I_z^A}{\mathrm{d}t} &= -R_1^A(I_z^A - I_{\mathrm{eq}}^A) - \sigma_{AB}(I_z^B - I_{\mathrm{eq}}^B),\\ \frac{\mathrm{d}I_z^B}{\mathrm{d}t} &= -R_1^B(I_z^B - I_{\mathrm{eq}}^B) - \sigma_{AB}(I_z^A - I_{\mathrm{eq}}^A).\end{aligned} \tag{14}$$

The coupling term, traditionally denoted by σ_{AB} (which has however nothing to do with the screening coefficient of Section 2.2), is the so-called cross-relaxation rate and is a relaxation parameters which depends *exclusively* on the dipolar interaction between nuclei A and B, contrary to auto-relaxation rates which are compounds of several contributions. For instance, if A is a carbon-13, the auto-relaxation rate can always be written as

$$R_1^A = R_{1,\mathrm{dip}}^A + R_{1,\mathrm{csa}}^A + R_{1,\mathrm{others}}^A. \tag{15}$$

In Equation (15), $R_{1,\,\mathrm{others}}^A$ encompasses all secondary interactions which are not included in the first two terms (for instance the interaction with an unpaired electron, the spin-rotation interaction, ...). By contrast, the expression of the cross-relaxation rate is simply

$$\sigma_{AB} = (K_{\mathrm{d}}/r_{AB}^6)[6\widetilde{J}_{\mathrm{d}}(\omega_A + \omega_B) - \widetilde{J}_{\mathrm{d}}(\omega_A - \omega_B)]. \tag{16}$$

This is the beauty of this quantity which provides specifically a direct geometrical information $(1/r_{AB}^6)$ provided that the dynamical part of Equation (16) can be inferred from appropriate experimental determinations. This cross-relaxation rate, first discovered by Overhauser in 1953 about proton–electron dipolar interactions,[8] led to the so-called NOE in the case of nucleus–nucleus dipolar interactions, and has found tremendous applications in NMR.[2] As a matter of fact, this review is purposely limited to the determination of proton–carbon-13 cross-relaxation rates in small or medium-size molecules and to their interpretation.

The simplest way to measure the proton–carbon-13 cross-relaxation rate is to saturate the proton transitions by means of decoupling procedures, which are normally used to remove the effect of proton–carbon J-couplings from carbon-13 spectra, thus leading to a single carbon peak (provided there exists no J-coupling with other nuclei). Referring to the first of Equation (14) and supposing that A is the carbon-13 nucleus, B being the proton coupled by dipolar interaction to A, one has

$$\frac{\mathrm{d}I_z^A}{\mathrm{d}t} = -R_1^A(I_z^A - I_{\mathrm{eq}}^A) + \sigma_{AB} I_{\mathrm{eq}}^B. \tag{17}$$

Assuming further that decoupling has been turned on a long time ago before the carbon-13 measurement so that a steady state is reached, one ends up with a steady state carbon polarization, I_{st}^A, obtained by setting $\mathrm{d}I_z^A/\mathrm{d}t$ to zero:

$$I_{\mathrm{st}}^A = \left(1 + \frac{\gamma_B}{\gamma_A}\frac{\sigma_{AB}}{R_1^A}\right) I_{\mathrm{eq}}^A. \tag{18}$$

Now, it can be seen from Equation (17) that a simple relaxation measurement under decoupling conditions yields directly R_1^A whereas I_{eq}^A can be measured by a standard experiment described in Section 5. One then arrives to the so-called NOE factor η given by

$$\eta = \frac{I_{\mathrm{st}}^A - I_{\mathrm{eq}}^A}{I_{\mathrm{eq}}^A} = \frac{\gamma_B}{\gamma_A}\frac{\sigma_{AB}}{R_1^A}. \tag{19}$$

It can be noticed that the maximum NOE factor (2 when A is a carbon-13 and B a proton) is reached under extreme narrowing (see Section 6) conditions and if R_1^A arises exclusively from the A–B dipolar interaction. On the other hand, the cross-relaxation rate σ_{AB} is easily deduced from the NOE factor and from the A specific relaxation rate

$$\sigma_{AB} = \frac{\gamma_A}{\gamma_B}\eta R_1^A. \tag{20}$$

In spite of the apparent simplicity of the method, its drawback comes from the fact that a two-spin system has been assumed. It provides merely global information spanning all protons prone two interact by dipolar coupling with the considered carbon. Selective information requires pulsed experiments stemming from the general solution of Equation (14) given below.

For this purpose, let us define A by $A = I_z^A - I_{\mathrm{eq}}^A$ and B by $B = I_z^B - I_{\mathrm{eq}}^B$, with $A(0) = K_A$, $B(0) = K_B$. Solomon equations can then be written as

$$\begin{aligned} \frac{\mathrm{d}A}{\mathrm{d}t} &= -R_1^A A - \sigma_{AB} B, \\ \frac{\mathrm{d}B}{\mathrm{d}t} &= -R_1^B B - \sigma_{AB} A. \end{aligned} \tag{21}$$

Their solution is as follows

$$\begin{aligned} A &= a_+ \mathrm{e}^{\lambda_+ t} + a_- \mathrm{e}^{\lambda_- t}, \\ B &= b_+ \mathrm{e}^{\lambda_+ t} + b_- \mathrm{e}^{\lambda_- t}, \end{aligned} \tag{22}$$

λ_+ and λ_- are both negative and are expressed as

$$\lambda_{\pm} = -\frac{R_1^A + R_1^B}{2} \pm \frac{1}{2}\sqrt{(R_1^A - R_1^B)^2 + 4\sigma_{AB}^2}. \tag{23}$$

The coefficients (a_+, a_-, b_+, b_- depend on all relaxation parameters and, of course, on the initial conditions). One has

$$\begin{aligned} b_+ &= -\frac{\sigma_{AB}}{\lambda_+ + R_1^B} a_+, \\ b_- &= -\frac{\sigma_{AB}}{\lambda_- + R_1^B} a_-, \end{aligned} \tag{24}$$

and

$$\begin{aligned} a_+ &= \frac{K_A/(\lambda_- + R_1^B) + K_B/\sigma_{AB}}{1/(\lambda_- + R_1^B) - 1/(\lambda_+ + R_1^B)}, \\ a_- &= \frac{K_A/(\lambda_+ + R_1^B) + K_B/\sigma_{AB}}{1/(\lambda_+ + R_1^B) - 1/(\lambda_- + R_1^B)}. \end{aligned} \tag{25}$$

The crucial point arises from λ_+ which may become very small, thus leading to the little known property of *long lived states*. For this purpose let us assume that R_1^B, in our case the proton longitudinal relaxation rate, is much greater than R_1^A and σ_{AB}, a common situation which, for λ_+, leads to a quantity which can be very small

$$\lambda_+ \cong -R_1^A + \frac{\sigma_{AB}^2}{R_1^B}, \tag{26}$$

$\lambda_- \cong -R_1^B$ is large and governs the first part of the evolution. Conversely, when the corresponding term in Equation (22) has almost completely decayed to zero, it essentially remains the term involving λ_+, which generates a long lasting signal. The amplitude of the latter (and therefore the possibility of its detection) depends on initial conditions via the coefficient a_+.

3.2. Longitudinal spin order: Extended Solomon equations

So far, we have not considered the so-called longitudinal two-spin order, represented by the product operator[9] $2I_z^A I_z^B$, a quantity related to the polarization of nuclei A and B. This spin state can be created in different ways. The easiest way is probably to let the system evolve under the sole J_{AB} coupling so as to obtain an antiphase doublet, for instance the B antiphase doublet represented by $2I_z^A I_x^B$ (corresponding to the two proton–carbon-13 satellites in an antiphase configuration).

Applying selectively on B a $(\pi/2)_y$ pulse transforms the latter spin state into $2I_z^A I_z^B$ (here x, y, z refer to the rotating frame). It turns out that the longitudinal order can also be created by relaxation. This is due to a coupling term which acts in the same way as the cross-relaxation rate but, this time, between A and B polarization and the longitudinal order. This coupling term is called cross-correlation rate[10] because it involves two relaxation mechanisms, namely the A–B dipolar interaction and the csa mechanism at A and B. In fact, two such cross-correlation terms are prone to interfere with the evolution of I_z^A andI_z^B. They will be denoted as $\sigma_{\mathrm{csa}(A),\,\mathrm{d}}$ and $\sigma_{\mathrm{csa}(B),\,\mathrm{d}}$; they complicate somewhat Equation (21) and give rise to the extended Solomon equations which can be written as (with $AB = 2I_z^A I_z^B$ and recognizing that the longitudinal order is zero at equilibrium)

$$\begin{aligned}\frac{\mathrm{d}A}{\mathrm{d}t} &= -R_1^A A - \sigma_{AB} B - \sigma_{\mathrm{csa}(A),\mathrm{d}} AB,\\ \frac{\mathrm{d}B}{\mathrm{d}t} &= -R_1^B B - \sigma_{AB} A - \sigma_{\mathrm{csa}(B),\mathrm{d}} AB,\\ \frac{\mathrm{d}AB}{\mathrm{d}t} &= -R_1^{AB} AB - \sigma_{\mathrm{csa}(A),\mathrm{d}} A - \sigma_{\mathrm{csa}(B),\mathrm{d}} B,\end{aligned} \tag{27}$$

R_1^{AB} is the longitudinal order auto-relaxation which may depend on all relaxation mechanisms affecting the spin system. We give below the dipolar and csa contributions

$$\begin{aligned}R_1^{AB} = (K_\mathrm{d}/r_{AB}^6)[3\widetilde{J}_\mathrm{d}(\omega_A) + 3\widetilde{J}_\mathrm{d}(\omega_B)] - (1/15)(\gamma_A B_0)^2(\Delta\sigma_A)^2\widetilde{J}_{\mathrm{csa}(A)}(\omega_A)\\ -(1/15)(\gamma_B B_0)^2(\Delta\sigma_B)^2\widetilde{J}_{\mathrm{csa}(B)}(\omega_B)\end{aligned}. \tag{28}$$

Conversely, the cross-correlation rates depend *solely* on the csa mechanism and on the dipolar interaction which is of prime importance here. It arises in fact from correlation functions of the form $\overline{b'(t)b(0)}$, where $b'(t)$ refers to the csa mechanism whereas $b(t)$ refers to the dipolar interaction. One has

$$\sigma_{\mathrm{csa}(A),\mathrm{d}} = -\left(\frac{1}{5}\right)\sqrt{\frac{2}{3}}(\gamma_A B_0)(\Delta\sigma_A)\left(\frac{\mu_0}{4\pi}\right)\left(\frac{\gamma_A\gamma_B\hbar}{r_{AB}^3}\right)\widetilde{J}_{\mathrm{csa}(A),\mathrm{d}}(\omega_A). \tag{29}$$

The various symbols have the same meaning as before while the spectral density $\widetilde{J}_{\mathrm{csa}(A),\mathrm{d}}(\omega_A)$ will be discussed in Section 4. For the moment, let us state that these cross-correlation rates can play a role only if the csa mechanism is important (i.e. for non-aliphatic carbons but certainly not for protons) and if measurements are performed at high

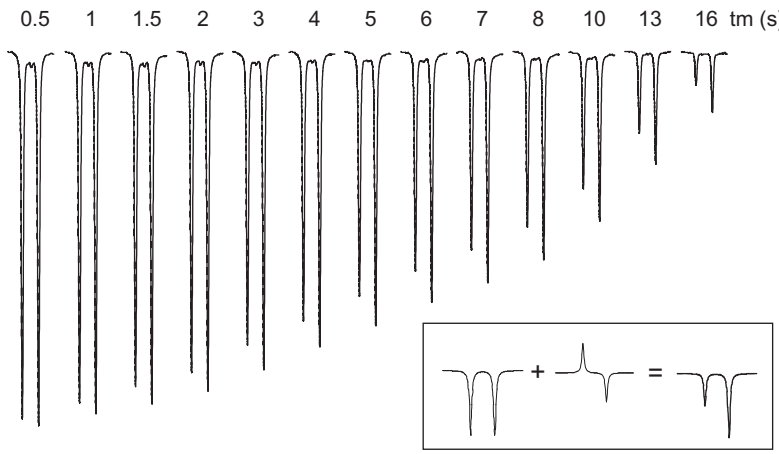

Figure 3 Creation of the longitudinal order by cross-correlation as a function of the mixing time t_m which follows the inversion of a carbon-13 doublet (due to a *J*-coupling with a bonded proton). The read-pulse transforms the longitudinal polarization into an in-phase doublet and the longitudinal order into an antiphase doublet. The superposition of these two doublets leads to the observation of an asymmetric doublet.

field (due to the term $\gamma_A B_0$ in Equation (29)). This means that, if A is a carbon-13 and B a proton, $\sigma_{\mathrm{csa}(B),\,\mathrm{d}}$ can be safely neglected in Equation (27). Nevertheless, the exploitation of Equation (27), which involves three simultaneous differential equations, relies necessarily on numerical procedures. In order to convince the reader that extended Solomon equations are not purely theoretical, we provide in Figure 3 an illustrative example showing the longitudinal order build-up.

Finally, it can be noted that there also exist dipolar–dipolar cross-correlation rates which involve two *different* dipolar interactions. These quantities may play a role, for instance, in the carbon-13 longitudinal relaxation of a CH_2 grouping.[11,12] Due to the complexity of the relevant theory and to their marginal effect under proton decoupling conditions, they will be disregarded in the following.

4. SPECTRAL DENSITIES

As seen from the above theoretical developments, accessing geometrical (and stereochemical) information implies at least an estimation of the dynamical part of the various relaxation parameters. The latter is represented by spectral densities which rest on the calculation of the Fourier transform of auto- or cross-correlation functions. These calculations require necessarily a model for describing molecular reorientation

(overall and internal) since this review is limited to *intra*-molecular relaxation mechanisms. Conversely, *inter*-molecular dipolar interactions would imply complex models involving, among other things, translational diffusion processes.[13] This aspect of nuclear spin relaxation will not be considered here.

4.1. Isotropic tumbling of a rigid molecule

Small-step rotational diffusion is the model universally used for characterizing the overall molecular reorientation. If the molecule is of spherical symmetry (or approximately; this is generally the case for molecules of important size), a single *rotational diffusion coefficient* is needed and the molecular tumbling is said isotropic. According to this model, correlation functions obey a diffusion type equation and we can write

$$\overline{b(t)b(0)} = \overline{b^2}\mathrm{e}^{-t/\tau_c}, \tag{30}$$

τ_c is called the correlation time and is equal to $1/6D_r$, where D_r is the rotational diffusion coefficient. For a simple Brownian motion, D_r can be expressed as a function of the radius a of the molecule (assumed to be spherical) and of the solvent viscosity η. This is the well-known Stokes-Einstein equation

$$D_r = \frac{k_B T}{8\pi a^3 \eta}, \tag{31}$$

where k_B is the Boltzmann constant and T the absolute temperature.

Qualitatively, τ_c can be viewed as the time necessary for a reorientation by one radian. τ_c is very weak (10^{-11}–10^{-12} s) for small size molecules in non-viscous solvents. Conversely, for large molecules (such as proteins in aqueous solution), it can reach much more important values (10^{-9} s or higher). All (normalized) auto-correlation spectral densities have the same expressions since, in the molecule, all directions are equivalent

$$\widetilde{J}(\omega) = \frac{2\tau_c}{1+\omega^2\tau_c^2}, \tag{32}$$

Equation (32) is as well valid for dipolar or csa auto-correlation spectral densities. As ω is an NMR frequency, thus smaller than 6.3 10^9 rad s^{-1}, $\widetilde{J}(\omega)$ is generally frequency independent for small or medium size molecules ($\omega^2\tau_c^2 \ll 1$) and simply equal to $2\tau_c$. Such a situation is called *extreme narrowing*. However, depending on the medium or on possible molecular associations, extreme narrowing conditions may no longer prevail and τ_c can be easily deduced from the evolution of relaxation parameters with the measurement frequency. This method, called relaxometry, can be employed whenever τ_c becomes larger than 10^{-10} s (see Figure 4).

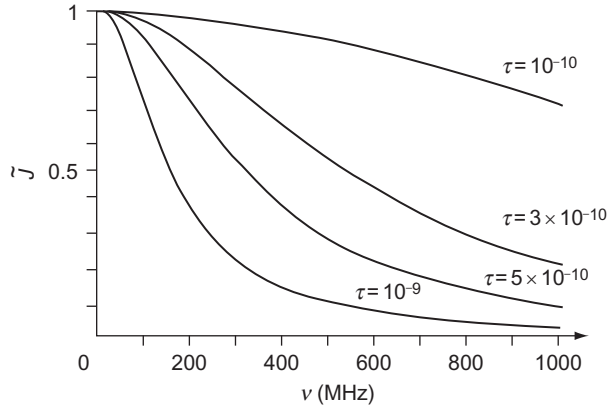

Figure 4 Normalized spectral densities as a function of $\nu = \omega/2\pi$ for different values of the correlation time τ (in s). They all start from 1 just to highlight their dependence with respect to the measurement frequency.

Concerning the cross-correlation spectral densities introduced in Equation (29), they are of the same form as Equation (32) with a geometrical factor depending on the angle $\theta_{\mathrm{d,\,csa}}$ between the two relaxation vectors: the vector joining the two nuclei for the dipolar interaction, and the largest shielding principal axis (or the symmetry axis of the shielding tensor if it is of axial symmetry). One has

$$\widetilde{J}_{\mathrm{csa}(A),\mathrm{d}}(\omega_A) = (1/2)(3\cos^2\theta_{\mathrm{d,csa}} - 1)\left(\frac{2\tau_{\mathrm{c}}}{1+\omega_A^2\tau_{\mathrm{c}}^2}\right). \tag{33}$$

4.2. Anisotropic tumbling of a rigid molecule

If the considered molecule cannot be assimilated to a sphere, one has to take into account a rotational *diffusion tensor*, the principal axes of which coincide, to a first approximation, with the principal axes of the molecular inertial tensor. In that case, three different rotational diffusion coefficients are needed.[14] They will be denoted as D_X, D_Y, D_Z and describe the reorientation *about* the principal axes of the rotational diffusion tensor. They lead to unwieldy expressions even for auto-correlation spectral densities, which can be somewhat simplified if the considered interaction can be approximated by a tensor of axial symmetry, allowing us to define two polar angles θ and ϕ describing the orientation of the relaxation vector (the symmetry axis of the considered interaction) in the (X, Y, Z) molecular frame (see Figure 5). As the tensor associated with dipolar interactions is necessarily of axial symmetry (the relaxation vector being

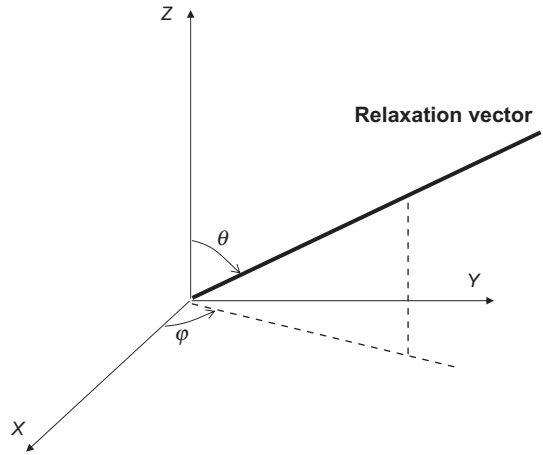

Figure 5 Definition of the polar angles in the principal axis system of the diffusion-rotation tensor.

the inter-nuclear vector) and because this review deals essentially with dipolar interactions, we shall limit ourselves to auto-correlation spectral densities in the case of an axially symmetric tensor.

From the pioneering works of Woessner,[15] Huntress[16] and Hubbard,[17] we can derive the following formulae[18]

$$\widetilde{J}_{\text{auto}}(\omega) = \sum_{k=-2}^{2} a_k \frac{(2/\lambda_k)}{1+\omega^2/\lambda_k^2} \tag{34}$$

with

$$\begin{aligned} &\lambda_0 = 4D_Z + 2D_+, \\ &\lambda_{\pm 1} = D_Z + 5D_+ \pm 3D_-, \\ &\lambda_{\pm 2} = 2D_Z + 4D_+ \pm [4(D_Z - D_+)^2 + 12D_-^2]^{1/2}, \\ &D_\pm = (D_X \pm D_Y)/2 \end{aligned} \tag{35}$$

and

$$\begin{aligned} &a_0 = (3/4)\sin^4\theta \sin^2 2\phi, \\ &a_1 = (3/4)\sin^2 2\theta \sin^2\phi, \\ &a_{-1} = (3/4)\sin^2 2\theta \cos^2\phi, \\ &a_{\pm 2} = \frac{1}{12D_-^2 + d_\pm^2}\left\{(9D_-^2)\sin^4\theta\cos^2 2\phi - (3D_- d_\pm)\right. \\ &\left.[\sin^2\theta\cos 2\phi(3\cos^2\theta - 1)] + \frac{d_\pm^2}{4}(3\cos^2\theta - 1)^2\right\}, \\ &\text{where } d_\pm = 2(D_Z - D_+) \mp [4(D_Z - D_+)^2 + 12D_-^2]^{1/2}. \end{aligned} \tag{36}$$

Fortunately, in the case of a rotational diffusion tensor with axial symmetry (such molecules are denoted ''symmetric top''), some simplification occurs. Let us introduce new notations: $D_{//} = D_Z$ and $D_\perp = D_X = D_Y$. Furthermore, we shall define effective correlation times:

$$\begin{aligned} 1/\tau_0 &= 6D_\perp, \\ 1/\tau_1 &= 5D_\perp + D_{//}, \\ 1/\tau_2 &= 2D_\perp + 4D_{//}. \end{aligned} \tag{37}$$

With these notations, one has

$$\begin{aligned} \widetilde{J}_{\text{auto}}(\omega) = \frac{1}{4}(3\cos^2\theta - 1)^2 \frac{2\tau_0}{1+\omega^2\tau_0^2} + \frac{3}{4}\sin^2 2\theta \frac{2\tau_1}{1+\omega^2\tau_1^2} \\ + \frac{3}{4}\sin^4\theta \frac{2\tau_2}{1+\omega^2\tau_2^2}. \end{aligned} \tag{38}$$

It can be noticed that at least two independent relaxation parameters in the symmetric top case, and three in the case of fully anisotropic diffusion rotation are necessary for deriving the rotation-diffusion coefficients, provided that the relevant structural parameters are known and that the orientation of the rotational diffusion tensor has been deduced from symmetry considerations or from the inertial tensor.

4.3. Local motions: The model free approach

Molecular internal motions are prone to affect relaxation parameters. A first approximation is to assume that they participate in the rotational diffusion anisotropy and to use the formulation of the preceding section. Indeed, for treating the internal rotation of a methyl grouping, one can use[19] an expression very close to Equation (38). It can also be assumed that the overall tumbling and internal motions are independent so that it is possible to devise models which account for the superposition of these two types of motion. These models,[20–24] depending on a number of parameters which may exceed the number of observables, will not be further detailed. We shall rather focus on the popular ''model free approach'', also called the Lipari–Szabo model[25] (the relevant expressions were actually derived earlier by Wennerström et al.[26]) which treats pragmatically the superposition of isotropic overall tumbling and *local* internal motions with a reasonable number of parameters. This approach is based on the fact that internal motions, considered globally, are represented by a correlation time τ_f (f for fast motions assumed to lead to extreme narrowing conditions) and an order parameter S which reflects their anisotropic character or rather their orientational restriction. S has the same meaning than in liquid crystals, reflecting a partial orientation with respect to a given local *director*. It is an empirical parameter defined as the mean of

$(1/2)(3\cos^2\theta - 1)$, θ being the angle between the relaxation vector and the director. It ranges from -0.5 to 1, the latter value corresponding to a uniform orientation while $S = 0$ indicates a pure random orientation (i.e. no preferred direction). $S = -0.5$ indicates that all relaxation vectors are perpendicular to the director. The overall tumbling is characterized by a correlation time τ_s (s for slow, this approach being really interesting when the overall tumbling is outside extreme narrowing conditions). The relevant auto-correlation spectral density, suitable for dipolar interactions (S would be the order parameter of the inter-nuclear direction), is of the form

$$\tilde{J}^{\mathrm{dip}}_{\mathrm{auto}}(\omega) = (1 - S^2)(2\tau_f) + S^2 \frac{2\tau_s}{1 + \omega^2\tau_s^2}, \tag{39}$$

where S, τ_f and τ_s have to be deduced from experimental data. It can be noted that $2\tau_s/(1 + \omega^2\tau_s^2)$ in Equation (39) can be substituted by Equation (34) or Equation (38) if the overall tumbling is anisotropic. Equation (39) would also be suitable for the csa contribution to relaxation rate provided that the csa tensor is of axial symmetry and that one defines a specific order parameter for the relevant symmetry axis. Let α the angle between the dipolar inter-nuclear direction and the csa symmetry axis. If Equation (39) is associated with the dipolar interaction, the homologous csa spectral density can be written as[27]

$$\begin{aligned}\tilde{J}^{\mathrm{csa}}_{\mathrm{auto}}(\omega) = {} & [1 - (1/4)(3\cos^2\alpha - 1)^2 S^2](2\tau_f) \\ & + (1/4)(3\cos^2\alpha - 1)^2 S^2 \frac{2\tau_s}{1 + \omega^2\tau_s^2}.\end{aligned} \tag{40}$$

Similarly,[27] the dipolar–csa cross-correlation spectral density can be expressed as follows

$$\tilde{J}^{\mathrm{dip,csa}}_{\mathrm{cross}}(\omega) = (1/2)(3\cos^2\alpha - 1)\left[(1 - S^2)(2\tau_f) + S^2 \frac{2\tau_s}{1 + \omega^2\tau_s^2}\right]. \tag{41}$$

The Lipari–Szabo approach has been essentially used in the study of large biomolecules,[21–24,28] less often for the medium size molecules as will be discussed in Section 6.

5. EXPERIMENTAL PROCEDURES

From now onward, we shall assume natural abundance for carbon isotopes, so that the signal we have to deal with arises from a single carbon-13 in the molecule under investigation. Moreover, most of the experiments described below imply, at one stage or another, proton

decoupling for removing any multiplet structure (due to *J*-couplings with protons) in such a way that every carbon gives rise to a singlet (except *J*-couplings with other nuclei such as ^{19}F, ^{31}P, ...). Another consequence of proton decoupling is, in principle, the destruction of proton magnetization so that the Solomon equation concerning carbon-13 (see Equation (14)) reduces to

$$\frac{dI_z^A}{dt} = -R_1^A(I_z^A - I_{st}^A), \tag{42}$$

where I_{st}^A is given by Equation (18). This is an important property meaning *that, under continuous proton decoupling, carbon-13 longitudinal relaxation is mono-exponential*. Very often (either in exploiting the NOE factor or the Solomon equations), the knowledge of the carbon-13 longitudinal relaxation time will be required. The forthcoming section is thus devoted to its measurement.

5.1. Measurement of ^{13}C longitudinal relaxation time

As explained above, these experiments have to be performed under continuous proton decoupling. The usual method is inversion-recovery[29] (Figure 6) which would require, between consecutive experiments or consecutive scans, a waiting time of $5T_1$ unless one has recourse to a variant dubbed ''Fast Inversion-Recovery''.[30]

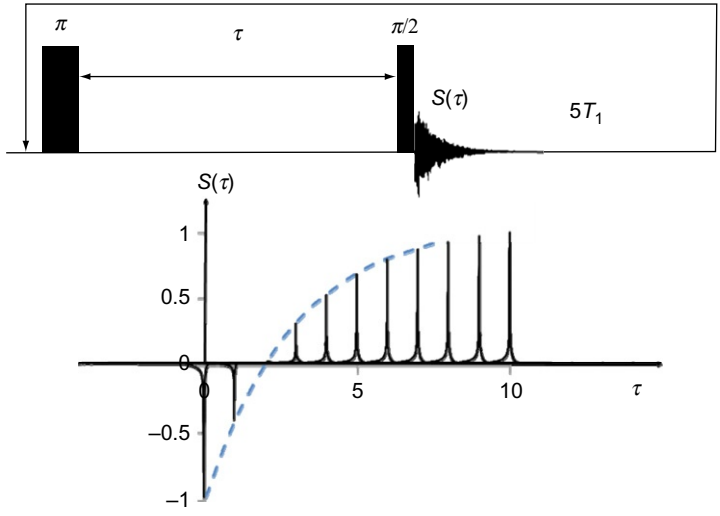

Figure 6 The inversion-recovery experiment. The dynamic range is twice the equilibrium magnetization.

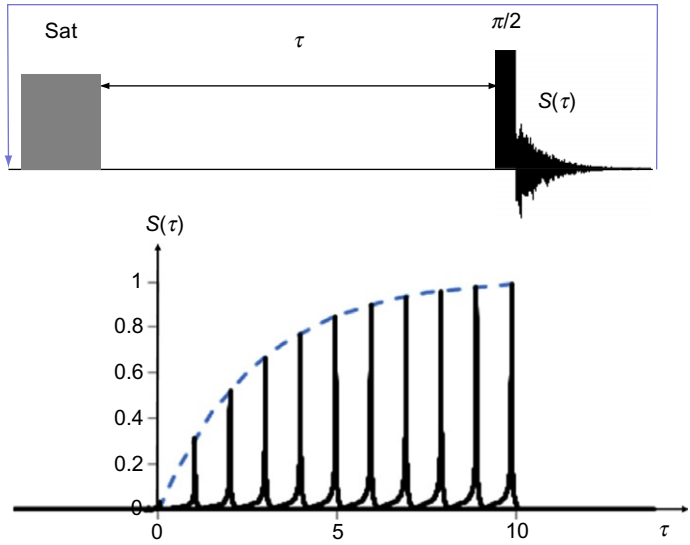

Figure 7 The saturation-recovery experiment. The dynamic range is equal to the equilibrium magnetization.

Saturation-recovery[31] (Figure 7) is an interesting alternative in the case of very long longitudinal relaxation times or when a proper inverting pulse is not available. It makes use of a saturation pulse (i.e. capable of destroying the whole carbon-13 magnetization) in place of the π pulse of the inversion-recovery experiment. Since magnetization starts always from zero, no waiting time is needed. The only drawback is a dynamic range half the one of the inversion-recovery experiment.

For both experiments and according to Equation (42), the experimental data can be adjusted according to

$$S(\tau) = S_{\mathrm{eq}}(1 - k\mathrm{e}^{-\tau/T_1}), \tag{43}$$

$1 < k < 2$ for the inversion-recovery experiment (k would be equal to 2 for a perfect 180° pulse and for a waiting time permitting full equilibrium recovery). k is around 1 for the saturation-recovery experiment (it would be strictly equal to 1 in the case of a perfect saturation; in practice, it can be either larger or smaller).

5.2. Measurement of the NOE factor

The NOE factor provides a global information, that is the sum of cross-relaxation rates of *all* protons which can interact by dipolar coupling with the considered carbon. It is therefore very useful when the considered

carbon is directly bound to one, two or three protons since the relevant dipolar interaction will overwhelm more remote interactions. As the C–H distance is normally known, the dynamical part of the cross-relaxation rate is, in that case, readily available (see Equation (16)) and can serve as a reference for further geometrical determinations. Now from Equation (19), it can be seen that I^A_{st} and I^A_{eq} have to be measured. In principle, the former is deduced from the usual proton-decoupled ^{13}C spectrum with a waiting time of five times the longest T_1 to restore equilibrium magnetization between scans. However, in experiments for which decoupling is substituted by a pulse train (this is the case in reverse two-dimensional experiments, mainly used for the study of large biomolecules), some caution must be exercised regarding the ability of actually saturating the proton spin system.[32] For obtaining I^A_{eq}, it suffices to run the normal experiment but with decoupling switched on during the fid acquisition. This can be achieved[33] that way because (i) decoupling is operative instantaneously, (ii) NOE does not affect transverse magnetization. However, since the proton spin state is modified during the pulse sequence (by gated decoupling), proton polarization *also* relaxes so that the recovery toward equilibrium needs a waiting time longer than $5T_1$. Various simulations have shown that a waiting time of $10T_1$ was safe in all circumstances.[34] The procedures for measuring I^A_{st} and I^A_{eq} are schematized in Figure 8.

In the early days of carbon-13 spectroscopy, high power decoupling was used and NOE measurements had to be carried out in such a way that temperature was identical for both experiments (interleaved experiments with shift of the proton frequency). With modern spectrometers, such

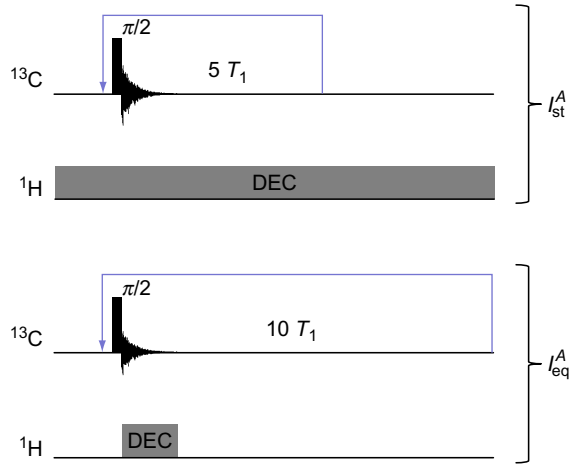

Figure 8 The two separate experiments for experimentally determining the NOE factor (see Equation (19)). DEC stands for decoupling.

precautions are no longer necessary thanks to decoupling schemes which permit low power decoupling and thanks to accurate temperature control.

5.3. The HOESY (Heteronuclear Overhauser Effect Spectroscopy) experiment

Initially, this is a two-dimensional experiment which is supposed to be the heteronuclear homolog of the NOESY experiment. It thus involves ^{1}H and ^{13}C pulses as well as proton decoupling during ^{13}C signal acquisition. This experiment, proposed simultaneously by Rinaldi[35] on the one hand, and Yu and Levy[36,37] on the other hand, provides only cross-peaks which indicate ^{1}H–^{13}C distance correlations. Evidently, at the onset, the method provides information about directly bonded ^{1}H–^{13}C nuclei, information which can be obtained through other more sensitive procedures. Its interest lies in other more remote correlations. Indeed, it has been mostly applied to inter-molecular dipolar interactions.[36–43] As described later, we shall be rather interested here in intra-molecular interactions associated with geometrical information not accessible by other correlation methods. The pulse sequences that we are using are shown in Figure 9 and will be

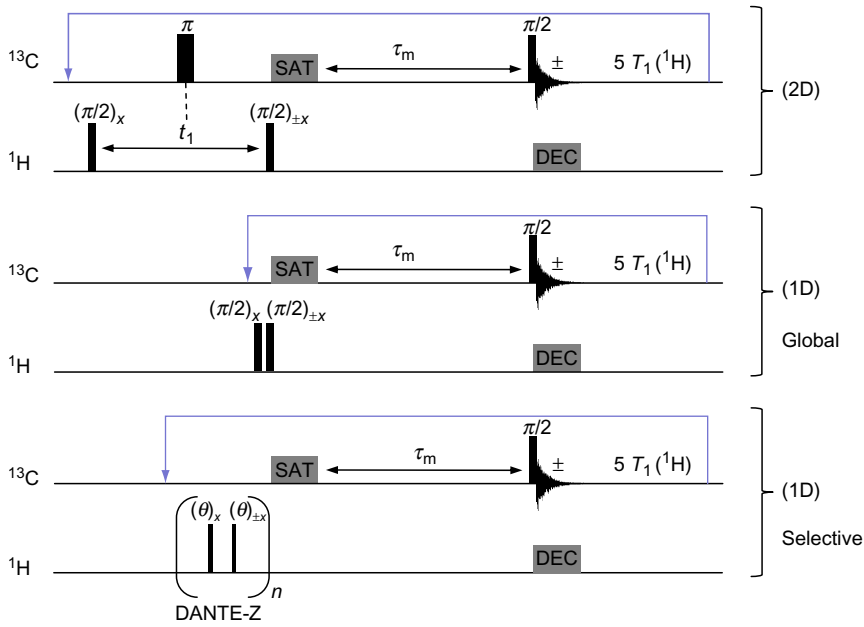

Figure 9 Three possible modes of the HOESY experiment.

now commented. We have found it useful to slightly modify the conventional sequences[44] by inserting a saturation procedure applied to carbon-13 prior to the mixing interval. This has two advantages: (i) the state of carbon polarization is perfectly defined at the beginning of the mixing period (it is actually zero), (ii) because time averaging is needed, the experiment can be repeated according to the proton relaxation time, usually much shorter than the carbon relaxation time. Furthermore, the 180° phase alternation of the second proton pulse along with the alternation of the acquisition sign has the effect of cancelling any recovery of carbon polarization by carbon relaxation during the mixing time. As a consequence, pure NOE spectra are obtained.

In the 2D mode, the evolution time t_1 plays its usual role for proton chemical shift labelling. The central π pulse refocuses all proton–carbon *J*-couplings (decoupling pulse), so that the v_1 dimension corresponds to proton chemical shifts, while the v_2 dimension (physically detected) corresponds to carbon chemical shifts. Without that π pulse, the correlation peaks appear at the position of the ^{13}C satellites in the proton spectrum, that is at more than 60 Hz on either side of the proton resonance. This can be a serious advantage for detecting remote correlations[45,46] which appear precisely at the proton resonance position. Amplitude modulation occurs in t_1 so that a two-dimensional spectrum in the absorption mode can be obtained, facilitating the experimental construction of build-up curves (signal amplitude as a function of the mixing time; see Figure 10). Thus an accurate measurement of the cross-relaxation rates can be achieved.

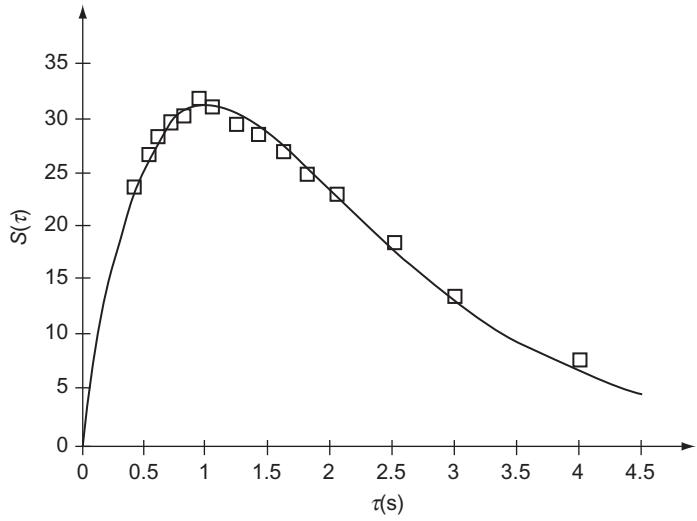

Figure 10 A typical HOESY build-up curve.

Whatever the method for extracting the cross-relaxation rates will be, a reference spectrum is needed. Actually it is furnished by the gated decoupling experiment shown at the bottom of Figure 8 with the same number of scans than in the HOESY experiment. Let us denote by I_{eq}^{C} the quantity which is measured that way. For a first estimation of the cross-relaxation rate, we can have recourse to the initial approximation which makes use of the data points corresponding to small values of the mixing time and seemingly varying linearly with the latter. Referring to Equation (22), these data points can be exploited to first order as indicated below

$$I_z^C(\tau_m) = I_z^C(0) + \left(\frac{dI_z^C}{dt}\right)_{t=0} \tau_m = 4\sigma I_{eq}^C \tau_m. \tag{44}$$

For deriving the above equation, we have taken into account the phase cycling of Figure 9 and the fact that $I_{eq}^{H} = 4I_{eq}^{C}$. The interesting result of Equation (44) is that the cross-relaxation rate can be deduced from the initial slope of the plot of I_z^C/I_{eq}^C as a function of τ_m. This initial slope is equal here to 4σ and would become $\sigma/4$ if we would attempt to perform the experiment the other way, that is from carbon-13 toward proton. Anyway, when one has at hand the full build-up curve, it is recommended to fit the experimental data according to Equation (22) or possibly to Equation (27) if one suspects a contribution from csa–dipolar cross-correlation rates. In the former case, this will provide not only the cross-relaxation rate σ (the parameter of interest) with an improved accuracy (because it is always difficult to decide what is the best initial slope) but also the longitudinal relaxation rates R_1^C and R_1^H. Notice that R_1^H can be affected by proton–proton cross-relaxation rates among the proton system[46] (the so-called spin diffusion phenomenon). Anyhow, the problem of sensitivity, related to the observation of carbon-13 (the low gyromagnetic constant nucleus), may be addressed. Inverse two-dimensional HOESY experiments[47–50] have been proposed. They consist in transferring NOE from the low gyromagnetic constant nucleus to the more sensitive high gyromagnetic constant nucleus which is detected. In principle this should lead to a sensitivity increase by a factor of 16 in the case of the pair ^{13}C–^{1}H. However, as the ^{1}H–^{13}C cross-relaxation rate is 16 times smaller than the ^{13}C–^{1}H cross-relaxation rate (see above), there is no net sensitivity increase and these experiments are of little value as far as sensitivity is concerned. Moreover, the gradients used in such experiments for suppressing unwanted signals and selecting coherences of interest may entail a loss of sensitivity by a factor of two, which must be further multiplied by the increase of noise associated with detection at a higher frequency. However, in particular instances, inverse HOESY experiments can reveal correlations not visible in the direct HOESY

experiments.[48,50] The true inverse HOESY experiment involves, by means of INEPT sequences, proton polarization transfer prior to the mixing time and proton detection together with the use of gradients as indicated above. This experiment has however been essentially devised for large biomolecules such as proteins.[51] As a matter of fact, because the INEPT transfer process is based on a well defined (large) *J*-coupling, it is well suited for carbon-13 or nitrogen-15 directly bound to (a) proton(s) and leads the cross-relaxation rate associated with the CH or NH bond. The method has been widely used for the amide proton of proteins[32] but, to the best of our knowledge, it has never been applied to the measurement of proton–carbon cross-relaxation rates in the case or small or medium size molecules. Nevertheless, it could probably be useful outside the extreme narrowing regime, along with measurements performed at different magnetic field values.

In difficult situations (weak cross-relaxation rates or strong overlap in the proton spectrum), when using carbon-13 detected HOESY experiments, one faces the unavoidable sensitivity problem. This problem can be alleviated by one-dimensional experiments, the easiest of which is shown in the middle of Figure 9. It is a global experiment, in the sense that the proton chemical shift labelling has been suppressed. As a consequence, the measured quantity is the sum of the cross-relaxation rates arising from *all* protons prone to interact by dipolar coupling with a given carbon-13. It can be noticed that the basic phase cycling (essential for a proper interpretation of the experimental data) has been maintained in this sequence. This experiment can be useful as a prelude of a two-dimensional HOESY experiment requiring the accumulation of many transients, in order to make sure that the spectrometer occupation for a long time will not be wasted. It can also be used quantitatively for carbons experiencing a single dipolar interaction with protons. In that case, it would provide a piece of information comparable to that provided by the NOE factor. Another one-dimensional experiment is a selective one[40] as shown in the bottom of Figure 9. This sequence allows one to determine the cross-relaxation rate produced by the selected proton. The DANTE-Z technique[52] is particularly well suited for achieving the selectivity process because it involves inherently the basic phase cycling of the HOESY experiment. Of course, other selective schemes can be used, combined for instance with a TOCSY sequence which can be valuable when the proton of interest (H) is not well separated from other multiplets. In that case, if H belongs to a *J*-coupling network possessing an isolated proton (H′), H′ is selected at the outset and its polarization is transferred to H by the TOCSY sequence just prior to the mixing interval of the HOESY experiment.[53]

6. EXAMPLES

6.1. Stereo and conformational studies

Early conformational studies by HOESY experiments are illustrated by the work of Batta and Köver[54] who were able to access oligosaccharide sequencing and conformational distribution around the glycosidic bond in model compounds. These determinations make use of relayed proton–proton–carbon cross-relaxation.

Another good example of what can be gained from HOESY experiments is provided by the work of Ancian et al.[53] about the preferential conformation of uridine in water. Through the TOCSY–HOESY experiment above described, these authors were able to show unambiguously that the torsion angle of the uracil group around the glycosidic bond lies in a range corresponding to the anti-form of the pyrimidine base with respect to the furanose ring.

The discrimination between E and Z isomers of the compound shown in Figure 11 constitutes a further example of the interest of selective HOESY experiments.[55]

This problem cannot be solved by the usual NMR experiments (COSY, NOESY, HSQC, HMBC, . . .). It turns out that the selective HOESY experiment (Figure 9, bottom) applied to proton H_5 provides an unambiguous

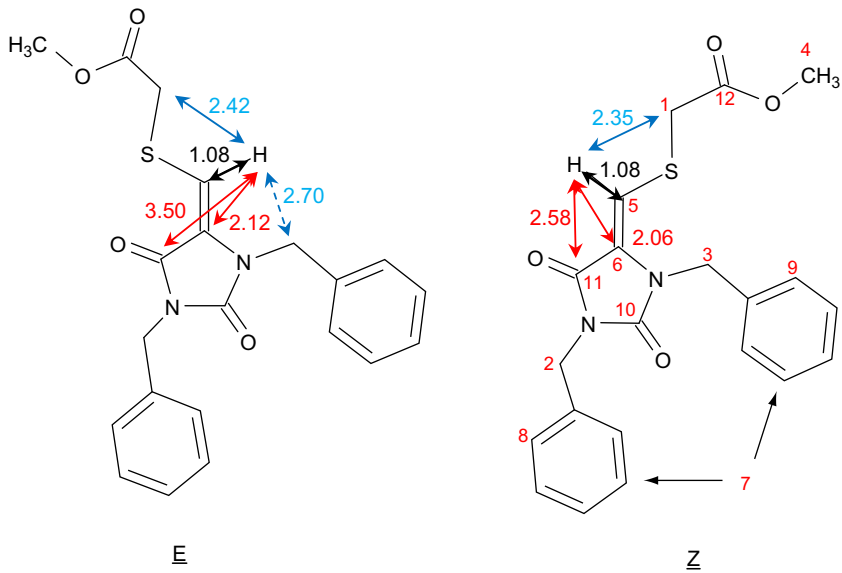

Figure 11 Two isomers with distances (in Å) obtained by quantum chemistry calculations. Solid lines: proton–carbon distances. Dashed lines: proton–proton distances.

answer: for both isomers, C_6 is close to H_5, but for the E isomer C_{11} is remote from H_5 whereas, in the Z isomer, H_5 is relatively close to C_{11} yet less close than C_6. It is exactly what is shown by Figure 12 where the peak intensities are in the ratio of the distances (given in Figure 11) to the power 6. It can therefore be concluded that we are in the presence of the Z isomer.

As a final example of this section, we present a HOESY two-dimensional experiment of aqueous micellized sodium octanoate.[46] In addition to one-bond ^1H–^{13}C correlation peaks, Figure 13 exhibits remote correlation peaks which indicate some spatial proximity between a given carbon and protons bound to a nearby carbon. Build-up curves (not shown) have been obtained at two different values of the magnetic field since, as expected, a slow motion corresponding to the micelle overall motion is superposed to local fast motions (segmental and rotational isomerism). The cross-relaxation rates deduced from these build-up curves can be interpreted according to the Lipari–Szabo approach which involves the correlation time τ_s associated with the global micelle tumbling, the correlation time τ_f associated with the fast local motions and an order parameter S which describes the restriction of the latter motions (see Equation (39)).

Taking into account spin diffusion among the proton spin system (multiple proton–proton cross-relaxation rates), one obtain order

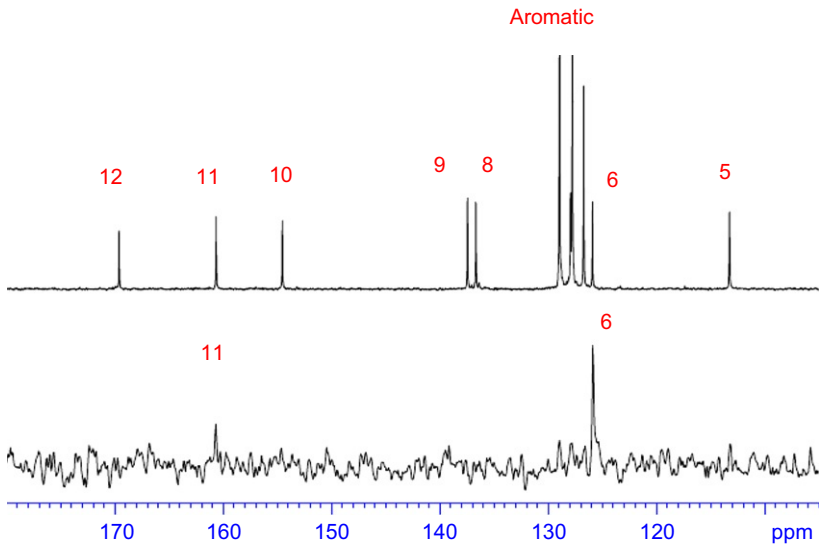

Figure 12 The ^{13}C responses (bottom) obtained by selectively inverting H_5 (bound to a carbon-12); they lead to the cross-relaxation rates σ_{H_5-C6} and σ_{H_5-C11}. A reference carbon-13 spectrum is shown at the top.

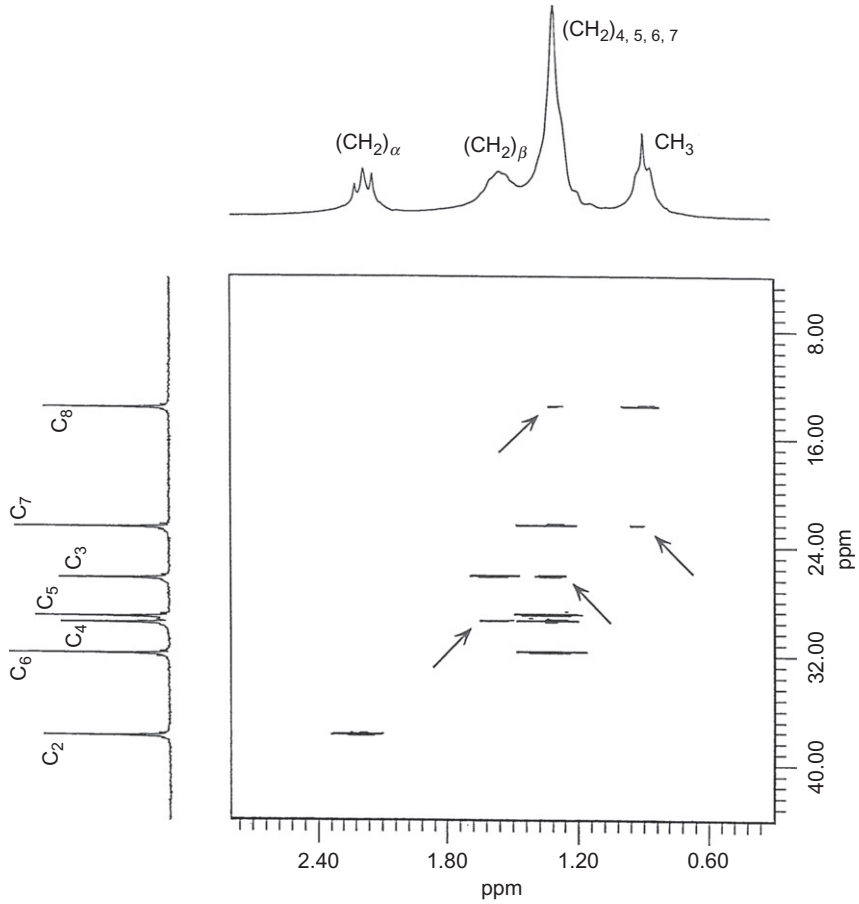

Figure 13 The HOESY two-dimensional spectrum of micellized sodium octanoate in aqueous solution. Besides one-bond carbon–proton correlations, remote correlations are observed (marked by an arrow).

parameters in agreement with those derived from extensive carbon-13 longitudinal relaxation measurements (at different magnetic fields). More interesting are the remote correlations, two of them being shown in more detail in Figure 14. It can be seen that they are relatively intense and devoid of symmetry (compare H_3–C_4 and H_4–C_3).

Attempts to interpret the corresponding build-up curves according to the Lipari–Szabo approach lead to inconsistent results (for instance, order parameters greater than unity). This indicates that these remote correlations are probably not of *intra*-molecular origin but would rather arise from *inter*-molecular dipolar interactions which could become significant when some contacts exist between neighbouring aliphatic chains. This

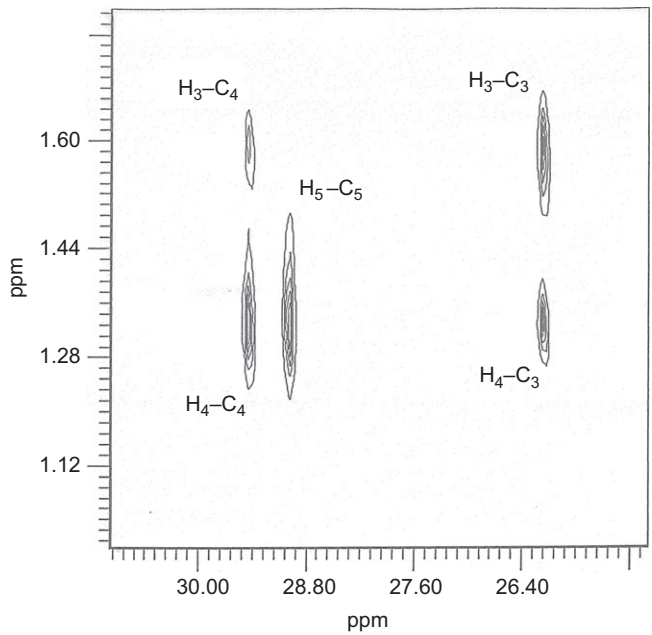

Figure 14 An excerpt of Figure 13 showing peaks associated with remote correlations.

can only occur for parts of the chain presenting some flexibility (due to rotational isomerism or segmental motions). This flexibility may not be the same at the C_3 or C_4 levels and this would explain the different intensities of the H_3–C_4 and H_4–C_3 peaks. Thus, in that case, the HOESY experiment brings information about aliphatic chain mobility. Indeed, the part of the chain located near the polar head is known to be rigid and this is confirmed by the absence of H_2–C_3 and H_3–C_2 correlations.

6.2. Geometrical determinations

During the seventies and the eighties, C–H distances in various medium size molecules were determined through proton–carbon-13 NOE cross-relaxation rates in a semi-quantitative way. These determinations followed the release of the seminal book by Noggle and Schirmer[56] and, most of the time, rested on the assumption of a single correlation time describing the overall motion of the molecule under investigation. These studies relied on global and selective NOE's. A complete bibliography can be found in the paper by Batta et al.,[57] who, in addition, treated an AMX spin system where A and M stand for two *J*-coupled protons and X for the observed carbon-13.

The previous approach is valid as long as the molecular reorientation can be described by a single correlation time. This excludes molecules involving internal motions and/or molecular shapes which cannot, to a first approximation, be assimilated to a sphere. Due to its shape, the molecule shown in Figure 15 cannot evidently fulfil the latter approximation and is illustrative of the potentiality of HOESY experiments as far as carbon–proton distances and the anisotropy of molecular reorientation are concerned.[45,58]

The HOESY spectrum is displayed in Figure 16. It has been obtained in the ''*J*-separated'' mode, that is without the central π pulse in the t_1 interval (see Figure 9, top) in such a way that direct correlations (one bond) appear at the location of carbon-13 satellites whereas possible remote correlations are visible at the proton resonance frequency (see Section 5.3). A first estimate of the molecular geometry can be deduced from quantum chemical calculations. Direct correlations (which involve one-bond C–H distances around 1.1 Å) can then be employed for deriving the three rotational diffusion coefficients which reveal a strong re-orientational anisotropy: expressed in terms of correlation times, this leads to $\tau_x = 18 \pm 5$, $\tau_y = 2.6 \pm 0.2$ and $\tau_z = 10.8 \pm 1.8$ ps. Evidently, it is out of the question to use the approximation of a single correlation time and Equations (34)–(36) must be used. The angles appearing in these equations can be assumed from the quantum mechanical calculations and the cross-relaxation rates derived from the build-up curves pertaining to remote correlations allow one to derive the relevant distances. They are collected in Table 1 and compared to those given by quantum mechanical calculations and crystallography.

The agreement between the three techniques is rather good, bearing in mind that quantum mechanical calculations totally ignore molecular

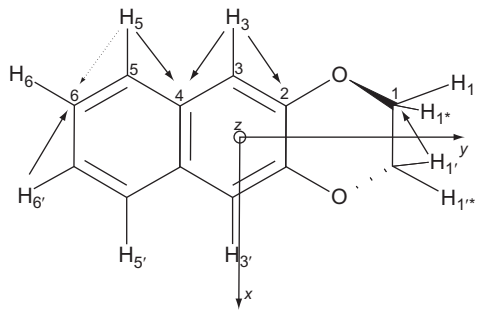

Figure 15 The model molecule used to demonstrate the possibilities of HOESY experiments in terms of carbon–proton distances and reorientational anisotropy. To a first approximation, the molecule is devoid of internal motions and its symmetry determines the principal axis of the rotation-diffusion tensor. Note that H_1, H_{1*}, $H_{1'}$, $H_{1'*}$ are non-equivalent. The arrows indicate remote correlations.

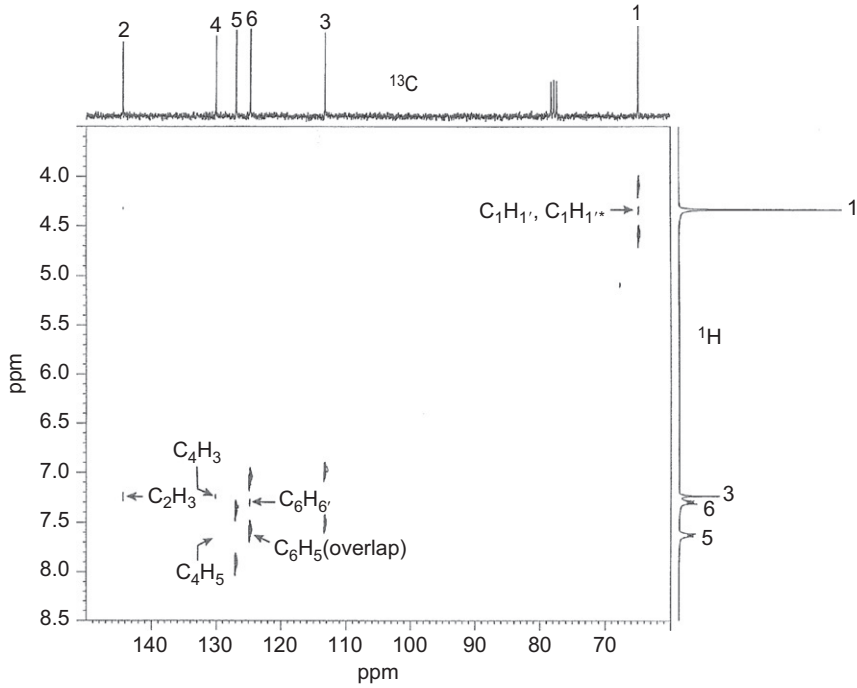

Figure 16 The *J*-separated HOESY spectrum of the molecule shown in Figure 15. Direct (one bond) correlations are located at the position of ^{13}C satellites in the proton spectrum. Arrows indicate remote correlations.

TABLE 1 Distances in Å derived from the HOESY experiment (r_{NMR}) and compared to results from crystallography (r_{RX}) and quantum mechanical calculations (r_{QM})

Vector	r_{NMR}	r_{RX}	r_{QM}
$C_1H_{1'}$	2.02	2.07	2.20
$C_1H_{1'*}$	1.96		2.21
C_2H_3	2.32	2.24	2.16
C_4H_3	2.14	2.07	2.19
C_4H_5	1.81	2.04	2.19
$C_6H_{6'}$	2.19	2.24	2.18

vibrations and that different vibrational averaging should be performed for r_{NMR} and r_{RX}.

In the case of a molecule with low symmetry and a reasonably known geometry, the inverse approach can be considered, that is determine not

only τ_x, τ_y and τ_z, but also the principal axis system of the rotation-diffusion tensor. The molecule shown in Figure 17 is a good example of such a study[59]: direct and remote correlations of a HOESY spectrum, along with an assumed geometry, lead to the orientation of the rotation-diffusion tensor principal axis system. Interestingly, it can be seen that this orientation has nothing to do neither with the inertia tensor, nor with the dipole moment direction. Again the reorientation is here strongly anisotropic: $\tau_x = 12.0 \pm 2.5$, $\tau_y = 32 \pm 04$ and $\tau_z = 4.1 \pm 1.0$ ps.

Still, in view of determining accurate C–H distances, a promising approach has been developed by Kowalewski et al.[60] It makes use of what these authors call a ''cryosolvent'', a mixture of D_2O and dimethyl sulfoxide (in a 2:1 molar ratio) which has the property of being very viscous at low temperature. As a consequence, any molecule in this cryosolvent is outside the extreme narrowing regime and relaxation parameters become frequency dependent. Their dependence upon the magnetic field will yield the correlation time(s) whereas their amplitudes lead to the interatomic distances. As an unambiguous example, these authors choose the hexamethylenetetramine (Figure 18) which possesses a high symmetry so that a single correlation time is required. Moreover, for carbon-13, the predominant relaxation mechanism should be the dipolar interaction with protons. With the longitudinal relaxation time and the NOE factor measured at two different magnetic fields, a C–H distance of 1.142 Å was found. This distance reduces to 1.108 Å after vibrational averaging and compares very well with other experimental

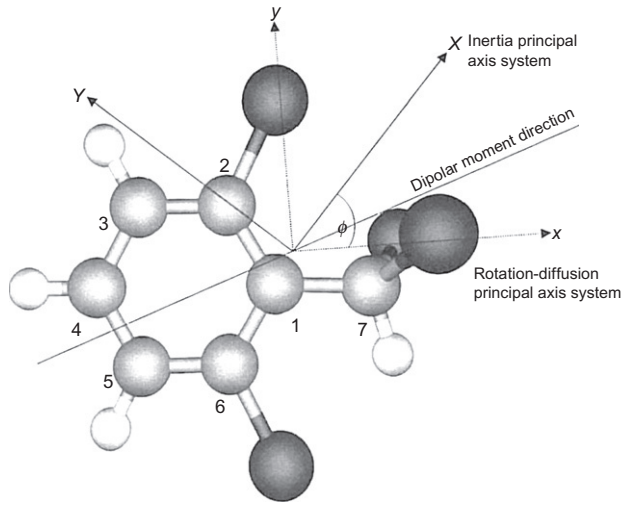

Figure 17 The α,α,2,6-tetrachlorotoluene. Small letters refer to the rotation-diffusion principal axis system.

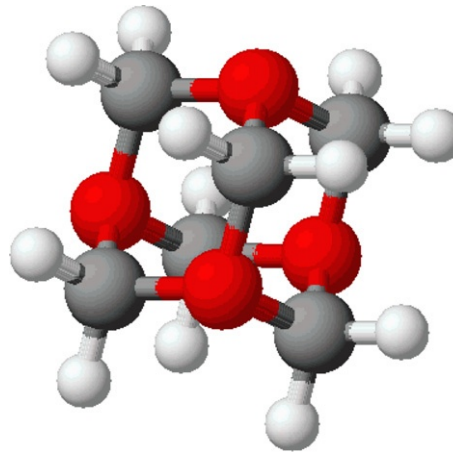

Hexamethylenetetramine

Figure 18 The molecule studied in a cryosolvent in order to determine by carbon-13 relaxation an accurate C–H distance.

determinations. This study validates the capability of spin relaxation for accessing molecular geometry. This feature has been confirmed and complemented by the measurement of cross-correlation relaxation rates.[61]

7. CONCLUSION

Through this review, it can be seen that the proton–carbon NOE have not been used as it probably deserves, as far as small or medium size molecules are concerned. As a possible perspective, one could envision extensive HOESY measurements at very high field (even combined with proton detection, a possibility for improving sensitivity not yet explored in the case of small or medium size molecules) in order to improve the spectral resolution and to obtain more and more remote correlations which could be useful for refining the geometrical parameters. Still toward this objective, another valuable approach is probably the use of cyosolvents. Altogether, one could dream of a sort of spin relaxation NMR crystallography.

ACKNOWLEDGEMENT

This work is part of the ANR project MULOWA (Grant Blan08-1_325450)

REFERENCES

1. F. Bloch, *Phys. Rev.*, 1946, **70,** 460.
2. D. Neuhaus and M. P. Williamson, *The Nuclear Overhauser Effect in Structural and Conformational Analysis*. Verlag Chemie, New York, 1989.
3. J. Jeener, B. H. Meier, P. Bachmann and R. R. Ernst, *J. Chem. Phys.*, 1979, **71,** 4546.
4. G. C. Levy, R. L. Lichter and G. L. Nelson, *Carbon-13 Nuclear Magnetic Resonance Spectroscopy*. 2nd edn., Wiley, New York, 1980.
5. D. Canet, *Nuclear Magnetic Resonance: Concepts and Methods*. Wiley, Chichester, 1996.
6. J. Kowalewski and L. Mäler, *Nuclear Spin Relaxation in Liquids: Theory, Experiments and Applications*. Taylor & Francis, New York, 2006.
7. I. Solomon, *Phys. Rev.*, 1955, **99,** 559; D. E. Woessner, *J. Chem. Phys.*, 1962, **37,** 647.
8. A. W. Overhauser, *Phys. Rev.*, 1953, **92,** 401.
9. O. W. Sorensen, G. W. Eich, M. H. Levitt, G. Bodenhausen and R. R. Ernst, *Prog. NMR Spectr.*, 1983, **16,** 163.
10. A. Kumar, R. C. R. Grace and P. K. Mahdu, *Prog. NMR Spectr.*, 2000, **37,** 191.
11. L. G. Werbelow and D. M. Grant, *Adv. Magn. Reson.*, 1977, **9,** 189.
12. D. Canet, *Prog. NMR Spectr.*, 1989, **21,** 203.
13. L. Nordstierna, P. V. Yushmanov and I. Furó, *J. Chem. Phys.*, 2006, **125,** 074704.
14. F. Perrin, *J. Phys. Rad.*, 1934, **V,** 33.
15. D. E. Woessner, *J. Chem. Phys.*, 1962, **37,** 647.
16. W. T. Huntress, Jr., *J. Chem. Phys.*, 1968, **48,** 3524.
17. P. S. Hubbard, *J. Chem. Phys.*, 1970, **52,** 563.
18. D. Canet, *Conc. Magn. Reson.*, 1998, **10,** 291.
19. A. Ericsson, J. Kowalewski, T. Liljefors and P. Stilbs, *J. Magn. Reson.*, 1980, **38,** 9.
20. D. E. Woessner, *in*: Encyclopedia of Nuclear Magnetic Resonance, D. M. Grant and R. K. Harris (eds.), Wiley, Chichester, 1996, p. 1068.
21. V. A. Daragan and K. H. Mayo, *Prog. NMR Spectr.*, 1997, **31,** 63.
22. M. W. F. Fischer, A. Majumdar and E. R. P. Zuiderweg, *Prog. NMR Spectr.*, 1998, **33,** 207.
23. D. M. Korzhnev, M. Billeter, A. S. Arseniev and V. Y. Orekhov, *Prog. NMR Spectr.*, 2001, **38,** 197.
24. P. Luginbühl and K. Wüthrich, *Prog. NMR Spectr.*, 2002, **40,** 199.
25. G. Lipari and A. Szabo, *J. Am. Chem. Soc.*, 1982, **104,** 4546.
26. H. Wennerström, B. Lindman, O. Söderman, T. Drakenberg and J. B. Rosenholm, *J. Am. Chem. Soc.*, 1979, **101,** 6860.
27. D. Canet, S. Bouguet-Bonnet and P. Mutzenhardt, *Conc. Magn. Reson.*, 2003, **19A,** 65.
28. D. Frueh, *Prog. NMR Spectr.*, 2002, **41,** 305.
29. R. L. Vold, J. S. Waugh, M. P. Klein and D. E. Phelps, *J. Chem. Phys.*, 1968, **48,** 3831.
30. D. Canet, G. C. Levy and I. R. Peat, *J. Magn. Reson.*, 1975, **18,** 199.
31. R. Freeman and H. D. W. Hill, *J. Chem. Phys.*, 1971, **54,** 3367.
32. F. Ferrage, A. Reichel, S. Battacharya, D. Cowburn and R. Ghose, *J. Magn. Reson.*, 2010, **207,** 294.
33. R. Freeman, H. D. W. Hill and R. Kaptein, *J. Magn. Reson.*, 1972, **7,** 327.
34. D. Canet, *J. Magn. Reson.*, 1976, **23,** 361.
35. P. L. Rinaldi, *J. Am. Chem. Soc.*, 1983, **105,** 5167.
36. C. Yu and G. C. Levy, *J. Am. Chem. Soc.*, 1983, **105,** 6994.
37. C. Yu and G. C. Levy, *J. Am. Chem. Soc.*, 1984, **106,** 6533.
38. W. Bauer and P. R. von Schleyer, *Magn. Reson. Chem.*, 1988, **26,** 827.
39. H. Seba and B. Ancian, *J. Chem. Soc. Chem. Commun.*, 1992, 996.
40. D. Canet, N. Mahieu and P. Tekely, *J. Am. Chem. Soc.*, 1992, **114,** 6190.
41. A. Belmajdoub, N. Mahieu, P. Tekely and D. Canet, *J. Phys. Chem.*, 1992, **96,** 1011.
42. N. Mahieu, P. Tekely and D. Canet, *J. Phys. Chem.*, 1993, **97,** 2764.

43. I. Furó, P. Mutzenhardt and D. Canet, *J. Am. Chem. Soc.*, 1995, **117,** 10405.
44. K. B. Köver and G. Batta, *Prog. NMR Spectr.*, 1987, **19,** 223.
45. P. Mutzenhardt, O. Walker, D. Canet, E. Haloui and I. Furó, *Mol. Phys.*, 1998, **94,** 565.
46. P. Palmas, P. Tekely, P. Mutzenhardt and D. Canet, *J. Chem. Phys.*, 1993, **99,** 4775.
47. W. Bauer, *Magn. Reson. Chem.*, 1996, **34,** 532.
48. K. Stott and J. Keeler, *Magn. Reson. Chem.*, 2003, **41,** 554.
49. T. M. Alam, D. M. Pedrotty and T. J. Boyle, *Magn. Reson. Chem.*, 2002, **40,** 361.
50. O. Walker, P. Mutzenhardt and D. Canet, *Magn. Reson. Chem.*, 2003, **41,** 776.
51. L. E. Kay, D. A. Torchia and A. Bax, *Biochemistry*, 1989, **28,** 8972.
52. D. Boudot, D. Canet, J. Brondeau and J. C. Boubel, *J. Magn. Reson.*, 1989, **83,** 428.
53. B. Ancian, D. Canet and P. Mutzenhardt, *Chem. Phys. Lett.*, 2001, **336,** 410.
54. Gy Batta and K. E. Köver, *Magn. Reson. Chem.*, 1988, **26,** 852.
55. M. Yemloul, S. Bouguet-Bonnet, L. A. C. Ba, G. Kirsch and D. Canet, *Magn. Reson. Chem.*, 2008, **46,** 939.
56. J. H. Noggle and R. E. Schirmer, *The Nuclear Overhauser Effect*. Academic Press, New York, 1971.
57. G. Batta, K. E. Köver and Z. Madi, *J. Magn. Reson.*, 1987, **73,** 477.
58. O. Walker, P. Mutzenhardt, J. P. Joly and D. Canet, *Chem. Phys. Lett.*, 2002, **357,** 103.
59. O. Walker, P. Mutzenhardt, E. Haloui, J.-C. Boubel and D. Canet, *Mol. Phys.*, 2002, **100,** 2755.
60. J. Kowalewski, M. Effemey and J. Jokisaari, *J. Magn. Reson.*, 2002, **157,** 171.
61. L. Ghalebani, P. Bernatowicz, S. N. Aski and J. Kowalewski, *Conc. Magn. Reson.*, 2006, **30A,** 100.

CHAPTER 3

NMR Studies of Optically Active Schiff Bases

Z. Rozwadowski

Contents

1. Introduction 126
2. Schiff Bases as Tools for Determination of Enantiomeric Purity and Absolute Configuration 127
   - 2.1. Determination of enantiomeric purity 127
   - 2.2. Determination of absolute configuration 132
3. Chiral Recognition of the Optically Active Schiff Bases 133
4. Product Identification and Conformation Studies 134
5. NMR Studies of Optically Active Schiff Base Equilibria 140
   - 5.1. Racemisation or epimerisation of imines 140
   - 5.2. Ring-chain equilibrium 142
   - 5.3. Proton transfer equilibrium 144
   - 5.4. Anomeric equilibrium 152
6. Conformation and Molecular Interactions of Biological Active Schiff Bases 153
   - 6.1. ^{31}P NMR studies of Schiff base derivatives of pyridoxal phosphate 153
   - 6.2. NMR studies of rhodopsin 155
   - 6.3. CP MAS NMR studies of proteorhodopsin or bacteriorhodopsin 158
7. Complexes of the Optically Active Schiff Bases 160
   - 7.1. Ti(IV) complexes 160
   - 7.2. Zr(IV) complexes 162
   - 7.3. V(V) complexes 162

Department of Inorganic and Analytical Chemistry, West Pomeranian University of Technology, Szczecin, Al. Piastów 42, 70-065 Szczecin, Poland

Annual Reports on NMR Spectroscopy, Volume 74
ISSN 0066-4103, DOI: 10.1016/B978-0-08-097072-1.00003-0

7.4. Mo(VI) complexes 163
7.5. Mn(III) complexes 164
7.6. Re(VII) complexes 164
7.7. Fe(II) complexes 165
7.8. Ru(II) complexes 166
7.9. Co(II, III) complexes 166
7.10. Rh(III) and Ir(III) complexes 167
7.11. Ni(II) complexes 168
7.12. Pt complexes 169
7.13. Zn(II) and Cd(II) complexes 171
7.14. Sn(II) complexes 172
7.15. Lanthanide complexes 173
7.16. U(IV) complexes 174
8. ^{9}Be NMR 176
9. ^{27}Al NMR 176
10. ^{29}Si MAS NMR 176
Acknowledgement 177
References 177

Abstract The review covers the use of NMR spectroscopy in studies of optically active Schiff bases based on selected results reported in the last decade. The first part of the review is devoted to formation of Schiff bases as products which facilitate determination of the enatiomeric purity of various compounds. The next part is dedicated to conformational studies and investigation of different types of equilibria in optically active Schiff bases. Another part is devoted to studies of selected metal complexes, derivatives of optically active Schiff bases. Results concerning investigation of biologically active compounds in which Schiff bases are formed as intermediate product of enzymatic reactions are presented in separate section.

Key Words: Schiff bases, Imines, Complexes, Optically active, Equilibria, NMR, CP MAS NMR.

1. INTRODUCTION

The Schiff bases being derivatives of aldehydes or ketones and various amines have received considerable attention because of their interesting physical and chemical properties, involvement in biologically important reactions and widespread application of their metal complexes. Increasing interest in optically active Schiff bases is connected with the discovery at the beginning of the 1990s of the so-called Jacobsen catalysts used in several asymmetric reactions showing excellent enantioselectivity.

Although NMR spectroscopy is an achiral technique, it can be successfully used in studies of optically active compounds when diastereomers are formed or they are formed with the help of some auxiliaries. Moreover, investigation of many optically active Schiff bases does not require enantiomeric differentiations, and results of NMR measurements of compounds of unknown chiral composition are sufficiently informative about structure, inter- and intramolecular interactions or dynamic processes. This chapter covers selected results of NMR studies of optically active Schiff bases reported in the past decade. Every year, dozens of articles concerning this type of compounds are published, but only some will be reviewed. The selection of topics has been made on the basis of the criterion of being of interest for the readers and includes the use of different NMR techniques in solution as well as in solid state along with NMR measurements of various types of nuclei. The first part of this chapter is devoted to formation of the Schiff bases as products which facilitate determination of enantiomeric purity of various optically active compounds. The next part is dedicated to conformational studies and investigation of different types of equilibria. Results concerning biologically active compounds such as rhodopsin, bacteriorhodopsin, proteorhodopsin in which Schiff bases are formed as intermediate product of enzymatic reactions, are presented in a separate section. The last part of this chapter is devoted to selected studies of metal complexes, derivatives of optically active Schiff bases. The papers concerning the use of NMR spectroscopy for product identification only have been omitted or just mentioned.

2. SCHIFF BASES AS TOOLS FOR DETERMINATION OF ENANTIOMERIC PURITY AND ABSOLUTE CONFIGURATION

NMR can be a powerful tool for determination of enantiomeric excess or absolute configuration of the optically active compounds, however, these processes require the use of some auxiliaries, for example, chiral lanthanide shift reagents or chiral derivatising agent. In many cases, the starting point for determination of enantiopurity of amines, amino acids or diols is the formation of chiral imines.

2.1. Determination of enantiomeric purity

2.1.1. Derivatives of myrtenal

In determination of the enantiomeric purity of aliphatic primary amines, the use of β-aminoalcohols and α-amino acids 1*R*(−)-myrtenal as a derivatising agent has been tested.[1]

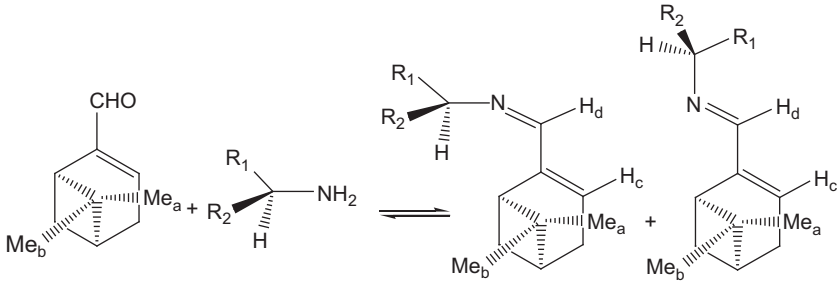

[1]

Derivatisation procedure, that is, formation of the Schiff bases [1], takes place directly in NMR tube before addition of deuterated solvents and usually does not require addition of other reagents (except amino acids when NaOH is added). For imines being derivatives of simple chiral amines, no significant differences in chemical shifts were observed. However, for compounds bearing more complex substituents especially aromatic groups, important differences between ^{1}H chemical shifts of the diastereoisomers are observed. The ring current effect increases the signal separation and allows determination of the enantiomeric purity by ^{1}H NMR. The largest differences in chemical shifts for both diastereomeric imines are observed for the signal of one methyl group Me(b) from the myrtenal moiety (ca. 0.01–0.18 ppm). This signal appears as a sharp singlet, which is often well resolved. Lower values have been measured for imine hydrogen H_d (ca. 0.01–0.14) and another methyl group Me(a) (ca. 0.01–0.05). The use of aromatic solvents like C_6D_6 and pyridine-d_5 twice increases the differences in chemical shifts of Me(a) protons.

Imines being derivatives of some primary amines, for example, 2-butylamine, 2-aminobutanol and (−)-myrtenal have been also studied by ^{13}C NMR.[2] It has been shown that for all compounds studied, it is possible to establish the *R*:*S* ratio (ratio of the enantiomers *R*:*S*). Two regions of the ^{13}C NMR spectra were useful in determination of the enantiomeric purity: ∼160 ppm assigned to imine carbon and ∼70 ppm assigned to carbon being stereo centre of the former amine. The differences in chemical shifts of both diastereoisomers were ca. 0.2–0.3 ppm. To avoid variations in the integration of the signals, a combined deconvolution and integration routine is required. Usually, estimation of the *R*:*S* ratio is possible within 15 min. The values depend on the number of scans, but the differences are in the acceptable range: for example, for the derivative of 1-phenylethylamine after 256 scans, the *R*:*S* ratio was 34.3:65.7; after 512 scans, it was 34.4:65.6; after 1k scans, 34.2:65.8; after 15k scans, 34.3:65.7. 2D ^{1}H, ^{15}N HMBC NMR spectra have also been used for evaluation of *R*:*S* ratio of Schiff base derivative of 1-phenylethylamine.

On the basis of automated peak picking and integration procedure, after less than 2 h, the enantiomeric purity was established. *R*:*S* ratio was 34.4:65.6, which is close to the values obtained from the ^{1}H or ^{13}C NMR spectra.

2.1.2. Derivatives of primary amines

Derivatization of the optically active aldehydes to imines has been used for determination of their enantiomeric excess. Chi et al.[3] have examined a series of chiral primary amines as a derivatizing agent in determination of the enantiomeric purity of the α-substituted δ-keto-aldehydes obtained from catalysed Michael additions. The imine proton signals were well resolved even if the reaction was not completed. The best results were obtained when chiral amines with —OMe or —COOMe groups were used [2]. The differences in chemical shifts of diastereomeric imine proton were ca. 0.02–0.08 ppm depending on amine. This method has been also used for identification of isomers of self-aldol condensation of hydrocinnamaldehyde.

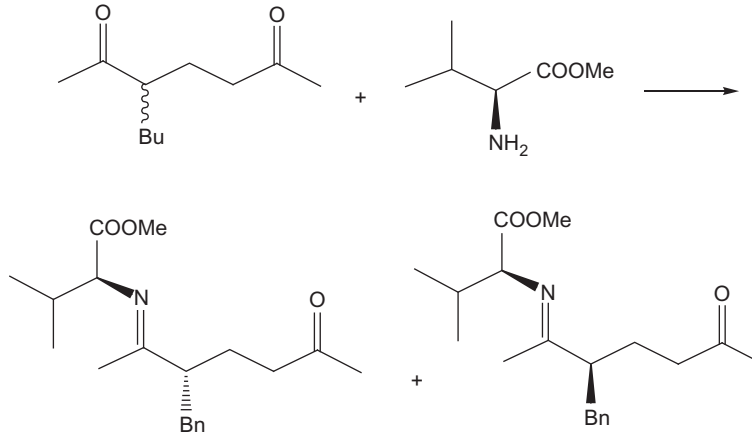

[2]

2.1.3. Derivatives of BINOL

In determination of the enantiomeric excess (ee%) of sulfinimines, the optically active (*S*)-BINOL (1,1′-bi-2-naphthol) has been used as chiral solvating agent.[4] In this method to the deuterated solution of the compounds studied, a portion of the solid (*S*)-BINOL was added and typical ^{1}H NMR spectra were recorded. The splitting of the proton signals due to the formation of Schiff bases diastereomers allowed concluding about the ee% value of the starting compound. If the separation of the imine signal was not satisfactory, another portion of the chiral solvating agent was added, even up to the ratio of 1:10.2. However, large excess of BINOL may

cause line broadening. The largest differences in chemical shifts of the imine signal 9.9 Hz (at 500 MHz) were observed when the ratio of sulfinimines to (*S*)-BINOL was 1:2.2 in C_6D_6. Lower values were measured in $CDCl_3$. Usually the use of benzene instead of $CDCl_3$ has twice increased separation of the signals. Comparison of the results obtained by means of HPLC chromatography with chiral column and the above-mentioned method has revealed an error of 1% in establishing the ee% value.

Derivatives of (*R*)-BINOL being chiral shift reagents were used in determination of the enantiomeric excess of amino acids[5] and 1,2-aminoalcohols[6]. Derivatives of (*R*)-BINOL and amino acids formed Schiff bases containing the OH··· N intramolecular hydrogen bond [3].[5] The splitting of the signal assigned to the proton engaged in the intramolecular hydrogen bond permitted determination of the *R*:*S* ratio. In a typical experiment, the amino acid was added to the solution of (*R*)-BINOL derivative in DMSO and after 5 min a typical ^1H spectrum was recorded. For a series of imines being derivatives of amino acids and amino acid esters, the differences in chemical shifts between both diastereoisomers were in the range 0.06–0.2 ppm. The highest value of 0.2 ppm was found for Schiff base derivative of valine, while the lowest one for alanine.

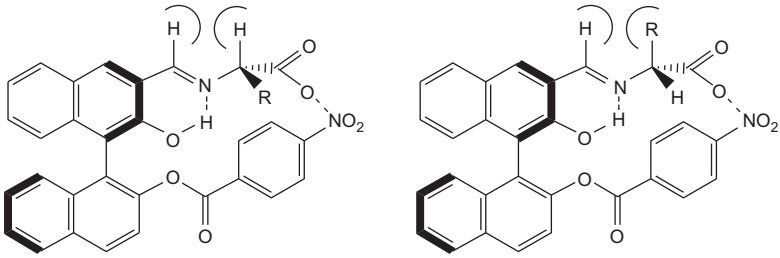

[3]

2.1.4. Three-component derivatives

Yeste et al.[7] have developed chiral derivatization protocols for determination of enantiopurity of chiral diols by the ^1H and ^{19}F NMR spectroscopy. Three-component method has required the treatment of diol with 2-formylphenylboronic acid and α-methyl-4-fluorobenzylamine [4].

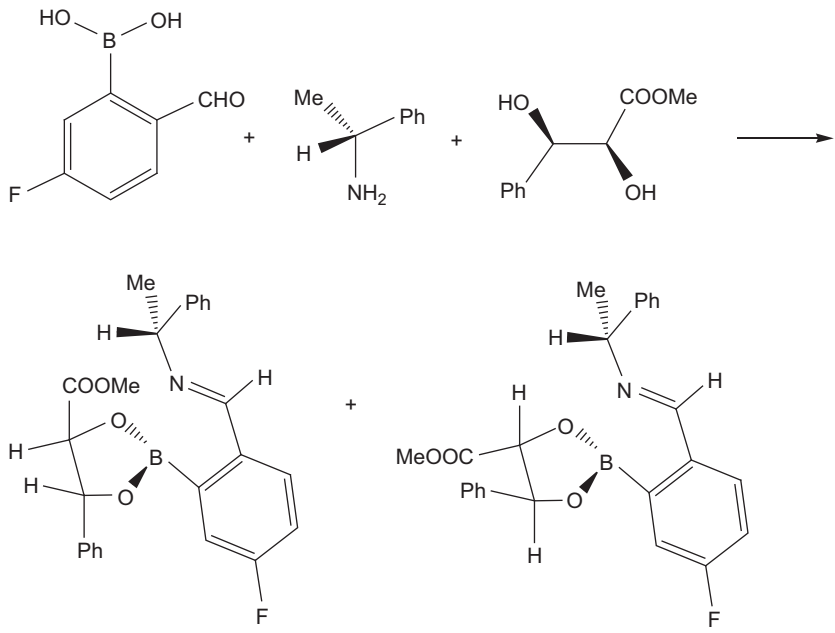

[4]

The imino-boronate esters obtained gave information on the enantiopurity of parent diols. The main advantages of this method were the use of commercially available components as chiral auxiliaries and their moisture insensitivity. The differences in ^{1}H chemical shifts of both diastereomers of the imine proton $\Delta\delta$ were in the range 0.05–0.35 ppm, while for the protons of the methyl group, 0.05–0.3 ppm. Usually higher values of $\Delta\delta$ ^{19}F (even up to 0.75 ppm) were observed in proton decoupled ^{19}F NMR spectra for pairs of diastereomeric imino-boronate esters. It was shown that the use of 4-fluoro-2-formylphenylboronic acid as a chiral derivatizing agent enables formation of diastereomeric imino-boronate esters with any chiral diol or chiral amine and determination of their enantiopurity. The values of $\Delta\delta^{1}H$ and $\Delta\delta^{19}F$ for mixtures of diastereomeric imines derived from 4-fluoro-2-formylphenylboronic acid were in the range 0.05–0.55 and 0.03–0.30 ppm, respectively. The chiral derivatizing protocol has been tested for determination of the enantiopurity of samples of methyl-(2*S*,3*R*)-dihydroxy-3-phenyl-propionoate with different ee% values. Analysis of the ^{1}H and ^{19}F NMR spectra revealed that diastereomeric excess values for each sample of imino-boronate esters were in a good agreement with the known enantiopurity of the starting diol.

A similar three-component protocol based on imino-boronate esters, derivatives of 2-formylphenolboronic acid, (*S*)-BINOL and amines has been developed by Perez-Fuertes et al.[8] for the determination of ee%

value of amines, and another one based on 2-formylphenolboronic acid and α-methylbenzylamine has been proposed for analysis of enantiomeric purity of diols.[9] Depending on the distance from the stereogenic centre, the chemical shift differences of diastereomeric imino-boronate esters were in the range from −0.67 up to 0.39 ppm.

2.2. Determination of absolute configuration

Chin et al. [5] have determined the absolute configuration of α-amino acids with hydrogen in α-position on the basis of the splitting of the OH signals in the ^{1}H NMR spectra of their imine derivatives with (*R*)-BINOL. On the basis of the theoretical computations, the authors have shown that hydrogen bond formed with L-alanine was shorter in comparison to that with D-alanine. The differences in hydrogen bond lengths were explained by steric interaction between the alanine methyl group and the imine hydrogen in D-alanine derivative. In consequence, the OH signal from Schiff base derivative of L-alanine was more downfield shifted in comparison to that of its D-enantiomer, which was the basis for determination of the absolute configuration of the amino acids. This procedure has been also successfully employed for assignment of the absolute stereochemistry of phenylethylamine.

In determination of the absolute configuration of α-chiral primary amines, BINOL derivatives were used as chiral derivatizing agent.[10] In this procedure, the chiral substrate was derivatized with *R* and *S* enantiomers of the 2′-methoxy-1,1′-binaphthalene-8-carbaldehyde and the ^{1}H spectra of both diastereomers were compared. Comparison of the chemical shift differences of the diastereomers has allowed determination of the absolute configuration of the chiral substrate [5].

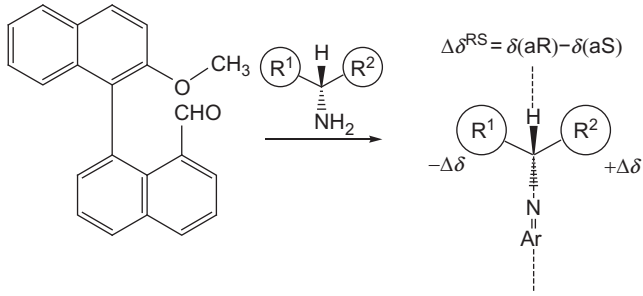

[5]

The origin of these differences was the diamagnetic effect of the naphthalene ring in BINOL fragment and different distances between the naphthalene ring and the groups on the stereogenic centre. It was shown that chemical shift of protons of the groups closer to the naphthalene ring on one side of the imino plane in *R*-derivative should be lower than that for *S*-derivative. The opposite situation should be observed for the groups on the

other side of the imino plane. On the basis of the differences in chemical shifts of the groups on the left and right sides of the imino plane, the authors have verified this method for a series of aliphatic amines, cyclic amines and amino acid esters of known configurations.

Perez-Fuertes et al.[8] have suggested the possibility of using the three-component chiral derivatizing approach for prediction of the absolute configuration of amines. Comparison of ^{1}H NMR spectra has shown significantly more deshielded signals of (*S,S*)-imino-boronate esters, derivative of α-amino esters than (*S,R*) diastereomers.

3. CHIRAL RECOGNITION OF THE OPTICALLY ACTIVE SCHIFF BASES

In chiral recognition of the optically active Schiff bases by NMR spectroscopy, the dirhodium method developed by Duddeck has been recently applied.[11,12] This method is very useful for chiral recognition of the compounds which cannot be recognised by lanthanide shift reagents. Dirhodium tetrakis-[(*R*)-α-methoxy-α-(trifluoromethyl)-phenylacetate] (dirhodium complex) used in this method forms kinetically labile 1:1 or 1:2 adducts with ligands, depending on the molar ratios of the components and the binding site in the ligand [6].

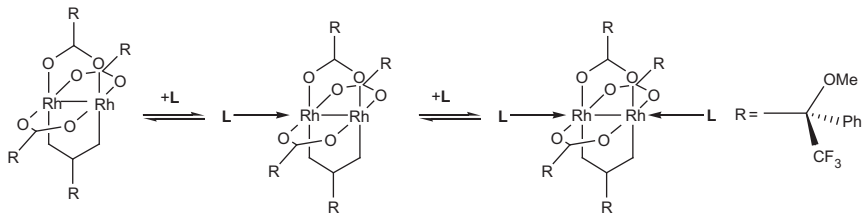

[6]

From the NMR spectra, two parameters can be extracted: the signal shift (Δδ) due to the change in the inductive and/or mesomeric influence of the complexing atom/group in the ligand and the signal dispersion (Δν) due to the presence of diastereomers. For the Schiff bases studied, the values of signal shifts ranged from ca. −0.5 to 1.5 ppm[11] in the ^{1}H spectra, from ca. −0.2 to 12.3 ppm[11] in the ^{13}C spectra and from −2.4 to 5.1 ppm[12] in the ^{15}N spectra, while the signal dispersion was from 3 to 67 Hz in the proton spectra (at 400 MHz),[11,12] 2.2–56 Hz (at 100 MHz) in the carbon spectra[11] and 2–48 Hz (at 60 MHz) in the nitrogen spectra.[12] Signal dispersion Δν, the most important parameter in chiral recognition, was observed at least for two protons and up to five protons. Similarly in the ^{13}C NMR spectra, the differences in chemical shift due to the presence of two diastereomers (Δν) were observed for a minimum two and maximum nine carbons[11]. The

highest values of the signal dispersion were measured for the position close to the stereogenic centre and for methine proton close to the anisotropic groups in the chiral Mosher acid residues. It should be mentioned that usually dirhodium complex does not cause a large signal shift, however, in the Schiff base studied, the high values of $\Delta\delta$ were observed because of a shift of the proton transfer equilibrium towards the NH-form. This case will be described in details in the Chapter 5.3. For some Schiff bases studied at low temperatures, a splitting of the proton donor group signal was observed. The splitting of this signal was explained by the presence of two adducts 2:1 and 1:1. The signal at a lower field was assigned to 2:1 adduct, while that at a higher field to 1:1 adduct. The temperature increase shifted the adduct formation equilibrium towards the 1:1 adduct.

Differences in the ^{1}H signals following from the presence of enantiomers were observed for Schiff bases being derivatives of gossypol [7], containing the crown ether moiety.[13] For Schiff bases being derivatives of racemic gossypol and L-phenylalanine amino acid methyl ester,[14] the presence of double signals of the naphthalene ring carbon atoms in the ^{13}C NMR spectra indicated the existence of diastereomers. In solution, the differences in chemical shifts were in the range from 0.01 ppm for carbon C-5 up to 0.84 ppm for carbon C-3. In the solid state, the double character of the signals was explained by the presence of hydrogen bonds of different strengths in the two parts of the symmetric molecule.

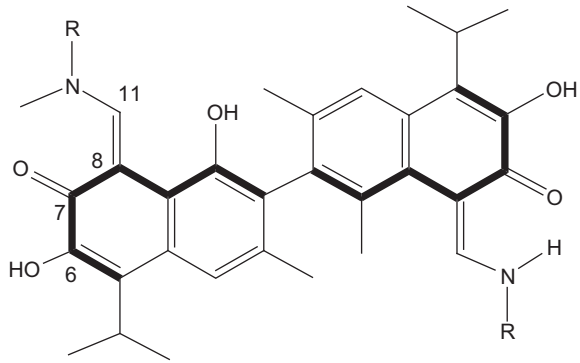

[7]

4. PRODUCT IDENTIFICATION AND CONFORMATION STUDIES

NMR spectroscopy has been widely used for identification of optically active Schiff bases.[15–18] It is also a valuable tool for determination of their conformations, suggesting the reaction pathway or simply for verification of their purity.[19–22] Selected examples are given below.

Durmaz et al.[19] have obtained novel calix[4]arene Schiff bases bearing chiral substituents [8] on the upper and lower rims, used in enantiomeric

recognition of amino acid derivatives by means of UV–vis spectroscopy. Although the ^{1}H and ^{13}C NMR spectroscopies have confirmed the structure of chiral imines, detailed description of the spectra was not presented.

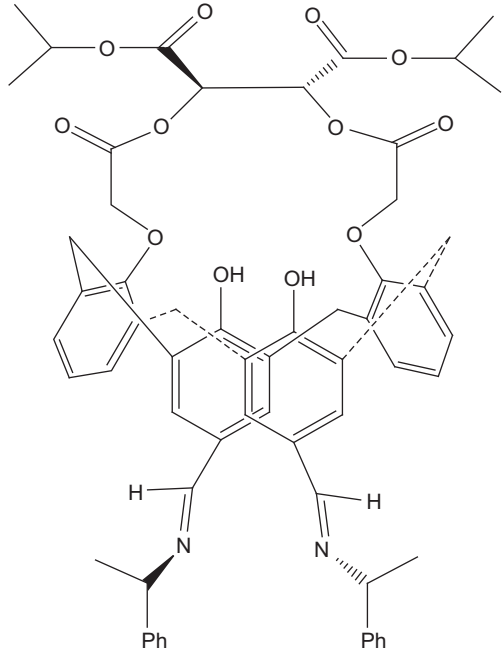

[8]

In the process of selective synthesis of macrocyclic Schiff bases, derivatives of chiral 1,4-diamines, the ^{1}H NMR spectra were taken to confirm the synthetic route without ^{1}H signals assignment.[20]

Gawroński et al.[21] have used NMR spectroscopy, especially NOE experiments in order to assign conformation of the chiral calixsalen-type macrocycles, products from the [3 + 3] cyclocondensation of the *trans*-1,2-diaminocyclohexane with hydroxydialdehydes. It was shown that the macrocycles had C_3-symmetrical structure and *s-syn* conformation of imine C—H/cyclohexane axial C—H bond systems and s-*trans* conformation of the bis-imine unit.

The 2D NOESY spectrum of the Schiff base being a derivative of histidine ethyl ester and 3-hydroxypyridin-4-carboxaldehyde has shown that in THF-d_8 solution the *E* conformation of the molecule is preferred.[22]

Recently, Bafquiren and Eddine have studied hindered Schiff base derivatives of *trans*-1,2-diaminocyclohexane.[23] The differences in chemical shifts found for imino carbons have indicated the presence of *anti*- and *syn*-geometric configurations. The intense NOESY effects between protons of naphthyl and alkyl units have proved the anti-configuration of the major stereoisomer.

Chiral Schiff bases are intermediates in the synthesis of peptidomimetic macrocycles which have been studied in detail by Bru et al.[24] and Alfonso et al. [9].[25]

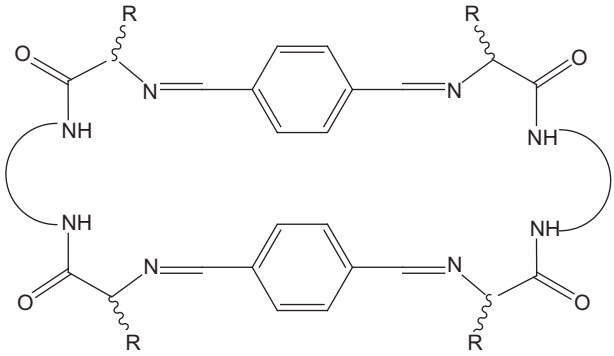

[9]

Simplification of the NMR spectra after 24 h as well as gCOSY, TOCSY, gHSQC experiments have suggested the symmetric conformation of the major component. The strong NOE effects between imino proton signals and α-proton of the peptidomimetic moiety have shown the connectivity between the substructures (peptidomimetic and aromatic). On the basis of the ^{1}H data for open-chain model, it was shown that the rate of formation of imine was lower for mismatch combination in comparison to that for the match combination of the diastereomers. Formation of the Schiff bases has been explained in terms of much favourable configurationally driven preorganization. The macrocyclisation process was dominated by a match/mismatch relationship of the relative configuration of the chiral centres in cyclic diamine and peptidic moieties.[25] The corrected combination of the chiral centres was (*R*,*R*)-cyclohexane-1,2-diamine and L-amino acids. Higher flexibility of the match diastereomer allowed adaptation of a folded conformation that led to macrocyclization.[25]

Spontaneous formation of the Schiff base [3 + 6] macrocycle being a derivative of 2,6-diformyl-4-methylphenol and polyamine has been shown by Schmidt et al. [10].[26]

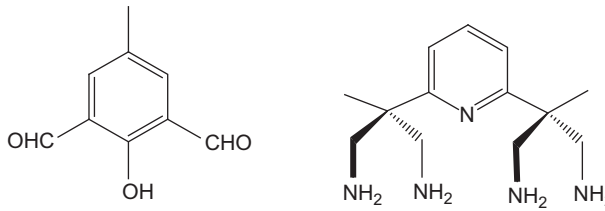

[10]

At 100 °C, the ROESY spectrum has shown chemical exchange of NH-protons and also pairwise chemical exchange of the methyl groups on the dialdehyde units, methine protons as well as the geminal CH_2 protons. This behaviour was explained as inversion of the whole molecule in an

umbrella-like fashion. On the basis of the chemical shift separation of the corresponding exchanging groups in the ^{1}H NMR spectra, a high barrier for the inversion process was established.

For 20- [11] and 40-membered [12] macrocyclic di- and tetra-Schiff bases being derivatives of (*R*)-BINOL, the chemical shift differences ($\Delta\delta$) measured for diastereotopic methylene protons of BINOL unit in $CDCl_3$ have suggested the presence of the partial rotation around the Ar—O—CH_2 bond.[27] The splitting of some ^{1}H signals in acetone-d_6 was explained as a result of a dynamic interconversion process on the NMR time-scale.

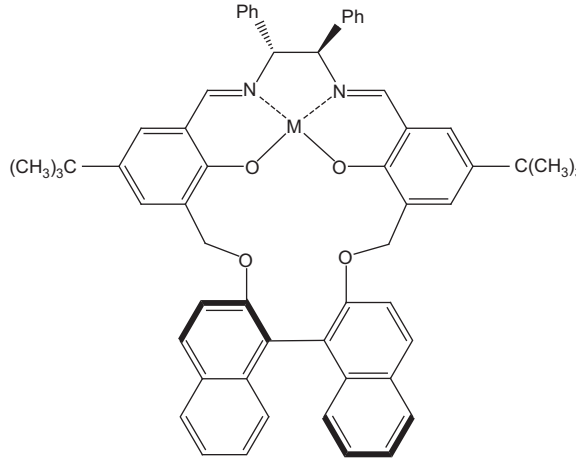

[11]

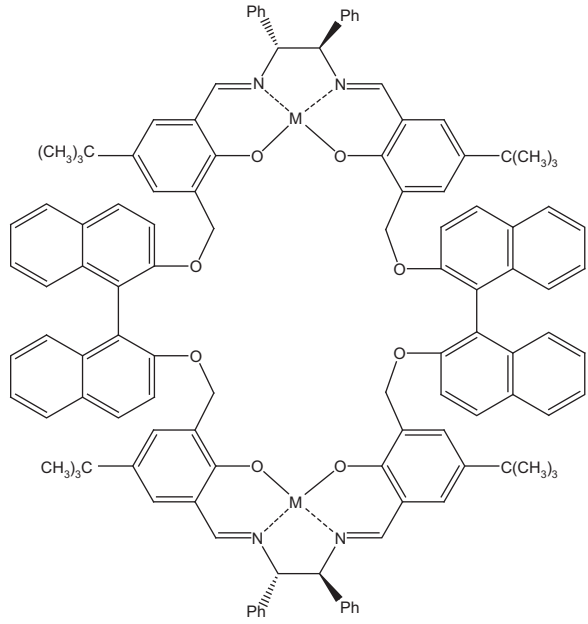

[12]

Tanaka et al.[28] have synthesised a series of (*S*)-chiral Schiff bases as the highly active (yield 69–99%) and enatioselective (ee 50–96%) catalysts in the reaction of addition of dialkylzinc to aldehydes. The stereochemistry of the asymmetric addition was suggested. In a transition state when *S*-chiral Schiff base was used as chiral source, the alkyl nucleophile attacked *Re* face of the activated aldehyde and formed the R-configuration alkylated product [13].

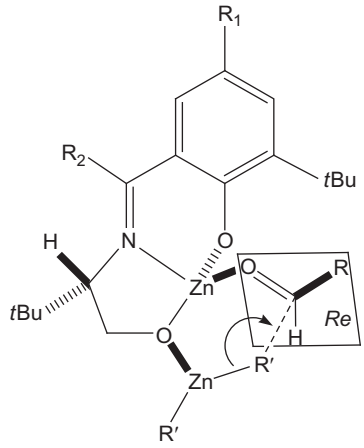

[13]

Structure of the chiral poly-Schiff base [14] has been studied by NMR spectroscopy.[29] It was shown that poly-Schiff bases have an interesting feature; their chiral forms can be self-assembled into nanometer-size fibrous architecture, while their racemic analogues did not show any self-assembling properties.

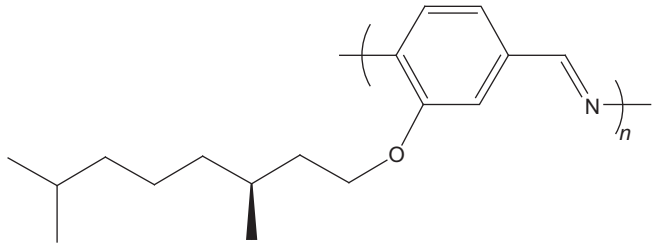

[14]

The ^{1}H NMR spectra have been used by dos Santos et al.[30] in determination of the degree of substitution (DS) in chitosan Schiff bases. The DS was found from the ratio between integrations of signals

of the imino proton and one of the pyranose ring protons. For the compounds studied, the DS value was in the range from 4.6% to 68.5%. The lowest DS values were found for derivatives of 5-chloro- and 5-bromosalicylaldehyde, while highest for the derivative of 5-nitro-salicylaldehyde. It was shown that inductive or/and field effects control the substitution degree.

The novel L-lysine modified cross-linked chitosan resin containing imine linkers [15] has been studied by the ^{13}C CP MAS spectroscopy.[31] However, as some ambiguous results were obtained and the resin was insoluble, instead of the resin a soluble model compound, derivative of chitosan oligosaccharide, has been obtained and investigated.

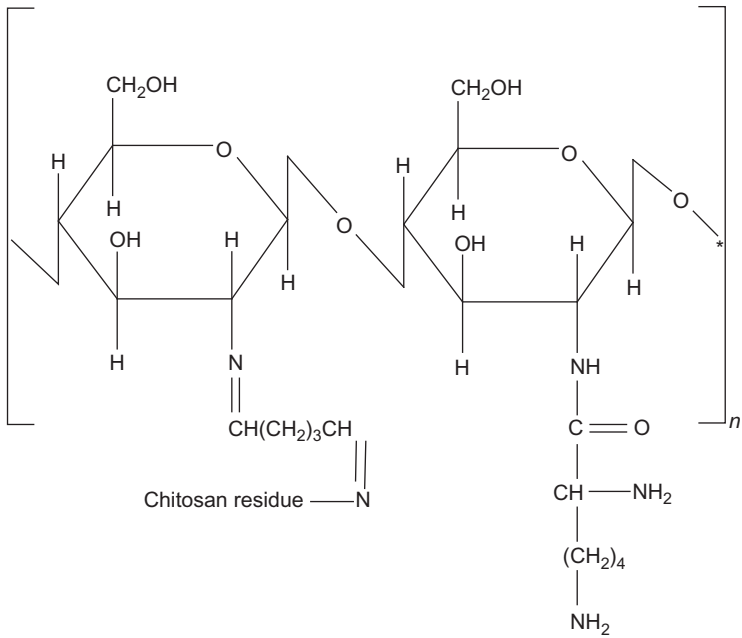

[15]

The NMR spectra have shown the formation of Schiff base as an intermediate product in the synthesis of the fully N-deacetylated oligomers from chitosan.[32] The mechanism of the Schiff base reaction leading to chain cleavage and formation of 5-hydroxymethyl-2-furfural has been proposed.

Rozwadowski et al.[33] have shown for Schiff base being derivatives of L-phenylalanine and 2-hydroxynaphthaldehyde [16] that shielding of the H-8 and H-α signals relative to the chemical shifts of these positions for other amino acid Schiff bases was connected with the anisotropy of the aromatic ring of the phenylalanine.

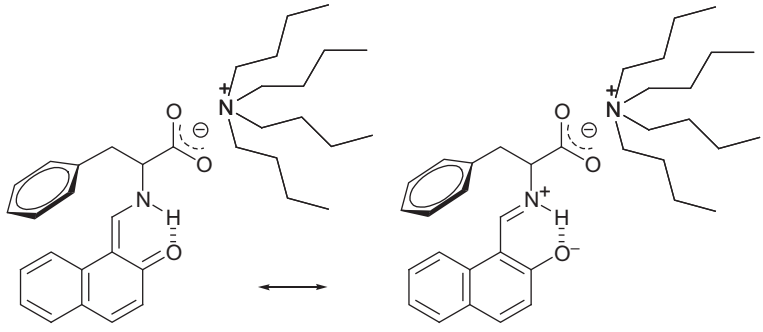

[16]

5. NMR STUDIES OF OPTICALLY ACTIVE SCHIFF BASE EQUILIBRIA

The NMR spectroscopy has been widely used in the studies of different types of equilibria like ring-chain tautomerism, racemisation or stereomutation and proton transfer equilibrium in Schiff bases.

5.1. Racemisation or epimerisation of imines

Possible racemisation of imines, derivatives of amino acids and *R*(−)-myrtenal, has been examined by Dufrasne et al.[1] After 72 h, no significant effect on chiral purity was observed. For imines being derivatives of chiral primary amines and the α-substituted δ-keto-aldehydes, no evidence of epimerisation has been indicated by the NMR measurements.[3] For a series of imines, being derivatives of amino acids or amino acid esters and (*R*)-BINOL reagents, Chin et al.[5] have tested the possibility of epimerization under experiment conditions. It was shown that *R*:*S* ratio has changed only slightly, and after 24 h, the difference was lower than 10%.

Park et al.[34,35] have used (*S*)-2-hydroxy-2′-(3-phenyl-uryl-benzyl)-1,1′-binaphthyl-3-carboxaldehyde for conversion of L-amino acids or peptides into D-amino acids [17].

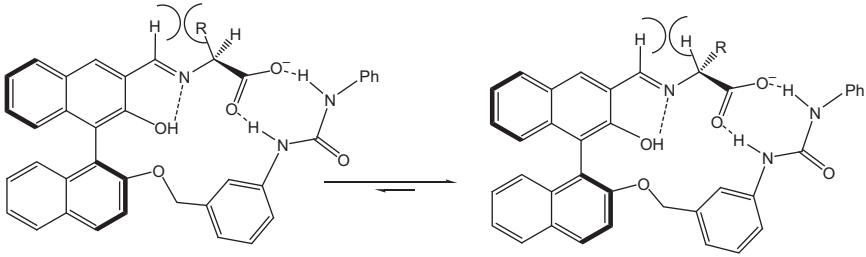

[17]

The chiral receptor has formed Schiff bases with a wide range of amino acids. It has been shown that, during Schiff base epimerisation, the chemical shifts of several signals have changed, for example, for derivative of L-alanine, the position of the phenolic hydrogen changed from 14.69 to 14.55 ppm and that of imine hydrogen from 8.78 to 8.70 ppm. The presence of the intramolecular hydrogen bonds has forced the orientation of the amino acid Schiff bases. Imine nitrogen was oriented towards the phenol OH group, while the carboxylate moiety was bonded to the uryl group. At equilibrium, the D/L ratio varied from 0 for valine derivative up to 20 for threonine derivative. The differences in the rate of deuteration of the α-proton between derivatives of D- and L-alanine have allowed prediction of the stepwise mechanism of the L-into-D conversion. DFT calculation has shown that the imine being a derivative of D-Ala is by 1.64 kcal/mol more stable than L-Ala and supported the mechanism suggested.

Dao et al.[36] have shown that for racemic *S*(+)-2-aminobutane-gossypolone-imine lowering temperature to 280 K has slowed the interconversion of the diastereomers.

For Schiff base being a derivative of gossypol and *R*-(+)-2-amino-3-benzyloxy-1-propanol, the conditions of the atropisomerisation were determined on the basis of the NMR spectra.[37] The ratio of the diastereomers was established on the basis of the integrals of selected ^{1}H signals (H-1 and H-11). The atropisomerisation of the gossypol Schiff base took place even if the samples were not exposed to the sunlight, however, this process was slower in the dark. The diastereopure Schiff bases were converted into a racemic mixture after ca. 12–14 h in the dark and ca. 3–3.5 h after irradiation of monochromatic light. The addition of a drop of water to acetonitrile solution accelerated the atropisomerisation. In this case, the 1:1 ratio of diastereomers was achieved after 45 min. The results obtained indicated that the atropisomerisation process cannot be considered as a simple photo-atropisomerisation.

The presence of the photoepimerization of the Schiff bases being derivatives of gossypol and L-amino acid methyl esters was also observed

by Przybylski and Brzeziński.[38] This process was relatively slow under laboratory conditions. Even after 7 days under diffuse light, both diastereomers were present in solution. It is worth mentioning that under the influence of diffused sunlight, the *L,L*-diastereoisomer was formed.

The dynamic NMR (DNMR) spectroscopy has been used in studies of stereomutations of non-symmetrical di-Schiff bases [18].[39] It was shown that the hindered Schiff bases exist in DMSO in two chiral conformations. The presence of a pair of conformers being in equilibrium was explained by the existence of two stereogenic axes $\alpha_{1,8}$ (aligned to C1—N8 bond) and $\alpha_{6,7}$ (aligned to C6—N7 bond) due to restricted rotation around two Ar—N bonds. The *trans* to *cis* interconversion as well as enantio- or diastereoisomerisation barriers for the compounds studied have been established using line shape analysis.

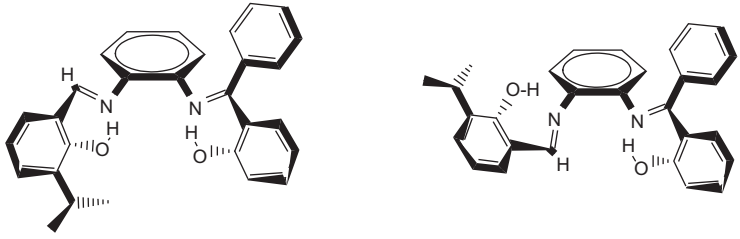

[18]

5.2. Ring-chain equilibrium

Talancon et al.[40] investigated the effects of substituents on the ring-chain tautomerism of Schiff bases being derivatives of norephedrine on the basis of ^{1}H and ^{13}C NMR measurements [19].

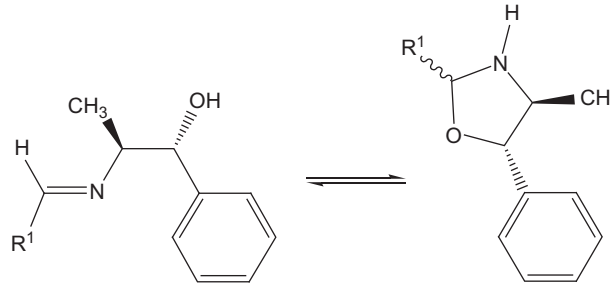

[19]

For ferrocenyl derivative, the spectra analysis has revealed the presence of a Schiff base in the *anti*-(E) form in equilibrium with two of the diastereomers of oxazolidines generated by 5-*endo-tring* process in the

$CDCl_3$ solution. Although formation of the oxazolidines has generated new stereogenic centre and four diastereomers are expected, in solution, the interchange of the proton in the NH unit can be responsible for the interconversion between isomers. Temperature measurements indicated a slight shift of the equilibrium towards oxazolidine form at lower temperatures and allowed determination of the ΔH and ΔS values. The position of equilibrium depended on the solvent and the mole fraction of the imine-form increased according to the solvent sequence: benzene < chloroform < acetone < methanol < DMSO. Similar behaviour has been observed for Schiff base with 5-methylthienyl unit, however, the presence of the 5-methylthienyl group increased the mole fraction of the open form. For the Schiff base containing 3-methylthienyl unit, the splitting of the imine carbon signal (difference in chemical shift ca. 0.9 ppm) suggested that the rotamers may exhibit different property to undergo *5-endo-trig* process. The differences in chemical shift of imine carbon observed for the Schiff bases studied indicated that steric effects can reduce the stability of the oxazolidines with 3-methylthienyl group in comparison to those for the oxazolidines with 5-methylthienyl group and hinder the free rotation of the thienyl ring leading to the existence of rotameric species in solution.

The ring-chain tautomerism has been also studied for di-Schiff base derivatives of C-substituted serinols [20].[41]

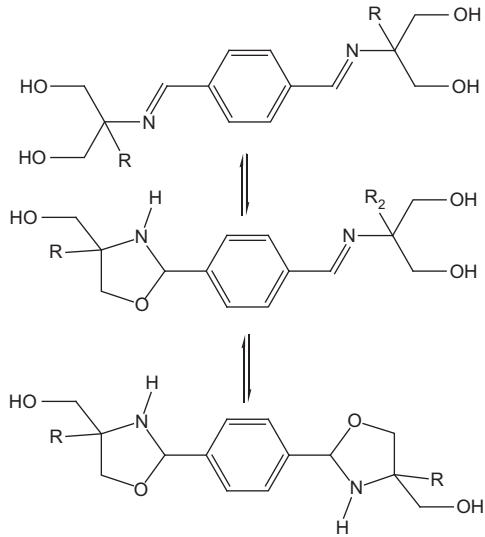

[20]

The composition of the forms being in equilibrium for chiral di-imines was deduced from ^{1}H NMR spectra. For the compounds studied, the equilibrium state was reached after 24 h. The absence of the intermediates

was explained by the increased acidity of the secondary hydroxyl group; their chemical shifts were 5.24 and 5.64 ppm, respectively. It has been shown that electronic factors dominate steric requirements regarding the stereochemistry of double oxazolidine.

5.3. Proton transfer equilibrium

The optically active Schiff bases containing intramolecular hydrogen bonds are of major interest because of their use as ligands for complexes employed as catalysts in enantioselective reactions or model compounds in studies of enzymatic reactions. In the studies of intramolecularly hydrogen bonded Schiff bases, the NMR spectroscopy is widely used and allows detection of the presence of proton transfer equilibrium and determination of the mole fraction of tautomers [21]. Literature gives a few names of tautomers in equilibrium. The OH-tautomer has been also known as OH-, enol- or imine-form, while NH tautomer as NH-, keto-, enamine-, or proton-transferred form. More detail information concerning the application of NMR spectroscopy for investigation of proton transfer equilibrium in Schiff bases is presented in reviews.[42–44]

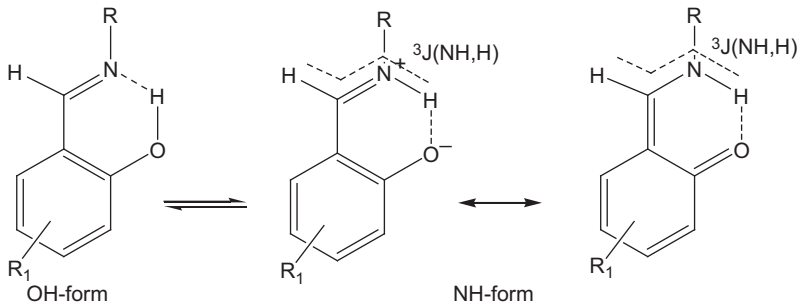

[21]

5.3.1. ^{1}H and ^{13}C NMR spectroscopy

The values of ^{3}J(NH,H) coupling constant observed for imine proton can be helpful in detection of the proton transfer processes and determination of mole fractions of tautomers in equilibrium. For NH-form, this value is close to 13 Hz, lower values usually indicate the presence of tautomeric equilibrium. It should be mentioned that the values below 2.4 Hz have not been reported. The chemical shift of C—OH (C-2 for imines, derivatives of aromatic ortho-hydroxyaldehydes or C-7 for gossypol derivatives) carbon to some extent can be informative, however, this value depends on type of substituents and should be interpreted with caution.

Analysis of the NMR data for symmetrical and unsymmetrical di-Schiff bases being derivatives of *trans*-1,2-diaminocyclohexane and various aromatic *ortho*-hydroxyaldehydes [22] has shown the presence of proton transfer equilibrium.[45,46]

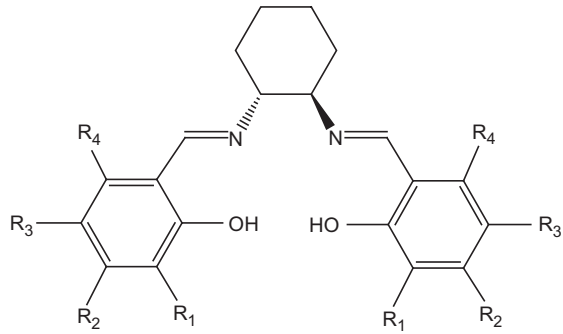

[22]

The values of ^{3}J(NH,H), varying from 5.8 to 10.2 Hz, were measured for di-imines with NH-form prevalent. Different positions of the tautomeric equilibrium have been reported for the Schiff bases being derivatives of rac-α-methylbenzylamine or rac-2-aminobutane and aromatic *ortho*-hydroxyaldehydes. Their ^{3}J(NH,H) values were in range from 2.4 to 13.4 Hz.[11,12] The Schiff bases being derivatives of gossypol have been studied by Przybylski et al. in detail.[47–51] Although the presence of tautomeric equilibrium was a possibility, the high values of ^{3}J(NH,H) coupling constant (12.09 Hz) and ^{13}C chemical shift of C—OH (C-7) carbon (173.63 and 173.69 ppm) observed in $CDCl_3$ solution for the Schiff base being derivative of gossypol and L-phenylalanine methyl ester[14] could indicate the existence of enamine–enamine tautomeric form. The splitting of carbon signal was explained by the presence of two diastereomers. Existence of other Schiff bases being derivatives of gossypol and 3,6-dioxadecylamine[47], 2-(aminomethyl)-18-crown-6 or 5-hydroxy-3-oxapentylamine[48] in the proton-transferred form was also confirmed. For the above-mentioned Schiff bases, the C-7 chemical shifts varied from 172.00 to 173.22 ppm. It has been shown that the value of chemical shift of carbon C-6 in position meta to the imine (~147 ppm) in solid state NMR can be related to the presence of the intramolecular hydrogen bond between the OH group at this position and the oxygen atom of C(7)=O carbonyl group in the proton transferred form.[49] Hansen et al.[52] have shown that for gossypol Schiff bases, the C-7 chemical shifts changed only slightly with temperature change or solvent presence. The ^{3}J(NH,H) values of 12–13 Hz as well as C-7 chemical shifts (172.1–177.0 ppm) indicated the presence of NH-form only.

For the Schiff base being a derivative of 2-hydroxynaphthaldehyde and threonine, the splitting of the imine proton signal (^3J(NH,H) = 6.5 Hz) has indicated the presence of proton transfer equilibrium in DMSO solution.[53] Results of NMR studies of the Schiff bases being derivatives of 2-hydroxynaphthaldehyde and amino acids, their lithium[54,55] and tetrabutylammonium salts[33] have been reported. The absence of proton transfer equilibrium and the existence of the above-mentioned compounds in NH-form in solution and in solid state were shown. For lithium salts in DMSO solution ^3J(NH,H), coupling constants varied from 10.6 to 13.0 Hz.[54] Similar values (12–13.1 Hz) were found for tetrabutylammonium salts in $CDCl_3$.[33] The δC-2 values depended on the solvent, temperature, type of salt and type of NMR measurements (solution or CP MAS) and varied from 178.9 to 182.5 ppm.[33,54,55] The highest values were found for lithium salts in D_2O.[55]

The NMR measurements for the Schiff bases being derivatives of (*R*)-1-(9-anthryl)-ethylamine and 2-(2′-pyridyl or quinolyl)acetophenone [23] have revealed the presence of the rigid conformation of the enamine form.[56]

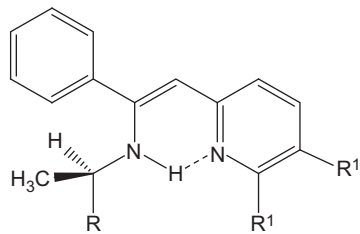

[23]

5.3.2. ^{15}N NMR spectroscopy

The δN chemical shift can be used in studies of tautomeric equilibrium for optically active Schiff bases, however, it depends not only on the position of equilibrium but also on the types of substituents. Usually values higher than −200 ppm (relative to nitromethane) indicate the presence of pure NH-form or equilibrium strongly shifted towards NH tautomer. Lower values of δ^{15}N imply the presence of tautomeric equilibrium.[42,44]

For the optically active Schiff bases [24], [25] in $CDCl_3$, the δ^{15}N values were in the range from −65.2 to −230.3 ppm and increased for the following series of derivatives: salicylaldehyde < 3-bromosalicylaldehyde < 5-nitrosalicylaldehyde < 4,6-dimethoxy-salicylaldehyde < 2-hydroxynaphthaldehyde which resulted from increased mole fraction of the NH-form.[12]

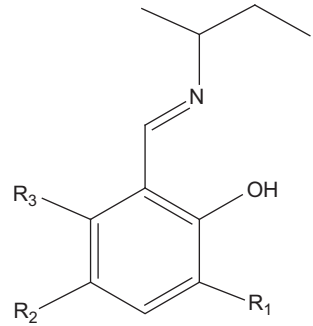

[24]

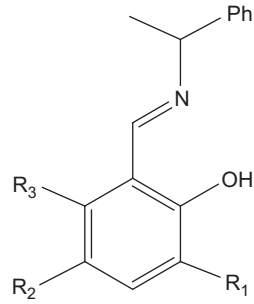

[25]

Formation of the adduct with dirhodium complex [6] has significantly changed the chemical shift of the compounds in which proton transfer occurred, for example, for the adduct of *N*-(5-nitrosalicylidene)-2-aminobutane, the chemical shift was −198.2, which was shielded by of 110 ppm in comparison to that in the starting Schiff base.[12] The large signal shift was due to the shift of the proton transfer equilibrium towards NH tautomer. For the adduct of *N*-(salicylidene)-2-aminobutane, existing in the OH-form, the ^{15}N chemical shift has changed from −87.5 to −84.6 ppm.

The values of $\delta^{15}N$ in the range from −75.6 to −217.1 ppm were measured for symmetrical and unsymmetrical di-Schiff bases being derivatives of *trans*-1,2-diaminocyclohexane [22] in chloroform solution and in solid state.[57]

The ^{15}N chemical shifts measured for the Schiff base being a derivative of gossypol [7] and L-phenylalanine methyl ester equal −243.7 ppm in $CDCl_3$ solution and −237.5 in solid state (relative to external

nitromethane) were typical of the NH-form.[14] For the derivative of L-arginine methyl ester, δ^{15}N CP MAS value of −187.3 ppm, deshielded in comparison to the other gossypol Schiff bases, was explained by a strong interaction of imine proton with the N atoms of arginine moiety. The ^{15}N chemical shift of crown Schiff base of ca. −350 ppm was explained by the interaction with O atoms of the crown.[48] For the Schiff bases being derivatives of L-alanine, L-phenylalanine and L-histidine methyl esters and 3-hydroxypyridin-4-carboxaldehyde, the values of δ^{15}N varied from −65.9 to −71.2 ppm and indicated that compounds studied exist mainly in OH-tautomeric form.[22] The existence of the Schiff bases being derivatives of glycine, L-alanine, L-phenylalanine, L-valine, L-leucine, their lithium salts and 2-hydroxynaphthaldehyde in NH-form in solid state was verified. The high negative values of ^{15}N CP MAS chemical shifts were in the range from ∼−203 to ∼−231 ppm.[54] The differences in chemical shifts were related to the type of amino acid moiety.

5.3.3. Deuterium isotope effects on chemical shifts

The measurement of deuterium isotope effects on chemical shifts is a useful tool for studies of tautomeric equilibrium (for details see the reviews [42–44]). The deuterium isotope effect $\Delta X(D)$ is defined as the difference between chemical shifts in deuterated and non-deuterated sample [26].

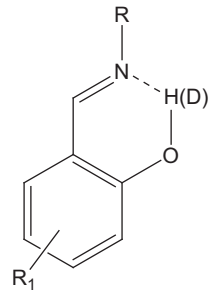

[26]

The deuterium isotope effects on chemical shift consists of: intrinsic isotope effect (direct perturbation of the shielding of X atom) and equilibrium isotope effect (perturbation of the equilibrium caused by the isotopic substitution). The values of deuterium isotope effects are to some extent independent of chemical shifts and allow determination of the mole fraction of the forms in equilibrium.

5.3.3.1. Deuterium isotope effects on ^{13}C chemical shifts In the studies of proton transfer equilibrium of Schiff bases, the most informative are deuterium isotope effects measured for carbons bonded with proton donor groups (C-2 or C-7 for gossypol derivatives). For imines in which

one proton is localised, the ΔC-2(D) values show weak temperature dependence and change in the range: 400–600 ppb for OH-form and −200 ÷ −250 ppb for NH-form. For the compounds in which the proton transfer equilibrium takes place, the ΔC-2(D) values varied from ∼+550 to ∼−550 ppb and showed temperature and solvent dependence.[42,43] The correlation between ΔC-2(D) values and mole fraction of the proton transferred forms found for Schiff bases has been shown in Figure 1.

Hansen et al.[52] measured the deuterium isotope effects for the Schiff base being a derivative of racemic gossypol [7]. The high negative value of deuterium isotope effect observed at carbon C-7 linked with proton donor group (−190 ÷ −240 ppb), solvent and temperature independent, clearly indicated the existence of this compound as enamine–enamine tautomer.

In the spectra of partially deuterated di-Schiff bases being derivatives of *trans*-1,2-diaminocyclohexane [22], an exceptional splitting of some ^{13}C signals into four lines instead of two was observed at low temperatures.[45,46] In order to explain such a behaviour, two hypotheses were considered (i) non-equivalence of two hydrogen bonds, (ii) interrelation between proton transfer equilibria in both hydrogen bonds. However, the first hypothesis was not taken into account due to existence of the splitting only in the di-Schiff bases in which proton transfer take place. Detailed analysis of the results has shown that a shift of the equilibrium in one intramolecular hydrogen bond due to deuteration induces in the other hydrogen bond a shift of the equilibrium in the opposite direction.

Measurements of the deuterium isotope effect for unsymmetrical di-Schiff bases fully confirmed the interrelation between proton transfer equilibria in both intramolecular hydrogen bonds.[46]

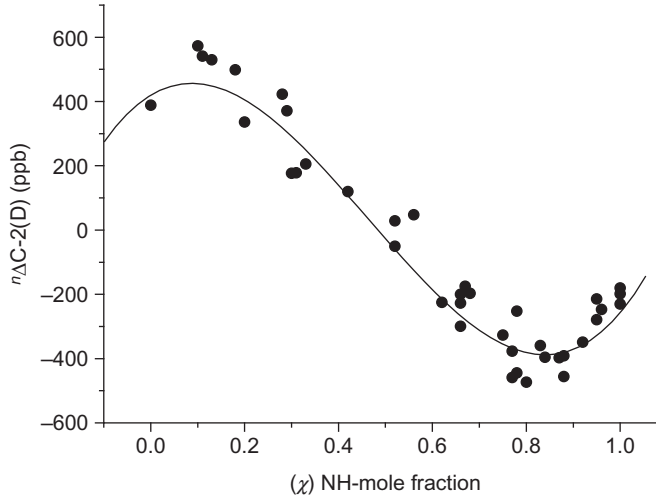

Figure 1 Correlation between ΔC-2(D) and mole fraction of the NH-form.[42–44]

Deuterium isotope effects on ^{13}C chemical shifts were measured for a series of Schiff bases being derivatives of 2-hydroxynaphthaldehyde and lithium salts of glycine, L-alanine, L-phenylalanine, L-valine, L-leucine, L-isoleucine, L-methionine in water.[55] The slow exchange on the NMR time-scale allowed observation of separate signals from both isotopomers (deuterated and non-deuterated) which is rather unusual in water. Large negative ΔC-2(D) values close to −200 ppb and their weak temperature dependence indicated the absence of proton transfer equilibrium. Comparable values of ΔC-2(D) in the range from −213 to −281 ppb measured for their tetrabutylammonium salt in $CDCl_3$ indicated that the type of amino acid moiety has rather small effect on the structure and mole fraction of NH tautomer.[33] Low values of the deuterium isotope effects determined for carboxylate carbon C-2′ of ∼50 ppb were interpreted as related to the presence of intermolecular hydrogen bonds between COO^- group and water molecules or to the long-range isotope effects. On the basis of the data for *N*-(2-hydroxynaphthylidene)-L-leucine methyl ester, it was shown that the presence of bifurcated hydrogen bond and the interaction between COO^- and NH stabilised the proton transferred form [27].

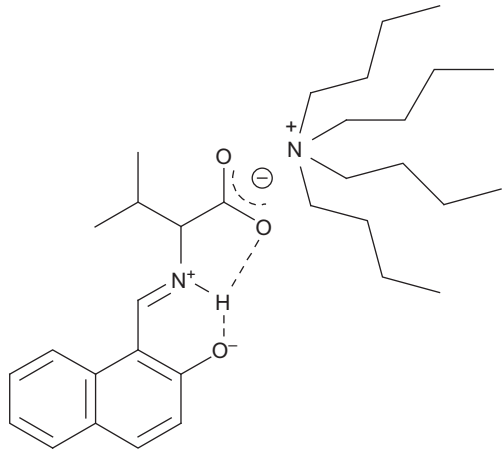

[27]

Deuterium isotope effects in $CDCl_3$ have been applied in studies of proton transfer equilibrium for optically active Schiff bases [24], [25] as well as their dirhodium tetracarboxylate adducts.[11] The ΔC-2(D) values were in the range from +541 to −546 ppb for imines and from +524 to −255 ppb for their adducts. Exceptionally low values of deuterium isotope effects of −20 ÷ −80 ppb were observed for the Schiff bases being derivatives of 3,5-dinitrosalicylaldehyde which exist in pure NH-form. This behaviour was explained by different electronic structures of the NH

tautomer; more zwitterionic than quinoidic [21]. For the Schiff bases in which the proton transfer equilibrium was present, formation of the adducts with dirhodium complex [6] shifted the tautomeric equilibrium towards pure NH-form. For example, the ΔC-2(D) value for rac-*N*-(5-nitrosalicylidene)-2-aminobutane changed from +530 ppm for imine to −230 ppb for its adducts. Most of the studied Schiff base adducts showed the following interesting feature: because of the presence of four species (non-deuterated and deuterated diastereomers), two sets of deuterium isotope effects were observed for some carbon atoms. The values of deuterium isotope effects were equal or very close for both diastereomers.

5.3.3.2. Deuterium isotope effects on ^{15}N chemical shifts Deuterium isotope effects on ^{15}N chemical shifts ΔN(D), similarly as for ΔC(D), can be employed in determination of mole fraction of the proton transferred form Schiff bases.[44] A similar correlation between the mole fraction of NH-form and ΔN(D) values was found (Figure 2). For the Schiff bases in which proton transfer takes place, the ΔN(D) values varied from −2 to +5 ppm and depend on solvent and temperature. The ΔN(D) values of ∼−2 ppm are typical of OH-form, while the values of ∼+2.5 ppm are typical of pure NH-form.

Deuterium isotope effects on ^{15}N chemical shift in $CDCl_3$ solution as well as in solid state were measured for a series of symmetrical and unsymmetrical di-Schiff bases being derivatives of *trans*-1,2-diaminocyclohexane and various aromatic *ortho*-hydroxy-aldehydes [22].[57] The ΔN(D) value determined in solid state for symmetrical di-Schiff base which was a derivative of salicylaldehyde was −1.8 ppm, which was typical of

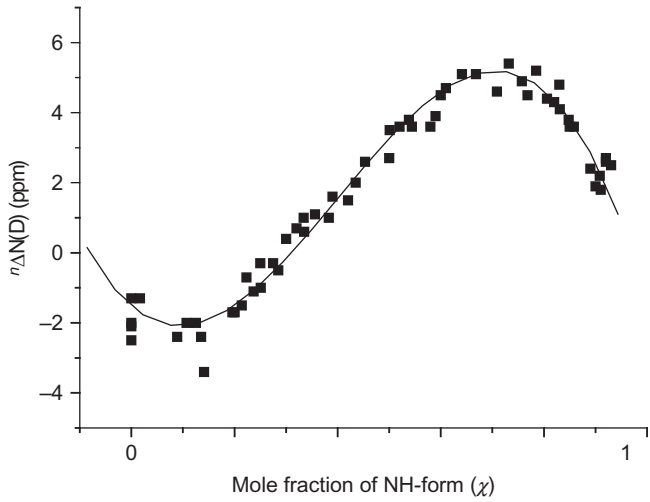

Figure 2 Correlation between ΔN(D) and mole fraction of the NH-form.[42,44]

the compounds existing exclusively in OH-tautomeric form. For symmetrical double Schiff base being a derivative of 2-hydroxynaphthaldehyde, the ΔN(D) CP MAS values −1.7 and +2.4 ppm have resulted in different mole fractions of the NH-form in both parts of the molecule. The data for the unsymmetrical compound being a derivative of 2-hydroxynaphthaldehyde and salicylaldehyde have shown that the proton transfer equilibrium in 2-hydroxynapthalidene moiety was strongly shifted towards NH-form (ΔN(D) CP MAS equal +5.4 ppm), while in salicylidene moiety, only the OH-form existed (ΔN(D) CP MAS equal −1.8 ppm).

The position of the proton transfer equilibrium for the Schiff bases being derivatives of rac-2-aminobutane [24] or rac-α-methylbenzylamine [25] and their adducts with dirhodium complex has been estimated in $CDCl_3$ solution on the basis of measurements of deuterium isotope effects on ^{15}N chemical shift.[12] It was shown that adduct formation significantly influenced the position of the equilibrium which was manifested by ΔN(D) values.

5.4. Anomeric equilibrium

The anomeric and tautomeric equilibria of the Schiff bases being derivatives of D-2-glucosamine have been studied by Kołodziej et al. [28].[58]

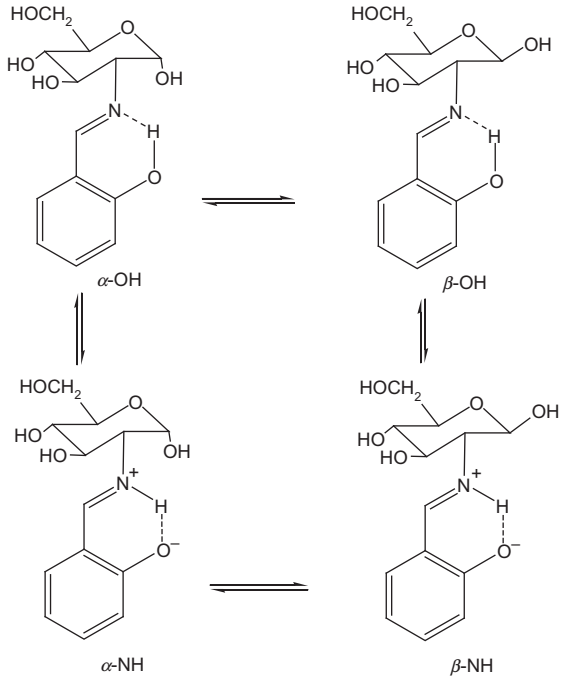

[28]

On the basis of the ^{1}H, ^{13}C, ^{15}N NMR spectra in solution and the ^{13}C and ^{15}N NMR spectra in solid state, the positions of both equilibria have been established. *N*-(salicylidene)-D-2-glucosamine existed in DMSO solution in the OH-tautomeric form as an anomeric mixture with predominance of the β form. For the Schiff bases being derivatives of 3,5-dichloro- and 3,5-dibromosalicylaldehyde, the proton transfer equilibrium was strongly shifted towards NH-form as an anomeric mixture with predominance of the α form. *N*-(3,5-dinitrosalicylidene)-D-2-glucosamine and *N*-(2-hydroxynaphthylidene)-D-2-glucosamine existed almost exclusively in the proton transferred NH-form, but in the former, α form prevailed in the anomeric mixture, while in latter, the β one was dominant. The results have shown that the relative stability of the anomeric forms depend on the position of the proton in the intramolecular hydrogen bond and the electronic structure of the NH tautomer. Similar studies for the Schiff bases being derivatives of glucosamine have been performed by Costamagna et al.[59]

6. CONFORMATION AND MOLECULAR INTERACTIONS OF BIOLOGICAL ACTIVE SCHIFF BASES

6.1. ^{31}P NMR studies of Schiff base derivatives of pyridoxal phosphate

The role of Schiff bases formed between pyridoxal phosphate and amino acid residues as intermediate products in many enzymatic reactions is well known and documented. NMR is an excellent tool for studies of the enzymatic processes involving Schiff bases formation.

^{31}P NMR spectroscopy is an excellent sensor of structural changes that occur along the reaction pathway [29], especially when monitoring the tightness of binding of the cofactor.

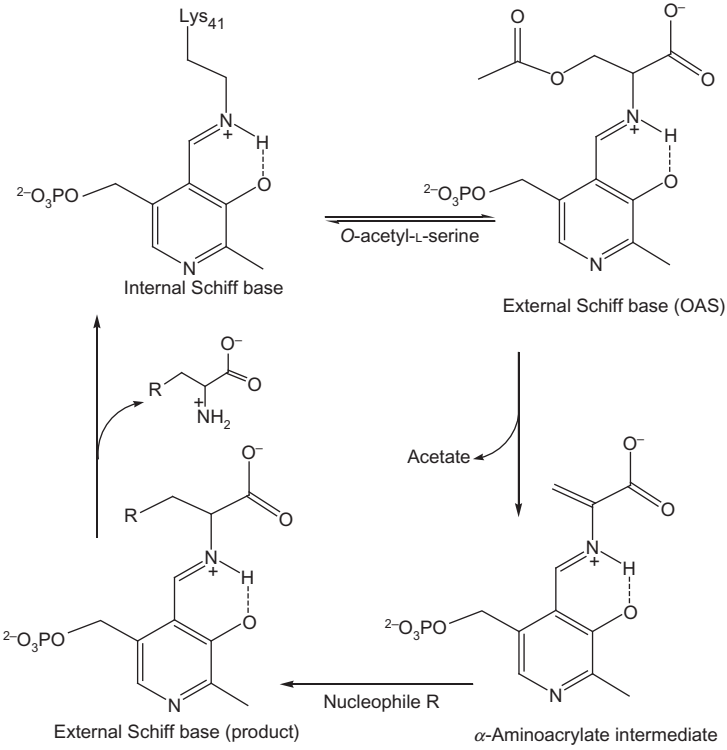

[29]

Chemical shift and line width are related and can be used to describe conformational changes. The δ^{31}P value of 5 ppm and the line width of 20 Hz indicate that dianionic 5′phosphate is very tightly bound to the active site and tumbles with the protein. Lower values of chemical shift indicate more loosely bound phosphate. Higher values of the line width indicate the presence of two conformers in equilibrium. If the open and close form undergo slow interconvertion, two signals are observed in the ^{31}P NMR spectra.

In a series of papers, Cook et al.[60–63] presented results of the ^{31}P NMR studies of pyridoxal 5′-phosphate dependent enzyme. *O*-acetylserine sulfhydrylase is the enzyme which catalyses the final step of biosynthesis of L-cysteine, the replacement of β-acetoxy group of *O*-acetyl-L-serine by thiol [30] in bacteria and plants.

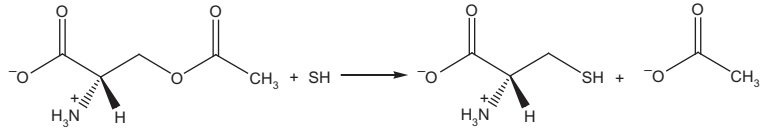

[30]

TABLE 1 ^{31}P NMR chemical shifts (ppm) and line width (in parentheses; Hz) of the wild type (WT) and mutant enzymes (H152A, K120Q)[60,61]

Intermediates	WT	H152A	K120Q
ISB	5.20 (20.5)	5.3 (24) 4.8 (22)	5.16 (19)
ESB_{serine}	4.4 (50)	4.22 (49)	4.4 (46)
$ESB_{lanthionine}$	5.3 (37.5)	5.48 (19) 5.06 (29)	5.16 (29)
AA	3.95 (18)	4.06 (14)	3.94 (18)

The behaviour of the mutant enzymes where, for example, histidine-152 has been changed to alanine is compared with that of wild type enzymes.[60] The ^{31}P NMR chemical shift values and signal width for H152A mutant enzyme have shown the presence of two conformers; open and closed forms of the enzyme that interconvert slowly on the NMR time scale. The tightness of the binding of the cofactor to the protein surface and its protonation state have been also discussed for intermediate Schiff bases in different steps of the catalytic cycle (Table 1).

In A- and B-isozymes of *O*-acetylserine sulfydrylase, δ^{31}P values of internal and external Schiff bases have been compared.[62] Higher value of ^{31}P chemical shift for B-isozyme suggested not only a tighter binding of the cofactor but also a torsional strain. The torsional angle, responsible for the rotation around C5—C5′ bond (of the 5′-phosphate fragment), has been reduced from 67.8° in isozyme-A to 55.6° in isozyme-B.

6.2. NMR studies of rhodopsin

Rhodopsin is a seven α-helix trans-membrane protein and visual pigment of the vertebrate rod photoreceptor cells that mediate dim light vision. In this photoreceptor, retinal is the chromophore bound by opsin protein, covalently linked to Lys296 by a Schiff base linkage. Kpega et al.[64] have studied ^{1}H NMR spectra of Schiff bases being derivatives of all-*trans* retinal and amino-β-cyclodextrins as a model of rhodopsin, where β-cyclodextrin plays a role of a binding pocket. On the basis of analysis of the chemical shift differences for the model compound in the presence and in the absence of adamantane carboxylate, it has been shown that the derivative of 3-amino-β-cyclodextrin forms dimer in water and retinoid is inserted into β-cyclodextrin cavity [31].

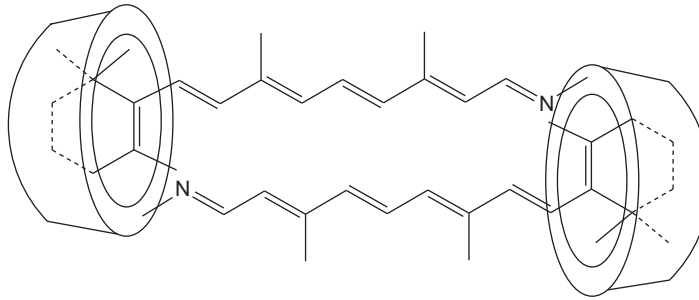

[31]

6.2.1. ^{1}H and ^{13}C CP MAS NMR

Recently, the CP MAS NMR spectroscopy has been widely used for the studies of rhodopsin making use of the sensitivity of the retinal chemical shifts to conformation of the chromophore and its molecular interaction within the protein-binding site.[65–70] 2D CP MAS techniques have used the incomplete assignment of the ^{1}H and ^{13}C signals for uniformly ^{13}C labelled chromophore in the natural membrane environment.[66] The proton ($\Delta\sigma^{H}_{lig}$) and carbon ($\Delta\sigma^{C}_{lig}$) NMR ligation shifts have been calculated using the data and results obtained for protonated Schiff base model *N*-(11-*cis*-12-s-*cis*-retylidene)-*n*-propyliminium trifluoro acetate. The NMR ligation shift values ($\Delta\sigma_{lig}$) reflect the differences in the electronic and spatial molecular structures between the model compound and the chromophore bound to the active site of the protein and can be used as a probe of ligand–protein interactions. The highest values of the $\Delta\sigma^{H}_{lig}$ up to -1.2 ppm were observed for the methyl protons of the ring moiety and indicated the non-bonding interactions between these groups and the aromatic amino acid residues Phe-208, Phe-212 and Trp-265 of transmembrane helix VI. The $\Delta\sigma^{H}_{lig}$ values in the polyene chain and $\Delta\sigma^{C}_{lig}$ value for methyl group C-20 confirmed non-planar conformation of the 12-s bond. Binding of the chromophore involves a chiral selection of the ring conformation, resulting in equatorial and axial positions for Me-16 and Me-17. The $\Delta\sigma$ ligation shifts were also analysed in the studies of an analogue of natural rhodopsin–isorhodopsin.[68]

For 10-fold ^{13}C labelled retinal, it has been shown that the differences between chemical shifts for polyene chain carbons of the chromophore in its native environment and detergent-solubilised system were small.[67] Analysis of the environment of the Schiff base has supported the model of stabilisation based on the protonation by a complex counterion. Three factors were responsible for the excessive positive charge in polyene (i) electronegative nitrogen, (ii) protonation and (iii) counterion strength.

TABLE 2 Bond lengths estimation from DQ solid state NMR of rhodopsin and bond length determined by X-ray diffraction on model compound (pm)[69]

$^{13}C_2$ pair	(2-retinylidene)-rhodopsin	N-*tert*-butyl-retinylideniminium perchlorate
10,11	146.9 ± 2.1	145.7 ± 0.7
11,12	139.3 ± 2.0	132.6 ± 0.7
12,13	144.0 ± 2.3	143.5 ± 0.7
13,14	139.8 ± 1.9	134.6 ± 0.7
14,15	145.8 ± 2.2	140.2 ± 0.7

Levitt et al.[69] have used the double quantum solid state NMR in the studies of bond lengths for a series of five ^{13}C labelled samples of rhodopsin. On the basis of DQ-filtered signal trajectories and numerical spin simulations of the signal points, the through-space dipole–dipole coupling between neighbouring ^{13}C nuclei has been estimated. Estimated dipole–dipole couplings have been converted into the internuclear distances (Table 2) [32].

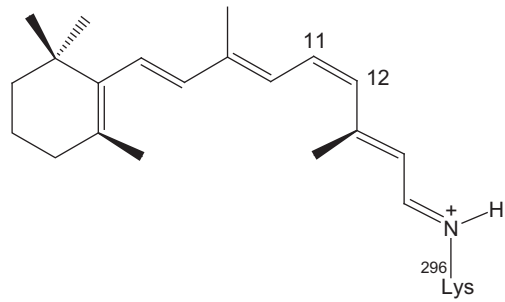

[32]

The carbon–carbon bond lengths determined indicated a perturbation in the electronic structure of the chromophore and a partial stabilisation of the positive charge away from protonated Schiff base and near C12. The authors postulate that the protein pocket assists the photoisomerisation by stabilising a positively charged conjugation defect in the polyene chain of the chromophore, leading to the local reduction in bond length alternation close to the isomerisation site, and that a water molecule, positioned and stabilised by a hydrogen bond network in the binding pocket, is responsible for solvation of the positive charge within the chain.

In CP MAS NMR studies of rhodopsin and their photoactivated state-metarhodopsin, Ahuja et al.[70] have used the measurements of the T_1 relaxation time. The T_1 values measured for C18 (0.34 s for rhodopsin

and 0.56 s for metaII) indicated the 6-s-*cis* conformation of retinylidene chain in the inactive and active states of rhodopsin.

6.2.2. ^{15}N CP MAS NMR

The values of the ^{15}N CP MAS chemical shift of Lys296 nitrogen bonded to retinal via the —C═N bond (Schiff base) was equal to 155.4 ppm for rhodopsin and 282.8 ppm for metarhodopsin (relative to 5.6 M aqueous NH_4Cl).[70] The results proved the imine bond polarisation, which facilitates Schiff base hydrolysis. The comparison between chemical shifts for metarhodopsin and model compounds suggested that Schiff base linkage of the all-*trans* retinal chromophore in MetaII is in a polar environment.

6.3. CP MAS NMR studies of proteorhodopsin or bacteriorhodopsin

The CP MAS NMR spectroscopy has been also extensively used for studies of proteins containing retinylidene chromophore like proteorhodopsin or bacteriorhodopsin. Bacteriorhodopsin is a protein component of purple membrane of *Halobacterium salinarium*.[71–75] This protein contains 248 amino acids residues, forming a 7-helix bundle and a retinal chromophore covalently bound to Lys-216 via a Schiff base linkage. It is a light-driven proton pump that translocates protons from the inside to the outside of the cell. After photoisomerization of retinal, the reaction cycle is described by several intermediate states (J, K, L, M, N, O). Between L and M intermediate states, a proton transfer takes place from the protonated Schiff base to the anionic Asp85 at the central part of the protein. In the M and/or N intermediate states, the global conformational changes of the protein backbone take place.

6.3.1. ^{13}C CP MAS NMR

Shi et al.[71] have assigned the backbone and side-chain chemical shifts for 103 of 238 residues of proteorhodopsin using solid state NMR spectroscopy. Analysis of the chemical shifts has allowed determination of protonation states of several carboxylic acids as well as boundaries and distortions of trans-membrane α-helices and secondary structure elements in the loops. It has been shown that internal Asp227, making a part of the counterion, is ionised, while Glu142 located close to the extracellular surface is neutral.

Lansing et al.[72] have determined the H-C14–C15-H dihedral angles analysing the correlation of anisotropic interactions for bacteriorhodopsin at different states of the photocycle. For protonated Schiff base (resting chromophore, bR_{568}), for proton loosing Schiff base (early M photocycle intermediate, M_0) and proton regaining Schiff base (late M photocycle intermediate, M_n), the angles were $164 \pm 4^\circ$, $147 \pm 10^\circ$ and $150 \pm 4^\circ$,

respectively. The results suggest that the protons of the C14–C15 moiety in bR_{568} are twisted out of the plane of the chromophore and that chromophore is in an activated state at the beginning of the photocycle. Greater distortion of M intermediates suggests that the Schiff base remains connected to the extracellular side of the protein during the first half of the photocycle.

Bacteriorhodopsin structure is far from being a rigid body at ambient temperature even in the 2D crystalline state. Saito et al.[73] have shown that analysis of ^{13}C solid state NMR signal intensities (SRI) as a function of temperature or pH provides information on the local or global dynamics in bacteriorhodopsin and their D85N mutants. For (1-^{13}C)Val or (3-^{13}C) Ala-labelled bacteriorhodopsin and D85N mutants, it was shown that global low-frequency motions with fluctuation frequencies in the order of 10^4 Hz are induced in the *M*-like state of D85N mutants. Suppressed or recovered intensities (SRI) permit distinction of the fluctuation frequencies above and under 10^4. Local fluctuation motion in the trans-membranes of bacteriorhodopsin was also studied by Kira et al.[74]

Other CP MAS studies of bacteriorhodopsin, proteorhodopsin as well as bathorhodopsin have been reported.[75–77]

6.3.2. ^{15}N CP MAS NMR

The ^{15}N–^{1}H HETCOR MAS technique has been used in the studies of proteorhodopsin and their H75M, H75N and H75W mutants.[78] The mutations have not influenced the ^{15}N chemical shift signals of protonated Schiff bases at 181.5 ppm, however, the presence of H75W strongly reduced their intensity. The deuterium isotope effect $\Delta N(D)$ of $+3$ ppm implied location of the proton close to nitrogen in the Schiff bases, however, its relatively low value suggested formation of a hydrogen bond to an electron donor, for example, water oxygen.

Dynamic nuclear polarisation (DNP) enhanced ^{15}N CP MAS NMR has been exploited by Mark-Jurkauskas et al.[79] in the studies of intermediates of the bacteriorhodopsin photocycle. The data for L intermediate were similar to those found for 13-*cis*,15-anti retylidene chloride, while those for K intermediate were similar to those of acid blue bacteriorhodopsin in which the Schiff base counterion was neutralised (Table 3). The ^{15}N chemical shifts observed have shown that for bacteriorhodopsin, the Schiff base in K intermediate state loses contact with its counterion and establishes a new one in L intermediate state. The proton energy stored at the beginning in the electrostatic modes has been transformed to torsional modes. The transfer of energy is facilitated by the reduction of bond order alternation in the polyene chain when the counterion interaction is initially broken and is driven by the attraction of the Schiff base to a new counterion. 3D CP MAS experiments of NCOCX, NCACX, CONCA and CAN(CO)CA types have been used in studies of proteorhodopsin.[71]

TABLE 3 ^{15}N chemical shifts of the Schiff bases in bacteriorhodopsin (ppm, reference liquid NH_3)[79]

Intermediate	$\delta^{15}N$
bR_{555}	173.5 ± 0.65
bR_{568}	165.2 ± 0.60
Iso-bR	175.4 ± 0.65
K	156.5 ± 0.72
L_{165}	165.2 ± 0.60
L_{174}	174.3 ± 1.02
L_{181}	181.2 ± 1.2
L_{185}	184.9 ± 1.0
M_o	318.4 ± 0.63
M_n	312.0 ± 0.65

The results of 15N CP MAS NMR studies for lysine, tryptophan and methionine labelled green variant of proteorhodopsin were presented by Shastri et al.[80]

7. COMPLEXES OF THE OPTICALLY ACTIVE SCHIFF BASES

The majority of papers on the optically active Schiff bases that appeared in literature in the past decade were related to their complexes with metals as they show interesting catalytic properties and biological activity. Many of these catalysts have revealed excellent enantioselectivity in various organic reactions. In the studies of chiral complexes of Schiff bases, apart from typical ^{1}H or ^{13}C NMR spectroscopy also NMR on the other nuclei like ^{15}N, ^{31}P and ^{19}F as well as ^{51}V, ^{119}Sn, ^{9}Be, ^{27}Al,^{20}Si, ^{95}Mo has been applied. These NMR measurements have permitted studies of the complex formation processes and provided some important information on their structure. Selected results are given below. It should be noted that paramagnetic properties of some metals were responsible for a strong shift of the resonance signals in ^{1}H NMR spectra and the spectral width range can cover over 300 ppm.

7.1. Ti(IV) complexes

The interactions between the chiral Schiff bases being derivatives of 2-aminoalcohols and substituted salicylic aldehydes and titanium (IV) isopropoxide [33] have been monitored by ^{1}H NMR spectroscopy.[81]

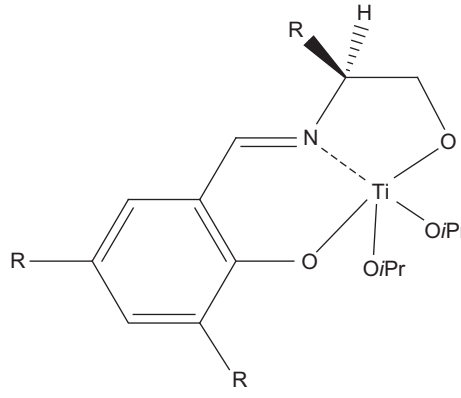

[33]

The appropriate ratio between chiral Schiff bases and Ti(Oi–Pr)$_4$ from catalytical point of view has been recommended. On the basis of the ^{1}H NMR measurements at −20 °C, the kinetic scheme for sulphide oxidation has been proposed.

Comparison of the ^{1}H NMR spectra of the titanium salen complex in chloroform and methanol solution has shown the interconversion of the di-μ-oxo Ti(salen) complex of the *cis*-β structure to monomeric square-planar salen complex.[82]

Belokon et al.[83] have investigated the formation of the homo-and bimetallic titanium complexes with di-Schiff base ligands, by means of ^{1}H NMR spectroscopy. The ligands have been shown to adapt the *cis*-β configuration in titanium (IV) complexes. Analysis of the ^{1}H NMR spectra has allowed determination of the population of the homobimetallic complexes derived from two different Ti(IV) complexes [34].

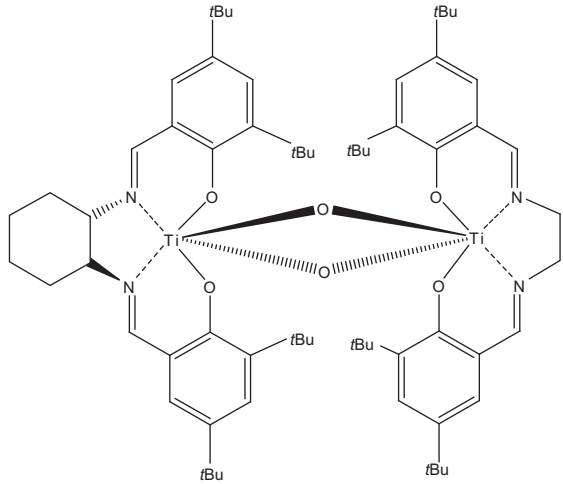

[34]

For example, the ratio of species being in equilibrium was 2:6:3 which does not correspond to the statistical ratio 1:1:2. The discrepancy was explained by perturbation in the equilibrium between mono- and dimeric forms of the complexes. For heterobimetallic complexes, the line broadening in the NMR spectra indicated dynamic exchange processes between various complexes. For a combination of the titanium complex being a derivative of 5-nitrosalicylaldehyde and the vanadium complex being a derivative of 3,5-di-*tert*-butylsalicylaldehyde, the absence of titanium dimer has been shown. This observation was explained by formation of the linear oligomeric or polymeric vanadium complexes which destabilise the bimetallic titanium complexes.

7.2. Zr(IV) complexes

^{1}H NMR data confirmed the α-*cis* geometry of the Zr(IV) Schiff bases complexes being derivatives of salicylaldehydes and (*R*),(*S*) or rac-α-methyl-benzyl amines NMR.[84] The broadening of the signals in ^{1}H NMR spectra indicated the presence of a dynamic process in solution on the NMR time scale. At low temperatures, the signals attributed to diastereomers have been split. On the basis of the stereochemistry of Zr(IV) complex being a derivative of salicylaldehyde and (*R*)-amine in the solid state, the major diastereomer was assigned as Λ-(*R*,*R*). For the complex being a derivative of rac-amine, the ^{1}H NMR spectra revealed additional resonances; except two set of signals corresponding to major and minor diastereomers, additional resonances were observed. These resonances have been assigned to the two additional diastereomers that arise from the complex containing one *R* and one *S* ligand: Δ-(*R*,*S*)/Δ-(*S*,*R*) and Λ(*S*,*R*)/Λ-(*R*,*S*). The results obtained have suggested low chiral induction from the ligand to the metal.

7.3. V(V) complexes

Domination of the *S*-diastereomers for the dioxovanadium(V) Schiff base complexes being derivatives of aromatic *ortho*-hydroxyaldehydes or ketones and (*S*)-(+)-2-(aminomethyl)-pyrrolidine [35] was shown and the molar ratio of the diastereomers was determined by means of integration of the ^{1}H signals.[85]

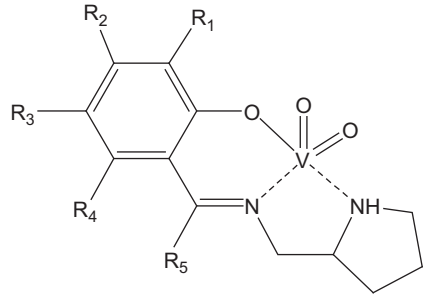

[35]

The negative values of $\Delta G^0(323)$ of -3.157 and -3.325 kJ/mol calculated for sterically hindered Schiff bases have indicated preference of the twist conformation of both five-membered chelate rings. In the ^{51}V NMR spectra in DMSO solution, two separate signals in range from -534 to -539 ppm typical of five coordinated V(V) complexes were observed. The large splitting of the signals at ca. 7.5 ppm was explained as a result of the presence of two diastereomers in which the chiral centre containing asymmetric carbon was separated from chiral vanadium centre by two bonds. Similar values of $\delta^{51}V$ in range from -547.8 to -554.0 ppm were found for vanadium complexes being derivatives of aromatic *o*-hydroxyaldehydes and 1,2-diphenyl-1,2-diaminoethane or (*R*)-1,2-diaminopropane in DMSO.[86]

7.4. Mo(VI) complexes

Interesting results of NMR study of Schiff base molybdenum(VI) *cis*-dioxo complexes, derivatives of α or β-D-glucosamines [36] have been published by Zhao et al.[87]

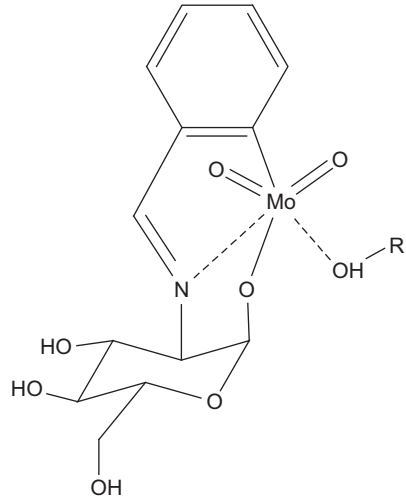

[36]

Comparison of the spectral data for ligands and complexes has revealed that the coordination of molybdenum is accompanied by the inversion of β- into α-configuration. When the C1-α configured ligand is used in the reaction with $MoO_2(acac)_2$, the complex formed remains in the original configuration of the ligand, while the C1-β configurated ligands form *cis*-configured complexes. This reaction has been suggested as a possible method for the conversion of a diastereomeric sugar-derived Schiff base into enantiomeric pure chiral one. The coordination of an ethanol molecule to the Mo centre has been confirmed. The ^{95}Mo NMR chemical shifts measured were similar to those obtained for the other *cis*-$[MoO_2]^{2+}$ complexes.

The significant differences between ^{15}N CP MAS chemical shifts observed for nitrogen atoms of the two imine moieties ($\Delta\delta$N varied from 26 to 29 ppm) in dioxo molybdenum (VI) complexes being derivatives of *trans*-1,2-diaminocyclohexane have indicated differences in the strength of the Mo—N bonding.[88] Also the differences in ^{13}C CP MAS spectra observed for both fragments of the molecule pointed to changes in the charge redistribution in the molecule induced by complexation and have suggested different arrangements of the two moieties. The asymmetric and non-planar structures of the complexes have been suggested.

7.5. Mn(III) complexes

The composition of (*R*,*R*)-(−)-N,N′-bis(3,5-di-*tert*-butylsalicylidene)-1,2-cyclohexane diamino-manganese(III) chloride and PhIO catalytic system has been monitored be means of ^{1}H NMR spectra.[89] Because of the paramagnetic properties of Mn(III), the resonance signals were observed in range from 30 to −35 ppm. The series of spectra recorded at different conditions (e.g. different temperatures, after addition of styrene or additional portion of PhIO) allowed assignment of signals in the spectra to various types of manganese species.

7.6. Re(VII) complexes

Methyltrioxorhenium(VII) (MTO) forms mono- or bis-complexes with di-Schiff bases being derivatives of various salicylaldehydes and *trans*-1,2-diaminocyclohexane [37].[90]

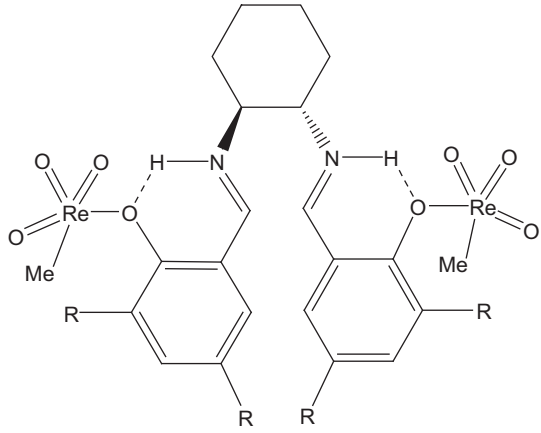

[37]

The small differences in chemical shifts of coordinated and uncoordinated MTO signals in ^{1}H NMR spectra indicate a weak MTO-Schiff base interaction in solution at room temperature. With decreasing temperature, this interaction strengthened. The authors suggested the shift of the proton transfer equilibrium towards NH-form. However, very small differences in chemical shift of OH signals in the spectra of the ligands and complexes (0–0.1 ppm) as well the lack of ^{3}J(NH,H) coupling constants for methine protons which should be measurable do not support their suggestions. For the 1:1 complex at low temperature (−60 °C), only the change in the line width was observed.

7.7. Fe(II) complexes

Bryliakov and Talsi[91,92] studied the mechanism of salen type di-Schiff base iron(III) catalysed reaction of enantioselective oxidation of sulphides employing detailed analysis of the ^{1}H NMR spectra. They have proved the formation of the iodosylbenzene(salen) iron active intermediate and proposed the catalytic cycle for the iron-catalysed asymmetric oxidation of sulphides. At −20 °C, a new signal appeared at 4.75 ppm and it was assigned to the *t*-Bu protons of the active intermediate. The spectral width of NMR measurements of paramagnetic complexes was of 500 ppm and the number of scans recorded was 1000–4000. It is worth noting that the enantioselectivity has been determined by NMR spectroscopy with the use of lanthanide chiral shift reagent.

7.8. Ru(II) complexes

NMR spectra of (*p*-cymene)ruthenium (II) Schiff base complex, derivative of (*S*)-(α-methylbenzyl) and 3,5-di-*tert*-butylsalicylaldimine, at room temperature in $CDCl_3$ solution evidenced the presence of diastereomers at the ratio of 88:12.[93] On the basis of a detailed analysis of 2D NMR spectra (ROESY) measured at 293 and 233 K, the (R_{Ru},S_C) configuration of the major diastereomer in solution was suggested.

7.9. Co(II, III) complexes

Products of the reaction between $CoCl_2$ and chiral tetradendate pyridylimine Schiff bases [38] have been studied by means of ^{1}H NMR.[94]

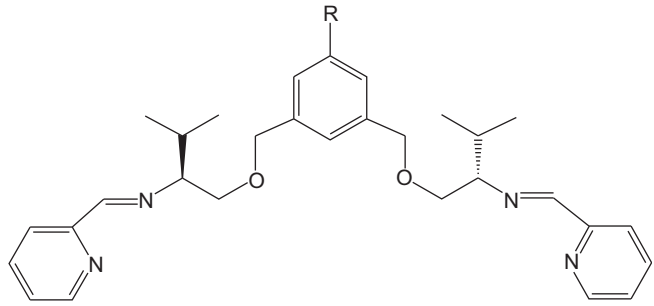

[38]

The ^{1}H NMR spectra of $[Co_2((S)\text{-L})_2Cl_2]^{2+}$ complexes in CD_3CN have shown signals paramagnetically shifted over a range of 110 ppm. The presence of the only one set of signals indicated its D_2-symmetric structure and highly diastereoselective formation. Similar results were observed for the complex obtained from the racemic ligand. The reaction of $CoCl_2$ with tetradendate Schiff bases yielded a racemic mixture of $[Co_2((S)\text{-L})_2Cl_2]^{2+}$ and $[Co_2((R)\text{-L})_2Cl_2]^{2+}$ complexes. The occurrence of the homochiral self-recognition was suggested. The chirality of the ligands predetermines the stereochemistry of the cobalt(II) centres.

The ^{1}H NMR titration has been used in studies of formation of the trinuclear mixed Co(III)–Co(II)–Co(III) complexes, derivatives of salen type ligands.[95] Although the ligands did not have the stereogenic centre, formation of the trinuclear complex with possible C_2 symmetry generated the element of chirality. The presence of the *cis* and *trans* isomers at a ratio of ca. 4:1 at 297.9 K was shown. The ^{1}H signals were assigned to the respective C_2 and C_{2h} isomers on the basis of T_1 and 2D EXSY measurements. The T_1 measurements allowed estimation of the distances between protons and Co(II) ion. The results obtained were in good agreement with the X-ray experimental data. With decreasing temperature, the total width of the ^{1}H spectrum increases from 190 to 330 ppm. The equilibrium

constants for *cis–trans* equilibrium were found in range from 6.3 (24.7 °C) to 21.7 (−60.4 °C). Because of the changes in intensity and ambiguous integration of the signals, the values of ΔH^0 and ΔS^0 were only estimated. The negative value of ΔS^0 for the complex with a bulky axial group was related to the loss of rotational freedom accompanying the transformation from *trans* into *cis* isomer.

The ^{1}H and ^{13}C NMR study of Co(III) complex, derivatives of Jacobsen's Schiff base, has shown the presence of equilibrium between high-spin pentacoordinated and low-spin hexacoordinated states dependent on the solvent.[96] In THF with increasing temperature, the equilibrium was shifted towards pentacoordinated state, while in the presence of a more strongly coordinated solvent (pyridine), only the hexacoordinated, paramagnetic complex was detected. The reaction enthalpy of $-(33 \pm 1)$ kJ/mol and an entropy of $-(164 \pm 3)$J/K/mol was calculated assuming the Curie's law is satisfied. On the basis of 2D NOESY spectra, the anion exchange of the octahedral complex was suggested. The diffusion coefficient values of D obtained for both enantiomers were almost the same, that is, 1.06 and 1.07 $\times$ 10^{-9} m^2/s for *R* and *S*, respectively, suggesting similar coordination properties of both enantiomers. For diamagnetic and paramagnetic Co(III) complexes, the ^{1}H and ^{13}C NMR were calculated.

For Co(II) complexes of salen type di-Schiff bases, analysis of paramagnetic spectra confirmed the influence of steric distortion in the coordination sphere on the chemical shifts of the protons in the proximity of Co(II).[97]

7.10. Rh(III) and Ir(III) complexes

Brunner et al.[98–100] have published a series of papers on epimerisation of chiral rhodium(III) and iridium (III) half-sandwich complexes [39].

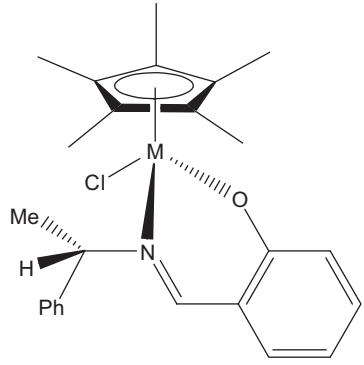

[39]

The kinetic studies of epimerisation were based on the integration of the signals at −35, −50 and −65 °C. The activation enthalpies and entropies were calculated. For complexes of (+)2-*N*-[(*S*)-1-phenylethyl] pyrrolcarbaldimine, the temperature increase led to increasing number of the (S_M, S_C) diastereomers because of epimerisation at the metal centre. At the equilibrium state, the (R_M,S_C):(S_M,S_C) ratio was 13:87 for Rh and 12:88 for Ir, respectively. For the complexes of (+)-*N*-[(*S*)-1-phenylethyl]salicylaldimine, the interconversion of the possible diastereomers was too fast and the kinetic parameters were established from the coalescence at 21 °C. The results have shown that rhodium complexes were more labile in the configuration at the metal centre than ruthenium ones.[98,99]

Boehm et al.[100] have synthesised and studied a series of half-sandwich rhodium (III) and iridium (III) complexes, derivatives of salicylaldehyde and L-amino acid esters. The diastereoselectivity has shown strong dependence on the type of metal as well as amino acid residue. The labile configuration of the metal atoms was suggested because of changes in the diastereomers ratio with increasing temperature. Fast epimerisation at the metal atom was suggested for some *S*-phenylalanine complexes.

7.11. Ni(II) complexes

Fox et al.[101–103] have studied the structure of Ni(II) complexes being derivatives of *trans*-1,2-diaminocyclohexane, using ^{1}H NMR spectroscopy. Chemical shift differences ($\Delta\delta$) between di-Schiff base and its nickel (II) complexes observed for aromatic protons were attributed to the ring currents [40].

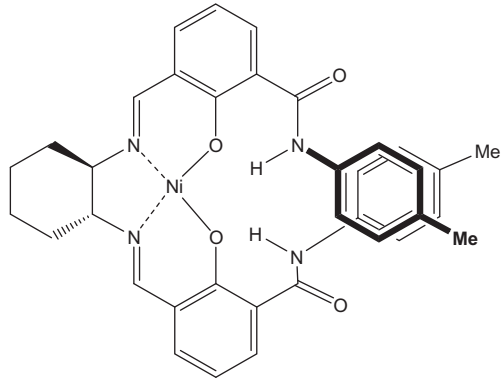

[40]

Chemical shift anisotropy evidenced the helical structure of the complexes. NOESY experiment also suggested the presence of a stable secondary structure. On the basis of the NOESY experiments, the

internuclear distances were calculated to be in good agreement with data from X-ray crystallography. Short internuclear distances between selected position confirmed the helical structure of the complex [41].

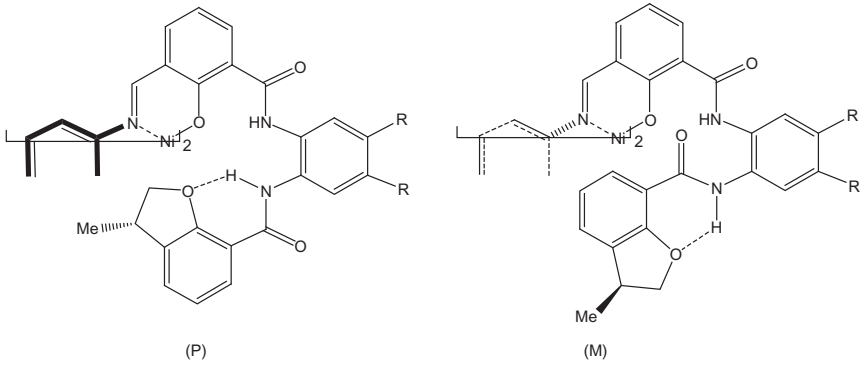

[41]

The temperature measurements in range from −40 to 23 °C revealed the presence of conformational equilibrium between conformers of the opposite helicity (M- and P-helix). The barrier of ∼13 kcal/mol of the chemical exchange was estimated. It was shown that peripheral stereocenters control the absolute sense of helicity in the foldamers studied.[103]

The NMR studies of di-Schiff bases Ni(II) complexes, derivatives (*1R,2R*)-1,2-diaminocyclohexane and 3- or 5-methoxysalicylaldehyde have been also presented by Szłyk et al.[97]

7.12. Pt complexes

For platinum(0) complexes, [42] analysis of the ^{1}H chemical shifts and coupling constants as well as results of 1D selective ROE experiments has allowed determination of the torsional angles ψ and Φ between glucose and imine units to be −60 and −110 °.[104]

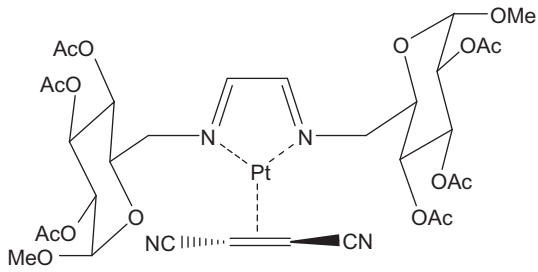

[42]

The results obtained have indicated the formation of a chiral pocket around the metal which was able to recognise selectively a single

enantioface of the prochiral alkene. The shift of the equilibrium towards one of the two possible diastereomers during complex formation has confirmed such ability. The platinum(II) complexes of the amino acid Schiff bases have been studied by ^{1}H NMR by Offiong et al.[105] Comparison of the ^{1}H chemical shifts between ligands and complexes has revealed the *trans*-geometry of the complexes and engagement of the azomethine group in bonding to the metal ion.

Ramirez et al.[106] have investigated the series of platinum complexes of chiral Schiff bases [43].

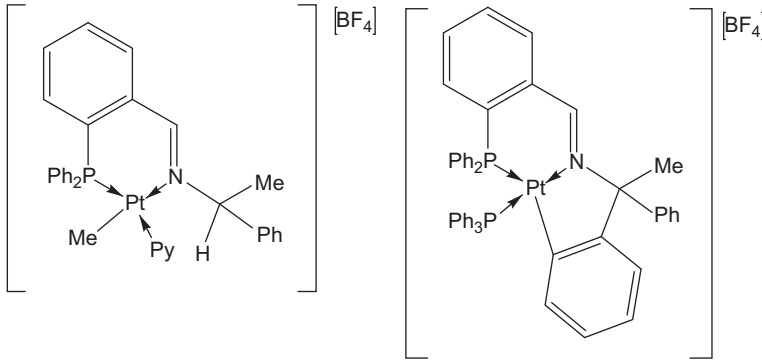

[43]

The proton signals have displayed long-range couplings with phosphorus and platinum atoms. For the basic neutral complexes, the ^4J(P,H) values were close to 2 Hz while ^3J(H, Pt) was almost 29 Hz. Higher values of ^3J(H,P) and ^2J(H, Pt) ca. 3 and 70 Hz, respectively, were observed for methyl groups bonded to platinum cationic complexes. The chemical shifts and coupling constants were typical of the methyl groups bonded to the metal centre in *trans* position to nitrogen atom. In the ^{31}P NMR spectra of neutral platinum complexes, the signals corresponding to both diastereoisomers were detected. For cationic complexes, the ^{31}P NMR chemical shift ranged from 11.95 to 20.90 ppm. For all the complexes, the ^1J(P,Pt) coupling constants varied in the range 1202–4159 Hz. The presence of the ^2J(P,P) coupling constants of 15 Hz between phosphorus atoms of Schiff base ligand and of triphenylphosphine confirmed the *cis* position of the phosphorus atoms and formation of the cyclometallated derivatives. In the ^{19}F NMR spectra of cationic complexes, the tetrafluoroborate anion had a typical chemical shift at -79.1 ppm.

7.13. Zn(II) and Cd(II) complexes

The recognition of barium containing crown ether bridged chiral Schiff base zinc complex [44] with the rigid bidendate guest 1,4-diazobicyclo-[2,2,2]octane (DABCO) was studied by ^{1}H NMR titration.[107]

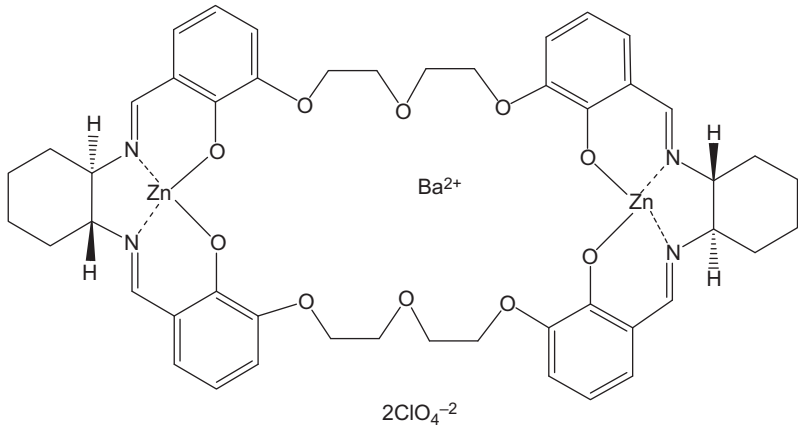

[44]

The results obtained have suggested a sandwich conformation of the host–guest complex in which DABCO was protected from the solvent and other molecules. The cross-peaks between coordinated DABCO and complex protons in the 2D ROESY spectra have indicated the accommodation of the DABCO molecule in the host cavity and confirmed the sandwich binding mode.

Differences between the ^{1}H NMR spectra of cadmium(II) or zinc(II) complexes, being derivatives of Schiff bases containing racemic [45] and enantiopure camphoric unit, have been observed by Jiang et al.[108] For enantiopure zinc(II) complex, the chemical shifts of azomethine, phenyl and camphoric methine protons were 8.20 and 8.01 ppm, 7.11 and 7.08 ppm, and 3.55 and 3.54 ppm, respectively. For the racemic analogue, these values were 8.34, 7.29 and 3.70 ppm in DMSO solution. On the basis of the CD spectra and the above-mentioned differences, it was shown that the use of enantiopure ligands results in the *RRSS* arrangement of the camphoric unit in the complex, while the use of the ramic one gives the *RSRS* arrangement.

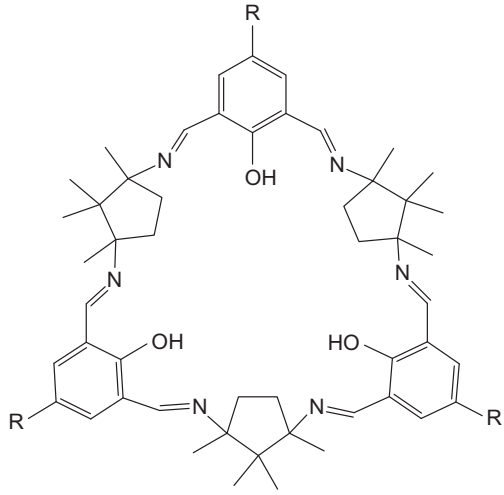

[45]

Szłyk et al.[109] have studied the di-Schiff bases Zn(II) complexes, being derivatives of (*1R,2R*)-1,2-diaminocyclohexane and 5-bromo- or 5-chloro-salicylaldehydes by means of ^{1}H and ^{13}C NMR in $CDCl_3$ and ^{13}C CP MAS NMR spectra.

7.14. Sn(II) complexes

Analysis of the ^{1}H and ^{13}C NMR spectra of the tin complexes, being derivatives of various di-Schiff bases, [46] has revealed the dependence of the position of tin centre on the type of linker between the two imine units and the metal coordination number.[110]

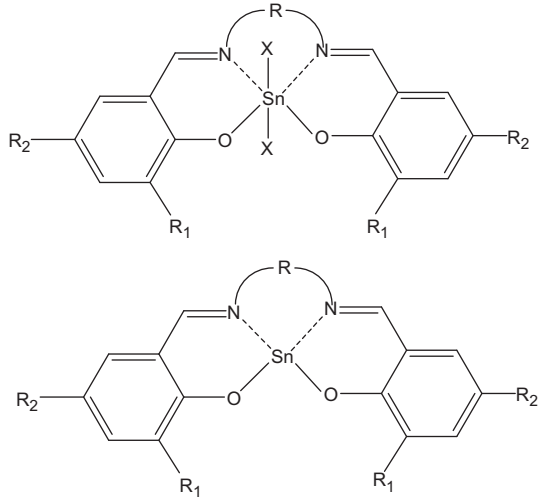

[46]

In Sn(II) complexes, the tin atom was located above the di-Schiff base coordination plane, while in Sn(IV) complexes, it was coplanar with the imine coordination framework. The position of the metal was supported by X-ray data. For the compounds studied, the ^{119}Sn chemical shift values varied from −501.4 to −1015.9 ppm. Increase in the coordination number from Sn(II) to Sn(IV) led to an increase in the tin shielding. The differences of up to 3.0 ppm between δ^{119}Sn values for the complexes, being derivatives of *R,R* and *S,S* 1,2-diaminocyclohexane, were observed.

For the tin(II) complexes of the fluorinated Schiff bases derived from amino acids, [47] the δ^{119}Sn chemical shifts in the range from −575 to −582 ppm suggested the four-coordinate square-planar geometry.[111]

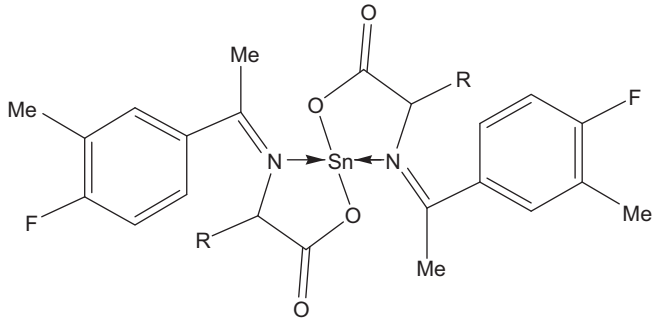

[47]

Thanks to the presence of the fluorine substituent on the salicylic ring, the ^{19}F NMR measurements could be performed. Similar values of the chemical shifts for the ligand (−75.2 ppm) and the complexes (from −70.2 up to −72.8 ppm) suggested that the fluorine atom was not involved in bonding.

For Sn(IV) complexes of amino acid Schiff bases, δ^{119}Sn chemical shift values in range from −192 to –384 were typical of pentacoordinated or hexacoordinated tin atom.[112] For all the compounds studied, the ^3J (Sn—N—CH) and ^3J(Sn—N=CH) coupling constants of 28–50 Hz were observed. The $^1J(^{119/117}\text{Sn},^{13}\text{C-}\alpha)$ values of 587–1031 Hz allowed calculation of the bond angle for the C—Sn—C fragment. For the complex being a derivative of di-*n*-butyltin(IV) oxide, the C—Sn—C angle was close to 127°, while for that being a derivative of diphenyltin(IV) oxide, it was close to 138°. The values of the bond angles suggested a slightly distorted trigonal bipyramidal geometry of the tin atom.

7.15. Lanthanide complexes

For the lanthanide Ce(III), Eu(III), La(III) complexes being derivatives of *R*-2,2′-diamino-1,1′-binaphthyl and 2,6-diformylpyridine, the formation of the macrocycle of D_2 symmetry was suggested.[113] The full assignment

of the signals in ^{1}H and ^{13}C NMR spectra of La(III) and Eu(III) complexes was made on the basis of COSY, NOESY and HMQC spectra. In the spectra of Ce(III) and Eu(III) complexes, the positions of proton signals were affected by the paramagnetic contributions. NOESY spectra have revealed that the naphthyl fragment of the molecule was positioned close to the azomethine group. This indicated a sizeable wrapping of the macrocycle around the lanthanide ion.

Assignment of the signals has been made for lanthanide complexes of nonadendate imino-phosphonate ligands [48].[114]

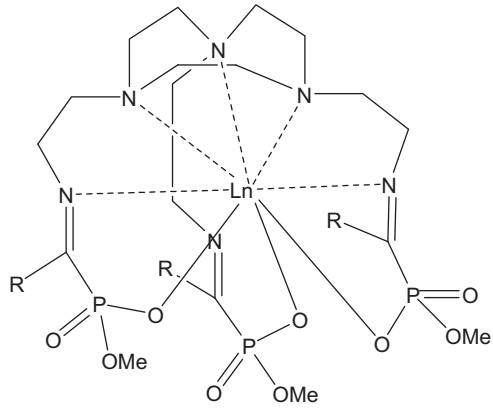

[48]

In the ^{1}H NMR spectra of paramagnetic Yb complex, each signal located in the range from 43.4 to −37.7 ppm consisted of four lines as a result of the presence of four diastereomers. Their intensity ratio was 70:10:10:10. On the basis of 2D COSY experiment, the ^{1}H chemical shifts of the major isomer were assigned to respective protons, and in accordance to X-ray data, the presence of (*RRR*)/(*SSS*) diastereomer was suggested. The ^{1}H spectra of diamagnetic Y and La complexes have not provided decisive evidence of the presence of different diastereomers; however, in the ^{31}P NMR spectra of the Y complex, four signals were observed. The signals at 14.74, 14.51 and 13.75 ppm were assigned to the minor diastereomers, while that at 14.67 ppm to the major one. In the ^{31}P NMR spectra of La complex, only one signal at 14.5 ppm was present. Hydrolysis of the complexes has been also studied.

7.16. U(IV) complexes

On the basis of the splitting of several ^{1}H signals in the 20- and 40-membered UO_2 complexes, [11], [12] being derivatives of (*R*)-binol, Amato et al.[27] have suggested the presence of a conformational equilibrium. For the 20-membered complex, the rate constant at 300 K was

estimated as 300 s^{-1}. On the basis of the temperature measurements for the 40-membered complex, the activation barrier (11.9 kcal/mol) of the interconversion equilibrium was calculated. The results of 2D experiments (NOESY, ROESY) have suggested that the exchange process might be associated with the flipping motion of the salicylidene units. The ability of di- and tetra-Schiff base uranyl macrocyclic complexes containing the (*R*)-BINOL unit M40 [11] and M20 [12] to recognise a series ammonium salts has been verified.[115] The 2D T-ROESY experiments of M40-tetrabutylammonium chloride complex have shown the dipolar correlation cross-peaks between OCH_2 protons of the BINOL unit and *N*-methylene and *N*-methyl protons of the salt. Such ROE contacts have indicated the proximity of the receptor and ammonium group and can evidence cation location inside the receptor and nearby the uranyl site. Splitting of the *N*-methylene proton signals after complexation has demonstrated that binding causes the loss of conformational freedom of butyl chains. The binding constants K in range from 112 to 1512 M^{-1} for the 20-membered macrocyclic complex and from 808 to 20826 M^{-1} for the 40-one have been estimated by means of ^1H NMR titration. Higher *K* values for the 40-membered macrocyclic complex have indicated its recognition ability of achiral ammonium salts, in contrast to their absence for the smaller macrocycles. Such behaviour was explained by the cavity size and the bulkiness of the guests. The binding efficiency of the tetrabutylammonium salts has increased with increasing counteranion hardness ($I^- < Br^- < Cl^-$) according to the hard Lewis acidic character of the uranyl centre. For chiral ammonium iodides, the formation of diastereomeric molecular complexes with M40 was observed. Comparison of the binding constants for achiral and chiral quaternary ammonium salts has shown that decreasing affinity of the receptor due to replacing the counteranion chloride by iodide was counterbalanced by the introduction of the stereocenter in the guest and generation of new guest–host interactions. The binding constants of the complexes of M40 with chiral salts were 968 M^{-1} for *R*-(α-methylbenzyl)-trimethylammonium iodide and 1668 M^{-1} for *S* enantiomer. The difference between the binding constants and the K_R/K_S ratio of 1.7 has implied the ability of M40 to discriminate between two enantiomers. The data collected for (*R*,*S*) and (*S*,*S*) proline derivatives have revealed that the change in configuration of the nitrogen stereocenter has a rather insignificant influence on the molecular recognition mechanism.

The stereochemistry and conformation of di-Schiff bases containing calix[4]arene unit U(IV) complexes have been deduced on the basis of the 2D TOCSY and T-ROESY measurements.[116]

Amato et al.[117] analysing the T-ROESY data have shown that formation of the uranyl(VI) complex maintained the symmetrical structure of the Schiff base containing two biphenyl units. The lack of dipolar contacts

between aromatic rings as well as between aromatic protons and isohexyloxy substituents suggested the presence of less hindered disc-shaped complex conformation in solution.

8. ^{9}Be NMR

The ^{9}Be NMR spectroscopy has been used in determination of the chiral binaphthyldiimine Be(II) complex [49].[118] The measured δBe value of 4.84 ppm and the line width of 40 Hz indicated the presence of a four-coordinate complex. The calculated ^{9}Be NMR parameters were in good agreement with experimental results.

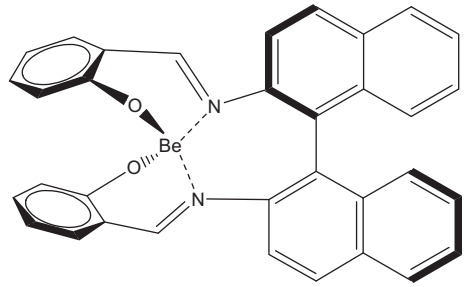

[49]

9. ^{27}Al NMR

Analysis of the ^{27}Al NMR spectra has confirmed the structure of the aluminium di-Schiff bases complexes being derivatives of *trans*-1,2-diaminocyclohexane.[119] The ^{27}Al chemical shift values of 6.57 and 39.48 ppm indicated the presence of dynamic equilibrium between five- and six-coordinated states in $CDCl_3$ solution.

10. ^{29}Si MAS NMR

Interesting results have been presented by Baleizao et al. for chiral vanadyl Schiff base complex [50].[120] The ^{29}Si MAS NMR spectra have confirmed covalent grafting of the vanadyl complex into the silicate skeleton.

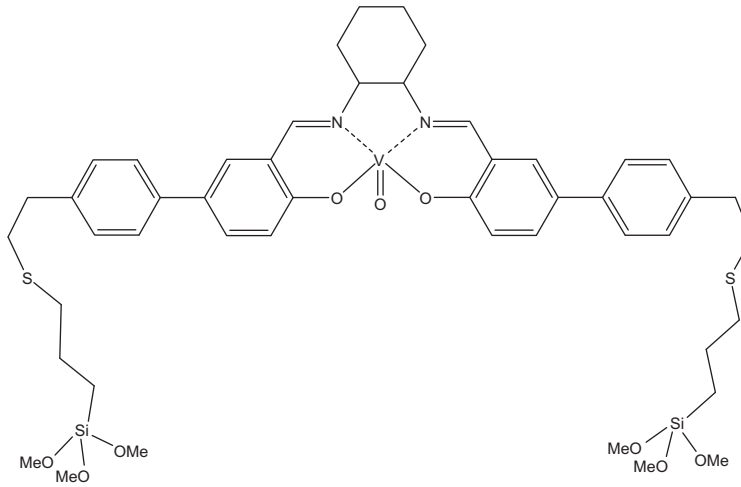

[50]

ACKNOWLEDGEMENT

The author thanks Prof. Teresa Dziembowska for helpful discussions and the Polish Ministry of Science and Higher Education for financial support under grants no. NN 204 338237 in the years 2009–2012.

REFERENCES

1. F. Dufrasne, M. Gelbcke and J. Nève, *Spectrochim. Acta A*, 2003, **59,** 1239.
2. F. Dufrasne, M. Gelbcke and M. Galanski, *Spectrochim. Acta A*, 2006, **65,** 869.
3. Y. Chi, T. J. Peelen and S. H. Gellman, *Org. Lett.*, 2005, **7,** 3469.
4. M. Ardej-Jakubisiak and R. Kawęcki, *Tetrahedron: Assymetry*, 2008, **19,** 2645.
5. J. Chin, D. C. Kim, H.-J. Kim, J. Chin, F. B. Panosyan and K. M. Kim, *Org. Lett.*, 2004, **6,** 2591.
6. K. M. Kim, H. Park, H.-J. Kim and W. Nam, *Org. Lett.*, 2005, **7,** 3525.
7. S. L. Yeste, M. E. Powell, S. D. Bull and T. D. James, *J. Org. Chem.*, 2009, **74,** 427.
8. Y. Perez-Fuertes, A. M. Kelly, A. L. Johnson, S. Arimori, S. D. Bull and T. D. James, *Org. Lett.*, 2006, **8,** 609.
9. A. M. Kelly, Y. Perez-Fuertes, S. Arimori, S. D. Bull and T. D. James, *Org. Lett.*, 2006, **8,** 1971.
10. H. Fukui and Y. Fukushi, *Org. Lett.*, 2010, **12,** 2856.
11. Z. Rozwadowski, *Magn. Reson. Chem.*, 2007, **45,** 605.
12. Z. Rozwadowski and B. Nowak-Wydra, *Magn. Reson. Chem.*, 2008, **46,** 974.
13. P. Przybylski, K. Jasiński, B. Brzeziński and F. Bartl, *J. Mol. Struct.*, 2002, **611,** 193.
14. P. Przybylski, W. Schilf and B. Brzeziński, *J. Mol. Struct.*, 2005, **734,** 123.
15. I. Karamé, M. L. Tommasino, R. Faure and M. Lemaire, *Eur. J. Org. Chem.*, 2003, 1271.
16. D. Sinha, A. K. Tiwari, S. Singh, G. Shukla, P. Mishra, H. Chandra and A. K. Mishra, *Eur. J. Med. Chem.*, 2008, **43,** 160.
17. W. T. Gao and Z. Zheng, *Molecules*, 2002, **7,** 511.

18. I. J. Patel and S. J. Parmar, *E-J. Chem.*, 2010, **7,** 617.
19. M. Durmaz, S. Alpaydin, A. Sirit and M. Yilmaz, *Tetrahedron: Asymmetry*, 2007, **18,** 900.
20. H.-B. Zhu, D.-H. Hu, H.-Z. Dong, G.-X. Li and S.-H. Gou, *Chin. J. Chem.*, 2007, **25,** 343.
21. M. Kwit and J. Gawroński, *Tetrahedron: Asymmetry*, 2003, **14,** 1303.
22. A. Perona, D. Sanz, R. M. Claramunt and J. Elguero, *Magn. Reson. Chem.*, 2008, **46,** 930.
23. H. Bafqiren and J. J. Eddine, *Tetrahedron*, 2010, **66,** 7028.
24. M. Bru, I. Alfonso, M. I. Burguete and S. V. Luis, *Tetrahedron Lett.*, 2005, **46,** 7781.
25. I. Alfonso, M. Bolte, M. Bru, M. I. Burguete and S. V. Luis, *Chem. Eur. J.*, 2008, **14,** 8879.
26. S. Schmidt, W. Bauer, F. W. Heinemann, H. Lanig and A. Grohmann, *Agnew. Chem. Int. Ed*, 2000, **39,** 913.
27. M. E. Amato, F. P. Ballistreri, A. Pappalardo, D. Sciotto, G. A. Tomaselli and R. M. Toscano, *Tetrahedron*, 2007, **63,** 9751.
28. T. Tanaka, Y. Sano and M. Hayashi, *Chem. Asian J.*, 2008, **3,** 1465.
29. J. Miyake, Y. Tsuji, A. Nagai and Y. Chujo, *Chem. Commun.*, 2009, 2183.
30. J. E. dos Santos, E. R. Dockal and E. T. G. Cavalheiro, *Carbohydr. Polym.*, 2005, **60,** 277.
31. Y. Xiao and X. Zhuo, *React. Funct. Polym.*, 2008, **68,** 1281.
32. K. Tømmeraas, K. M. Vårum, B. E. Christensen and O. Smidrød, *Carbohydr. Res.*, 2001, **333,** 137.
33. Z. Rozwadowski, *Magn. Reson. Chem.*, 2006, **44,** 881.
34. H. Park, K. M. Kim, A. Lee, S. Ham, W. Nam and J. Chin, *J. Am. Chem. Soc.*, 2007, **129,** 1518.
35. H. Park, R. Nandhakumar, J. Hong, S. Ham, J. Chin and K. M. Kim, *Chem. Eur. J.*, 2008, **14,** 9935.
36. V.-T. Dao, M. K. Dowd, M.-T. Martin, C. Gaspard, M. Mayer and R. J. Michelot, *Eur. J. Med. Chem.*, 2004, **39,** 619.
37. P. Przybylski, M. Kwit, K. Pyta, R. Pankiewicz, G. Schroeder, J. Gawroński and B. Brzeziński, *Tetrahedron: Asymmetry*, 2010, **21,** 973.
38. P. Przybylski and B. Brzeziński, *Biopolymers*, 2002, **67,** 61.
39. A. D. Cort, F. Gasparrini, L. Lunazzi, L. Mandolini, A. Mazzanti, C. Pasquini, M. Pierini, R. Rompietti and L. Schiaffino, *J. Org. Chem.*, 2005, **70,** 8877.
40. D. Talancón, R. Bosque and C. López, *J. Org. Chem.*, 2010, **75,** 3294.
41. C. Maiereanu, M. Darabantu, G. Plé, C. Berghian, E. Condamine, Y. Ramondenc, I. Silaghi-Dumitrescu and S. Mager, *Tetrahedron*, 2002, **58,** 2681.
42. T. Dziembowska and Z. Rozwadowski, *Curr. Org. Chem.*, 2001, **5,** 289.
43. T. Dziembowska, P. E. Hansen and Z. Rozwadowski, *Prog. Nucl. Magn. Reson. Spectrosc.*, 2004, **45,** 1.
44. P. E. Hansen, T. Dziembowska and Z. Rozwadowski, *Curr. Org. Chem.*, 2009, **13,** 194.
45. K. Ambroziak, Z. Rozwadowski, T. Dziembowska and B. Bieg, *J. Mol. Struct.*, 2002, **615,** 109.
46. Z. Rozwadowski, K. Ambroziak, T. Dziembowska and M. Kotfica, *J. Mol. Struct.*, 2002, **643,** 93.
47. P. Przybylski, W. Lewandowska and B. Brzeziński, *J. Mol. Struct.*, 2006, **797,** 92.
48. P. Przybylski, W. Schilf, B. Kamieński, B. Brzeziński and F. Bartl, *J. Mol. Struct.*, 2005, **748,** 111.
49. P. Przybylski, W. Schilf, B. Kamieński, B. Brzeziński and F. Bartl, *Magn. Reson. Chem.*, 2008, **46,** 534.
50. P. Przybylski, M. Włodarz, B. Brzeziński and F. Bartl, *J. Mol. Struct.*, 2004, **691,** 227.
51. P. Przybylski, G. Bejcar, A. Huczyński, G. Schroeder, B. Brzeziński and F. Bartl, *Biopolymers*, 2006, **82,** 521.
52. Q. T. That, K. P. P. Nguyen and P. E. Hansen, *Magn. Reson. Chem.*, 2005, **43,** 302.
53. Y. Özcan, S. İde, İ. Şakiyan and E. Logoglu, *J. Mol. Struct.*, 2003, **658,** 207.
54. Z. Rozwadowski, K. Ambroziak, M. Szypa, E. Jagodzińska, S. Spychaj, W. Schilf and B. Kamieński, *J. Mol. Struct.*, 2005, **734,** 137.
55. Z. Rozwadowski, *J. Mol. Struct.*, 2005, **753,** 127.

56. M. Roje and V. Šunjić, *Chirality*, 2002, **14,** 625.
57. T. Dziembowska, K. Ambroziak, Z. Rozwadowski, W. Schilf and B. Kamieński, *Magn. Reson. Chem.*, 2003, **41,** 135.
58. B. Kołodziej, E. Grech, W. Schilf, B. Kamieński, M. Makowski, Z. Rozwadowski and T. Dziembowska, *J. Mol. Struct.*, 2007, **844–845,** 32.
59. J. Costamagna, E. Lillo, B. Matsuhiro, M. D. Noseda and M. Villagrán, *Carbohydr. Res.*, 2003, **338,** 1535.
60. C.-H. Tai, W. M. Rabeh, R. Guan, L. Schnackerz and P. F. Cook, *Arch. Biochem. Biophys.*, 2008, **472,** 115.
61. C.-H. Tai, W. M. Rabeh, R. Guan, K. D. Schnackerz and P. F. Cook, *Biochim. Biophys. Acta*, 2008, **1784,** 629.
62. R. Guan, S. A. Nimmo, K. D. Schnackerz and P. F. Cook, *Arch. Biochem. Biophys.*, 2009, **487,** 85.
63. H. Tian, R. Guan, E. Salsi, B. Campanini, S. Bettati, V. P. Kumar, W. E. Karsten, A. Mozzarelli and P. F. Cook, *Biochemistry*, 2010, **49,** 6093.
64. K. Kpega, M. Murtha and N. Nesnas, *Bioorg. Med. Chem. Lett.*, 2006, **16,** 1523.
65. S. Ahuja, E. Crocker, M. Eilers, V. Hornak, A. Hirshfeld, M. Ziliox, N. Syrett, P. J. Reeves, H. G. Khorana, M. Sheves and S. O. Smith, *J. Biol. Chem.*, 2009, **284,** 10190.
66. A. F. L. Creemers, S. Kiihne, P. H. M. Bovee-Guerts, W. J. DeGrip, J. Lugtenburg and H. J. M. de Groot, *Proc. Natl. Acad. Sci. USA*, 2002, **99,** 9101.
67. M. A. Verhoeven, A. F. L. Creemers, P. H. M. Bovee-Guerts, W. J. DeGrip, J. Lugtenburg and H. J. M. de Groot, *Biochemistry*, 2001, **40,** 3282.
68. A. F. L. Creemers, P. H. M. Bovee-Guerts, W. J. DeGrip, J. Lugtenburg and H. J. M. de Groot, *Biochemistry*, 2004, **43,** 16011.
69. M. Carravetta, X. Zhao, O. G. Johannessen, W. C. Lai, M. A. Verhoeven, P. H. M. Bovee-Guerts, P. J. E. Verdegem, S. Kiihne, H. Luthman, H. J. M. de Groot, W. J. DeGrip, J. Lugtenburg and M. H. Levitt, *J. Am. Chem. Soc.*, 2004, **126,** 3948.
70. S. Ahuja, M. Eilers, A. Hirshfeld, E. Y. C. Yan, M. Ziliox, T. P. Sakmar, M. Sheves and S. O. Smith, *J. Am. Chem. Soc.*, 2009, **131,** 15160.
71. L. Shi, M. A. M. Ahmed, W. Zhang, G. Whited, L. S. Brown and V. Ladizhansky, *J. Mol. Biol.*, 2009, **386,** 1078.
72. J. C. Lansing, M. Hohwy, C. P. Jaroniec, A. F. L. Creemers, J. Lugtenburg, J. Herzfeld and R. G. Griffin, *Biochemistry*, 2002, **41,** 431.
73. H. Saitô, A. Kira, T. Arakawa, M. Tanio, S. Tuzi and A. Naito, *Biochim. Biophys. Acta*, 2010, **1798,** 167.
74. A. Kira, M. Tanio, S. Tuzi and H. Saitô, *Eur. Biophys. J.*, 2004, **33,** 580.
75. Y. Kawase, M. Tanio, A. Kira, S. Yamaguchi, S. Tuzi, A. Naito, M. Kataoka, J. K. Lanyi, R. Needleman and H. Saitô, *Biochemistry*, 2000, **39,** 14472.
76. A. Gansmüller, M. Concistrè, N. McLean, O. G. Johannessen, I. Marín-Montesinos, P. H. M. Bovee-Geurts, P. Verdegem, J. Lugtenburg, R. C. D. Brown, W. J. DeGrip and M. H. Levitt, *Biochim. Biophys. Acta*, 2009, **1788,** 1350.
77. N. Pfleger, M. Lorch, A. C. Woerner, S. Shastri and C. Glaubitz, *J. Biomol. NMR*, 2008, **40,** 15.
78. N. Pfleger, A. C. Wörner, J. Yang, S. Shastri, U. A. Hellmich, L. Aslimovska, M. S. M. Maier and C. Glaubitz, *Biochim. Biophys. Acta*, 2009, **1787,** 697.
79. M. L. Mark-Jurkauskas, V. S. Bajaj, M. K. Hornstein, M. Belenky, R. G. Griffin and J. Herzfeld, *Proc. Natl. Acad. Sci. USA*, 2008, **105,** 883.
80. S. Shastri, J. Vonck, N. Pfleger, W. Haase, W. Kuehlbrandt and C. Glaubitz, *Biochim. Biophys. Acta*, 2007, **1768,** 3012.
81. K. P. Bryliakov and E. P. Talsi, *J. Mol. Catal. A*, 2007, **264,** 280.
82. B. Saito and T. Katsuki, *Tetrahedron Lett.*, 2001, **42,** 8333.
83. Y. N. Belokon, W. Clegg, R. W. Harrington, M. North and C. Young, *Inorg. Chem.*, 2008, **47,** 3801.
84. A. J. Chmura, D. M. Cousins, M. G. Davidson, M. D. Jones, M. D. Lunn and M. F. Mahon, *Dalton Trans.*, 2008, 1437.

85. E. Kwiatkowski, G. Romanowski, W. Nowicki and M. Kwiatkowski, *Polyhedron*, 2006, **25,** 2809.
86. G. Romanowski, E. Kwiatkowski, W. Nowicki, M. Kwiatkowski and T. Lis, *Polyhedron*, 2008, **27,** 1601.
87. J. Zhao, X. Zhou, A. M. Santos, E. Herdtweck, C. C. Romão and F. E. Kühn, *Dalton Trans.*, 2003, 3736.
88. W. Schilf, B. Kamieński, Z. Rozwadowski, K. Ambroziak, B. Bieg and T. Dziembowska, *J. Mol. Struct.*, 2004, **700,** 61.
89. K. P. Bryliakov, D. E. Babushkin and E. P. Talsi, *Mendeleev Commun.*, 2000, **10,** 1.
90. Z. Xu, M.-D. Zhou, M. Drees, H. Chaffey-Millar, E. Herdtweck, W. A. Herrmann and F. E. Kuehn, *Inorg. Chem.*, 2009, **48,** 6812.
91. K. P. Bryliakov and E. P. Talsi, *Angew. Chem. Int. Ed.*, 2004, **43,** 5228.
92. K. P. Bryliakov and E. P. Talsi, *Chem. Eur. J.*, 2007, **13,** 8045.
93. R. K. Rath, M. Nethaji and A. R. Chakravarty, *Polyhedron*, 2002, **21,** 1929.
94. S. G. Telfer, T. Sato, R. Kuroda, J. Lefebvre and D. B. Leznoff, *Inorg. Chem.*, 2004, **43,** 421.
95. L. Mechi, P. Siega, R. Dreos, E. Zangrando and L. Randaccio, *Eur. J. Inorg. Chem.*, 2629.
96. S. Kemper, P. Hrobárik, M. Kaupp and N. E. Schlörer, *J. Am. Chem. Soc.*, 2009, **131,** 4172.
97. E. Szłyk, M. Barwiołek, R. Kruszynski and T. J. Bartczak, *Inorg. Chim. Acta*, 2005, **358,** 3642.
98. H. Brunner, A. Köllnberger, T. Burgemeister and M. Zabel, *Polyhedron*, 2000, **19,** 1519.
99. H. Brunner, A. Köllnberger and M. Zabel, *Polyhedron*, 2003, **22,** 2639.
100. A. Böhm, H. Brunner and W. Beck, *Z. Anorg. Allg. Chem*, 2008, **634,** 274.
101. F. Zhang, S. Bai, G. P. A. Yap, V. Tarwade and J. M. Fox, *J. Am. Chem. Soc.*, 2005, **127,** 10590.
102. Z. Dong, G. P. A. Yap and J. M. Fox, *J. Am. Chem. Soc.*, 2007, **129,** 11850.
103. Z. Dong, R. J. Karpowicz, S. Bai, G. P. A. Yap and J. M. Fox, *J. Am. Chem. Soc.*, 2006, **128,** 14242.
104. C. De Castro, A. Molinaro, F. Giordano, I. Orabona and F. Ruffo, *Carbohydr. Res.*, 2002, **337,** 651.
105. O. E. Offiong, E. Nfor and A. A. Ayi, *Transition Met. Chem.*, 2000, **25,** 369.
106. P. Ramírez, R. Contreras, M. Valderrama and D. Boys, *J. Organomet. Chem.*, 2006, **691,** 491.
107. F. Gao, W.-J. Ruan, J.-M. Chen, Y.-H. Zhang and Z.-A. Zhu, *Spectrochim. Acta A*, 2005, **62,** 886.
108. J.-C. Jiang, Z.-L. Chu, W. Huang, G. Wang and X.-Z. You, *Inorg. Chem.*, 2010, **49,** 5897.
109. E. Szłyk, A. Wojtczak, A. Surdykowski and M. Goździkiewicz, *Inorg. Chim. Acta*, 2005, **358,** 467.
110. H. Jing, S. K. Edulji, J. M. Gibbs, Ch.L. Stern, H. Zhou and S. T. Nguyen, *Inorg. Chem.*, 2004, **43,** 4315.
111. H. L. Singh, *Spectrochim. Acta A*, 2010, **76,** 253.
112. N. Kobakhidze, N. Farfán, M. Romero, J. M. Méndez-Stivalet, M. G. Ballinas-López, H. García-Ortega, O. Domínguez, R. Santillan, F. Sánchez-Bartéz and I. Gracia-Mora, *J. Organomet. Chem.*, 2010, **695,** 1189.
113. J. Lisowski, M. Paluch and T. Lis, *J. Inclusion Phenom. Macrocycl. Chem.*, 2006, **55,** 123.
114. L. Tei, A. J. Blake, C. Wilson and M. Schröder, *Dalton Trans.*, 2004, 1945.
115. M. E. Amato, F. P. Ballistreri, S. Gentile, A. Pappalardo, G. A. Tomaselli and R. M. Toscano, *J. Org. Chem.*, 2010, **75,** 1437.
116. M. E. Amato, F. P. Ballistreri, A. Pappalardo, G. A. Tomaselli, R. M. Toscano and D. J. Williams, *Eur. J. Org. Chem.*, 2005, 3562.
117. M. E. Amato, F. P. Ballistreri, A. Pappalardo, G. A. Tomaselli and R. M. Toscano, *Molecules*, 2010, **15,** 1442.
118. P. G. Plieger, K. D. John and A. K. Burrell, *Polyhedron*, 2007, **26,** 472.
119. J. Yang, Y. Yu, Q. Li, Y. Li and A. Cao, *J. Polym. Sci. A*, 2005, **43,** 373.
120. C. Baleizão, B. Gigante, D. Das, M. Álvaro, H. Garcia and A. Corma, *J. Catal.*, 2004, **223,** 106.

CHAPTER 4

Probing Interactions Between Small Molecules and Polymers by Means of NMR Spectroscopy

Sara Cozzolino, Paolo Sequi, and **Massimiliano Valentini**[1]

Contents

1. NMR Techniques in the Liquid State 182
   1.1. High resolution NMR spectroscopy 182
   1.2. Relaxation time measurements 187
   1.3. Diffusion NMR 192
2. Solid-State NMR 200
   2.1. Magic-angle spinning 201
   2.2. Decoupling 201
   2.3. Cross polarization 202
   2.4. Heteronuclear and homonuclear dipolar recoupling under magic-angle spinning 202
   2.5. Ligand–receptor interactions 204
3. Supramolecular Chemistry 207

References 210

Abstract

Interactions between small molecules and polymers, or species with a biological relevance as proteins and enzymes, are of high significance in several research fields, above all physics, chemistry, biology and medicine. The type and the strength of the interactions rule most of the occurring processes and determine the main characteristics of the systems. Drug-receptor, signal transduction, cellular

Agricultural Research Council—Research Centre for Plant Soil System, Instrumental Centre of Tor Mancina, S.P. Pascolarese—Strada della Neve Km 1, Monterotondo, Rome, Italy
[1] Corresponding author.

Annual Reports on NMR Spectroscopy, Volume 74
ISSN 0066-4103, DOI: 10.1016/B978-0-08-097072-1.00004-2

recognition are only a few examples of binding phenomena where a profound understanding of the interaction is indispensable.

In the next pages, a brief overview of known application of NMR spectroscopy for assessing interactions between small molecules and polymers is reported with the aim of underlying the importance of NMR in this research area.

Key Words: Binding affinity, H-bonding, Preferred sites, NMR pulse sequence

1. NMR TECHNIQUES IN THE LIQUID STATE

1.1. High resolution NMR spectroscopy

In the past years, many new NMR liquid-state-based screening methods were developed in order to characterize binding phenomena, mainly for medical and pharmaceutical applications but also in food, environmental and soil sciences. The improvement of NMR hardware systems and the development of new sequences optimized for molecular characterization purposes proved to be a powerful tool for elucidation of the structure of complex matrixes, among them polymeric systems. The analysis of protein chemical shifts can reveal preferred interactions between specific portion of the protein and a ligand. This is a fundamental goal in drug discovery research, where therapeutic events strongly depend on the selectivity and affinity of agonists, antagonists, and inhibitors for biological targets. There are powerful two-dimensional (2D) NMR experiments that can be used to monitor efficiently specific groups in a protein. Particularly interesting are the HSQC (heteronuclear single quantum coherence) and TROSY (transverse relaxation optimized spectroscopy) experiments. In a ^{15}N-labelled protein, all amino acids, except proline, give rise to single peaks in an ^{1}H–^{15}N HSQC or TROSY spectrum. Using a variety of procedures, the ^{15}N–^{1}H cross peaks can be assigned to specific backbone resonances in the protein. When a ligand is added, the resonances are selectively shifted or broadened. The chemical shifts of protein amides are very sensitive to interactions with ligands, so that the HSQC approach is a very helpful approach, even for the assay of ligands weakly binding to proteins ($K_d < 41$ mm).[1] The δ variation can be therefore used to localize the binding sites, and resonances that experience significant chemical-shift perturbation can be mapped on to a known structure.

This kind of shift mapping has been used extensively in NMR studies of protein–ligand interactions. Shuker et al.[1,2] used this method to advantage in a lead generation approach that effectively covalently links two

weakly binding ligands located in adjacent binding sites. ^{1}H and ^{15}N NMR studies have been undertaken by Morgan et al.[3] on complexes of *Lactobacillus casei* dihydrofolate reductase (DHFR) formed with analogues of the antibacterial drug brodimoprim (2,4-diamino-5-(3′,5′-dimethoxy-4′-bromobenzyl)pyrimidine) in order to monitor interactions between carboxylate groups on the ligands and basic residues in the protein. DHFR is an enzymes essential for cellular growth, and it has proved a useful target for antifolate drugs as 2,4-diamino-5-(3′,5′-dimethoxy-4′- bromobenzyl) pyrimidine, that act by inhibiting the enzyme in malignant and parasitic cells. A similar approach for ligand screening involves ^{13}C isotopic enrichment of methyl groups on protein side chains. This method has the disadvantage of the high cost for ^{13}C enrichment and the clear advantage of a larger signal intensity in ^{1}H–^{13}C HSQC with respect to the ^{1}H–^{15}N HSQC.[1] Fesik and co-workers devised an ingenious approach for the selective ^{13}C labelling of side-chain methyl groups by using inexpensive $^{13}CH_3I$.[4] Dissociation constants can also be obtained by monitoring chemical-shift changes of the backbone amide as a function of ligand concentration.[5] Transferred nuclear Overhauser enhancement (trNOE) is another popular NMR method for rapid drug–protein interaction elucidation. In general, the observation of transfer NOE allows the analysis of bound ligand conformations without requiring the complete knowledge of the complex protein NMR spectrum. The experiments of trNOE is based on the distinction of free and bound molecules on the basis of their correlation time τ_c. Small molecules have short correlation times, whereas large molecules, such as high molecular weight proteins, have longer τ_c. The correlation time determines sign and size of the NOE. Low or medium molecular weight molecules, for example, below 1–2 kDa, have short τ_c and exhibit positive NOEs, no NOEs, or very small negative NOEs depending upon the molecular weight, shape and the field strength applied. Large molecules, such as proteins, polysaccharides or nucleic acids, have longer τ_c and show large negative NOEs reaching. The correlation time of a small molecule that binds to a large one is determined by the large molecule during the life time of the complex. Upon dissociation of the complex, the small ligand tumbles back with its own characteristic correlation time. During a standard NOESY experiment, the large negative NOEs of the bound ligand will be transferred to the sharp signals of the free ligand. Consequently, in a 2D NOESY spectrum, positive cross peaks are detected for protein ligands whereas signals from free compounds are negative or disappear. The NOEs that are observed under such circumstances are called transferred NOES (trNOEs) and contain information on the conformation of the bound ligand, the so-called bioactive conformation. One advantage of trNOE experiment is that it usually works properly when a 10–20-fold excess of ligand is present, in agreement with the expression.[6]

$$N_b \times \sigma_b \succ\succ N_f \times \sigma_f \quad (1)$$

where N_b and N_f are the number of ligand molecules in the bound and free states, respectively, and σ_b and σ_f are the cross-relaxation rates of the ligand in the bound and free states, respectively. As cross relaxation rates of high molecular biomolecules weight are much larger than cross relaxation rates of small molecules, inequality (1) is usually satisfied for a 10–20-fold excess of ligand; in fact, σ_f sometimes is so small that it does not play any significant role. Usually, tetra- and pentasaccharides have a molecular weight that NOEs are close to zero. It is worth to note that the observation of trNOEs is only possible under certain conditions. In general, it can be said that trNOEs are only observable for large proteins with dissociation constant values in the range between 10^{-6} and 10^{-3}. Background signals due to large proteins are generally not observed, or can be efficiently suppressed by a T_2 or a $T_{1\rho}$ filter.[7] The dipole–dipole relaxation is the source of NOEs, and therefore the observation of trNOEs depends critically on the kinetics of the association/dissociation process of a protein–ligand complex; in particular, it is fundamental that the complex dissociation is fast on the relaxation time scale.[8] A fast or slow exchange process on the chemical-shift time scale plays no role in observing trNOEs, as it is always the signal of the free ligand that carries the information of the bound state. In other words, it is critical that a large amount of ligand molecules samples the protein binding site frequently enough during the NOESY mixing time experiment; in practice, exchange frequencies of 50–100 Hz are sufficient to allow trNOE to be observed. Various experimental implementations of trNOE have been exploited, for example, one-dimensional (1D) selective saturation transfer and 1D- and 2D transient NOE.[9,10] A scheme published by Shuker[2] is actually very utilized to produce ligand with a high binding affinity. It consists in the optimization of ligands by mapping proximal binding sites with a large number of molecules and subsequently linking two ligands.

A technique based on the transfer NOE experiment for the direct identification from a mixture of compounds with binding activity was reported by Meyer.[10] Development of novel drugs often involves the compound libraries screening. A biologically active component can be identified when the pure compound is tested *in vivo* or *in vitro*. Authors used the trNOE to detect in a mixture of oligosaccharides the compounds with binding affinity with *A. aurantia* agglutinin, a lectin that recognizes α-L-Fuc-(1 → 6)-β-D-GlcNAc-OMe. Two libraries were chosen, one with six and the second with 15 carbohydrate derivatives both containing the α-L-Fuc-(1 → 6)-β-D-GlcNAc-OMe oligosaccharide. The time dependence of NOE build-up of the proton pairs H_1^F-H_6proS^{GN} and H_6proS^{GN}-H_6pro-R^{GN}of the oligosaccharide shows positive NOEs, being highest when the mixing time is ca. 1000 ms. In the presence of *A. aurantia* agglutinin, strong

negative transfer NOEs are observed; their build-up is very fast and the maximum is reached already for a mixing time below 300 ms. Based on these data, it is possible to recognize which molecules among a mixture bind to the protein. In fact, ^{1}H and transfer NOESY spectra, the latter recorded in presence and in absence of lectin, of the carbohydrates containing oligosaccharides of interest were able to identify the species with binding affinity to lectin. This approach is straightforward when spectra of compounds are known and signals correctly assigned; in case of unknown mixtures, additional NMR experiments to identify molecules, for example, 2D homonuclear and heteronuclear correlations, etc., are necessary.

A similar approach was used by Henrichsen, who studied the interactions between selectins and ligands present on the surface of leukocytes.[11] The latter are cells of the immune system involved in defending the organism from infectious disease and foreign materials. The interaction between selectins and ligands on leukocytes involves as a first step a ''rolling'' of the leukocytes, which leads to further specific interactions with other membrane proteins, and then the migration of selectin-leukocytes system into the target tissues. The bioactive components towards E-selectin were identified from a mixture of sialyl Lewis tetrasaccharide derivatives by performing NOESY spectra of the pure library and trNOESY spectra of the library in the presence of E-selectin. In agreement with ELISA activity data, only one component with binding activity towards selectin was found. trNOE experiments are now commonly applied to large proteins with dissociation constants ranging from 10^{-7} to 10^{-3} M. A disadvantage of this approach is connected with the need of high ligand concentrations, which therefore must be soluble.

Another NMR-based screening compounds procedure for binding activity to proteins was proposed by Mayer in 1999[12,13] and is addressed as saturation transfer difference (STD) spectroscopy. It is based on the transfer of saturation from the protein to the ligands with a binding affinity. Macromolecules are composed of a large system of protons tightly coupled by dipole–dipole interactions; consequently, the longitudinal relaxation rate R_1 of protons in proteins is dominated by the cross relaxation rate. Selective saturation of a single protein resonance will result in a rapid spread of the magnetization over the entire protein via the spin-diffusion mechanism. Intermolecular magnetization transfer from protein to ligand leads to progressive saturation of ligand resonances, which corresponds to a decrease of ligand signal in the ^{1}H spectrum, depending upon the proximity to the protein protons. Protons of non-binding substances will not be experienced by this saturation transfer, so that peak intensity remains unchanged. Subtracting the difference between the ^{1}H spectrum recorded with off-resonance irradiation and that obtained with selective saturation of protein (STD NMR spectrum),

the identification of binding species is achieved. The intensity of the STD NMR signal increases as a function of ligand excess as long as ligand molecules received no or little saturation bind to receptor, that is, large dissociation constant rates result in a larger effect at higher ligand-to-protein ratios. Therefore, the degree of saturation depends on (1) size of the protein; (2) offset and the duration of the on-resonance irradiation; (3) dissociation rate constant k_{off} and (4) excess of ligand. Mayer demonstrated the goodness of the method to detect peptides, glycopeptides and typical representatives of drug candidates, such as aromatic and heterocyclic compounds.

A very interesting approach based on STD NMR is also reported by the same authors for the characterization of binding interactions at atom level, addressed as Group Epitope Mapping (GEM).[12] They chose the well-studied system of galactose binding to the 120-kDa lectin *Ricinus communis* agglutinin I, that is, RCA120. As ligands, they used methyl α-D-galactoside and a biantennary decasaccharide by performing titration, competition and saturation time experiments. For a careful evaluation of the STD effect, they introduce the STD amplification factor defined as:

$$\text{STD amplification factor} = \frac{I_0 - I_{sat}}{I_0} \times \left[\text{ligand}\right]_{excess} \quad (2)$$

where I_0 is the NMR intensity of a signal in the off-resonance NMR spectrum, I_{sat} is the intensity of the same signal in the on-resonance NMR spectrum and $I_0 - I_{sat}$ is the intensity of the STD NMR spectrum. The STD value represents the relative intensity of the STD signal, thus providing a quick and reliable system for knowing the amplification of the protein information observed in the STD signals of the ligand. Such factor can be used to compare the STD effect of resonances of the two sugars in competitions and titration experiments, even if the concentration of the protein is not the same. The analysis of the saturation transfer effects of methyl-β-D-galactoside showed that the H_2, H_3 and H_4 protons are the most saturated, clearly indicating the close proximity of such atoms to lectin, in agreement with results reported in the literature. This approach works very well also for ligands with a small binding affinity. It is the case of biantennary decasaccharide, for which the binding epitopes were mapped to the terminal β-D-Gal-(1–4)-*N*-acetyl-D-glucosamine residues located at the non-reducing end of the two carbohydrate chains. The binding contribution of the terminal galactose residue was found larger than those of the second-last GlcNAc moieties. It was reported that the GlcNAc residues bind ''edge-on'' with the region from H_2 to H_4, making intense contacts with the protein. Analysis of STD NMR data acquired under competitive conditions proved that the two saccharides bound at the same receptor site, thereby ruling out unspecific binding.

As previously underlined, the identification of complex mixture only partially assigned requires additional NMR experiments, especially 2D ones. The saturation transfer effect is applicable to any 2D NMR experiment, such as TOCSY, NOESY, COSY, allowing to record 2D-STD NMR spectra capable of revealing structural information.[7,14] This is properly argued by Mayer in the study of binding behaviour of some saccharides by means of TOCSY experiments. The STD TOCSY spectrum contains only cross peaks originated from the binding of *N*-acetylglucosamine component, allowing unambiguous identification of interacting species among a complex partially assigned mixture.

Another helpful method in the field of drug discovery is NOE pumping.[15] In this experiment, the magnetization is transferred from the protein to the ligand selectively by applying a diffusion filter. Ligands in fast exchange, which experienced magnetization transfer from the protein, are detected, whereas all other small molecules do not give rise to signals to NMR. Also water–ligand observed via gradient spectroscopy, that is, Water LOGSY,[16] can elucidates the interaction matter; the protein magnetization is selected through water molecules bound to protein using a selective pulse followed by a mixing time, during which magnetization is transferred from water to the protein and to ligands. The magnetization can be also directly transferred from bulk water to the ligand. In the latter case, the NOE is positive and small, giving negative signals in the spectrum. The NOEs arising via the protein are negative, that is, positive signals are present in the spectrum due to the larger auto-correlation time of the protein. Recent works reported Water LOGSY experiments to probe for bulk water accessibility to derive the orientation of a bound ligand, the so-called SALMON method, that is, solvent accessibility and protein ligand binding studied by NMR spectroscopy.[17,18]

1.2. Relaxation time measurements

The relevant contribute of relaxation measurements on the use of NMR spectroscopy in studying interactions can be argued by considering the relationship between relaxation rates and spectral density function; being the latter related to the correlation time, which accounts for the molecular motion. Therefore, spin–lattice and spin–spin can be used to probe interactions between, in principle, every species bearing an active NMR nucleus.

^{1}H longitudinal and transverse relaxation constants are the most measured parameters in investigating small molecules/polymer interactions, as the high natural abundance of the proton nuclei ensures a rapid measurement and excellent signal to noise.

In the case of water/polymers interactions, several heterogeneous systems are based on, for example, hydrogels, soils, foodstuffs, etc. and

the most meaningful data for elucidating the aggregation between the two components are the T_1 and T_2 of water molecules.

In polymeric hydrogels, water represents a significant proportion, and thus elucidating its interaction with the polymeric structure is fundamental for understanding properties, such as biocompatibility, transport of small molecules, etc.[19,20] Polymer dynamics is strongly influenced by the water plasticizing effect, and at the same time, the boundaries of the polymeric matrix cause the motion of water molecules to be anisotropic and restricted.[19,20] Consequently, ^{1}H T_1 and T_2 analysis are informative for both water and polymer dynamics, as well as for their interaction. However, other processes need to be taken into account for a correct interpretation of relaxation data. In particular, the chemical exchange of protons between water molecules and some functional groups of the polymer can occur. Moreover, magnetization transfer between water and polymer can also be present.[21–23]

Recent works reported the study of interactions in poly(amidoamine) hydrogel by using ^{1}H low resolution NMR.[24,25] They studied the polymer swelling phenomenon by hydrating the sample from a water percentage of ca. 68% up to ca. 90%. A bi-exponential behaviour for the spin–lattice rate constants at each hydration levels was observed with the shortest value of about 300 ms being constant for all hydrated samples, on the contrary, the longest constant increases with the hydration level, accordingly with its relative populations, from 0.8 s up to ca. 2 s. A careful analysis of the inversion recovery data suggested that the short T_1 value accounts for the polymer and hydrogen-bound water molecules, while the other component for the remaining water. Moreover, the analysis of population contributing to the short T_1 value was related to the number of hydrogen-bound water molecules per polymer unit, allowing to identify carbonyl and protonated amino groups as the main sites of interaction. Also the spin–spin relaxation was helpful, as it allowed the authors to elucidate the hydration mechanism. Again, they found two T_2 values for all samples, with the exception of the most hydrated one, which revealed three T_2 components. The shortest one, ca. 500 μs, was assigned to water strongly interacting with the polymer, that is, bound and belonging to a hydration layer. The second component was attributed to water with a larger degree of mobility within the hydrogel structure, and finally the longest one to the free water. They rationalized that the polymer is uniformly plasticized already at moderate hydration level and that the hydration process occurs stepwise. Firstly, water saturates the hydration layer, then the polymer meshes until the hydrogel is completely swollen, the remaining water is located outside the matrix and behaves as free water.

In food chemistry, the water distribution and its interaction with polymeric structures plays a fundamental role as it determines important food quality parameters. ^{1}H low resolution NMR proved to be an

excellent technique, and many study on vegetables, meat, fish products and others foods were performed in the past years.[26–31] NMR relaxometry was also applied by Ritota et al. on rice flour mixed with distilled water, to obtain starch–water samples, in order to investigate starch–water interactions[32] The relaxation data were interpreted according to the diffusive and chemical exchange model. The gelatinisation mechanism, important in the field of food quality and processing, was followed by performing: (a) solid–liquid ratio; (b) transverse and longitudinal relaxation determinations of starch–water samples increasing the temperature from 20 to 77 °C. The optimization of the CPMG acquisition parameters allowed the authors to detect a quadric–exponential behaviour for the curves up to 54 °C, and a tri-exponential above this temperature due to the gelatinisation process. Table 1 reported the measured data; the T_2 values of component *a* linearly increased with temperature according to a dominant dipolar mechanism contribution, while the trend for components *b* and *c* is characterized by a flat minimum, according to a diffusive exchange mechanism contribution. The *d* component, almost independent from temperature, indicated interactions with starch, suggesting that diffusion is not playing a significant role, which supports the fast chemical exchange assumption. The slowly relaxing component is associated to extra-granular bulk water, whose motion unaffected by the presence of starch granules behaving therefore as free water. This is argued by considering the T_2/T_1 ratio, which is close to one, and from the disappearing of the bulk water component by reducing the water content until the water saturation of starch is reached. The others components indicate the presence of interactions of water molecules with starch and are associated to water molecules inside the polymer granules. The fastest relaxation rate, T_{2d} of about 3.0 ms at 20 °C, is assigned to molecules entrapped within the amylopectin or amylose helices in the crystalline phase of starch. This spin–spin process is essentially dominated by a fast chemical exchange with amylopectin or amylase exchangeable OH protons. The two intermediate relaxing components, $T_{2b} = 85$ and $T_{2c} = 32$ ms, are ascribed to non-exchangeable hydrogen atoms of more mobile sub-granular starch structures: amylose and amylopectin CH protons, as well as to water protons interacting by diffusion with structured amylose and amylopectin in the starch amorphous regions. These water molecules are likely to interact with the polysaccharide structure by diffusion from bulk to biopolymer interface, acting as a relaxation sink, so that T_2 is controlled by diffusive exchange. The observation of two different T_2 values may be consistent with either the difference in the mobility and crystallinity of amylose and amylopectin chains or by a polydispersion in the radius (and geometry) of diffusive domains.

The Hill equation[33] relates the T_2 relaxation rate with the starch exchangeable hydrogen molar fraction and with the rate constant of

TABLE 1 ^{1}H relaxation times values and signal percentages at different measuring temperatures in 1:3 starch–water samples

T (°C)	T_{2a} (ms)	%*a*	T_{2b} (ms)	%*b*	T_{2c} (ms)	%*c*	T_{2d} (ms)	%*d*
20	1056 ± 2	35 ± 1	85 ± 1	33 ± 1	32 ± 1	17 ± 1	3.1 ± 0.1	15 ± 1
31	1370 ± 5	40 ± 1	74 ± 1	33 ± 1	26 ± 1	13 ± 1	3.0 ± 0.1	14 ± 1
40	1623 ± 9	37 ± 1	70 ± 1	34 ± 1	25 ± 1	14 ± 1	2.8 ± 0.1	15 ± 1
54	689 ± 23	12 ± 1	73 ± 1	44 ± 1	22 ± 1	26 ± 1	2.5 ± 0.1	18 ± 1
58	–	–	72 ± 1	50 ± 1	24 ± 1	35 ± 1	3.0 ± 0.1	15 ± 1
60	–	–	67 ± 1	48 ± 1	25 ± 1	38 ± 1	3.3 ± 0.1	14 ± 1
64	–	–	69 ± 1	62 ± 1	29 ± 1	32 ± 1	3.2 ± 0.1	6 ± 1
77	–	–	82 ± 1	62 ± 1	37 ± 1	35 ± 1	2.7 ± 0.2	3 ± 1

chemical exchange between water and biopolymer; the latter is obtained from the T_2 dependence on the inter-pulse in the CPMG sequence. Based on this, authors found that starch protons accessible to exchange with polymer are about 69%. When a starch suspension is heated in a water excess, gelatinisation process takes place and severe changes are observed in the system. The slowest spin–spin relaxation rate increases linearly with temperature, according to the dominant dipolar mechanism contribution from bulk water. At the temperature equal to 54 °C, the amount of extra-granular water decreases until disappearing at 58 °C. At the same time, the population associated to water molecules interacting with amorphous regions inside starch granules is observed to increase. On the contrary, population of water associated to starch crystalline regions decreases. This is in agreement with the starch gelatinisation mechanism in which the first stage of gelatinisation in excess of water is the uptake of water by the amorphous background region of starch granules, followed by their rapid expansion.[34] Such swelling exerts a strong destabilizing effect on the organized structures within the crystalline lamellae. At the end, they are disrupted and the crystallinity is progressively lost.

Also ^{13}C spin–spin and spin–lattice relaxation can be of great help in elucidating interactions between polymer and small molecules, for example, in the case of salts/polymers. The dissolution of alkali metal salts in polymers give rise to conductive materials, with interesting applications in many electrochemical devices.[35,36] However, one of the main problem in improving the conductivity properties is the ion aggregation. Plasticizers are small molecules with a high permittivity values capable of improving ion dissociation and mobility, thus increasing the conductivities without changing the material properties. On this topic, relevant

studies have been reported by Forsyth in the 1990s.[37–39] The effect of a number of plasticizers on the copolymer ethylene oxide and propylene oxide (3PEG) was investigated by means of ^{13}C NMR; spin–lattice relaxation times and the conductivity behaviour were used to asses important features of this system. They added to the copolymer *N*,*N*′-dimethylformamide (DMF), *N*-methylformamide (NMF), propylene carbonate (PC) and tetraglyme plasticizers, in order to compare the effects of each species on the individual carbon sites of the polymer backbone. Interactions were assessed by an increase of the T_1 relaxation times for all the ^{13}C resonances, a general trend found for all the plasticizer considered, and were attributed to an increase of local mobility. Normalized T_1 values were used to compare the behaviour of the different plasticizers, and it was observed that the C_3 carbon resonance was the most influenced. The comparison of viscosity of the different plasticizers and their effects on the T_1 allowed the authors to conclude that the mobility of the plasticizer is not the unique parameter influencing polymer flexibility, specific interactions between the highly polar molecules and the polymer backbone occurred.

The case of interactions between salts and polymers was argued by a clear decreases of the T_1 relaxation values of the polymer carbons as a result of the coordination of the ether polymer molecules with the alkali metal. The same behaviour was observed in the presence of plasticizers, indicating that the polymer ether molecules are still involved in the alkali metal coordination.

^{1}H and ^{13}C relaxation measurements can also be used in the presence of paramagnetic centres for evaluating aggregation phenomena. In fact, when aggregated, many paramagnetic molecules lack paramagnetism due to the antiferromagnetic coupling between metal ions, being readily distinguishable from monomer species.[40,41]

In the absence of an endogenous centre, the specificity of relaxation data can be improved by introducing in known positions paramagnetic probes. The unpaired electron spin enhances the relaxation rate of the surrounding nuclei in a distance-dependent fashion. In this way, it is possible to evaluate specific interaction sites between a marked polymer and the small molecules.

This approach was followed by Yushmanov for the localization of papaverine in ionic micelles.[42] Another interesting application was reported by Chien[43]; who measured ^{19}F NMR relaxation times of trifluoromethyl labelled atrazine induced by paramagnetic probes gadolinium ethylenediamine tetraacetic acid and 2,2,6,6-tertramethyl-piperidine-*N*-oxyl. The results showed that atrazine solubilized by humic micelles occupied a hydrophobic domain accessible only to neutral hydrophobic molecules.

1.3. Diffusion NMR

1.3.1. General theory

Pulsed field gradient NMR (PFG-NMR) spectroscopy has been successfully used for probing interactions in several research fields.[44–53] The method was developed by Stejskal and Tanner more than 40 years ago[54] and allows the measurement of self-diffusion coefficient, D, which is defined as the diffusion coefficient in absence of chemical potential gradient.

In principle, the diffusion coefficient of a molecular species under given conditions, for example, solvent and temperature, depends on its ''effective'' molecular weight, size and shape. Therefore, it is obvious that diffusion can be used to map intermolecular interactions. The easiest situation occurs when the interacting species are very different in size, as the diffusion coefficient of the low molecular weight component will be largely reduced when interacting. However, even in more complicated systems, it is still possible to study interactions by taking into account the correct shape of all species involved.[55,56] Further, as the general approach compares the D values of the aggregates with those measured for the isolated species, temperature and viscosity in both experiments must be exactly the same.

The general law describing the diffusion process of a fluid is the Fick's second law, Equation (3), which expresses the dependence of the molecular concentration with time[57,58]:

$$\frac{\partial c(\mathbf{r},t)}{\partial t} = \nabla \mathbf{D} \nabla c(\mathbf{r},t) \tag{3}$$

where $\mathbf{D}$ is the diffusion coefficient tensor of rank two. In case of self-diffusion, the diffusion process takes place without a concentration gradient and the diffusion theory considers the probability $P(\mathbf{r}_0,\mathbf{r},t)$, known as *Green's function* or *diffusion propagator*,[59] that a particle moves from an initial position $\mathbf{r}_0$ to $\mathbf{r}$ during the time t. Assuming an isotropic motion, the Fick's second law is:

$$\frac{\partial P(\mathbf{r}_0,\mathbf{r},t)}{\partial t} = \nabla D \nabla P(\mathbf{r}_0,\mathbf{r},t) \tag{4}$$

where D is now the isotropic self-diffusion coefficient, that is, a scalar.For fluids with isotropic and unrestricted motion and in homogeneous medium, as $\mathbf{r}$ approaches to ∞, P approaches zero and the solution of the Equation (4) is:

$$P(\mathbf{r}_0,\mathbf{r},t) = (4\pi t D)^{-3/2} \exp\left(-\frac{(\mathbf{r}-\mathbf{r}_0)^2}{4Dt}\right) \tag{5}$$

which states that the radial distribution function is Gaussian and it is completely characterized by the self-diffusion coefficient D. The mean-square displacement for the case of free diffusion is given by[60]:

$$\left\langle (\mathbf{r}-\mathbf{r_0})^2 \right\rangle = \frac{\int (\mathbf{r}-\mathbf{r_0})^2 P(\mathbf{r_0},\mathbf{r},t)d\mathbf{r_0}d\mathbf{r}}{\int P(\mathbf{r_0},\mathbf{r},t)d\mathbf{r_0}d\mathbf{r}} \tag{6}$$

so that:

$$\left\langle (\mathbf{r}-\mathbf{r_0})^2 \right\rangle = 6Dt \tag{7}$$

Thus, for unbounded molecules, the mean-square displacement changes linearly with time. It is well known that the self-diffusion coefficient D in infinitely dilute solution is related to molecular size according to equation:

$$D = \frac{kT}{f} \tag{8}$$

where k is the Boltzmann constant, T the temperature expressed in K, and f is the friction coefficient. The latter depends on size and shape of the diffusing species. In the simplest case of a sphere having radius r moving with constant velocity in a continuous medium with viscosity η, f was demonstrated by Stokes to be equal to $6\pi\eta r$,[61] and thus Equation (8) becomes the well-known Stokes–Einstein equation:

$$D = \frac{kT}{6\pi\eta r} \tag{9}$$

Several NMR pulse sequences have been developed for measuring the diffusion coefficient. The most successful and currently used experiment is the modified spin-echo experiment (PGSE) proposed by Stejskal in 1967.[62] As the echo signal is due to the transversal components of magnetic moments, the echo attenuation normalized for the attenuation due to relaxation can be written as[63]:

$$\frac{I(2\tau)}{I(2\tau)_{g=0}} = E(\mathbf{g},\Delta) = \int\int \rho(\mathbf{r_0})P(\mathbf{r_0},\mathbf{r},t)\cdot \exp[i\gamma\cdot\delta\cdot\mathbf{g}(\mathbf{r}-\mathbf{r_0})]d\mathbf{r_0}d\mathbf{r} \tag{10}$$

where $p(\mathbf{r_0})P(\mathbf{r_0},\mathbf{r},t)$ is the probability that a spin starting from $\mathbf{r_0}$ moves to $\mathbf{r}$ in the time Δ and:

$$I(2\tau)_{g=0} = I(0)\exp[-2\tau/T_2] \tag{11}$$

Considering the probability described in Equation (5), the spherical polar coordinates and setting $\mathbf{g} = g_z$ and $\mathbf{R} = \mathbf{r_1} - \mathbf{r_0}$, the final expression for the echo attenuation is:

$$E(g, \Delta) = \exp\left(-\gamma^2 g^2 D \delta^2 \Delta\right) \tag{12}$$

The intensity of the NMR signal at 2τ will be:

$$I(2\tau) = I(0) \exp\left[-\left(2\tau/T_2 + \gamma^2 g^2 D \delta^2 \Delta\right)\right] \tag{13}$$

This experiment has two limitations: (a) nuclei with short T_2 are difficult to be detected and (b) multiplets produce a distorted signal phase after π pulse which inverts the coupled spin states. Both limitations are partially overcome by the stimulated echo experiment (STE).[64,65] The main difference with the experiment previously described is that the echo attenuation due to the diffusion competes with T_1 rather than with T_2. The equation analogous to Equation (13) is now:

$$I(\tau_1 + \tau_2) = I(0) \cdot 0.5 \exp\left[-(\tau_2 - \tau_1)/T_1 + 2\tau_1/T_2 + \gamma^2 g^2 D \delta^2 \Delta\right] \tag{14}$$

which normalized for the attenuation due to T_1 and T_2 relaxation processes becomes:

$$\frac{I(\tau_1 + \tau_2)}{I(\tau_1 + \tau_2)_{g=0}} = E(g, \Delta) = \exp\left[-\gamma^2 g^2 D \delta^2 \Delta\right] \tag{15}$$

where

$$I(\tau_1 + \tau_2)_{g=0} = I(0) \cdot 0.5 \exp[-(\tau_2 - \tau_1)/T_1 + 2\tau_1/T_2] \tag{16}$$

Equations (12) and (15) can also be expressed as:

$$\ln(E(g, \Delta)) = -\gamma^2 g^2 \delta^2 \Delta D \tag{17}$$

If one does not use the short gradient pulse (SGP) approximation, the term Δ has to be substituted with $(\Delta - \delta/3)$. In the case of a monodisperse system, the plot of $\ln(E)$ versus $\gamma^2 g^2 \delta^2 \Delta$ is a straight line having the absolute value of the slope equal to the self-diffusion coefficient. For polydisperse sample, the signal intensity decay can be interpreted in terms of a distribution of diffusing species:

$$\frac{I}{I_0} = \int_0^\infty P(D) \exp(-kD) dD \tag{18}$$

where $k = \gamma^2 g^2 \delta^2 \Delta$ and $P(D)$ is the normalized distribution of self-diffusion coefficients D. $P(D)$ can be obtained by the numerical inversion of Equation (18) after the assumption of a mathematical form for the

self-distribution coefficient distribution. However, as the signal is noisy, the $P(D)$ obtained by a simple non-negative least square fit would lead to a multiple peaks, which is a mathematically ill-posed problem.[66–68] To avoid misleading data interpretation, the so-called regularization function, or smoothing function, must be used. A widely adopted mathematical algorithm is CONTIN[66,68] which implements a Tikhonov regularization coupled with non-negativity constraints in the framework of least-squares programming.

An important technical development of the PFG and STD experiments was introduced at the beginning of the 1990s; the Diffusion Ordered Spectroscopy, that is DOSY.[69,70] It provides a convenient way of displaying the molecular self-diffusion information in a bi-dimensional array, with the NMR spectrum in one dimension and the self-diffusion coefficient in the other. While the chemical-shift information is obtained by Fast Fourier Transformation (FFT) of the time domain data, the diffusion information is obtained by an Inverse Laplace Transformation (ILT) of the signal decay data. The goal of DOSY experiment is to separate species spectroscopically (not physically) present in a mixture of compounds; for this reason, DOSY is also known as ''NMR chromatography.''[71]

More recently, three-dimensional (3D) pulse sequences with DOSY have been presented; where a diffusion coordinate is added to the conventional 2D map. As in the conventional 2D spectra, these experiments reduce the probability of signal overlap by spreading the NMR frequency of the same species over a 2D plane, and distribute the diffusion coefficient.

1.3.2. Applications of diffusion NMR

In principle, the interaction of small molecules within a swollen polymer is one of the easiest situation to be proven, due to the large difference in size of species involved. Changes in the small molecule diffusivity will occur as a result of specific interactions between the diffusant and the polymeric matrix.

Griffiths[72] investigated the behaviour of three diffusant molecules, that is, toluene, aniline and phenol, as a function of weight fraction for two polymers: $PEG_{76}PPG_{29}PEG_{76}$, that is a block copolymer comprising poly(ethylene glycol), poly(propylene glycol) and poly(ethylene glycol), and (polyvinyl acetate). All the investigated systems were analysed using the stretched exponential Equation (19) describing the diffusion of spheres in polymer solutions:

$$\frac{D}{D_0} = \exp(-\alpha\varphi^{\nu}) \tag{19}$$

where D is the self-diffusion coefficient of the probe, ϕ is the polymer weight fraction and D_0 is the diffusion coefficient at $\phi = 0$. They found

that the reduction of diffusion coefficients are related to interaction strength between the two species. For both $PEG_{76}PPG_{29}PEG_{76}$ and PVAc, α was constant for all the three diffusants suggesting that it accounts for the obstruction experienced by the diffusant molecule within the polymeric environment. On the contrary, v decreased from 1.0 to 0.39 for $PEG_{76}PPG_{29}PEG_{76}$ and from 1.0 to 0.66 for PVAc, accordingly to H-bonding strength (toluene < aniline < phenol). Thus v reflects the strength of H-bonding, and Equation (19) can be used to differentiate obstruction from specific interactions. If the small molecule is water, care must be taken in measuring the diffusion coefficients due to the fact that intense signal contribution to NMR signal arising from bulk water is always present; in this case, organic solvents are preferred.

The association of a protein with a small molecule is a biological relevant processes which can be also investigated by means of PFG-NMR by choosing in the NMR spectrum a resonance belonging to the ligand.[45] For this application, the experiment is particularly quick and reliable, as the D value of the small molecule decreases largely when the species is associated with the protein. If the ligand exchange between the free and the bound-to-protein states is slower than the chemical shift and diffusion time scales, distinct resonances and diffusion coefficients will be observed.[73] When fast exchange occurs, the observed diffusion coefficient will be a weighted average of the free and bound diffusion coefficient in agreement with the equation[74]:

$$D_0 = (D_f \cdot f_f) + (D_b \cdot f_b) \tag{20}$$

where D_f and f_f are the diffusion coefficient and the molar fraction of the free species, while D_b and f_b refer to bound system.

In principle, in both slow and fast exchange limits, the analysis of the ligand–protein interaction could be performed by a direct integration of the two well-separated resonances of free and bound ligand and by the analysis of their chemical shift. However, these methods are limited by the broadness of the protein–ligand NMR spectra, and numerical values of association constants are barely obtainable.

PFG-NMR measurements are preferably performed in the fast exchange regime; the ligand resonance intensity can be monitored over a range of gradient amplitudes. This improves the precision of the diffusion measurement, as larger amounts of data points can be used for D calculation. The fast exchange regime is assured preparing solutions with a large excess of the ligand. Moreover, in order to obtain an accurate D value, the measurements should be performed with a short Δ delay, otherwise the signal of the free ligand, which moves faster than the ligand–protein aggregate, is preferentially attenuated. Consequently, the D_0 value in Equation (20) decreases due to spectral editing of the fraction

f_f of the free ligand. In this condition, D_0 will no longer represent a real-weighted average of the ligand in the free and bound states as a decrease of the f_f value with Δ will be observed. The case of 1:1 ligand–protein equilibrium is described by the equation:

$$LP \underset{K_2}{\overset{K_1}{\Leftrightarrow}} L + P \tag{21}$$

The binding constant K_d in the fast diffusion limit is obtained according to[45,74]:

$$K_d = \frac{[L][P]}{[LP]} = P_{tot}\left(\frac{D_b - D_0}{D_0 - D_f}\right) + L_{tot}\left(\frac{D_0 - D_b}{D_b - D_f}\right) \tag{22}$$

P_{tot} being the total protein concentration, L_{tot} the total ligand concentration, D_b and D_f the diffusion coefficients of bound and free ligand, respectively. K_d can be obtained by the measurement of D_0 and by independent measurements of diffusion coefficients of ligand and protein, the latter being a good approximation for the diffusion coefficient of the bound ligand. $\Delta D = D_f - D_0$ versus ligand concentration calculated with Equation (22) for different K_d values has been largely discussed.[45,74] Independently from K_d value, ΔD converges to zero when ligand concentration becomes large with respect to the protein amount; however, the behaviour of ΔD at low ligand:protein molar ratios changes according to K_d value. When binding affinity is high, that is, low K_d and low ligand:protein molar ratios, almost all ligand molecules are bound to the protein and the observed diffusion coefficient is equal to the one of the protein. When K_d increases, the equilibrium favours the free ligand, and even at low ligand:protein molar ratios, the observed ligand diffusion coefficient D_0 reflects a substantial fraction of free ligand. For intermediate ligand:protein molar concentration, that is, from 1:1 to 1:10, the observed D value depends upon both ligand concentration and K_d. This is the best range for the evaluation of the affinity of several ligands towards a specific protein binding site.

Derrick studied the interaction of L-tryptophan and ibuprofen with human serum albumin (HSA),[74] which is an abundant transport blood protein capable of binding efficiently several species.[75] They acquired ^{1}H NMR spectra of L-Tryptophan–HSA system for different ligand:protein molar ratios, that is 3:1, 5:1, 7:1 and 10:1. The aromatic resonances of L-Tryptophan are difficult to be observed due to the overlap with HSA signals, even at 10:1 molar ratio, so that the spectral subtraction was performed. D values of L-Tryptophan were calculated by integration of the subtracted spectra and were in good agreement with those predicted by computer simulations. In the case of ibuprofen, only for 140:1 molar ratio, the resonances of ibuprofen are clearly visible; also in this case, the

protein spectrum subtraction was necessary. Dissociation constants were calculated assuming a single binding site with a 1:1 stoichiometry, and the obtained K_d were in agreement with literature data for lower HSA sites affinity. The latter increased regularly with the ligand concentration, indicating successive saturation of the available HSA low-affinity binding sites.[75,76]

A class of systems extensively investigated by means of PFG-NMR are colloids. They are usually hydrophobically modified water-soluble polymers, that is, polymers with a water-soluble skeleton bearing one or more hydrophobic units, which allow the self-assembling of the polymer in water solution and the interaction with surfactants.[77]

A gelatine–SDS model system was studied by means of PFG-NMR by Miller.[78] It was found that by adding 1%, 2% or 5% (w/w) of SDS to the gelatine polymer, the diffusion coefficient of SDS itself decreases about one order of magnitude with respect to *D* of pure SDS. Micellar size is the same in water and in gelatine, so that the decrease of the *D* value was attributed to the strong interaction between micelles. Further, they observed that the diffusion coefficient of gelatine was similar to the one of SDS micelles, and argued that a gelatine chain is wrapped around the SDS micelle, so that gelatine and SDS diffuse as a single species. Persson studied the behaviour of the polymer obtained by end-capping dodecyl groups to polyethylene oxide ($C_{12}EO_{200}C_{12}$) at different SDS concentrations.[79] The *D* distributions obtained by CONTIN algorithm showed a narrowing of the distribution width by increasing SDS amount. This was attributed to the rearrangement of the hydrophobic framework, which changed from an inter-polymer association to an intra-polymer one. Griffiths also investigated the interactions between SDS and a self-assembling copolymer of vinyl-pyrollidone and vinyl-acetate.[72] Diffusion coefficient of SDS monotonically decreases as SDS concentration increases, while no significant variations were observed for the copolymer. Consequently, either the polymer and polymer–surfactant complexes have a similar dimension or the binding of SDS does not change the polymer's structure. A large number of articles reports the use of PFG-NMR for quantifying the binding degree of the small molecule phenol with $C_{18}Ex$ surfactant micelles.[80,81] It was observed the interesting correlation between the degree of phenol binding and micelle size and shape, the latter also assessed by small-angle neutron scattering.

The isotherm characterizing the binding phenomenon of small molecules with surfactant micelles or polymers has been largely studied by means of PFG-NMR.

The two-state mobility model[82,83] was used to describe such system, Equation (23), which states that the phenol self-diffusion coefficient is a weighted average of free and micelle-bound ones:

$$\bar{D}_s^{\text{phenol}} = \frac{C_{\text{free}}}{C_{\text{total}}} D_s^{\text{phenol,nosurfactant}} + \frac{C_{\text{micelle-bound}}}{C_{\text{total}}} D_s^{\text{micelle}} \quad (23)$$

When $D_s^{\text{phenol}} \gg D_s^{\text{micelle}}$, significant binding of phenol to micelles occurs, $\bar{D}_s^{\text{phenol}}$ is largely reduced. From the binding isotherm, an estimation of phenol molecules per surfactant molecule can be obtained.

For more complicated systems, the DOSY experiment provides several advantages, it combines the selectivity of high-resolution NMR with the hydrodynamic information derived from PFG-NMR. It allows to separate the molecular species according to their diffusion coefficients and simultaneously monitoring the structures and sizes of the components. An example is reported by Chen,[84] who considered the binding isotherm and size of the bovine serum albumin (BSA) and SDS complex. The fraction of SDS bound to BSA was determined from self-diffusion measurements, and it was found that saturation corresponds to a weight ratio of SDS-to-BSA equal to 1.9. Diffusions and chemical shifts information were obtained simultaneously for all species in solution and showed that at low binding levels both ends of SDS interact with protein, whereas for increasing binding number, the protein is denatured. At the saturation stage, micelle-like clusters of surfactant molecules are formed.

Colloidal drug carriers with relevant medical application can be obtained from derivatization of hyaluronic acid (HA).[85] The limited number of receptors on cell surfaces, the non-inflammatory properties and the enzymatic degradability make HA appealing in the biomedical field, that is, viscosurgery,[86] ophthalmic surgery and osteoarthritis therapy.[87] HA, a linear polysaccharide formed by alternating D-glucuronic acid (GlcUA) and *N*-acetyl-D-glucosamine (GlcNAc) units, is a biocompatible polymer playing important roles in cell adhesion, growth and migration and acting as a signalling molecule in cell motility, inflammation, wound healing and cancer metastasis through its receptors, mainly the CD44 antigen. HA-based systems have been extensively studied by Di Meo, and some bioconjugates were synthesized for in antitumor therapy.[88–90] In a recent work, spermidines were linked via one primary amino group to HA (soluble amide derivatives) and via both primary amino groups to different HA chains (cross-linked amide derivatives).[89] The aim was to obtain HA derivatives with a high affinity for NO molecules through specific covalent bonds with the secondary amine groups of spermidine. Authors used DOSY maps to evaluate the linkage between spermidine and the polymer. The diffusion coefficients measured for the HA-spermidine and for free spermidine sample were found to be 5.51×10^{-12} and 1.87×10^{-9} m^2/s, respectively. Moreover, it is also possible to establish the presence of low molecular weight compounds such as free spermidine, which may impair the determination of the true percentage of the grafting of spermidine onto HA. Finally, DOSY data indicated that no low

molecular weight impurities are present in the sample; allowing the degree of grafting to be calculated.

Hydrophobically modified HA derivatives,[91] obtained through the partial esterification of the HA carboxyl groups with methylprednisolone (45% in HYCp45 and 60% in HYCp60),[92] have been deeply studied.[93] A key point prior to any *in vivo* study of the biomaterial is the assessment of the so-called ''stealth character'' of the species itself. Such characteristic corresponds to be invisible towards the immune system, so that colloids are not recognized as foreign objects by body fluid components, as plasma proteins fibrinogen, BSA and lipidic components.[94,95]

The *D* values of HYCp45 and HYCp60 with DPPC (zwitterionic liposome at physiological pH) and DPPG (anionic liposome at physiological pH) were measured in order to evaluate polar and/or apolar interactions. Further, the apolar interactions of HA derivatives with two relevant plasma proteins, that is, BSA and fibrinogen, were also investigated. The observed diffusion coefficients suggested that the functionalization of HA with hydrophobic methylprednisolone groups reduced the hydrodynamic size of the polymer, probably due to the loss of coordinated water molecules around the newly formed esters and to a more compact form of the macromolecule arising from hydrophobic association. The presence of DPPC and DPPG liposomes increased the macromolecular mobility, and this was explained by taking into account the loss of sensitivity of the PFG-NMR technique for materials with low mobility; in fact, nuclei with restricted motion, thus short T_2, give broader resonances in the spectrum. Moreover, HA derivatives are characterized by a large molecular weight polydispersity. As polymers with higher molecular weight are absorbed preferentially, the PFG-NMR signals are influenced by the least interacting polymers (with a smaller size). Despite these considerations, the change of *D* values indicates the presence of some interactions between HA/HA derivatives and phospholipids as confirmed by dynamic light scattering and *Z* potential measurements. Comparing the diffusion coefficients obtained for HA-based materials interacting with DPPC and DPPG, it is evident that DPPC liposomes show stronger interactions than DPPG ones, probably due to the different electrostatic organization. In fact, DPPC liposome has a fractional positive character which can attract negatively charged carboxylic groups, while the anionic liposome DPPG does repel them.

2. SOLID-STATE NMR

The NMR technique applied in the solid-state offers the unique opportunity of studying interactions between low-affinity ligand and insoluble targets, such as membrane protein, humic substances or to investigate the aggregation occurring at the organic/inorganic interface of

multi-component materials. The role of solid-state NMR is in continuous growth, allowing the detection of many nuclei and, for each of them, the analysis of different physical–chemical properties. Moreover, there is no limitation on the molecular mass for solid-state NMR. All these characteristics make SS-NMR a powerful approach for obtaining details at a microscopic level.

Atoms and molecules in solid state are subject to restricted motions, so that all the interactions which are orientation dependent are not averaged by molecular motion and the spectra are complex; it is therefore fundamental to apply approaches able to increase the resolution and the S/N.

2.1. Magic-angle spinning

This approach consists of spinning the sample around an axis inclined at the magic angle with respect to the applied external field,[96] which is able to average to zero the nuclear dipole–dipole interactions between magnetic moments. This is valuable for polymers, where the anisotropic spin interactions are so strong that becomes hard to extract any kind of structural information. The advances in spectrometer hardware and ceramics technology made possible to reach high rotation frequencies allowing the desired resolution to be achieved. The spin frequency depends on the diameter of the rotor according to[97]:

$$v = \frac{\sqrt{3}}{\pi}\sqrt{\frac{T\Delta}{\rho}}\frac{1}{D} \tag{24}$$

where T is the tensile strength of the material, Δ is the relative wall thickness of the rotor, ρ the density of the material and D the rotor diameter.

2.2. Decoupling

The actual limit on the rates of spinning depends primarily on the tensile strength of the rotor material, provided that the necessary precautions concerning rotor balancing and bearing lubrication are taken. The spinning rates are often not fast enough to average the strong heteronuclear dipolar coupling with ^{1}H or other abundant active nuclei nearby. For this reason, the high power decoupling technique must be applied for the observation of dilute spins like ^{13}C.

2.3. Cross polarization

Cross polarization is the technique routinely used for increasing the sensitivity in the NMR dilute spins, such as ^{13}C, using the reserve of abundant spins which usually are ^{1}H.

This sensitivity enhancement arises through two mechanisms:

- an increase of population difference between α and β of abundant species;
- a decrease of time between successive free induction decays (FID) due to relaxation time shortening.

The first step consists of preparing the abundant spin system in a state with an artificially low temperature applying a $\pi/2$ pulse followed by an on-resonance $-y$ ^{1}H contact pulse. This field acts to maintain, to some extent, the ^{1}H magnetization along $-y$ and is known as spin-lock field $B_1(^{1}H)$. Then the dilute spin system is allowed to come into thermal contact with the cold system of abundant spins. In this way, heat flows from the dilute spin system to the cold abundant spin system, which produces a large drop in the spin temperature of the dilute spin system. This step is achieved by applying an RF radiation $B_1(X)$ on dilute spin system and then adjusting the oscillating magnetic field amplitudes to satisfy the Hartmann–Hahn condition: $\omega_{1X} = \omega_{1^1H}$. This thermal contact will lead a slight warming of the spin temperature of the abundant nuclei and a considerable cooling of the dilute nuclei with a decrease of spin temperature of dilute spin system down to[98]:

$$T_X^{cp} = T^1H = \left(B_1\left(^1H\right)/B_0\right)T_L = \left(\gamma_X/\gamma^1H\right)\left(B_1\left(^1H\right)/B_0\right)T_L \qquad (25)$$

The ''decrease'' of the spin temperature means an increase of population difference between the upper and lower energy spin states and consequently an increased sensitivity of the NMR experiment. From Equation (25), the temperature of dilute spins has been lowered by a factor γ_X/γ^1_H, that is, ¼ when $X = {}^{13}C$. This means an increased sensitivity of the FID resonance experiment equal to about 4 for the ^{13}C nuclei. Because the X signal is created from the magnetization of dilute nuclei, the repetition time of NMR experiment depends on the spin–lattice relaxation time of the abundant spin species, protons, which is usually much shorter than the spin–lattice relaxation times of the dilute nuclei. This, a further advantage of cross polarization, delay between two scans can be very short, even in the order of few tens of milliseconds.

2.4. Heteronuclear and homonuclear dipolar recoupling under magic-angle spinning

In case of interest on investigating molecular structure via distance measurements between two nuclear spins, the suppression of dipole–dipole interactions under MAS is undesirable. In this case, a reintroduction of the

heteronuclear, or homonuclear, dipole–dipole coupling under magic-angle spinning in a controlled fashion must be carried out.

Rotational-Echo, DOuble-Resonance (REDOR) is a MAS experiment for measuring internuclear distances between heteronuclear spin pairs. This experiment makes use of simple rotor-synchronized π pulses to recover the heteronuclear dipolar interaction.[99,100] In particular, π pulses are applied at the centre and at the end of each rotor period to the S spin leading to the incomplete refocusing of the heteronuclear interaction by the MAS. The incomplete averaging of the heteronuclear interaction gives an enhanced dephasing of proximal I spins. Typically, measurements are performed using a spin-echo applied to the I spins in the presence and then in the absence of the train of π pulses applied to the S spin. Data is typically analysed by monitoring the ratio of the dephased/nondephased signal intensity (S/S_0) as a function of the dephasing period, and the resulting plots are analysed to extract the strength of the heteronuclear coupling, and hence the distance between the heteronuclear spin pair I and S. Analysis of these dephasing curves is aided by their weak dependence on the relative orientations and other anisotropic parameters, such as the chemical shielding anisotropy. However, attention is required in order to include any coupling which may arise from interactions with natural abundance spins in close proximity. The determination of weaker couplings from these dephasing curves requires the efficient decoupling of the protons, which otherwise would lead to a rapid decay of the overall signal for extended dephasing periods and a concurrent drop in sensitivity and accuracy. REDOR has been extensively used to measure heteronuclear couplings between isolated heteronuclear spin pairs. Methods using frequency selective pulses have also been developed to determine accurate heteronuclear dipolar couplings in uniformly labelled samples.[101] The selectivity of REDOR is highly reliant on the sites being sufficiently well resolved such that the selective π pulses only affect a particular spin. These methods may prove complementary to broadband techniques (such as CP), enabling detailed distance information to be obtained from uniformly labelled samples, once proximity has been established.

For coupled homonuclear spins, the method is more complicated due to the non-commutation among the chemical shifts of the nuclei and their chemical-shift interactions. For this reason, different recoupling techniques have been developed to meet different interaction conditions, all comprising into two groups: the rotational and the multiple pulse RF irradiation. Pulse sequences of the first group provide a means of measuring distances between weak coupling spins most conveniently with significant chemical-shift differences (>50 ppm). In these cases, the chemical-shift interactions dominate, and recoupling is achieved by matching the rotor frequency to a multiple of the isotropic chemical-shift difference

between the two nuclei $\Delta\delta = m\omega_r$.[102–104] For spins with small chemical-shift differences (< 50 ppm), homonuclear recoupling with less sensitivity is desired. This is achieved by modulating the Hamiltonian with multiple pulse irradiation, and a broad range of RF pulse schemes have been developed for this purpose.[105] The multiple pulse irradiation is also used for correlation spectroscopy of multiple spins over a broad range of chemical shifts.

2.5. Ligand–receptor interactions

The development of novel pharmaceuticals species is tightly related to the mechanism of interactions between drugs and target integral membrane proteins. Solid-state NMR is highly attractive for these biological systems for two main reasons: there is no limitation on molecular mass and it enables to study the membrane protein systems in their native forms.

The affinity of a ligand for a receptor is controlled by two rate constants: the on-rate k_{on} and the off-rate $k_{off.}$[106] Ligands with high affinity for a membrane receptor have dissociation constants $K_d = k_{off}/k_{on} \leq 10$ μM and are difficult to be studied with liquid-state NMR, as they are almost completely associated with receptor binding sites, producing broad signals. Therefore, in the case of ligands with high receptor affinities, SS-NMR is the most rational choose.

Several works have been reported for macroscopically orientated biological membranes.[106–109] The biomembrane alignment can be carried out mechanically or magnetically. The first one relies on the deposition of lipid bilayers on the surface of a rigid support (glass plates) such that the bilayer normal is perpendicular to the surface of the support itself. Small peptides and the lipid bilayers can be dissolved in organic solvents which are successively removed under vacuum.[105] The re-hydration of the system in a chamber of an optimized temperature, humidity and time gives rise to the desired orientation.

Large systems have harsh conditions, which represents a problem for the membrane integrity; in this case, the centrifugation of the bilayers onto the support surface under the conditions of fully hydration and normal temperature is preferred.[110]

Magnetic alignment relies on the negative diamagnetic anisotropy of the acyl chains within the lipids that compose the lipid bilayer.[111,112] In the presence of a magnetic field, this results in preferential alignment of the acyl chains perpendicular to the magnetic field. The appropriate addition of a surfactant with the lipid bilayer results in planar lipid bilayers that align perpendicularly with the field, whereas the addition of lanthanide ions, having a positive diamagnetic anisotropy, and chelating lanthanide lipids results in bilayers parallel to the magnetic field.[105,113] The main advantage of magnetic orientation is due to the

fact that the system is continuously fully hydrate and thus maintains its activity. NMR experiments on oriented samples can be carried out with or without MAS. In static conditions, the orientation dependence of all the anisotropic interactions can be exploited and this allows the alignment of bounds, chemical groups or domains of the ligand relative to the receptor to be argued. However, the most reported application concerns the study of the quadrupolar tensor orientation using the NMR signal of ligands deuterated in specific positions, which allows an unambiguous identification of the signal of the ligand. In addition to it, the deuterium involves large quadrupolar interactions giving a great sensibility to study changes in orientation of the labelled groups. An excellent demonstration is reported by Ulrich, who studied the orientation of the retinal chromophore within the proton pump bacteriorhodopsin.[107,108] They performed different NMR experiments labelling the methyl groups of the chromophore chain in specific positions and analysed the quadrupolar tensor orientation. They were able to study the orientation of the methyl groups with respect to the membrane normal and thus to obtain the conformation of the retinal within the membrane itself. The same system was investigated after it was exposed to light in order to investigate conformational changes of the protein in relation to its function as proton pump.

Information on the orientation and the structure of ligands can be also extracted by rotating the orientated sample at a frequency ωr, whose value is below $\omega r < \delta_{\text{aniso}}$. This approach is known as MAOSS (magic-angle oriented sample spinning) and provides spectra with a set of spinning sidebands depending on the anisotropic interactions involved and on their orientation with respect to the magnetic field.[105] Applications of MAOSS are reported by Grobner[110]; who studied the structure and the orientation of the retinal in the G-protein coupled receptor rhodopsin during the cycle of photoexcitation. Similarly to the static technique, they deuterated some specific position of the receptor and then analysed carefully the spinning sidebands coming from the incomplete average of the quadrupolar interactions. Changes in the orientation of the b-ionone ring at the beginning of the photoexcitation cycle, that is, before protein conformational changes occur, were detected. A similar approach was followed for the investigation of interactions between acetylcoline and nicotinic acetylcholine receptor.[114] They demonstrated that the ammonium group of the receptor is positioned outwards the binding site and oriented at an angle of 40° with respect to the membrane normal.

A well-known and established NMR approach is CP-MAS, which provides good sensitivity and spectral resolution for both weak and strong interacting ligands. In fact, it is possible to distinguish the free ligand and the bound to the membrane on the basis of their differing dynamics. The polarization transfer from the ^{1}H to ^{13}C is mediated by the

dipole–dipole interactions, which in turn depend on the mobility of the molecules and on the efficiency of the spin-diffusion process. The transfer is absent for the free ligand, as it experiences a Brownian motion averaging the orientation-dependent interactions. On the contrary, species associated to membranes have a reduced mobility and the cross polarization will be efficient. CP-MAS was used to study interactions between a wide range of ligands and integral membrane proteins, including several bacterial transporters.

An exhaustive study is reported by Patching,[115] who investigated the binding affinities of two transporter protein ligands from *Escherichia coli*, both characterized by antibiotic resistance, toxin secretion and tumour growth, one is a nucleoside transporter, that is, NupC, and the other a glucuronide transporter, namely GusB, using variable contact time ^{13}C CP-MAS experiments. The affinities of two ^{13}C-labelled substrates were examined: the GusB substrate methyl [1-^{13}C]-β-D-glucuronide ([13C]MG) and the NupC substrate [1′-^{13}C]uridine. They used a combination of the Monte Carlo approach with CP-MAS experiments performed at different contact times to obtain the relationship between binding constants K_d and k_{off} and the evolution of the CP-MAS NMR signal intensity with contact time: binding constants can be extracted and the ligand affinity quantified. The method was tested using notable values of binding constants and the reproducibility proved by collected two intensity profile versus contact time for each ligand–protein system.

A potential limitation of the CP-MAS method is the requirement for appropriately labelled ligands not always available. To overcome this problem, it has been suggested the detection of ^{19}F nucleus, which is 100% NMR active and is very often contained in pharmacologically active compounds.

Problems can also occur if the membrane has abundant nuclei which give resonances in the same chemical-shift region of the ligand. Different approaches can be of help, as the use of ^{13}C depleted media to express the protein, to perform a spectral subtraction or to applied solid-state NMR experiments *ad hoc* for the system under investigation. In the latter strategy are enclosed cross polarization with inversion of polarization (CPPI) and 2D homonuclear correlation magic-angle spinning NMR spectroscopy. The CPPI experiment takes advantage from different CP characteristics of the signal of the bound ligand.[116] The homonuclear MAS–NMR correlation spectroscopy helps in recognizing weak resonances belonging to the ligand, which would otherwise be overlapped with the intense resonance of abundant material. Different implementations of this 2D spectroscopy were reported.[117]

As previously hinted, structure assessment through the interatomic distances determination can be done by recoupling techniques. Till few

years ago, measurements were performed on samples where isolated spin pairs were introduced and using selective recoupling methods that recouple two spins at a time. The reason is that the polarization transfer dynamics in such systems is simple. This approach can be easily reached experimentally for small molecules, but for more complicated systems, as ligands receptors, it is expensive and time consuming for the labelling of many spins.

Recently, numerous studies reported the application of homonuclear and heteronuclear selective recoupling schemes on uniformly labelled ligand interacting with membrane receptors. The polarization exchange curves were fitted with the two-spin model and showed that it is possible to determine internuclear distances up to 4.5 Å.[118]

A complementary as well as fundamental information to elucidate the structure of small molecules bound to membrane proteins is the knowledge of torsion angles. This was extensively performed for the assessment of the torsion angle between specific labelled sites of the ligand. Double quantum coherence is monitored under the action of the heteronuclear dipolar couplings arising from the adjacent protons. Examples were reported by Lansing[119]; where retinal chromophore structure in bacteriorhodopsin was elucidated.

3. SUPRAMOLECULAR CHEMISTRY

Supramolecular chemistry takes into consideration the weak and reversible non-covalent interactions between molecules, which include H-bonding, metal coordination, hydrophobic forces, van der Waals forces, π–π interactions, and covers different research fields, for example, molecular recognition, host–guest chemistry, mechanically interlocked and nanochemistry.

High resolution solid-state NMR represents an emerging technique for supramolecular species; it is able to investigate the microscopic environment at each individual site in a solid material allowing a complete characterization of the local interactions. Recent contributions have been reported by Chierotti[120] on weak interactions, most likely H-bonds and van der Waals contacts, in the molecular self-assembly of crystal engineering. The latter concerns the construction of crystalline materials from discrete molecular building blocks using non-covalent interactions. These weak connections can cooperatively assemble molecules, thanks to the large number of directional interactions. H-bonding is fundamental for its specificity, directionality, selectivity and easiness for manipulation. Their strengths can vary from 5 to hundreds of kJ mol^{-1}, depending upon the molecules and whether they are in the gas phase or in solution. HBs can be divided according to their strength into three categories, namely

strong, moderate and weak.[121] In weak HBs, the heavy atoms are separated by less than the sum of their van der Waals radii, while in strong HBs, the heavy atom distances are 2.4–2.55 Å for O···H···O, 2.6–2.7 Å for N···H···N and 2.5–2.6 Å for N···H···O.

IR and NMR are the most accepted techniques for the investigation of HB; in particular, solid-state NMR is to be preferred as the signal is not averaged by molecular motion. Its versatility allows to investigate directly atoms involved in the HB or those in their proximity; that is, the ^{1}H atom and ^{13}C, ^{15}N, ^{17}O, ^{29}Si, ^{31}P. The proton chemical shift can be used to detect hydrogen bonds and to evaluate their strength. Many authors have reported that ^{1}H is increasingly deshielded with increasing HB strength, and that the magnitude of the shift is directly correlated with the length of the HB.[122–125]

The ^{15}N chemical shift is also a useful parameter for the study of the HB, as it is very sensitive to the presence of the HB due to its wide chemical-shift range. The change in ^{15}N chemical shift can be up to 50–100 ppm for complete protonation. The shifts can occur to a higher or lower frequency according to the type of nitrogen atom involved and to the type of interaction occurring. For example, the ^{15}N isotropic chemical shifts are in the order of 100 ppm towards lower frequencies for aromatic amines and about 25 ppm towards higher frequencies for aliphatic amines. In OQC–OH···N(Py) interaction, the ^{15}N chemical shift was used to probe the protonation state of the N atom: it was found that in moderate strength O—H···N, the shift was below 20 ppm; in symmetric bonds, O···H···N around −60 ppm; and in ionic bonds, $^{-}$O···H–N^{+} ca. 100.54 ppm.[120]

HB interactions have also been studied by ^{13}C-CP-MAS spectroscopy. The carbon chemical-shift tensors of the COOH group obtained from the sideband intensity of low speed spinning NMR spectra provide a reliable criterion for assigning the protonation state of compounds. Several studies demonstrated that the principal elements of the nuclear shielding tensor change significantly with the protonation of carboxylic groups in different compounds such as amino acids DABCO–glutaric and other similar adducts.[126] Chierotti gave a careful explanation on how HB can be gained by investigating H/D isotope effect. Generally speaking, the replacement of the HB proton by a deuteron leads to a primary and a secondary influence on the H/D geometric isotope effect. When the hydrogen is replaced by a deuterium, the smaller heavy atom-hydrogen distance decreases, but the distance from the larger atom increases even more, leading to a widening of the HB. This geometry modification leads also to an H/D isotope effect on the chemical shift of the neighbour atoms. The shift experienced by atoms involved in the interaction depends on the strength of the HB and on the position of the H atom along the heavy atom axes, that is, only strong HBs give an isotope effect. This behaviour was

properly illustrated in the study of the isotope effect on the ^{15}N chemical shift, which measured for a series of supramolecular adducts obtained by grinding DABCO with several deuterated dicarboxylic acids (malonic, succinic, etc.). No shifts on deuteration was observed in the cases of the DABCO–malonic and DABCO–glutaric adducts, both characterized by weak HBs, whereas a low-frequency shift was found for the adducts with succinic, adipic, pimelic, suberic and azelaic acids; for all of them, the deuteration decreases the O–D distance and then increases the N–D distance, confirming the formation of an LBHB. The host–guest complexes are included in the field of supramolecular chemistry and some works reported the application of solid-state NMR for their investigation.[127–130] They are composed of two or more molecules, or ions, that are held together in unique structural relationships by non-covalent forces, which play a critical role in maintaining the 3D structure. Solid-state NMR was particularly suitable for the study of a class of host–guest complexes known as tweezers.[123] In these systems, the guest has a concave–convex topology and shows propensity for selectively forming complexes with electron deficient aromatic and aliphatic compounds and organic cations. Some of these systems can be studied by ^{1}H liquid-state NMR by exploiting the large upfield shifts of the substrate resonances upon complexation caused by host aromatic ring currents. However, when the complex formation and dissociation in $CDCl_3$ at room temperature is fast with respect to the NMR timescale, the solid-state approach is preferred. The reason is that the guest remains complexed on the timescale of the NMR experiment, and thus the structure and dynamics of the host–guest complex can be probed directly. The ^{1}H Double Quantum MAS is the most rational choice for a detailed study. In a 2D spectrum, as the DQ frequency corresponding to a given DQ Coherence is the sum of the two SQ frequencies, DQCs between like and unlike spins can be usually distinguished; in the first case, a single peak is observed, while in the second, two resonances are found. To a first approximation, which is fully valid in the limit of short recoupling times and for an isolated spin pair, it can be shown that the DQ peak intensity is inversely proportional to r^{6}.[123] Thus, it is reasonable to assume that the ^{1}H resonance shifts of the guest are sensitive to aromatic ring current effects and H-bonding, so that DQ peaks can reveal the intimate contact between host and guest molecules. Some experiments for host–guest interactions performed with ^{1}H DQ MAS sequence were reported by Brown,[123] encompassing inclusion compound formed by the polymer poly(dimethylsiloxane) with γ-cyclodextrin, the linear-chain alkane C_9H_{20} with tris(*o*-phenylenedioxy)spirotriphosphazene which forms a supramolecular structure with channels of diameter of ca. 4.5 Å and the trapping of solvent molecules in supramolecular organic nanotubes formed by calyx[4]hydroquinone (CHQ) crystallised from a water/acetone mixture.

REFERENCES

1. S. W. Homans, *Angew. Chem. Int. Ed.*, 2004, **43,** 290–300.
2. S. B. Shuker, P. J. Hajduk and R. P. Meadows, *Science*, 1996, **274,** 1531.
3. W. D. Morgan, B. Birdsall, P. M. Nieto, A. R. Gargaro and J. Feeney, *Biochemistry*, 1999, **38,** 2127–2134.
4. P. J. Hajduk, D. J. Augeri, J. Mack, R. Mendoza, J. G. Yang, S. F. Betz and S. W. Fesik, *J. Am. Chem. Soc.*, 2000, **122,** 7898.
5. L. Fielding, *Prog. Nucl. Magn. Reson. Spectrosc.*, 2007, **51,** 219–242.
6. D. Neuhaus and M. Williamnson, Wiley-VCH, New York, 1989.
7. C. Ludwig and U. L. Guenther, *Front. Biosci.*, 2009, **14,** 4565–4574.
8. T. Peters, Carbohydrates in Chemistry and Biology, Wiley-VCH, New York, pp. 1003–1023.
9. H. N. B. Moseley, E. V. Curto and N. R. Krishna, *J. Magn. Reson. B*, 1995, **108,** 243–261.
10. B. Meyer, T. Weimar and T. Peters, *Eur. J. Biochem.*, 1997, **246,** 705–709.
11. D. Henrichsen, B. Ernst, J. L. Magnani, W. T. Wang, B. Meyer and T. Peters, *Angew. Chem. Int. Ed.*, 98–102.
12. M. Mayer and B. Meyer, *J. Am. Chem. Soc.*, 2001, **123,** 6108–6117.
13. M. Mayer and B. Meyer, *Angew. Chem. Int. Ed.*, 1999, **38,** 1784–1788.
14. A. J. Benie, R. Moser, E. Bauml, D. Blaas and T. Peters, *J. Am. Chem. Soc.*, 2003, **125,** 14–15.
15. E. Y. X. Chen and T. J. Marks, *Chem. Rev.*, 2000, **100,** 1391–1434.
16. C. Dalvit, G. Fogliatto, A. Stewart, M. Veronesi and B. Stockman, *J. Biomol. NMR*, 2001, **21,** 349–359.
17. C. Ludwig, P. J. A. Michiels, X. Wu, K. L. Kavanagh, E. Pilka, E. Jansson, U. Oppermann and U. L. Günther, *J. Med. Chem.*, 2008, **51,** 1–13.
18. C. Ludwig, P. J. A. Michiels, A. Lodi, J. Ride, C. Bunce and U. L. Günther, *ChemMedChem*, 2008, **3,** 1371–1376.
19. V. J. McBrierty, S. J. Martin and F. E. Karasz, *J. Mol. Liq.*, 1999, **80,** 179–205.
20. A. M. Math and A. B. Scranton, *Biomaterials*, 1996, **17,** 547–557.
21. H. T. Edzes and E. T. Samulski, *J. Magn. Reson.*, 1978, **31,** 207.
22. R. G. Bryant and J. P. Korb, *Magn. Reson. Chem.*, 2005, **23,** 167.
23. J. R. Zimmerman and W. E. Brittin, *J. Phys. Chem.*, 1957, **61,** 1328.
24. L. Calucci, C. Forte and E. Ranucci, *J. Chem. Phys.*, 2008, **129,** 064511.
25. L. Calucci, C. Forte and R. Elisabetta, *Biomacromolecules*, 2007, **8,** 2936–2942.
26. R. Gianferri, V. D'Aiuto, R. Curini, M. Delfini and E. Brosio, *Food Chem.*, 2007, **105,** 720–726.
27. R. Gianferri, M. Maioli, M. Delfini and E. Brosio, *Int. Dairy J.*, 2007, **17,** 167–176.
28. B. P. Hills, S. F. Takacs and P. S. Belton, *Food Chem.*, 1990, **37,** 95–111.
29. R. J. S. Brown, F. Capozzi, C. Cavani, M. A. Cremonini, M. Petracci and G. Placuccie, *J. Magn. Reson.*, 2000, **147,** 89–94.
30. C. A. Toussaint, F. Médale, A. Davenel, B. Fauconneau, P. Haffray and S. Akoka, *J. Sci. Food Agric.*, 2002, **82,** 173–178.
31. F. P. Duval, M. Cambert and F. Mariette, *Appl. Magn. Reson.*, 2005, **28,** 29–40.
32. M. Ritota, R. Gianferri and R. B. Elvino Brosio, *Food Chem.*, 2008, **110,** 14–22.
33. B. P. Hills, K. M. Wright and P. S. Belton, *Mol. Phys.*, 1989, **67,** 1309–1326.
34. J. W. Donovan, *Biopolymers*, 1979, **18,** 263–275.
35. M. Forsyth, D. R. MacFarlane, J. Hey and P. Meakin, Advances hindered (or bulky) have less influence on the polymer relax- in Science and Technology, New Horizons for Materials. , 1995.
36. D. R. MacFarlane, J. Sun, P. Meakin, P. Fasolopoulos, J. Hey and M. Forsyth, *Electrochim. Acta*, 1995, **40,** 2131.
37. M. Forsyth, P. Meakina and D. R. MacFarlanea, *J. Mater. Chem.*, 1997, **7,** 193–201.

38. M. Forsyth, P. M. Meakin and D. R. Macfarlanet, *Electrochim. Acta*, 1995, **40,** 2339–2342.
39. M. Forsyth, P. Meakin, D. R. MacFarlane, G. Bulme and M. Reid, *J. Mater. Chem.*, 1994, **4,** 1149–1151.
40. Y. Xu, V. E. Yushmanov and P. Tang, *Biosci. Rep.*, 2002, **22,** 175–195.
41. V. E. Yushmanov, T. T. Tominaga, I. E. Borissevitch, H. Imasato and M. Tabak, *Magn. Reson. Imaging*, 1996, **14,** 255–261.
42. V. E. Yushmanov, H. Imasato, J. R. Perussi and M. Tabak, *J. Magn. Reson. B*, 1995, **106,** 236–244.
43. Y. Y. Chien, E. G. Kim and W. F. Bleam, *Environ. Sci. Technol.*, 1997, **31,** 3204–3208.
44. P. S. Pregosin, *Prog. Nucl. Magn. Reson. Spectrosc.*, 2006, **49,** 261–288.
45. L. H. Lucas and C. K. Larive, *Concepts Magn. Reson. Part A*, 2004, **20A,** 24–41.
46. A. Napoli, M. Valentini, N. Tirelli, M. Muller and J. A. Hubbell, *Nat. Mater.*, 2004, **3,** 183–189.
47. S. Cozzolino, M. G. Sanna and M. Valentini, *Magn. Reson. Chem.*, 2008, **46,** S16–S23.
48. M. Valentini, H. Ruegger and P. S. Pregosin, *Helv. Chim. Acta*, 2001, **84,** 2833–2853.
49. M. Valentini, M. Vaccaro, A. Rehor, N. Napoli, J. A. Hubbell and N. Tirelli, *J. Am. Chem. Soc.*, 2004, **126,** 2142–2147.
50. R. Baciocchi, G. Zeroni, M. Valentini, M. Mazzotti and M. Morbidelli, *J. Phys. Chem. A*, 2002, **106,** 10461–10469.
51. A. Pichota, P. S. Pregosin, M. Valentini, M. Wörle and D. Seebach, *Angew. Chem., Int. Ed. Engl.*, 2000, **39,** 153–156.
52. M. Valentini, P. S. Pregosin and H. Ruegger, *Organometallics*, 2000, **19,** 2551–2555.
53. M. Valentini, P. S. Pregosin and H. Ruegger, *J. Chem. Soc., Dalton Trans.*, 4507–4510.
54. E. O. Stejskal, *J. Chem. Phys.*, 1965, **43,** 3597–3603.
55. E. L. Cussler, Diffusion: Mass Transfer in Fluid Systems. Cambridge University Press, Cambridge, 1984.
56. J. P. Hansen and I. R. McDonald, Theory of Simple Liquids. Academic Press, London, 1976.
57. G. Arfken, *Mathematical Methods for Physicists*. Academic Press, New York, 1995.
58. J. Crank, The Mathematics of Diffusion. Academic Press, Oxford University, Oxford, 1975.
59. J. Kärger and W. Heink, *J. Magn. Reson.*, 1983, **51,** 1–7.
60. R. Lenk, Fluctuations, Diffusion and Spin Relaxation. Elsevier, Amsterdam, 1986.
61. J. T. Edward, *J. Chem. Educ.*, 1970, **47,** 261–270.
62. B. D. Boss, E. O. Steiskal and J. D. Ferry, *J. Phys. Chem.*, 1967, **71,** 1501–1505.
63. J. E. Tanner and E. O. Stejskal, *J. Chem. Phys.*, 1968, **49,** 1768–1777.
64. P. Stilbs, *Prog. Nucl. Magn. Reson. Spectrosc.*, 1987, **19,** 1–45.
65. J. E. Tanner, *J. Chem. Phys.*, 1970, **52,** 2523–2527.
66. S. W. Provencher, *Comput. Phys. Comm.*, 1982, **27,** 213–227.
67. R. La Manna, *Concepts Magn. Reson.*, 2005, **26A,** 78–90.
68. S. W. Provencher, *Comput. Phys. Comm.*, 1982, **27,** 229–242.
69. D. Wu, A. Chen and C. S. Johnson, *J. Magn. Reson. A*, 1995, **115,** 123–126.
70. C. S. Johnson, Jr., *Prog. Nucl. Magn. Reson. Spectrosc.*, 1999, **34,** 203–256.
71. Y. Cohen, L. Avram and L. Frish, *Angew. Chem. Int. Ed.*, 2005, **44,** 520–554.
72. P. C. Griffiths, A. Y. F. Cheung, J. A. Davies, A. Paul, C. N. Tipples and A. L. Winnington, *Magn. Reson. Chem.*, 2002, **40,** S40–S50.
73. D. E. Wemmer and P. G. Williams, *Methods Enzymol.*, 1994, **239,** 739–767.
74. T. S. Derrick, E. F. McCord and K. L. Cynthia, *J. Magn. Reson.*, 2002, **155,** 217–225.
75. T. Peters, *The Plasma Proteins. Structure, Function and Genetic Control*. Academic Press, New York, 1975.
76. U. Kragh-Hansen, *Pharm. Rev.*, 1981, **33,** 17–53.

77. B. M. Discher, Y. Y. Won, D. S. Ege, J. C. M. Lee, F. S. Bates, D. E. Discher and D. A. Hammer, *Science*, 1999, **284,** 1143–1146.
78. L. W. Miller DD, B. J. Antalek, A. J. Williams and J. M. Hewitt, *Langmuir*, 1994, **10,** 68–71.
79. K. Persson, P. C. Griffiths and P. Stilbs, *Polymer*, 1996, **37,** 253–261.
80. C. N. Tipples. Cardiff University, 2000.
81. M. J. Rosen, *Surfactants and Interfacial Phenomena*. Wiley, New York, 1989.
82. P. C. Griffiths, P. Stilbs, A. M. Howe and T. H. Whitsides, *Langmuir*, 1996, **12,** 5302.
83. R. Wimmer, F. L. Aachmann, K. L. Larsen and S. B. Peterson, *Carbohydr. Res.*, 2002, **337,** 841.
84. A. Chen, D. H. Wu and C. S. Johnson Jr., *J. Phys. Chem.*, 1995, **99,** 828–834.
85. T. C. Laurent, The Chemistry, Biology and Medical Application of Hyaluronan and Its Derivatives. Portland Press, London, 1998.
86. M. V. Shah, UCLA, 2003.
87. R. Day, P. Brooks, P. G. Conaghan and M. Petersen, *J. Rheumatol.*, 2004, **31,** 775–782.
88. C. Di Meo, L. Panza, D. Capitani, L. Mannina, A. Banzato, M. Rondina, D. Renier, A. Rosato and V. Crescenzi, *Biomacromolecules*, 2007, **8,** 552–559.
89. C. Di Meo, D. Capitani, L. Mannina, E. Brancaleoni, D. Galesso, G. De Luca and V. Crescenzi, *Biomacromolecules*, 2006, **7,** 1253–1260.
90. C. Di Meo, L. Panza, F. Campo, D. Capitani, L. Mannina, A. Banzato, M. Rondina, A. Rosato and V. Crescenzi, *Macromol. Biosci.*, 2008, **8,** 670–681.
91. R. Romeo, N. Nastasi, L. M. Scolaro, M. R. Plutino, S. Albinati and A. Macchioni, *Inorg. Chem.*, 1998, **37,** 5460–5466.
92. E. Payan, J. Y. Jouzeau, F. Lapicque, K. Bordji, G. Simon, P. Gillet, M. Oregan and P. Netter, *J. Controlled Release*, 1995, **34,** 145–153.
93. A. Taglienti, R. Cellesi, V. Crescenzi, P. Sequi, M. Valentini and N. Tirelli, *Macromol. Biosci.*, 2006, **6,** 611–622.
94. D. E. Owens and N. A. Peppas, *Int. J. Pharm.*, 2006, **307,** 93–102.
95. B. D. Ratner and S. J. Bryant, *Annu. Rev. Biomed. Eng.*, 2004, **6,** 41–75.
96. M. J. Duer, Solid State NMR Spectroscopy, Principles and Applications. University of Cambridge, Cambridge, Blackwell Publishing, 2002.
97. A. Samoson, T. Tuherm, J. Past, A. Reinhold, T. Anupõld and I. Heinmaa, *Top. Curr. Chem.*, 2004, **246,** 15–31.
98. E. O. Stejskal and J. D. Memory, High Resolution NMR in the Solid State. Oxford University Press, New York, 1994.
99. I. Sack and S. Vega, *J. Magn. Reson.*, 2000, **145,** 52–61.
100. T. Gullion, *Concepts Magn. Reson.*, 1998, **10,** 277–289.
101. C. P. Jaroniec, B. A. Tounge, J. Herzfeld and R. G. Griffin, *J. Am. Chem. Soc.*, 2001, **123,** 3507–3519.
102. D. P. Raleigh, M. H. Levitt and R. G. Griffin, *Chem. Phys. Lett.*, 1988, **146,** 71–76.
103. M. H. Levitt, D. P. Raleigh, F. Creuzet and R. G. Griffin, *J. Chem. Phys.*, 1990, **92,** 6347–6364.
104. P. R. Costa, B. Q. Sun and R. G. Griffin, *J. Am. Chem. Soc.*, 1997, **119,** 10821–10830.
105. M. Williamnson, *Concepts Magn. Reson. A*, 2009, **34A,** 144–172.
106. D. A. Middleton, NMR methods for characterising ligand-receptor and drug-membrane interactions in pharmaceutical research. *Annu. Rep. NMR Spectrosc.*, 2007, **60,** 39–75.
107. A. S. Ulrich, I. Wallat, M. P. Heyn and A. Watts, *Nat. Struct. Biol.*, 1995, **2,** 190–192.
108. A. S. Ulrich, A. Watts, I. Wallat and M. P. Heyn, *Biochemistry*, 1994, **33,** 5370–5375.
109. G. Grobner, I. J. Burnett, C. Glaubitz, G. Choi, A. J. Mason and A. Watts, *Nature*, 2000, **405,** 810–813.
110. G. Grobner, A. Taylor, P. T. F. Williamson, G. Choi, C. Glaubitz and J. A. Watts, *Anal. Biochem.*, 1997, **254,** 132–138.

111. R. R. Vold and R. S. Prosser, *J. Magn. Reson. B*, 1996, **113,** 267–271.
112. C. R. Sanders and J. P. Schwonek, *Biochemistry*, 1992, **31,** 8898–8905.
113. C. R. Sanders, B. J. Hare, K. P. Howard and J. H. Prestegard, *Prog. Nucl. Magn. Reson. Spectrosc.*, 1994, **26,** 421–444.
114. P. T. F. Williamson, A. Verhoeven, K. W. Miller, B. H. Meier and A. Watts, *Proc. Natl. Acad. Sci. USA*, 2007, **104,** 18031–18036.
115. S. G. Patching, G. Psakis, S. A. Baldwin, J. Baldwin, P. J. Henderson and D. A. Middleton, *Mol. Membr. Biol.*, 2008, **25,** 474–484.
116. A. N. Appleyard, R. B. Herbert, P. J. F. Henderson, A. Watts and P. J. R. Spooner, *Biochim. Biophys. Acta*, 2000, **1509,** 55–64.
117. A. Lange, K. Giller, S. Hornig, M. F. Martin-Eauclaire, O. Pongs and S. Becker, *Nature*, 2006, **440,** 959–962.
118. P. T. F. Williamson, A. Verhoeven, M. Ernst and B. H. Meier, *J. Am. Chem. Soc.*, 2003, **125,** 2718–2722.
119. J. C. Lansing, M. Hohvy, C. P. Jaroniec, A. F. L. Creemers, J. Lugtenburg and J. Herzfeld, *Biochemistry*, 2002, **41,** 431–438.
120. M. R. Chierotti and R. Gobetto, *Chem. Commun.*, 1621–1634.
121. P. A. Frey, *Magn. Reson. Chem.*, 2001, **39,** S190–S198.
122. G. A. Jeffrey, An Introduction to Hydrogen Bonding. University Press, Oxford, 1997.
123. S. B. Brown, *Macromol. Rapid Commun.*, 2009, **30,** 688–716.
124. T. Kameda and I. Ando, *J. Mol. Struct.*, 1997, **412,** 197.
125. K. Yamauchi, S. Kuroki, I. Ando, A. Shojii and T. Ozaki, *Chem. Phys. Lett.*, 1999, **302,** 435.
126. D. Braga, L. Maini, G. de Sanctis, K. Rubini, F. Grepioni, M. R. Chierotti and R. Gobetto, *Chem. Eur. J.*, 2003, **9,** 5538–5548.
127. T. Schaller, U. P. Buchele, F. G. Klarner, D. Blaser, R. Boese, S. P. Brown, H. W. Spiess, F. Koziol, J. Kussmann and C. Ochsenfeld, *J. Am. Chem. Soc.*, 2007, **129,** 1293.
128. S. P. Brown, T. Schaller, U. P. Seelbach, F. Koziol, C. Ochsenfeld, F. G. Klarner and H. W. Spiess, *Angew. Chem. Int. Ed Engl.*, 2001, **40,** 717.
129. C. Ochsenfeld, F. Koziol, S. P. Brown, T. Schaller, U. P. Seelbach and F. G. Klarner, *Solid State Nucl. Magn. Reson.*, 2002, **22,** 128.
130. J. Zienau, J. Kussmann, F. Koziol and C. Ochsenfeld, *Chem. Phys.*, 2007, **9,** 4552.

CHAPTER 5

Using 1,1- and 1,*n*-ADEQUATE 2D NMR Data in Structure Elucidation Protocols

Gary E. Martin

Contents

1. Introduction 217
2. Long-Range Heteronuclear Shift Correlation: HMBC and Related experiments 218
3. 1,1-ADEQUATE 219
   - 3.1. Sample requirements 221
   - 3.2. ADEQUATE data acquisition and processing 224
   - 3.3. Extracting correlation information from 1,1-ADEQUATE spectra 225
   - 3.4. Modulation of 1,1-ADEQUATE responses 228
4. Applications of 1,1-ADEQUATE and ACCORD-ADEQUATE Experiments 230
   - 4.1. 5,6-Dihydrolamellarin 232
   - 4.2. 4,5-Dibromopyrrol-2-carboxylic acid 234
   - 4.3. 2-[1-(4-Chlorobenzyl)-1*H*-indol-3-yl]-2-oxo-*N*-pyridin-4-yl acetamide 235
   - 4.4. Jamaicamide 236
   - 4.5. Phormidolide 236
   - 4.6. Confirmation of the medermycin/lactoquinomycin-A structure 237
   - 4.7. Cytosporacin 238
   - 4.8. Piperidylrifamycins 239
   - 4.9. Leucanthoside-A 240
   - 4.10. Withanolides 242

Merck Research Laboratories, Discovery & Preclinical Sciences, Global Chemistry—Structure Elucidation Group, Summit, New Jersey, 07901, USA

Annual Reports on NMR Spectroscopy, Volume 74
ISSN 0066-4103, DOI: 10.1016/B978-0-08-097072-1.00005-4

4.11. 3,4-Dihydroxy-2-quinolin-2-ylpyrido[3,2,1-*jk*] carbazol-6-ones 242
4.12. Phakellin and isophakellin 243
4.13. Rhodoptilometrin 245
4.14. Retrorsine and delcosine 245
4.15. 3,4-Epoxynephthenol acetate 247
4.16. Differentiating (2-pyrrole)cysteine S-oxide from (3-pyrrole)cysteine S-oxide 247
5. 1,*n*-ADEQUATE 248
5.1. Application of 1,*n*-ADEQUATE to 5,6-dihydrolamellarin 251
5.2. Application of 1,*n*-ADEQUATE for highly substituted aromatic compounds 252
5.3. Measurement of $^{1}J_{CC}$, $^{2}J_{CC}$, and $^{3}J_{CC}$ coupling constants 253
5.4. Applications of 1,*n*-ADEQUATE in the elucidation of the structures of phakellin and isophakellin alkaloids 253
5.5. 1,*n*-ADEQUATE of retrorsine 255
6. The *n*,1- and *m*,*n*-ADEQUATE Experiments 256
6.1. *n*,1-ADEQUATE of strychnine 257
6.2. Application of *n*,1-ADEQUATE to 5,6-dihydrolamellarin 262
6.3. Comparison of 1,*n*- and *n*,1-ADEQUATE 263
6.4. *m*,*n*-ADEQUATE of strychnine 263
6.5. Application of *m*,*n*-ADEQUATE to 5,6-dihydrolamellarin 266
7. Using 1,1-ADEQUATE Data in Conjunction with CASE Methods 267
8. Covariance NMR Methods 269
8.1. Unsymmetrical indirect covariance and generalized indirect covariance processing using ADEQUATE data 271
8.2. HSQC-1,1-ADEQUATE 272
8.3. Applications of HSQC-1,1-ADEQUATE 277
8.4. HSQC-1,*n*-ADEQUATE of strychnine 283
8.5. HSQC-1,*n*-ADEQUATE of retrorsine 285
9. Conclusions 287
References 288

Abstract

Modern structure elucidation methods are heavily reliant on a variety of two-dimensional NMR methods. Direct heteronuclear shift correlation methods *via* $^{1}J_{XH}$ and long-range correlation methods *via* $^{n}J_{XH}$, in particular, have become the cornerstone of modern structure elucidation protocols. Unfortunately, the inherent ambiguity in the number of bonds across which long-range heteronuclear correlations are observed can complicate the determination of novel structures, even

leading in some cases to erroneously reported structures. Various NMR experiments have been devised to circumvent problems inherent to the interpretation of long-range heteronuclear correlation methods; the 1,1- and 1,*n*-ADEQUATE experiments are among the methods developed. The 1,1- and 1,*n*-ADEQUATE experiments begin with an initial $^{1}J_{CH}$ transfer of magnetization followed by either a $^{1}J_{CC}$ or $^{n}J_{CC}$ carbon–carbon transfer, respectively, in an out-and-back sense. Thus, the 1,1-ADEQUATE experiment provides exclusively the identity of protonated and non-protonated carbons that are adjacent to the proton–carbon pair involved in the initial one-bond heteronuclear transfer. The 1,*n*-ADEQUATE experiment correspondingly provides long-range carbon–carbon connectivity information, primarily *via* $^{3}J_{CC}$ although $^{2}J_{CC}$ correlations are observed in some cases. The acquisition and interpretation of 1,1- and 1,*n*-ADEQUATE spectra are discussed in addition to the much less frequently utilized *n*,1- and *n*,*m*-ADEQUATE experiments. Applications of these experiments found in the literature through early 2011 are surveyed. Finally, the utilization of the newly developed unsymmetrical and generalized indirect covariance processing methods to calculate HSQC-1,1- and HSQC-1,*n*-ADEQUATE spectra is also discussed. These processing methods afford a convenient, diagonally symmetric carbon–carbon correlation spectrum in addition to allowing sample sizes, and/or data acquisition times to be reduced through the five- to as much as twentyfold gain in sensitivity inherent to the covariance processing method. Examples are shown and the interpretation of these data is also discussed.

Key Words: 1,1-ADEQUATE, 1,*n*-ADEQUATE, *n*,1-ADEQUATE, *n*,*m*-ADEQUATE, Structure elucidation, Unsymmetrical indirect covariance, Generalized indirect covariance, Carbon–carbon correlation.

1. INTRODUCTION

Two-dimensional (2D) NMR is irrefutably the cornerstone of modern structure elucidation methods.[1] Despite the inherently low sensitivity of NMR compared to other forms of analytical spectroscopy such as mass spectrometry and vibrational spectroscopy, NMR methods provide the means of establishing atom-to-atom connectivities that cannot be established by other methods. Supplemented by accurate mass measurements and fragmentation pathway information, NMR data can facilitate the elucidation of most small molecule structures.

Typical structure elucidation protocols using NMR methods rely on one-dimensional (1D) ^{1}H and ^{13}C reference spectra, when sufficient sample is available to acquire a ^{13}C reference spectrum, in conjunction with a

series of 2D NMR experiments. Proton–proton connectivities are established using gradient homonuclear COSY or TOCSY spectra. Direct $^{1}H–^{13}C$ correlations can be established by using either HMQC or HSQC spectra.[2] The latter is preferred, providing better digital resolution in the F_1 frequency domain than the former.[3] Quaternary carbons can be linked to protonated carbon fragments using $^{1}H–^{13}C$ long-range heteronuclear shift correlation methods, most typically gradient HMBC when modern spectrometers and probeheads are employed.[4] Heteroatoms can often be spanned via long-range heteronuclear correlations. With the advent of cryogenic NMR probes, supplementing the usual ensemble of 2D NMR experiments with a long-range $^{1}H–^{15}N$ GHMBC experiment has become a facile undertaking.[5–10] Stereochemical considerations in a structure determination can be addressed either using homonuclear scalar (J_{HH}) coupling constants or through-space relaxation information that can be extracted from NOESY or ROESY spectra, with the latter generally preferred for small molecules.

2. LONG-RANGE HETERONUCLEAR SHIFT CORRELATION: HMBC AND RELATED EXPERIMENTS

HMBC/GHMBC is undeniably an extremely powerful and useful experiment. The pulse sequence is quite simple and easily implemented. For $^{1}H–^{13}C$ experiments, unwanted direct correlation responses are eliminated by a single or two stage low-pass J filter. In contrast, for $^{1}H–^{15}N$ long-range heteronuclear correlation experiments, it is generally preferable to allow the direct ($^{1}J_{NH}$) correlation responses to ''leak'' into the spectrum as ~90–95 Hz doublets since the likelihood of a direct correlation response overlapping a long-range response is quite low.

The primary drawback of the HMBC/GHMBC is the indeterminate nature of the long-range correlations observed. *A priori* there is no simple way to differentiate $^{2}J_{CH}$ from $^{3}J_{CH}$ correlations. In addition, there are also instances in which $^{4}J_{CH}$ correlations can be observed with strong intensity, allowing them to be mistaken for shorter range correlations. The question of differentiating $^{2}J_{CH}$ from $^{3}J_{CH}$ and longer range correlations was first addressed by Reynolds and co-workers with the development of the ^{13}C-detected XCORFE experiment.[11] The 2J3J-HMBC experiment was the first of the proton-detected long-range heteronuclear shift correlation experiments that allowed for the specific identification of $^{2}J_{CH}$ correlations.[12] The H2BC experiment and variants subsequently developed by Sørensen and co-workers[13–15] allows edited long-range sub-spectra to be generated. Unfortunately, all of the experiments that allow the differentiation of $^{2}J_{CH}$ correlations from longer range correlations only work for protonated carbon resonances.

A second inherent problem with the HMBC/GHMBC experiment is the choice of the long-range delay optimization. A cursory survey of the literature shows that the most frequently chosen long-range optimization, at least for natural product structure elucidation, is probably 10 Hz. Optimization for 8 or 5 Hz is also frequently utilized. The congruence of the actual long-range coupling and the delay optimization determines the long-range correlation intensity. For long-range couplings that are well matched to the optimization, long-range correlation intensity will be good. As the mismatch between the delay and the optimization becomes more severe, long-range correlation intensities correspondingly decrease.

To address the problem of long-range delay optimization, Wagner and Berger[16] initially reported the development of the ACCORD-HMBC experiment that employs accordion-optimization of the long-range delay to circumvent the problem of the variability of long-range heteronuclear delays. Quite simply, the long-range delay begins at the smallest optimization (at the longest delay since this is an inverse relationship) for the shortest duration of the evolution period for the second frequency domain. As the duration of the evolution time is progressively incremented during the digitization of the second frequency domain, the delay optimization is correspondingly decremented. In this manner, a predefined range of long-range delay optimizations is sampled in a single long-range heteronuclear correlation experiment. Martin and co-workers[17] have examined the effects of long-range delay optimization ranges on the correlation responses observed in the ACCORD-HMBC experiment, showing the F_1 dispersion of long-range correlations to be dependent on the number of increments of the evolution time in the second frequency domain. The IMPEACH-MBC[18] and CIGAR-HMBC[19] experiments were subsequently developed to circumvent the digitization dependent short-comings of the ACCORD-HMBC experiment.

The various long-range heteronuclear shift correlation experiments and considerations of their optimization have been reviewed by Martin.[20] The limitation of the experiments designed to differentiate $^2J_{CH}$ from long-range range correlations to only protonated carbon resonances highlights the need for investigators to have available alternative methods that allow the unequivocal establishment of ^2J correlations.

3. 1,1-ADEQUATE

The heteronucleus-detected INADEQUATE experiment, first reported in 1981 by Freeman and co-workers, is elegantly capable of establishing the identity of adjacent neighbour carbons via $^1J_{CC}$ couplings.[21–24] Major drawbacks of the INADEQUATE experiment are extreme insensitivity and prodigious sample requirements. To an extent, the sensitivity and

sample limitations of the experiment have been overcome by the development of small volume high sensitivity and cryogenic NMR probes.[25–27] A version of the INADEQUATE experiment using proton detection[28] has been reported. Proton-excitation variants of the INADEQUATE experiment have included INEPT-INADEQUATE,[29] DEPT-INADEQUATE,[30] C-relayed H,C-COSY,[31,32] and INEPT-INADEQUATE.[33–36] The proton-detected ADEQUATE experiment provides investigators with a higher sensitivity alternative to the INADEQUATE experiment that allows carbon–carbon connectivity information to be derived for all but contiguous non-protonated carbons.[37,38] To circumvent the problem of optimizing the $^{1}J_{CC}$ coupling-based delays, an ACCORD-ADEQUATE experiment was reported by Williamson and co-workers.[39] The broadband version of the 1,1- and 1,*n*-ADEQUATE experiment used to generate the example data contained in this chapter employed the pulse sequence using CHIRP pulses described by Köck, Kerssebaum, and Bermel.[40] A *J*-modulated version of the experiment, JM-ADEQUATE has been described by Kövér and Forgó[41] and further investigated using various refocusing pulses by Thiele and Bermel.[42] A multiplicity-edited variant of the 1,1-ADEQUATE experiment has also been described by Parella and Sánchez-Ferrando.[43]

Several variations of the ADEQUATE experiment are possible. We will begin with the 1,1-ADEQUATE experiment, which exploits $^{1}J_{CH}$ and $^{1}J_{CC}$ couplings to allow for the identification of adjacent neighbour carbons. Other variants of the experiment are 1,*n*-, *n*,1-, and *m*,*n*-ADEQUATE.[40] The schematic representation of the magnetization transfer in the various types of ADEQUATE experiments is shown in Figure 1.

The ADEQUATE pulse sequences are shown in Figure 2. 1,1-ADEQUATE begins with an HSQC-type coherence transfer from a proton to its directly attached carbon via $^{1}J_{CH}$. Magnetization is dephased during the ensuing delay due to $^{1}J_{CC}$ and ^{13}C–^{13}C double quantum (DQ) coherence is excited at the beginning of the evolution period, t_1. Following the evolution period, magnetization is transferred back to the starting proton and detected. Hence, although the experiment is still dependent on two adjacent ^{13}C nuclides, the sensitivity of the experiment is significantly increased over that of the INADEQUATE experiment since the experiment is based on proton excitation/detection.

Correlation responses are observed in a 1,1-ADEQUATE spectrum for protonated adjacent neighbour carbon resonances at the F_1 ^{13}C shift of the carbon being interrogated and at the F_2 frequencies of the protons attached to the adjacent neighbour carbons to which magnetization was transferred during the ^{13}C–^{13}C DQ out-and-back step of the experiment. Figure 3A shows the multiplicity-edited GHSQC spectrum of strychnine (**1**); Figure 3B shows the 60 Hz optimized 1,1-ADEQUATE spectrum of **1**. Hence, at the ^{13}C shift of C15 as an example, correlation responses are

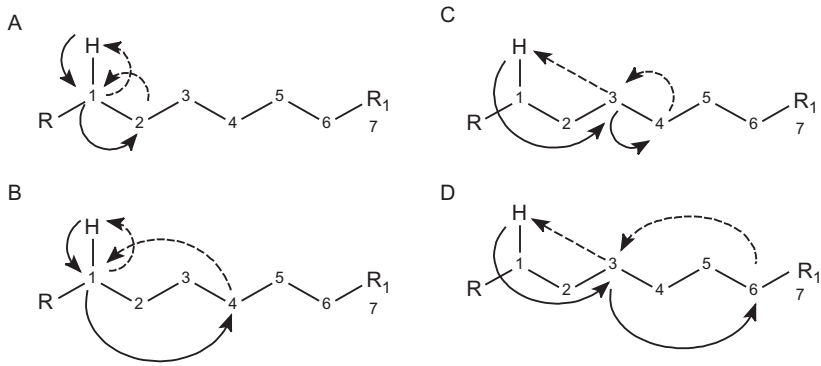

Figure 1 Schematic representations of the various forms of the ADEQUATE experiment. (A) The simplest, and perhaps most useful form of the experiment is the 1,1-ADEQUATE experiment whose prefix derives from the fact that it relies on $^{1}J_{CH}$ and $^{1}J_{CC}$ couplings. Solid arrows designate the magnetization transfers "out"; dashed arrows designate the magnetization transfers "back" in this "out-and-back" experiment. (B) The 1,*n*-ADEQUATE experiment also begins with $^{1}J_{CH}$ transfer followed by a long-range $^{13}C–^{13}C$ transfer via $^{n}J_{CC}$ coupling. (C) The *n*,1-ADEQUATE experiment, rather than beginning with a $^{1}J_{CH}$ transfer begins, instead, with a $^{n}J_{CH}$ transfer followed by a $^{1}J_{CC}$ transfer to the adjacent neighbour carbon of the carbon to which magnetization was initially long-range transferred. (D) Finally, the *m*,*n*-ADEQUATE sequence utilizes long-range couplings for both magnetization transfers, giving it the capability of spanning the largest potential number of atoms.

detected at the F_2 frequencies of the H14 and H16 proton resonances (Figure 3B). Alternatively, correlation responses are observed at the ^{13}C shifts of C14 and C16 at the F_2 shifts of the anisochronous H15 methylene protons (see Section 3.3).

3.1. Sample requirements

1,1-ADEQUATE is considerably more sensitive than the INADEQUATE experiment but it is still not nearly as sensitive as, for example, multiplicity-edited HSQC. Early reports that appeared during the development of the ADEQUATE experiments were generally studies that were performed employing instruments that were not equipped with cryogenic NMR probes. During a 2008 study of tetracyclic pyrrole-imidazole alkaloids, Myer and Köck,[47] using a 600-MHz spectrometer equipped with a cryoprobe, began to explore ADEQUATE data acquisition requirements. The authors noted that although all data used for structure elucidation were acquired in ~20 h, that in the case of a 21-mg sample of one of the compounds that usable data with all of the responses observed could be recorded in 6 h and that six of nine correlations were still observed in a 3-h

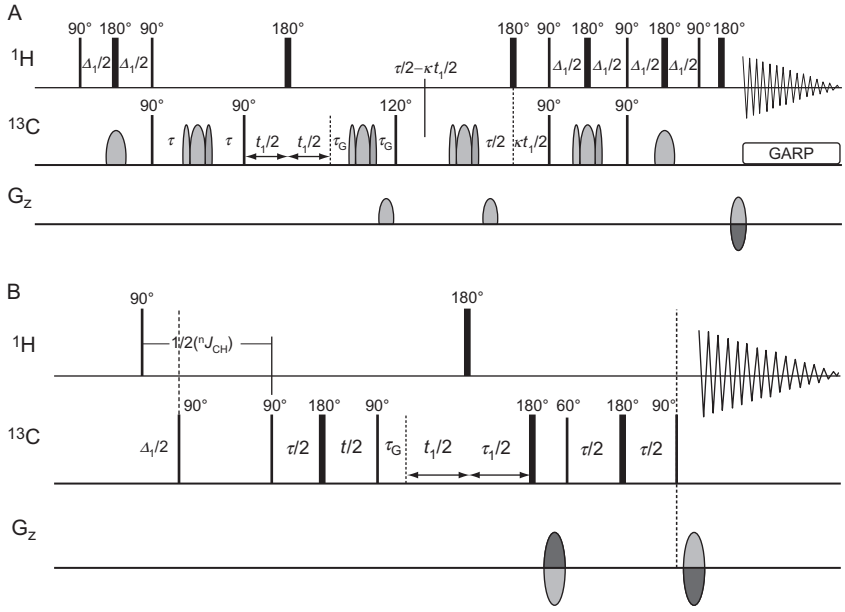

Figure 2 (A) Pulse sequence used to acquire the 1,1- and 1,*n*-ADEQUATE experiments shown in this review.[37,38,40] (B) Pulse sequence used to acquire the *n*,1- and *m*,*n*-ADEQUATE spectra shown in this review.[37,38] Typically, unless a fully aromatic compound is being investigated, a compromise $^1J_{CH}$ optimization of 140–145 Hz should be used for variants of the ADEQUATE experiment. For the 1,1-ADEQUATE experiment, $^1J_{CC}$ couplings will generally be in the range of 30–60 Hz but may range to as large as 80 Hz.[44,45] Work by Cheatham and co-workers[46] suggested that optimization of the $^1J_{CC}$ delay for 60 Hz was most useful in that correlations between adjacent sp^2 carbons are observed with good sensitivity while correlations between adjacent sp^3 and sp^2 carbon pairs are still observed with sufficient sensitivity to provide useful correlations.

experiment. For another of the alkaloids, a 5.5-mg sample gave seven of nine possible 1,1-ADEQUATE correlations in a 38-h acquisition. Finally, using a 2.5-mg sample of the same alkaloid, the authors noted that only three correlations were observed in a 77-h experiment prompting the suggestion that this represented the bottom limit for minimum sample size. More recently, Cheatham and co-workers[46] further confirmed that high-quality ADEQUATE data could be acquired overnight with samples of ~5 mg using a spectrometer equipped with a 5-mm cryogenic NMR probe. Most recently, Martin and Hilton[48] have shown that it is possible acquire high-quality 1,1-ADEQUATE data using a sub-milligram sample of strychnine (**1**) overnight in a 1.7-mm Micro CryoProbe.™ When Micro CryoProbe technology is combined with covariance data processing methods (see Section 8), data acquisition times can be significantly reduced and/or sample requirements can be pushed still lower.[49,50]

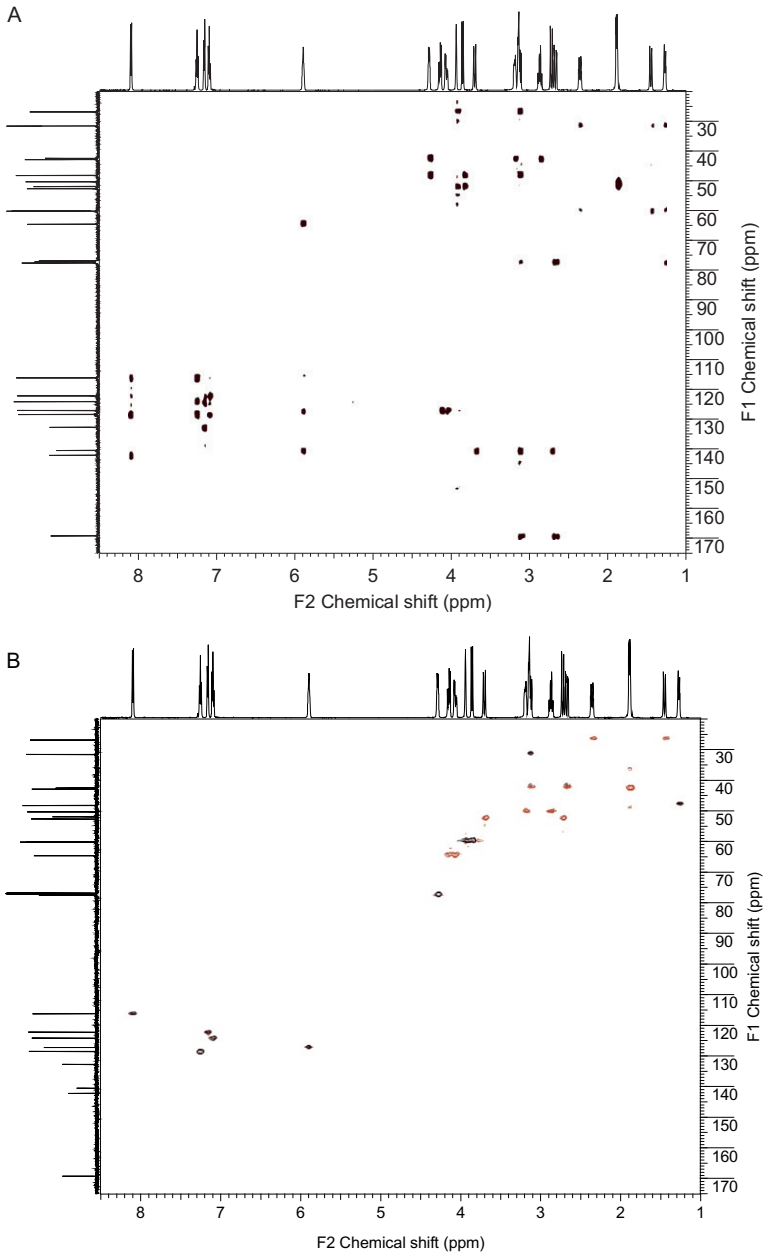

Figure 3 (A) Plot of the 60 Hz optimized 1,1-ADEQUATE spectrum of a sample of strychnine (**1**). The spectrum is flanked by high resolution ^{1}H and ^{13}C reference spectra. (B) Plot of the multiplicity-edited GHSQC spectrum of **1**. Methylene resonances are inverted and plotted in grey; methine resonances have positive intensity and are plotted in black. There are no methyl resonances in the spectrum of strychnine but would have positive intensity if any were present.

3.2. ADEQUATE data acquisition and processing

The full ADEQUATE phase cycle is 16 transients. Practically, the length of the phase cycle will not be a limitation in most instances and most samples will necessitate several complete passes through the phase cycle, constituting an overnight acquisition.

Relaxation requirements, since the ADEQUATE experiment is a proton-detected experiment, are not as stringent as for an INADEQUATE experiment, and there is generally no advantage to doping the sample with $Cr(OAc)_3$ or other relaxation promoting agents. Typically, a 3-s interpulse delay is sufficient. When ADEQUATE data are to be acquired using a 5-mm gradient inverse-detection cryogenic NMR probe, investigators should recall that it is advantageous to prepare the sample in a 3-mm tube rather than a 5-mm tube. First, sample requirements for an equivalent concentration are reduced. Second, the reduction in thermal noise from the sample itself is greater than losses of signal intensity due to filling factors providing an increase in signal-to-noise (s/n) ratios.[27]

Data shown as examples in this review were typically acquired as 2K $\times$ 128 or 2K $\times$ 160 point files. Data were processed with linear prediction or zero-filling prior to the first Fourier transform. Data were uniformly linear predicted to 512 points in the second dimension followed by zero-filling to afford final data matrices that were 2K $\times$ 1K points.

Delay optimization is another point that warrants discussion. Optimization of the delay for one-bond heteronuclear couplings, as with HSQC experiments, can be set to a compromise value of $\sim$140–145 Hz. For most types of molecules, that value will work well. Some classes of heterocycles have resonances with one-bond heteronuclear couplings of 200 Hz or larger and these resonances will not respond as well as resonances whose one-bond couplings are closer to the optimization value. Protonated acetylenic carbons, which have one-bond heteronuclear couplings in the vicinity of 250 Hz, will not afford a response with the compromise setting for the one-bond heteronuclear coupling suggested above.

In contrast, the optimization of the delay for the $^1J_{CC}$ homonuclear coupling is more of a challenge. One-bond carbon–carbon couplings range from approximately 30 to 80 Hz.[44,45] The recent report by Cheatham and co-workers[46] recommended optimization of the $^1J_{CC}$ delay for 60 Hz, asserting that correlations to aliphatic carbons are still observed with reasonable intensity and that correlations between sp^2 carbons are observed, whereas the latter might be missed if the experiment is optimized for a smaller $^1J_{CC}$ coupling. This problem has been addressed by the development of the ACCORD-ADEQUATE pulse sequence reported by Williamson and co-workers.[39] The issue of response modulation is considered further below (see Section 3.4).

3.3. Extracting correlation information from 1,1-ADEQUATE spectra

Once acquired, processed, and plotted, carbon–carbon connectivity information can be extracted from a 1,1-ADEQUATE spectrum. There are multiple ways of going about this task and whichever method is used is probably best determined by the preferences of the individual investigator.

Parella and Sánchez-Ferrando[43] have discussed the extraction of connectivity information from 1,1-ADEQUATE spectra in a fashion analogous to what follows. Referring to the GHSQC spectrum shown in Figure 3A, the ^{1}H chemical shift of any proton resonance in the spectrum defines a F_2 correlation axis (column). Responses will be observed along that axis at the F_1 ^{13}C shift of carbons that are adjacent (i.e. correlated via $^{1}J_{CC}$) to the carbon that is directly bound to the proton in question. Responses are observed to both protonated and quaternary carbons along the vertical, F_2 axis. Using this approach to the interpretation of the data, there is, of course, no direct response in the 1,1-ADEQUATE spectrum for the heteronuclide pair that is being interrogated. As an alternative, if one considers the horizontal F_1 axis for a given proton–carbon pair (row), responses will be observed along that axis at the proton (F_2) shift (s) of protons that are directly bound to carbons that are coupled via $^{1}J_{CC}$ to the carbon of the heteronuclide pair being considered. There are no correlations along the horizontal F_1 axis to adjacent quaternary carbons since they have no directly attached proton that would allow a response.

As noted in the analysis of Parella and Sánchez-Ferrando,[43] by considering the number of carbons to which $^{1}J_{CC}$ correlations are observed, the presence of heteroatoms such as oxygen and nitrogen can be inferred, supplementing ^{13}C chemical shift considerations. An aliphatic methine carbon as an example would be expected to exhibit $^{1}J_{CC}$ correlations to three other carbons. Assuming that all available carbon–carbon correlations are observed, the absence of one of the correlations, in conjunction with the ^{13}C shift of the methine in question, can be used to infer the presence of a heteroatom attached to the methine carbon. Chemical shift considerations in this analysis are applicable to nitrogen or oxygen, which produce significant downfield shifts, but not necessarily to sulphur, which has an electronegativity identical to carbon.

Another alternative for the interpretation of 1,1-ADEQUATE data is available by overlaying HSQC and 1,1-ADEQUATE spectra. By plotting the two spectra in different colours, as was done in Figure 4, the direct ^{1}H/^{13}C heteronuclear correlation response is visible and provides a guide for interpretation that is sometimes convenient. A further alternative would be to overlay 1,1-ADEQUATE and GHMBC spectra; responses appearing in both are identified as $^{2}J_{CH}$ correlations and all remaining

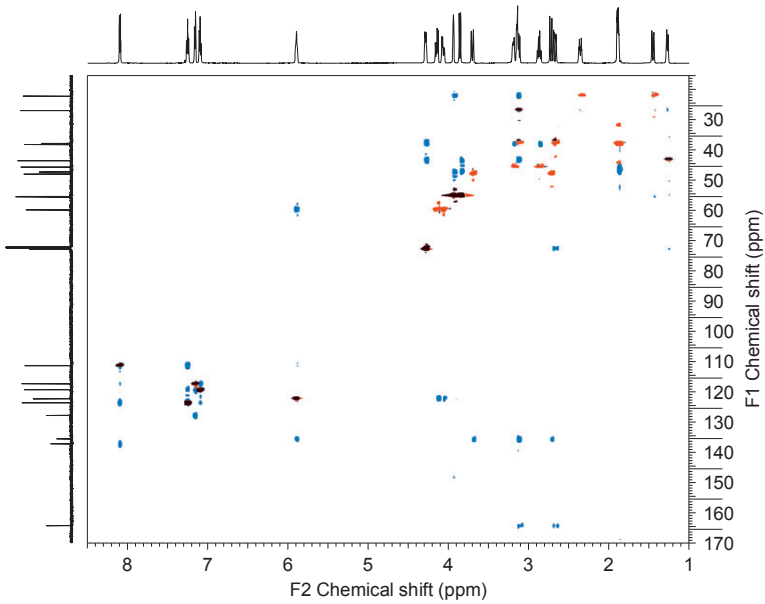

Figure 4 Overlaid multiplicity-edited GHSQC (CH_2 responses are shown in light grey; CH/CH_3 responses are shown in dark grey) and 60 Hz 1,1-ADEQUATE (black correlations) spectra of strychnine (**1**).

correlations must arise from ${}^{n}J_{CH}$ coupling pathways, where $n \geq 3$.[37] A further alternative for the extraction of adjacent ${}^{13}C$–${}^{13}C$ connectivity is available in the form of unsymmetrical indirect covariance (UIC) or generalized indirect covariance (GIC) processing of HSQC and 1,1-ADEQUATE spectra to afford HSQC-1,1-ADEQUATE spectra (see Sections 8.2 and 8.4).

Figure 5 shows the aliphatic region of the overlaid multiplicity-edited GHSQC and 60 Hz optimized 1,1-ADEQUATE spectra of strychnine (**1**), the two alternative methods for identifying neighbouring carbons are illustrated. Beginning from the anisochronous 15-methylene protons enclosed in the elongated black box, solid horizontal arrows designate correlations from the adjacent C14 and C16 carbons that are observed at the F_2 shifts of their directly attached protons and the F_1 shift of C15. Moving to the H16/C16 direct correlation response, the dashed arrow identifies C15 as a carbon adjacent to C16 in the structure. In similar fashion, the H14/C14 direct response likewise identifies C15 as an adjacent carbon.

Using either of the methods just described in successive steps allows the identification of progressively larger fragments of the chemical structure of the molecule being studied or elucidated. In the case of strychnine, **1**, shown

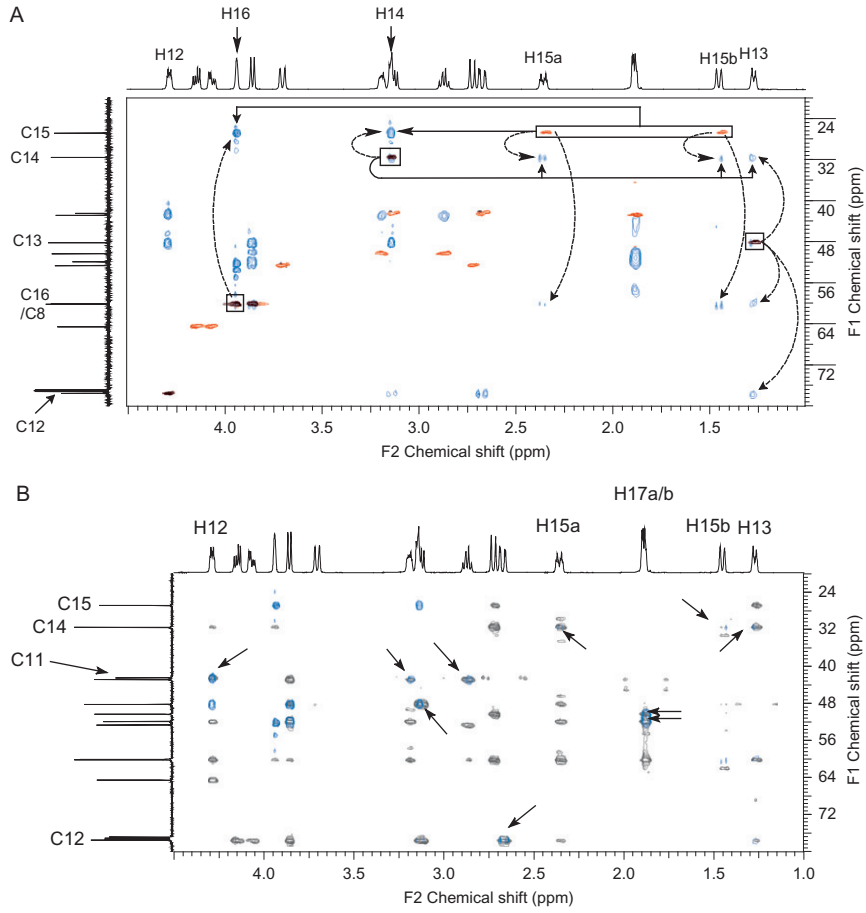

Figure 5 (A) Segment of the overlaid multiplicity-edited GHSQC and 60 Hz 1,1-ADEQUATE spectra of **1** showing the partial interpretation of the 1,1-ADEQUATE data. The H13/C13 through H16/C16 direct responses in the GHSQC spectra are enclosed in black boxes; the spectra are annotated with pertinent ^{1}H and ^{13}C resonance assignments. Beginning from the anisochronous H15a/b methylene resonances (light grey correlations), solid horizontal arrows denote the 1,1-ADEQUATE responses (black correlations) that correlate C15 with C14 and C16 observed at the F_2 ^{1}H chemical shifts of H14 and H16, respectively. Dashed vertical arrows from boxed direct responses designate the 1,1-ADEQUATE correlation responses at the F_1 frequencies of the adjacent neighbour carbons. (B) Segment of the overlaid 8 Hz GHMBC and 60 Hz 1,1-ADEQUATE spectra of **1.** The GHMBC correlations are plotted in grey and the 1,1-ADEQUATE correlations are plotted in black. Overlapped resonances in the two spectra are $^{2}J_{CH}$ correlations of adjacent carbons designated by arrows. Other non-overlapped correlations are $^{n}J_{CH}$ correlations where $n \geq 3$.

below, the segments of the structure were assembled as contiguous pieces. Solid dark or light grey carbon–carbon bonds denote 1,1-ADEQUATE correlations observed between adjacent protonated carbons; dashed dark or light grey carbon–carbon bonds denote correlations observed in the 1,1-ADEQUATE spectrum between adjacent protonated and non-protonated carbons. Bonds between pairs of non-protonated carbons or carbon-heteroatom bonds shown in black cannot be determined from the 1,1-ADEQUATE spectrum.

Segments of the aliphatic region of the 8 Hz GHMBC and 60 Hz 1,1-ADEQUATE spectra are shown in Figure 5B. Correlations designated by arrows in the spectrum that appear in both spectra correspond to $^{2}J_{CH}$ correlations in the GHMBC data. Other responses in the GHMBC spectrum that do not coincide with responses in the 1,1-ADEQUATE spectrum must therefore arise from $^{n}J_{CH}$ correlations where $n \geq 3$.

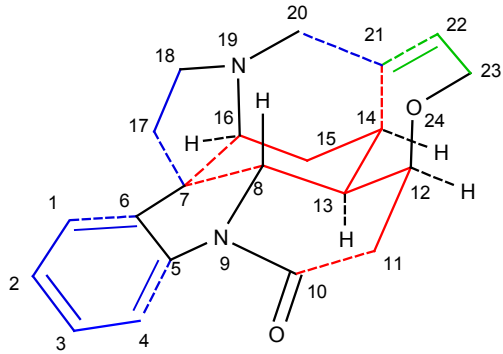

[1]

3.4. Modulation of 1,1-ADEQUATE responses

The ACCORD-ADEQUATE experiment reported by Williamson and co-workers[39] incorporated accordion-optimization of the $^{1}J_{CC}$ delay to circumvent problems associated with missing responses in the investigation of the structure of a marine natural product (see Section 4.4). Cheatham and co-workers[46] have recommended optimizing the $^{1}J_{cc}$ delay for 60 Hz, suggesting that this optimization provides a greater likelihood of observing correlations between sp^2 carbons in addition to aliphatic correlations whereas correlations involving sp^2 carbons may be missed when $^{1}J_{CC}$ delays are optimized for smaller potential couplings (see Section 4.14).

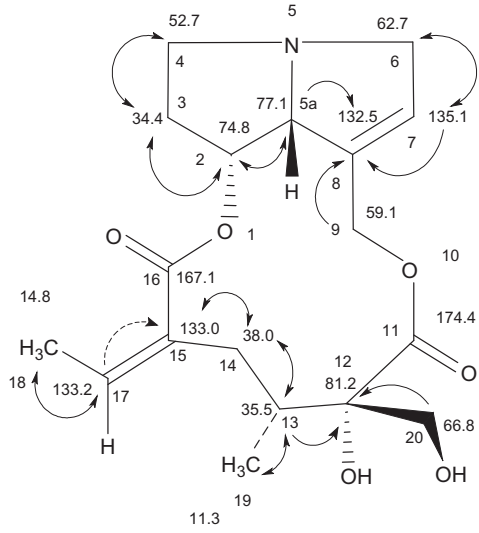

[2]

Using retrorsine (**2**) as a model compound, it was interesting to note that the correlation between the C17 and C15 sp^2 carbons (dashed arrow) was not observed (Figure 6) when a 60-Hz optimized 1,1-ADEQUATE spectrum was acquired.[51] Cheatham and co-workers,[46] however, reported observing this correlation although the $^1J_{CC}$ optimization used when the correlation was observed was not specifically noted (see **22**). In an effort to observe the C15–C17 correlation, a 40-Hz 1,1-ADEQUATE spectrum was acquired in which the correlation was observed. A series of spectra optimized in 5 Hz steps over the range from 30 to 65 Hz was acquired to probe the modulation of this correlation. Segments of four of the spectra of this series are shown in Figure 7; the slices through the F_1 frequency domain at the F_2 shift of the H17 vinyl proton are shown as a horizontal "stack" plot in Figure 8 over the range from 30 to 55 Hz. The individual spectral segments show the C17 resonance intensity as a function of the experiment optimization. The 30 and 35 Hz optimized spectra both have good C17 response intensity that has fallen to about 50% in the 40 Hz spectra and has gone to almost zero in the 55 Hz spectrum.

The data shown in Figures 7 and 8 clearly underscore the need to exercise caution before assigning an unknown structure if a critical 1,1-ADEQUATE correlation is not observed with a given optimization for $^1J_{CC}$. The acquisition of a spectrum with an additional $^1J_{CC}$ optimization or the acquisition of an ACCORD-ADEQUATE[39] spectrum should be considered. The 1,*n*-ADEQUATE correlations for retrorsine (**2**) are discussed below in Section 5.5.

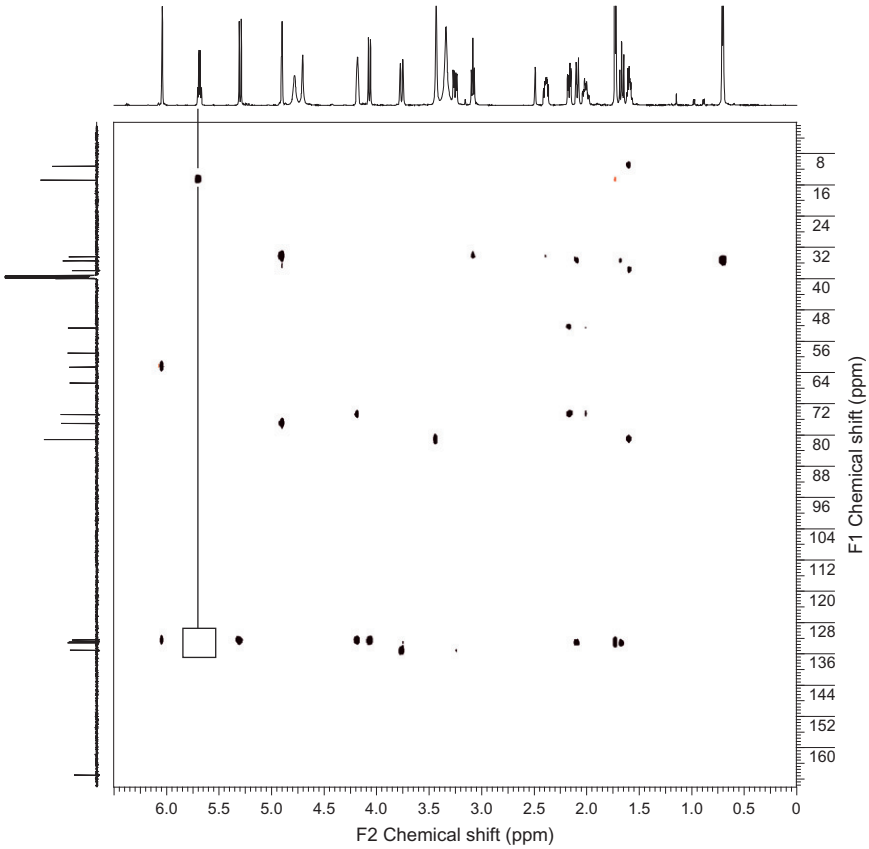

Figure 6 60 Hz Optimized 1,1-ADEQUATE spectrum of retrorsine (**2**). The correlation between the C15 and C17 sp^2 carbons was not observed (open boxed region). This correlation was, however, reported by Cheatham and co-workers[46] although the optimization used when the correlation was observed was not specifically noted. In contrast, the correlation was observed when the $^1J_{CC}$ delay was optimized for smaller values of the coupling constant from 30 to 45 Hz (see Figures 7 and 8).

4. APPLICATIONS OF 1,1-ADEQUATE AND ACCORD-ADEQUATE EXPERIMENTS

Unlike HMBC/GHMBC and related long-range heteronuclear chemical shift correlation experiments, which have hundreds of reported applications in the published literature, there are considerably fewer reported applications of 1,1-ADEQUATE and related long-range variants in the literature. In part, the dearth of reported applications can be attributed to the considerably lower sensitivity of these experiments relative to, for example HMBC/GHMBC. Sensitivity concerns are largely ameliorated,

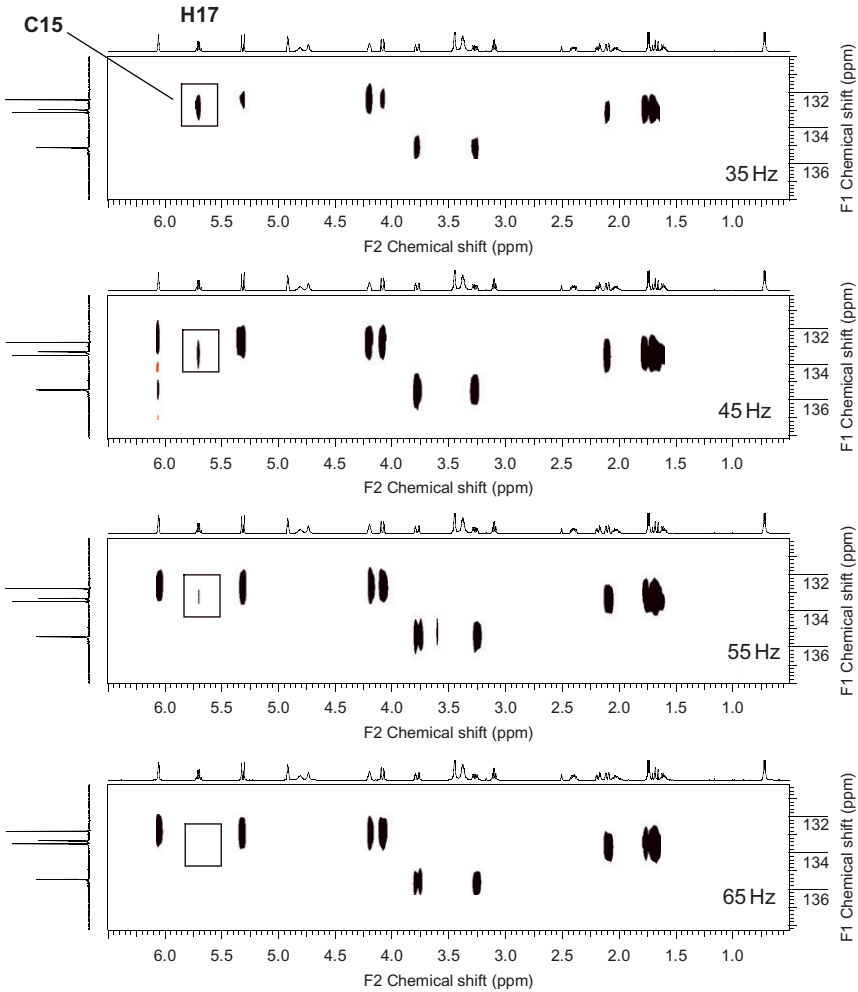

Figure 7 Segments of the sp^2 carbon region of a series of 1,1-ADEQUATE spectra of retrorsine (**2**) in which the $^1J_{CC}$ coupling was optimized over the range from 35 to 65 Hz.[51] In the 35 and 45 Hz spectra, the C17–C15 correlation (boxed regions) is observed with good intensity. In the 55 Hz spectrum, the intensity of this correlation has decreased significantly and in the 65 Hz spectrum, the response is completely absent (see also Figure 8).

however, by high-field instruments equipped with high-sensitivity small volume probes or cryogenic probes.[25,26] As the use of UIC and GIC processing becomes more widespread, it is likely that the utilization of 1,1-ADEQUATE and related experiments will be further spurred.[49,50,52] A further stimulus may also be found in the benefits that derive from the unequivocal identification of adjacent carbon neighbours that can be

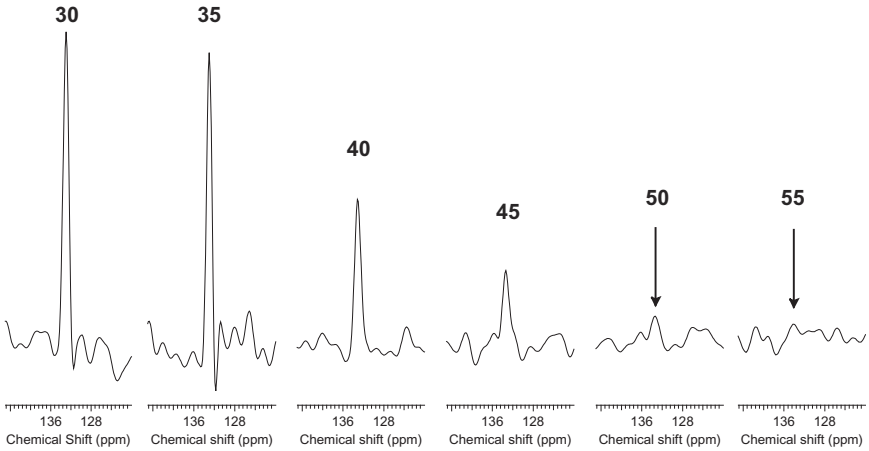

Figure 8 F_2 Slices through a series of 1,1-ADEQUATE spectra of retrorsine (**2**) at the F_2 shift of the H17 resonance.[51] The optimization is shown above the individual spectral segments. The correlation shown in the individual traces is that from the C17 sp^2 resonance to the C15 sp^2 resonance. The absence of this response in the 60 Hz optimized spectrum (see Figure 7) prompted the acquisition of the series of spectra shown.

accomplished using 1,1-ADEQUATE. While HMBC/GHMBC correlations cannot differentiate $^2J_{CH}$ from $^3J_{CH}$ correlations, adjacent neighbour carbons are unequivocally identified via $^1J_{CC}$ couplings in 1,1-ADEQUATE data. There are already several reports in the literature that have noted the synergy of using ADEQUATE data in conjunction with CASE (computer-assisted structure elucidation) programs.[46,47,53]

4.1. 5,6-Dihydrolamellarin

One of the initial reports of the family of ADEQUATE experiments combined correlation data from a number of the experimental variants in the elucidation of the structure of the complex marine natural product 5,6-dihydrolamellarin (**3**).[37,38] Data were acquired using a 14-mg sample of **3** dissolved in 80 μL in a 2.5-mm tube on a 500-MHz spectrometer. Acquisition times were identically 65 h for both the *n*,1- and *m*,*n*-ADEQUATE (also referred to as *n*,*n*-ADEQUATE—the *m*,*n*- notation used here is intended to differentiate the two couplings) spectra. The authors made the important point that proton-deficient molecules may require $^nJ_{CH}$ long-range heteronuclear correlations where $n \geq 4$ to complete the elucidation of the structure. Portions of the molecular structure were assembled using correlations from a conventional ^1H–^{13}C GHMBC spectrum. Structural fragments that could not be linked together from the correlations in the GHMBC spectrum were subsequently linked together to complete the elucidation of the structure through the extensive use of 1,

n-, *n*,1-, and *m*,*n*-ADEQUATE correlation pathways as shown by **3**. As shown schematically in Figure 1, the 1,1-ADEQUATE experiment establishes the identity of adjacent carbons (i.e. carbons corresponding exclusively to $^{2}J_{CH}$ correlations in a GHMBC experiment) via the $^{1}J_{CH}$ and $^{1}J_{CC}$ coupling pathways. To reach somewhat further out from the starting point, the 1,*n*- and *n*,1-ADEQUATE experiments can next be employed. The former again begins with $^{1}J_{CH}$ and then transfers magnetization from the directly bound carbon to a remote carbon, typically three bonds removed, by $^{n}J_{CC}$ where $n = 3$ (see Section 5). These correlations are the equivalent of $^{4}J_{CH}$ correlations in a GHMBC experiment. In comparison, the *n*,1-ADEQUATE experiment begins with a long-range heteronuclear transfer via $^{n}J_{CH}$, typically three-bonds as in a GHMBC experiment, although $^{2}J_{CH}$ and $^{4}J_{CH}$ transfers cannot be excluded, followed by a $^{1}J_{CC}$ transfer to the adjacent carbon. Hence, from a sensitivity standpoint, the *n*,1-ADEQUATE experiment would be correspondingly less sensitive than a 1,*n*-ADEQUATE experiment in the same sense that a GHMBC experiment is less sensitivity than a GHSQC experiment. Assuming that a three-bond heteronuclear correlation is the starting point, the *n*,1-ADEQUATE experiment also provides the means of identifying carbons via what would be the equivalent of $^{4}J_{CH}$ correlations. Finally, the *m*,*n*-ADEQUATE spectrum is the most far-reaching and is capable of spanning as many as six bonds or even seven bonds. The first step of the *m*,*n*-ADEQUATE experiment employs a long-range $^{n}J_{CH}$ coupling followed nominally by a $^{3}J_{CC}$ magnetization transfer. In the case where the initial $^{m}J_{CH}$ magnetization transfer is via four bonds, the *m*,*n*-ADEQUATE experiment can possibly span seven bonds. Examples of correlations via 1,*n*-, *n*,1-, and *m*,*n*-ADEQUATE used in the elucidation of the structure of 5,6-dihydrolamellarin (**3**) are shown schematically on the structure (see also structures **28**, **42**, and **45**). The individual steps of the *n*,1- and *m*,*n*-ADEQUATE correlation pathways are delineated by compound long-range correlation arrows on structures **42** and **45**.

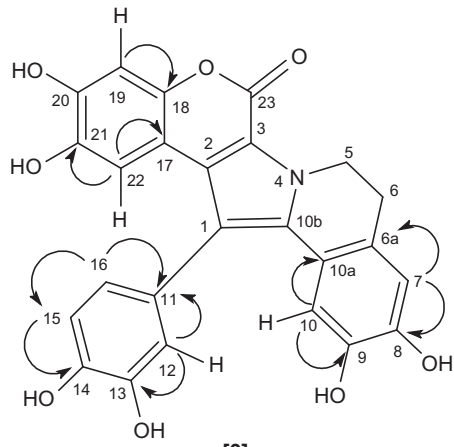

[3]

In addition to the papers describing the elucidation of the structure of 5,6-dihydrolamellarin (**3**), the molecule was also used as a model compound in the modification of the 1,1- and 1,*n*-ADEQUATE pulse sequences to allow the determination of the $^{1}J_{CC}$, $^{2}J_{CC}$, and $^{3}J_{CC}$ carbon–carbon coupling constants at natural abundance.[54] The modified version of the 1,1-ADEQUATE spectrum afforded $^{1}J_{CC}$ couplings directly from doublet splittings along the F_1 frequency axis. The measured $^{1}J_{CC}$ coupling constants could then be used for the calibration of cross-peak intensities in the 1,*n*-ADEQUATE spectrum to allow the measurement of the $^{2}J_{CC}$ and $^{3}J_{CC}$ coupling constants.

4.2. 4,5-Dibromopyrrol-2-carboxylic acid

Following the development of the family of ADEQUATE experiments used in the elucidation of the structure of 5,6-dihydrolamellarin (**3**) just discussed, the next application of ADEQUATE spectral data rather interestingly was reported in conjunction with an evaluation of the COCON (COnstitutions from CONnectivities) CASE program.[53] The structure of 4,5-dibromopyrrol-2-carboxylic acid (**4**) is relatively simple; 1,1-ADEQUATE correlations from the H3/C3 resonant pair identified the flanking C2 and C4 carbon resonances. The availability of the 1,1-ADEQUATE correlations reduced the number of structures generated by the program from 10 to 3, which differed only in the assignments of some of the carbon resonances. The authors also applied the COCON program to the structure of manzacidin A (**5**), but no 1,1-ADEQUATE data were recorded; the authors instead were dealing with 1,1-ADEQUATE correlations that would be theoretically available had the data been acquired. A second paper that dealt with the probable impact of the availability of 1,1-ADEQUATE data with the COCON CASE program was also reported by the same authors in 1999, but again no actual 1,1-ADEQUATE data were reported.[55] Ascomycin, aflatoxin B_1, 11-hydroxyrotenone, and haemoventosin were used as model compounds in that study.

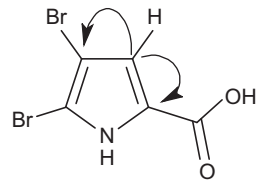

[4]

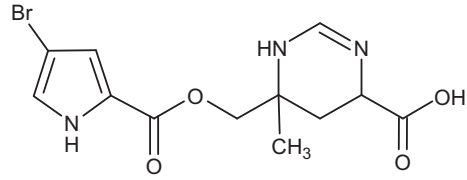

[5]

4.3. 2-[1-(4-Chlorobenzyl)-1*H*-indol-3-yl]-2-oxo-*N*-pyridin-4-yl acetamide

In 2001, Knaack and co-workers[56] reported an application of the 1,1-ADEQUATE experiment in the course of synthesizing and characterizing a biologically active 2-[1-(4-chlorobenzyl)-1*H*-indol-3-yl]-2-oxo-*N*-pyridin-4-yl acetamide (**6**). Treatment of 1-(4-chlorobenzyl)-1*H*-indole with oxalyl chloride afforded the corresponding oxoacetyl chloride that was finally subjected to aminolysis with 4-aminopyridine to afford the final product of the reaction scheme, **6**. Although the NMR data supported the *N*-benzyl structure, a 1,1-ADEQUATE spectrum was acquired to provide additional confirmation of the structure of **6**.

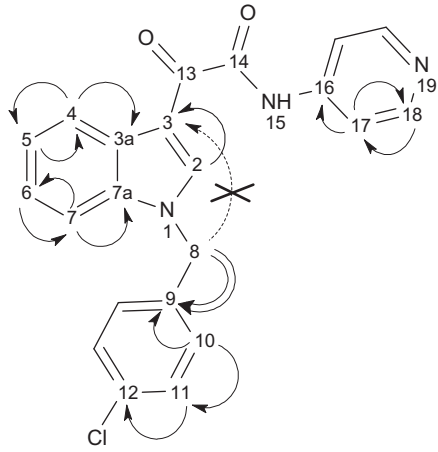

[6]

A $^{1}J_{CC}$ 55 Hz optimized 1,1-ADEQUATE spectrum was recorded over 2 days 13 h as a 2K × 256 data file with 352 transients accumulated/t_1 increment. The observed 1,1-ADEQUATE correlations are shown on the structure. The expected correlation (double-tailed arrow) was observed from the 8-benzyl to the 9-aromatic carbon resonance. The corresponding absence of a correlation from C8 to C3 (dashed arrow) confirmed that

N-benzylation had occurred as expected rather than substitution at the 2-position of the indole nucleus.

4.4. Jamaicamide

Williamson and co-workers[39] reported the development of the ACCORD-ADEQUATE experiment in 2001 in conjunction with the elucidation of the structure of the marine natural product jamaicamide (**7**). The acquisition of several statically optimized GHMBC and 1,1-ADEQUATE spectra failed to establish a key connectivity between the 18-vinyl and 19-amide carbonyl resonances. The ACCORD-ADEQUATE experiment employs the accordion-optimization of the $^{1}J_{CC}$-based delay in the pulse sequence to cover a range of potential carbon–carbon coupling constants. Using a 58-mM sample of **7**, an ACCORD-ADEQUATE spectrum optimized over the range of 40–70 Hz for the $^{1}J_{CC}$ delay was acquired and did contain the critical correlation between the 18-vinyl and 19-amide carbonyl (dashed arrow). The data were acquired as 2K × 180 points with 256 transients accumulated/t_1 increment. Data were linear predicted in the second frequency domain to 360 files and then zero-filled to afford a final data matrix 1K × 1K. Visual comparison of the conventional 1,1-ADEQUATE and ACCORD-ADEQUATE spectra reproduced in the report shows the latter to contain considerably more correlations than the former.

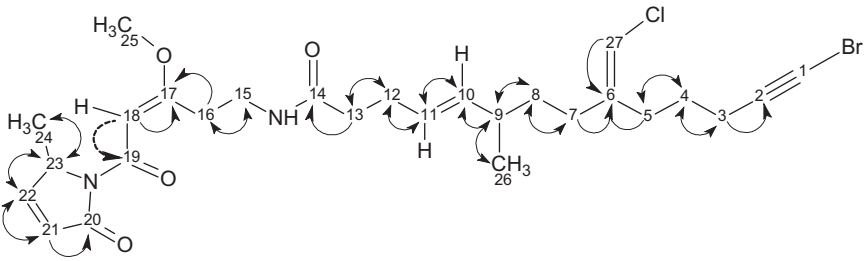

[7]

4.5. Phormidolide

Following the initial report of the development of the ACCORD-ADEQUATE experiment and the application of the technique to jamaicamide (**7**) discussed above, there were several additional applications of the technique by Williamson and co-workers. The next application to appear was the elucidation of the structure of phormidolide (**8**), a toxic metabolite of the marine cyanobacterium *Phormidium* sp.[57] Elucidating the structure of **8** was a complex undertaking that utilized a wide range of 2D NMR methods for the establishment of the overall skeletal structure, including ACCORD-ADEQUATE.[39] ^{13}C-enriched phormidolide (**8**) was prepared by feeding the cyanobacterium doubly labelled [1,2-$^{13}C_2$]acetate that afforded a sample

that was ~6% enriched. The acetate incorporation was analyzed using the INADEQUATE[21–24] experiment, which led to the deduction of a significant portion of the complex molecular structure. There were, however, gaps in the carbon skeleton that it was necessary to fill-in through the acquisition of a 30–55 Hz optimized ACCORD-ADEQUATE experiment. Correlations derived from the ADEQUATE data are denoted by arrows on the structure of **8**. The stereochemical assignment of many of the centres in the molecule was subsequently derived from *J*-based confirmation analysis experiments.

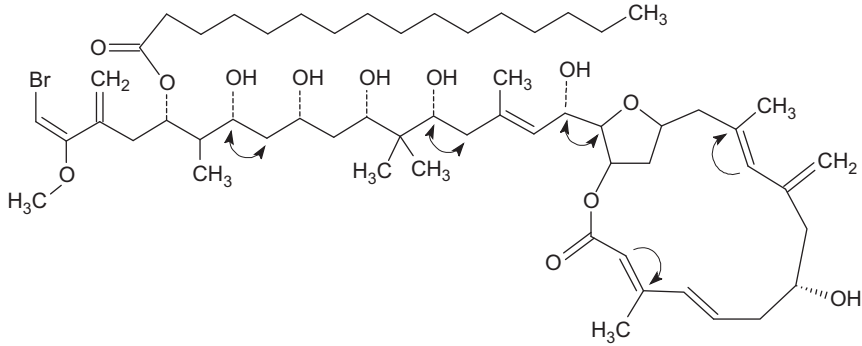

[8]

4.6. Confirmation of the medermycin/lactoquinomycin-A structure

The structure of the antibiotic, **9**, which has been variously named lactoquinomycin-A and medermycin, was first reported by Okabe and coworkers in 1985.[58] In early 2002,[59] a communication was published reporting that the original structure, **9**, was incorrect based on synthesis and that the substituted tetrahydropyran ring was attached to the 6-position to give **10**, rather than the 8-position as originally reported. The authors based their conclusion on the fact that a key intermediate was identified as 6-bromo-3-hydroxybenzaldehyde rather than the 4-bromo-3-hydroxy benzaldehyde as previously reported.[60]

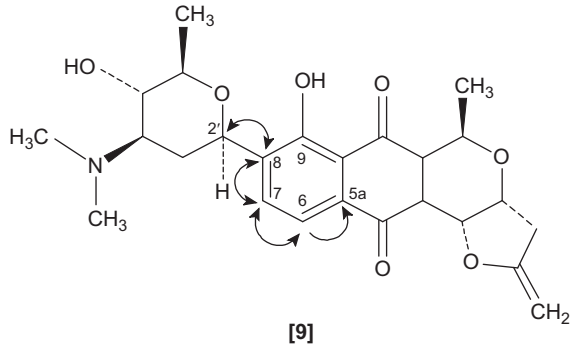

[9]

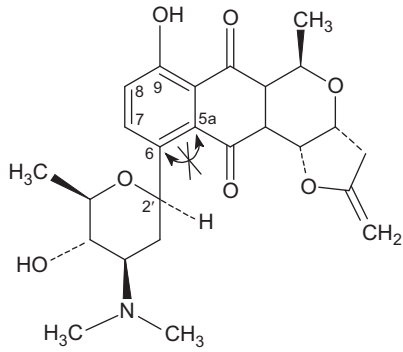

[10]

Employing an authentic sample of the antibiotic from a reference compound collection, Williamson and co-workers[61] re-investigated the structure of the molecule using a full array of 2D NMR methods that included the acquisition of an ACCORD-ADEQUATE spectrum. Correlations in the GHMBC spectrum for **9** were predominantly $^{2}J_{CH}$ or $^{3}J_{CH}$ correlations with the exception of the $^{4}J_{CH}$ correlation from H7 to the carbonyl resonance. In contrast, if the correct structure was **10**, the observed GHMBC correlations would have to include $^{4}J_{CH}$ and $^{5}J_{CH}$ correlations to account for the data. As shown by **9**, from the ACCORD-ADEQUATE spectrum, the H6 resonance was correlated to the aromatic C7 methine and C5a quaternary carbons. H7 was correlated, in turn, to C6 and C8, the latter was further correlated to the C2a' methine position in the tetrahydropyran ring. The key correlation from H6 to C5a observed in the spectrum is not possible for **10**. Hence, the correct structure was confirmed to be **9**, as originally reported.

4.7. Cytosporacin

One of the compounds found in a screening search for potential novel antibiotic and anticancer agents was a red compound isolated from the fermentation broth of *Cytospora rhizophorae* ATCC38475.[62] From a feeding experiment that utilized [1,2-$^{13}C_2$]sodium acetate, a considerable portion of the skeleton of cytosporacin, **11**, was established using a ^{13}C–^{13}C INADEQUATE experiment.[21–24] Several key features of the structure, however, could not be resolved solely from the other 2D NMR experiments and the INADEQUATE data, prompting the acquisition of an

ACCORD-ADEQUATE spectrum using a 500-MHz spectrometer equipped with a 5-mm cryoprobe. The data were acquired as 180 hypercomplex points in the second frequency domain using 256 transients/t_1 increment. The broad 14-vinyl methylene resonance was located in the structure based on correlations in the ACCORD-ADEQUATE spectrum from H14 to C13 and from H12 to both C11 and C13. The C18 aromatic methine resonance afforded ADEQUATE correlations to the flanking C17 and C19 non-protonated carbons and, finally, the C23 methine provided a correlation to the C22 non-protonated carbon.

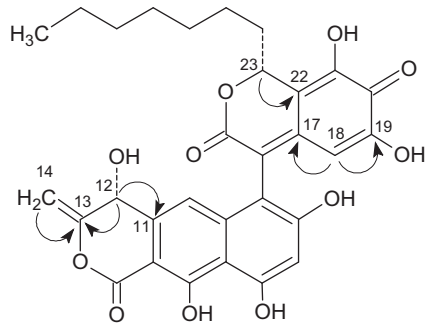

[11]

4.8. Piperidylrifamycins

Following the reports of Knaack[56] and those of Williamson and co-workers,[39,57,61,62] there was a gap of several years before the next reported application of 1,1-ADEQUATE data appeared in the literature. Rubio and co-workers,[63] in a study of several spiro-piperidylrifamycins reported the use of 1,1-ADEQUATE data to confirm the assignments of the C2 and C4 quaternary carbon resonances flanking the H3 methine proton of the rifamycin analogue whose structure is shown by **12**. While there were undoubtedly numerous other 1,1-ADEQUATE correlations observed in the 50 Hz optimized spectrum, they were not reported by the authors. The data were acquired by taking 128 transients/t_1 increment with 256 points used to digitize F_1. Sample sizes were noted as ranging from 30 to 50 mg but the specific sample size used to acquire the 1,1-ADEQUATE data was not specified.

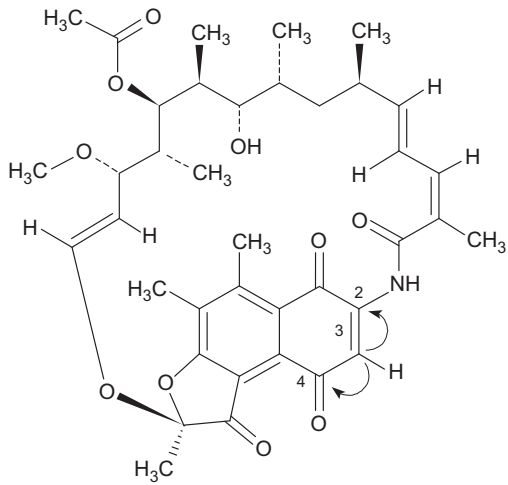

[12]

4.9. Leucanthoside-A

In 2006, Milosavljević and co-workers[64] reported a study of the complete ^{1}H and ^{13}C NMR assignment of a new triterpenoid saponin, leucanthoside-A (**13**), from *Cephalaria leucantha* L. In the course of determining the structure and assigning the spectra, the authors made extensive use of the normal ensemble of 2D NMR experiments in use for the characterization of natural product structures: HSQC, HMBC, DQF-COSY, TOCSY, and NOESY. The authors supplemented the aforementioned list of experiments with 2D *J*-resolved, DINE-(Double INEPT-Edited)-HSQC, and 1,1-ADEQUATE spectra. The authors made no mention of the use of the connectivity information derived from the 1,1-ADEQUATE spectrum in the assembly of the triterpene nucleus of the molecule but reported extensive tabulations of the 1,1-ADEQUATE correlations that were used to sequence and assign the saccharide resonances of the tri- and di-saccharide sub-units, **14** and **15**, respectively, linked to the triterpene nucleus.

The identities of the individual sugars were established by acid hydrolysis of a portion of the sample followed by paper chromatography and comparison with authentic samples. It was interesting to note that one of the sugars was the rarely encountered β-D-allose that has only been found in a few saponins. Regrettably, only scant details were reported on the acquisition conditions used for the 1,1-ADEQUATE spectrum.

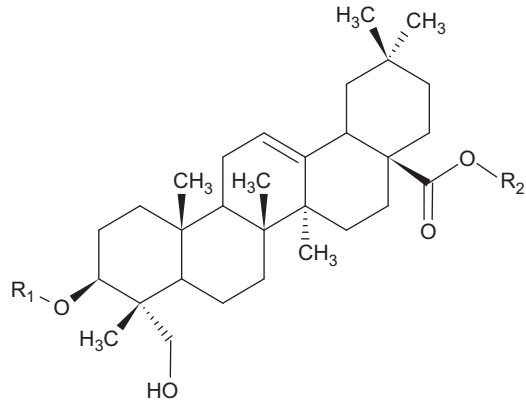
H3C
CH3
CH3
H3C
CH3
O
R2
O
R1
O
H3C
HO

[13]

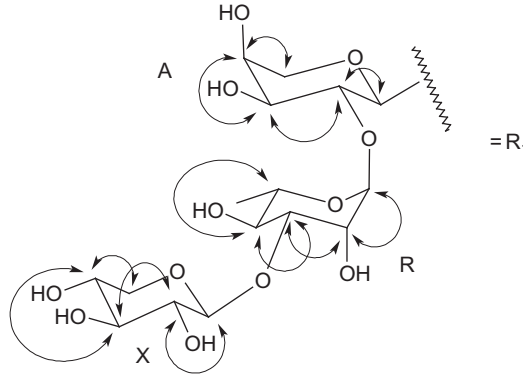
HO
A
HO
O
O
= R1
HO
O
OH
R
O
O
HO
HO
X
OH

[14]

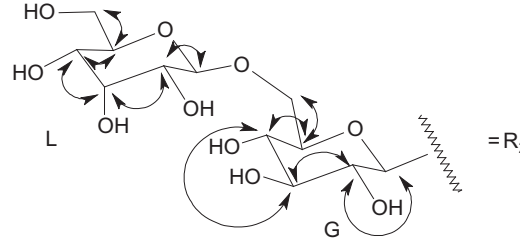
HO
O
HO
O
OH
OH
L
O
HO
HO
OH
= R2
G

[15]

4.10. Withanolides

In 2007, Christen and co-workers[65] reported the elucidation of the structures of a series of withanolides from the leaves of *Withania adpressa*, a plant endemic to the Sahara of Morocco and Algeria. The observed 1,1-ADEQUATE correlations for one of the molecules characterized are shown on **16**. The data were recorded at 600 MHz but unfortunately no further experimental details were reported. It is also interesting to note that there were no correlations reported involving the 11- and 12-positions in the C-ring of the steroid nucleus.

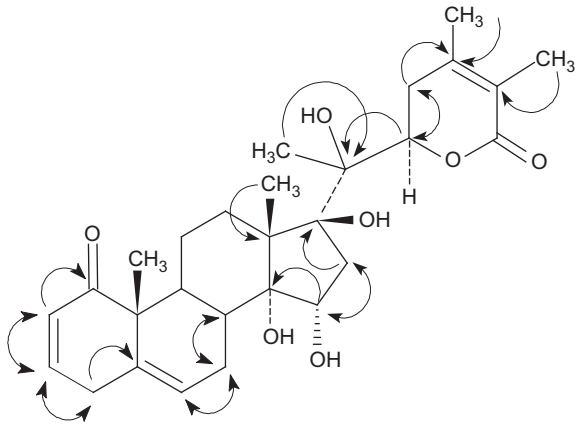

[16]

4.11. 3,4-Dihydroxy-2-quinolin-2-ylpyrido[3,2,1-*jk*]carbazol-6-ones

In 2007, Stadlbauer and co-workers[66] reported the use of 1,1-ADEQUATE data to identify quaternary carbons located two-bonds from various protons in the structure of a quinolinylpyrido[3,2,1-*jk*]carbazolone (**17**). For the acquisition of the 1,1-ADEQUATE data, the authors used a very large 200 mg sample of **17** but did not give details of the optimization, digitization, or acquisition time for the experiment. 1,1-ADEQUATE correlations observed are shown on the structure.

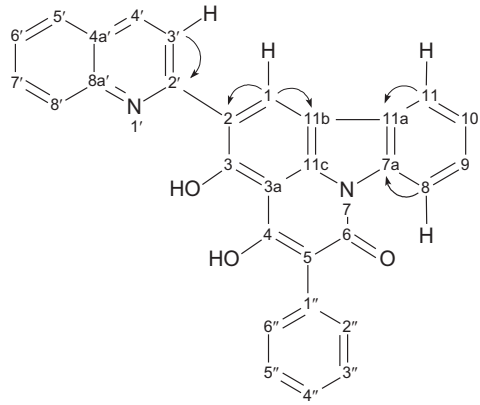

[17]

4.12. Phakellin and isophakellin

Myer and Köck reported a study of several tetracyclic pyrrole-imidazole alkaloids isolated from marine sponges in 2008 that extensively utilized 1,1- and 1,*n*-ADEQUATE data.[47] The results from the 1,1-ADEQUATE experiments on these alkaloids are shown immediately below, the 1,*n*-ADEQUATE results are discussed in Section 5.4. Usefully, the authors provided considerable information on the range of the $^{1}J_{CC}$ coupling constants and on sample requirements (see Section 3.1). In the case of bromophakellin (**18a**), the $^{1}J_{CH}$ couplings range from 194 Hz for C4H4 to 135 Hz for C11H11. The $^{1}J_{CC}$ couplings for C4–C5 and C11–C10 were 77 and 38 Hz, respectively, the largest and smallest of those contained in the molecule. The 1,1-ADEQUATE experiment performed on **18a** was optimized with $^{1}J_{CH} = 155$ Hz and $^{1}J_{CC} = 55$ Hz. When smaller samples and shorter acquisition times were employed in an effort to determine sample requirements, the H4–C5 and H10–C11 correlations proved to be the most difficult to observe.

The ADEQUATE data were combined with GCOSY, HSQC, ^{1}H–^{13}C, and ^{1}H–^{15}N GHMBC data as input for the COCON CASE program. Four different data sets were prepared as input for the program. Data set A was comprised of the correlations from the GCOSY and ^{1}H–^{13}C GHMBC spectra. Data set B contained the same data as A supplemented by the 1,1-ADEQUATE correlations. Data set C was comprised of the correlations from the GCOSY, and the ^{1}H–^{13}C and ^{1}H–^{15}N GHMBC data. Finally, data set D was comprised of the full ensemble of available 2D correlation data. In the case of bromophakellin (**18a**), the inclusion of the ^{1}H–^{15}N GHMBC data had a slightly greater impact than the inclusion of the

1,1-ADEQUATE data. For data set A, the program generated 1310 structures when hybridization states were not pre-defined. In contrast, data sets B, C, and D led to the generation of 27, 16, and 4 structures, respectively. Complete 1,1-ADEQUATE correlations reported for the bromo- and dibromophakellins (**18a**, **18b**) and the bromo- and dibromoisophakellins (**19a**, **19b**) are shown on the structures.

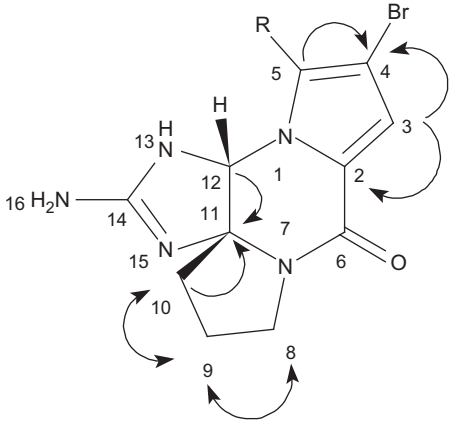

[18a] R = –H

[18b] R = –Br

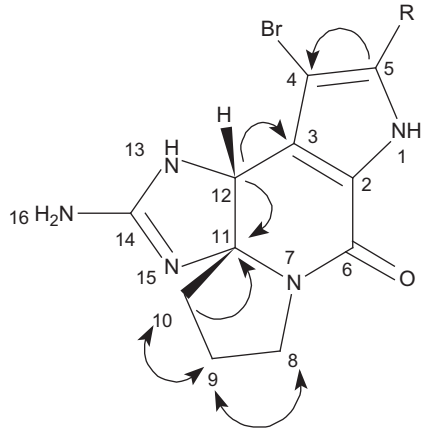

[19a] R = –H

[19b] R = –Br

4.13. Rhodoptilometrin

In 2009, Wright and colleagues[67] used a combination of ^{1}H–^{13}C HMBC and 1,1-ADEQUATE to assign the structure of rhodoptilmetrin (**20**) isolated from the echinoderm *Colobometra perspinosa*. During the structure elucidation process, comparison of the NMR data recorded for **20** with data contained in the literature suggested the possibility of the regioisomer whose structure is shown by **21**. The data were acquired at 600 MHz using a spectrometer equipped with a cryogenic probe but, unfortunately, details of the 1,1-ADEQUATE data were not reported.

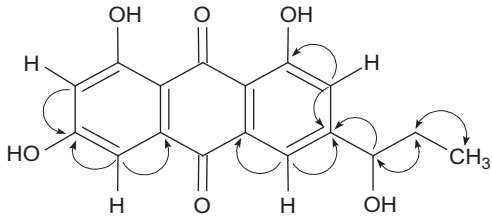

[20]

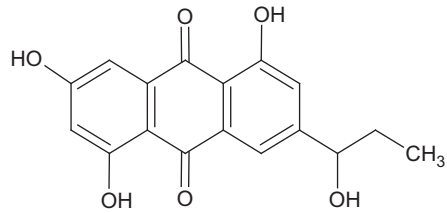

[21]

4.14. Retrorsine and delcosine

As a part of a further investigation of the impact of 1,1-ADEQUATE data on CASE programs, Cheatham and co-workers[46] employed retrorsine (**22**) and delcosine (**23**) as model compounds. HMBC and 1,1-ADEQUATE data were acquired for **22** and a suite of HMBC, H2BC, and 1,1-ADEQUATE spectra were acquired for **23**. Usefully, the authors also reported details of their efforts to optimize the acquisition of the 1,1-ADEQUATE data used as input for the CASE investigation. Strychnine (**1**) was used by the authors to explore the optimization of experimental conditions. Using a 600-MHz instrument equipped with a 5-mm cryoprobe, the authors compared s/n for various 1,1-ADEQUATE correlations of strychnine using 10 mg samples in 5 mm tubes, and both 5 and 2.5 mg samples in 3 mm tubes. Acquisition times of 15 h were used for these measurements.

The authors' work demonstrated that even samples as small as 2.5 mg could be studied yielding data with s/n > 5:1. They further demonstrated for samples with aromatic rings that 60 Hz optimization of the experiment was beneficial and that correlations to aliphatic carbons with smaller $^{1}J_{CC}$ couplings did not experience a serious adverse impact due to the larger optimization but the reverse was not true. Correlations to aromatic carbons were not amenable to optimization biased toward aliphatic carbons (e.g. 40 Hz). Correlations observed in the 1,1-ADEQUATE spectrum of retrorsine (**22**) are shown on the structure. Complete 1,1-ADEQUATE correlations were not shown for delcosine (**23**) but the authors noted that the key correlations shown on the structure that were observed in the 1,1-ADEQUATE data were not observed in the H2BC spectrum acquired. The impact of the availability of the 1,1-ADEQUATE data on the Structure Elucidator CASE program is discussed in Section 7.

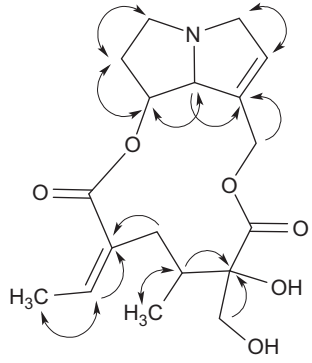

[22]

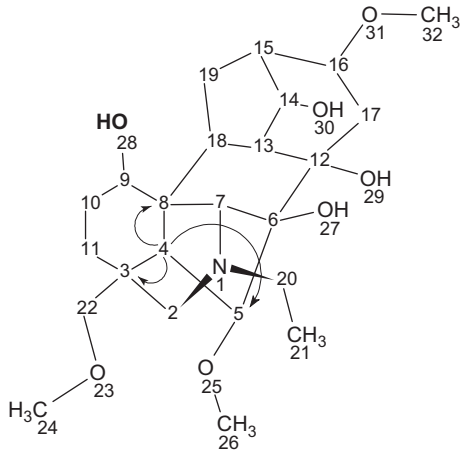

[23]

Finally, retrorsine, **22**, has also recently been used as a model compound for a study by the author and co-workers that investigated the 1,1- and 1,*n*-ADEQUATE spectra of the molecule in conjunction with unsymmetrical and generalized indirect covariance processing to afford the corresponding HSQC-1,1-ADEQUATE and HSQC-1,*n*-ADEQUATE spectra, respectively.[51]

4.15. 3,4-Epoxynephthenol acetate

In another 2010 study, Wright and co-workers[68] utilized 1,1-ADEQUATE data in the elucidation of the structure of a 3.4-epoxynephthenol acetate (**24**) from the Indonesian soft coral *Nephthea* sp. Cembranoid diterpenes contain a 14-membered macrocyclic ring that can be challenging to characterize in terms of linking together the contiguous protonated carbon segments of the molecule. Using a combination of long-range correlations observed in a ^{1}H–^{13}C GHMBC spectrum and correlations observed in a 1,1-ADEQUATE spectrum, it was possible to link together the contiguous protonated carbon segments to assemble the structure shown below. Correlations observed in the 1,1-ADEQUATE spectrum are shown on the structure.

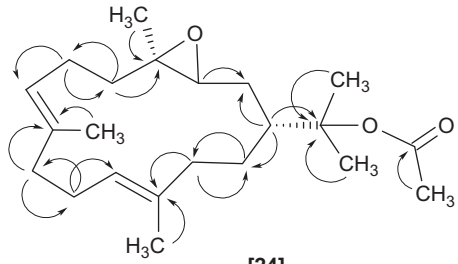

[24]

4.16. Differentiating (2-pyrrole)cysteine S-oxide from (3-pyrrole)cysteine S-oxide

The most recent application of 1,1-ADEQUATE of which the author is aware is the early 2011 report of Schraml et al.[69] The isomeric S-(2-pyrrole) cysteine S-oxide (**25**) and S-(3-pyrrole)cysteine S-oxide (**26**) both have AMX proton spin systems with comparable coupling constants that do not allow differentiation of the substitution of the pyrrole ring. The ^{13}C resonances of the two molecules are likewise quite similar and are also not amenable to the unequivocal assignment of the substitution pattern. In contrast, the $^{1}J_{CC}$-derived connectivity information from the 1,1-ADEQUATE spectrum provides an unequivocal assignment of the substitution pattern for the isomeric structures.

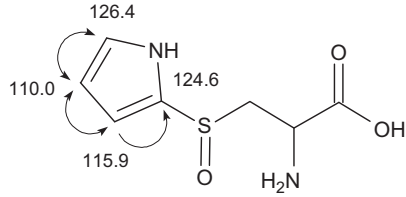

[25]

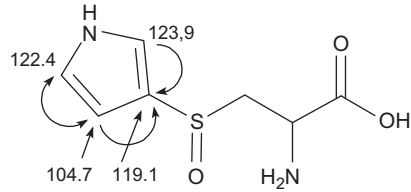

[26]

Because of the relatively narrow spectral widths, Schraml and co-workers[69] were able to acquire fewer t_1 increments (64) to digitize the second frequency domain. Coupling constants were optimized as: $^1J_{CH} = 181$ Hz and $^1J_{CC} = 62$ Hz. Data were linear predicted from 64 to 128 files in the second frequency domain and then zero-filled to afford a final data matrix of 1K $\times$ 1K points. The sample size and data acquisition times were not reported but the authors noted that the data were acquired using a 500-MHz spectrometer equipped with a 5-mm broadband switchable probe. The authors further commented that while the application of the 1,1-ADEQUATE experiment had been demonstrated only for the pyrrole system of **25** and **26**, that extension to other heterocyclic systems was obvious, as was the utility of 1,1-ADEQUATE data as input for CASE programs, noting the work of Cheatham and co-workers[46] discussed in Section 7.

5. 1,*n*-ADEQUATE

While the number of references in the literature pertaining to applications of the 1,1-ADEQUATE experiment is sparse, there is almost a complete dearth of papers citing applications of the 1,*n*-ADEQUATE experiment. Aside from the development of the ADEQUATE family of experiments in which the 1,*n*-ADEQUATE experiment was described, and some correlations for 5,6-dihydrolamellarin (**3**) that were reported in the elucidation of that structure (see Section 4.1), there are only a few papers that appear in literature searches.

The 5 Hz optimized 1,*n*-ADEQUATE spectrum of strychnine (**1**) is shown in Figure 9.[70] The high resolution 600 MHz proton spectrum is shown in Figure 10A and compared to slices extracted at the F_1 frequency of the C15 methylene resonance in the 5 Hz optimized 1,*n*-ADEQUATE spectrum (B) and the 60 Hz optimized 1,1-ADEQUATE spectrum (C). The adjacent carbons (via $^1J_{CC}$) show correlations in the 5 Hz optimized 1,*n*-ADEQUATE spectrum that are unsuppressed but all possible three-bond

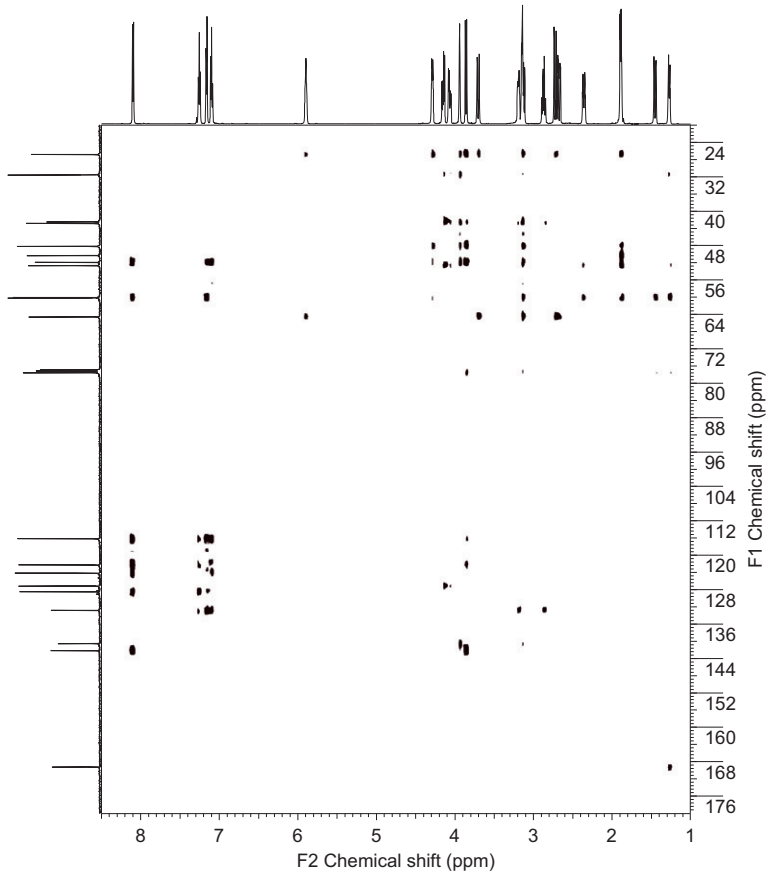

Figure 9 1,*n*-ADEQUATE spectrum of strychnine (**1**) optimized for 5 Hz. The data were acquired using a sample of ~1.8 mg in 40 μL of deuterochloroform in a 1.7-mm NMR tube at 600 MHz using a 1.7-mm Micro CryoProbe. The data were acquired as 1K × 160 points with 320 transients/t_1 increment and a 3-s interpulse delay giving an acquisition time of 48 h 17 min. The data were linear predicted to 1K points in the first dimension and from 160 to 512 point in the second frequency domain followed by zero-filling to give a final 1K × 1K data matrix.

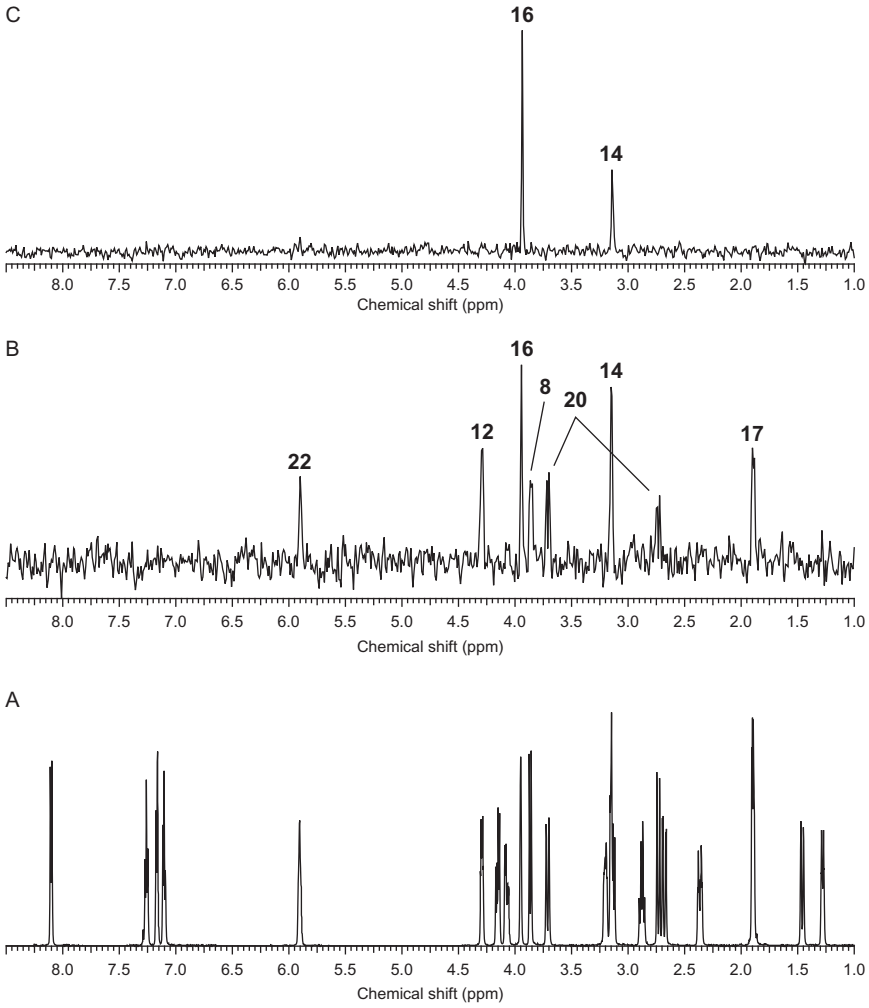

Figure 10 (A) 600 MHz ^{1}H reference spectrum of strychnine (**1**) in deuterochloroform. (B) Slice taken through the 5 Hz optimized 1,*n*-ADEQUATE spectrum of **1** at the F_1 shift of the C15 methylene resonance. (C) Comparison slice taken through the 60 Hz optimized 1,1-ADEQUATE spectrum of **1** at the F_1 shift of the C15 methylene resonance.

correlations are also observed in the trace shown in B. These correlations are summarized for C15 on **27**.

Usefully, 1,1-ADEQUATE spectra provide $^{1}J_{CC}$ correlations that are equivalent to $^{2}J_{CH}$ correlations in GHMBC spectra, while 1,*n*-ADEQUATE spectra provide $^{3}J_{CC}$ correlations that correspond to $^{4}J_{CH}$ correlations in GHMBC spectra. When these data are combined with GHMBC spectra, which contains predominantly $^{3}J_{CH}$ correlations, a series of successive

"shells" of neighbouring carbons, each one bond further removed, is identified. These data should prove to be an extremely useful set of input data for CASE programs (see Section 7) or for interpretation by a skilled spectroscopist.

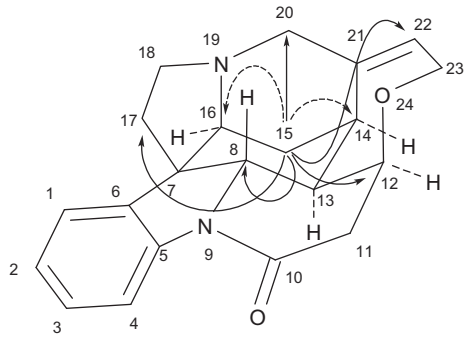

[27]

5.1. Application of 1,*n*-ADEQUATE to 5,6-dihydrolamellarin

The elucidation of the structure of 5,6-dihydrolamellarin[37,38] served as the development vehicle for the entire family of ADEQUATE experiments. Hence, this work also represented the first reported application of the 1,*n*-ADEQUATE experiment. Two important 1,*n*-ADEQUATE correlations were observed in the benzopyrone portion of the molecule and are shown by **28**. The C19 resonance was correlated via three bonds to the C23 carbonyl. The C22 carbon was correlated via three bonds to the C3 quaternary carbon adjacent to the C23 carbonyl.

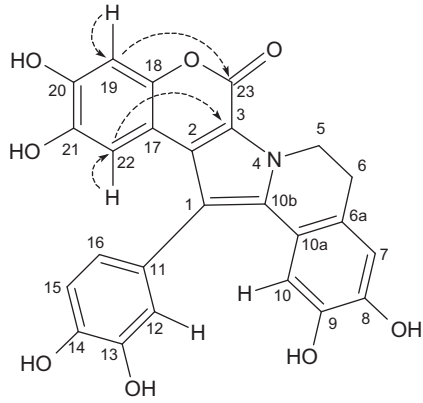

[28]

5.2. Application of 1,*n*-ADEQUATE for highly substituted aromatic compounds

The second reported application of the utilization of 1,*n*-ADEQUATE data in the elucidation of a structure is found in the 1996 report of Köck and co-workers[71] describing the characterization of an intermediate in the synthesis of euglobal-G1 (**29**) and euglobal-G2 (**30**). The synthesis employed a route that involved the acylation of a highly substituted benzaldehyde (see Scheme 1). While there were two possible acylation products, only a single product was formed in the reaction and it was necessary to unequivocally assign the structure.

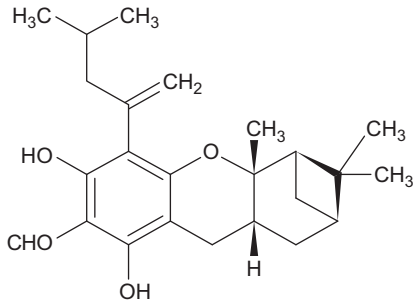

[29]

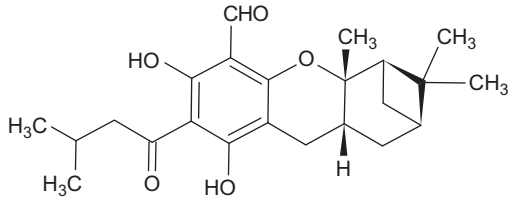

[30]

As will be noted from even a cursory look at the structures of the two acylation products shown in Scheme 1, there is but a single aromatic methine resonance, that, regardless of which substitution product

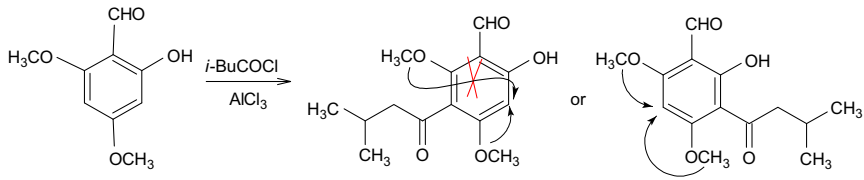

[31] **[32]** **[33]**

Scheme 1 Synthetic route for the preparation of a highly substituted aromatic intermediate in the synthesis of euglobal-G2 [**30**]. The two possible product structures are shown with key long-range couplings. Based on the 1,*n*-ADEQUATE data, **33** was the sole product of the reaction.

formed, would afford a $^{3}J_{CH}$ correlation to the quaternary carbon bearing the acyl side chain. Hence, an assignment strategy other than the conventional GCOSY/GHSQC/GHMBC protocol was necessary. In the case of **32**, the 1,*n*-ADEQUATE experiment will afford a correlation from one of the two O-methyl groups to the aromatic methine but not from both. In contrast, for **33**, both O-methyl groups will correlate to the aromatic methine in a 1,*n*-ADEQUATE experiment as shown in Scheme 1. The observation of both possible correlations to the protonated aromatic methine resonance confirmed the structure of the product formed as **33**.

5.3. Measurement of $^{1}J_{CC}$, $^{2}J_{CC}$, and $^{3}J_{CC}$ coupling constants

The next application of the 1,*n*-ADEQUATE experiment found in a SciFinder search is the 1996 report of Griesinger and co-workers[72] for the measurement of $^{n}J_{CC}$ coupling constants. Various ^{13}C-detected methods for the determination of carbon–carbon coupling constants have been reported and reviewed by Krividin and Della[73] but, as would be expected, these methods suffer from the inherently low sensitivity that typifies ^{13}C-detected methods. In contrast, ^{1}H excitation/detection using variants of the ADEQUATE experiment can lead to gains in sensitivity as great as 64-fold.[74–76] Despite the higher sensitivity of proton-detected methods, measuring times can still be lengthy because of the requirement for higher F_1 digital resolution when coupling constants are to be measured. In the case of the 14 mg sample of 5,6-dihydrolamellarin (**3**) used as the model compound for the study, the 1,1-ADEQUATE spectrum utilized 768 increments in the F_1 dimension with an acquisition time of 63 h; the 1,*n*-ADEQUATE data were acquired using 192 t_1 increments requiring an acquisition time of 47 h. It will be interesting to see the impact of non-uniform sampling (NUS) on experiments such as this that require high F_1 digital resolution.

5.4. Applications of 1,*n*-ADEQUATE in the elucidation of the structures of phakellin and isophakellin alkaloids

A series of 1,1-ADEQUATE experiments were performed (see Section 4.12) in the course of elucidating the structures of a series of bromo- and dibromophakellins (**18a, -b**) and bromo- and dibromoisophakellins (**19a, -b**).[47] Those data were combined with the data from other 2D NMR spectra and used as input for the COCON CASE program. In addition, however, the authors also acquired 1,*n*-ADEQUATE spectra for the four alkaloids that revealed additional correlations not observed in the GHMBC spectra. The observed 1,*n*-ADEQUATE correlations are shown below on structures **34**–**37**. Unfortunately, the specific optimization of the long-range $^{n}J_{CC}$ delay used by the authors was not specified. While there was some variability among the 1,*n*-ADEQUATE correlations

observed in the series of mono- and dibromophakellin and isophakellin alkaloids, all of the correlations were via $^{3}J_{CC}$ with no $^{2}J_{CC}$ correlations observed. Hence, all of the correlations reported for the 1,*n*-ADEQUATE spectra were the equivalent of $^{4}J_{CH}$ GHMBC correlations. The 1,*n*-ADEQUATE correlations are denoted by dashed arrows to differentiate them from the 1,1-ADEQUATE correlations shown for **18a**, **18b**, **19a**, and **19b** that are denoted by solid arrows. Dashed double headed arrows denote mutually 1,*n*-ADEQUATE coupled resonances.

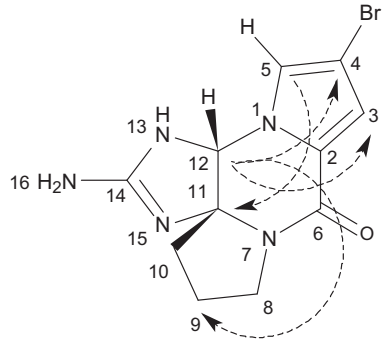

[34]

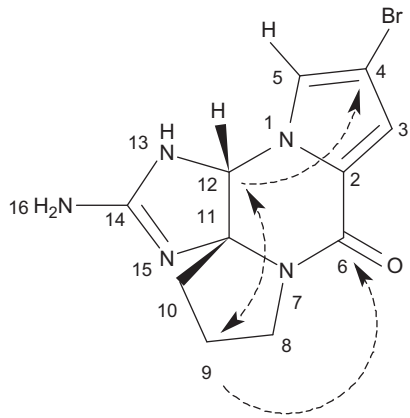

[35]

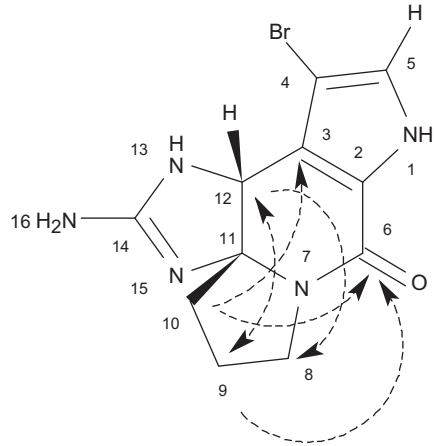

[36]

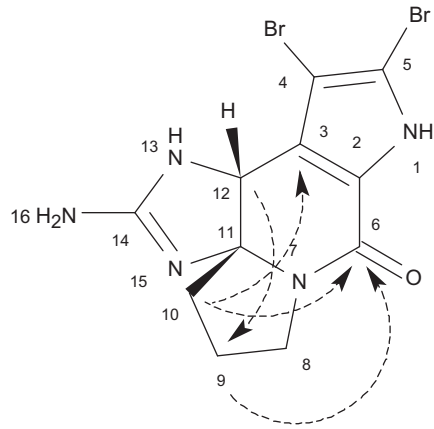

[37]

5.5. 1,*n*-ADEQUATE of retrorsine

Retrorsine (**22**) was recently used as a model compound in a study of carbon–carbon correlations observed in 1,1-ADEQUATE and 1,*n*-ADEQUATE spectra. It was noted by Martin and co-workers[51] that modulations of $^{1}J_{CC}$ correlations between pairs of sp^2 carbons and from an sp^3 carbon to an sp^2 carbon can lead to gaps in the connectivity network being determined for adjacent carbons (see Figures 7 and 8 and also Section 3.4). In addition to the investigation of the 1,1-ADEQUATE correlations of the

molecule, correlations observed in the 5 Hz optimized 1,*n*-ADEQUATE spectrum of retrorsine were also examined and are summarized by **38**.

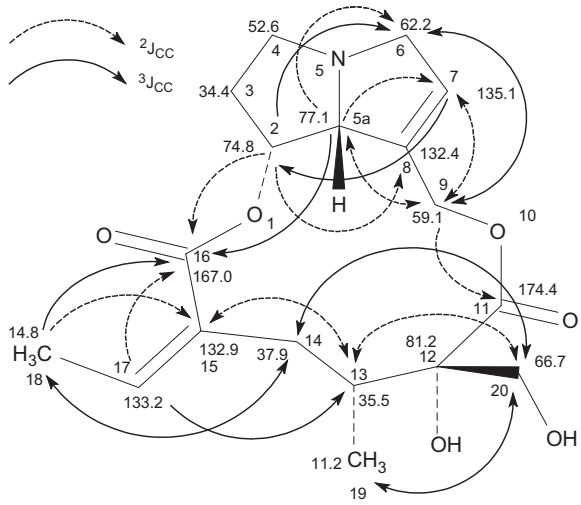

[38]

The high degree of functionality of the 12-membered ring of retrorsine leads to the observation of a significant number of $^2J_{CC}$ correlations in addition to the $^3J_{CC}$ correlations that might normally be expected. In addition, two of the methylene resonances of the pyrrazolidine nucleus (C3 and C4) showed no long-range carbon–carbon correlations at all.

In addition to the investigation of the adjacent and long-range carbon–carbon couplings of retrorsine, the authors also investigated the covariance processing of both types of adequate data with multiplicity-edited GHSQC spectra affording the corresponding HSQC-1,1-ADEQUATE and HSQC-1,*n*-ADEQUATE spectra (see Sections 8.3.3 and 8.5, respectively).

6. THE *n*,1- AND *m*,*n*-ADEQUATE EXPERIMENTS

The 1,*n*-ADEQUATE experiment described in Section 5 provides, in many cases, a means of establishing the equivalent of $^4J_{CH}$ correlations via the successive $^1J_{CH}$ and $^nJ_{CC}$ magnetization transfers. When, for example, the delay for the $^nJ_{CC}$ coupling is optimized for 5 Hz for strychnine (**1**), a significant number of the observed correlations (other than unsuppressed $^1J_{CC}$ correlations—see Figures 9 and 10) are those due to $^3J_{CC}$ coupling pathways. The exception is for carbon atoms flanked by an sp^2 carbon or a heteroatom such as oxygen or nitrogen.

In the latter cases, a mix of $^{2}J_{CC}$ and $^{3}J_{CC}$ correlations is observed presumably since the electronic effects of the heteroatom can be expected to increase the size of the $^{2}J_{CC}$ coupling somewhat. The *n*,1-ADEQUATE experiment described by Köck and co-workers,[37,38] which first employs a $^{n}J_{CH}$ HMBC-type transfer followed by a $^{1}J_{CC}$ transfer would be expected to afford connectivity information comparable to that of the 1,*n*-ADEQUATE experiment (see Section 5). However, differences between the pulse sequence used for 1,1- and 1,*n*-ADEQUATE and that for *n*,1- and *m*,*n*-ADEQUATE (see Figure 2) lead to the detection of the evolved ^{13}C–^{13}C DQ coherence frequencies in the *n*,1- and *m*,*n*-ADEQUATE experiments rather than as single quantum coherence in the case of the 1,1- and 1,*n*-ADEQUATE experiments. Hence, connectivity information must be extracted from the spectrum by calculating the DQ frequencies of the carbons correlated by the $^{1}J_{CC}$ magnetization transfer step for both the *n*,1- and *m*,*n*-ADEQUATE experiments. This facet of the experiment renders it less readily interpretable since the ^{13}C reference spectrum can no longer be plotted along the F_1 frequency axis. Further, since the experiment begins with a long-range $^{n}J_{CH}$ HMBC-type magnetization transfer, the experiment is correspondingly less sensitivity than the 1,*n*-ADEQUATE experiment in the same sense that HMBC experiments are less sensitive than HSQC experiments.

6.1. *n*,1-ADEQUATE of strychnine

An *n*,1-ADEQUATE spectrum of strychnine (**1**) recorded using a $^{n}J_{CH}$ delay optimized for 8 Hz and a $^{1}J_{CC}$ delay optimized for 50 Hz is shown in Figure 11.[77] The spectrum was recorded with the F_1 frequency range set for 350 ppm with the transmitter located at 175 ppm just downfield of the C10 carbonyl resonance. To illustrate the interpretation of an *n*,1-ADEQUATE spectrum, correlations for the C14 methine resonance will be considered. Obviously, based on the structure of strychnine (**1**), there are three carbon–carbon correlations possible from C14 to the C13 methine, the C15 methylene, and C21 quaternary vinyl carbons.

Alternatively, the transmitter could be located in the centre of the spectrum. The choice was made, however, to record the spectrum with the F_1 spectral width set to 350 ppm to intentionally spread out the correlations in the F_1 frequency domain to avoid potential response overlaps.

Perhaps, the simplest means of approaching the interpretation of an *n*,1-ADEQUATE spectrum is to compare the observed correlations with those of a GHMBC spectrum acquired with the same $^{n}J_{CH}$ optimization. As an example, correlations observed from the H23a/b protons (see **39**) in

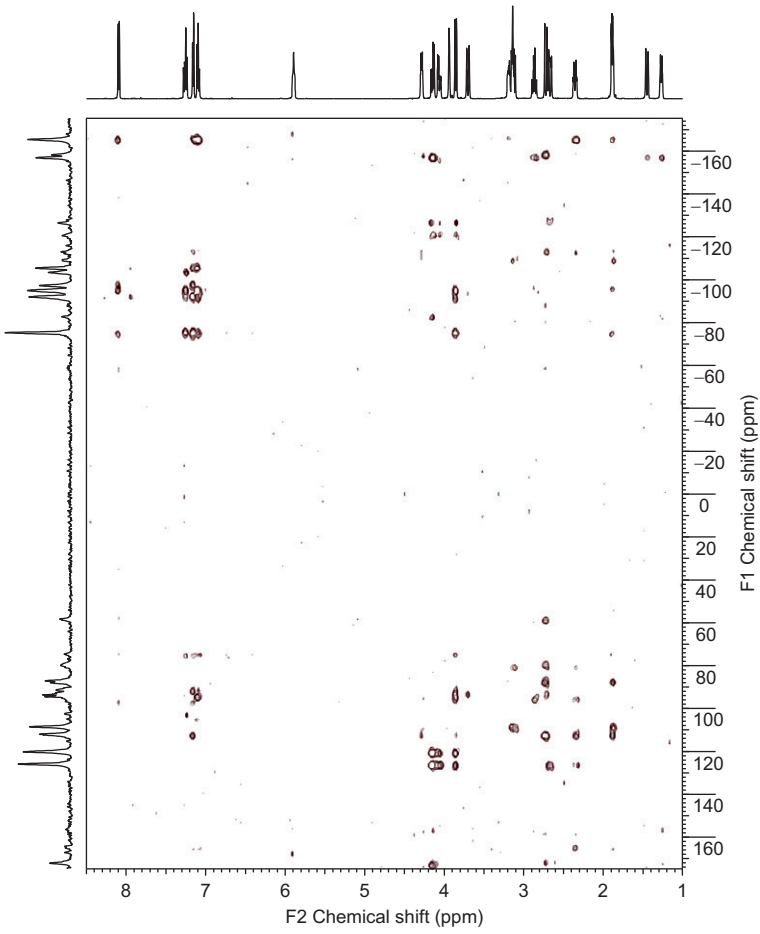

Figure 11 *n*,1-ADEQUATE spectrum of strychnine (**1**) recorded with the $^{n}J_{CH}$ and $^{1}J_{CC}$ delays optimized for 8 and 50 Hz, respectively. The data were acquired using a 25-mg sample of **1** dissolved in 600 μL of deuterochloroform in a 5-mm NMR tube. The data were acquired using a 500-MHz spectrometer equipped with a 5-mm cryoprobe with the inner coil doubly tuned to $^{1}H/^{19}F$ and the outer coil tuned to ^{13}C. The data were acquired using 4096 points in the t_2 domain with 256 increments of the evolution time, t_1, accumulating 512 transients/t_1 increment giving an acquisition time of 96 h. The data were processed using a combination of linear prediction and zero-filling to afford a final data matrix of 2K × 4K points. Relative to the sensitivity of the 1,*n*-ADEQUATE experiment, the *n*,1-ADEQUATE experiment is substantially less sensitive.

the *n*,1-ADEQUATE spectrum should generally also be observed in the GHMBC spectrum. In the case of **39**, this step would identify the $^{n}J_{CH}$ coupled partner as C14. At that point, knowing the offset of C14 relative to the transmitter, the resonances that can be $^{1}J_{CC}$ coupled to C14 are C13, C15, and C21.

Correlations in the F_1 dimension are a function of the algebraic sum of the $^{1}J_{CC}$ coupled resonances relative to the transmitter according to Equation (1):

$$(\delta C_A + \delta C_B) - \delta_{xmtr}. \quad (1)$$

The ^{13}C chemical shifts, offsets relative to the transmitter, calculated and observed DQ frequencies for the correlations to C14 are summarized in Table 1.

The potential carbon–carbon correlations from C14 are shown in grey on the structures that follow; the observed correlation is denoted by a solid grey bond while the other correlations are designated by dashed grey bonds.

Beginning with the C14–C21 correlation, which would be expected to be observed at +172.0 ppm in the DQ frequency (F_1) domain (see Table 1) of the spectrum shown in Figure 11, correlations from the H23a/b, H20b, and very weakly from the H13 proton are observed at a DQ frequency of +172.5 ppm (see Figure 12). The $^{n}J_{CH}$ correlations observed from the 8 Hz "*n*" portion of the *n*,1-ADEQUATE experiment are summarized by **39**.

TABLE 1 Chemical shifts, offsets relative to the transmitter, calculated and observed double quantum frequencies for selected ^{13}C resonances of strychnine (**1**)

Resonance	Chemical shift[a] (δ) (ppm)	Offset from transmitter[b] (ppm)	Calc. DQ frequency for C14 correlation[c] ($\delta C_A + \delta C_B$)	Calc. DQ frequency after folding[d]	Obs. DQ frequency
C14	31.6	−143.4	–	–	–
C13	50.3	−124.6	−268.0	93.0	93.4
C15	26.8	−148.2	−291.6	58.4	58.0
C21	140.4	−34.6	−178.0	173.0	172.5

[a] Chemical shifts are in ppm downfield of TMS.
[b] The transmitter was located 175 ppm downfield of TMS.
[c] Double quantum (DQ) frequencies are calculated according to Equation (1).
[d] The DQ frequency range was ±175 ppm. DQ frequencies >−175 ppm are folded in from the bottom of the spectrum and hence are observed at pseudo-positive DQ frequencies.

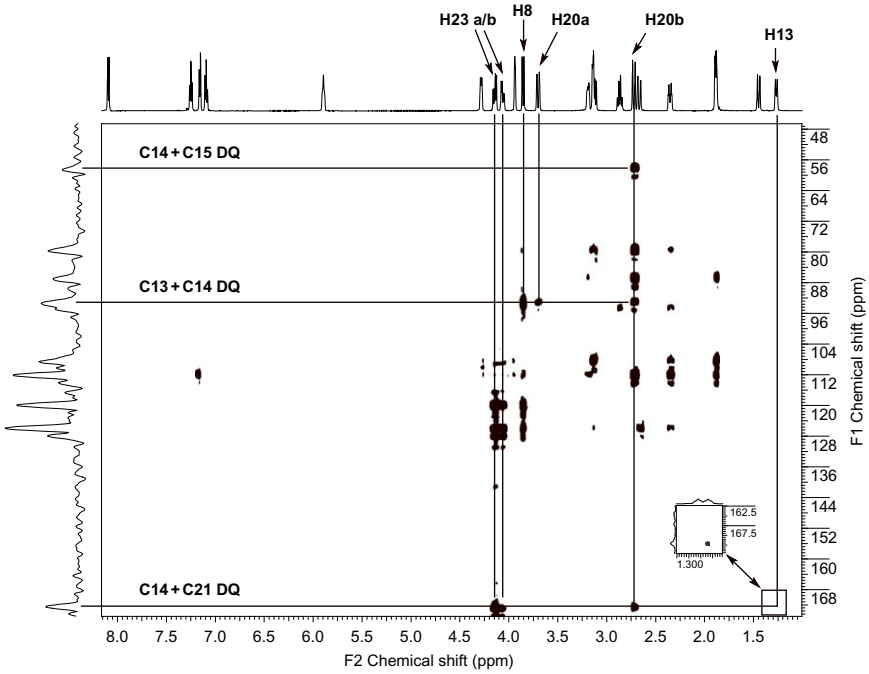

Figure 12 Expansion of the positive double quantum frequency range of the *n*,1-ADEQUATE spectrum shown in Figure 1. The correlation responses for the three possible carbon–carbon correlations from C14 are shown (see also Table 4 and **39**, **40**, and **41**). The very weak $^{2}J_{CH}$ correlation from H13 to C14 at the C14 + C21 DQ frequency is shown in the inset.

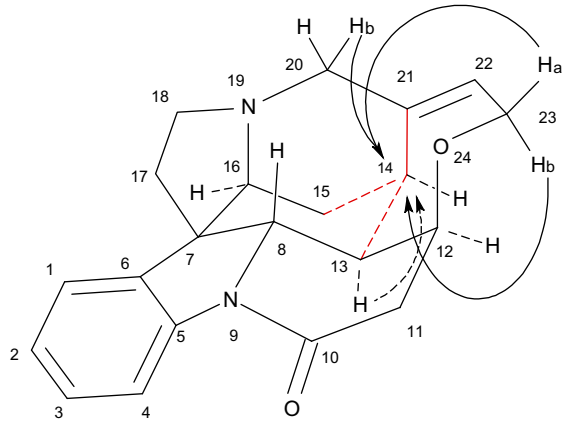

[39]

The calculated C14–C13 DQ correlation frequency (Table 1) is −268.0 ppm; correlations were expected to be observed at +93 ppm

after folding in F_1. Correlations are observed from the H20a, H20b, and H8 protons at +93.4 ppm (see Figure 12). The observed correlations are shown by **40**.

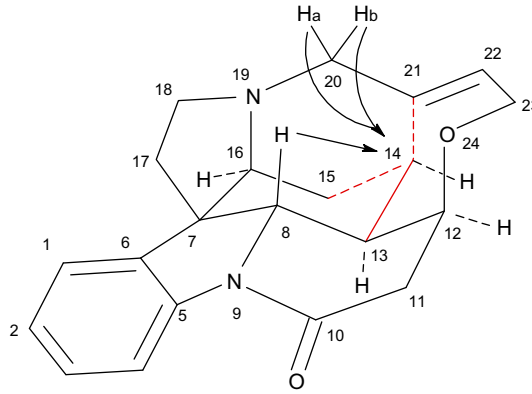

[40]

Finally, the calculated C14–C15 DQ correlation frequency (Table 1) is −291.6 ppm, with correlations expected at +58.4 ppm after folding in F_1. A single correlation is observed from the H20b proton at a DQ frequency of +58 ppm; the correlation pathway is shown by **41**.

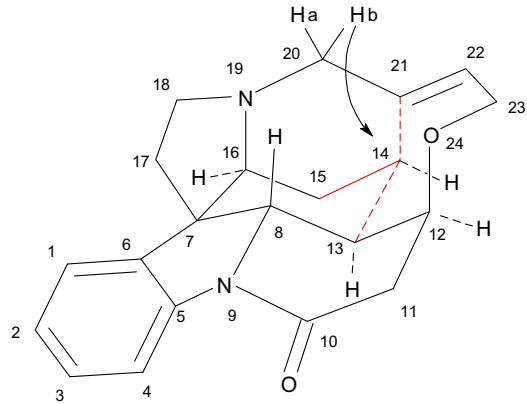

[41]

It is interesting to note from even the examination of just the three carbon–carbon correlation pathways from C14, that there is no uniformity in the $^{n}J_{CH}$ correlations observed to C14 from the various protons among these correlations. Further, while the observed $^{n}J_{CH}$ correlations are predominantly three-bond correlations, a weak two-bond correlation from H13 to C14 was among the correlations observed. Hence, the *n*,1-ADEQUATE experiment suffers from the same potential ambiguities of the correlation pathways as the GHMBC experiment.

6.2. Application of *n*,1-ADEQUATE to 5,6-dihydrolamellarin

The sole application of the *n*,1-ADEQUATE experiment reported in the literature is found in the report of the initial development of the experiment during the elucidation of the structure of 5,6-dihydrolamellarin (see Sections 4.1, 5.1 and 6.5).[38] The correlation pathway (see Figure 1C) begins with a $^{n}J_{CH}$ long-range transfer analogous to that of an HMBC/GHMBC experiment. There is no way to differentiate between various long-range heteronuclear couplings, which can range from $^{2}J_{CH}$ to $^{4}J_{CH}$ couplings, although $^{3}J_{CH}$ will likely predominate as in an HMBC/GHMBC spectrum. There were several useful *n*,1-ADEQUATE correlations observed in the spectrum of 5,6-dihydrolamellarin as shown by **42**. The data were acquired using a 14-mg sample of the molecule dissolved in 80 μL of solvent in a 2.5-mm tube using a 500-MHz spectrometer equipped with a 2.5-mm conventional probe. A total of 384 transients were accumulated per each of the 256 t_1 increments giving an acquisition time of 2 days 17 h with a 2-s interpulse delay. The $^{n}J_{CH}$ delay was optimized for 69 ms, which corresponds to ~7.25 Hz; the $^{1}J_{CC}$ delay was optimized for 55 Hz.

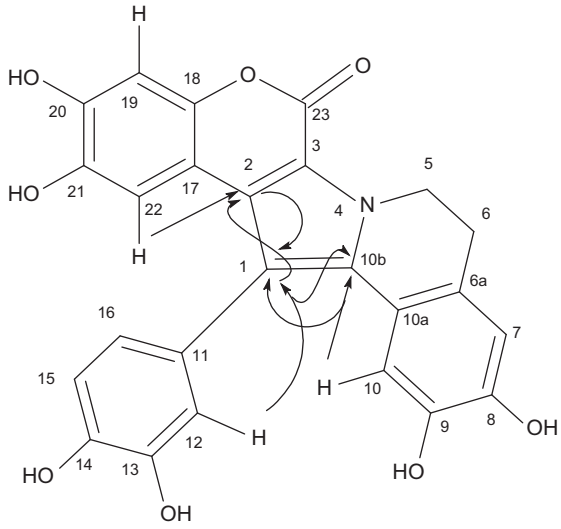

[42]

It is interesting to note that all of the initial $^{n}J_{CH}$ correlations observed were via three bonds in the case of 5,6-dihydrolamellarin while in the case of strychnine, as shown by **39**, both two- and four-bond $^{n}J_{CH}$ coupling pathways have also been observed.

6.3. Comparison of 1,*n*- and *n*,1-ADEQUATE

The extraction of correlation information from the 1,*n*- and *n*,1-ADEQUATE experiments highlights the inherent differences of the information content of the two experiments. Comparing Figures 10B and 12 shows some of the differences. The $^{1}J_{CH}$ initial transfer in the 1,*n*-ADEQUATE experiment followed by the $^{n}J_{CC}$ long-range out-and-back step (see Figure 1B) collects all of the long-range carbon–carbon correlation responses in a single F_1 trace (Figure 10B) at the ^{13}C shift of the carbon in question (F_1) or along the axis defined by the proton shift in question (F_2). In contrast, the nature of the *n*,1-ADEQUATE spectrum is such that, for C14, there are three separate DQ frequencies at which the $^{1}J_{CC}$ out-and-back transfers are observed (see Figure 12). Hence, at least in the opinion of the author, the interpretation of the 1,*n*-ADEQUATE experiment is more facile than for the *n*,1-ADEQUATE experiment.

From a sensitivity standpoint, the *n*,1-ADEQUATE experiment, at least in the author's experience, ranges from two to four times less sensitive than the 1,*n*-ADEQUATE experiment. This difference in relative sensitivity reflects the relative difference in sensitivity between an HSQC and HMBC experiments with which 1,*n*- and *n*,1-ADEQUATE begin, respectively.

6.4. *m*,*n*-ADEQUATE of strychnine

The related *m*,*n*-ADEQUATE (also referred to as *n*,*n*-ADEQUATE) experiment uses the same pulse sequence as the *n*,1-ADEQUATE experiment (see Figure 2) with the exception that the delay for the transfer of ^{13}C–^{13}C magnetization is optimized for $^{n}J_{CC}$ rather than $^{1}J_{CC}$ as in the *n*,1-ADEQUATE experiment (compare Figure 1C and D). In principle, the *m*,*n*-ADEQUATE experiment allows up to as many as six or in some cases seven bonds to be spanned by the successive $^{m}J_{CH}$ and $^{n}J_{CC}$ long-range magnetization transfers. The potential very long "reach" of this experiment is unfortunately counterbalanced by the significant losses in sensitivity inherent to the $^{m}J_{CH}$ and $^{n}J_{CC}$ long-range coupling pathways employed in the successive magnetization transfers. Thus, just as the 1,*n*-ADEQUATE experiment is correspondingly less sensitive than the 1,1-ADEQUATE experiment, the *m*,*n*-ADEQUATE experiment is also correspondingly less sensitive than the *n*,1-ADEQUATE experiment. In parallel with the *n*,1-ADEQUATE experiment, the *m*,*n*-ADEQUATE experiment is also detected via the ^{13}C–^{13}C DQ frequencies of the carbons correlated through the $^{n}J_{CC}$ magnetization transfer employed in the experiment.

A further detractor from the *m*,*n*-ADEQUATE experiment is the inherent ambiguity of the two long-range magnetization transfers. As in the HMBC/GHMBC experiment, the $^{m}J_{CH}$ transfer step may afford

long-range couplings where m ranges from two- to four-bonds. The $^{n}J_{CC}$ long-range transfer, while it gives predominantly three-bond carbon–carbon correlations in the case of strychnine, can lead to some two-bond carbon–carbon correlations when the carbon to which magnetization is transferred in the initial $^{m}J_{CH}$ step is flanked by a heteroatom (e.g. oxygen or nitrogen). In addition, since $^{1}J_{CC}$ correlations are not suppressed, n,1-ADEQUATE type correlations may also be observed in m,n-ADEQUATE spectra.

An m,n-ADEQUATE spectrum of strychnine (**1**) is shown in Figure 13.[78] The data were acquired with the $^{m}J_{CH}$ magnetization transfer optimized for 8 Hz and the $^{n}J_{CC}$ delay for the creation of long-range ^{13}C–^{13}C DQ coherence optimized for 5 Hz. Two of the relatively few correlations observed in the spectrum, which took 72 h of spectrometer time to acquire are analyzed below. As with an n,1-ADEQUATE spectrum, the simplest way to begin the interpretation of the data is to compare the correlations observed in the m,n-ADEQUATE spectrum to those of a GHMBC spectrum recorded with the same optimization of the $^{m}J_{CH}$ long-range delay. In contrast to the n,1-ADEQUATE experiment shown in Figures 11 and 12, the m,n-ADEQUATE spectrum shown in Figure 13 was recorded with the transmitter located in the centre of the carbon spectrum.

The first correlation is observed at ~40 ppm (~−48 ppm relative to the transmitter position) in the F_1 frequency domain at the F_2 shifts of the anisochronous H11 methylene protons in Figure 13. Rather than an $^{m}J_{CH}$ transfer across three bonds, instead a $^{2}J_{CH}$ transfer is observed, probably an effect of the oxygen of the oxepin ring being attached to C12 as shown by **43**. The $^{n}J_{CC}$ long-range correlation in this case is to the C7 resonance.

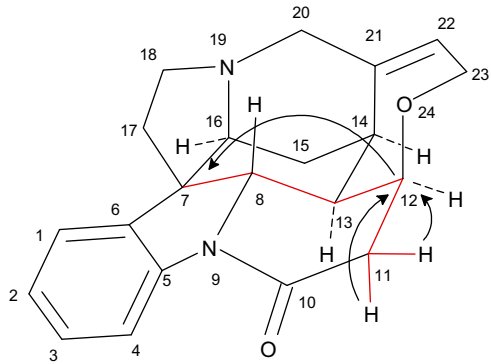

[43]

As shown above, one must first determine the carbon to which the proton long-range correlations are observed. Referring to a GHMBC spectrum will, of course, provide insight into which carbons are

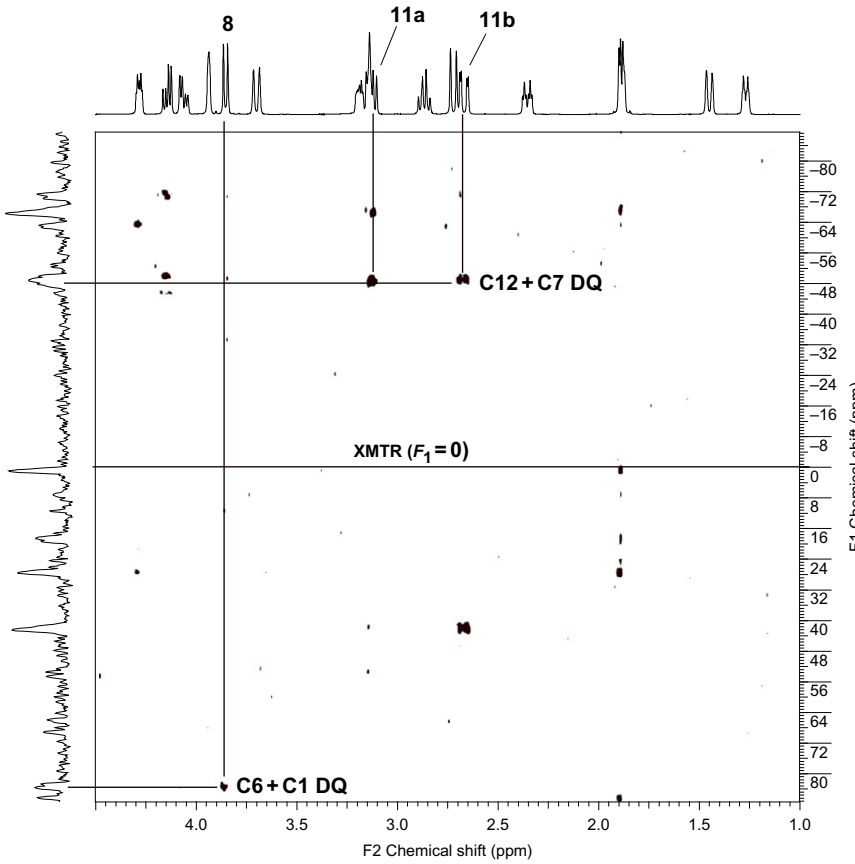

Figure 13 *m*,*n*-ADEQUATE spectrum of a 25-mg sample of strychnine (see structures **43**–**44**) recorded with the $^{m}J_{CH}$ magnetization transfer optimized for 8 Hz and the $^{n}J_{CC}$ delay for the creation of long-range ^{13}C–^{13}C double quantum coherence optimized for 5 Hz. The data were recorded in 48 h using a 500-MHz spectrometer equipped with a gradient triple resonance cryoprobe with the inner coil doubly tuned for $^{1}H/^{19}F$. The data were acquired with the transmitter located in the centre of the F_1 spectral window using 160 increments of the evolution period, t_1, with 256 transients accumulated/t_1 increment. There were relatively few correlations observed in the spectrum, with none to showing at any of the sp^2 proton shifts; two long-range correlations are shown on the spectrum.

long-range coupled to the proton or protons in question. Next, one must consider each of the carbons that could be accessed via $^{n}J_{CC}$ where $n = 2$ or 3. The DQ frequency at which the correlations are observed is the algebraic sum of the offsets of the carbons in question relative to the transmitter (Equation (1)).

In the case of the other correlation shown in Figure 13 as an example, the ${}^{m}J_{CH}$ long-range magnetization transfer occurs across the anticipated three bonds from the H8 doublet to the C6 quaternary aromatic carbon. Next, the ${}^{n}J_{CC}$ correlation, rather than occurring via two- or three bonds where $n = 2$ or 3, instead is via an uncanceled ${}^{1}J_{CC}$ coupling from C6 to C1 as shown by **44**.

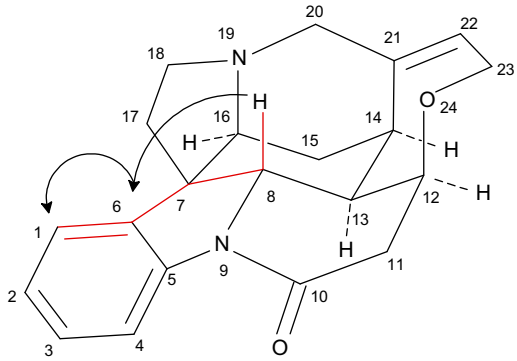

[44]

Aside from the initial applications of the *n*,1- and *m*,*n*-ADEQUATE experiments in the elucidation of the structure of 5,6-dihydrolamellarin (**3**, see Sections 4.1, 5.1 and 6.5), the author is unaware of any reported applications of these experiments in the literature.[38] Given the potential ambiguities associated with the two long-range magnetization transfer steps of the latter, coupled with the very low sensitivity and the fact that correlations are observed in F_1 at the DQ frequency of the coupled carbons rather than at the ${}^{13}C$ shift as in the 1,1- or 1,*n*-ADEQUATE experiments, it is probably quite likely that the *m*,*n*-ADEQUATE experiment will continue to be very sparingly utilized for structure elucidation.

6.5. Application of *m*,*n*-ADEQUATE to 5,6-dihydrolamellarin

The only reported application of the *m*,*n*-ADEQUATE experiment for structure elucidation was again in the initial report of the development of the experiment using 5,6-dihydrolamellarin.[38] Only two correlations were reported by the authors. Both began with an initial ${}^{3}J_{CH}$ correlation from H19 and H22 to C17 and C2, respectively. The subsequent long-range transfers were also via three bonds from C17 to C10b and from C2 to C10a, respectively as shown by **45**.

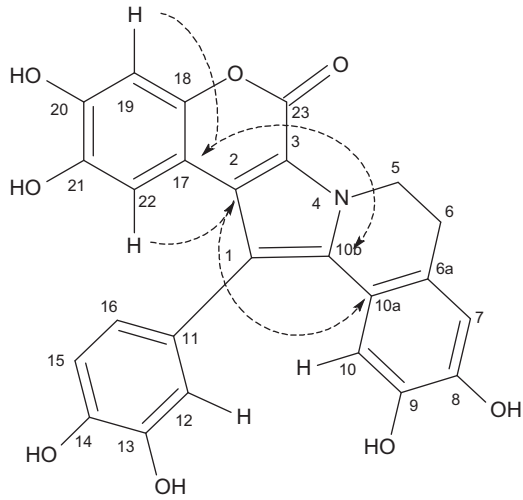

[45]

The long-range delays $^{m}J_{CH}$ and $^{n}J_{CC}$ were optimized for 69 and 44 ms, respectively, which correspond to ~7.25 and ~11.4 Hz, respectively. The authors did not report the digitization or the acquisition time for the *m*,*n*-ADEQUATE experiment.

7. USING 1,1-ADEQUATE DATA IN CONJUNCTION WITH CASE METHODS

To date, there have been four reports published that have examined the impact of 1,1-ADEQUATE correlation data on structure generation times and the number of structures generated for various CASE programs.[46,47,53,55] The first of the studies discussed above used limited 1,1-ADEQUATE data in a COCON computation run for the relatively simple molecule 4,5-dibromopyrrol-2-carboxylic acid (**4**).[53] In the same report, the authors considered the effect of 1,1-ADEQUATE correlations that would theoretically be expected for manzacidin A (**5**), however no 1,1-ADEQUATE data were actually acquired. The results for **4** and **5** are summarized in Table 2.

A follow-up study by Köck and colleagues[55] further explored the potential impact of the availability of 1,1-ADEQUATE data on computational runs for several larger natural product molecules including ascomycin, aflatoxin B_1, 11-hydroxyrotenone, and haemoventosin, using theoretically expected correlations. Again, not surprisingly, the availability of 1,1-ADEQUATE correlation data had a significant impact on structure generation times and on the number of structures generated by the program.

TABLE 2 Results of COCON computation runs for 4,5-dibromopyrrol-2-carboxylic acid (**4**) and manzacidin-A (**5**)[53]

NMR correlation data employed	**4**	**5**
COSY, HMBC	10	190
COSY, HMBC, 1,1-ADEQUATE Non-ADEQ = 0[a]	3	40
COSY, HMBC, 1,1-ADEQUATE Non-ADEQ = 1[a]	3	24

[a] Non-ADEQ represents a flag in the COCON CASE program that relates to bonds between two carbon atoms. 0 denotes that there are no prohibited correlations. 1 denotes a condition in which at least one of the involved carbons is protonated in which there should be a 1,1-ADEQUATE correlation observed.

TABLE 3 Numbers of structures generated for bromo- and dibromophakellins (**18a** and **18b**) and the corresponding bromo- and dibromoisophakellins (**19a** and **19b**)[47]

	Data set A GCOSY, $^{1}H–^{13}C$ GHMBC	Data set B GCOSY, $^{1}H–^{13}C$ GHMBC, 1,1-ADEQUATE	Data set C GCOSY, $^{1}H–^{13}C$ and $^{1}H–^{15}N$ GHMBC	Data set D GCOSY, $^{1}H–^{13}C$ and $^{1}H–^{15}N$ GHMBC, 1,1-ADEQUATE
18a R = H	1,310	27	16	4
18a R = H pre-def hyb.	26	6	5	2
18b R = Br	236,161	16,578	1,105	176
18b R = Br pre-def hyb.	264	62	20	4
19a R = H	212	53	21	7
19a R = H pre-def hyb.	8	4	4	2
19b R = Br	31,286	10,225	311	218
19b R = Br pre-def hyb.	67	36	14	5

The most recent report of Myer and Köck[47] afforded a more robust assessment of the value of 1,1-ADEQUATE data as a part of the input data set for the COCON CASE program. The output of the structure generation for the brominated phakellins (**18a, b**) and brominated isophakellin (**19a, b**) alkaloids is summarized in Table 3. Structures generated without specified hybridization are noted on the first line for each compound that can be compared with the number of structures generated when pre-defined hybridization was employed on the second line for each

compound. Clearly, the pre-defined hybridization has a very significant impact on the numbers of structures generated by the COCON CASE program.

Another very interesting study was that reported by Cheatham and co-workers.[46] Table 4 summarizes the results found for retrorsine (**22**) for which a good set of 1,1-ADEQUATE data were available. The synergy between ^{1}H–^{13}C GHBMC and 1,1-ADEQUATE noted by Myer and Köck[47] was further confirmed in the study by Cheatham and co-workers.[46] The synergy can be seen by examining the number of structures that pass filtration and the structure generation times shown in Table 4. Combining HMBC and COSY spectral data in the input table was also a synergistic combination but the number of structures generated was somewhat larger and generation times were longer than for the HMBC + 1,1-ADEQUATE data combination. In the study of delcosine (**23**) that was also contained in the report of Cheatham and co-workers,[46] the utility of H2BC data was contrasted to 1,1-ADEQUATE data. In that portion of the study, HMBC alone was the least effective data set followed, in order of improvement by HMBC + H2BC, HMBC + COSY, and finally, HMBC + 1,1-ADEQUATE giving the fastest results. Interestingly, in terms of the number of structures generated, the HMBC + H2BC was the least synergistic pairing although there were only small differences in the total number of structures generated by any of the data sets.

8. COVARIANCE NMR METHODS

Covariance NMR processing methods represent a compliment, at least in the author's opinion, to the Fourier transform. Covariance processing methods do not create new information that is not contained within the NMR data sets on which they operate. Rather, these methods establish correlations between nuclear spins through statistical covariance.[79–81] The interested reader is referred to the recent review of Snyder and Brüschweiler[52] and references cited therein for further information. Briefly, covariance NMR processing methods can be further sub-divided into direct and indirect covariance methods. The former can be applied to homonuclear 2D NMR spectra such as COSY, TOCSY, NOESY, and ROESY affording spectra in which the F_1 frequency domain is endowed with the same digital resolution as the F_2 domain. In addition to increasing spectral resolution, covariance processing can also reduce experimental time.

Covariance processing can also be applied to heteronuclear 2D NMR experiments. As first demonstrated in a report by Zhang and Brüshweiler,[82] an ''indirect'' covariance spectrum can be obtained by multiplying a spectrum by its transpose according to Equation (2):

TABLE 4 The impact of various of 2D NMR data on the number of structures generated and generation times for retrorsine (**22**) using the Structure Elucidator CASE program[46]

Data set	Number of correlations	Total correlations	Extended correlations[a]	Structures generated		Generation time
				Total	After filtration	
HMBC	60	36	1	1148	0	>16 h
1,1-ADEQUATE	30	13	0	1,166,231	533	4 h 40 min
HMBC + 1,1-ADEQUATE	60 + 30	38	1	8	2	<1 s
HMBC + COSY	60 + 29	37	2	10,921	7	1 h 10 min

[a] Extended correlations refer to the number of correlations that had to be lengthened, for example, from two- to three-bonds during the structure generation process.

$$C_{\text{indirect}} = \left(F \cdot F^{\text{T}}\right)^{1/2}. \tag{2}$$

The resulting spectrum, C_{indirect}, is a symmetric matrix whose axes are defined by the indirect dimension, F_1. Applying indirect covariance processing to a non-symmetric data matrix such as heteronuclear ^{1}H–^{13}C HSQC-TOCSY spectrum affords a symmetric homonuclear ^{13}C–^{13}C TOCSY spectrum analogous to that described originally by Turner.[22]

8.1. Unsymmetrical indirect covariance and generalized indirect covariance processing using ADEQUATE data

Indirect covariance processing has been further extended by the work of Martin and co-workers[83,84] and by Kupče and Freeman[85] to include the reconstruction of non-symmetric spectra from pairs of spectra, *F* and *G*, that share a common frequency domain according to Equation (3):

$$C = F \cdot G^{\text{T}}. \tag{3}$$

These processing methods have been labelled UIC[83] and projection reconstruction.[86] Matrix multiplication according to Equation (3) can be used to multiply a ^{1}H–^{13}C HSQC spectrum by a ^{1}H–^{13}C HMBC spectrum to yield a ^{13}C–^{13}C correlation spectrum based on heteronuclear scalar couplings.[84] In parallel to their seminal paper on 2D NMR in which Aue et al.[87] noted that a diverse range of 2D NMR experiments are possible from three fundamental pulse sequence ''building blocks'', a myriad of mathematic combinations of 2D NMR experiments is likewise possible using UIC although, obviously, many will not provide useful correlation spectra. HSQC spectra have been combined with various homo- and heteronuclear 2D spectra affording a high sensitivity, time-saving route to the former and access to experimentally inaccessible correlation data in the case of the latter.[83,87–94]

At present, there are two computational methods for performing indirect covariance calculations on pairs of spectra. The first method, reported by the author and co-workers,[83,84] was given the name UIC. More recently, Synder and Brüschweiler[95] described a method that gives similar data that they termed GIC. Both processing methods operate on pairs of 2D NMR spectra that share a common frequency domain. The UIC method leads to an asymmetric data matrix that is not amenable to matrix-square-root transformation. In contrast, the GIC method affords a symmetric matrix that can be subjected to matrix-square-root transformation. In simple terms, GIC processing begins with the creation of a modified or combined matrix from the two matrices being co-processed that can be denoted as *FG*. The combined matrix, *FG*, is then multiplied by its transpose, FG^{T}, as shown in Equation (4), after which the desired matrix

root can be calculated. It has been suggested by Snyder and Brüschweiler[95] that the GIC calculation may reduce artefacts in the resulting covariance spectra. In the authors' experience, GIC matrices generally have a s/n ratio that is comparable to that of the matrix obtained by Equation (3) after UIC processing.[49,51,70,96,97]

$$C = \left(FG{\cdot}FG^{\mathrm{T}}\right)^{\lambda}. \tag{4}$$

The information content resulting from both processing methods is identical insofar as correlation information is concerned. The matrix-square-root transformation can minimize artefacts due to relay effects and chemical shift near degeneracy (pseudo-relay effects[80–82,98]). The application of covariance methods to compute HSQC-1,1-ADEQUATE spectra is described in the following section.

8.2. HSQC-1,1-ADEQUATE

Using strychnine (**1**) as a model compound, Martin et al.[49] showed that subjecting a multiplicity-edited GHSQC spectrum and a 60-Hz optimized 1,1-ADEQUATE spectrum to UIC processing afforded the HSQC-1,1-ADEQUATE spectrum shown in Figure 14 that identifies adjacent carbon–carbon correlations from the 1,1-ADEQUATE spectrum in a diagonally symmetric manner analogous to the familiar COSY spectrum. Beginning from the C15-methylene resonance (26.4 ppm), a correlation is observed diagonally to the C14-methine resonance (27.1 ppm). Tracing correlations horizontally along the F_1 frequency axes defined by the ^{13}C shifts of C15 and C14, the next adjacent carbons, C16 and C13, respectively, can be identified. Successive steps allow the correlation network to be expanded outward as shown in the expansion of the aliphatic region of the spectrum presented in Figure 14 and shown in grey by **46**. Correlations between protonated and non-protonated adjacent carbons are not diagonally symmetric. These correlations are designated by dashed lines in Figures 14 and 15. There are also several artefact responses that are identified by being enclosed in black boxes in Figures 14 and 15. In this manner, the central "core" of strychnine's carbon skeleton can be assembled in a facile manner without any knowledge of the molecule's proton assignments. It should be emphasized that new information is not created by covariance processing methods. Rather, these methods provide an alternative visualization of the extant data that may be more readily extractable than that of the component spectra from which the covariance spectrum was calculated.

It is also important to note that UIC or GIC processing methods, when calculating hyphenated spectra such as HSQC-COSY/TOCSY[83] or HSQC-1,1-ADEQUATE,[49] can afford a significant gain in s/n ratios as shown in

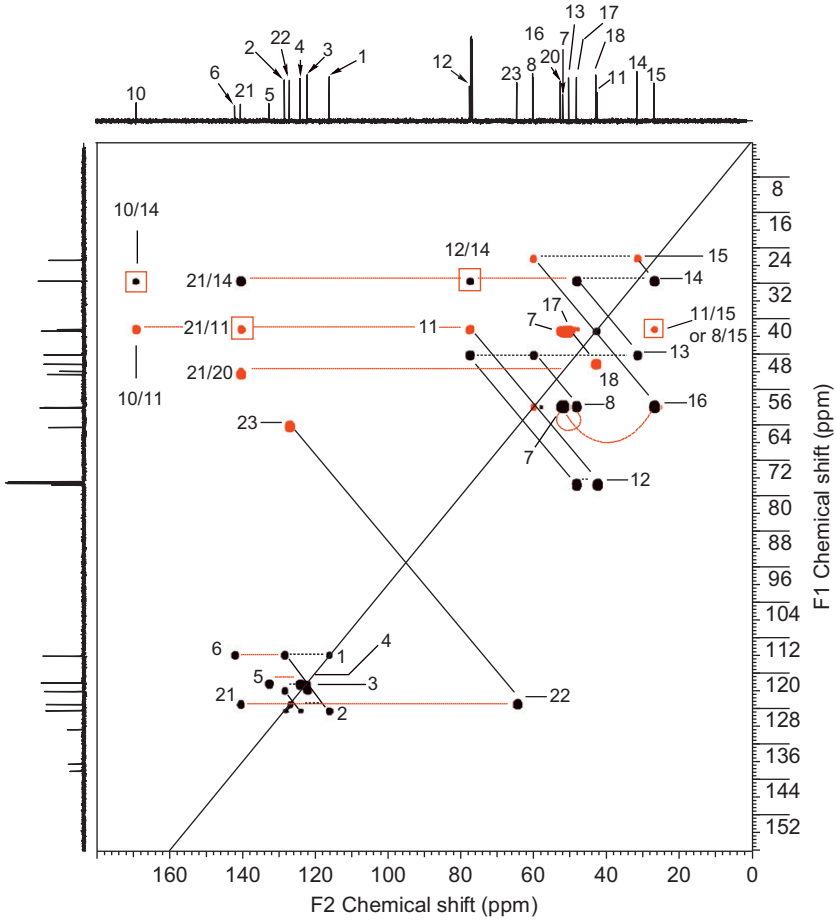

Figure 14 HSQC-1,1-ADEQUATE spectrum calculated using UIC processing from a multiplicity-edited GHSQC and a 60-Hz optimized 1,1-ADEQUATE spectrum recorded for a sample of strychnine (**1**). Covariance processing of this pair of spectra, which share a common frequency domain in the proton spectrum in F_2, leads to a $^{13}C–^{13}C$ autocorrelated spectrum. Resonance multiplicity information encoded in the multiplicity-edited GHSQC spectrum is retained in the covariance calculated spectrum. Methylene resonances have negative intensity and are plotted in grey; methine and methyl resonances (**1** has none of the latter) have positive intensity and are plotted in black. The spectrum is diagonally symmetric with adjacent carbons correlated via $^{1}J_{CC}$ observed flanking the diagonal, for example, the C15–CH_2 (26.4 ppm) correlation to the C14–CH (27.1 ppm) resonance in the upper right corner of the spectrum. Tracing horizontally (dashed horizontal black line) along either of the F_1 frequency axes defined by the ^{13}C shift of either C14 or C15, other correlations can be identified to extend the $^{13}C–^{13}C$ connectivity network beyond in the initial correlated pair of resonances. Spurious responses are boxed in black.

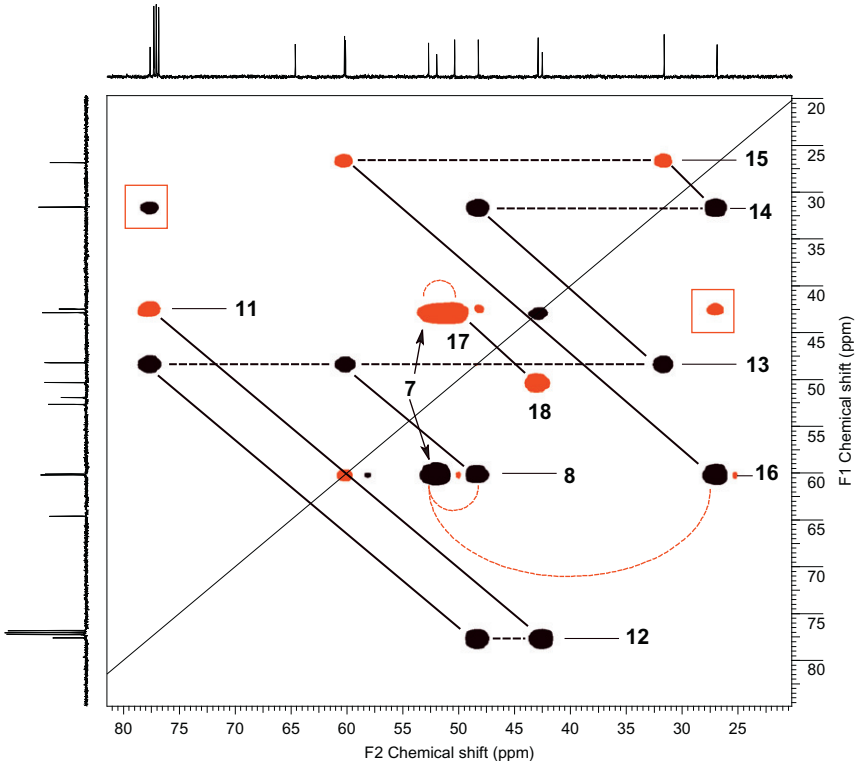

Figure 15 Annotated 60 Hz HSQC-1,1-ADEQUATE spectrum of strychnine (**45**) showing the ^{13}C–^{13}C connectivity network that defines the central "core" of the molecule as shown in grey by **46**. Correlations from methylene carbons are inverted and plotted in grey; correlations from methine carbons have positive intensity and are plotted in black. There are no methyl correlations, which would also have positive intensity. Adjacent carbons are defined by solid black lines perpendicular to the diagonal. Dashed horizontal black lines define correlations to adjacent protonated carbon resonances, for example, C15 (26.4 ppm) to C16 (60.3 ppm). Dashed curved lines define correlations between adjacent protonated and non-protonated carbons. These responses, in contrast to those between adjacent protonated carbons, are not diagonally symmetric. Responses enclosed in black boxes are artifacts that arise from the overlap of H14 and one of the anisochronous H11 methylene proton resonances.

Figures 16 and 17. Covariance processing methods can thus reduce data acquisition times for lower sensitivity experiments such as 1,1- or 1,*n*-ADEQUATE when these data are going to be interrogated following covariance processing.[50] Alternatively, when the increased s/n of

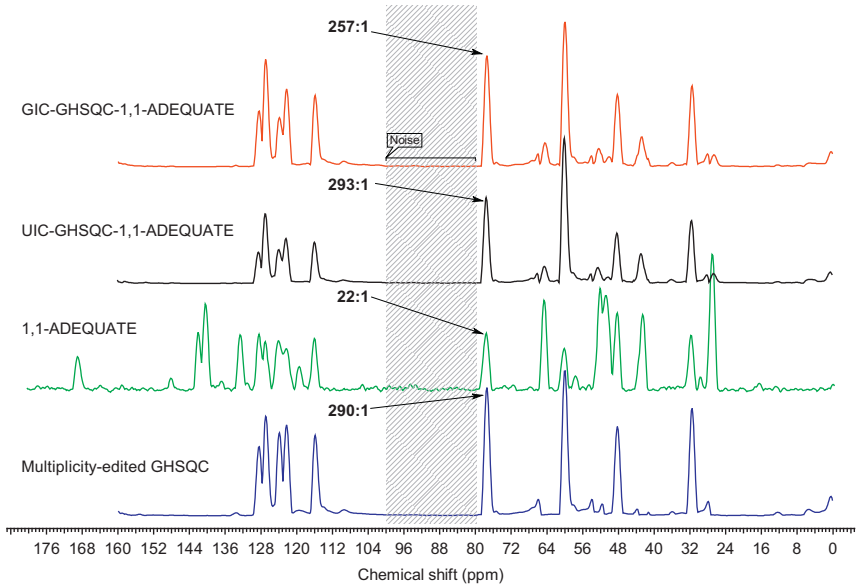

Figure 16 Comparison of the F_1 projections of the multiplicity-edited GHSQC, 60 Hz 1,1-ADEQUATE, the UIC calculated HSQC-1,1-ADEQUATE, and GIC calculated HSQC-1,1-ADEQUATE spectra (power 0.5) of strychnine (**1**). While Snyder and Brüschweiler have noted[52] that signal-to-noise (s/n) measurements of covariance spectra may not be the most viable means of making comparisons, in the present example, the differences are so dramatic that they still allow valid conclusions to be drawn. The C12 (77.6 ppm) resonance provides a convenient s/n comparator. The region from 80 to 100 ppm, which is devoid of responses in the spectrum of strychnine, was used to define the "noise" region for the measurement. There is certainly no question that multiplicity-edited GHSQC is a high-sensitivity experiment as attested by a s/n for the C12/H12 correlation response of 290:1. In comparison, the C12 resonance of the 60 Hz 1,1-ADEQUATE spectrum is a much more modest 22:1. In contrast, the s/n for the C12 resonance in the HSQC-1,1-ADEQUATE spectra calculated using UIC and GIC methods was 293:1 and 257:1, respectively.

responses in HSQC-1,1-ADEQUATE spectra are taken into consideration, sample size reductions can be factored into the structure elucidation strategy. Indeed, work by Hilton and Martin[48] demonstrated for the first time the acquisition of 1,1-ADEQUATE data for a sub-milligram sample of strychnine (**1**) overnight.

A subsequent more detailed study of data requirements for the 1,1-ADEQUATE spectrum when HSQC-1,1-ADEQUATE spectra were to be calculated[50] showed that it was possible to reduce the sample size still further to below 0.5 mg (~1.4 μmole).

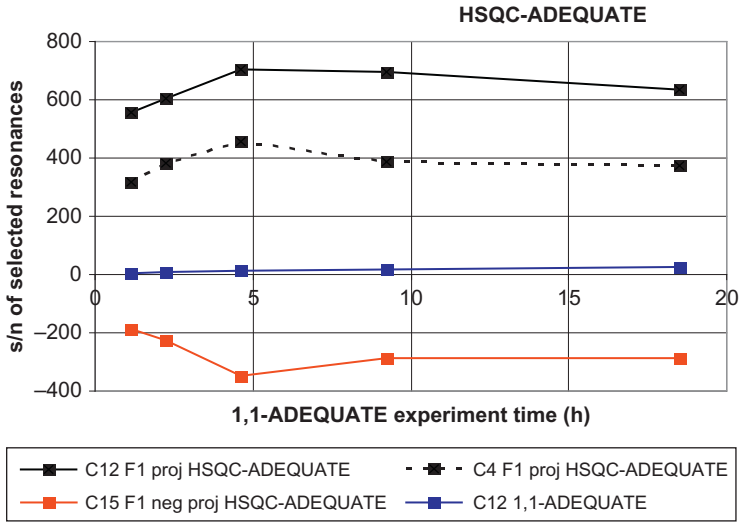

Figure 17 Signal-to-noise measurements for selected resonances of strychnine (**1**) in HSQC-1,1-ADEQUATE spectra calculated as a function of data acquisition time for the 1,1-ADEQUATE spectra used in the calculation.[50]

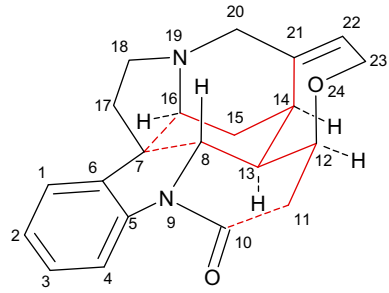

[46]

The point just made about HSQC-1,1-ADEQUATE s/n versus data acquisition time requirements is illustrated very dramatically by the curves shown in Figure 16 for several resonances for strychnine (**1**).[50] Despite the relatively low s/n for the C12 methine resonance in the 1,1-ADEQUATE spectra acquired with varied acquisition times, the corresponding gains in s/n of several resonances tracked in the HSQC-1,1-ADEQUATE spectra calculated from the 1,1-ADEQUATE spectra demonstrates the advantage inherent in the covariance calculated

HSQC-1,1-ADEQUATE spectra. When 1,1-ADEQUATE data are to be utilized in conjunction with UIC or GIC co-processing, acquisition times and/or sample sizes may be reduced. In the former case, with an ~10 mg sample of strychnine (**1**), acquisition times could be reduced to approximately 4 h while still giving very usable HSQC-1,1-ADEQUATE spectra. Using the latter tact, the authors demonstrated that it was possible to reduce the sample size to <0.5 mg of **1** over a weekend when the data were acquired using a 600-MHz 1.7 mm Micro CryoProbe.[50] Clearly, for applications such as this, there appears to be considerable potential for the utilization of UIC or GIC co-processing of multiplicity-edited GHSQC and 1,1-ADEQUATE spectra.

8.3. Applications of HSQC-1,1-ADEQUATE

Since the initial reports of HSQC-1,1-ADEQUATE spectra are very recent,[49,50] there are only the reports by the author and co-workers in the literature. Aside from the initial work done using strychnine (**1**) as a model compound, applications to the complex antifungal agent posaconazole (**47**)[96] and the cyclin-dependant kinase inhibitor dinaciclib (**48**)[97] are the only other applications that have been reported.

8.3.1. Application of HSQC-1,1-ADEQUATE to posaconazole

The complex triazole-derived antifungal agent posaconazole (**47**) has been the focus of several recent reports that have dealt with the assignment of the $^{1}H–^{15}N$ correlations in the molecule[99] and the impact of the availability of long-range $^{1}H–^{15}N$ correlation data on structure generation times using CASE programs.[100]

Figure 18A shows the overlaid multiplicity-edited GHSQC and 60 Hz 1,1-ADEQUATE spectra of posaconazole (**47**). As will be noted from an inspection of the overlaid spectra, there is an overlap of the C46 and C47 resonances of the aliphatic side chain attached to the triazolone ring that can be seen more clearly in the expansion shown in Figure 18B. In contrast, when the data are subjected to GIC processing with power = 0.5, the overlap between the C46 and C47 resonances is clearly resolved (Figure 18C). In addition, the weak correlation between the C3 and C4 resonances of the tetrahydrofuryl moiety in the structure is also observed despite the fact that this correlation was not visible in the overlaid spectrum shown in A. This feature of the spectrum can be attributed to the sensitivity enhancement inherent to the covariance processing method.[50]

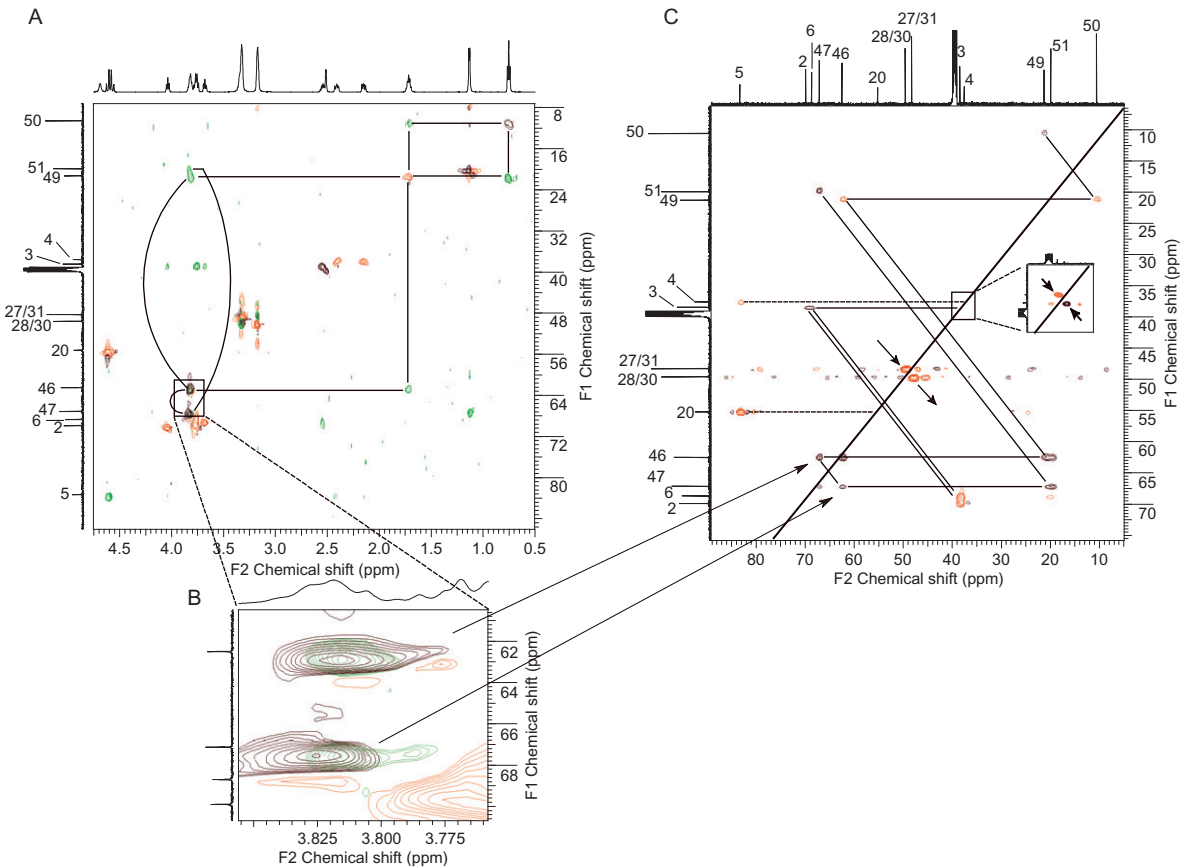

Figure 18 (A) Overlaid multiplicity-edited GHSQC and 60 Hz optimized 1,1-ADEQUATE spectra of posaconazole (**47**).[96] Correlations in the GHSQC spectrum are plotted in medium grey for methine and methyl resonances and in light grey for methylene resonances. Correlations from the 1,1-

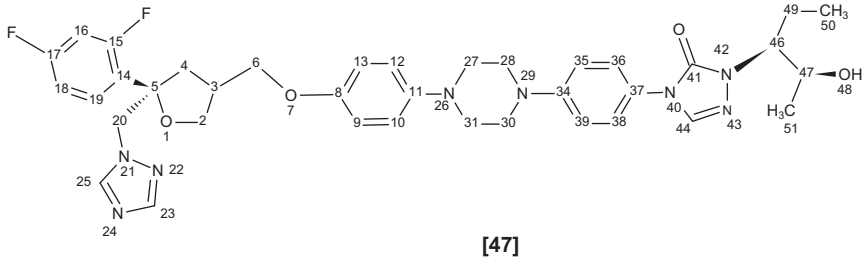

[47]

8.3.2. Application to the cyclin-dependant kinase inhibitor dinaciclib

The other application of HSQC-1,1-ADEQUATE to structure elucidation/spectral assignment that has appeared was for the cyclin-dependant kinase-2 inhibitor dinaciclib (**48**).[97] The overlaid multiplicity-edited GHSQC and 40 Hz optimized 1,1-ADEQUATE spectra are shown in

ADEQUATE spectrum are plotted in black. The connectivity network for the side chain (C46–C51) is traced out in the spectrum. The overlap of the correlations for the C46 and C7 methine resonances creates a point of ambiguity that could be problematic if dealing with an unknown structure. Likewise, there is overlap of the C49 and C51 responses to which C46 and C47, respectively, are correlated. It should also be noted that there is no correlation observed linking the C3 methine and C4 methylene resonances in the tetrahydrofuran moiety in the structure. (B) Expansion showing the overlap of the C46 and C47 methine resonances. (C) HSQC-1,1-ADEQUATE spectrum calculated using general indirect covariance (GIC) processing. Correlations between vicinal protonated carbons are diagonally symmetric analogous to the distribution of connectivity information in a familiar COSY spectrum. Correlations between non-protonated and vicinal protonated carbons are observed at the F_2 frequency of the non-protonated carbon and the F_1 frequency of the protonated member of the pair. Correlations to the C5 non-protonated carbon from the C4 and C20 methylene resonances are denoted by dashed horizontal lines. Correlation networks for all of the aliphatic resonances of the molecule are traced out. The ambiguity of the C46 and C47 methine resonances is clearly resolved in the HSQC-1,1-ADEQUATE spectrum. As shown in the inset in C, there is a diagonally symmetric correlation establishing the connectivity between the C3 methine and C4 methylene resonances although it is below the threshold used to prepare the contour plot. Correlations for methylene carbons are inverted and plotted in grey; correlations for methine and methyl resonances have positive intensity and are plotted in black.

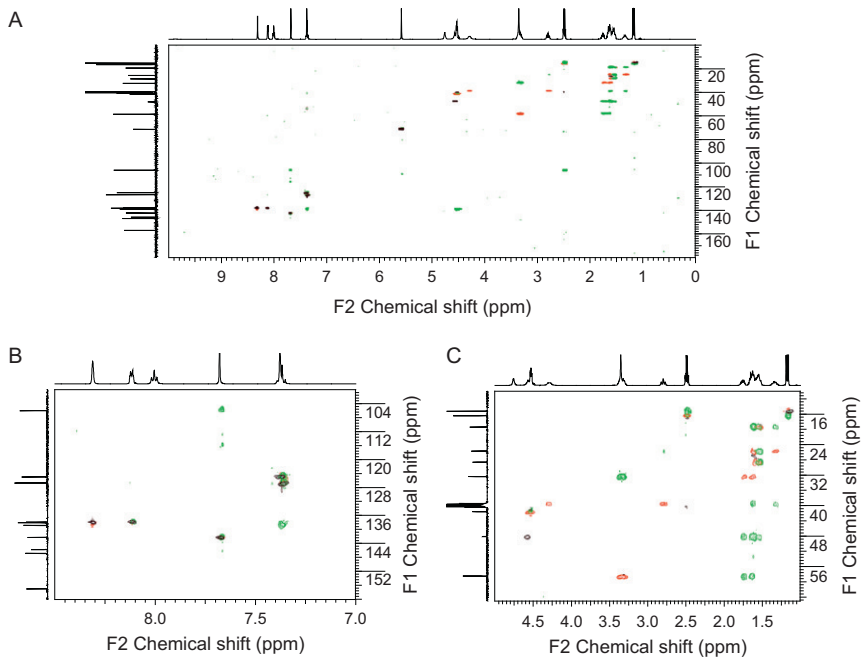

Figure 19 (A) Overlaid multiplicity-edited GHSQC and 40 Hz optimized 1,1-ADEQUATE spectra of the CDK-2 inhibitor dinaciclib (**48**).[97] The methine and methyl responses from the multiplicity-edited GHSQC spectrum are plotted in medium grey while the methylene resonances are inverted and plotted in light grey. The responses from the overlaid 40 Hz optimized 1,1-ADEQUATE spectrum are plotted in black. (B) Expansion of the aromatic region of the overlaid spectra. (C) Expansion of the aliphatic region of the overlaid spectra.

Figure 19. Correlations in the HSQC-1,1-ADEQUATE spectrum allow the overlapped resonances of the 2-(β-hydroxyethyl)piperidine moiety incorporated in the structure to be assigned (Figures 20 and 21). There are, however, resonance overlaps that complicate the HSQC-1,1-ADEQUATE spectrum by virtue of artefact responses contained in the spectrum that are enclosed in boxes in Figure 21. Given the considerable overlap in the proton spectrum, the presence of artefact responses in the GIC processed HSQC-1,1-ADEQUATE spectrum is not surprising. It is also somewhat uncertain whether or not the 1,1-ADEQUATE spectrum itself would be tractable because of the proton resonance overlaps.

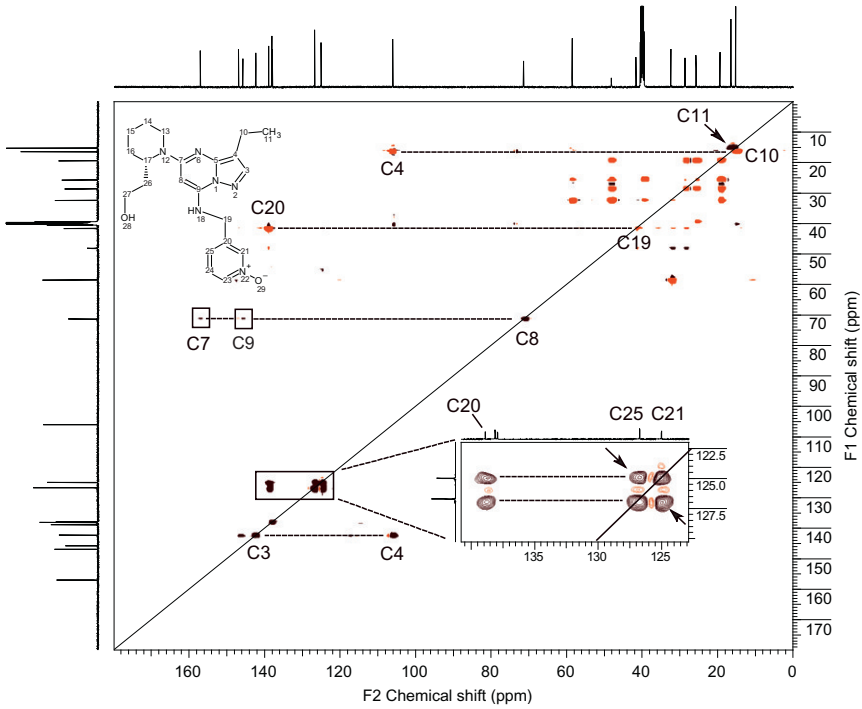

Figure 20 HSQC-1,1-ADEQUATE spectrum of **48** calculated using GIC processing[95] with power = 0.5. Adjacent protonated carbons (correlated via $^{1}J_{CC}$) are diagonally symmetric and indicated by solid black lines perpendicular to the diagonal as shown in Figure 21. Resonance multiplicity information that was phase encoded in the multiplicity-edited GHSQC spectrum is retained in the HSQC-1,1-ADEQUATE spectrum. Methylene correlations are inverted and plotted in grey; methine and methyl correlations have positive intensity and are plotted in black. Correlations between protonated and non-protonated adjacent carbons are diagonally asymmetric and are observed at the F_1 shift of the protonated carbon at the F_2 frequency of the non-protonated resonance. The correlations between protonated and non-protonated adjacent carbons are designated by dashed horizontal black lines. The sensitivity of the HSQC-1,1-ADEQUATE spectrum is governed by the much higher sensitivity GHSQC experiment rather than the lower sensitivity of the 1,1-ADEQUATE experiment.[49,50,52]

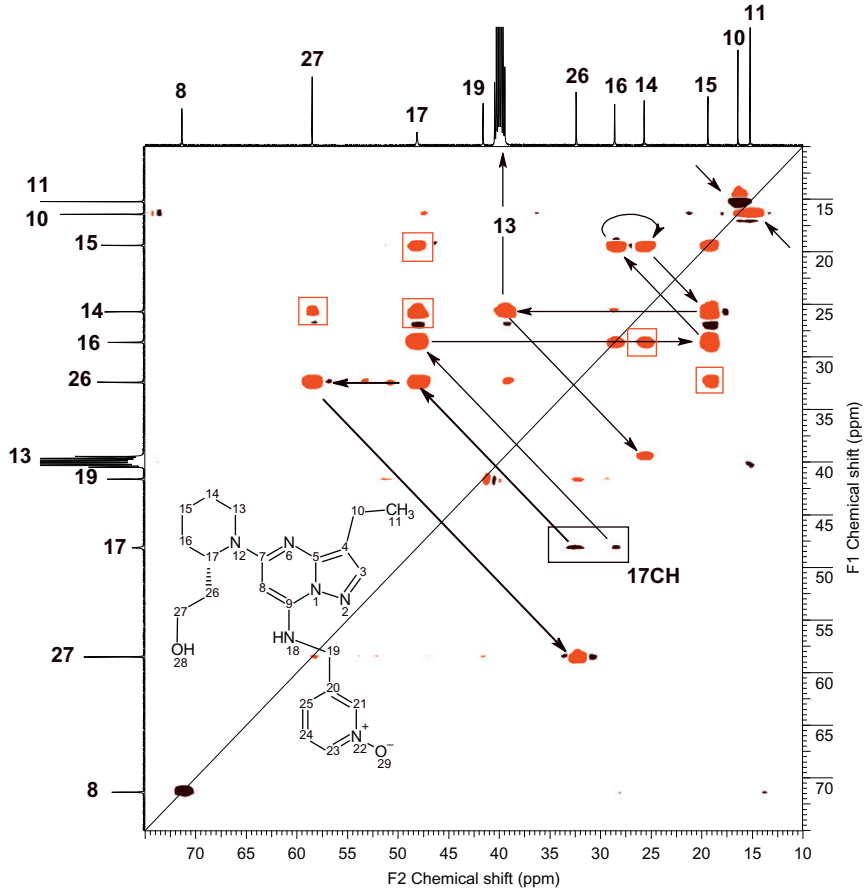

Figure 21 Expansion of the aliphatic region of the HSQC-1,1-ADEQUATE spectrum of the CDK-2 inhibitor dinaciclib (**48**). The connectivity network is traced out for the 2-(β-hydroxyethyl)piperidine moiety contained in the structure. Methylene resonances are inverted and plotted in grey; methine and methyl resonances have positive intensity and are plotted in black.

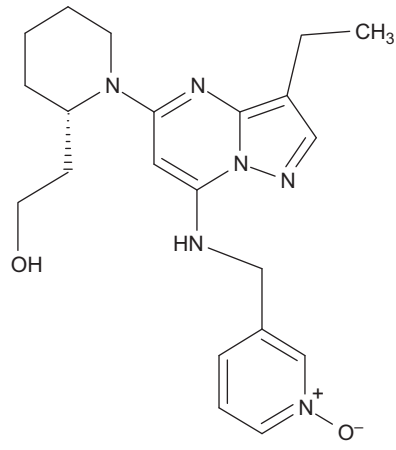

[48]

8.3.3. Application of HSQC-1,1-ADEQUATE to retrorsine

In a manner analogous to the other examples shown above, multiplicity-edited GHSQC and 1,1-ADEQUATE spectra of retrorsine can also be co-processed using either unsymmetrical[84] or generalized indirect covariance methods[95] to afford an HSQC-1,1-ADEQUATE spectrum. The 1,1-ADEQUATE data used for the calculation were acquired using a 1.6-mg sample of retrorsine dissolved in 30 μL of solvent in a 1.7-mm tube using a Bruker 600 MHz three channel spectrometer equipped with a 1.7-mm Micro CryoProbe. As with previous examples, the spectrum is diagonally symmetric with respect to adjacent protonated carbon correlations and diagonally asymmetric for correlations between adjacent protonated and non-protonated carbons. In the specific case of the correlations between the C9-methylene and C8 non-protonated sp^2 carbons and the C17 sp^2 methine and C15 non-protonated sp^2 carbons, breaks in the carbon–carbon connectivity network were observed as a function of the observation of the $^1J_{CC}$ optimization of the 1,1-ADEQUATE spectrum used in the calculation of the HSQC-1,1-ADEQUATE spectrum.[51] When the 1,1-ADEQUATE data were to be co-processed with multiplicity-edited GHSQC data, the acquisition time for the former could be reduced to ~5 h.

8.4. HSQC-1,*n*-ADEQUATE of strychnine

In the same sense that multiplicity-edited GHSQC and 1,1-ADEQUATE 2D NMR spectra can be combined using either UIC[83,84] or GIC,[52,95] the same can also be done with 1,*n*-ADEQUATE data. Thus, the HSQC-1,*n*-ADEQUATE spectrum of strychnine (**1**) is shown in Figure 22.

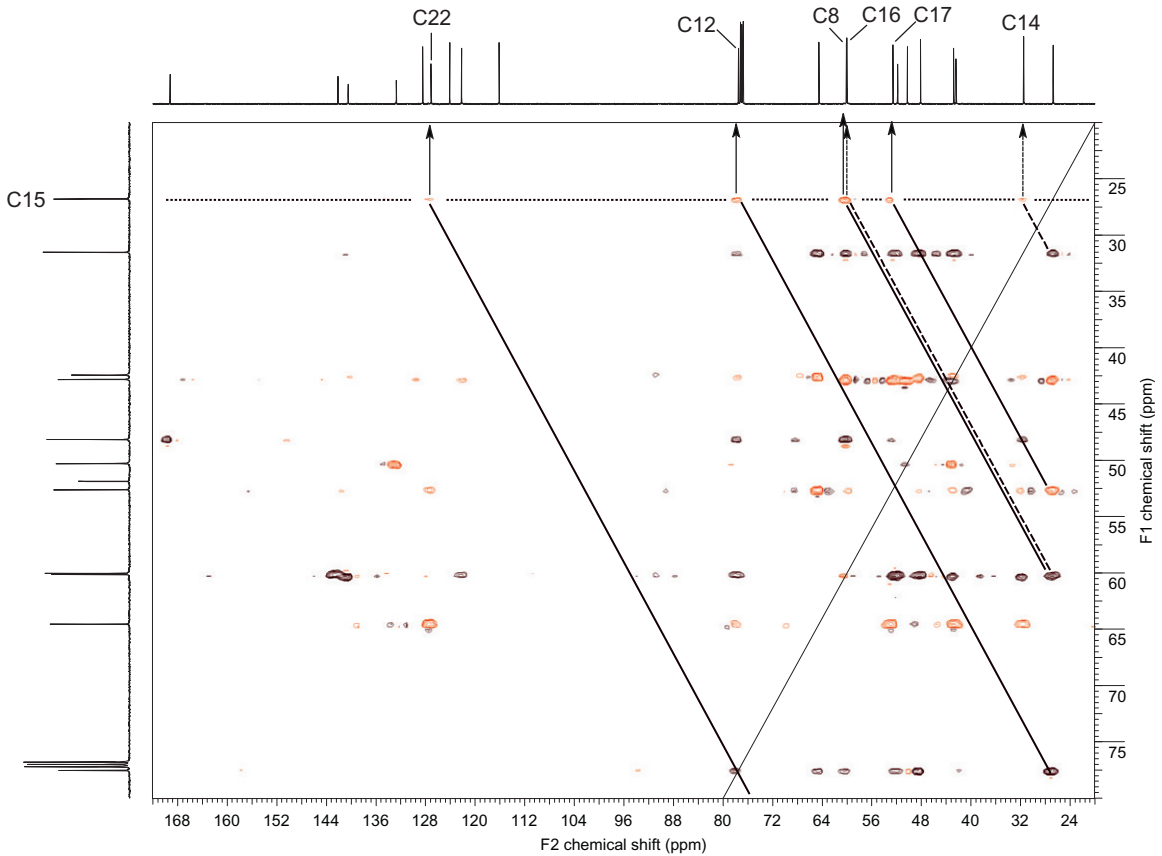
C22
C12
C8
C16
C17
C14
C15
168 160 152 144 136 128 120 112 104 96 88 80 72 64 56 48 40 32 24
F2 chemical shift (ppm)
25 30 35 40 45 50 55 60 65 70 75
F1 chemical shift (ppm)

Once again, the spectrum is diagonally symmetric and retains the phase-encoded multiplicity information of the multiplicity-edited GHSQC spectrum used in the calculation. As noted in Section 5, the pulse sequence used did not cancel the 1,1-ADEQUATE correlations so that correlations from C15 to both adjacent carbons, C14 and C16, were also observed in the spectrum via $^{1}J_{CC}$ in addition to the desired $^{n}J_{CC}$ ($n = 3$) correlations that are equivalent to $^{4}J_{CH}$ correlations in a GHMBC spectrum. Correlations via $^{1}J_{CC}$ are designated by dashed lines perpendicular to the diagonal; correlations via $^{3}J_{CC}$ are denoted by solid lines perpendicular to the diagonal. The utility of calculated HSQC-1,*n*-ADEQUATE spectra remains to be determined and as of the date of this writing, there have been no applications of the method reported in the literature.

8.5. HSQC-1,*n*-ADEQUATE of retrorsine

Analogous to the calculation of the HSQC-1,*n*-ADEQUATE spectrum of strychnine (**1**) (see Section 8.4 and Figure 22), a 7-Hz 1,*n*-ADEQUATE spectrum of retrorsine (**38**) and a multiplicity-edited GHSQC spectrum were co-processed using the GIC method of Snyder and Brüschweiler[95] to afford the HSQC-1,*n*-ADEQUATE spectrum shown in Figure 23. The spectrum is diagonally symmetric for long-range carbon–carbon correlations between protonated carbons and diagonally asymmetric for long-range correlations between protonated and non-protonated carbons. Once again, a significant increase in the signal intensity of the long-range carbon–carbon correlations is observed following covariance processing. Using the region from 95 to 100 ppm as representative noise, the s/n ratio of the 18 h 30 min 7 Hz optimized 1,*n*-ADEQUATE spectrum of retrorsine was 29:1 using the C5a methine carbon resonance as a benchmark. In contrast, the HSQC-1,*n*-ADEQUATE spectrum shown in Figure 23 gave a s/n ratio of 461:1, a 16-fold increase in s/n. Further, the diagonally symmetric nature of the spectrum allowed the identification of long-range carbon–carbon correlations from the C20 methylene to the C13 methine and C14 methylene resonances that were below the threshold of the contour plot at the F_2 frequency of C20 (see inset in Figure 23).

Figure 22 HSQC-1,*n*-ADEQUATE spectrum of strychnine (**1**) calculated from a multiplicity-edited GHSQC and a 1,*n*-ADEQUATE spectrum optimized with $^{1}J_{CH} = 145$ Hz and $^{n}J_{CC} = 5$ Hz.[70] The C15 F_1 chemical shift is designated by the horizontal dotted line. Carbon–carbon correlations, both one-bond and long-range, are diagonally symmetric. The one-bond correlations are designated by the dashed lines perpendicular to the diagonal; long-range $^{3}J_{CC}$ correlations from C15 are denoted by the solid lines perpendicular to the diagonal. The correlations shown are summarized by **27** (see Section 5). Methylene correlations are inverted and are plotted in grey; methine and methyl correlations have positive intensity and are plotted in black.

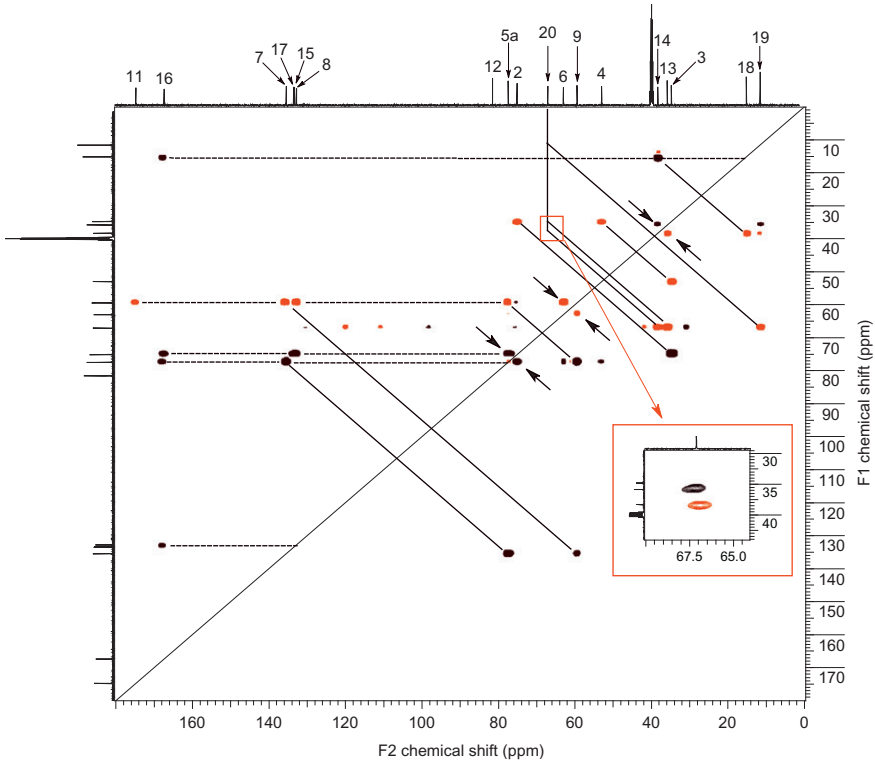

Figure 23 HSQC-1,*n*-ADEQUATE spectrum calculated from the multiplicity-edited GHSQC and 7 Hz optimized 1,*n*-ADEQUATE spectra of retrorsine (**38**).[51] Methylene correlations are inverted and are plotted in grey; methine and methyl correlations have positive intensity and are plotted in black. The spectrum is diagonally symmetric for long-range correlations between protonated carbon pairs and diagonally asymmetric for long-range correlations between protonated and non-protonated carbons. The latter are observed at the F_2 frequency of the non-protonated carbon at the F_1 shift of the protonated carbon. Correlations from the C20 resonance at the C20 chemical shift (66.7 ppm) are below the threshold used to prepare the plot shown. The inset shows the diagonally symmetric correlations to the C13 and C14 methine and methylene correlations. In like manner, a correlation is also observed from the 19-methyl resonance to C20 that is below the threshold of the contour plot (not shown). Nevertheless, correlations can be identified by virtue of the diagonal symmetry of the spectrum, allowing weaker counterparts to be readily identified thereby confirming the correlation.

It is logical to assume that the enhanced s/n ratio for co-processed 1,*n*-ADEQUATE data, coupled with the diagonally symmetric nature of the HSQC-1,*n*-ADEQUATE spectrum will allow the acquisition of useful spectral data for smaller samples or in shorter periods of time than would otherwise be possible. Indeed, useable HSQC-1,*n*-ADEQUATE spectra were obtained for 1,*n*-ADEQUATE data recorded in just over 9 h.

9. CONCLUSIONS

The 1,1-ADEQUATE experiment provides a method for the unequivocal identification of carbons adjacent to the carbon of a proton–carbon heteronuclide resonant pair. The method operates for both protonated and non-protonated adjacent carbons, unlike experiments such as 2J3J-HMBC,[12] H2BC,[13,14] and HAT-H2BC[15] that operate only for protonated adjacent carbon resonances. The low sensitivity of the 1,1-ADEQUATE experiment can, in part, be circumvented by resorting to cryogenic NMR probes.[27,46,48] Data acquisition times and/or sample size requirements can also be reduced by taking advantage of the sensitivity gain inherent in UIC or GIC co-processing of the data with a multiplicity-edited GHSQC spectrum.[49,50] While resonance overlaps in the proton spectrum can lead to artifact responses in HSQC-1,1-ADEQUATE spectra, the spectra can still be successfully employed to track out the carbon skeleton of molecules with greater facility than the 1,1-ADEQUATE experiment itself or with alternatives such as HSQC-TOCSY. To at least some extent, these factors can be expected to promote somewhat greater utilization of at least the 1,1- and 1,*n*-ADEQUATE experiments in the future.

There have been only a few reported applications of 1,*n*-ADEQUATE data and a dearth of *n*,1-, and *m*,*n*-ADEQUATE applications aside from the initial reported applications during the development of the experiments and the elucidation of the structure of 5,6-dihydrolamellarin (**3**).[38] The 1,*n*-ADEQUATE experiment has been sparsely utilized, first in the characterization of a highly substituted aromatic compound employed in the synthesis of euglobal-G1 (**29**) and euglobal-G2 (**30**) (see Section 5.2).[62] More recently, 1,*n*-ADEQUATE has also been employed as a part of the strategy for the elucidation of the structure of a series of mono- and dibromophakellin (**34** and **35**) and isophakellin (**36** and **37**) alkaloids (see Section 5.4).[47] In part, the lack of applications of the 1,*n*-ADEQUATE experiment can likely be attributed to the considerably lower sensitivity of the experiment relative even to the 1,1-ADEQUATE experiment. However, given the significant gain in s/n that can be attained through UIC or GIC processing of experiments such as 1,1- or 1,*n*-ADEQUATE with a multiplicity-edited GHSQC spectrum, more applications of the experiment in the form of hyphenated HSQC-1,*n*-ADEQUATE spectra may be seen in the future. The almost complete lack of applications of the *n*,1- and *m*,*n*-ADEQUATE experiments can be attributed, in part, to correspondingly lower sensitivity than the 1,*n*-ADEQUATE experiment coupled with the fact that the signal is detected in the second frequency domain at the DQ frequency of the correlated carbon resonances making the interpretation of the data considerably more challenging than for 1,1- or 1,*n*-ADEQUATE spectra. Further, since each carbon–carbon correlation pathway gives rise to a response at a

separate F_1 frequency serving to further complicate the interpretation of the data, it is unlikely that either of these experiments will see very many potential applications in the future.

REFERENCES

1. W. F. Reynolds and R. G. Enriquez, *J. Nat. Prod.*, 2002, **65,** 221–244. G. E. Martin, C. E. Hadden and D. J. Russell, Solution NMR spectroscopy. *in*: Handbook of Spectroscopy, G. Gauglitz and T. Vo-Dinh (eds.), *In* 2003, Vol. 1, Wiley-VCH, 2003, pp. 209–268. N. Bross-Walch, T. Kühn, D. Moskau and O. Zerbe, *Chem. Biodiversity*, 2005, **2,** 147–177L. L. Lohr, B. L. Marquez and G. E. Martin, Nuclear magnetic resonance spectroscopy. *in*: Comprehensive Analytical Chemistry, S. Ahuja and N. Jespersen (eds.), *In* 2007, Vol. 47, Elsevier, Amsterdam, 2007, pp. 259–318.
2. T. D. W. Claridge, High-Resolution NMR Techniques in Organic Chemistry. Pergamon, Amsterdam, 1999, pp. 224–239.
3. W. F. Reynolds, S. McLean, L.-L. Tay, M. Yu, R. G. Enriquez, D. M. Estwick and K. O. Pascoe, *Magn. Reson. Chem.*, 1997, **35,** 455–462.
4. A. Bax and M. F. Summers, *J. Am. Chem. Soc.*, 1986, **108,** 2093.
5. R. C. Crouch, W. Llanos, K. G. Mehr, C. E. Hadden, D. J. Russell and G. E. Martin, *Magn. Reson. Chem.*, 2001, **39,** 555–563.
6. G. E. Martin and C. E. Hadden, *Magn. Reson. Chem.*, 2000, **38,** 251–256.
7. G. E. Martin and A. J. Williams, Long-range ^{1}H–^{15}N heteronuclear shift correlation. *in*: Annual Reports on NMR Spectroscopy, G. A. Webb (ed.), 2005, Vol. 55, , 2005, pp. 1–119.
8. R. Marek and A. Lyčka, *Curr. Org. Chem.*, 2002, **6,** 35–66.
9. R. Marek, A. Lyčka, E. Kohlemainen, E. Sievanen and J. Toušek, *Curr. Org. Chem.*, 2007, **11,** 1154–1205.
10. G. E. Martin, M. Solntseva and A. J. Williams, Applications of ^{15}N NMR spectroscopy in alkaloid chemistry. *in*: Modern Alkaloids: Structure, Isolation, Synthesis and Biology, E. Fattorusso and O. Taglialatela-Scafati (eds.), Wiley, New York, 2008, pp. 409–476.
11. W. F. Reynolds, D. W. Hughes, M. Perpick-Dumont and R. G. Enriquez, *J. Magn. Reson.*, 1985, **63,** 413–417.
12. V. V. Krishnamurthy, D. J. Russell, C. E. Hadden and G. E. Martin, *J. Magn. Reson.*, 2000, **146,** 232–239.
13. N. T. Nyberg, J. O. Duus and O. W. Sørensen, *J. Am. Chem. Soc.*, 2005, **127,** 6154–6155.
14. N. T. Nyberg, J. O. Duus and O. W. Sørensen, *Magn. Reson. Chem.*, 2005, **43,** 971–974.
15. A. J. Benie and O. W. Sørensen, *J. Magn. Reson.*, 2007, **184,** 315–321.
16. R. Wagner and S. Berger, *Magn. Reson. Chem.*, 1998, **36**(S19), S44–S46.
17. G. E. Martin, C. E. Hadden, R. C. Crouch and V. V. Krishnamurthy, *Magn. Reson. Chem.*, 1999, **37,** 517–528.
18. C. E. Hadden, G. E. Martin and V. V. Krishnamurthy, *J. Magn. Reson.*, 1999, **140,** 274–280.
19. C. E. Hadden, G. E. Martin and V. V. Krishnamurthy, *Magn. Reson. Chem.*, 2000, **38,** 143–147.
20. G. E. Martin, Qualitative and quantitative exploitation of heteronuclear coupling constants. *in*: Annual Reports on NMR Spectroscopy, G. A. Webb (ed.), *In* 2002, Vol. 46, Academic Press, New York, 2002, pp. 37–100.
21. A. Bax, R. Freeman and T. A. Frenkiel, *J. Am. Chem. Soc.*, 1981, **103,** 2102–2104.
22. D. L. Turner, *J. Magn. Reson.*, 1983, **49,** 175–178.
23. A. Bax and T. H. Mareci, *J. Magn. Reson.*, 1983, **535,** 360–363.
24. G. Bodenhausen, H. Kogler and R. R. Ernst, *J. Magn. Reson.*, 1984, **58,** 370–399.

25. G. E. Martin, Cryogenic NMR probes: applications. *in*: Encyclopedia of Nuclear Magnetic Resonance, Vol. 9: Advances in NMR, D. M. Grant and R. K. Harris (eds.), 2002, pp. 33–35.
26. G. E. Martin, Microprobes and methodologies for spectral assignments: applications. *in*: Encyclopedia of Nuclear Magnetic Resonance, Vol. 9: Advances in NMR, D. M. Grant and R. K. Harris (eds.), 2002, pp. 98–112.
27. G. E. Martin, Small-volume and high-sensitivity NMR probes. *in*: Annual Reports on NMR Spectroscopy, G. A. Webb (ed.), 2005, Vol. 56, , 2005, pp. 1–96.
28. P. Keller and K. Vogele, *J. Magn. Reson.*, 1986, **68,** 389–392.
29. O. W. Sørensen, R. Freeman, T. A. Frenkiel, T. H. Mareci and R. Shuck, *J. Magn. Reson.*, 1982, **46,** 180–184.
30. S. W. Sparks and P. D. Ellis, *J. Magn. Reson.*, 1985, **62,** 1–11.
31. H. Kessler, W. Bermel and C. Griesinger, *J. Magn. Reson.*, 1985, **62,** 573–579.
32. H. Kessler, W. Bermel, C. Griesinger, P. Hertl, E. Streich and H. Rieker, *J. Org. Chem.*, 1986, **51,** 596–612.
33. Y. Q. Gosser, K. P. Howard and J. H. Prestegard, *J. Magn. Reson.*, 1993, **101B,** 126–133.
34. J. Chung, J. R. Tolman, K. P. Howard and J. H. Prestegard, *J. Magn. Reson.*, 1993, **102B,** 137–147.
35. J. K. Pratum and B. S. Moore, *J. Magn. Reson.*, 1993, **102B,** 91–97.
36. J. Weigelt and G. Otting, *J. Magn. Reson.*, 1995, **113A,** 128–130.
37. M. Köck, B. Rief, W. Fenical and C. Griesinger, *Tetrahedron Lett.*, 1996, **37,** 363–366.
38. B. Reif, M. Köck, R. Kerssebaum, H. Kang, W. Fenical and C. Griesinger, *J. Magn. Reson.*, 1996, **118A,** 282–285.
39. R. T. Williamson, B. L. Marquez, W. H. Gerwick and F. E. Koehn, *Magn. Reson. Chem.*, 2001, **39,** 544–548.
40. M. Köck, R. Kerssebaum and W. Bermel, *Magn. Reson. Chem.*, 2003, **41,** 65–69.
41. K. Kövér and P. Forgó, *J. Magn. Reson.*, 2004, **166,** 47–52.
42. C. M. Thiele and W. Bermel, *Magn. Reson. Chem.*, 2007, **45,** 889–894.
43. T. Parella and F. Sánchez-Ferrando, *J. Magn. Reson.*, 2004, **166,** 123–128.
44. V. Wray, Carbon–carbon coupling constants: a compilation of data and a practical guide. *In* Progress in Nuclear Magnetic Resonance Spectroscopy 1979, Vol. 13, 1979, pp. 177–256.
45. K. Komieiska-Trela, One-bond ^{13}C–^{13}C spin–spin coupling constants. *in*: Annual Reports on NMR Spectroscopy, G. A. Webb (ed.), 1995, Vol. 30, Academic Press, New York, 1995, pp. 131–230.
46. S. Cheatham, M. Kline, R. R. Sasaki, K. Blinov, M. E. Elyashberg and S. G. Molodtsov, *Magn. Reson. Chem.*, 2010, **48,** 571–574.
47. S. W. Myer and M. Köck, *J. Nat. Prod.*, 2008, **71,** 1524–1529.
48. B. D. Hilton and G. E. Martin, *J. Nat. Prod.*, 2010, **73,** 1465–1469.
49. G. E. Martin, B. D. Hilton and K. A. Blinov, *Magn. Reson. Chem.*, 2011, **49,** 248–252.
50. G. E. Martin, B. D. Hilton, M. R. Willcott, III and K. A. Blinov, *Magn. Reson. Chem.*, 2011, **49,** 350–358.
51. G. E. Martin, B. D. Hilton and K. A. Blinov, *J. Nat. Prod.*, submitted for publication, 2011.
52. D. A. Snyder and R. Brüschweiler, Multidimensional correlation spectroscopy by covariance NMR. *in*: Multidimensional NMR Methods in the Solution State, G. A. Morris and J. W. Emsley (eds.), John Wiley and Sons, Ltd., Chichester, 2010, pp. 97–105.
53. T. Lindel, J. Junker and M. Köck, *J. Mol. Model.*, 1997, **3,** 364–368.
54. B. Reif, M. Köck, R. Kerssebaum, J. Schleucher and C. Griesinger, *J. Magn. Reson.*, 1996, **112B,** 295–301.
55. J. Junker, W. Maier, T. Lindel and M. Köck, *Org. Lett.*, 1999, **1,** 737–740.

56. M. Knaack, P. Emig, J. W. Bats, M. Kiesel, A. Müller and E. Günther, *Eur. J. Org. Chem.*, 3843–3847.
57. R. T. Williamson, A. Boulanger, A. Vulpanovici, M. A. Roberts and W. H. Gerwick, *J. Org. Chem.*, 2002, **67,** 7927–7936.
58. T. Okabe, K. Nomoto, H. Funabashi, S. Okuda, H. Suzuki and N. Tanaka, *J. Antibiot.*, 1985, **38,** 1333–1336.
59. P.-M. Leo, C. Morin and C. Philouze, *Org. Lett.*, 2002, **4,** 2711–2714.
60. K. Tatsuta, H. Ozeki, M. Yamaguchi, M. Tanaka and T. Okui, *Tetrahedron Lett.*, 1990, **31,** 5495–5498.
61. R. T. Williamson, L. A. McDonald, L. R. Barbieri and G. T. Carter, *Org. Lett.*, 2002, **4,** 4659–4662.
62. H. He, J. E. Janso, R. T. Williamson, H. Y. Yang and G. T. Carter, *J. Org. Chem.*, 2003, **68,** 6079–6082.
63. E. Rubio, I. Merino, A.-B. Garcia, M.-P. Cabal, C. Ribas and M. Bayod-Jasanda, *Magn. Reson. Chem.*, 2005, **43,** 269–282.
64. D. Godevac, B. Mandić, V. Vajs, N. Menkković, S. Macura and S. Milosavljević, *Magn. Reson. Chem.*, 2006, **44,** 731–735.
65. L. H. Abdeljebber, M. Humam, P. Christen, D. Jennerat, B. Vitorg, S. Amzazl, A. Benjouad, K. Hostettman and K. Bekkouche, *Helv. Chim. Acta*, 2007, **90,** 346–352.
66. H. V. Dang, N. S. Habib, T. Kappe, K. Zangger and W. Stadlbauer, *J. Heterocyclic Chem.*, 2007, **44,** 161–165.
67. A. D. Wright, J. L. Nielson, D. M. Tapiolas, C. A. Motti, S. P. B. Ovenden, P. S. Kearns and C. H. Liptrot, *Mar. Drugs*, 2009, **7,** 565–575.
68. H. I. Januar, E. Chasanah, C. A. Motti, D. M. Tapiolas, C. H. Liptot and A. D. Wright, *Mar. Drugs*, 2010, **8,** 2142–2152.
69. J. Schraml, R. Kubec and P. Kučerová, *Magn. Reson. Chem.*, 2011, **49,** 147–150.
70. G. E. Martin, B. D. Hilton, M. R. Willcott, III and K. A. Blinov, *Magn. Reson. Chem.*, **49**, in press, 2011.
71. M. Köck, B. Reif, M. Gerlach and M. Reggelin, *Molecules*, 1996, **1,** 41–45.
72. B. Reif, M. Kock, R. Kerssebaum, J. Schleucher and C. Griesinger, *J. Magn. Reson.*, 1996, **112B,** 295–301.
73. L. B. Krividin and E. W. Della, *Prog. NMR Spectrosc.*, 1991, **23,** 301–610.
74. P. Keller and K. Bogele, *J. Magn. Reson.*, 1986, **68,** 389–392.
75. T. K. Pratum and B. S. Moore, *J. Magn. Reson.*, 1993, **102B,** 91–97.
76. J. Wright and G. Otting, *J. Magn. Reson.*, 1995, **113A,** 128–130.
77. G. E. Martin, C. W. Anklin and W. Bermel, unpublished results.
78. G. E. Martin, unpublished results.
79. R. Brüschweiler and F. Zhang, *J. Chem. Phys.*, 2004, **120,** 5253–5260.
80. R. Brüschweiler, *J. Chem. Phys.*, 2004, **121,** 409–414.
81. N. Trbovic, S. Smirnov, F. Zhang and R. Brüschweiler, *J. Magn. Reson.*, 2004, **171,** 277–283.
82. F. Zhang and R. Brüschweiler, *J. Am. Chem. Soc.*, 2004, **126,** 13180–13181.
83. K. A. Blinov, N. I. Larin, W. J. Williams, K. A. Mills and G. E. Martin, *J. Heterocyclic Chem.*, 2006, **43,** 163–166.
84. K. A. Blinov, N. I. Larin, A. J. Williams, M. Zell and G. E. Martin, *Magn. Reson. Chem.*, 2006, **44,** 107–109.
85. Ē. Kupče and R. Freeman, *J. Am. Chem. Soc.*, 2008, **128,** 6020–6021.
86. R. Freeman and Ē. Kupče, Multidimensional NMR by projection-reconstruction. *in*: Multidimensional NMR Methods in the Solution State, G. A. Morris and J. W. Emsley (eds.), John Wiley and Sons, Ltd., Chichester, 2010, pp. 73–83.
87. W. P. Aue, E. Barotholdi and R. R. Ernst, *J. Chem. Phys.*, 1976, **64,** 2229–2251.

88. G. E. Martin, B. D. Hilton, P. A. Irish, K. A. Blinov and A. J. Williams, *J. Nat. Prod.*, 2007, **70,** 1393–1396.
89. G. E. Martin, B. D. Hilton, K. A. Blinov and A. J. Williams, *J. Heterocyclic Chem.*, 2008, **45,** 1109–1113.
90. K. A. Blinov, A. J. Williams, B. D. Hilton, P. A. Irish and G. E. Martin, *Magn. Reson. Chem.*, 2007, **48,** 544–546.
91. G. E. Martin, P. A. Irish, B. D. Hilton, K. A. Blinov and A. J. Williams, *Magn. Reson. Chem.*, 2007, **45,** 624–627.
92. G. E. Martin, B. D. Hilton, P. A. Irish, K. A. Blinov and A. J. Williams, *Magn. Reson. Chem.*, 2007, **45,** 883–888.
93. G. E. Martin, B. D. Hilton, P. A. Irish, K. A. Blinov and A. J. Williams, *J. Heterocyclic Chem.*, 2007, **44,** 1219–1222.
94. G. E. Martin, B. D. Hilton, K. A. Blinov and A. J. Williams, *J. Nat. Prod.*, 2007, **70,** 1966–1970.
95. D. A. Snyder and R. Brüschweiler, *J. Chem. Phys. A*, 2009, **113,** 12898–12903.
96. G. E. Martin, *J. Heterocyclic Chem.*, 2011, **48,** in press.
97. G. E. Martin and D. Sunseri, *J. Pharm. Biomed. Anal.*, 2011, **55,** 895–901.
98. G. E. Martin, B. D. Hilton, K. A. Blinov and A. J. Williams, *Magn. Reson. Chem.*, 2008, **46,** 138–143.
99. G. E. Martin, W. Feng and B. D. Hilton, *J. Heterocyclic Chem.*, 2011, **48,** 948–951.
100. B. D. Hilton and G. E. Martin, *J. Heterocyclic Chem.*, 2011, **48,** in press.

CHAPTER 6

Recent Developments in HMBC Studies

Julien Furrer

Contents

1. Introduction 294
2. Basic Theory-Analysis of the Basic HMBC Experiment 296
   - 2.1. The standard HMBC pulse sequence 296
   - 2.2. Analysis of the basic HMBC pulse sequence: residual $^{1}J_{CH}$ signals 296
   - 2.3. Analysis of the standard HMBC pulse sequence: missing and weak long-range correlations 299
   - 2.4. A typical example 300
3. Suppression of Direct $^{1}J_{CH}$ Responses 301
   - 3.1. The low-pass J filters 302
   - 3.2. Other recent purging sequences for efficient $^{1}J_{CH}$ suppression 309
4. Enhancing Weakly or Missing $^{n}J_{CH}$ Correlations 317
   - 4.1. Accordion optimized HMBC experiments 317
   - 4.2. Broadband HMBC 318
   - 4.3. *J*-compensated HMBC 321
5. Differentiating Between $^{2}J_{CH}$ and $^{3,4}J_{CH}$ Connectivities 324
   - 5.1. The ^{2}J,^{3}J-HMBC experiment 324
   - 5.2. The HMBC–RELAY experiment 326
   - 5.3. The H2BC experiment: Suppressing three or higher correlations 329
6. Editing HMBC Spectra 332
   - 6.1. The edited HMBC 332
   - 6.2. The HAT-HMBC experiment 334
7. Improving the F_1 Resolution 335

Department für Chemie und Biochemie, Universität Bern, Freiestrasse 3, Bern, Switzerland

Annual Reports on NMR Spectroscopy, Volume 74
ISSN 0066-4103, DOI: 10.1016/B978-0-08-097072-1.00006-6

7.1. Constant-time HMBC experiments 335
7.2. The 10-ppm HMBC experiment 335
7.3. Combining 10- and 9.9-ppm HMBC experiments 338
7.4. The DENA element 339
8. Accelerating HMBC Experiments 340
8.1. Principles of fast experiments 340
8.2. The IMPACT-HMBC experiment 341
8.3. Other methods for accelerating HMBC measurements 345
9. Measurement of Long-Range Coupling Constants 347
10. Time-Shared (TS) HMBC Experiments 348
10.1. The CN-HMBC experiment: concerted recording of $^{1}H–^{13}C$ and $^{1}H–^{15}N$ HMBC spectra 348
11. Conclusion and Outlook 349
Acknowledgments 351
References 351

Abstract Since its introduction, the HMBC—Heteronuclear Multiple Bond Correlation—experiment has modernized NMR spectroscopy in small to medium molecule applications. The experiment provides information about which protons are near to different carbons or to another heteronucleus, but not directly bonded to. This experiment can provide a huge amount of information about molecular structure, since the long-range proton–carbon correlations can include quaternary carbons, in addition to protonated carbons. Impressive examples for structure elucidation of organic molecules, peptides, or natural products have been published in the last 20 years. After a short introduction into the basic theory, this manuscript will give to the reader an overview of the last developments and improvements of HMBC experiments, ranging from pulse sequences dedicated for suppressing one-bond correlations to HMBC pulse sequences that allow distinguishing between $^{2}J_{CH}$ and $^{3}J_{CH}$ cross-peaks.

Key Words: NMR, Heteronuclear Long-range correlation, HMBC, CT-HMBC, ACCORD-HMBC, IMPEACH-MBC, BIRD-HMBC, G-BIRD-HMBC, CIGAR-HMBC, IMPACT-HMBC, TS-HMBC, Broadband-HMBC, H2BC, edited HMBC, 10-ppm HMBC, $^{1}J_{CH}$ artefacts suppression, Spectral editing

1. INTRODUCTION

The structure determination of organic molecules in solution—constitution, configuration, and conformation—is probably the most important application of high-resolution NMR spectroscopy. Among all existing

two-dimensional (2D) experiments, the Heteronuclear Multiple Bond Correlation (HMBC) NMR experiment[1] has probably been the most widely used 2D heteronuclear NMR method in the field of structural elucidation of complex organic molecular structures.[2] Nowadays, it has become the most popular techniques for multiple-bond (or long-range) heteronuclear chemical shift correlation. It provides a wealth of structural information, and eventually the full assignment, through long-range correlation signals for ^{13}C, ^{1}H spin pairs. It can span quaternary carbons or heteronuclei, providing a way to link different molecular fragments into a complete structure. It has therefore rapidly become the standard way of detecting the presence of long-range couplings in small- to medium-size molecules and for building and checking molecular skeletons. This experiment is ideally suited when a carbonyl moiety or other non-protonated carbon group is involved.

The HMBC is a fascinating experiment in the sense that it provides valuable information through selection of the magnetization associated with small heteronuclear long-range couplings, while the magnetization associated with large heteronuclear one-bond couplings can be efficiently eliminated.[1] One of the breakthroughs in the development of the HMBC experiment was the introduction of pulsed field gradients (PFGs) in the early 1990s.[3–9] Using PFGs, high quality spectra, can be obtained in standard conditions, allowing the analysis of very small but informative cross-peaks. Today, the advantages offered by the incorporation of PFGs into high-resolution NMR pulse sequences, combined with advanced software tools available to acquire and process multidimensional NMR experiments, have allowed to record and process the HMBC sequence with PFGs just by clicking a button or executing a predefined macro, making it available to the non-experienced NMR users and for being used with automatic sample changers.

Based on a different approach than the widespread HSQC sequence,[10,11] the basic 2D HMBC pulse sequence is closely related to the HMQC pulse sequence[12–14] but incorporates the following modifications. A low-pass *J*-filter[15] (consisting of a delay $\tau - 90°(^{13}C)$ cluster) is included directly after the initial $90° \, ^{1}H$ pulse to minimize direct $^{1}J_{CH}$ responses. As discussed before, the long-range coupling evolution delay Δ is optimized to $0.5/^{n}J_{CH}$. A refocusing period is usually omitted, for limiting signal loss due to T_2 relaxation. Proton acquisition is performed without ^{13}C decoupling, although this remains in principle possible.[16] In spite of well-known deficiencies, such as weakly observed or missing long-range correlations and unwanted residual $^{1}J_{CH}$ signals, the basic HMBC experiment has been retained over the years and widely used in analytical laboratories. Only from the late 1990s there has been a surge of interest in the development of new inverse-detected long-range correlation experiments.

Recent results have been summarized in a number of articles, especially in this journal.[17–19] This review will focus on newly developed HMBC pulse sequences and application on small to medium-sized organic molecules. After a short introduction into basic theory, a selection of pulse sequences and a look at the large variety of applications will complete the overview of the HMBC experiment. Finally, a brief summary and outlook to future perspectives of HMBC will be given.

2. BASIC THEORY-ANALYSIS OF THE BASIC HMBC EXPERIMENT

2.1. The standard HMBC pulse sequence

The pulse sequence for a standard gradient-selected HMBC (gsHMBC)[20] experiment is shown in Figure 1. The HMBC experiment is closely related to HMQC and uses the same principles with some differences. For analyzing the HMBC pulse sequence in terms of product operators,[23] we should now separate the magnetization which evolves under the one-bond heteronuclear scalar coupling $^1J_{CH}$, which will be termed H^d in the following, from the magnetization which evolves under the long-range scalar couplings $^nJ_{CH}$, H^r.[24] The whole pulse sequence can be analyzed as briefly presented below starting from point 1 to 6.

2.2. Analysis of the basic HMBC pulse sequence: residual $^1J_{CH}$ signals

2.2.1. Evolution of the H^r magnetization under the heteronuclear long-range scalar coupling $^nJ_{CH}$

The analysis is straightforward for the H^r coherence associated with heteronuclear long-range couplings. For simplifying the calculations, we assume that the long-range heteronuclear coupling $^nJ_{CH}$ exactly matches the condition $\Delta = 0.5/(^nJ_{HC})$.

$(1 \rightarrow 2)$

$$\begin{aligned} H_Z^r \xrightarrow{(90^\circ)H_X} -H_Y^r \xrightarrow{\pi^1 J_{CH}\tau 2H_Z C_Z} & -H_Y^r \cos(\pi^n J_{CH}\tau) + 2H_X^r C_Z \sin(\pi^n J_{CH}\tau) \\ \xrightarrow{\tau=0.5/(^1J_{HC})} & -H_Y^r \xrightarrow{(90^\circ)C_X} -H_Y^r \end{aligned} \tag{1}$$

$(2 \rightarrow 3)$

$$\begin{aligned} -H_Y^r \xrightarrow{\pi^n J_{CH}\Delta 2H_Z C_Z} & -H_Y^r \cos(\pi^n J_{CH}\Delta) \\ & + 2H_X^r C_Z \sin(\pi^n J_{CH}\Delta) \xrightarrow{\Delta=0.5/(^nJ_{HC})} 2H_X^r C_Z \end{aligned} \tag{2}$$

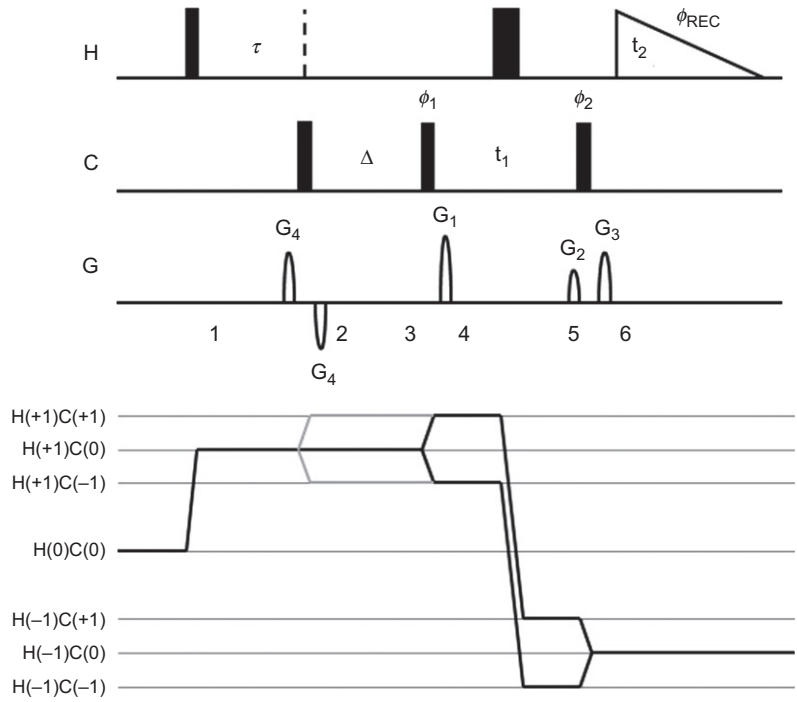

Figure 1 Pulse sequence of a basic gradient-selected $^{1}H–^{13}C$ HMBC experiment and the corresponding coherence transfer diagram[21,22] of the magnetization evolving under the long-range scalar couplings $^{n}J_{CH}$, H^{r}. Thin bars represent 90° pulses, thick bars 180° pulses. Δ is the long-range coupling evolution delays and is set to an average value $0.5/^{n}J_{CHave}$. τ is the one-bond coupling evolution delay and should be set to an average value $0.5/^{1}J_{CHave}$. Gradient pulses are represented by sine-shaped and denoted by G_1–G_4. They can be for instance applied in the ratio: 50:30:40.1:35. The following basic phase cycle is sufficient for obtaining clean spectra: $\phi_1 = x, -x$; $\phi_2 = x, x, -x, -x$; $\phi_{rec} = x, -x, -x, x$. Phases not shown are applied along the x-axis.

During the delay Δ, the proton coherence associated with long-range heteronuclear couplings is fully converted into anti-phase (AP) magnetization. The second 90° pulse applied on the ^{13}C channel converts this AP magnetization into heteronuclear multiple quantum coherences ($2H_XC_Y$).

$(3 \rightarrow 4)$

$$-2H_X^rC_Z \xrightarrow{(90^\circ)C_X} 2H_X^rC_Y \tag{3}$$

The next step in the HMBC sequence is the t_1 evolution period, during which the magnetization of interest is labelled with the ^{13}C chemical shift information.

$(4 \rightarrow 5)$

$$-2H_X^r C_Y \xrightarrow{t_1/2-(180^\circ)H_X-t_1/2} -2H_X^r(C_Y \cos\Omega_C t_1 + C_X \sin\Omega_C t_1) \tag{4}$$

The last 90° pulse applied on the ^{13}C channel is aimed to convert the heteronuclear multiple quantum magnetization into observable proton AP magnetization.

$(5 \rightarrow 6)$

$$-2H_X^r(C_Y \cos\Omega_C t_1 + C_X \sin\Omega_C t_1) \xrightarrow{(90^\circ)C_X} -2H_X^r(C_Z \cos\Omega_C t_1 + C_X \sin\Omega_C t_1) \tag{5}$$

During the acquisition time t_2, the AP proton magnetization term $2H_XC_Z$ will be converted into observable proton magnetization.

$$-2H_X^r C_Z \cos\Omega_C t_1 \xrightarrow{\pi^n J_{CH} t_2 2H_Z C_Z} \xrightarrow{\Omega_H H_Z t_2} -H_Y^r \cos(\Omega_C t_1)\sin(\pi^n J_{CH} t_2)\cos(\Omega_H t_2) + \text{non detectable terms} \tag{6}$$

The observable ^1H signals that originate from ^1H–^{13}C multiple quantum coherences are modulated by ^{13}C chemical shift. These terms produce cross-peaks at δ_C in F_1 and at δ_H in F_2 split into a doublet due to the long-range $^nJ_{CH}$ couplings. These peaks are expected cross-peaks in the HMBC spectrum as they indicate correlations between carbon and remote protons through the long-range $^nJ_{CH}$ couplings. As HMBC experiments are recorded without ^{13}C broadband decoupling, the ^1H signals are also modulated by long-range $^nJ_{CH}$ heteronuclear couplings as well as potential homonuclear proton–proton $^nJ_{HH}$ couplings. Signals of proton–carbon spin pairs are theoretically completely removed during the low-pass J filter.

However, molecules are made of different chemical groups and therefore a wide range of one-bond heteronuclear $^1J_{CH}$ couplings coexist rather than one single value. Consequently, for most of the carbon–proton spin pairs, the delay τ effectively set in the experiment will not match the condition $\tau = 0.5/(^1J_{CH})$. A considerable amount of transverse ^1H magnetization may then survive the filtering process, depending on the violation degree.

2.2.2. Evolution of the H^d magnetization under the one-bond scalar coupling $^1J_{CH}$

$(1 \rightarrow 2)$

$$\begin{aligned} H_Z^d \xrightarrow{(90^\circ)H_X} -H_Y^d \xrightarrow{\pi^1 J_{CH}\tau 2H_Z C_Z} -H_Y^d \cos(\pi^1 J_{CH}\tau) + 2H_X^d C_Z \sin(\pi^1 J_{CH}\tau) \\ \xrightarrow{(90^\circ)C_X} -H_Y^d \cos(\pi^1 J_{CH}\tau) - 2H_X^d C_Y \sin(\pi^1 J_{CH}\tau). \end{aligned} \tag{7}$$

The behaviour of the $2H_XC_Y$ heteronuclear multiple quantum term has been described above. The difference now is that this term is attenuated by the factor $\sin(\pi J_{CH}\tau)$. The spurious transverse H^d magnetization will survive the low-pass J filter, even after the dephasing G_4 gradient pair, because this coherence matches the condition for a gradient echo to occur. In the subsequent parts of the HMBC sequence, this spurious proton H^d term will evolve like the desired proton H^r magnetization associated with heteronuclear long-range couplings:

(2 → 6)

$$\cdots \xrightarrow{(90^\circ)C_X} -2H_X^d \cos\left(\pi^1 J_{CH}\tau\right) \sin\left(\pi^1 J_{CH}\Delta\right)\left(C_Z \cos\Omega_C t_1 + C_X \sin\Omega_C t_1\right). \quad (8)$$

During the acquisition time t_2, the term $-2H_X{}^dC_Z$ will be converted into observable proton magnetization.

As HMBC experiments are recorded without ^{13}C broadband decoupling, these ^1H signals are also modulated by one-bond $^1J_{CH}$ heteronuclear couplings as well as potential homonuclear proton–proton $^nJ_{HH}$ couplings. These terms produce cross-peaks at δ_C in F_1 and at δ_H in F_2 split into a doublet due to the direct heteronuclear coupling $^1J_{CH}$. These cross-peaks are not desired in HMBC spectra as they indicate a correlation between a carbon and its directly bound proton H through the one-bond heteronuclear coupling $^1J_{CH}$. Such a correlation is found in HSQC/HMQC spectra and is usually called a $^1J_{CH}$ artefact in HMBC spectra.

It can be seen that those terms (Equation (8)) contain additional attenuation sine and cosine factors, due to the evolution of the one-bond heteronuclear coupling during the delays τ and Δ. The resulting spurious cross-peaks should in principle be less intense than the true HMBC cross-peaks. The absolute intensity of the signals can be in theory a criterion to discriminate between long-range cross-peaks and $^1J_{CH}$ artefacts. However, the intensity of long-range cross-peaks $^nJ_{CH}$ is also dependent on the evolution during Δ, and frequently the discrimination between weak long-range responses $^nJ_{CH}$ and unwanted $^1J_{CH}$ artefacts remains tricky or even impossible. The occurrence of direct $^1J_{CH}$ responses in the final spectrum prevents the use of ^{13}C broadband decoupling.

2.3. Analysis of the standard HMBC pulse sequence: missing and weak long-range correlations

The second drawback of the basic HMBC experiment is due to the actual range of $^nJ_{CH}$ spin coupling constants, which vary from 1 to 50 Hz. Usually HMBC spectra are recorded with a compromise by setting the corresponding delay in the sequence to about 70 ms to allow an optimum transfer for correlation signals where the spin coupling constant is about 7 Hz. Under these conditions, several important connectivities may yield

only very small correlation signals or are completely lost. The analyses of the basic HMBC sequence have shown that the proton coherence associated with long-range heteronuclear couplings evolve during the delay Δ as:

$$-\mathrm{H}_Y^{\mathrm{r}} \xrightarrow{\pi^{\mathrm{n}} J_{\mathrm{CH}} \Delta 2\mathrm{H}_Z\mathrm{C}_Z} -\mathrm{H}_Y^{\mathrm{r}} \cos\left(\pi^{\mathrm{n}} J_{\mathrm{CH}} \Delta\right) + 2\mathrm{H}_X^{\mathrm{r}}\mathrm{C}_Z \sin\left(\pi^{\mathrm{n}} J_{\mathrm{CH}} \Delta\right) \xrightarrow{\Delta = 0.5/\left({}^{\mathrm{n}}J_{\mathrm{HC}}\right)} 2\mathrm{H}_X^{\mathrm{r}}\mathrm{C}_Z. \quad (9)$$

During the delay Δ, the proton coherence associated with long-range heteronuclear couplings is fully converted into AP magnetization, assuming that the long-range heteronuclear coupling ${}^{n}J_{\mathrm{CH}}$ exactly matches the condition $\Delta = 0.5/({}^{n}J_{\mathrm{HC}})$. However, organic molecules have a wide range of long-range heteronuclear coupling constants ${}^{n}J_{\mathrm{CH}}$. Thus, for most of the carbon–proton spin pairs of a molecule, the delay Δ effectively set in the experiment will not match the condition $\Delta = 0.5/({}^{n}J_{\mathrm{CH}})$ and a significant loss of transverse magnetization will result. Actually, as the intensity of long-range couplings follows a sine function, there are gaps of zeros occurring for certain values. It is therefore typical to find weak ${}^{n}J_{\mathrm{CH}}$ correlations or even missing ${}^{n}J_{\mathrm{CH}}$ correlations in HMBC spectra.[25] Although an experienced spectroscopist would probably not be misled by these characteristics, inexperienced users and computer programs might mistake missing or weak peaks.

Various approaches have been suggested to overcome these problems. They will be briefly presented in the next sections.

2.4. A typical example

The HMBC spectrum recorded on a sample of 50 mmol cyclosporine A (Figure 3) dissolved in C_6D_6 using the pulse sequence depicted in Figure 1 is shown in Figure 2.

In this spectrum, the dashed rectangles denote regions plagued with residual ${}^{1}J_{\mathrm{CH}}$ signals, which arise from the intense methyl groups of cyclosporine. Clearly, these residual ${}^{1}J_{\mathrm{CH}}$ signals may interfere with long-range correlations and may hamper the analysis, especially for inexperienced users and if computer programs are used to partially perform the attribution. The dashed circle displays a region with weak or missing long-range correlations. As mentioned above, it is usual to find weak ${}^{n}J_{\mathrm{CH}}$ or missing ${}^{n}J_{\mathrm{CH}}$ correlations in HMBC spectra. However, weak long-range correlations may be overlooked or mixed up with noise, and missing long-range correlations may impede the structure elucidation of a compound, because the attribution of the resonances could not be performed unambiguously. It would be therefore of great interest for chemists and scientists in general to have HMBC pulse sequences at their disposal that are able to provide artefact-free spectra, and with improved properties for detecting long-range correlations.

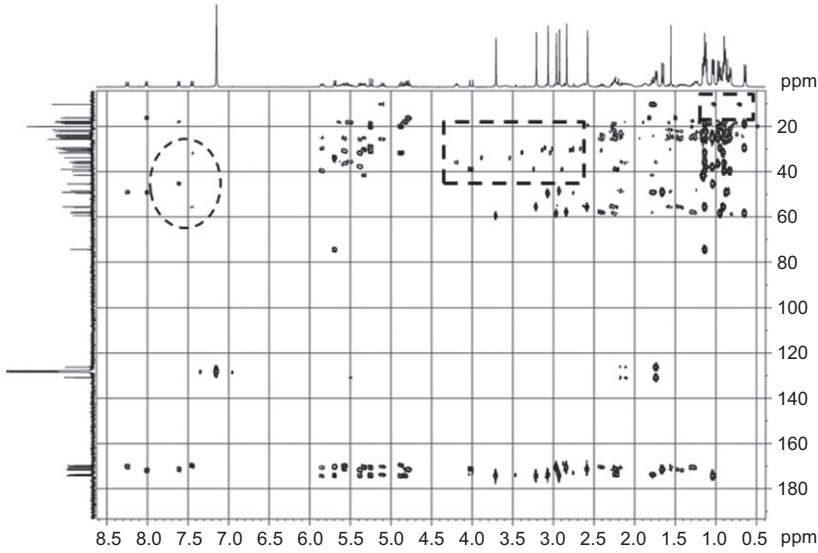

Figure 2 HMBC spectrum recorded on a sample of 50 mmol cyclosporine dissolved in C_6D_6 using the standard HMBC pulse sequence depicted in Figure 1 and recommended acquisition and processing parameters.[27]

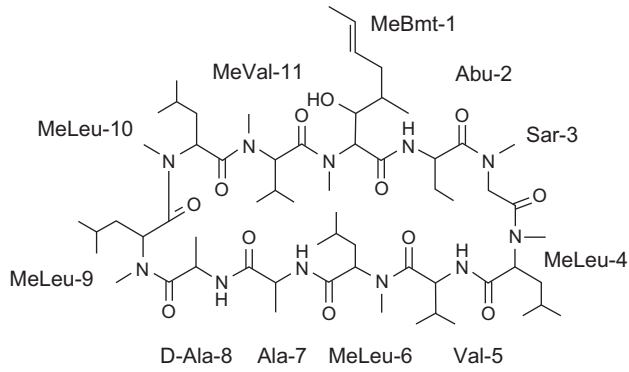

Figure 3 Cyclosporine A. The amino-acid residues were abbreviated following the notation given by Kessler.[26]

3. SUPPRESSION OF DIRECT $^1J_{CH}$ RESPONSES

In its standard implementation, the suppression of the undesired one-bond correlations is far from complete using a one-step low-pass J filter HMBC pulse sequence. Effective modifications are needed to achieve this goal when there is a wide range of $^1J_{CH}$ values. There are several kinds of pulse

sequences that may be utilized in the preparation part of the HMBC experiment to remove the transverse proton magnetization associated with protons directly attached to ^{13}C so that they do not give observable signals.[25,28–30] The higher orders of the low-pass J filter, which have been developed almost 30 years ago, represent a valuable option. It seems however that they have remained little known from a large majority of scientists. We will thus first develop the concept of heteronuclear low-pass *J*-filters, and subsequently review the newest effective one-bond correlation suppression methods.

3.1. The low-pass J filters

Applied to the purpose of ^{1}H–^{13}C HMBC experiments, the heteronuclear low-pass *J*-filter (LPJF, Figure 4) is a pulse element that suppresses the magnetization H^{d} associated with large one-bond heteronuclear coupling constants $^{1}J_{CH}$, while leaving virtually unaffected the magnetization H^{r} associated with small long-range heteronuclear coupling constants $^{n}J_{CH}$.

The simple one-step low-pass J filter has severe deficiencies if the sample has a wide range of one-bond heteronuclear coupling constants $^{1}J_{CH}$, which is practically always the case of organic, inorganic, and biomolecular compounds. For most of the carbon–proton spin pairs, the delay τ effectively set in the filter will not match the condition $\tau = 0.5/(^{1}J_{CH})$ and a significant amount of transverse magnetization survives even after the purging 90° carbon pulse.

3.1.1. Overall response of N-low-pass *J*-filters

In 1983, Kogler et al. had proposed that the low-pass J filtering process can be repeated and improved several times with different intervals $\tau_1, \tau_2, \ldots$ in order to properly eliminate all $^{1}J_{CH}$ peaks when a wide range of one-bond coupling constants $^{1}J_{CH}$ is present in the molecule under study (Figure 4).[15] After the low-pass J filter, as shown by Equation (8), the

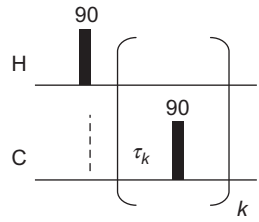

Figure 4 General scheme for constructing *N*-steps low-pass J filters. Low-pass filtering process can be repeated and improved several times with different intervals $\tau_1, \tau_2, \ldots$ in order to properly eliminate all $^{1}J_{CH}$ peaks when a wide range of one-bond coupling constants $^{1}J_{CH}$ is present in the molecule.

magnetization term responsible for the occurrence of $^1J_{CH}$ artefacts in HMBC spectra is $-\ H_Y{}^d \cos(\pi^1 J_{CH}\tau)$.

The overall response of a low-pass *J*-filter with N ^{13}C pulses and N delays τ_k can be numerically evaluated using the function f_{LPN}:

$$f_{LPN} = \prod_{k=1}^{N} \cos\left(\pi^1 J_{CH}\tau_k\right). \tag{10}$$

For a one-step low-pass J filter, the one-bond responses f_{LP1} are expected to be proportional to

$$f_{LP1} \propto \left|\cos\left(\pi^1 J_{CH}\tau_1\right)\right|. \tag{11}$$

For a two-step low-pass J filter, the one-bond responses f_{LP2} and f'_{LP2} are expected to be proportional to

$$f_{LP2} \propto \left|\cos^2\left(\pi^1 J\tau_1\right)\right|, \quad \text{if the same delay} \tau_1 \text{ is used twice,} \tag{12}$$

$$f'_{LP2} \propto \left|\cos\left(\pi^1 J_{CH}\tau_1\right)\cos\left(\pi^1 J_{CH}\tau_2\right)\right|, \quad \text{if the delays } \tau_1 \text{ and } \tau_2 \text{ are different.} \tag{13}$$

For a three-step low-pass J filter, the one-bond responses f_{LP3} and f'_{LP3} are expected to be proportional to

$$f_{LP3} \propto \left|\cos^3\left(\pi^1 J_{CH}\tau_1\right)\right|, \quad \text{if the same delay } \tau_1 \text{ is used thrice,} \tag{14}$$

$$f'_{LP3} \propto \left|\cos\left(\pi^1 J_{CH}\tau_1\right)\cos\left(\pi^1 J_{CH}\tau_2\right)\cos\left(\pi^1 J_{CH}\tau_3\right)\right|, \quad \text{for three different delays } \tau_1, \tau_2 \text{ and } \tau_3. \tag{15}$$

In the same way, four-, five- and *N*-step low-pass J filters can be designed, which can be evaluated using the four-bond responses f_{LP4} and f'_{LP4}, the five-bond responses f_{LP5} and f'_{LP5} and the *N*-bond responses f_{LPN} and f'_{LPN}, respectively. In order to match the effective $^1J_{CH}$ coupling range of the sample, the optimum choice for $N = 1$, 2, 3, 4 and 5 as a function of the $^1J_{CH}$ coupling constant are given in Table 1. The theoretical variation of the residual transverse proton magnetization as a function of the $^1J_{CH}$ range for f_{LP1}, f_{LP2}, f'_{LP2}, f_{LP3}, f'_{LP3}, f_{LP4}, f'_{LP4}, f_{LP5} and f'_{LP5} is shown in Figure 5 and the maximal residual transverse proton magnetizations given in Table 2.

Obviously, the one-step low-pass J filter produces the narrowest profile and is therefore the less efficient in removing direct correlations in HMBC spectra, while the five-step tuned low-pass J filter (f'_{LP5}) offers the most broadband profile. For this filter, the intensity of the residual $^1J_{CH}$ signals remains below 0.11% for the range $125 < {}^1J_{CH} < 225$ Hz, which is remarkable. Interestingly, as long as the $^1J_{CH}$ couplings range of the molecule remains moderate ($\sim$60 Hz), the four- and five-step filters

TABLE 1 Optimal duration of the τ_i delays for maximal $^1J_{CH}$ suppression as a function of the minimum ($^1J_{CHmin}$) and maximum ($^1J_{CHmax}$) coupling constant values

Number N of steps and associated attenuation function f'_{LPN}	Best set of τ_i for maximal $^1J_{CH}$ suppression as a function of the minimum (J_{min}) and maximum (J_{max}) coupling constant values		Corresponding values for $^1J_{CHmin} = 125$ Hz and $^1J_{CHmax} = 250$ Hz (ms)
2	τ_1	$\frac{0.5}{(J_{min}+0.146(J_{max}-J_{min}))}$	3.49
f'_{LP2}	τ_2	$\frac{0.5}{(J_{max}-0.146(J_{max}-J_{min}))}$	2.16
3	τ_1	$\frac{0.5}{(J_{min}+0.07(J_{max}-J_{min}))}$	3.74
f'_{LP3}	τ_2	$\frac{1}{(J_{max}+J_{min})}$	2.67
	τ_3	$\frac{0.5}{(J_{max}-0.07(J_{max}-J_{min}))}$	2.07
4	τ_1	$\frac{0.5}{(J_{min}+0.04(J_{max}-J_{min}))}$	3.85
f'_{LP4}	τ_2	$\frac{0.5}{(J_{min}+0.31(J_{max}-J_{min}))}$	3.05
	τ_3	$\frac{0.5}{(J_{max}-0.31(J_{max}-J_{min}))}$	2.37
	τ_4	$\frac{0.5}{(J_{max}-0.04(J_{max}-J_{min}))}$	2.04
5	τ_1	$\frac{0.5}{(J_{min}+0.02(J_{max}-J_{min}))}$	3.92
f'_{LP5}	τ_2	$\frac{0.5}{(J_{min}+0.21(J_{max}-J_{min}))}$	3.31
	τ_3	$\frac{1}{(J_{max}+J_{min})}$	2.67
	τ_4	$\frac{0.5}{(J_{max}-0.21(J_{max}-J_{min}))}$	2.23
	τ_5	$\frac{0.5}{(J_{max}-0.02(J_{max}-J_{min}))}$	2.02

Corresponding values in ms for $^1J_{CHmin} = 125$ Hz and $^1J_{CHmax} = 250$ Hz.

optimized for a single coupling value (f_{LP4} and f_{LP5}) provide similar results as compared to the tuned variants (f'_{LP4} and f'_{LP5}). This situation would typically arise for molecules possessing only aliphatic and aromatic groups, for which the range of direct $^1J_{CH}$ couplings is roughly $120 < {}^1J_{CH} < 170$ Hz. For this type of molecules, the use of either the filters optimized for a single coupling value or the tuned filters provides identical results. On the other hand, for molecules possessing a broader range of direct $^1J_{CH}$ couplings, the use of the four- or five-step tuned low-pass J filters is more adequate and strongly advocated. For instance, this category encompasses molecules possessing aliphatic, acetylenic and aromatic groups, for which the range of direct $^1J_{CH}$ couplings can be comprised between 110 and 260 Hz.

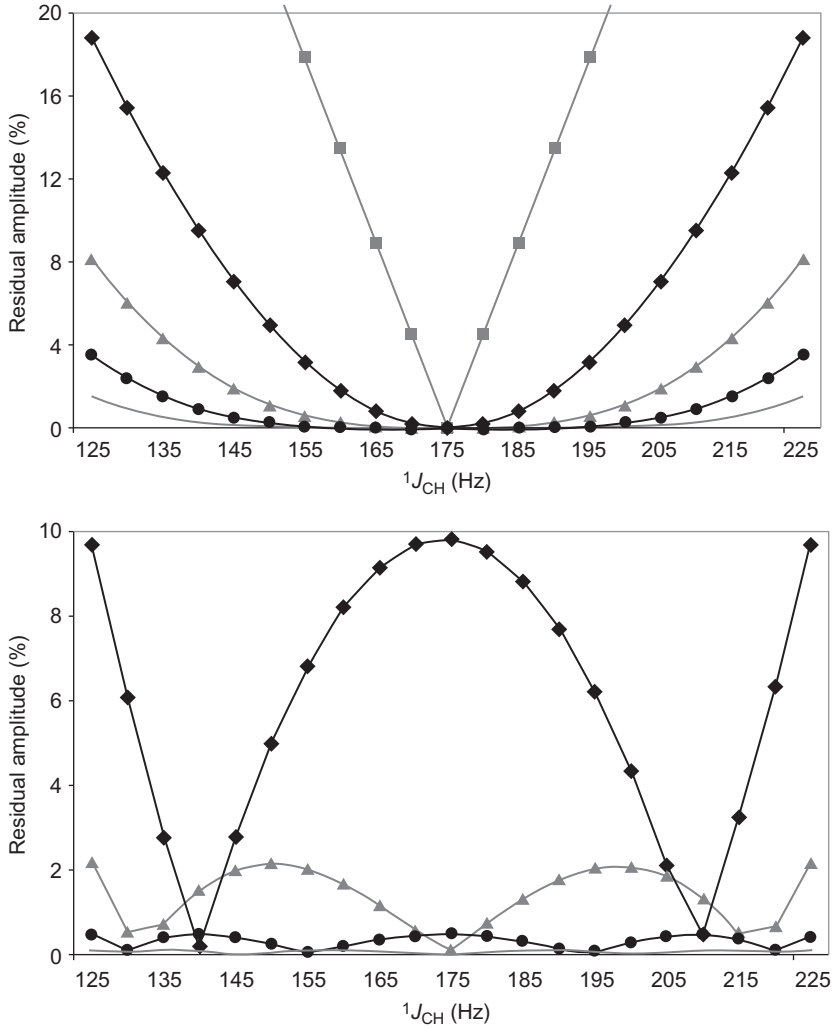

Figure 5 Theoretical residual transverse proton magnetization as a function of the $^1J_{CH}$ range for the f_{LP1} (■), f_{LP2} (◆), f_{LP3} (▲), f_{LP4} (●), f_{LP5} (−) (top) and f'_{LP2} (◆), f'_{LP3} (▲), f'_{LP4} (●), and f'_{LP5} (−) (bottom) functions.

3.1.2. Attenuation of the long-range magnetization after *N*-step low-pass J filters

Unavoidably, the efficiency of the different low-pass J filters in removing direct correlations induces attenuation of the signals associated with long-range couplings. For some molecules, the choice of the most suitable low-pass J filter may be first determined by the attenuation of those signals. Neglecting relaxation, pulse imperfections and offset effects, the

TABLE 2 Maximal residual transverse proton magnetization and maximal attenuation for $^{n}J_{CH}$ coupling constants <8 Hz; <20 Hz and <30 Hz for one-, two-, three-, four- and five-step low-pass J filters

Number N of steps and associated attenuation function f_{LPN}	Maximum residual amplitude (%) for 125 Hz $< J <$ 225 Hz	Maximum attenuation (%) for $J <$ 8 Hz; f_{AT}	Maximum attenuation (%) for $J <$ 20 Hz; f_{AT}	Maximum attenuation (%) for $J <$ 30 Hz; f_{AT}
1				
f_{LP1}	43.4	0.3	1.6	3.6
2				
f_{LP2}	18.8	0.5	3.2	7.1
f'_{LP2}	9.8	0.6	3.6	8.0
3				
f_{LP3}	8.2	0.8	4.8	10.5
f'_{LP3}	2.2	0.9	5.4	11.8
4				
f_{LP4}	3.5	1.0	6.3	13.8
f'_{LP4}	0.49	1.2	7.1	15.5
5				
f_{LP5}	1.5	1.3	7.8	16.8
f'_{LP5}	0.11	1.5	8.8	19.0

maximum attenuation for signals associated with long-range couplings after a N-step low-pass J filter can be calculated using the following function f_{AT}:

$$f_{AT} = \prod_{k=1}^{N} \cos\left(\pi^{n} J_{CH} \tau_k\right). \tag{16}$$

The results for 1, 2, 3, 4 and 5 filtration cycles N for $^{n}J_{CH} < 8$ Hz, <20 Hz and <30 Hz are given in Table 2.

Obviously, the weakest attenuation is obtained with the one-step low-pass J filter, while the largest attenuation is expected with the five-step low-pass J filters. Fortunately, for most of chemical functionalities, heteronuclear long-range coupling constants $^{n}J_{CH}$ values remain below 10 Hz, and the effect of the low-pass J filters on the intensity of the signals associated with long-range couplings remain secondary. On the other hand, for some chemical functionalities, like acetylenic, aldehyde or furanyl, much higher long-range coupling values can exist, and intensity losses cannot be neglected. For instance, when a five-step low-pass J filter is used, the loss of intensity reaches 9% for a 20-Hz and 19% for a 30-Hz long-range coupling constant. Thus, if those chemical functionalities are

present, the three-step low-pass J filter seems more appropriate: the suppression of residual $^{1}J_{CH}$ signals remain excellent (2.2%) and the signals associated with $|^{n}J| < 30$ Hz are not attenuated by more than 11.8%.

For non-experienced users, which may prefer to use one single experimental parameter set suitable for all samples, or for being used in automatic mode, we found experimentally that the three-step low-pass J filter offers the best compromise between $^{1}J_{CH}$ suppression and $^{n}J_{CH}$ attenuation. It provides excellent results for nearly all molecules, and only in very special cases a four- or a five-step low-pass J filter will be required.

3.1.3. Experimental verification

The efficiency of the various low-pass J filters may be appreciated by considering the HMBC spectra of 1,3-butadiynyl (*tert*-butyl) diphenylsilane (Figure 6), which provides a stringent test because of the extensive range of $^{1}J_{CH}$ coupling constants present.

Partial plots extracted from HMBC spectra recorded with the five different low-pass J filters are shown in Figure 7. Clearly, ambiguities may arise, particularly if accidental degeneracy in chemical shifts causes true long-range correlations and residual $^{1}J_{CH}$ correlations to overlap.

Likewise, the attenuation of the long-range signals $^{n}J_{CH}$ is demonstrated by selected F_2 sections taken through the 2D HMBC spectra. Figure 8 shows the responses at the ω_2 frequencies of C-2 at 68.73 ppm and C-3 at 78.46 ppm.

The results shown in Figure 8 are in good agreement with the theoretical results shown in Table 2. The value of the $^{2}J_{C2H1}$ coupling is very large, 49 Hz, and the attenuation during the respective low-pass J filters is subsequent (left). It must be pointed out that relaxation has not been

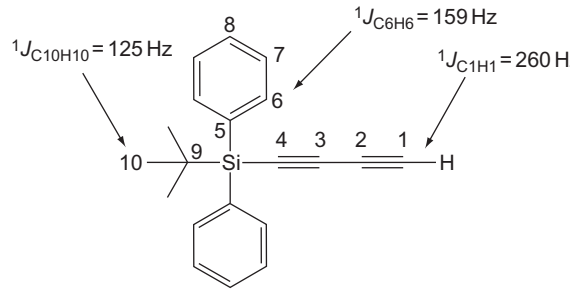

Figure 6 Structure and carbon atoms numbering of the 1,3-butadiynyl (*tert*-butyl) diphenylsilane molecule. The values of three representative $^{1}J_{CH}$ coupling constants are indicated.

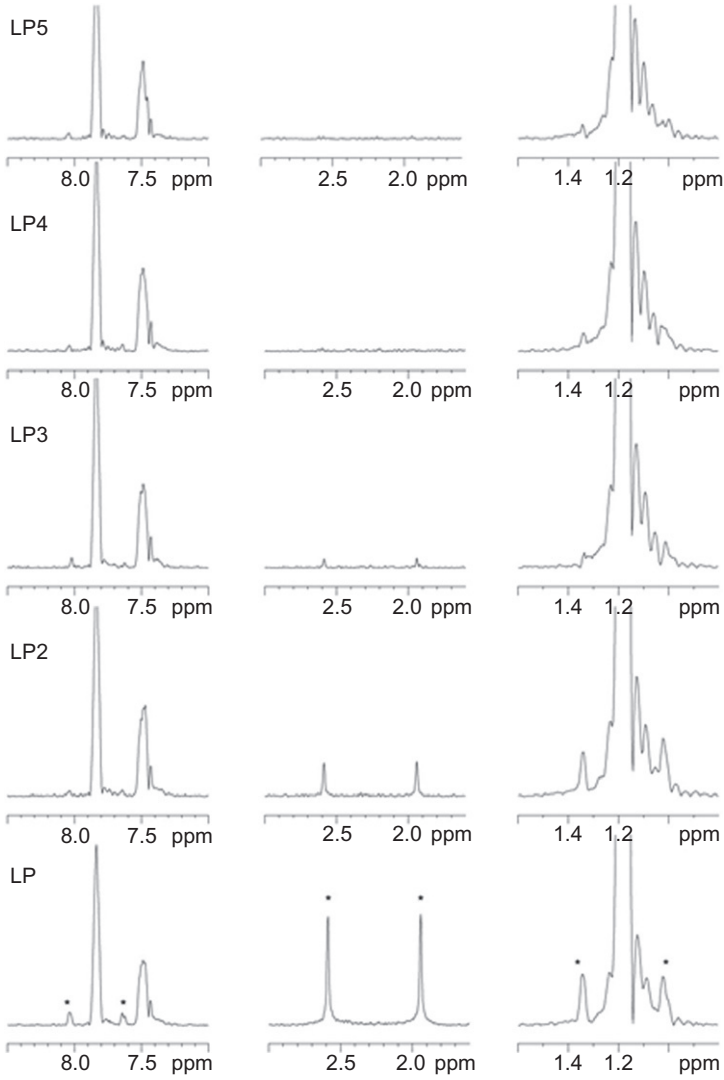

Figure 7 Comparison of $^{1}J_{CH}$ artefact's intensity illustrated with 1D rows taken from HMBC experiments recorded using a one-step low-pass J filter (denoted LP), a two-step LPJF (denoted LP2), a three-step LPJF (denoted LP3), a four-step LPJF (denoted LP4), and a five-step LPJF (denoted LP5) showing the $^{1}J_{CH}$ artefacts and $^{n}J_{CH}$ responses of C-6 at 135.6 ppm (left), C-1 at 67.2 ppm (middle) and C-10 at 27 ppm (right) of the 1,3-butadiynyl (*tert*-butyl) diphenylsilane molecule dissolved in $CDCl_3$. The delays were adjusted according to the extreme range of coupling constants for this molecule (125–260 Hz) following the strategy indicated in Table 2. The same vertical scale is used for all spectra. Residual $^{1}J_{CH}$ signals are denoted with stars.

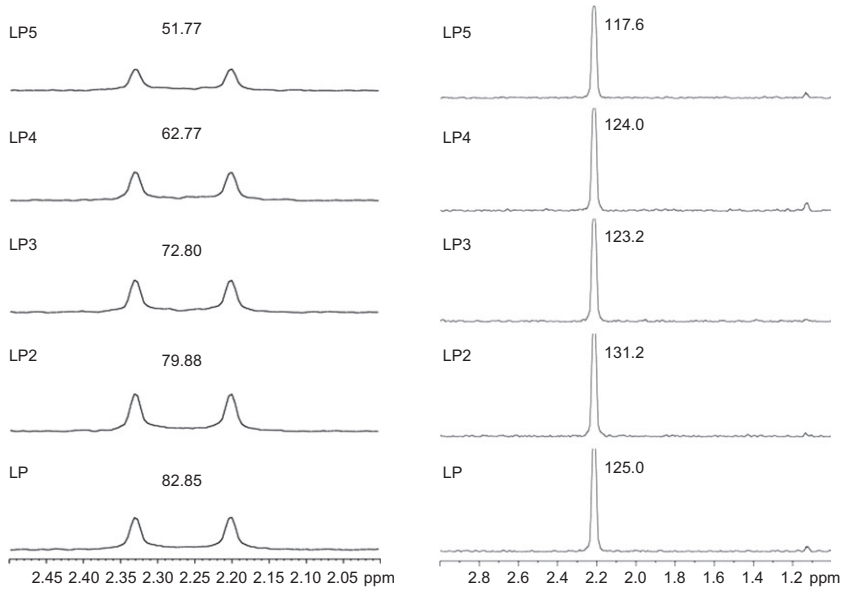

Figure 8 Comparison of $^{n}J_{CH}$ intensity illustrated with 1D rows taken from HMBC experiments recorded using a one-step low-pass J filter (denoted LP), a two-step LPJF (denoted LP2), a three-step LPJF (denoted LP3), a four-step LPJF (denoted LP4), and a five-step LPJF (denoted LP5) showing the $^{n}J_{CH}$ response of C-2 (left) and the $^{n}J_{CH}$ response of C-3 (right) of the 1,3-butadiynyl (*tert*-butyl) diphenylsilane molecule dissolved in $CDCl_3$. The measured signal-to-noise (obtained using the sino macro) are indicated on the top of each peak.

included in the calculations, but the effect should be negligible with a small-size molecule like the 1,3-butadiynyl (*tert*-butyl) diphenylsilane molecule. If a more standard long-range coupling is considered, for example the $^{3}J_{C3H1}$ cross peak (right), with a coupling value of 6 Hz, the attenuation is negligible, as expected from Table 2.

3.2. Other recent purging sequences for efficient $^{1}J_{CH}$ suppression

3.2.1. The BIRD-HMBC experiment

A recent and efficient alternative for $^{1}J_{CH}$ signals suppression is the incorporation of a BIRD^{r,X} element[24,31] in the middle of the long-range couplings evolution period, as described for the BIRD-HMBC experiment, shown in Figure 9.[32] This experiment starts with a BIRD^{r,X} element with

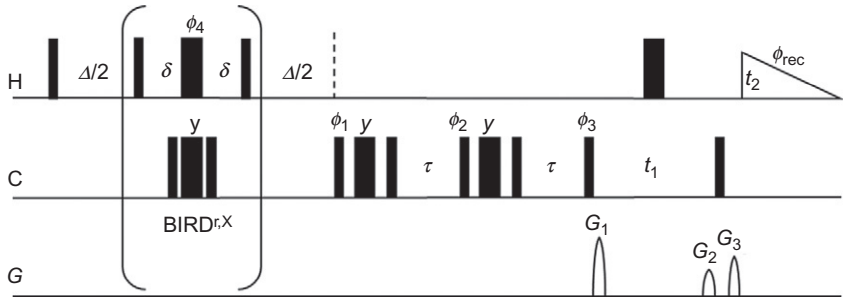

Figure 9 Timing diagram of the BIRD-HMBC pulse sequence for the detection of $^{n}J_{CH}$ correlations, including an additional two-step low-pass J filter. Thin and thick bars represent 90° and 180° pulses, respectively. ^{13}C 180° pulses are replaced by 90°y −180°x −90°y composite pulses. δ is set to 0.5/($^{1}J_{CH}$) and Δ is set to 0.5/($^{n}J_{CH}$). Phases are cycled as follows: $\phi_1 = y, y, -y, -y$; $\phi_2 = x, -x$; $\phi_3 = 8(x), 8(-x)$; $\phi_4 = 4(x), 4(-x)$; $\phi_{rec} = 2(x, -x), 4(-x, x), 2(x, -x)$. Phases not shown are along the x-axis. Gradient pulses are represented by filled half-ellipses denoted by G_1–G_3. They should be applied in the ratio: 50:30:40.1.

the delay δ adjusted for direct couplings positioned in the middle of the long-range heteronuclear coupling constants evolution period, Δ. Using such a BIRD element, a different concept for $^{1}J_{CH}$ coherences suppression is introduced: instead of being filtered out, the unwanted $^{1}J_{CH}$ coherences are sampled together with the long-range coupling coherences. Following the properties of a BIRD^{r,X} element, described in the above sections, the long-range coupling constants have evolved into pure AP coherences ($H_X C_Z$) after the second delay Δ, whereas $^{1}J_{CH}$ coherences have evolved under the influence of chemical shifts into pure proton in-phase (IP) coherences (H_Y and H_X).

3.2.1.1. *Evolution of the H^r magnetization under the long-range coupling $^{n}J_{CH}$*

$$\begin{aligned} H_Z^r &\xrightarrow{(90^\circ)H_X} -H_Y^r \xrightarrow{\Delta-\mathrm{BIRD}^{r,X}-\Delta} H_Y^r \cos\left(\pi^n J_{CH} 2\Delta\right) \\ &- 2H_X^r C_Z \sin\left(\pi^n J_{CH} 2\Delta\right) \xrightarrow{\Delta=0.25/\left({}^{n}J\right)} -2H_X^r C_Z \end{aligned} \tag{17}$$

$$\begin{aligned} H_Z^d \xrightarrow{(90^\circ)H_X} &- H_Y^d \xrightarrow{\Delta-\mathrm{BIRD}^{r,X}-\Delta} - H_Y^d \cos\left(\pi^n J_{CH} 2\delta\right) - 2H_X^d C_Z \sin\left(\pi^n J_{CH} 2\delta\right) \\ &+\text{Identical terms in } -H_X \text{ and } -2H_Y C_Z \\ &\left(\text{The evolution under the influence of chemical shifts has been neglected}\right) \end{aligned} \tag{18}$$

For efficiently eliminating these potential intense $^1J_{CH}$ coherences, low-pass J filtering has to be introduced immediately after the long-range evolution period. The best suppression results are obtained using a filter element consisting of a $(90°)_{\pm x}$–$(180°)_y$–$(90°)_x$ ^{13}C composite pulse immediately followed by a delay set to $\delta = 0.5/(^1J_{HC})$ and applied once or as a two-step filter. This composite pulse allows long-range coupling coherences to be selectively and differently labelled ($\pm H_XC_Y$) from scan to scan. When the receiver phase is set accordingly, the long-range coupling coherences co-added. The signals of the spurious $^1J_{CH}$ coherences evolve into AP coherences during the filter delay δ and, as they are not labelled by the composite ^{13}C pulse, are cancelled in subsequent scans.

Evolution of the H^r magnetization during the low-pass J filter:

$$-2H_X^rC_Z \xrightarrow{(90°)C_{\pm X}-(180°)C_Y-(90°)C_X} \mp 2H_X^rC_Z \xrightarrow{\delta=0.5/(^1J_{HC})} \mp 2H_X^rC_Z. \qquad (19)$$

Evolution of the H^d magnetization during the low-pass J filter:

$$\begin{aligned} -H_Y^d &\xrightarrow{(90°)C_{\pm X}-(180°)C_Y-(90°)C_X} -H_Y^d \xrightarrow{\delta} -H_Y^d \cos(\pi {}^1J_{CH}\delta) \\ &- H_X^dC_Z \sin(\pi {}^1J_{CH}\delta) \xrightarrow{\delta=0.5(^1J_{HC})} -H_X^dC_Z. \end{aligned} \qquad (20)$$

On the other hand, $^1J_{CH}$ coherences which survive the BIRD filter have evolved as H_XC_Z and H_YC_Z AP coherences. They will be therefore labelled together with long-range coupling coherences and would give rise to unwanted $^1J_{CH}$ residual peaks in the HMBC spectrum. In the course of the filter delay δ, fortunately, these H_XC_Z and H_YC_Z AP coherences evolve back for the most part into IP coherences H_X and H_Y. They are therefore not transformed into multiple quantum coherence by the $90°_x$ ^{13}C pulse and are filtered out by the selection gradients G_1, G_2, and G_3.

H^d magnetization:

$$\begin{aligned} -2H_Y^dC_Z &\xrightarrow{(90°)C_{\pm X}-(180°)C_Y-(90°)C_X} \pm 2H_Y^dC_Z \xrightarrow{\delta} \mp H_X^d \cos(\pi {}^1J_{CH}\delta) \\ &\pm 2H_Y^dC_Z \sin(\pi {}^1J_{CH}\delta) + \text{Identical terms in } H_Y. \end{aligned} \qquad (21)$$

The low-pass J filter efficiency obtained may be improved by implementing a second low-pass J filter element. Taking advantage of the double-difference principle, this two-step filter is expected to yield high degrees of $^1J_{CH}$ signal suppression.

3.2.2. The G-BIRD-HMBC experiment

Experimentally, the BIRD-HMBC sequence has its merits, but it turns out that it inadequately suppresses $^1J_{CH}$ correlations when large $^1J_{CH}$ coupling constant ranges are present. While for moderate $^1J_{CH}$ ranges the additional low-pass J filters of the original BIRD-HMBC sequence allow

excellent $^1J_{CH}$ suppression, their efficiency for large $^1J_{CH}$ coupling constant ranges remains insufficient. As noticed by Burger et al., the excellent suppression achieved using the original BIRD-HMBC scheme has to be mainly attributed to the additional low-pass J filters, as the filter performances of a single BIRD pulse deteriorate rapidly when the delays between the pulses are mismatched.[33] Recently, to overcome this weakness, an improved version of the BIRD-HMBC experiment, the G-BIRD-HMBC experiment, has been proposed (Figure 10).[35]

3.2.2.1. The double G-BIRD filter In comparison to the original version, the G-BIRD-HMBC experiment, outlined in Figure 10, starts with a double G-BIRD^{r,X} filter[33,36,37] with the delays δ and δ' adjusted for direct heteronuclear couplings, instead of a single BIRD^{r,X} pulse. As for the original scheme, the double G-BIRD filter is positioned in the middle of the long-range evolution delays Δ, optimized for heteronuclear long-range couplings values. This double G-BIRD filter strategy follows the idea of the double pulsed field gradient spin echo (DPFGSE) introduced by Shaka et al.[36] For the G-BIRD-HMBC experiment, we use a DPFGSE sequence in which the refocusing element is the G-BIRD^{r,X} element.[38] Each BIRD filter is tuned to two different heteronuclear coupling constants by using different values for the delays of the filters. The combination of the

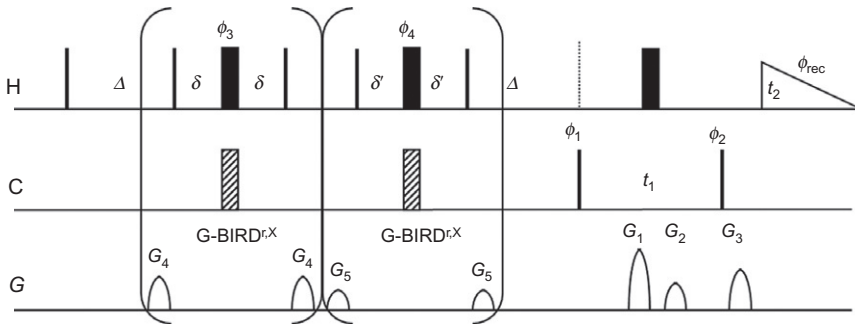

Figure 10 Timing diagram of the G-BIRD-HMBC experiment. Thin bars represent 90° pulses, thick bars 180° pulses. The rectangular ^{13}C 180° pulses are replaced by BIP pulses,[34] indicated as shaded rectangles. At 400 MHz, a 192-μs BIP 720-100-10 which inverts well over ± 10.6 kHz with inhomogeneity compensation of ($B_1/B_1^0 = 1 \pm 0.1$) is adequate. Δ are the long-range couplings evolution delays and are set to an average value $0.25/^nJ_{CH}$. δ and δ' are the one-bond couplings evolution delays and should be set to an average value $0.5/^1J_{CHave}$ for a double G-BIRD filter or $0.5/[^1J_{CHmin} + 0.146(^1J_{CHmax} - {}^1J_{CHmin})]$ and $0.5/[^1J_{CHmax} - 0.146(^1J_{CHmax} - {}^1J_{CHmin})]$, respectively, for a double tuned G-BIRD filter. Gradient pulses are represented by filled half-ellipses denoted by G_1–G_5. They can be applied in the ratio: 50:30:40.1:34:−22. The following phase cycles were applied: $\phi_1 = x, -x$; $\phi_2 = x, x, -x, -x$; $\phi_3 = y, y, -y, -y$; $\phi_4 = -y, -y, y, y$; $\phi_{rec} = x, -x, -x, x$. Phases not shown are applied along the *x*-axis.

DPFGSE sequence with double tuned filters has been first proposed by Ogura et al.[39] These filters demonstrate very high filtering efficiency for isotope-filtered, isotope-edited NOESY spectra.[40]

Optimal results for a double-G-BIRD sequence are obtained when the phase of the central proton 180° pulse is shifted by 180° from the first G-BIRD to the second. This strategy was shown to provide excellent suppression over a substantial variation in the nominal flip angles over a large range of resonance offsets.[33] For further improving the performances and the tolerance to resonance offsets of the G-BIRD-HMBC experiment, the 180° pulses on both the proton and carbon channels have been replaced with BIP pulses.[34] Depending on the effective range of $^1J_{CH}$ coupling constants of the molecule being investigated, the delays δ and δ' of the G-BIRD pulses can be set either to a standard average value $^1J_{CHave}$, or, following the dual low-pass J filter strategy, to $0.5/[^1J_{min} + 0.146(^1J_{max} - {}^1J_{min})]$ and $0.5/[^1J_{max} - 0.146(^1J_{max} - {}^1J_{min})]$, respectively. Compared to the original BIRD-HMBC, the double G-BIRD^{r,X} filter is expected to suppress the residual one-bond coupling signals more efficiently. Therefore, the two ^{13}C 180° composite pulses, acting as supplementary low-pass J filters in the original BIRD-HMBC experiment, have been removed from the improved pulse sequence. The rest of the G-BIRD-HMBC sequence is identical to the basic HMBC and to the BIRD-HMBC sequence.

3.2.2.2. Leaking intensity after a double G-BIRD filter The leaking intensity of residual one-bond couplings for a single G-BIRD and a double tuned G-BIRD filters as a function of the heteronuclear coupling $^1J_{CH}$ can be calculated for a single ^{1}H–^{13}C pair. The equation used for calculating the intensity of the leaking magnetization I_{leak} is[41]:

$$I_{leak}^{G-BIRD} = 0.5 \times \left(1 - \cos\left(\pi {}^1J_{CH} 2\delta\right)\right), \tag{22}$$

$$I_{leak}^{doubleG-BIRD} = 0.25 \times \left(1 - \cos\left(\pi {}^1J_{CH} 2\delta\right)\right) \times \left(1 - \cos\left(\pi {}^1J_{CH} 2\delta'\right)\right), \tag{23}$$

where δ and δ' are the delays between the pulses of the BIRD cluster. The curves shown in Figure 11A were optimized for one-bond coupling values ranging from 120 to 170 Hz, whereas the curves shown in Figure 11B were optimized for one-bond coupling values between 125 and 260 Hz. In Figure 11A, the delays δ and δ' were adjusted to J values of 127 and 163 Hz, respectively (double tuned G-BIRD), according to the dual low-pass J filter strategy, or to an average value of 145 Hz (G-BIRD). In Figure 11B, the delays δ and δ' were adjusted to J values of 145 and 240 Hz (double tuned G-BIRD), or to an average value of 190 Hz (G-BIRD). It can be seen from the curves that the leaking intensity after a single G-BIRD filter can already reach 7% for the moderate 120–170 Hz range. According to these theoretical curves and as claimed by Burger et al., the excellent suppression

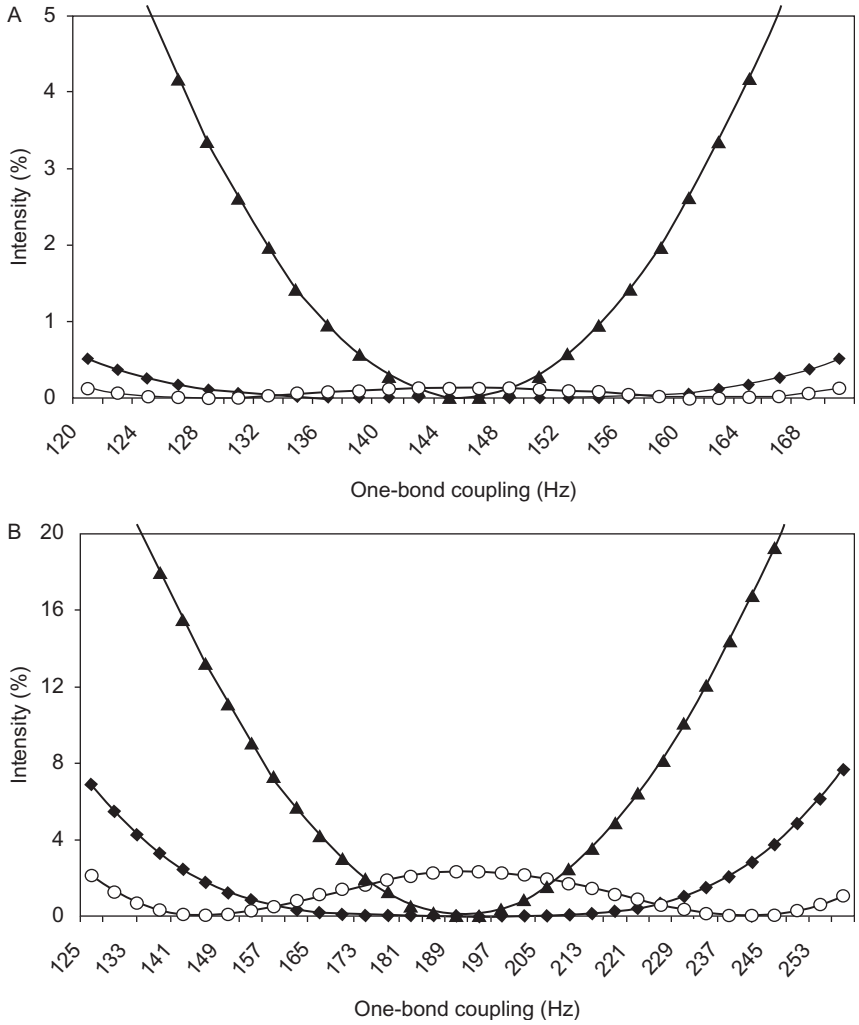

Figure 11 Leaking intensity of residual one-bond couplings for single (filled triangles), double (filled diamonds) and double tuned G-BIRD (open circles) filters as a function of the heteronuclear coupling $^1J_{CH}$. The intensities are calculated for a single ^{1}H–^{13}C pair. The equations used for calculating the intensities of the leaking magnetization are: I(G-BIRD) $= 0.5 \times (1 - \cos(\pi {}^1J_{CH} 2\delta))$; I(double G-BIRD) $= 0.25 \times (1 - \cos(\pi {}^1J_{CH} 2\delta))$; I(double tuned G-BIRD) $= 0.25 \times (1 - \cos(\pi {}^1J_{CH} 2\delta)) \times (1 - \cos(\pi {}^1J_{CH} 2\delta'))$, where δ and δ' are the delays between the pulses of the BIRD cluster ($\delta = 0.5/{}^1J_{CH}$). The curves shown in (A) were optimized for one-bond coupling values ranging from 120 to 170 Hz, whereas the curves shown in (B) were optimized for one-bond coupling values between 125 and 260 Hz. In (A), the delays δ were adjusted to a *J*-value of 145 Hz, for the single and double G-BIRD filters. For the double tuned G-BIRD, the delays δ and δ' were adjusted to *J* values of 127 and 163 Hz, respectively, according to the dual low-pass J filter strategy. In (B), the delays δ were adjusted to a *J*-value of 190 Hz, for the single and double G-BIRD filters. For the double tuned G-BIRD, the delays δ and δ' were adjusted to *J* values of 145 and 240 Hz.

achieved using the original BIRD-HMBC scheme has to be mainly attributed to the additional low-pass J filters, as the filter performances of a single BIRD pulse deteriorate rapidly when the delays between the pulses are mismatched. As proven by Figure 11A, the filter properties of the double tuned G-BIRD filter are excellent. The leaking intensity remains below 0.5%. Much impressive is the suppression achieved by the double tuned G-BIRD filter for larger ranges of one-bond coupling constants. The curves shown in Figure 11B demonstrate that the leaking intensity is always less than 3% using the double tuned G-BIRD filter, while it reaches up to 25% for a single G-BIRD element. As shown in the previous section, during the filter delay δ, the coherences associated with $^1J_{CH}$ coupling constants evolve back for the most part into IP coherences H_X and H_Y and are therefore not transformed into multiple quantum coherence by the $90°_x$ ^{13}C pulse and filtered out by the selection gradients G_1, G_2, and G_3. While the additional low-pass J filters of the original BIRD-HMBC sequence allow excellent $^1J_{CH}$ suppression for moderate $^1J_{CH}$ ranges, their efficiency for large $^1J_{CH}$ coupling constant ranges remains insufficient. Indeed, most of the coherences associated with $^1J_{CH}$ coupling constants evolve back for the most part into AP coherences H_XC_Z and H_YC_Z and will be labelled together with long-range coupling coherences and detected.

The limits of the original BIRD-HMBC sequence and the excellent $^1J_{CH}$ filter quality of the double tuned G-BIRD element is exemplified in the spectra obtained with the molecule 1,3-butadiynyl (*tert*-butyl) diphenylsilane (Figure 6). This molecule provides a stringent test, since it contains all together aliphatic, aromatic and acetylenic protons, and the corresponding $^1J_{CH}$ coupling constant values vary from 125 to 260 Hz.

In Figure 12, these three illustrative rows extracted from a BIRD-HMBC, a double G-BIRD-HMBC, and a double tuned G-BIRD-HMBC spectra are shown. In this figure, vertical arrows denote the residual $^1J_{CH}$ signals. Clearly, intense residual $^1J_{CH}$ signals are noticeable using the original BIRD-HMBC sequence, especially for aromatic and aliphatic protons (Figure 12A, D and G). The double G-BIRD filter provides contrasting results. While the residual $^1J_{CH}$ signals of aromatic and aliphatic protons are better eliminated (Figure 12B and H), those of acetylenic protons remain more intense (Figure 12E). On the other hand, the double tuned G-BIRD-HMBC filter is very efficient over the full range of $^1J_{CH}$ coupling constants (Figure 12C, F and I). The residual $^1J_{CH}$ signals are almost completely eliminated, as demonstrated in Figure 12C and F.

Compared to the original BIRD-HMBC, the improved G-BIRD-HMBC scheme demonstrate an intrinsically better sensitivity and signal losses due to imperfect pulses and offset effects are attenuated by the incorporation of improved inversion pulses. For usual one-bond coupling constant ranges, optimal $^1J_{CH}$ signals suppression is easily achieved by adjusting the value of the delays δ and δ' of the G-BIRD elements to an average

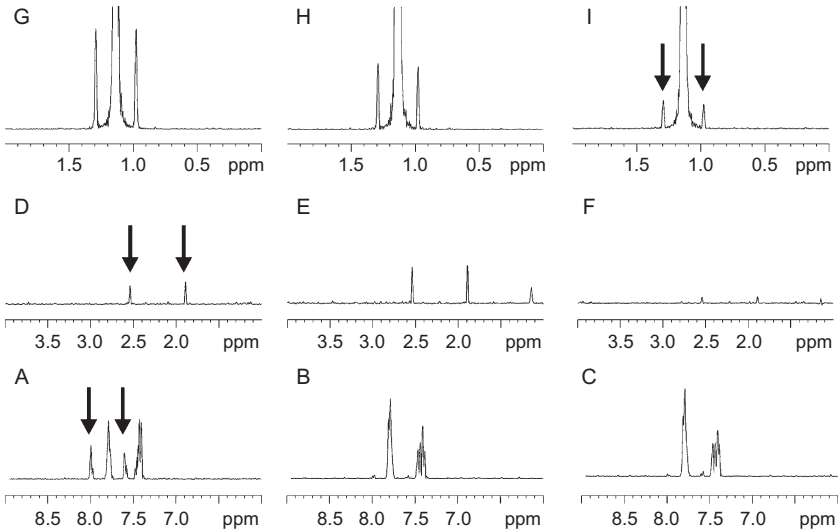

Figure 12 Comparison of $^{1}J_{CH}$ artefacts intensity illustrated with 1D rows taken from a BIRD-HMBC (A), (D) and (G) a G-BIRD-HMBC (B), (E) and (H) and a double tuned G-BIRD-HMBC (C), (F) and (I) experiments showing the $^{1}J_{CH}$ artefacts and $^{n}J_{CH}$ responses of C-6 at 135.6 ppm (A), (B) and (C), C-1 at 67.2 ppm (D), (E) and (F) and C-10 at 27 ppm (G), (H) and (I) of the 1,3-butadiynyl (*tert*-butyl) diphenylsilane molecule dissolved in $CDCl_3$. For the BIRD-HMBC and G-BIRD-HMBC experiments, the delays δ were adjusted to a *J*-value of 190 Hz, as an average value for the extreme range of coupling constants for this molecule (125–260 Hz). For the double tuned G-BIRD-HMBC, the $^{1}J_{CH}$ max and $^{1}J_{CH}$ min values were set to 240 and 145 Hz, respectively. The corresponding values for the δ and δ' delays were 3.13 and 2.17 ms, adjusted to *J* values of 160 and 230 Hz, respectively. For both G-BIRD-HMBC experiments, 192 μs BIP 720-100-10 pulses have been used for ^{13}C inversion. The same vertical scale is used for all spectra. Residual $^{1}J_{CH}$ signals are denoted with arrows.

J-value. For larger ranges, on the other hand, optimal suppression requires the use of a double tuned G-BIRD filter. Using this filter, excellent suppression for all type of one-bond constants present in a molecule can be achieved. In turn, both the sensitivity and the $^{1}J_{CH}$ purging are superior to the original BIRD-HMBC scheme.

3.2.3. The clean and adiabatic clean HMBC experiments

It has been observed and shown above that the expected degree of suppression is observed for weakly coupled spins systems. However, that is not the case for strong coupling. Even perfectly tuned delays in the low-pass J filters or going to higher-order filters have little effect on the intensity of one-bond artefacts in HMBC spectra in the presence of strong coupling. Sørensen et al. have introduced in 2008 a modified HMBC experiment, clean HMBC, where good suppression of unwanted one-bond correlations peaks is achieved even in the case of strong coupling (Figure 13).[42]

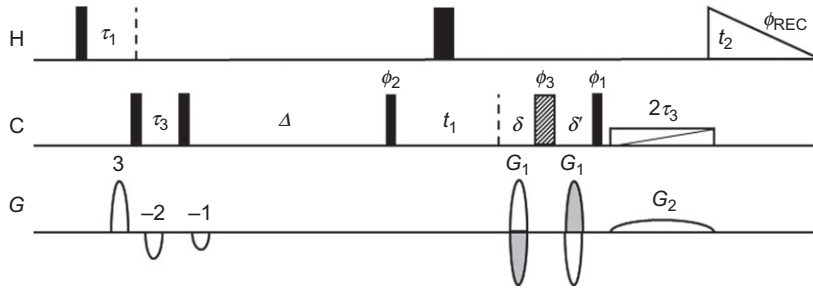

Figure 13 Timing diagram for the clean HMBC experiment with an initial second-order and terminal adiabatic low-pass *J*-filter.[42,43] The recommended delays for the filters are the same than for a third-order low-pass J filter. δ and δ' are gradient delays, where $\delta' = \delta + t_1$ accounts for the delay of the first point in the ^{13}C dimension. The integral over each gradient pulse G_1 is $\gamma_H/2\gamma_C$ times the integral over gradient G_2 in order to achieve coherence selection. The recommended phase cycle is $\phi_1 = x, x, x, x$; $\phi_2 = x, x, 4(-x), x$, and x and $\phi_3 = 4(x), 4(y), 4(-x), 4(-y)$ with the receiver phase $\phi_{REC} = x, x$.

In strongly coupled systems, it is not possible to eliminate chemical shifts by refocusing nor is it possible to describe the evolution in terms of an effective Hamiltonian.[44] A 90° or a 180° pulse leads to coherence transfer between various transitions, and a multitude of new effective precession frequencies may appear in the F_1 dimension. A detailed analysis shows artefacts resulting of strong coupling induced by the 180° pulse applied on the ^1H channel can be efficiently removed by applying a LPJF before acquisition.[42] Likewise, artefacts present in HMBC with a terminal LPJF are suppressed by an LPJF in the beginning of the sequence as in conventional HMBC.

The best and easiest way to implement such an experiment is to use adiabatic inversion pulses, in order to introduce heterogeneity for evolution under ^{13}C–^1H scalar or residual dipolar couplings by means of a frequency-swept 180° pulse on ^{13}C that inverts ^{13}C nuclei at different positions in the NMR sample at different times (Figure 13).[40,45] This filter is robust with respect to pulse miscalibration and operates efficiently without the need to cycle the phases of pulses that otherwise is a common feature of non-destructive LPJFs.

4. ENHANCING WEAKLY OR MISSING $^nJ_{CH}$ CORRELATIONS

4.1. Accordion optimized HMBC experiments

In the late 1990s, various approaches have been suggested to overcome the problem of weak and missing long-range correlations. The relative merits of several sequences proposed for this purpose have recently been

thoroughly evaluated and discussed and thus will be only briefly mentioned here. Fuhirata and Seto have first addressed the problem by converting HMBC into a three-dimensional (3D) experiment by independently incrementing the delay period for $^{n}J_{CH}$ to produce a third frequency axis.[46] However, this involves a considerable increase in experiment time and/or a sacrifice of ^{13}C resolution and thus, is not a reasonable solution to the problem. An alternative approach to compensate for the variation of $^{n}J_{CH}$ is the ACCORD-HMBC sequence of Wagner and Berger.[47] This sequence decrements the $^{n}J_{CH}$ delay in concert with the incrementation of t_1. While this allows one to observe cross-peaks for a wide range of $^{n}J_{CH}$ values, it simultaneously increases F_1 modulation, sacrificing ^{13}C resolution.[48] In an attempt to address both problems, Martin and Krishnamurthy have developed modified versions of ACCORD-HMBC with the inspired acronyms IMPEACH-MBC and CIGAR-HMBC.[49,50] These allow optimization for a wide range of $^{n}J_{CH}$ while allowing one to control the extent of f_1 modulation from complete elimination to enhancement. The reader must become aware that there is unavoidably a conflict between the benefits of sampling a range of $^{n}J_{CH}$ and signal losses due to relaxation during extra delays incorporated into the IMPEACH-MBC and CIGAR-HMBC pulse sequences. However, the elimination of f_1 modulation in CIGAR makes it much easier to interpret the spectrum, particularly in the crowded regions. Thus it appears that the CIGAR sequence is the best of the existing HMBC sequences in terms of information content and ease of interpretation, at least for small to intermediate size molecules. For larger molecules, signal loss due to relaxation will be a serious problem. However, the resolution advantages may also be more important for larger molecules. A recent accordion-BIRD-HMBC experiment has also been recently proposed, with superior suppression of $^{1}J_{CH}$ coupling constants.[51]

4.2. Broadband HMBC

4.2.1. Principles and theory

As we have seen before, the basic HMBC pulse sequence contains a delay Δ for the creation of ^{1}H magnetization AP with respect to long-range heteronuclear *J*-coupling constants, which leads to the amplitude factor of $\sin(\pi^{n}J_{CH}\Delta)$ on the cross-peak intensities. When a molecule contains a broad range of heteronuclear long-range couplings, a statically optimized HMBC is only optimal for one coupling constant value. Because of the amplitude factor $\sin(\pi^{n}J_{CH}\Delta)$, the risk that cross-peaks are weakly observed or missing increases in concert with the mismatch between the actual coupling and the coupling value set in the long-range evolution delay Δ. In the previous section, we have seen that accordion optimization can be implemented to equalize intensities, however at a cost of

significant sensitivity losses. To cope with this problem, Sørensen et al. have proposed in the broadband HMBC experiment.[52,53] The approach they suggest is not a new idea, but it has the merit to provide a way to determine suitable sets of delays as a function of the *J*-coupling constant ranges and transverse relaxation times T_2. The broadband HMBC consists of recording a series of spectra with different Δ delays by the pulse sequence shown in Figure 14 and then co-adding them in absolute-value mode.

In a heteronuclear two-spin system the build-up of AP magnetization for coherence transfer during a delay Δ is determined by the amplitude function

$$f(\Delta, J, T_2) = \sin(\pi J \Delta) e^{-\Delta/T_2}, \tag{24}$$

where T_2 is the transverse relaxation time. This function has its maximum at[53]

$$\Delta_m(J, T_2) = \frac{1}{\pi J} \arctan(\pi J T_2) = \Delta_m(J, L) = \frac{1}{\pi J} \arctan(J/L), \tag{25}$$

where $L = 1/(\pi T_2)$ is the lorentzian linewidth in Hertz associated with an averaged relaxation time T_2. It can be estimated from Equation (25) that the sine function in Equation (24) has a dominating influence on the product for small linewidths while the damping by the exponential

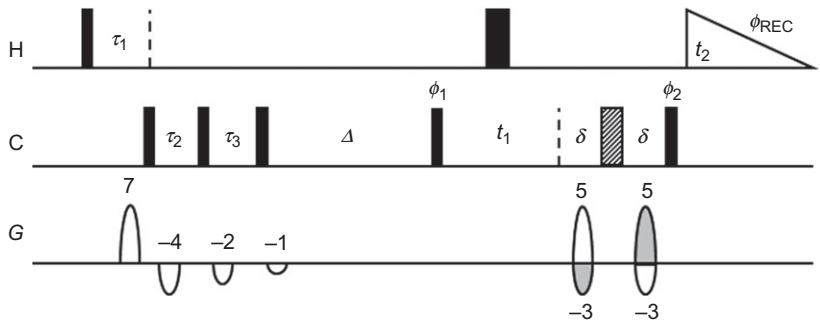

Figure 14 Broadband-HMBC pulse sequence. Thin and thick bars represent 90° and 180° pulses, respectively. Pulsed field gradients are indicated as bell shapes. Pulse phases with the prefix ϕ indicate independent two-step phase cycles with alternating receiver phase. The ratio of the heteronuclear gradient echo gradients after t_1 is +5: −3 for echo selection and −3: +5 for antiecho selection. Δ is the HMBC delay tuned according to $^nJ_{CH}$ and δ is the gradient delay. The length of the delays τ_1, τ_2, and τ_3 follow the rules of the three-step low-pass J filter given in Table 1. The following basic phase cycle is sufficient for obtaining clean spectra: $\phi_1 = x, -x$; $\phi_2 = x, x, -x, -x$; $\phi_{rec} = x, -x, -x, x$. Phases not shown are applied along the *x*-axis.

function grows with increasing linewidth to the extent that the maxima in Equation (25) become rather insensitive to J for large linewidth. Thus, a single Δ delay is adequate in that limit, whereas Δ_m is strongly dependent on J for small molecules with long T_2 relaxation times.

Inserting Equation (25) into Equation (24) yields the maximum amplitude as a function of the J-coupling constant and the linewidth.

$$f_m(J,L) = \frac{J}{L} \cdot \frac{1}{\sqrt{1+(J/L)^2}} e^{-\arctan(J/L)/(J/L)}. \tag{26}$$

These optima can only be obtained by setting the delay $\Delta = \Delta_m(J, L)$ individually according to Equation (25). Obviously, this is neither possible for all J nor for all T_2 values simultaneously. Calculations and optimizations performed by the authors were summarized in tables. In these tables, the reader can find representative sets of delays Δ corresponding to the line widths 0.5, 1, 2, and 3 Hz. For instance, a broadband HMBC for 1 Hz line widths can be recorded using four different values for the delay Δ: 97.4, 80.0, 67.8, and 59.0 ms. This setting ensures 75% of the maximal transfer for ${}^nJ_{CH}$ comprise between 2.43 and 8.83 Hz. For comparison, a static HMBC optimized for ${}^nJ_{CH} = 7.7$ Hz ($\Delta = 65$ ms) ensures 75% of the maximal transfer for ${}^nJ_{CH}$ comprise between 3.03 and 10.83 Hz and a static HMBC optimized for ${}^nJ_{CH} = 5$ Hz ($\Delta = 100$ ms) ensures 75% of the maximal transfer for ${}^nJ_{CH}$ comprise between 1.40 and 6.90 Hz. The authors also developed so-called *ultra*-HMBC experiments, optimized for high sensitivity at very small long-rang coupling constants. For instance, an *ultra*-HMBC for 2 Hz linewidths can be recorded using four different values for the delay Δ: 181.1, 160.0, 115.0, and 99.3 ms. This setting ensures 75% of the maximal transfer for ${}^nJ_{CH}$ comprise between 0.03 and 4.03 Hz.[53]

The main advantage of this approach is that gaps of zero transfer amplitude are avoided throughout the range of long-range heteronuclear J-couplings of interest. As for accordion-optimized experiments, this can be of particular advantage when recording spectra of unknown substances. In addition, specially tailored ultra-broadband HMBC are parameterized in order to observe very small coupling constants while maintaining non-vanishing cross-peaks for the larger J's.

4.2.2. Practical applications

In practical applications, it can be a factor that the above approach by virtue of the cycle over Δ values has a higher minimum number of scans per t_1 value than the standard experiment and its various accordion versions. For dilute samples, this does not matter but for concentrated samples the instrument time can be longer than required considering the inherent sensitivity.

It seems that the broadband HMBC is more effective for small molecules, as emphasized by Equations (24)–(26). For cyclosporine, indeed, as shown by Figures 15 and 16, there is no advantage in recording broadband and *ultra*-broadband HMBC as compared to standard optimized HMBC schemes. On the contrary, the *ultra*-broadband HMBC spectrum shown in Figure 16 does not exhibit more cross-peaks than the standard HMBC (Figure 15A), and there is besides a severe sensitivity loss.

4.3. *J*-compensated HMBC

Another method to cope with the problem of weak or missing long-range correlations in HMBC spectra is to implement so-called *J*-compensated sequences. The problem of incomplete coherence conversion by spin–spin coupling is actually similar to the problems associated with the inhomogeneity of radiofrequency pulses, which can be minimized by replacing the RF pulse by appropriate composite or adiabatic pulses. By using this parallelism between RF pulses and spin–spin coupling, Wimperis and Bodenhausen have devised *J*-compensated INEPT sequences that are less

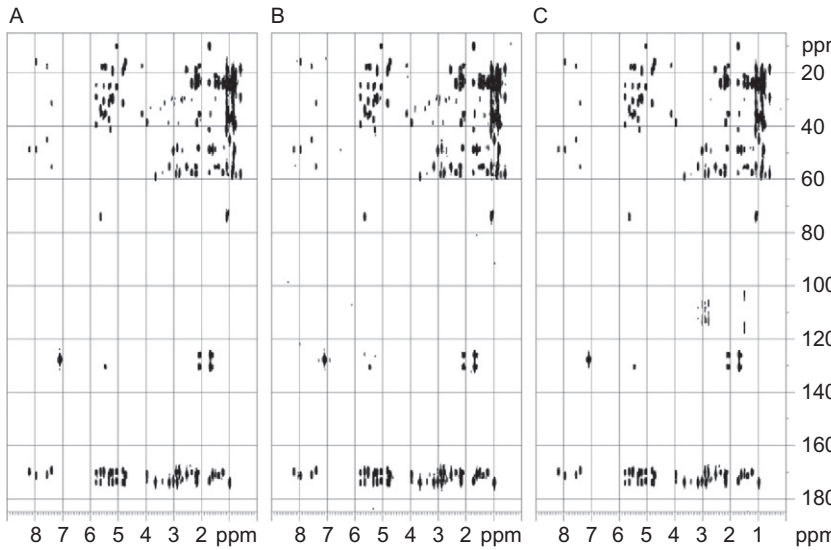

Figure 15 HMBC and broadband HMBC spectra of cyclosporine in C_6D_6 recorded with the pulse sequence shown in Figure 14. (A) HMBC spectrum recorded with $\Delta = 65.0$ ms and 32 scans. (B) HMBC spectrum where two subspectra of 16 scans each recorded with $\Delta = 65.0$ ms and 120 ms, and co-added in absolute-value mode. (C) broadband HMBC spectrum where four subspectra of eight scans each were recorded with $\Delta = 96.7$, 84.4, 81.8, and 80.8 ms, respectively, and co-added in absolute-value mode.

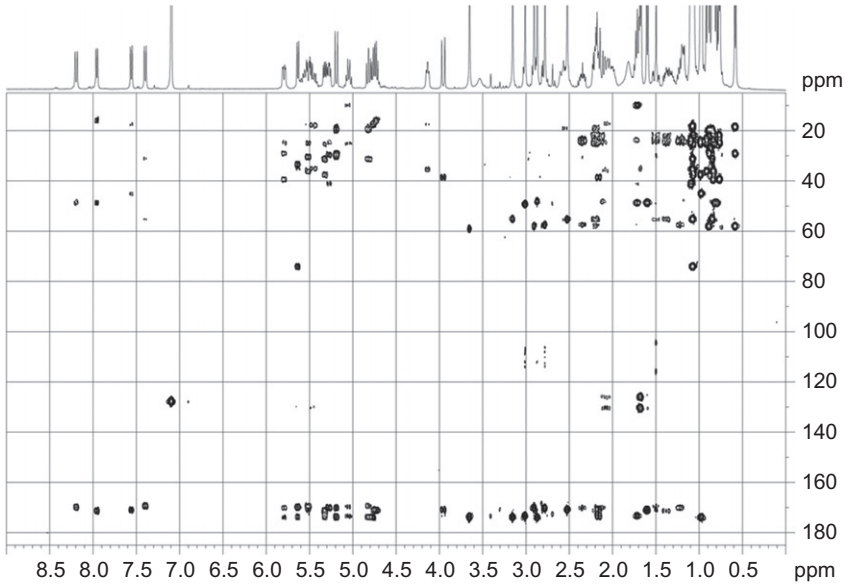

Figure 16 *ultra*-HMBC spectrum of cyclosporine in C_6D_6 recorded with the pulse sequence shown in Figure 14 where four subspectra of eight scans each were recorded with $\Delta = 181.1$, 160.0, 115.0, and 99.3 ms, respectively, and co-added in absolute-value mode.

sensitive to variation in $^1J_{CH}$.[54] Subsequently, *J*-compensated sequences, termed INEPT-CR,[55] and *J*-compensated DEPT sequences,[56] were shown to be less sensitive to variations in J_{CH} than standard INEPT and DEPT experiments. More recently, the implementation of *J*-refocusing techniques into a PGSE-type experiment (*J*-PGSE) and HMBC has proven to improve the spectra as compared to standard PGSE and HMBC experiments.[57,58] Overall, it turns out that the major drawback of all *J*-compensated experiments is that they incorporate more RF pulses and delays than the conventional experiments. This makes them longer in duration and therefore more susceptible to signal loss through relaxation. In their contribution, however, Torres et al. could develop short *J*-compensated sequences,[57] which are highly desirable as their duration is extended by only 50% compared with conventional experiments. Of the various developed and investigated *J*-compensated HMBC experiments, the so-called HMBC-J45 + 90A and HMBC-J45 + 90B, which use an excitation pulse of the form $45_x90_{(x+120)}$ and $45_x90_{(x+90)}$, respectively, were shown to be more effective over a wider range of $^nJ_{CH}$ values and they were less prone to pulse-calibration imperfections (Figure 17). These two experiments are unusual in that their pulse sequences start with an RF pulse of less than 90°.

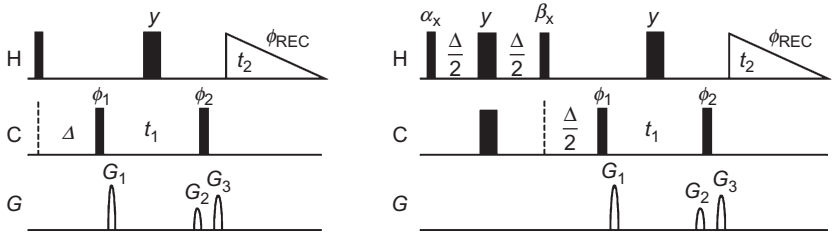

Figure 17 Pulse sequences for the standard HMBC (without low-pass J filters) (A), and for the *J*-compensated HMBC-J45 + 90A ($\alpha = 30°$, $\beta = 120°$) or HMBC-J45 + 90B ($\alpha = 45°$, $\beta = 90°$) (B). The gradient ratios G_1:G_2:G_3 can bet set as normally implemented in the gradient-selected HMBC experiment, that is 50:30:40.1. The basic phase cycle can also be applied: $\phi_1 = (x, -x)_2$; $\phi_2 = x, x, -x, -x$; and $\phi_R = x, -x, -x, x$.

In this chapter, various pulse sequences for detecting a large range of long-range coupling constants have been presented and their advantages and potential disadvantages have been discussed. The pioneer ACCORD-HMBC has early shown its limit, since the skewed of the F_1 responses is more disturbing than helping. Improved pulse sequences, such as IMPEACH-MBC, CIGAR-HMBC or CT-accordion (G)BIRD-HMBC, provides the means of suppressing the otherwise disturbing F_1 homonuclear coupling modulation while still allowing broad ranges of potential long-range couplings to be sampled in a single experiment. Experimentally, it turns out that these improved accordion-based experiments have undoubtedly their merits. While a broad range of long-range couplings can be effectively sampled in a single experiment, this is achieved at a cost of a severe sensitivity loss compared to a statically optimized HMBC. Usually, to obtain a comparable sensitivity, these experiments must be recorded using twice as much scans as the corresponding statically HMBC experiment. The reason is obvious: all these pulse sequences contain much more pulses, especially on the ^{13}C channel, and are significantly longer, due to the constant-time construction, compared to a statically optimized HMBC. Usually, it is advisable to record two different statically optimized HMBC and to sum up the data. The broadband HMBC presented above does provide a more uniform excitation over a range of heteronuclear long-range coupling constants. The main advantage of this approach is that gaps of zero transfer amplitude are avoided throughout the range of long-range heteronuclear *J*-couplings of interest. The remedy is both simple and effective as it just consists of co-adding spectra recorded with different delays in the pulse sequence. In addition, the provided tables help the users to find the suitable sets of delays Δ corresponding to the desired long-range coupling range as well as to the size of the compound under study.

5. DIFFERENTIATING BETWEEN $^{2}J_{CH}$ AND $^{3,4}J_{CH}$ CONNECTIVITIES

HMBC spectra provide a wealth of correlations over multiple bonds, and while this on one hand is highly attractive, it poses the problem of distinguishing particularly between two- and three-bond correlations. Several methods have been proposed to this end, and will be briefly exposed in the following.

5.1. The ^{2}J,^{3}J-HMBC experiment

5.1.1. Principles: The STAR element

In 2000, Krishnamurthy et al. have presented the ^{2}J,^{3}J-HMBC experiment (Figure 20), that affords for the first time the means of unequivocally differentiating between $^{2}J_{CH}$ from $^{3}J_{CH}$ correlations.[59] Their approach is based on a further derivative of the constant-time variable delay introduced in the IMPEACH-MBC experiment. The user-definable J-scaling factor of the CIGAR-HMBC is used in the new experiment, the ^{2}J,^{3}J-HMBC experiment, to differentiate between $^{2}J_{CH}$ from $^{3}J_{CH}$ correlations. This new pulse sequence element has been given the acronym STAR (*S*electively *T*ailored *A*ccordion F_1 *R*efocused) operator.

5.1.2. Evaluation of the STAR element

The behaviour of all magnetization of interest during the STAR operator will be described subsequently. To understand correctly the behaviour of the F_1 response of a given long-range CH spin–pair, one needs to investigate the fate of all couplings during the STAR element. For clarity, we will use a hypothetical C_1H_1—C_2H_2—C_3H_3 fragment, sketched in Figure 18.

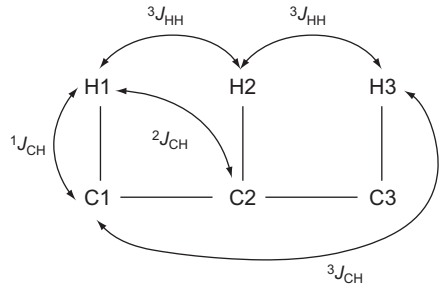

Figure 18 Hypothetical C_1H_1—C_2H_2—C_3H_3 fragment within a more complex molecule, with heteronuclear coupling constants $^{1}J_{H1C1}$, $^{2}J_{H1C2}$, $^{1}J_{H2C1}$, $^{2}J_{H2C1}$, respectively, and homonuclear coupling constants $^{3}J_{H1H2}$, $^{3}J_{H1H3}$, respectively.

The STAR element includes a BIRD^{d,X} pulse whose effect is inverse to that of the BIRD^{r,X} pulse employed in BIRD-HMBC experiments. It behaves like a 180° for the ^{13}C and the protons that is directly attached to it, but as a 0° for all other protons, including the active proton of a long-range CH spin pair. It follows that the direct coupling $^{1}J_{C1H1}$ and the geminal coupling $^{3}J_{H2H3}$ are active (have evolved) after a BIRD^{d,X} filter, while the long-range heteronuclear couplings $^{2}J_{C1H2}$ and $^{3}J_{C1H3}$, as well as the geminal coupling $^{3}J_{H1H2}$ remain inactive (Table 3).

5.1.2.1. Evaluation for the ^{1}H–^{1}H homonuclear couplings ($^{2}J_{CH}$) According to Table 3, the vicinal component ($^{3}J_{H1H2}$) of magnetization in the long-range response that is two-bond coupled to a protonated carbon is refocused during the course of the BIRD^{d,X} pulse. Therefore, it experiences modulation, which serves as a pseudo-evolution for this coupling (Figure 19).

5.1.2.2. Evaluation for the ^{1}H–^{1}H homonuclear couplings ($^{3}J_{CH}$) According to Table 3, the vicinal component ($^{3}J_{H2H3}$) of magnetization in the long-range response that is three-bond coupled to a protonated carbon is active during the course of the BIRD^{d,X} pulse. Therefore, it does not exhibit an F_1 skew. Homonuclear modulation during the evolution time t_1 is still present, as in standard HMBC experiments (Figure 19).

In Figure 21, a $^{2}J,^{3}J$-HMBC spectrum recorded on cyclosporine is shown. A specific region is exemplified and magnified in (A). For

TABLE 3 Relevant interactions which effectively influence the different spins of the hypothetical $C_1H_1—C_2H_2—C_3H_3$ described in Figure 19 during a BIRD^{d,X} filter

	$^{3}J_{H1H2}$	$^{1}J_{C1H1}$	$^{2}J_{C1H2}$	$^{3}J_{C1H3}$	$^{3}J_{H2H3}$	δ_{1H}	$\delta_{H2,H3}$	δ_{13C}
BIRD^{d,X}	*Inactive*	Active	Inactive	Inactive	*Active*	Inactive	Active	Inactive

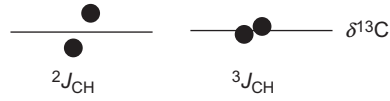

Figure 19 Schematic effect of the STAR operator on $^{2}J_{CH}$ and $^{3}J_{CH}$ couplings. The vicinal component of magnetization in the long-range response that is two-bond coupled to a protonated carbon experiences modulation, which serves as a pseudo-evolution for this coupling. In contrast, the vicinal component of magnetization in the long-range response that is three-bond coupled to a protonated carbon does not exhibit a F_1 skew. Homonuclear modulation during the evolution period t_1 is still present, as the full experiment is not a constant-time experiment.

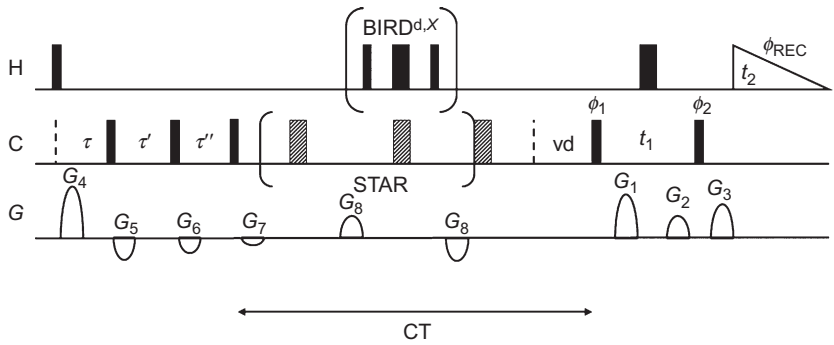

Figure 20 Timing diagram of the suggested $^{2}J,^{3}J$-HMBC experiment, including a LPJF3 for efficient 1JCH suppression. The sequence is virtually identical to the CIGAR-HMBC pulse sequence. The STAR operator is also a constant-time variable element. In this fashion, scalable F_1 modulation can be specifically introduced for $^{2}J_{CH}$ cross-peaks into the spectrum independently of the digitization employed in the second frequency domain.

comparison, the same region from a standard is shown in (B). This region shows the ^{n}J correlations from the amide protons to the neighbouring aliphatic groups. In the $^{2}J,^{3}J$-HMBC spectrum, the distinction between ^{2}J and ^{3}J correlation is obvious. For instance, at a chemical shift of 8.00 ppm (NH Ala 7), two cross-peaks can be found: the cross peak at 49.5 ppm shows the typical F_1 skew characteristic of a ^{2}J-correlation, while the cross peak at 16.6 ppm is similar in the $^{2}J,^{3}J$-HMBC and in the HMBC spectrum. Therefore, in this simple example, the cross peak at 49.5 ppm belongs to the αC while the cross peak at 16.6 ppm belongs to the βC.

While the $^{2}J,^{3}J$-HMBC experiment, also known as STAR-HMBC, has undeniably its merits, it also suffers from a severe sensitivity penalty which results from the extended pulse sequence and additional delays, pulses and gradients as compared to the standard HMBC sequence. For instance, the $^{2}J,^{3}J$-HMBC spectrum shown in Figure 21 has been recorded using 64 scans, for a total experimental time of 184 min, while for obtaining approximately the same signal-to-noise ratio, the corresponding HMBC spectrum could be recorded with only 8 scans and 23 min.

5.2. The HMBC–RELAY experiment

In 2003, Sprang and Bigler have developed a pulse sequence, HMBC–RELAY, subsequently improved in 2004, that yields two simultaneously detected types of long-range correlation spectra.[60,61] One spectrum shows all $^{n}J_{CH}$ connectivities while the other shows exclusively $^{2}J_{CH}$ connectivities. Their method uses homonuclear $^{3}J_{HH}$ couplings between the protons of adjacent carbons, as already been exploited for the XCORFE

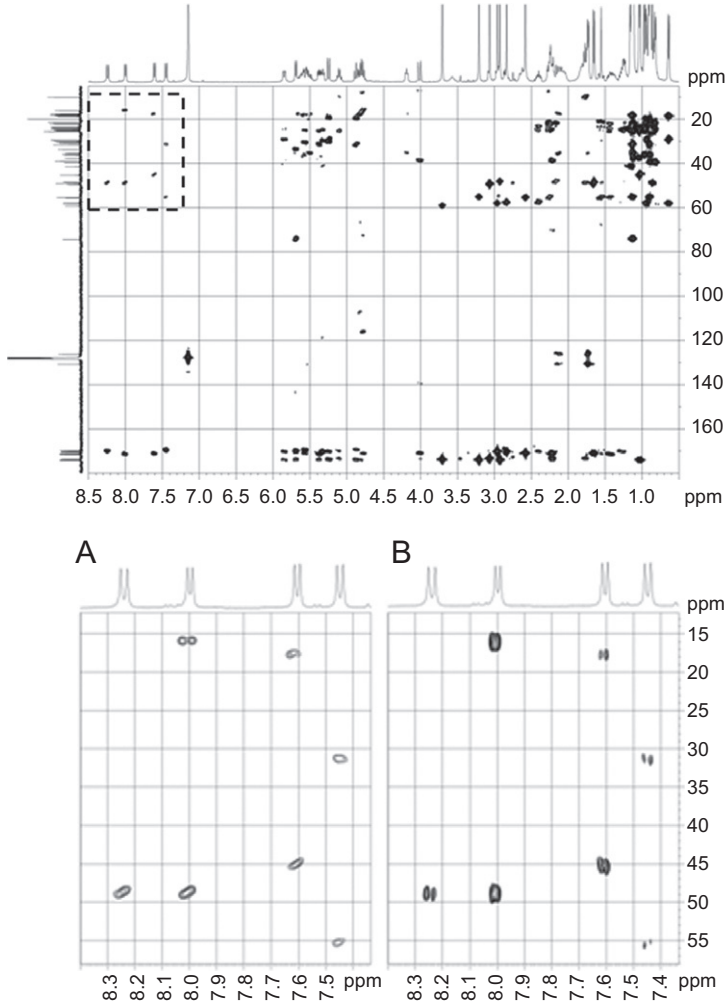

Figure 21 $^{2}J,^{3}J$-HMBC spectrum recorded on cyclosporine (left). The region labelled by a dashed box is exemplified in (A). For comparison, (B) shows the corresponding region taken from a standard HMBC.

experiment[62] that creates split signals for $^{2}J_{CH}$ and collapsed signals for $^{3,4}J_{CH}$ connectivities as well as for the $^{2}J,^{3}J$-HMBC pulse sequence presented above. Based on the idea of the HMSC experiment[63] that uses a single sequence to simultaneously detect $^{1}J_{CH}$ and $^{n}J_{CH}$ couplings and presents them in two subspectra, their goal was to develop a pulse sequence that detects $^{2}J_{CH}$ and $^{n}J_{CH}$ connectivities simultaneously and allows the calculation of the corresponding subspectra. The HMBC–RELAY sequence is depicted in Figure 22.

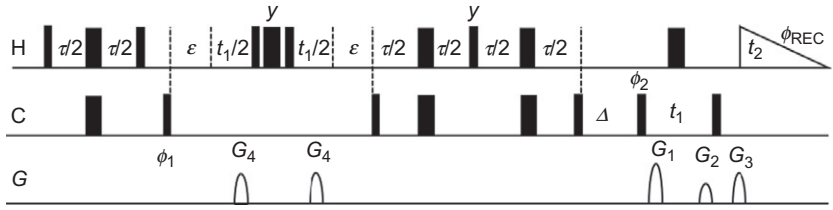

Figure 22 Pulse sequence of the HMBC–RELAY experiment. Filled and open bars represent 90° and 180° pulses, respectively. All other phases are set as *x*, excepted otherwise stated. A two-phase cycle *x*, $-x$ is used for the pulse phases ϕ_1 and ϕ_2 and the receiver phase. In order to separate the $^2J_{CH}$ and the $^nJ_{CH}$ spectra, two FIDs have to be acquired for each t_1 increment with the phase ϕ_1 set as *x*, $-x$ and $-x$, *x*, respectively (*interleaved* mode of detection) and have to be stored separately. By using a composite $90°x\ -180°y\ -90°x$ pulse instead of a single $180°x$ ^{1}H pulse, artefacts arising from misadjusted ^{1}H pulse lengths are suppressed. The delays are calculated according to $\tau/2 = [0.25/^1J_{CH}]$, $\varepsilon = [0.25/^3J_{HH}]$ and $\Delta = [0.5/^nJ_{CH}]$. The ^{13}C chemical shift evolution delay t_1 must be equal for both evolution periods.

5.2.1. Principles

In the HMBC–RELAY experiment, the discrimination between $^nJ_{CH}$ and $^2J_{CH}$ requires using two-independent coherence pathways, which significantly lengthen the pulse sequence. The detection of $^nJ_{CH}$ is achieved using an HMBC mechanism whereas the detection of $^2J_{CH}$ works by a C, H,H-RELAY mechanism. Since Δ is adjusted to $^nJ_{CH}$ couplings (i.e. 8–12 Hz), this should not attenuate the cosine dependence of the cosine term containing the $^2J_{CH}$ magnetization. Indeed, most $^2J_{CH}$ coupling constants are in the range of 1–6 Hz, and there will be only moderate or even almost no evolution under the influence of heteronuclear coupling in Δ. Consequently, most signals in the ^2J spectrum are expected to be of adequate intensity. In order to separate the $^2J_{CH}$ and the $^nJ_{CH}$ spectra, two FIDs have to be acquired for each t_1 increment and have to be stored separately (interleaved mode of detection). With the phase of the first carbon 90 pulse set as x and $-$x, the $^2J_{CH}$ responses are selectively encoded as $+$ or $-$, whereas the ''mixed'' $^2J_{CH} + {}^nJ_{CH}$ responses are not affected. Therefore, subtraction of the two FIDs acquired for each t_1 will add up the pure $^2J_{CH}$ responses, but will cancel the ''mixed'' $^2J_{CH} + {}^nJ_{CH}$ responses. Conversely, co-addition will add up the ''mixed'' $^2J_{CH} + {}^nJ_{CH}$ responses, but will cancel the pure $^2J_{CH}$ responses.

5.2.2. Evaluation

The HMBC–RELAY experiment has merit, but suffers from several deficiencies. First, $^2J_{CH}$ signals for quaternary carbons are missing since the transfer of coherences from carbon to protons is restricted to proton-bearing carbons. This is also the drawback of the $^2J,^3J$-HMBC experiment.

Second, the detection of $^{n}J_{CH}$ and $^{2}J_{CH}$ requires using two-independent pathways, which significantly lengthen the pulse sequence and the number of pulses, especially 180° pulses. The consequence is a strong intensity drop as compared to a standard HMBC experiment, especially for $^{2}J_{CH}$ correlations. Third, the COSY transfer of the $\pm$ $H_{1x}H_{2z}$ coherence into $\pm$ $H_{1z}H_{2x}$ through homonuclear ^{1}H–^{1}H couplings depends on the magnitude of the J_{HH} coupling constant. Therefore, potential missing $^{2}J_{CH}$ correlations and /or undesired $^{3}J_{CH}$ or $^{4}J_{CH}$ correlations can hamper the analysis of the $^{2}J_{CH}/^{n}J_{CH}$ maps. In the case of completely unknown compounds, this drawback might seriously complicate the analysis (Figure 23).

5.3. The H2BC experiment: Suppressing three or higher correlations

5.3.1. Principles

In 2005, Sørensen et al. have reported a novel experiment, H2BC, which should in principle overcome the drawbacks of the $^{2}J,^{3}J$-HMBC and HMBC–RELAY experiments. The experiment, shown in Figure 24, leads to an HMBC-type spectrum almost exclusively showing only two-bond correlations and markedly also two-bond correlations that are absent in HMBC spectra.[64] Virtually, H2BC can be understood as an HMQC-COSY experiment designed to the needs of small molecule heteronuclear NMR spectroscopy. The H2BC experiment relies on $^{1}J_{CH}$ and $^{n}J_{HH}$ couplings for coherence transfer and is fully independent of long-range $^{n}J_{CH}$ couplings, the HMBC amplitude factor $\sin(\pi^{n}J_{CH}\Delta)$. Furthermore, heteronuclear decoupling can be employed during acquisition, which compares favourably with HMBC where either the peaks are AP with respect to $^{n}J_{CH}$ or an additional refocusing delay Δ is introduced. In addition, the authors have made the H2BC a constant-time experiment that suppresses all homo- and heteronuclear couplings in the indirect dimension F_1.

5.3.2. Experimental verification

As indicated by the authors, H2BC spectra only show peaks involving protonated ^{13}C spins, but ^{1}H can be attached to any type of atom if $^{3}J_{HH}$ does not vanish. The discrimination between two- and three-bond correlations in H2BC is based solely on the size of $^{n}J_{HH}$ coupling constants, and as these do not uniformly vanish for $n > 3$, there is no absolute guarantee that a peak in an H2BC spectrum represents a two-bond correlation. It must be kept in mind that unusual large $^{4}J_{HH}$ coupling constants can lead to three-bond correlation peaks in H2BC spectra. However, as a rule of thumb, correlations that are strong in an H2BC spectrum and weak in an HMBC spectrum indicate two-bond correlations, while vice versa is indicative of a three-bond correlation. Possible remaining ambiguities

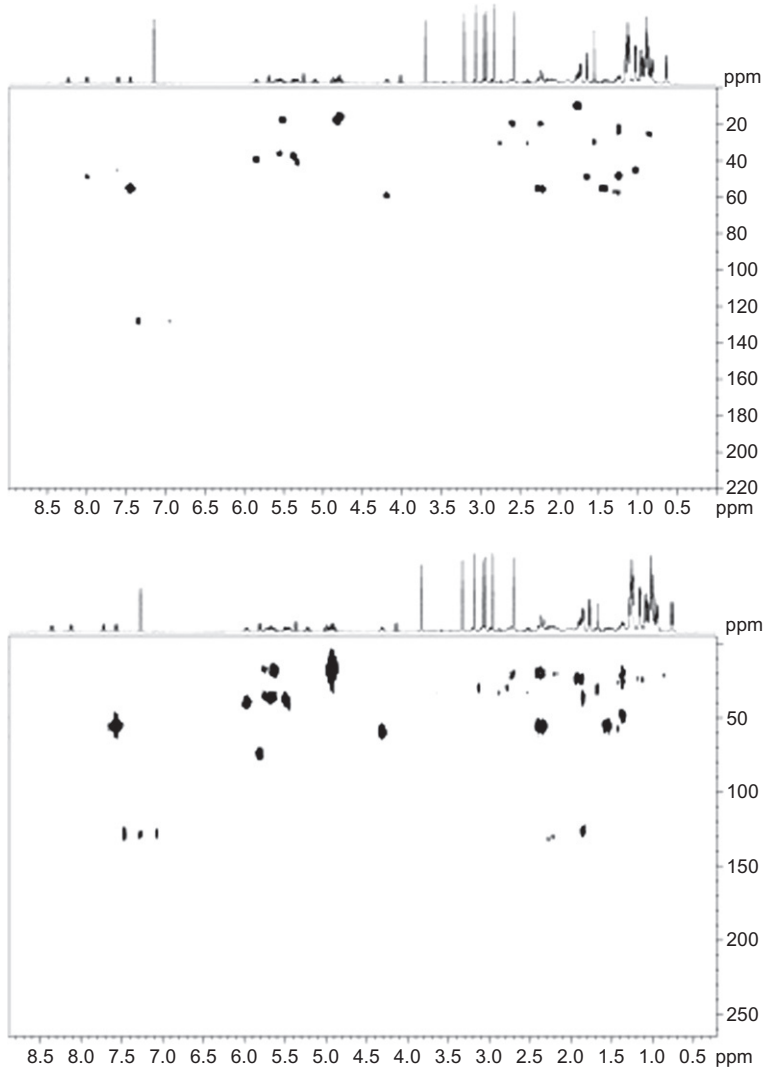

Figure 23 HMBC–RELAY spectra recorded on cyclosporine. Top: experiment optimized for $J_{HH} = 6$ Hz. Bottom: experiment optimized for $J_{HH} = 8$ Hz.

associated with peaks of similar intensities in H2BC and HMBC must be resolved based on the clear two- and three-bond assignments.

A further refinement of the H2BC has been subsequently presented by the same authors. It consists in a version that allows editing H2BC spectra, that is, an experiment that edits into two subspectra according to the number of protons attached to ^{13}C nuclei being odd or even.[65,66]

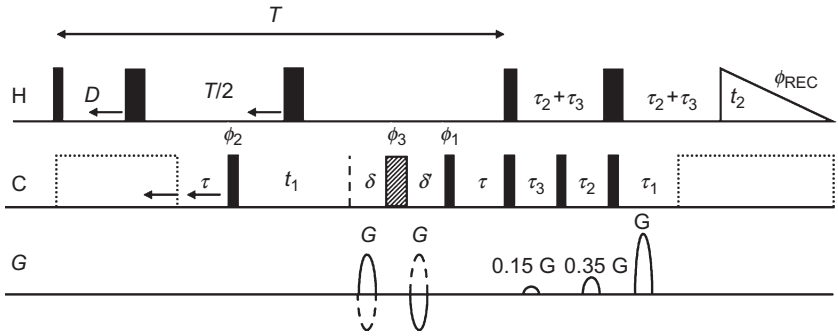

Figure 24 H2BC pulse sequence. Thin and thick bars represent 90° and 180° pulses, respectively, while, and the dashed boxes represent ^{13}C decoupling. $\tau = \tau_2 = 1/[^1J_{max} + {}^1J_{min}]$, $\tau_1 = 0.5/[^1J_{min} + 0.07(^1J_{max} - {}^1J_{min})]$, $\tau_3 = 0.5/[^1J_{max} - 0.07(^1J_{max} - {}^1J_{min})]$ and $\delta' = \delta + t(90_H)$, where δ is the gradient delay. T denotes the constant-time delay. The gradient strength is G and $-G$ for echo and antiecho selection, respectively. The recommended phase cycle is $\phi_1 = x, -x, -x, x$, $\phi_2 = x, x, 4(-x), x, x$, $\phi_3 = 4(x), 4(y), 4(-x), 4(-y)$, $\phi_{REC} = x, -x$.

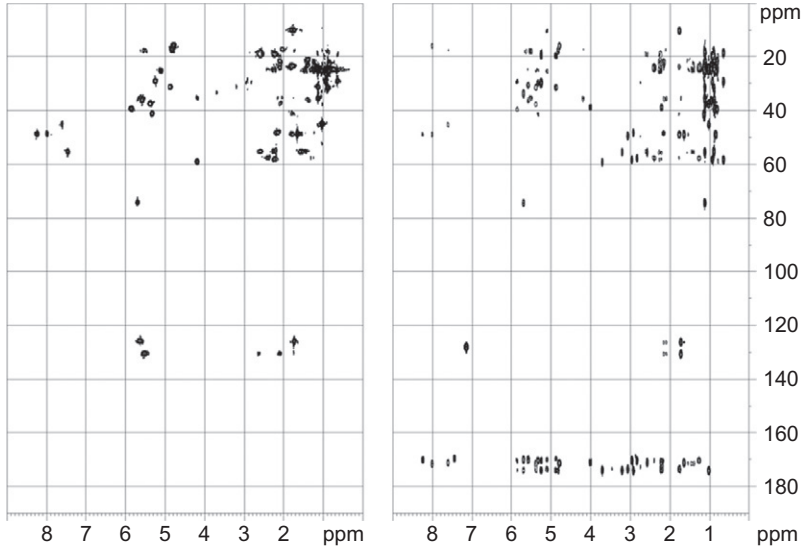

Figure 25 H2BC spectrum recorded on cyclosporine (left), compared with a standard gradient-selected HMBC (right).

Figure 25 shows a comparison between an H2BC (left) and an HMBC (right) spectrum of cyclosporine recorded under identical conditions and using the same contour levels. The spectra are quite complementary, as

H2BC shows all possible two-bond correlations, while in HMBC, some two-bond peaks are very weak or even missing.

As shown by the authors, the almost exclusivity of two-bond correlations in H2BC makes it possible to extract INADEQUATE-type connectivity information by overlaying H2BC and HSQC spectra. Also, the complementarity of HSQC, H2BC, and HMBC spectra could be used for a semi-automated analysis of this package of spectra based on the H2BC–HMBC rule of thumb mentioned above and the unique one-bond correlations in HSQC.

6. EDITING HMBC SPECTRA

6.1. The edited HMBC

All HMBC experiments that have been examined so far yield a general map of correlations based on non-vanishing $^{n}J_{CH}$ coupling constants, and typically exhibits good sensitivity for two- and three-bond correlations. H2BC yields almost exclusively a map of $^{2}J_{CH}$ of protonated carbons. H2BC and HMBC are therefore quite complementary and are recommended for studying small molecules. It is not uncommon that the number of peaks in HMBC spectra exceeds 100. With such a large number of peaks comes also the risk of overlap that can obscure weak peaks or cause ambiguities. Hence it would be of great interest to edit HMBC spectra into independent subspectra with a reduced risk of overlap. In 2006, Sørensen et al. have proposed such an experiment to edit HMBC spectra. The principle of edited HMBC experiments consists of combining data obtained by two similar sequences where CH and CH_3 signals are inverted in the latter. These two data sets are added and subtracted to yield the C + CH_2 and CH + CH_3 subspectra, respectively.[67,68]

6.1.1. Principles

The pulse sequences suitable for editing HMBC spectra are outlined in Figure 26. The authors have proposed the following design of the edited HMBC pulse sequence pair: ^{13}C coherence is excited from a remote proton via long-range $^{n}J_{CH}$ couplings in HMBC experiments in the form of heteronuclear zero- and double-quantum coherences. These coherences have the same multiplet structure as ^{13}C single-quantum coherence if long-range couplings are ignored. In analogy with early ^{13}C editing experiments, these coherences can be probed whether the number of directly attached protons is odd or even. As noted by the authors, the standard spectrum can be obtained by any variant of the HMBC pulse sequence, but for the purpose of editing it is necessary to adapt the standard pulse sequence to ensure that the only effective difference to the up–down pulse sequence

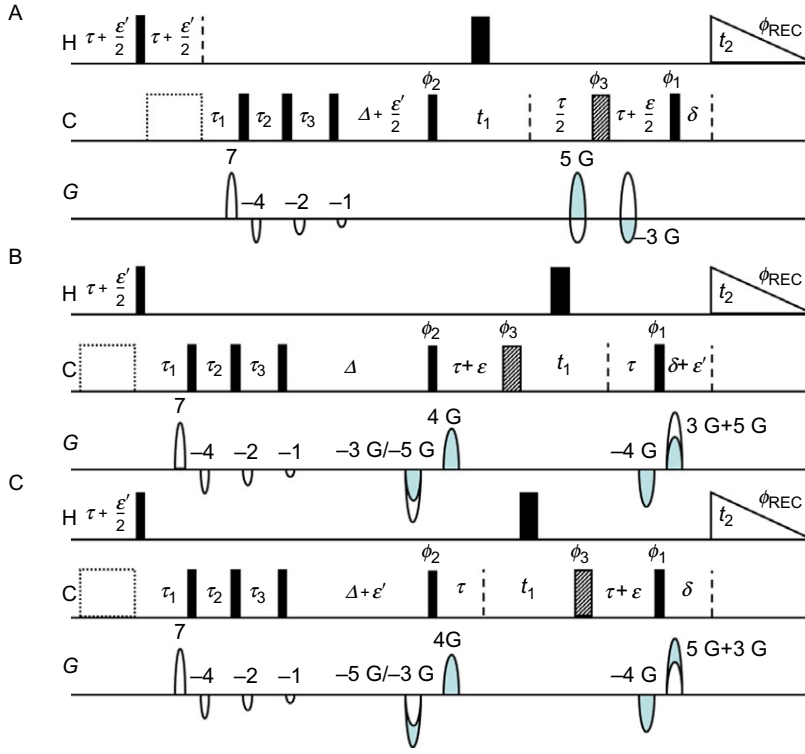

Figure 26 Proposed HMBC pulse sequences[68] for editing into two subspectra according to the number of directly attached protons being odd or even: Filled and open bars refer to 90° and 180° pulses, respectively, while the dashed open boxes represent ^{13}C decoupling. Recommended phase cycle: $\phi_1 = x, -x, x, -x$; $\phi_2 = x, x, 4(-x), x, x$; $\phi_3 = 4(x), 4(y), 4(-x), 4(-y)$; $\phi_{REC} = x, -x$. (A) Standard HMBC pulse sequence. (B) up–down "−" HMBC pulse sequence inverting ^{13}CH and ^{13}CH$_3$ peaks relative to the standard sequence. (C) up–down "+" HMBC pulse sequence inverting ^{13}CH and ^{13}CH$_3$ peaks relative to the standard sequence and in the opposite sense to the up–down "−" sequence. The data of the different pulse sequences are recorded in an interleaved manner. After formation of the required two linear combinations in the time domain, the data are processed in the same way as other HMBC-type data.

is that the latter includes a $1/^1J_{CH}$ evolution of heteronuclear couplings during the time of heteronuclear two-spin coherence.

The current version required recording three different pulse sequences, such as *J* cross-talk (i.e. an ''even signal'' in the ''odd subspectrum'' or *vice versa* caused by deviation, ΔJ, of an actual $^1J_{CH}$ from the value used in setting the τ delays) are minimized.[69] It is however possible to obtain edited spectra by using one reference and one up–down sequence.

6.1.2. Experimental verification

See Figure 27

6.2. The HAT-HMBC experiment

Subsequent to the edited HMBC experiments, Benie and Sørensen have introduced the HAT-HMBC (Homonuclear J ATtenuated) experiment that is conceptually a hybrid of the H2BC and HMBC.[70] The experiment aims at establishing two-bond correlations absent or very weak in H2BC spectra because of vanishing $^{3}J_{HH}$ coupling constants. Such peaks ($^{3}J_{HH} = 0$, $^{2}J_{CH} \neq 0$) can be observed in HMBC spectra, but often their identification will remain unobvious. The HAT-HMBC aimed at identifying

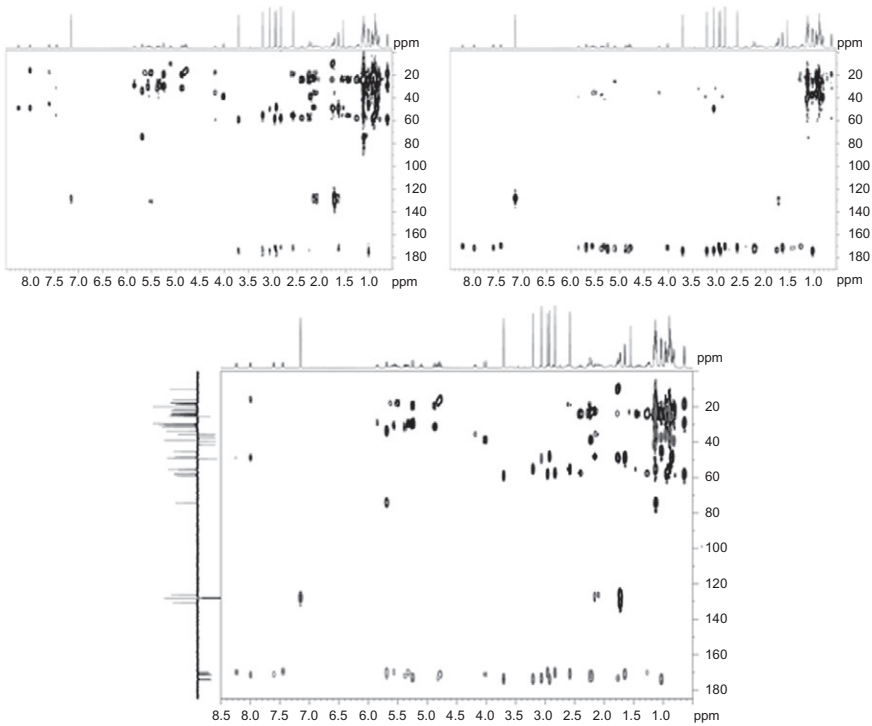

Figure 27 Edited broadband HMBC spectrum of cyclosporine using the pulse sequences shown in Figure 26 in an interleaved manner. The two subspectra, CH + CH_3 (left) and C + CH_2 (right), exemplify the editing properties. The spectrum in the bottom displays the two subspectra, CH + CH_3 (black) and C + CH_2 (grey) in the same frame. The number of scans was 32 for each of the 128t_1 increments, the relaxation delay was 1 s, and the range for the third-order low-pass *J*-filter was 115 Hz $< {}^{1}J_{CH} <$ 165 Hz. The spectra were processed to maintain the absorptive profiles in F_1 while a magnitude mode was done in F_2.

those two-bond correlations. Similar to the edited HMBC, the central idea of the HAT-HMBC is to create an additional 180° phase difference in the multiplet structure in HMBC peaks with respect to the $^{n+1}J_{HH}$ coupling constant between the proton(s) attached to a ^{13}C and a remote proton separated by n bonds.

In comparison to the HMBC pulse sequence, the HAT-HMBC experiment includes an evolution period $0.5/^{1}J_{CH}$ introduced between the two 90° ^{13}C pulses surrounding t_1 yielding an additional 180° phase difference of multiplet components. As for the edited HMBC experiments, the 90° evolution under $^{1}J_{CH}$ of the individual $^{1}J_{CH}$ doublet components can be chosen positive or negative, depending whether the 180° ^{13}C pulse is applied before or after the 180° ^{1}H pulse, respectively (Figure 26). Subsequent addition and subtraction of the HAT "−" and HAT "+" data sets allow editing into two subspectra according to the number of protons attached to the ^{13}C being even (i.e. C and CH_2 groups) or odd (i.e. CH and CH_3 groups).

7. IMPROVING THE F_1 RESOLUTION

7.1. Constant-time HMBC experiments

As in the case of HMQC, ^{1}H multiple structure appears along f_1 as well as f_2, limiting ^{13}C resolution. Various approaches have been suggested to overcome these problems. f_1 modulation can be eliminated by replacing the variable evolution time t_1 with a constant-time period[71] incorporating a ^{13}C 180° pulse which is incrementally moved through the time period to generate ^{13}C chemical shift information. This can significantly improve ^{13}C resolution with minimal loss in sensitivity and is particularly useful for disentangling crowded regions[72,73] (Figure 28).

7.2. The 10-ppm HMBC experiment

We have seen in the previous chapters that standard HMBC experiments usually have low signal resolution in the carbon-13 dimension. When a 250-ppm HMBC spectrum is acquired using 128–512 time increments signals have a typical width as large as 1 (ppm) in the carbon dimension. The measured chemical shifts have four significant figures among which one is to the right of the decimal separator while 1D carbon spectra provide five figures. Close pairs of carbons are therefore unresolved making it difficult or impossible to assign signals. This is quite likely to occur in the study of mixtures of isomers, oligomers, polyketals, etc. but may also happen with the simplest molecules. The use of band–selective HMBC experiments greatly enhances the resolution in the carbon

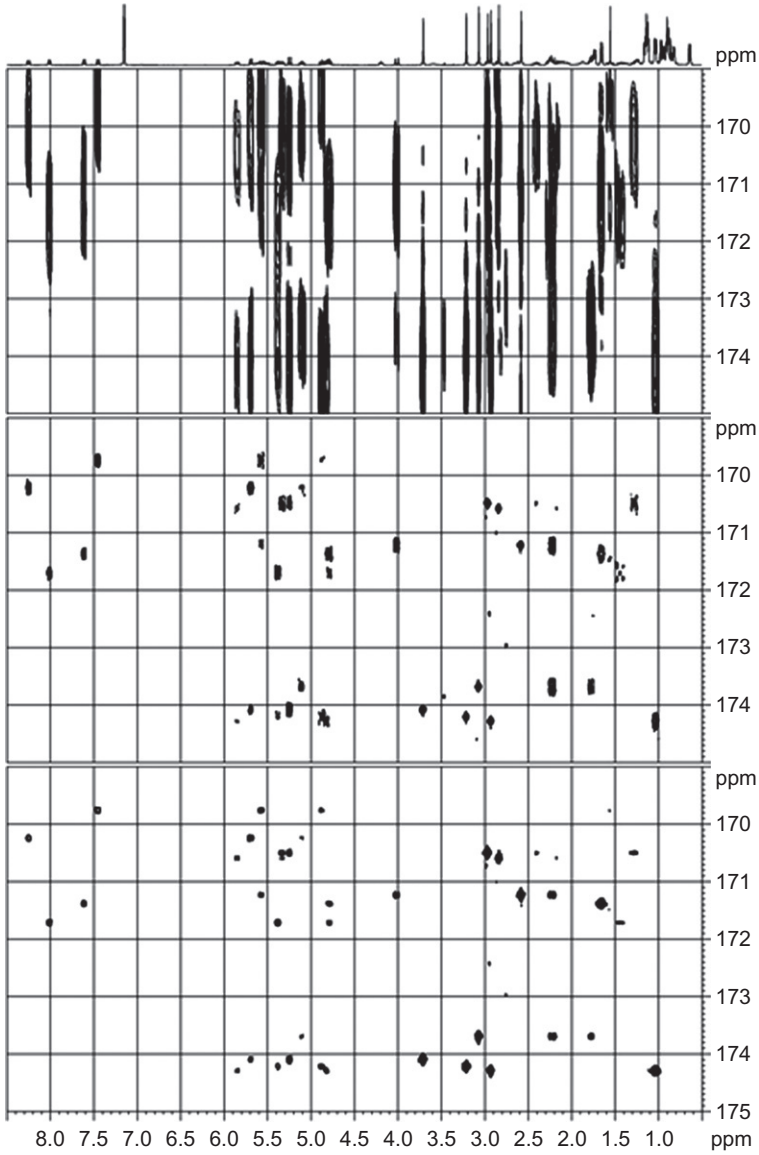

Figure 28 Excerpts of an HMBC (top), BS-HMBC (middle) and CT-BS-HMBC (bottom) spectra showing the carbonyl part of cyclosporine using the standard HMBC pulse sequence and the CT–BS-HMBC of Claridge.[73] The conventional non-selective HMBC was acquired with a 200-ppm ^{13}C window. The band-selective (middle) and the constant-time band-selective (bottom) HMBC were acquired with a 6-ppm window cantered at 172 ppm. Selective excitation was achieved with a ^{13}C 1 ms 180° seduce-1 pulse.

dimension.[73–77] However, in case of very crowded spectra, the full assignment of all signals may require recording several band–selective HMBC experiments, which may be impractical due to time constraints.

7.2.1. Principles

Recently, Jeannerat et al. have proposed to record ''10-ppm spectra'' to avoid all these problems (Figure 29).[78] Their experiment uses the properties of ''spectral aliasing'', the phenomenon making signals outside the spectral boundaries appearing as back-folded (or ''aliased'') into the smaller window. Determining the correct chemical shifts in 10-ppm-aliased spectra is straightforward, thanks to a property of the modulo function. When looking at the spectra of 10-ppm scales, it is possible to rely simply on one digit on the left of the period and two on the right. One must ignore the first two digits of the observed chemical shift. The combination of the values observed in the full-width and the 10-ppm spectra generates carbon chemical shifts with five digital figures. Pairing the signals is obvious even if signals accidentally overlap in the 10-ppm spectrum.

For those purposes, the authors used constant-time version of the sensitivity-enhanced HMBC sequence,[79] combined with a two-step low-pass J filter. Constant-time experiments have no coupling structures in the carbon dimension making it easy to identify the centre of signals in

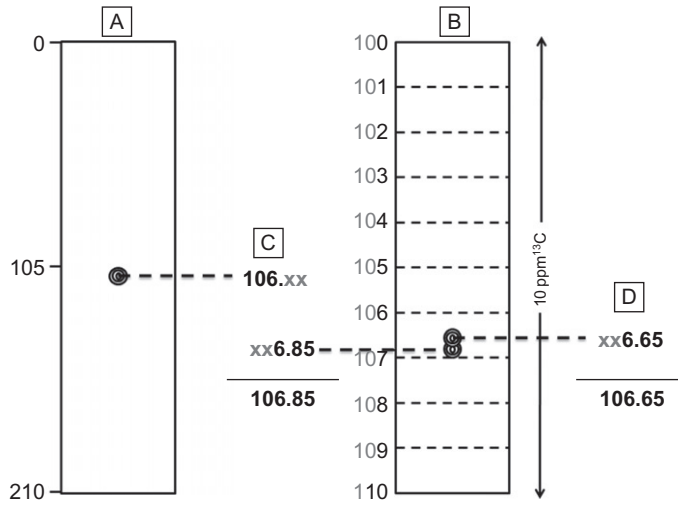

Figure 29 A 10-ppm spectrum (B) corresponds to a normal spectrum (A) cut into 10-ppm broad stripes that overlap except that signals are nearly 20 times narrower compared to a normal full 210-ppm spectrum. (C) The three digital figures of the chemical shift of the full spectrum (A) can be combined with the partially complementary three figures of the 10-ppm spectrum (B) to provide precise carbon chemical shifts (C & D). Signals overlapping in (A) may be resolved in (B).

crowded spectra. Secondly, using the phase-sensitive scheme, the long t_1-evolution times of 10-ppm experiments are not gradient coded, which avoids the signals of small molecules to be significantly damped due to molecular diffusion.

Figure 30 shows the potential of the 10-ppm approach. The full-width HMBC spectra (left) do not allow a clear discrimination of all cross-peaks. For instance, the correlation between the proton resonance of $CH_3\delta_2$ MeLeu 9 at 0.82 ppm and the close pair of carbons at 22.1 and 22.2 ppm remains ambiguous and it is not possible to attribute the resonance of the $CH_3\delta_1$ MeLeu 9. In the 10-ppm spectrum, the achieved resolution clearly shows that this correlation can be unambiguously attributed, and that the exact resonance of the $CH_3\delta_1$ MeLeu 9 is 22.2 ppm.

7.3. Combining 10- and 9.9-ppm HMBC experiments

The simplicity of the logic for analyzing 10-ppm HMBC spectra is noticeable, but going back and forth between the high- and low-resolution spectra may be quite tedious whether they are printed on paper or

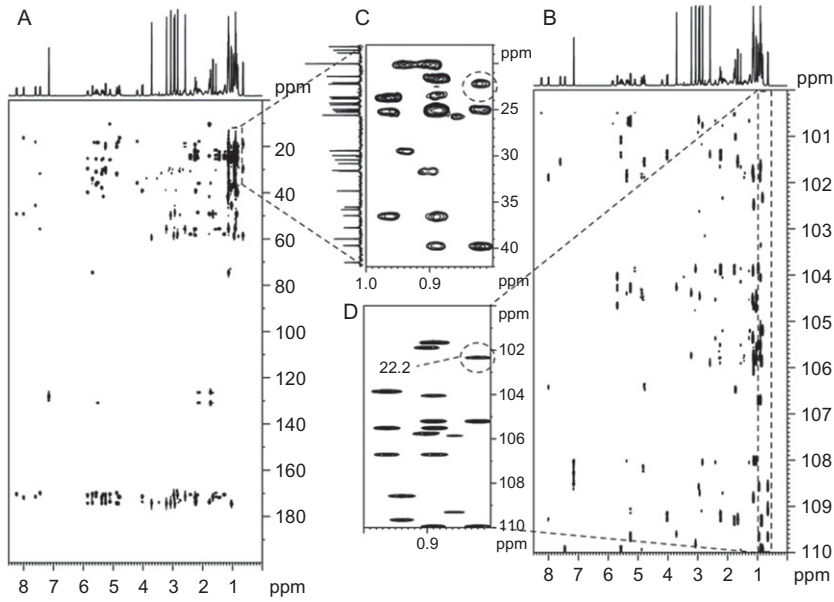

Figure 30 Standard full-width (200 ppm) HMBC (A), and the corresponding 10-ppm HMBC spectrum of cyclosporine (B). The excerpts (C) and (D) show the region comprising the methyl resonances of cyclosporine and the ambiguous resonance discussed in the text is highlighted with a dashed circle. Both experiments have been recorded using the same parameters, with the exception of the ^{13}C spectral width, which was set to 10 ppm for recording (B).

displayed on a computer screen. Foroozandeh and Jeannerat have introduced a new combination, 10 and 9.9 ppm, where both spectra have high resolution and can simply be overlapped, making their analysis much easier and convenient.[80] In the 10-ppm-aliased spectrum, the position of the signals provides the basis for the determination of the chemical shifts. In the complementary 9.9-ppm spectrum, signals are shifted in a quantized manner relative to the signals in the 10-ppm spectrum according to the first two digits of the high-order chemical shift. A readily made correction ruler allows one to determine the full six-digit chemical shift by reporting the rounded distances between the signals to the increments to add to the observed chemical shifts (Figure 31).

7.4. The DENA element

As an alternative to independently record two separate 10- and 9.9-ppm spectra, Foroozandeh and Jeannerat have also introduced a new pulse sequence element, the DENA element (Differential Evolution for

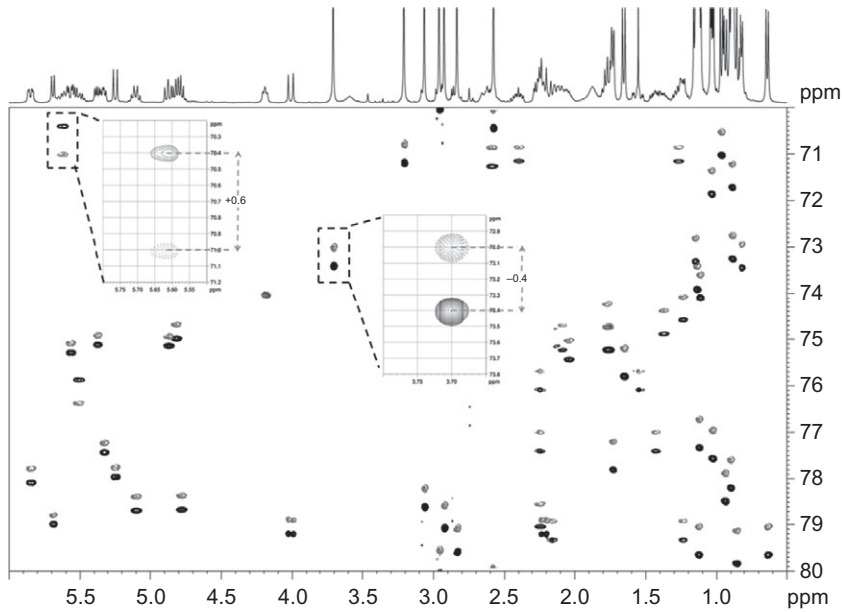

Figure 31 Superposition of the 10-ppm HMBC spectrum (filled black peaks) with the 9.9-ppm HMBC spectrum (dotted grey contours) of Cyclosporine A. In the 9.9-ppm spectrum, the chemical shifts are shifted in a quantized manner relative to the signals in the 10-ppm spectrum according to the first two digits of the high-order chemical shift. The two insets show the actual difference $\Delta\delta$ between the cross-peaks in the two spectra for the H–C(ε) and the CH_3N resonances of MeBmt 1.

Non-ambiguous Aliasing) to obtain a similar result in a single experiment.[80] This element can be included in a sensitivity-enhanced HSQC experiment only, and comprises an additional chemical shift evolution period active for one of the two components of the carbon magnetization. This component is then further sine modulated by $t_1' = 0.001t_1$ to provide a signal pattern coding the high-order chemical shift. The DENA-HSQC (HMBC) gives thus rise to the reference ''10-ppm'' signals and to the pair of IP ''satellites'' observed above and below the reference signal. Since $t_1' = 0.001t_1$, these two satellites turn out to be located at the positions of the signals in the 10.1- and 9.9-ppm spectra, respectively. The principal advantage of the DENA-HSQC sequence compared to the overlap of the 10- and 9.9-ppm spectra is to require only half of the acquisition time to record the 10- and 9.9-ppm spectra separately. On the other hand, the DENA-HSQC experiment spreads the magnetization over three signals with 1/4:1/2:1/4 relative amplitudes, that is, 25% of the sensitivity obtained using the classical SE-HSQC.

8. ACCELERATING HMBC EXPERIMENTS

8.1. Principles of fast experiments

The development of experiments containing low number of RF pulses and delays to improve sensitivity has been an active research area. For instance, applied to proteins, the FHSQC scheme allows a sensitivity gain for fast exchanging protons.[81] In 1997, Ross et al. have introduced the fast-HMQC experiment[82] using Ernst angle pulses.[44,83] They find that for an HMQC with an initial pulse of 120° and a 200-ms recovery delay, a remarkable gain in sensitivity is possible. Recently, Schanda and Brutscher have optimized the idea of the fast-HMQC experiment for the purpose of protein NMR spectroscopy.[84–86] They have introduced band-*S*elective *O*ptimized-*F*lip-*A*ngle *S*hort-*T*ransient (SOFAST) HMQC experiments for fast acquisition of 2D heteronuclear correlation spectra. Fast data acquisition in SOFAST-HMQC is realized by using very short inter-scan delays. SOFAST-HMQC combines the advantages of a small number of radio-frequency pulses, Ernst angle excitation to obtain an increased signal to noise ratio for high repetition rates of the experiment. As SOFAST-HMQC relies on standard data sampling in the indirect dimension, it is therefore easily implemented on any commercially available high-field NMR spectrometer. The idea to develop a (SO)FAST-HMBC for organic molecules, and generally for smaller molecules, naturally follows from these newly developed experiments.

8.1.1. Principles and theory

The development of a FAST-HMBC rather than a SOFAST-HMBC experiment appears more judicious for being applied to organic molecules, since the essence of the SOFAST-HMQC method is to use band-selective pulses that allow optimizing longitudinal relaxation.[87] The method is therefore purely dedicated to protein NMR spectroscopy. However, it was shown that the application of a non-90° excitation pulse in HMQC experiments also results in a significant gain in sensitivity if the sequence is applied at very high repetition rate or run on compounds with long T_1 relaxation times, provided that the first 90° excitation pulse is set to the Ernst angle α_{ernst}.[82]

In practice, any available HMBC pulse sequence could be used to record fast-HMBC spectra.[88] As HMBC are recorded without broadband heteronuclear decoupling, the duty cycle is no longer an issue with FAST-HMBC schemes, as it is using the standard SOFAST-HMQC or FAST-HMQC pulse sequences.

8.1.2. Experimental verification

The Ernst angle α_{ernst} of the initial proton pulse can be easily determined experimentally by incrementing the initial proton pulse from, for example, zero to 40 μs and keeping the ^{13}C t_1 evolution period at a fixed value of ca. 10 μs. Different angles can be determined as a function of the repetition rate T_{RD} considered. Figure 32 shows the time course for the intensity of cyclosporine and isopropylidene glycerol.

It turns out from the spectra shown in Figure 32 that for molecules having long T_1 (>3 s), specifically small molecules or macromolecules, a significant gain in sensitivity compared to the standard setup using 1 s repetition and 90° excitation can be obtained by optimizing both the Ernst angle and the repetition rate. If the inter-scan delay is kept short (<1 s), a much higher gain in the relative sensitivity is achieved in an experiment using optimized Ernst angle excitation versus 90° pulsing. On the other hand, for medium-size molecules having short T_1 (<1 s), like cyclosporine, the gain in sensitivity compared to the standard setup using 1 s repetition and 90° excitation by optimizing both the Ernst angle and the repetition rate is moderate. For those molecules, it is therefore advocated to use a standard 90° excitation.

8.2. The IMPACT-HMBC experiment

Shorten or even eliminate the relaxation delay is only effective for relatively fast-relaxing nuclei, and can lead, if decoupling is turned on, to serious radio-frequency heating problems if the relaxation delay is very short. Recently, Kupče and Freeman have introduced an alternative

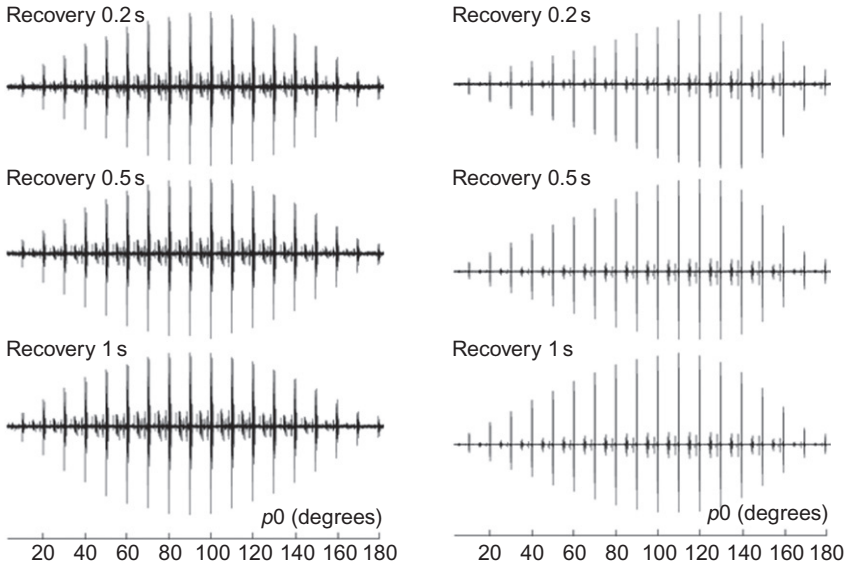

Figure 32 Ernst angle determination for cyclosporine (left) and isopropylidene glycerol (right). The plots show the behaviour of the proton spectrum with increasing flip-angle of the initial hard pulse. Spectra were collected over 10 ppm using a 1D HMBC experiment, as 2 K data points, and using 4 transients. For cyclosporine, it can be seen that the maximum signal amplitude is attained for an Ernst angle between 90° and 100°, whatever the recovery delay value. For isopropylidene glycerol, on the other hand, the maximum signal amplitude is attained for an Ernst angle of 110° for a recovery delay of 1 s, of 120° for a recovery delay of 0.5 s, and of 130° for a recovery delay of 0.2 s. A gain of approximately 50% is realized for the last case using optimized Ernst angle versus 90° excitation.

scheme, which speeds the recovery of longitudinal proton magnetization by sharing polarization with nearby protons. This method has been called acceleration by sharing adjacent polarization (ASAP).[89]

8.2.1. Principles

The essence of the ASAP method is based on the different spin–lattice relaxation behaviour of these two types of protons. In the case of a HMBC experiment, the acceptor protons are those directly bound to ^{13}C with large spin–spin couplings; they are the spins that give rise to the final spectrum. By contrast, the donor protons have negligible couplings to ^{13}C and are therefore essentially unaffected by this polarization transfer sequence, which simply returns them to the z axis. In their method, Kupče and Freeman have proposed to replace the usual relaxation delay with a short cross-polarization (HOHAHA) interval. This offers a

significant reduction in cycle time and an improvement in overall sensitivity. In liquid samples, the mixing is mediated by the scalar coupling, and the interchange of polarization is cyclic, with a period set by the appropriate proton–proton coupling constant.

The magnitudes of the intensity enhancements can be evaluated from traces extracted at a ^{13}C frequency of 137 ppm. The enhancement factors are 1.75 for normal cross-polarization, and 1.85 when the ''Ernst angle'' is included. Through these spectra, the benefits of the ASAP modification in HMBC experiments is obvious. Cross polarization causes a net transfer of longitudinal magnetization from the donor protons to the acceptor protons during the interval normally devoted to spin–lattice relaxation; this interval can thus be shortened significantly. This contributes to the effectiveness of this simple modification of HMBC and more generally of standard pulse sequences.

Recently, a robust, sensitive, and versatile HMBC experiment for rapid structure elucidation has been proposed. The suggested IMPACT-HMBC experiment eliminates the weaknesses of the basic HMBC experiment and the overall performance of the pulse sequence is improved significantly. In addition, it can be recorded with short recovery times, which is useful in routine analysis by NMR when the experimental time is limited.

The IMPACT-HMBC is derived from the band-selective, constant-time HMBC experiment described by Claridge et al.[73] As shown schematically (Figure 33), the experiment starts with a cross-polarization period (ASAP period), which speeds the recovery of longitudinal proton magnetization and transfers polarization from nearby spins, allowing the use of considerably shortened relaxation delays between scans. In addition, the ASAP mixing has proven to be very effective in suppressing the noisy F_1 ridges that often occur in 2D spectra recorded with short relaxation delays. The suitable length of the ASAP period that provides a satisfactory balance between the gains and losses of polarization must be determined experimentally, and it turns out that a mixing in the order of 40 ms represents a good choice. The rest of the sequence combines the phase-sensitive HMBC scheme and a classical constant-time element, which suppresses proton couplings to other protons and the heteronucleus. The resolution in the ^{13}C dimension can be therefore markedly enhanced. For keeping the maximum flexibility, the 180° on the ^{13}C channel can be set as a broadband pulse or as a band-selective pulse for enhancing the resolution.

8.2.2. Experimental verification

The potential advantages of the IMPACT-HMBC experiment are readily shown in Figures 34 and 35. In Figure 34, the full-width HMBC spectrum, recorded using the standard HMBC pulse sequence, is shown on the left. This spectrum combines strong residual $^1J_{CH}$ correlations and F_1 ridges

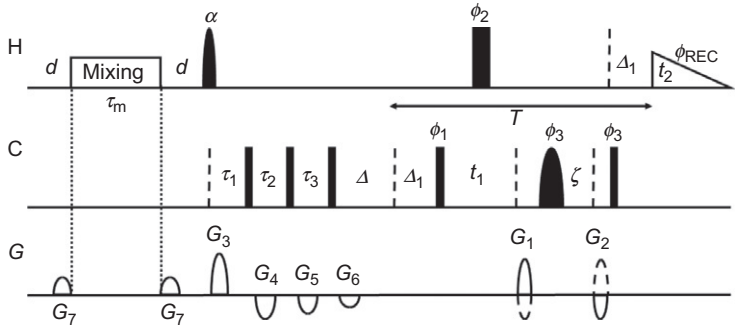

Figure 33 The sequence of the proposed IMPACT-HMBC experiment.[90] Narrow solid bars indicate 90° pulses and wide bars 180° pulses. The first pulse on the ^{1}H channel is shown as a sine shape and its length α can be set according to the Ernst angle. The 180° pulse on the ^{13}C channel is shown as a half-sine shape, and can be set as a broadband or band-selective pulse. $^{1}J_{CH}$ correlations are suppressed using a three-step low-pass *J*-filter, and the delays τ_1, τ_2 and τ_3 are set as previously described.[15] The delay Δ is for the evolution of $^{n}J_{CH}$. The delays Δ_1 are decremented as t_1 is incremented such that the period T remains constant.[72] Delay ζ is set to guarantee no ^{13}C chemical shift evolution for the first t_1 value, $\zeta = (t_1)_0 + p_{180H}$, where $(t_1)_0$ is the initial value of t_1, and p_{180H} is the duration of the proton 180° pulse.[79] The standard relaxation delay is replaced with a mixing sequence (DIPSI-2[91] or TanhTan mixing[92]) of length τ_m flanked by field gradients pulses and relaxation delays d. Gradient ratios: G_1:G_2:G_3:G_4:G_5:G_6:G_7 = 5:−3:4:−2.5:−1:−0.5:−1.5 (odd experiments) and 3:−5:4:−2.5:−1:−0.5:−1.5 (even experiments). The phases of the pulses are ϕ_1 = x, −x; ϕ_2 = x, x, −x,−x; ϕ_3 = 4(x), 4(−x); ϕ_{REC} = 2(x, −x), 2(−x, x) and x when not specified.

that obscure the long-range correlations. The same region, but using the IMPACT-HMBC pulse sequence (Figure 33). As demonstrated by the figure, the IMPACT-HMBC sequence combines signals with no coupling structure, optimal $^{1}J_{CH}$ suppression, absence of F_1 ridges, and very good signal to noise ratio using a minimum experimental time. As the proposed HMBC experiment incorporates a constant-time element, its potential disadvantage is the lower sensitivity. This is due to the longer duration of the sequence, as defined by the fixed period T and hence relaxation losses prior to collection of each FID. Relaxation losses may be particularly important if the chosen band is narrow. These losses should therefore be balanced against the benefits of the improved peak dispersion.

The superiority of the IMPACT-HMBC experiment is readily shown in Figure 35. Figure 35A shows the full-width HMBC spectrum, recorded on a sample of isopropylidene glycerol using the standard low-pass gradient-selected HMBC pulse sequence. This spectrum combines strong residual $^{1}J_{CH}$ correlations and F_1 ridges that obscure the long-range correlations. Figure 35B shows the same region, but using the proposed IMPACT-HMBC pulse sequence (Figure 33). As demonstrated by

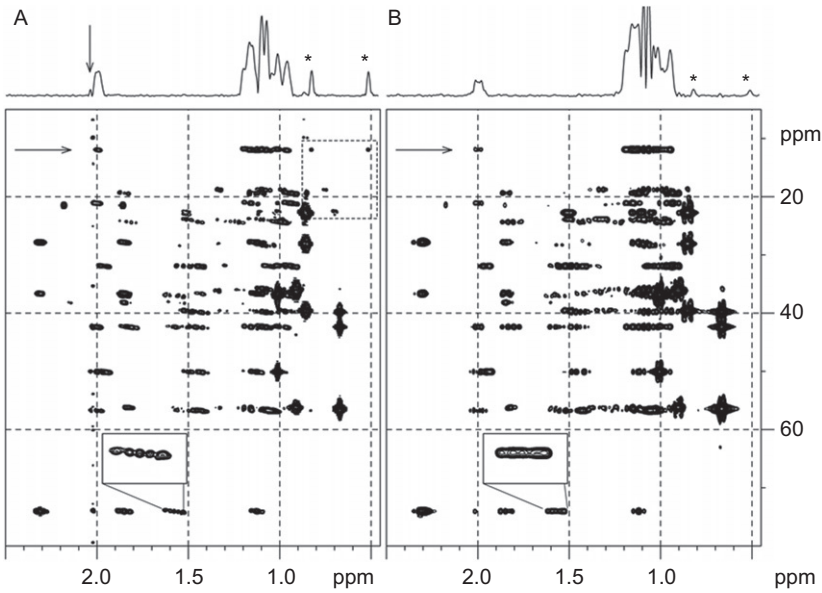

Figure 34 Excerpts of two-dimensional HMBC spectra of cholesteryl acetate recorded on a Bruker AvanceII 400 MHz spectrometer (A) with the standard HMBC pulse sequence (Figure 1), and (B) with the IMPACT-HMBC experiment depicted in Figure 30. The same contour levels are used for all spectra. In (A), F_1 ridges are still visible (indicated by a vertical arrow), while they are very efficiently suppressed in (B). The proposed sequence results in signals with no coupling structure, as a result of the incorporation of a constant-time period. The improved peak dispersion is shown for the correlation between C-3 and H-2 (expanded in the small boxes). Asterix and the dashed box indicate residual $^1J_{CH}$ signals. The measurement duration was 22 min for both experiments. (A) Recorded with 256 increments, 4 transients, and a recovery delay of 1 s. (B) Recorded with 256 increments, 8 transients, and a recovery delay of 0.2 s. The flip angle α was set to 90°. The typical F_2 rows (at the ^{13}C chemical shift of C-18, indicated by the horizontal arrows and depicted on the top of the spectra) show the signal enhancements.

Figure 35B, the IMPACT-HMBC spectrum combines optimal $^1J_{CH}$ suppression, absence of F_1 ridges, and very good signal to noise ratio using a minimum experimental time. It should be also stated that the attribution of the resonances can be correctly performed only in the case of the IMPACT-HMBC spectrum (Figure 35B).

8.3. Other methods for accelerating HMBC measurements

Some ''fast methods'' such as single-scan experiments,[93,94] Hadamard[95] and projection–reconstruction techniques[96] take a few seconds to produce 2D spectra, but suffer from a lack of spectral resolution. As mentioned

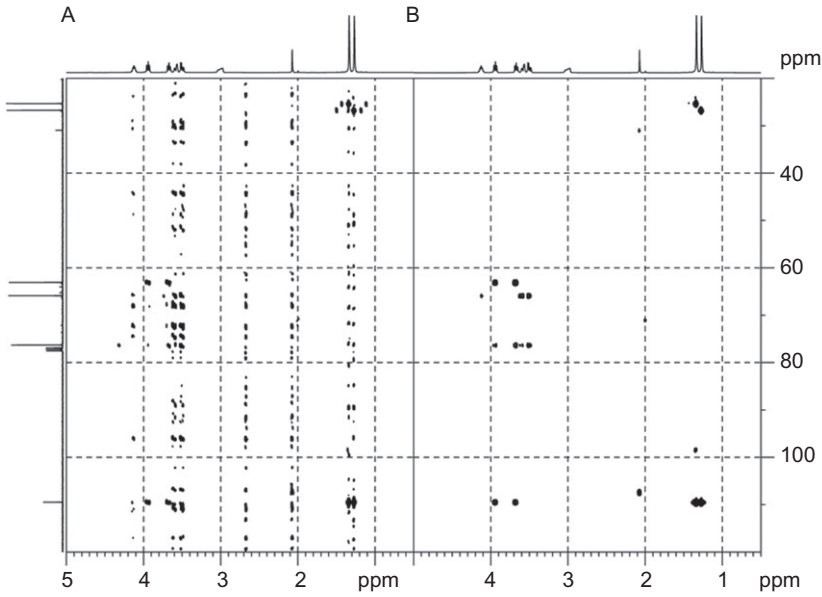

Figure 35 Two-dimensional HMBC spectra of isopropylidene glycerol recorded at 400 MHz with (A) the standard HMBC experiment, and (B) with the IMPACT-HMBC experiment. The spectra have been recorded using 128 increments, 2 transients, and a recovery delay of 0.2 s. The flip angle α was set to 130°. Measurement duration for both experiments approximately 2 min.

before, SOFAST experiments rely on selective pulses and small tilt angles to minimize the recovery times and record HMBC experiments in about 15 s.[84–86] Recently the combination of Hadamard and SOFAST experiments[97] or single-scan experiments[98] have also been proposed. Using these combinations, it seems possible to record 2D experiments within a few seconds. The SPEED method[99] avoids time incrementation and alternatives like Time-Shared,[100] or PANSY[101] are interesting as well. Recently, a Novel SMAll Recovery Times (SMART) method[102] that uses orthogonal PFGs in three spatial directions to select the desired pathways and suppress interference effects has been introduced and seems very promising. It allows a drastic reduction of the time required for 2D NMR experiments by completely skipping the recovery delay between successive experiments. 2D spectra of dilute compounds can be recorded in about 0.1 s per increment in the indirect domain. The only drawback of the method is the hardware requirement, since x, y, and z gradients must be available. According to the authors, it seems possible that the SMART method could also be used when only a single gradient axis is available, but there is currently no result available.

9. MEASUREMENT OF LONG-RANGE COUPLING CONSTANTS

The quantitative measurement of long-range proton-heteronucleus, mainly proton–carbon coupling constants, for small and medium-size organic compounds at natural abundance has been an interesting topic among the years.[103] From the values of theses coupling constants, dihedral angles can be characterized by means of Karplus-type relationships. There are numerous NMR methods to perform such measurements. A survey of recent heteronuclear correlation experiments for the measurement of heteronuclear coupling constants can be found elsewhere.[104–106]

Among those experiments, some are based on the basic HMBC/HMQC scheme and provide a quantitative or qualitative measure of long-range heteronuclear coupling constants without the need for techniques such as selective excitation or chemical shift filters.[107–111] Another idea is to use a reference experiment for coupling extraction, for example by acquiring a corresponding reference HSQC with identical phase distortions due to ^{1}H–^{1}H couplings.[105,112–114] The current most efficient experiment available, the so-called CBC-HSQMBC experiment, combines all existing pulse elements for obtaining the cleanest possible multiplets. It can be seen as a derivative from HMBC experiments. Basically, the CBC-HSQMBC experiment combines the LR-CAHSQC[115] with a BIRD^{r,X}-CPMG-HSQMBC[116,117] with the BIRD^{r,X} filter element replaced by a so-called CAGEBIRD filter.[118] The pulse sequence of the CBC-HSQMBC experiment is depicted in Figure 36.

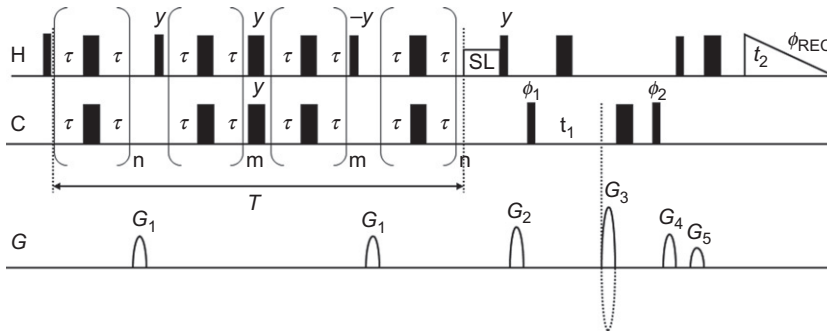

Figure 36 Pulse sequences for the CBC-HSQMBC experiment. Narrow and thick bars represent 90° and 180° RF pulses, respectively. Pulse phases are along *x* unless indicated otherwise. Phase cycles are: $\phi_1 = x, -x$; $\phi_2 = x, x, -x, -x$; $\phi_{REC} = x, -x, -x, x$. The long-range polarization transfer delay T is typically set to 62.5 ms to roughly correspond to the usual transfer delay for the long-range coupling of 8 Hz. The CPMG-delay τ should be set equal or larger than 100 μs.

Coupling constants can be extracted quite reliably from CBC-HSQMBC spectra. However, the coupling extraction procedure is not yet implemented in any available software, which renders the use of these experiments obscure for non-NMR expert's users. Some homemade programs are however available. In addition, the coupling determination from HMBC-type spectra is not sign-sensitive. This strongly limits the use for the determination of long-range residual dipolar couplings RDCs, since the sign of RDCs contains valuable structural information.

Another interesting possibility relies on the recording of two complementary IP and AP data separately and then added/subtracted to provide spin-state-selective α/β-HSQMBC spectra.[119] In these types of IPAP spectra, the magnitude of $^{n}J_{CH}$ can be directly determined by simple analysis of the relative displacement between α- and β-cross-peaks.

Carbohydrates and especially oligosaccharides represent a special category for NMR spectroscopists. The structural characterization of oligosaccharides by NMR spectroscopy has remained challenging because of the lack of experimental parameters and the intrinsic high mobility in solution. For instance, the conformation around the exocyclic glycosidic bonds cannot unambiguously be determined from measurement of inter-residue ^{1}H–^{1}H NOE measurements.

To this end, Ilin et al. have developed the Γ-HMBC experiment,[120] which is itself based on an experiment developed by Vincent and Zwahlen for measuring dipole–dipole cross-correlation in polysaccharides.[121] These experiments allow determining the conformation around glycosidic bonds based on $^{3}J_{CH}$ couplings and C–H-dipolar cross-correlated relaxation.

10. TIME-SHARED (TS) HMBC EXPERIMENTS

10.1. The CN-HMBC experiment: concerted recording of ^{1}H–^{13}C and ^{1}H–^{15}N HMBC spectra

10.1.1. The concept of time-sharing

TS experiments are based on the simultaneous evolution of different frequencies in the indirect dimension of a multidimensional experiment. The concept has been described several years ago in order to obtain different spectra in a single NMR experiment.[100,122–128] These experiments were originally applied to obtain heteronuclear correlation TS-HMQC and TS-HSQC or 3D and 4D NOESY-edited spectra in doubly labelled proteins. Recently, the successful implementation and application of these types of experiments have been demonstrated on small molecules at natural abundance. Examples have been reported for TS-HSQC, TS-HSQC-TOCSY, TS-HSQMBC and TS-HMBC pulse schemes.[129–133] Parella et al. have subsequently proposed the MATS technique[134] (multiple-FID acquisition-time-shared evolution), the time-effective collection of

multiple NMR spectra by combining the individual features associated with the TS evolution of independent coherences and the acquisition of different FID signals within the same scan.

All these methods show a general applicability for any type of small organic and organometallic compounds of low- and medium molecular weight containing nitrogens in their chemical structures, namely, peptides, nucleotides, natural products or organometallic complexes. For instance, of particular interest is the simultaneous acquisition of C-HMBC and N-HMBC spectra for simultaneous detection of ^{13}C and ^{15}N connectivities to both protonated and non-protonated centres. Another possible application of TS-HMBC-based experiments is the simultaneous measurement of proton–carbon and proton–nitrogen coupling constants. As experimentally demonstrated, the main advantage of the acquisition of TS experiments over the conventional separate acquisition of two equivalent experiments is an important sensitivity gain per time unit around the theoretical 41% for both ^{13}C and ^{15}N, with the same acquisition and processing setup requirements.[135]

11. CONCLUSION AND OUTLOOK

The HMBC experiment has been introduced about 25 years ago, and, as shown in this manuscript, its main goal is to provide correlation signals for C, H spin pairs indicating connectivities over two and three bonds. It is therefore widely used to build a molecular skeleton, and can be considered as one of the key experiments for characterizing the structure of small- to medium-sized molecules. Owing to the fact that for a large majority of scientists the main purposes of an HMBC experiment remain the detection of long-range couplings, we have particularly detailed the first sections describing the suppression of residual $^{1}J_{CH}$ signals. We hope that this will assist a newcomer in choosing between the various schemes available, in order to get spectra of the highest quality.

Starting from the late 1990s, there has been a surge of interest in the development of new inverse-detected long-range correlation experiments. In this manuscript, it has been the intention of the author to describe a selection of new HMBC variants that can be useful for resonance assignments and structure determination. The basic unifying features of pulse sequences have been presented so that the underlying mechanics of even complicated sequences become more transparent. In addition, some mathematical derivations have been given in great detail for the basic HMBC scheme with the hope that this will help a newcomer to understand the latest pulse sequence techniques more easily.

The band-selective constant-time HMBC, or the ultra resolved 10-ppm HMBC, aiming at providing a better resolution in the ^{13}C dimension,

represent in our view powerful new variants for any molecule exhibiting crowded spectra, since they allow the users to discriminate between ^{13}C resonances separated by only a few hertz.

For some classes of molecules or for resolving specific structural problems, it may be essential to detect $^{4}J_{CH}$—or $^{5}J_{CH}$ correlations, which depend on very small coupling values. Various pulse sequences that sample wide ranges of long-range coupling constants have been presented and their advantages and potential disadvantages have been discussed. The broadband HMBC provides a fairly uniform excitation over a range of heteronuclear long-range coupling constants, and the main advantage of this approach is that gaps of zero transfer amplitude are avoided throughout the range of long-range heteronuclear *J*-couplings of interest. It turns out that it is more advisable to record two or more different statically optimized HMBC and to sum up the data than to record a single experiment that samples larger ranges of long-range coupling constants.

HMBC experiments for unequivocally differentiating between $^{2}J_{CH}$ and $^{3}J_{CH}$ correlations are also potentially attractive at first sight. However, all these sequences only provide peaks involving protonated ^{13}C spins, and the discrimination between two- and three-bond correlations is based solely on the size of $^{n}J_{HH}$ coupling constants. In our opinion that sample wide ranges of long-range coupling constants, these experiments present more potential disadvantages than actual advantages for the users. A more attractive variant is the edited HMBC experiment. This experiment yields two subspectra, one containing the C + CH_2, the second the CH + CH_3 peaks, respectively. These two subspectra can be co-added, leading to an edited HMBC spectrum. Similar to the edited-HSQC experiment, this HMBC can be viewed as an HMBC-DEPT experiment and is very useful for attributing resonances when the structures are unknown or only partly known. The major advantage for the users is that the edited HMBC spectra can be obtained fully automatically, and that the experiment can be used under automated conditions.

Since about one decade, the development of fast experiments containing low number of RF pulses and delays to improve sensitivity and reduce the experimental time has been an active research area. It is likely that this area will involve many NMR spectroscopists for the next years. Current ''fast methods'' such as non-linear sampling, Hadamard and SMART techniques take a few seconds to produce 2D spectra. While these methods are currently rather mysterious for most of the scientists, there is absolutely no doubt that they will be provided by the NMR manufacturers in the next years. It is therefore likely that most of the HMBC spectra will be obtained in only a few minutes in a near future, which opens new perspectives.

ACKNOWLEDGMENTS

The author thanks the University of Neuchâtel, the University of Berne, and the Swiss National Fonds (SNF 200021-131867) for financial support. Once again the author very much thanks current (University of Berne) and previous colleagues (University of Neuchâtel) for the great scientific environment provided by them and their groups.

REFERENCES

1. A. Bax and M. Summers, *J. Am. Chem. Soc.*, 1986, **108,** 2093–2094.
2. G. Bifulco, P. Dambruoso, L. Gomez-Paloma and R. Riccio, *Chem. Rev.*, 2007, **107,** 3744–3779.
3. A. Maudsley, A. Wokaun and R. R. Ernst, *Chem. Phys. Lett.*, 1978, **55,** 9–14.
4. R. E. Hurd, *J. Magn. Reson.*, 1990, **87,** 422–428.
5. R. E. Hurd and B. K. John, *J. Magn. Reson.*, 1991, **91,** 648–653.
6. A. L. Davis, E. D. Laue, J. Keeler, D. Moskau and J. Lohman, *J. Magn. Reson.*, 1991, **94,** 637–644.
7. A. L. Davis, E. D. Laue, J. Keeler and D. Moskau, *J. Magn. Reson.*, 1992, **98,** 207–216.
8. J. R. Tolman, J. Chung and J. H. Prestergard, *J. Magn. Reson.*, 1992, **98,** 462–467.
9. J. Ruiz-Cabello, G. W. Vuister, C. Moonen, P. Van Gelderen, J. Cohen and P. C. M. Van Zijl, *J. Magn. Reson.*, 1992, **100,** 282–302.
10. G. Bodenhausen and D. Ruben, *Chem. Phys. Lett.*, 1980, **69,** 185–189.
11. T. J. Norwood, J. Boyd and I. D. Campbell, *FEBS Lett.*, 1989, **225,** 369–371.
12. L. Müller, *J. Am. Chem. Soc.*, 1979, **101,** 4481–4484.
13. A. Bax, R. H. Griffey and B. L. Hawkins, *J. Am. Chem. Soc.*, 1983, **105,** 7188–7190.
14. A. Bax and S. Subramanian, *J. Magn. Reson.*, 1986, **67,** 565–569.
15. H. Kogler, O. W. Sørensen, G. Bodenhausen and R. R. Ernst, *J. Magn. Reson.*, 1983, **55,** 157–163.
16. K. Furihata and H. Seto, *Tetrahedron Lett.*, 1995, **36,** 2817–2820.
17. G. E. Martin, Qualitative and quantitative exploitation of heteronuclear coupling constants. *in*: Annual Reports on NMR Spectroscopy, G. A. Webb (ed.), Vol. 46, Academic Press, 2002, pp. 37–100.
18. G. E. Martin and A. J. Williams, Long-Range ^{1}H–^{15}N Heteronuclear Shift Correlation. *in*: Annual Reports on NMR Spectroscopy, G. A. Webb (ed.), Vol. 55, Academic Press, 2005, pp. 1–119.
19. W. Schoefberger, J. Schlagnitweit and N. Müller, Recent Developments in Heteronuclear Multiple-Bond Correlation Experiments. *in*: Annual Reports on NMR Spectroscopy, G. A. Webb (ed.), Vol. 72, Academic Press, 2011, pp. 1–60.
20. W. Wieland, L. Dieter, K. Rainer and B. Wolfgang, *Magn. Reson. Chem.*, 1993, **31,** 287–292.
21. G. Bodenhausen, H. Kogler and R. R. Ernst, *J. Magn. Reson.*, 1984, **58,** 370–388.
22. A. Bain, *J. Magn. Reson.*, 1984, **56,** 418–427.
23. O. W. Sørensen, G. W. Eich, M. H. Levitt, G. Bodenhausen and R. R. Ernst, *Prog. Nucl. Magn. Reson. Spectrosc.*, 1983, **16,** 163–192.
24. D. Uhrín, T. Lipatj and K. E. Kövér, *J. Magn. Reson. A*, 1993, **101,** 41–46.
25. G. E. Martin and A. S. Zektzer, *Magn. Reson. Chem.*, 1988, **26,** 631–652.
26. H. Kessler, H. R. Loosli and H. Oschkinat, *Helv. Chim. Acta*, 1985, **68,** 661–681.
27. T. E. Burrow, R. G. Enriquez and W. F. Reynolds, *Magn. Reson. Chem.*, 2009, **47,** 1086–1094.
28. O. W. Sørensen, N. C. Nielsen, H. Bildsøe and H. J. Jacobsen, *J. Magn. Reson.*, 1986, **70,** 54–70.

29. A. Meissner, D. Moskau, N. C. Nielsen and O. W. Sørensen, *J. Magn. Reson.*, 1997, **124,** 245–249.
30. T. Parella, F. Sanchez-Ferrando and A. Virgili, *J. Magn. Reson. A*, 1995, **112,** 241–245.
31. J. R. Garbow, D. P. Weitkamp and A. Pines, *Chem. Phys. Lett.*, 1982, **93,** 504–508.
32. R. Burger, C. Schorn and P. Bigler, *Magn. Reson. Chem.*, 2000, **38,** 963–969.
33. C. Emetarom, T. L. Hwang, G. Mackin and A. J. Shaka, *J. Magn. Reson. A*, 1995, **115,** 137–140.
34. M. A. Smith, H. Hu and A. J. Shaka, *J. Magn. Reson.*, 2001, **151,** 269–283.
35. J. Furrer and D. Thévenet, *Magn. Reson. Chem.*, 2009, **47,** 239–248.
36. T. L. Hwang and A. J. Shaka, *J. Magn. Reson. A*, 1995, **112,** 275–279.
37. G. Mackin and A. J. Shaka, *J. Magn. Reson. A*, 1996, **118,** 247–255.
38. S. Heikkinen and I. Kilpeläinen, *J. Magn. Reson.*, 1999, **137,** 93–99.
39. K. Ogura, H. Terasawa and F. Inagaki, *J. Biomol. NMR*, 1996, **8,** 492–498.
40. C. Zwahlen, P. Legault, S. F. J. Vincent, J. Greenblatt, R. Konrat and L. E. Kay, *J. Am. Chem. Soc.*, 1997, **119,** 6711–6721.
41. T. N. Pham, T. Lipatj, K. Bromek and D. Uhrin, *J. Magn. Reson.*, 2002, **157,** 200–209.
42. P. Würtz, P. Permi, N. C. Nielsen and O. W. Sørensen, *J. Magn. Reson.*, 2008, **194,** 89–98.
43. S. Meier, A. J. Benie, J.Ø. Duus and O. W. Sørensen, *ChemPhysChem.*, 2009, **10,** 893–895.
44. R. R. Ernst, G. Bodenhausen and A. Wokaun, Principles of Nuclear Magnetic Resonance in One and Two Dimensions. Clarendon Press, Oxford, 1987.
45. Ē. Kupče and R. Freeman, *J. Magn. Reson.*, 1997, **127,** 36–48.
46. K. Furihata and H. Seto, *Tetrahedron Lett.*, 1996, **37,** 8901–8902.
47. R. Wagner and S. Berger, *Magn. Reson. Chem.*, 1998, **36,** S44–S47.
48. G. E. Martin, C. E. Hadden, R. C. Crouch and V. V. Krishnamurthy, *Magn. Reson. Chem.*, 1999, **37,** 517–523.
49. C. E. Hadden, G. E. Martin and V. V. Krishnamurthy, *J. Magn. Reson.*, 1999, **140,** 274–279.
50. C. E. Hadden, G. E. Martin and V. V. Krishnamurthy, *Magn. Reson. Chem.*, 2000, **38,** 143–147.
51. J. Furrer, *Magn. Reson. Chem.*, 2006, **44,** 845–850.
52. A. Meissner and O. W. Sørensen, *Magn. Reson. Chem.*, 2000, **38,** 981–984.
53. T. Schulte-Herbrüggen, A. Meissner, A. Papanikos, M. Meldal and O. W. Sørensen, *J. Magn. Reson.*, 2002, **156,** 282–288.
54. S. Wimperis and G. Bodenhausen, *J. Magn. Reson.*, 1986, **69,** 264–282.
55. O. W. Sørensen, J. C. Madsen, N. C. Nielsen, H. Bildsøe and H. J. Jakobsen, *J. Magn. Reson.*, 1988, **77,** 170–174.
56. A. M. Torres and R. E. D. McClung, *J. Magn. Reson.*, 1991, **92,** 45–63.
57. A. M. Torres, W. A. Bubb, D. J. Philp and P. W. Kuchel, *J. Magn. Reson.*, 2008, **194,** 81–88.
58. A. M. Torres, G. Zheng and W. S. Price, *Magn. Reson. Chem.*, 2010, **48,** 129–133.
59. V. V. Krishnamurthy, D. J. Russel, C. E. Hadden and G. E. Martin, *J. Magn. Reson.*, 2000, **146,** 232–239.
60. T. Sprang and P. Bigler, *Magn. Reson. Chem.*, 2003, **41,** 177–182.
61. T. Sprang and P. Bigler, *Magn. Reson. Chem.*, 2004, **42,** 55–60.
62. C. Bauer, R. Freeman and S. Wimperis, *J. Magn. Reson.*, 1984, **58,** 526–532.
63. R. Burger, C. Schorn and P. Bigler, *J. Magn. Reson.*, 2001, **148,** 88–94.
64. N. T. Nyberg, J.Ø. Duus and O. W. Sørensen, *J. Am. Chem. Soc.*, 2005, **127,** 6154–6155.
65. N. T. Nyberg, J.Ø. Duus and O. W. Sørensen, *Magn. Reson. Chem.*, 2005, **43,** 971–976.
66. B. O. Petersen, E. Vinogradov, W. Kay, P. Würtz, N. T. Nyberg, J.Ø. Duus and O. W. Sørensen, *Carbohydr. Res.*, 2006, **341,** 550–555.
67. N. T. Nyberg and O. W. Sørensen, *Magn. Reson. Chem.*, 2006, **44,** 451–454.
68. A. J. Benie and O. W. Sørensen, *Magn. Reson. Chem.*, 2006, **44,** 739–743.
69. J. C. Madsen, H. Bildsøe, H. J. Jakobsen and O. W. Sørensen, *J. Magn. Reson.*, 1986, **67,** 243–257.

70. A. J. Benie and O. W. Sørensen, *J. Magn. Reson.*, 2007, **184,** 315–321.
71. G. W. Vuister and A. Bax, *J. Magn. Reson.*, 1992, **98,** 428–435.
72. K. Furihata and H. Seto, *Tetrahedron Lett.*, 1998, **39,** 7337–7340.
73. T. D. W. Claridge and I. Perez-Victoria, *Org. Biomol. Chem.*, 2003, **1,** 3632–3634.
74. A. Bax and D. Marion, *J. Magn. Reson.*, 1988, **78,** 186–191.
75. G. Gasmi, G. Massiot and J. M. Nuzillard, *Magn. Reson. Chem.*, 1996, **34,** 185–190.
76. C. Gaillet, C. Lequart, P. Debeire and J.-M. Nuzillard, *J. Magn. Reson.*, 1999, **139,** 454–459.
77. J. M. Bernassau and J. M. Nuzillard, *J. Magn. Reson. B*, 1994, **103,** 77–81.
78. B. Vitorge, S. Bieri, M. Humam, P. Christen, K. Hostettmann, O. Muñoz, S. Loss and D. Jeannerat, *Chem. Commun.*, 2009, **2009,** 950–952.
79. D. O. Cicero, G. Barbato and R. Bazzo, *J. Magn. Reson.*, 2001, **148,** 209–213.
80. M. Foroozandeh and D. Jeannerat, *ChemPhysChem.*, 2010, **11,** 2503–2505.
81. S. Mori, C. Abeygunawardana, M. O'Neil Johnson and P. C. M. Van Zijl, *J. Magn. Reson. B*, 1995, **108,** 94–98.
82. A. Ross, M. Salzmann and H. Senn, *J. Biomol. NMR*, 1997, **10,** 389–396.
83. R. R. Ernst, VIth international Conference on Magnetic Resonance in Biological Systems, , 1974Kandersteg, Switzerland.
84. P. Schanda and B. Brutscher, *J. Am. Chem. Soc.*, 2005, **127,** 8014–8015.
85. P. Schanda, E. Kupče and B. Brutscher, *J. Biomol. NMR*, 2005, **33,** 199–211.
86. P. Schanda, *Prog. Nucl. Magn. Reson. Spectrosc.*, 2010, **55,** 238–265.
87. K. Pervushin, B. Vögeli and A. Eletsky, *J. Am. Chem. Soc.*, 2002, **124,** 12898–12902.
88. J. Furrer, unpublished results..
89. E. Kupče and R. Freeman, *Magn. Reson. Chem.*, 2007, **45,** 2–4.
90. J. Furrer, *Chem. Commun.*, 2010, **46,** 3396–3398.
91. A. J. Shaka, C. J. Lee and A. Pines, *J. Magn. Reson.*, 1988, **77,** 274–293.
92. W. Peti, C. Griesinger and W. Bermel, *J. Biomol. NMR*, 2001, **18,** 199–205.
93. L. Frydman, T. Scherf and T. Lupulescu, *Proc. Natl. Acad. Sci. USA*, 2002, **99,** 15858–15863.
94. A. Tal and L. Frydman, *Prog. Nucl. Magn. Reson. Spectrosc.*, 2010, **57,** 241–292.
95. Ē. Kupče, T. Nishida and R. Freeman, *Prog. Nucl. Magn. Reson. Spectrosc.*, 2003, **42,** 95–122.
96. E. Kupče and R. Freeman, *J. Am. Chem. Soc.*, 2004, **126,** 6429–6440.
97. P. Schanda and B. Brutscher, *J. Magn. Reson.*, 2006, **178,** 334–339.
98. A. Tal, B. Shapira and L. Frydman, *Angew. Chem. Int. Ed Engl.*, 2009, **48,** 2732–2736.
99. E. Kupče and R. Freeman, *Magn. Reson. Chem.*, 2007, **45,** 711–713.
100. M. Sattler, M. Maurer, J. Schleucher and C. Griesinger, *J. Biomol. NMR*, 1995, **5,** 97–102.
101. E. Kupče, R. Freeman and B. K. John, *J. Am. Chem. Soc.*, 2006, **128,** 9606–9607.
102. B. Vitorge, G. Bodenhausen and P. Pelupessy, *J. Magn. Reson.*, 2010, **207,** 149–152.
103. M. Eberstadt, G. Gemmecker, D. F. Mierke and H. Kessler, *Angew. Chem. Int. Ed Engl.*, 1995, **34,** 1671–1695.
104. B. L. Marquez, W. H. Gerwick and R. T. Williamson, *Magn. Reson. Chem.*, 2001, **39,** 499–530.
105. K. Kobzar and B. Luy, *J. Magn. Reson.*, 2007, **186,** 131–141.
106. T. Parella, 2D methods for the measurement of long-range proton–carbon coupling constants. *in*: Multidimensional NMR Methods for the Solution State, G. A. Morris and J. W. Emsley (eds.), John Wiley & Sons Ltd, Chichester, 2010, pp. 305–314.
107. V. V. Krishnamurthy, *J. Magn. Reson. A*, 1996, **121,** 33–41.
108. K. Furihata and H. Seto, *Tetrahedron Lett.*, 1999, **40,** 6271–6275.
109. K. Furihata, M. Tashiro and H. Seto, *Magn. Reson. Chem.*, 2009, **47,** 814–818.
110. K. Furihata, M. Tashiro and H. Seto, *Magn. Reson. Chem.*, 2010, **48,** 179–183.
111. K. Furihata, M. Tashiro and H. Seto, *Magn. Reson. Chem.*, 2011, **49,** 53–58.
112. J. J. Titman, D. Neuhaus and J. Keeler, *J. Magn. Reson.*, 1989, **85,** 111–131.

113. L. Verdier, P. Sakhaii, M. Zweckstetter and C. Griesinger, *J. Magn. Reson.*, 2003, **163,** 353–359.
114. R. A. E. Edden and J. Keeler, *J. Magn. Reson.*, 2004, **166,** 53–68.
115. H. Koskela, I. Kilpelainen and S. Heikkinen, *J. Magn. Reson.*, 2003, **164,** 228–232.
116. K. E. Kövér, G. Batta and K. Fehér, *J. Magn. Reson.*, 2006, **181,** 89–97.
117. V. J. Lacerda, G. V. J. da Silva, M. G. Constantino, C. F. Tormena, R. T. Williamson and B. L. Marquez, *Magn. Reson. Chem.*, 2006, **44,** 95–98.
118. H. Koskela, I. Kilpeläinen and S. Heikkinen, *J. Magn. Reson.*, 2004, **170,** 121–126.
119. S. Gil, J. F. Espinosa and T. Parella, *J. Magn. Reson.*, 2010, **207,** 312–321.
120. S. Ilin, C. Bosques, C. Turner and H. Schwalbe, *Angew. Chem. Int. Ed Engl.*, 2003, **42,** 1394–1397.
121. S. J. F. Vincent and C. Zwahlen, *J. Am. Chem. Soc.*, 2000, **122,** 8307–8308.
122. O. W. Sørensen, *J. Magn. Reson.*, 1990, **89,** 210–216.
123. B. T. Farmer, *J. Magn. Reson.*, 1991, **93,** 635–641.
124. R. Boelens, M. Burgering, R. H. Fogh and R. Kaptein, *J. Biomol. NMR*, 1994, **4,** 201–213.
125. M. Mariani, M. Tessari, R. Boelens, H. Vis and R. Kaptein, *J. Magn. Reson. B*, 1994, **104,** 294–297.
126. D. Uhrín, J. Bramham, S. J. Winder and P. N. Barlow, *J. Biomol. NMR*, 2000, **18,** 253–259.
127. D. Frueh, H. Arthanari and G. Wagner, *J. Biomol. NMR*, 2005, **33,** 187–196.
128. D. Frueh, D. Vosburg, C. Walsh and G. Wagner, *J. Biomol. NMR*, 2006, **34,** 31–40.
129. P. Nolis and T. Parella, *J. Magn. Reson.*, 2005, **176,** 15–26.
130. P. Nolis, M. Pérez and T. Parella, *Magn. Reson. Chem.*, 2006, **44,** 1031–1036.
131. P. Nolis and T. Parella, *J. Biomol. NMR*, 2007, **37,** 65–77.
132. M. Pérez-Trujillo, P. Nolis, W. Bermel and T. Parella, *Magn. Reson. Chem.*, 2007, **45,** 325–329.
133. M. Perez-Trujillo, P. Nolis and T. Parella, *Org. Lett.*, 2007, **9,** 29–32.
134. P. Nolis, M. Pérez-Trujillo and T. Parella, *Angew. Chem. Int. Ed.*, 2007, **46,** 7495–7497.
135. T. Parella and P. Nolis, *Concepts Magn. Reson. A*, 2010, **36A,** 1–23.

CHAPTER 7

Highly Customized NMR Systems Using an Open-Resource, Home-Built Spectrometer

Kazuyuki Takeda

Contents

1. Introduction 356
2. Design Concepts 357
   - 2.1. Field-Programmable Gate Array (FPGA) 357
   - 2.2. Architecture 359
   - 2.3. RF transmitter 359
   - 2.4. Signal acquisition 362
   - 2.5. Operation at higher intermediate frequency 363
   - 2.6. Polar plot option in the software 367
3. Applications 368
   - 3.1. Conventional NMR measurements 368
   - 3.2. A compact NMR and MRI systems 372
   - 3.3. Customized NMR systems 374
   - 3.4. The role of nuclear magnetization in a levitating body by the magneto-Archimedes effect 382
   - 3.5. Active compensation of RF pulse transients 386
4. Summary 390

Acknowledgement 391

References 392

Division of Chemistry, Graduate School of Science, Kyoto University, Kyoto, Japan

Annual Reports on NMR Spectroscopy, Volume 74
ISSN 0066-4103, DOI: 10.1016/B978-0-08-097072-1.00007-8

Abstract An integrated Field-Programmable Gate Array (FPGA)-based NMR spectrometer is described, with an emphasis on its applications to non-conventional NMR experiments, some of which are accompanied with modification to the hardware and software of the system.

Key Words: NMR spectrometer, Field-programmable gate array, Customization

1. INTRODUCTION

Recently, the author has published papers on design and fabrication of a home-built NMR spectrometer,[1,2] called the OPENCORE NMR spectrometer. The design resources of the spectrometer, such as circuit board drawings and programming source codes, etc., are freely available.[3] In the sense that information required to reproduce the spectrometer are open to the public, what the author does may look similar to uploading an open-source free software. However, the operational hardware cannot be reproduced in a straightforward way in practice, because one need to fabricate the hardware physically, making sure that the system is mechanically robust, electrical contacts are all fine for a number of device pins and connectors, power supplies are stable enough, and noises flying around the laboratory do not disturb the system, and so on.

To the author's knowledge, several groups have built the OPENCORE NMR spectrometers, those shown in Figure 1, presumably knowing that they have to deal with these problems by themselves, in contrast to using commercial systems.

The purpose of this review is to show that such an open-design NMR spectrometer, in spite of such difficulties and further potential problems, can be used to realize highly customized experimental systems with, if a necessary, modification to the hardware and the software. In the following, we describe features specific to the OPENCORE NMR spectrometer, and then we show its applications to various circumstances, some of which are standard NMR experiments, while others can only be realized using a customized system. The former cases may help researchers aiming at equipping the experimental setup with a low cost. More importantly, the latter cases encourage one to modify the system to build a specialized setup according to the purpose of the research. In this context, we believe that the OPENCORE NMR project contributes to push exciting NMR researches forward.

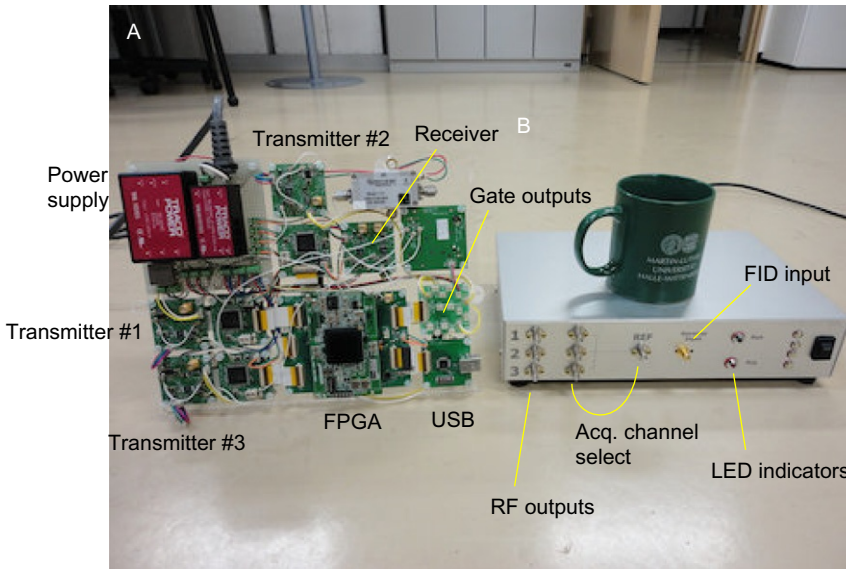

Figure 1 (A) An OPENCORE NMR spectrometer with an exposed assembly. The circuit boards are mounted on an acrylic plate, which is propped on a stand. The entire parts of the spectrometer can be placed inside a chassis, as shown in (B). For a feel of the size of the spectrometer, a coffee mug is also shown.

2. DESIGN CONCEPTS

2.1. Field-Programmable Gate Array (FPGA)

One of the important keywords of the project is FPGA. An FPGA is a semiconductor device in which digital circuits can be built. Figure 2A shows an example of the FPGA chip. Interestingly, the digital modules can be built simply by writing codes in a hardware description language, like software development. For the readers who are not familiar with the word FPGA, it may be worth showing here a simple example of FPGA development. Let us suppose that we are interested in building an inverter circuit converting the logic high (low) to logic low (high). The circuit implementing this function is also known as a NOT gate, and is described with a symbol shown in Figure 2B. In VHDL, which is one of the hardware description languages, the NOT circuit can be written as follows:

$$b <= \text{not } a;$$

here, a and b are Boolean variables taking either 1 or 0 corresponding to logic high and low. On the development software, one can assign physical

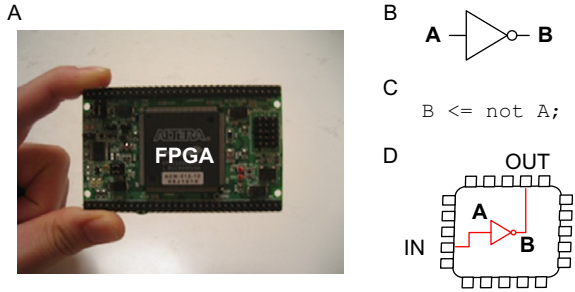

Figure 2 (A) An FPGA breadboard. In order to build a NOT gate as an example, whose symbol is depicted in (B), a VHDL code shown in (C) suffices. On the development software, one can assign physical pin connections, as schematically described in (D). Then, the FPGA is connected to the personal computer via a download cable, and finally, the circuit is physically built into the FPGA chip.

connections of the input and output to the device pins, and write the module into the FPGA chip using a download cable. In this way, a customized device can be built, as schematically depicted in Figure 2D. Although this example is too simple to be of practical interest, this procedure can be used to build *any* digital circuit within the limitation set by the circuit size and the operation speed of the FPGA chip in use. Nowadays, typical FPGA chips equip with more than 10^4 logic elements and can operate at clock frequencies exceeding 100 MHz.

Attractive features of the FPGA are as follows:

(i) Circuit components are reusable. That is, once a module has been developed, it can be used again in other occasions, or can be called from other modules.
(ii) Circuits are re-configurable as many times as needed.
(iii) Individual modules built inside the FPGA chip run in parallel. This contrasts with a microprocessor, which also does digital jobs, but in a successive way.
(iv) A personal computer suffices for development.

A digital module built into the FPGA chip is called a core module. In this project, the author has built a set of core modules dedicated for an NMR spectrometer. They include pulse programmers for controlling over the system, direct digital synthesizers (DDS) for generating RF signals with arbitrary phase modulation, a digital quadrature demodulators for converting the NMR signals into the rotating-frame representation, digital low-pass filters used to prevent the white noises outside the spectral width of interest from aliasing into view, and an interface module for command/data communication with a personal computer. The OPENCORE NMR spectrometer has been named after the *open*-resource *core* modules for an NMR spectrometer.

A unique design concept of the spectrometer is to let a single chip of FPGA undertake all digital jobs required for an NMR spectrometer, to fully exploit the above merits of the FPGA to build the system. On the other hand, the price to pay would be that the performance of some core modules may be lower than that of function-dedicated devices. Nevertheless, considering remarkable progress in the circuit size and the speed of the latest available FPGA devices, we may be optimistic about significant improvement in the ability and the performance of the integrated FPGA-based NMR spectrometer in near future.

2.2. Architecture

The principle of operation of RF transmission and signal acquisition has been described in the Refs. 1,2. Here we briefly overview the architecture of the spectrometer, to the extent that is sufficient for the discussion of the system customization described below.

Figure 3 shows a block diagram of the spectrometer. The modules depicted inside the area surrounded by the bold lines have been built into the FPGA chip. By default, the spectrometer can equip with up to three equivalent and independent RF transmitters, while there is a single receiver. The observation channel is selected by manually plugging the cable from one of the three reference signals of the transmitters to the receiver (Figure 1B).

In addition to the RF transmission and signal acquisition, the spectrometer can export/accept trigger signals. For example, the spectrometer can trigger external devices, such as an oscilloscope, and the spectrometer can wait for the trigger signal from, for example, a sample spinning controller to run a rotor-synchronized sequence. Furthermore, it is possible to synchronize two or more spectrometers, so that extension of the system to quadruple-resonance and/or dual-channel signal acquisition is straightforward.

2.3. RF transmitter

Each of the three transmitters has two separate frequency synthesizers based on DDS. For the sake of convenience, we henceforth refer to them as DDS(I) and DDS(II).

In DDS(I), the phase of the RF signal is tunable, while its frequency f_1 is fixed at either 20 MHz or 180 MHz, as described below. On the other hand, DDS(II) creates RF signals at various frequencies f_2. In order to create an RF pulse at frequency f of interest, the two signals are mixed using an RF mixer. The frequency f_2 generated by DDS(II) can be chosen so that either the sum $f_1 + f_2$ or the difference $|f_2 - f_1|$ matches with f. Since the signal from the output of the mixer contains a number of image

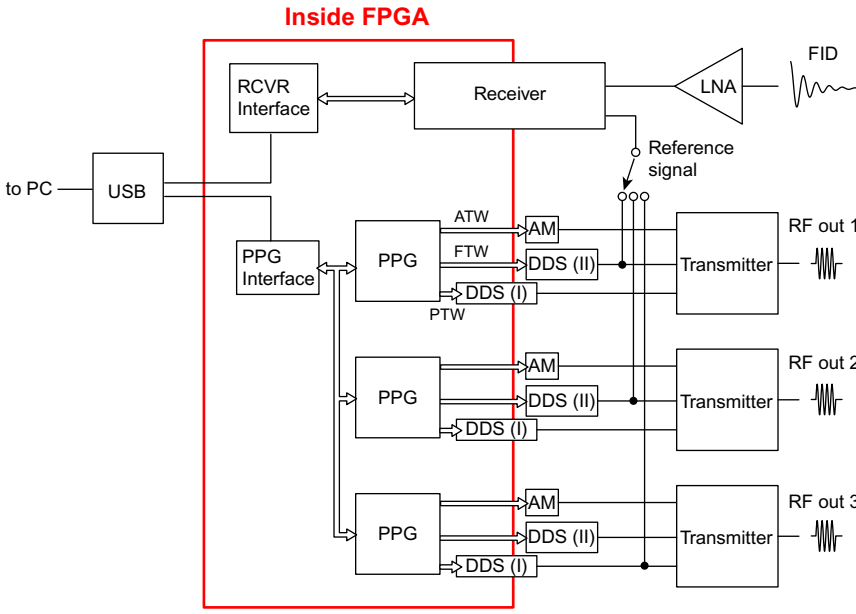

Figure 3 A block diagram describing the architecture of the OPENCORE NMR spectrometer. The modules located within the area indicated by the red rectangle have been built inside a single FPGA chip. Those which cross the FPGA boundary have both the digital and analog functions, so that the latter have been built outside the FPGA. The glossary is as follows. PPG, Pulse ProGrammer; DDS, Direct Digital Synthesizer; AM, Amplitude Modulator; RCVR, ReCeiVeR; FTW, Frequency-Tuning Word; PTW, Phase-Tuning Word; ATW, Amplitude-Tuning Word; LNA, Low Noise Amplifier.

frequencies, an RF filter is used to extract the relevant Fourier component at f. Insertion of the filter is done manually.

Here, it is important to realize which of $f_1 + f_2$ or $|f_2 - f_1|$ is used as well as the sign of the gyromagnetic ratio of the nuclear spin species under measurement. As extensively discussed by Levitt,[4] the issue on the signs of RF frequencies and phases used in NMR spectroscopy is delicate and can cause a number of practical problems. In 2000, Levitt and Johannessen[5] put forth recommendations for ''future'' NMR instruments, proposing that the sign of the phases should be inverted if (i) the gyromagnetic ratio is positive and the sum $f_1 + f_2$ is employed, or if (ii) the gyromagnetic ratio is negative and the difference $|f_2 - f_1|$ is used. In the OPENCORE spectrometer, the frequency mixing scheme is explicitly visible, and the user is requested to set up the source frequencies and the right RF filter accordingly. The above instruction can thus be applied straightforwardly.

The RF signal at f thus generated is sent to an analog multiplier to adjust its level. The signal, so far being a continuous wave, is then gated by an RF switch to make a pulse.

In the transmitter, one has to control the frequency, the phase, and the amplitude of the signal. In addition, the gating signals for pulse modulation, power amplifier unblanking, and other optional triggers to an oscilloscope and/or peripheral devices are required. A set of digital signals to implement all of these functions are generated by the pulse programmer. In the OPENCORE NMR spectrometer, three separate and equivalent pulse programmers have been built into the FPGA chip in order to manipulate the three RF channels independently. The operations of the three pulse programmers can be triggered with one another, so that they can run in either a synchronous or an asynchronous way. In many cases, the former mode is convenient, while the latter is useful for asynchronous sequences, such as TPPM decoupling.[6,7]

The individual pulse programmer operates at a clock frequency of 160 MHz, and the digital control signals can be generated with the minimum width and increment of 25 and 6.25 ns, respectively.

DDS is a technology to generate signal waves by digital signal processing, and can be an alternative to the traditional analog signal synthesis. In the design of DDS, a phase wheel is conceptually considered (Figure 4A). DDS(I) operates at a clock frequency of 160 MHz and employs 10-bit digital resolution. The circumference of the phase wheel is divided into $2^{10} = 1024$ points, and the value corresponding to sin of its

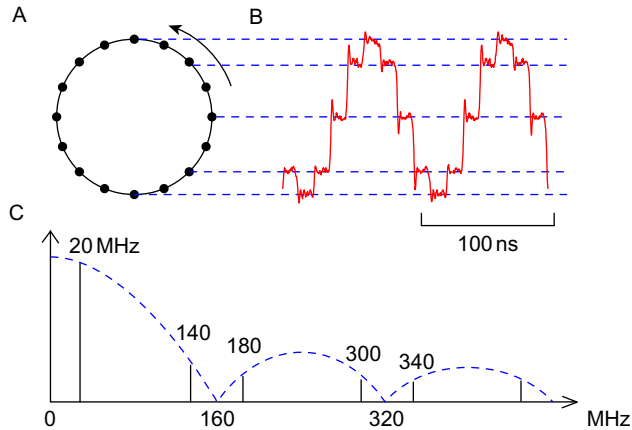

Figure 4 (A) A DDS phase wheel. (B) A signal from the frequency-fixed, phase-tunable DDS(I). The signal is updated at a rate of 160 MHz. (C) The spectral decomposition of the signal. Either the fundamental wave at 20 MHz or the second-order image frequency at 180 MHz is used for the intermediate frequency.

phase is assigned to each point. The output level of the DA converter is determined accordingly. At the leading edge of the 160 MHz clock, the phase wheel is rotated by 45°. One whole rotation takes eight steps, so that the fundamental wave at 20 MHz is generated, as shown in Figure 4B.

In order to implement the phase-tunable DDS, the phase wheel is also shifted according to phase modulation and phase cycling. The digital signal carrying the amount of the additional phase shift is given to DDS (I) by the pulse programmer.

DDS(II) has exceptionally been built completely outside the FPGA, as a tentative solution to cover the second frequency f_2 of up to ~400 MHz. In DDS(II), a DDS-dedicated LSI AD9858 (Analog Devices) is used.[8] It operates at a clock frequency of 1 GHz. The theoretical limit of the maximum frequency of the fundamental wave is given by half the sampling frequency, that is 500 MHz, whereas the realistic limitation is loosely given by ~0.4 time the clock frequency.[9] This DDS-chip is also capable of jumping/sweeping frequencies. This feature can be exploited in the NMR experiments that require frequency modulation.

2.4. Signal acquisition

The NMR signal in the form of FID is sent to the input of the receiver circuit. In the receiver, the frequency of the signal is converted into the intermediate frequency. This is done by mixing the signal with the reference signal from one of the three RF channels, and then passing the signal through an appropriate RF filter. Next, the signal is digitized by a 14-bit analog-to-digital converter (ADC) with a sampling rate of 80 MHz.

As the design concept is to let the FPGA do all digital jobs, the signal is immediately sent to the FPGA once it has been digitized. The first processing stage is digital quadrature demodulation, which converts the digitized signal into a pair of in-phase (real) and quadrature (imaginary) components. The demodulation is performed with respect to the reference phase of the transmitter. Since the transmitter phase is determined by that of DDS(I), the clocks driving DDS(I) and the demodulator are synchronized with each other, ensuring that the signals can be accumulated in a reproducible way.

The signal bandwidth is given by half the sampling frequency, that is $80/2 = 40$ MHz in the present case, and the in-phase and quadrature signal components are updated every 25 ns. This gives the minimum time interval that the spectrometer can record the signals. In many practical cases, however, the spectral width of interest is much narrower, ranging from several tens of kHz to, at most, a few MHz. The signals sampled at such a fast rate can be used to process the data by digital filtration, in order to prevent the noises spreading outside the spectrum from aliasing into view. For this purpose, two separate Finite Impulse

Response (FIR) filters have been implemented in the FPGA. Finally, the in-phase and quadrature signal pair is stored in a memory, also built inside the FPGA, according to the acquisition phase indicated by the pulse programmer.

2.5. Operation at higher intermediate frequency

The NMR spectrometer originally supported frequencies up to 400 MHz. However, even higher frequencies may be of interest, considering the recent progress in the magnet technology pushing the proton resonance frequency up to 1 GHz. One straightforward way would be frequency up-conversion by mixing the signal with that from another source. In this case, the system needs an additional up-converter in the transmitter and a down-converter in the receiver.

Here, we show another way of extending the frequency by increasing the intermediate frequency only with a slight hardware modification.[10] This strategy is specific to the current design of the spectrometer, in which the DDS operates at twice the ADC clock frequency and generates a fundamental wave at one quarter the ADC clock frequency. In the present case, the ADC sampling rate is 80 MHz, while DDS(I) operates at 160 MHz and generates a 20-MHz signal. This specific combination enables us to exploit one of the image frequencies of the DDS, and at the same time to use the scheme called the super-Nyquist sampling or undersampling in the receiver.

The signal generated by the DDS is composed of a number of image frequencies in addition to the fundamental frequency. Figure 4C illustrates the spectrum for the case of DDS(I). So far, it has been implicitly assumed that the fundamental wave is selected by cutting off the image components using a low-pass filter. Now instead, let us suppose that one of the image frequencies is extracted by passing the signal through a band-pass filter. Interestingly, the even order images have the same phase as that of the fundamental wave,[9] so there is nothing to be modified with regard to pulse programming for RF-phase modulation. For example, when we extract the second-order image signal through a band-pass filter, it can be used as an alternative phase-tunable signal wave with a fixed frequency at 180 MHz. Thus, the transmitter can deal with the higher frequency by a factor of $180 - 20 = 160$ MHz as compared to the original configuration.

Naturally, there should be something we have to do in the receiver, because the ADC is required to digitize signals at the intermediate frequency that is higher than its sampling rate. At a glance, this may appear to be impossible. Nevertheless, it is possible by the super-Nyquist sampling. In the conventional sampling, we are interested in only those Fourier components of the signal lying in the region from zero to the

Nyquist limit given by half the sampling rate. However, aliasing occurs for the higher frequencies, as schematically described in Figure 5A. What we usually do is to eliminate them by a low-pass filter in advance to ADC (Figure 5B). Now let us suppose that the low-pass filter is replaced by such a band-pass filter that extracts the region indicated by the red square in Figure 5C. This region, called the fifth Nyquist zone, has a centre frequency of 180 MHz and a width of 40 MHz. It can thus cover the frequency range cantered at the new intermediate frequency.

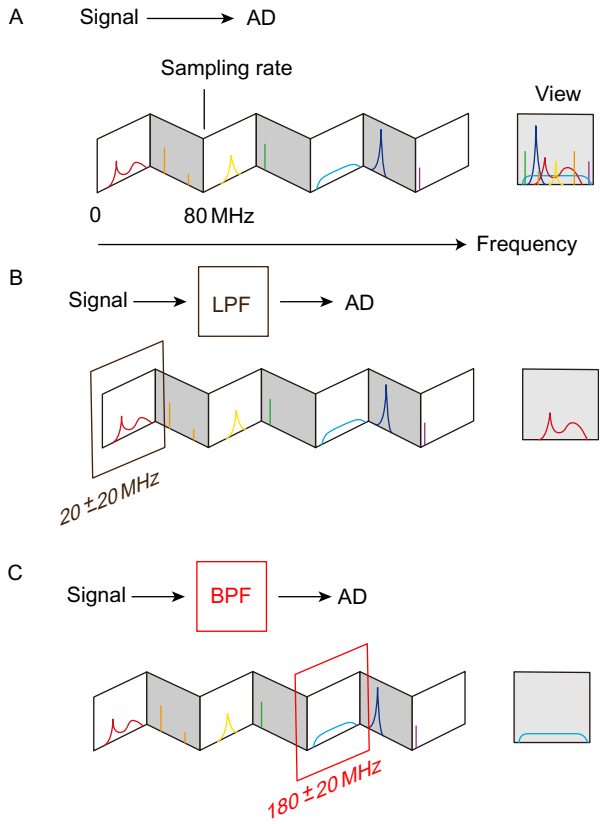

Figure 5 In digital signal sampling, the spectral bandwidth is limited by half the sampling rate, and those frequency components lying outside the bandwidth appear into view, in an analogous way with a projection view on a folded paper, as schematically described in (A) for the case of the sampling rate of 80 MHz. (B) In the traditional sampling, the signal passes through a low-pass filter, to obtain only those signal components having the frequencies ranging from 0 to 40 MHz, which is known as the Nyquist frequency. (C) In this work, super-Nyquist sampling is employed to extract the fifth Nyquist zone ranging over 180 $\pm$ 20 MHz by replacing the low-pass filter by a band-pass filter.

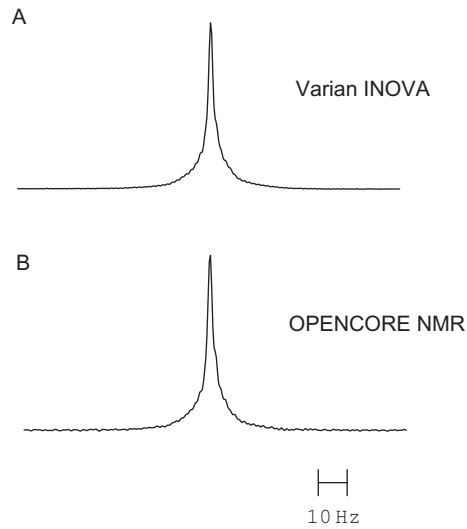

Figure 6 Liquid-state ^{1}H spectra in chloroform acquired in 11.7 T (A) on a Varian INOVA 500 MHz spectrometer, and (B) OPENCORE NMR spectrometer. The intermediate frequency was 180 MHz. In the transmitter, the 180-MHz DDS image was used, while super-Nyquist sampling was employed in the receiver.

Figure 6 demonstrates the feasibility of the idea of DDS-image combined with super-Nyquist sampling. Figure 6A shows a liquid-state ^{1}H NMR spectrum in chloroform obtained at a resonance frequency of 500 MHz using a Varian INOVA spectrometer. After the measurement, we replaced the spectrometer with the OPENCORE spectrometer, while keeping the sample and the probe as they were, and we obtained the spectrum shown in Figure 6B. Here, the intermediate frequency at 180 MHz was extracted from the output signal of DDS(I) using a 180-MHz band-pass filter, and was mixed with a signal at 320 MHz to produce the RF pulse at 500 MHz. In addition, another 180 MHz band-pass filter was employed between the mixer circuit of the receiver and the ADC. Figure 7A and B shows a circuit diagram and a snapshot of a handmade 180 MHz band-pass filter. Its transmission characteristic was found to be satisfactory, as demonstrated in Figure 7C.

The price to pay for getting the higher intermediate frequency in such a convenient way would be the less clock-jitter tolerance, so that the apparent resolution of the resonance line can be degraded compared with that obtained in the conventional detection scheme. For this reason, we demonstrated the high-resolution liquid-state NMR experiment, in which the resonance line width was on the order of Hz. In fact, we observed a drift of the peak position when we used a less stable clock

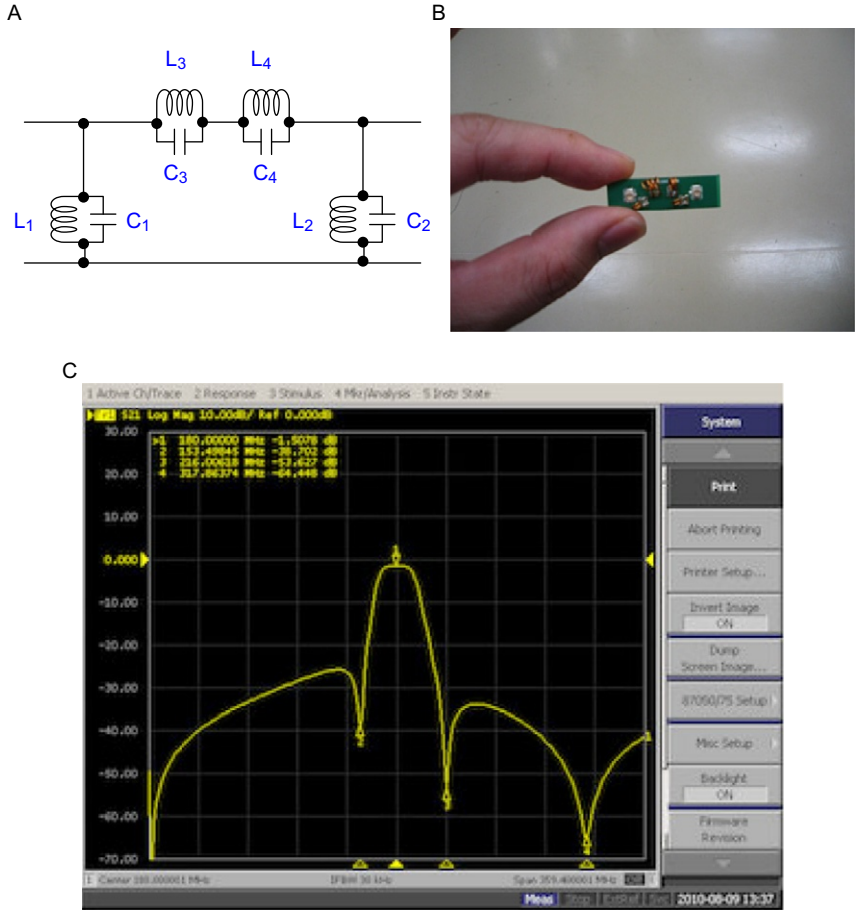

Figure 7 (A) A circuit diagram for a 180-MHz band-pass filter used for extracting the image signal of DDS(I) at 180 MHz signal and applying the super-Nyquist sampling. (B) A snapshot of the 180-MHz band-pass filter. The capacitances are as follows: $C_1 = C_2 = 100$ pF (GQM2195C2E101JB12, Murata), $C_3 = 39$ pF (GQM2195C2E390JB12), and $C_4 = 22$ pF (GQM2195C2E220JB12). The inductors were wound with a 0.4-mm coated copper wire. The diameters and the numbers of turns were 2 mm and two for L_1 and L_2, 3 mm and four for L_3, and 3 mm and three for L_4. (C) The S_{21} parameter of the filter measured using a network analyzer. The centre frequency and the span were 180 and 400 MHz.

for the system; a long time signal averaging resulted in the apparent broader peak. Nevertheless, when the OPENCORE spectrometer was driven by a good clock, such as that from a PTS synthesizer, the quality of the spectrum was as satisfactory as that obtained on the commercial spectrometers.

2.6. Polar plot option in the software

Since the software is also home built, a number of unique functions can be added to it. An example of such is the way that the data is plotted. In addition to the conventional data plotting scheme, the parametric plot of the real and the imaginary data on the *xy*-plane is supported. This option enables one to ''see'' the precession of the transverse nuclear magnetization in the rotating reference frame with respect to the carrier frequency.

Figure 8 shows screenshots of the console software displaying ^{79}Br FIDs measured in a powder sample of KBr under magic angle spinning for various carrier frequencies. When the ^{79}Br Larmor frequency was higher than the carrier frequency, the trajectory of the transverse magnetization was a spiral. As the carrier frequency increased and approached to the Larmor frequency, the decaying magnetization rotated more slowly, and at on-resonance, the ^{79}Br magnetization decayed without

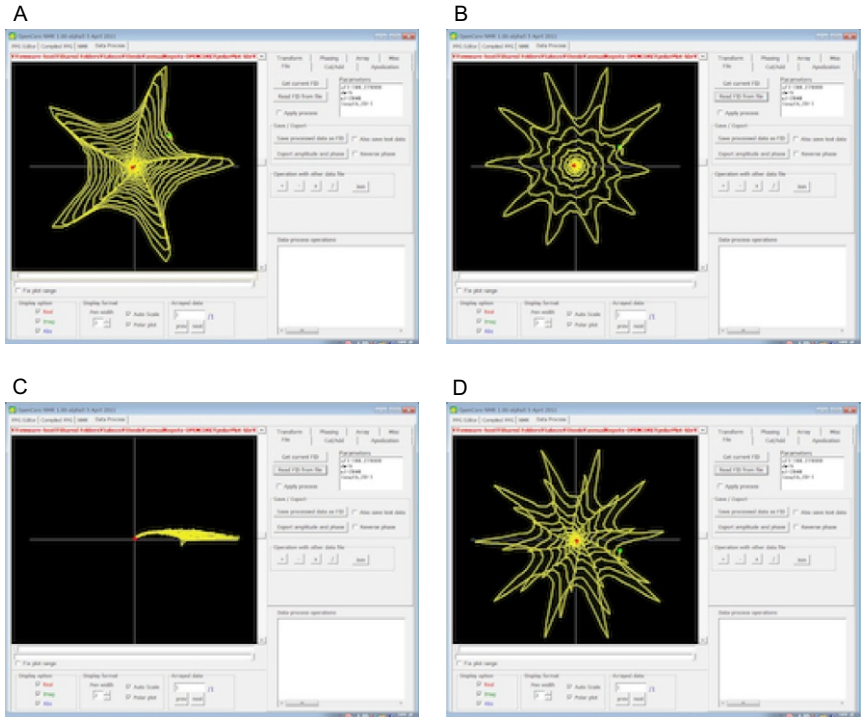

Figure 8 Polar plots of the in-phase and quadrature components of the ^{79}Br NMR signal in a powder sample of KBr in a magnetic field of 7 T under MAS at 5.1 kHz. The carrier frequencies were (A) 100.280545 MHz, (B) 100.281545 MHz, (C) 100.282545 MHz, and (D) 100.283545 MHz. The ^{79}Br resonance frequency was 100.282545 MHz.

any apparent precession. For the carrier frequency higher than the Larmor frequency the rotating frame magnetizations drew a spiral line in the opposite direction. In all the screenshots, the rotational echoes appeared as spikes.

The polar plot shown here is nothing more than the parametric plot of the real and imaginary component of the signal. In this sense, a generic graph-plotting software can be used to obtain the same figure. What is special about this plotting option *on the spectrometer software* is that it provides real-time visualization of the processing transverse magnetization. This feature is not only amusing, but also instructive to understand that the spectrometer is transforming the FID into the rotating-frame representation.

3. APPLICATIONS

3.1. Conventional NMR measurements

Using the OPENCORE NMR spectrometer, standard solid-state NMR experiments have been demonstrated in Ref. 2. They include ^{1}H–^{13}C CPMAS with TPPM decoupling, ^{13}C–^{15}N dipolar recoupling under MAS, ^{1}H FSLG, ^{13}C–^{13}C 2D exchange, and so on. Here we show two more examples, where the spectrometer was used to implement standard pulse sequences, but in somewhat demanding circumstances in terms of sensitivity.

The first one concerns microcoil MAS,[11–15] which is an effective strategy for high-resolution solid-state NMR of volume limited samples. Although the microcoil enables NMR studies of such a small sample that cannot to be measured with the conventional probe, the sensitivity is in general low. Thus, the loss of the signal intensity or contamination of any extra noises in the spectrometer would seriously degrade the quality of the spectrum and should be avoided. Figure 9A shows a ^{13}C CPMAS spectrum of amyloid-β labelled with ^{13}C at the 35-Met and 42-Ala amino acid residues. The amount of the sample was $\sim$0.1 mg, and magic angle coil spinning (MACS) was utilized.[16] In MACS, a tank circuit composed of a microcoil and a chip capacitor is inserted into a rotor, and is spun at the magic angle together with the rotor. RF irradiation at the sample inside the microcoil and NMR signal acquisition are done wirelessly by the inductive coupling between the microcoil and the sample coil of the probe. Here, we used a doubly tuned MACS resonator at the ^{1}H and ^{13}C Larmor frequencies to perform the double-resonance experiment.[17]

In the next example, the OPENCORE NMR spectrometer was used with a cryo-coil MAS probe,[18] in which the sample coil and the

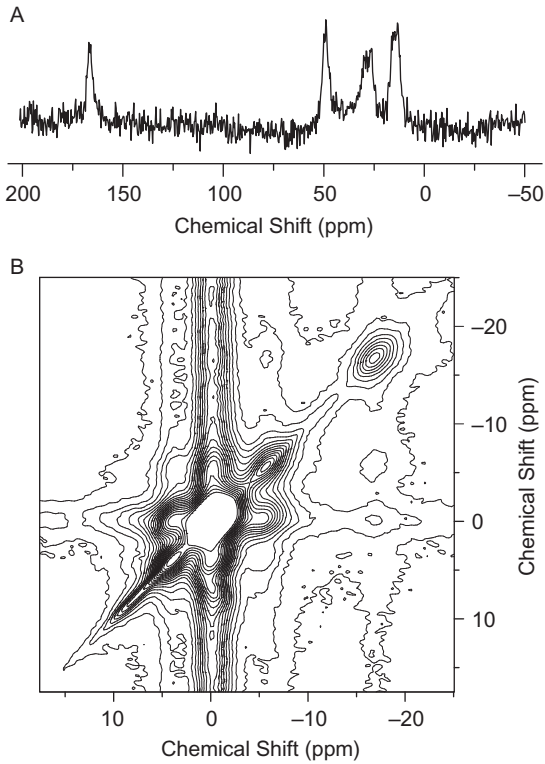

Figure 9 (A) A ^{13}C CPMAS spectrum of synthesized Aβ42, which was partially ^{13}C-labelled at the 35-Met and 42-Ala amino acid residues. The sample with a weight of $\sim$0.1 mg was packed into a capillary, which, together with a MACS insert tuned doubly at 300 and 75 MHz, spun in a magnetic field of 7 T at 10 kHz. The ^{13}C NMR signals were accumulated over 180,000 times with a recycle delay of 1 s. (B) 2D ^{6}Li exchange spectrum in 95% ^{6}Li labelled $LiCoO_2$ measured using a cryo-coil MAS probe. The amount of the sample was 225.9 mg. The mixing time, the carrier frequency, and the spinning frequency were 200 ms, 44.35 and 3 kHz.

preamplifier can be cooled to cryogenic temperatures, while the spinning sample can be kept at ambient temperatures. The effect of cooling the circuit is to reduce the resistance and thereby the thermal noise. Moreover, increase in the Q factor of the circuit enhances the signal intensity.

Figure 9B shows a ^{6}Li 2D exchange NMR spectrum obtained in $LiCoO_2$ obtained using the cryo-coil MAS probe. This sample has been of interest as a cathode material for Li ion batteries. In general, the sensitivity of ^{7}Li NMR is much higher than that of ^{6}Li NMR, as the former has a larger natural abundance and gyromagnetic ratio. One drawback of ^{7}Li is its relatively large quadrupole moment, often degrading the spectral resolution and obscuring the structure of interest. For this reason, the

sensitivity-challenging ^{6}Li NMR was performed using the cryo-coil MAS probe that enables ^{6}Li 2D NMR within a realistic experimental time. In this case, the intensity of the thermal noise in the probe was much smaller compared to the conventional cases. Thus, in order to exploit the high-performance of the probe, the spectrometer was required to be silent enough not to generate or pick up unwelcome extra noises.

Experiments demonstrated above are also feasible in the commercial spectrometers. Next, we show examples of highly customized experimental setups utilizing the OPENCORE NMR spectrometer.

A network analyzer is a device used to measure S parameters of the circuit of interest for various frequencies, and is a useful tool in NMR spectroscopy for probe tuning, RF-filter characterization, and so on. Here we demonstrate that a simple network analyzer can be implemented by the OPENCORE NMR spectrometer. Figure 10A describes a diagram for measurement of the S_{11} parameter, that is, the reflection. Using a hybrid junction, the RF signal coming out of the transmitter is forwarded to the test circuit, and the reflected signal is directed to the receiver. Figure 10B shows a pulse sequence for the analyzer. While opening the transmitter gate, the frequency is linearly swept over the range of interest, and the reflected signal is acquired. When one needs to measure the S_{21} parameter, that is, the transmission, the hybrid junction may be replaced by the circuit of interest, and the same pulse sequence works for this purpose.

In order to demonstrate probe tuning using this scheme, a setup shown in Figure 11A was assembled. Here, the X channel of a Varian

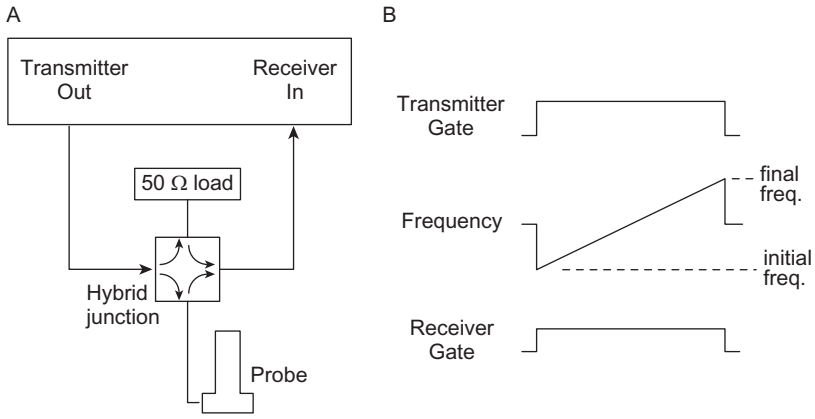

Figure 10 (A) A wiring diagram to let the OPENCORE NMR spectrometer act as a network analyzer. The RF irradiation from the transmitter is fed to a hybrid junction, and the reflection from the probe or any passive device of interest is led to the receiver. (B) A pulse sequence for implementing a network analyzer. The RF frequency is linearly swept over the range of interest, while the receiver gain is opened and the signal is acquired.

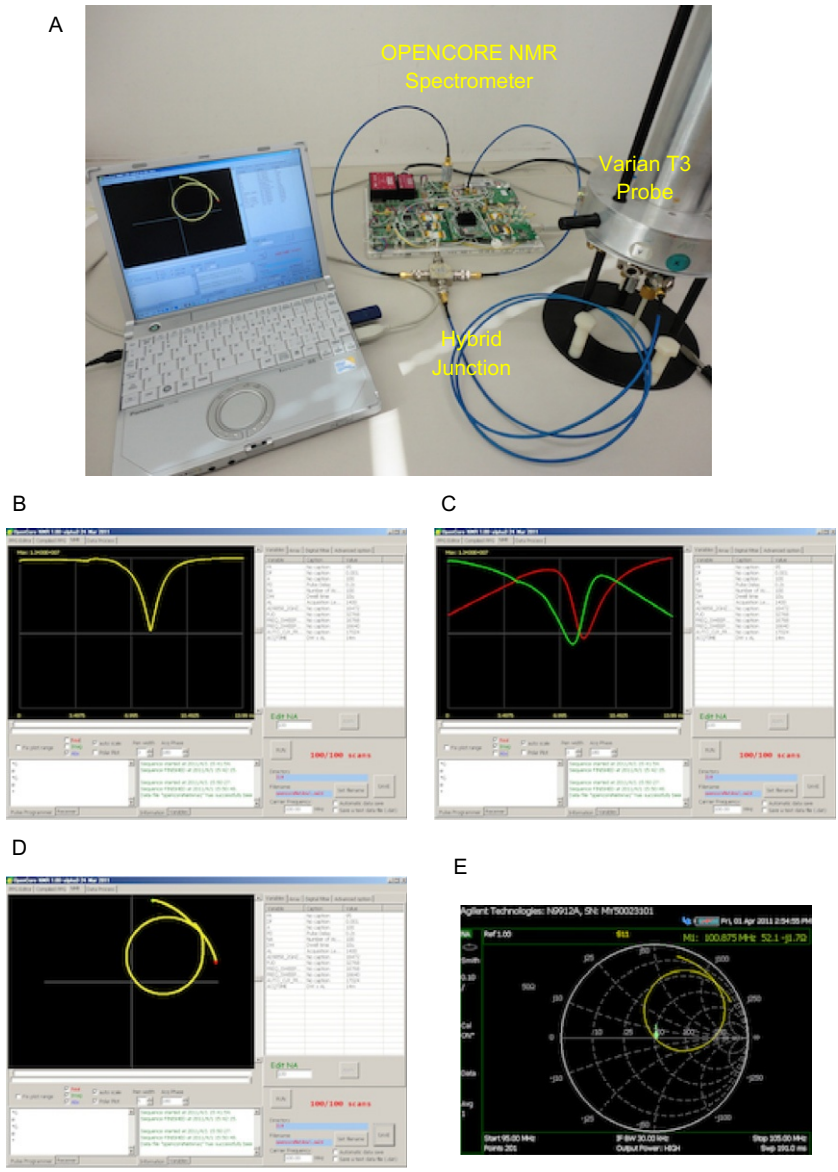

Figure 11 (A) A snapshot of an experimental setup arranged to implement the wiring diagram described in Figure 10. The X channel of a Varian 3.2 mm T3-probe was tuned at 100.875 MHz, and the pulse sequence described in Figure 10B was performed with initial and final frequencies of 95 and 105 MHz. The frequency was altered every 1.0 μs by 1.0 kHz for 14.0 m, and the signal reflecting from the probe was acquired with a sampling interval of 10 μs. (B) The magnitude profile of the probe reflection as a function of the frequency. (C) The in-phase (red line) and quadrature (green) components of the

3.2 mm T3-probe was tuned at 100.875 MHz, and the sequence described in Figure 10A was implemented over the frequencies ranging from 95 to 105 MHz. By switching the mode of the DDS(II) to the frequency-sweep mode, the frequency was altered every 1.0 μs by 1.0 kHz for 14.0 ms, while the signal reflecting from the probe was acquired with a sampling interval of 10 μs.

Figure 11B shows the magnitude of the reflecting signal as a function of the frequency. This should be equivalent to what one sees on the screen of the commercial spectrometers running probe tuning. For minimizing the reflection at a certain frequency, the magnitude may be sufficient. In general, however, the phase of the reflected signal with respected to that of the incident signal is also important, and therefore, it would be convenient if the real and imaginary components can be plotted, as shown in Figure 11C. In this context, the polar plot option discussed above is relevant. As demonstrated in Figure 11D and E, what we see in the parametric plot of the real and imaginal components of the reflected signal corresponds to the S_{11} parameter measured by the network analyzer and plotted in the Smith-chart format.

3.2. A compact NMR and MRI systems

In the conventional NMR system used in chemical analyses, downsizing of the spectrometer alone may not be appealing, unless other parts of the system, such as a superconducting magnet, a power amplifier, etc., are also miniaturized. On the other hand, the small-sized spectrometer would find interest in various unconventional scenes. In this section, we show examples of such.

Figure 12A shows an MRI system packed into a bookshelf, which was developed for educational purposes. In this experimental setup, the static field was provided by a NEOMAX 1 T permanent magnet (Hitachi Metals, Ltd.), which is shown in Figure 12B. The size of the magnet was $73 \times 73 \times 139$ mm, and the sample coil could be inserted via its 17×5 mm slit. In order to perform MRI experiments using this specific magnet, we developed an MRI probe and field-gradient driver circuits. A sample coil with a diameter of 2 mm was wound, and three sets of gradient coils along the x, y, and z directions were built into the probe that fit in the magnet bore. In addition, modifications were made to the OPEN-CORE NMR spectrometer, so that it can generate waveforms for field-

reflection signal, and (D) its polar representation. For comparison, the S_{11} parameter measured on a network analyzer (Agilent N9912A) is shown in (E).

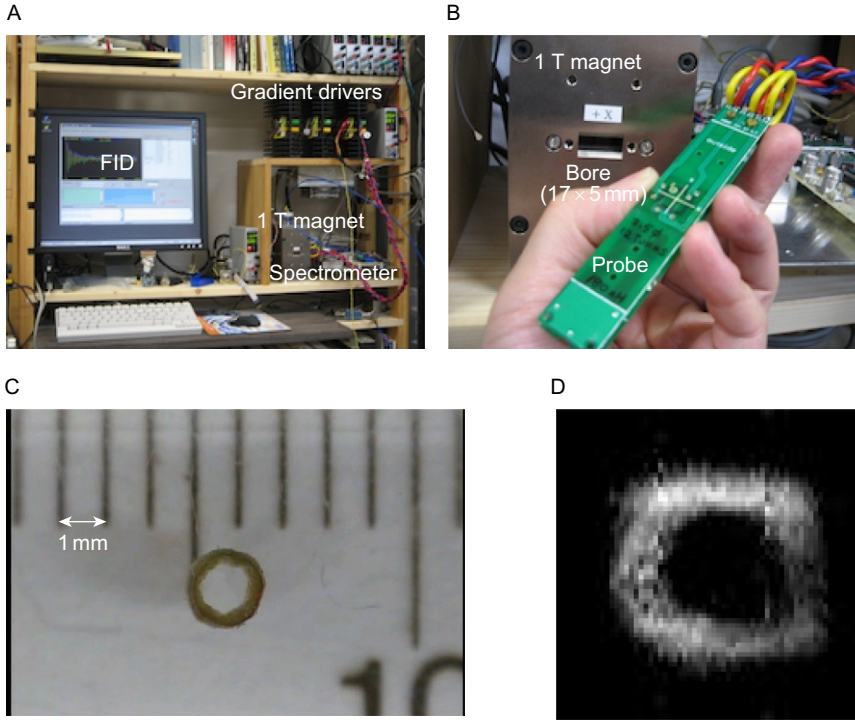

Figure 12 (A) An MRI system in a book shelf. (B) A 1-T permanent magnet with a bore size of 17 × 5 mm, and a home-built probe equipped with a sample coil with a diameter of 2 mm and *X*, *Y*, *Z* field-gradient coils. (C) A slice of a stem of dandelion, and (D) its ^{1}H MRI image acquired on this system.

gradient pulses. Using this hardware, we carried out an MRI experiment in a stem of dandelion (Figure 12C), and obtained the ^{1}H image, as demonstrated in (Figure 12D).

With this size of the sample coil, the RF power level required to excite the ^{1}H magnetization was relatively low, so that a tiny power amplifier with the output level of as small as ~1 W sufficed. This, together with the above permanent magnet, made the entire NMR system mobile outside the laboratory. By packing the system into a pair of attaches cases, the NMR system was carried to the author's home, and ^{1}H NMR experiments were performed, as demonstrated in Figure 13A. We carried the mobile system on trains, in order to demonstrate NMR experiments at various places. Figure 13B and C are snapshots demonstrating ^{1}H NMR in an intensive NMR course for graduate students, where an explanation was given how the demodulated FID looks like when the carrier frequency was varied.

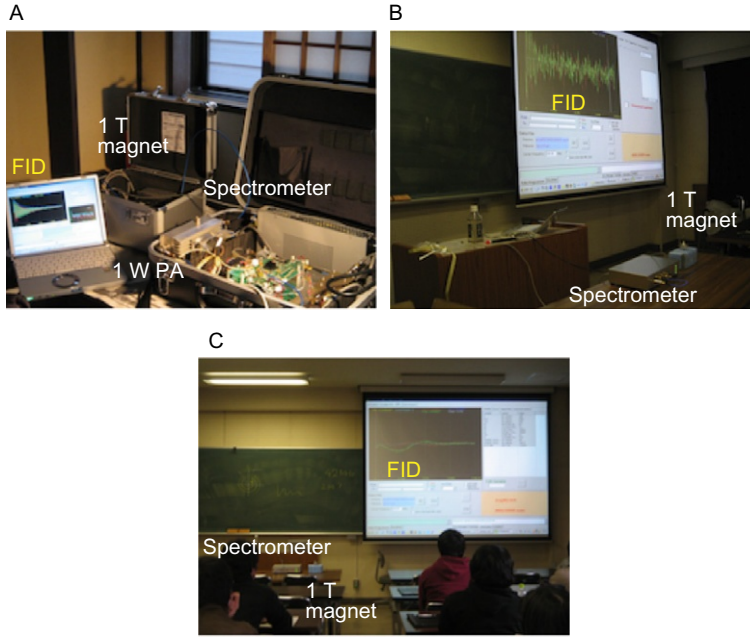

Figure 13 Snapshots of a portable NMR system serving as a science toy and an education tool. ^{1}H NMR experiments in water performed (A) at the author's home, and (B and C) in a class room at University of Fukui. A 1 T permanent magnet was used, and the ^{1}H resonance frequency was 42.6 MHz.

The spectrometer can also be used for a simple magnetic-field monitoring device. Figure 14A is a snapshot of the OPENCORE NMR spectrometer brought into a clinical whole-body MRI room in a hospital. In order to measure the magnetic field and its homogeneity, a palm-top probe was developed, and placed inside the 3 T horizontal magnet at positions of interest, as shown in Figure 14B. ^{1}H NMR signals were measured in water filled in a 3-mm glass tube, and obtained the spectrum shown in Figure 14C. Here, the resonance line width of $\sim$1 kHz was ascribed to the magnetic-field inhomogeneity, as confirmed by the spin-echo experiments demonstrated in Figure 14D.

3.3. Customized NMR systems

3.3.1. An NMR system using a field-variable, cryogen-free superconducting magnet

Figure 15A shows a desktop NMR system using the OPENCORE NMR spectrometer and a cryogen-free, field-variable superconducting magnet (Cryogenics). The desktop superconducting magnet, shown in

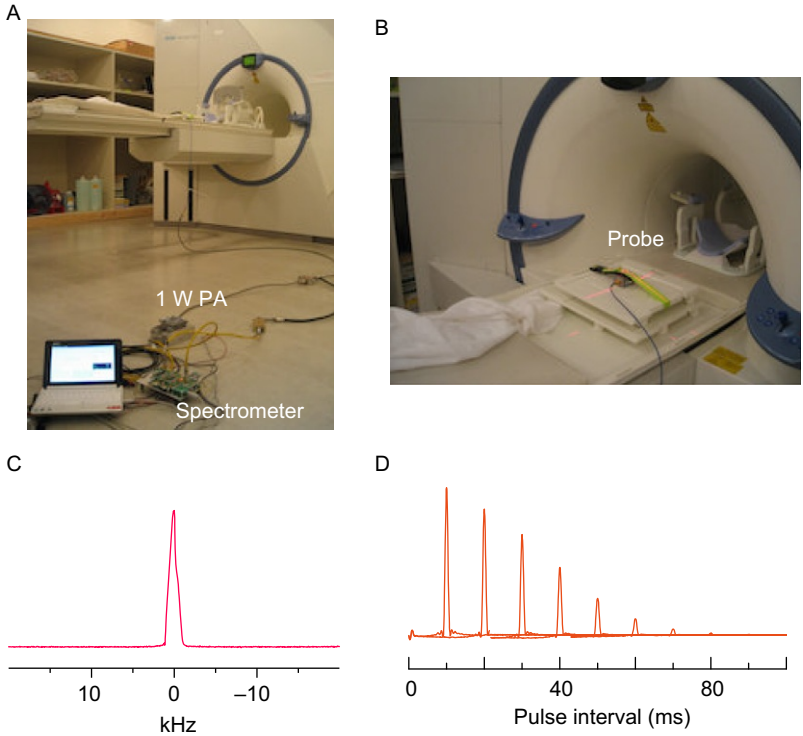

Figure 14 (A) An experimental setup for monitoring the magnetic field in a clinical MRI system in Kyoto University hospital. (B) An NMR probe placed at the head position. (C) A ^{1}H NMR spectrum in H_2O. The resonance frequency was 123.225 MHz, and the signal was accumulated over four times. (D) ^{1}H spin echoes.

Figure 15A, has an external refrigerator to keep the temperature of the magnet wire below 4 K. The magnetic field can be varied from 0 to 7 T by heating a part of the wire of the magnet, breaking superconductivity, and altering the electric current flowing through it. By switching the heater off, the magnet begins to run in the persistent-current mode again. The magnet bore has a diameter of 50 mm.

This system has been developed to acquire NMR spectra with such broad resonance lines that a single RF pulse cannot excite all the spin packets at once. In such a case, it is more convenient to vary the external field and fix the carrier frequency than to change the carrier frequencies with a constant field magnet, because the latter require probe re-tuning at every increment of the carrier frequencies. Moreover, it can alter the efficiency and phase response of the circuit, putting questions on the quantitative analyses of the data.

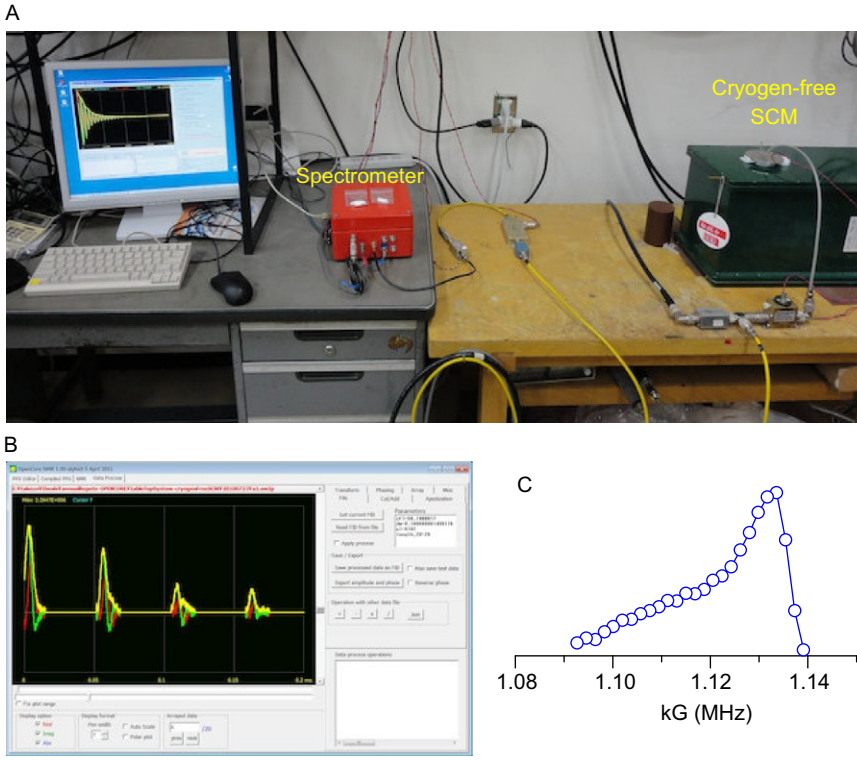

Figure 15 (A) A desktop NMR system using the OPENCORE NMR spectrometer and a cryogen-free, field-variable superconducting magnet (Cryogenics), in which the magnetic field can be varied between 0 and 7 T. (B) A screenshot displaying ^{195}Pt spin echoes obtained in platinum powder (290 mg) using the CPMG sequence. The interval between the echoes was 50 μs. (C) Magnetic-field dependence of the ^{195}Pt spin-echo intensity. The resonance frequency was 50.74 MHz, and the experiments were performed at 77-K by immersing the sample into a liquid-nitrogen dewar, which was put in the magnet.

In order to perform array experiments by increasing/decreasing the external magnetic field, the spectrometer software has been modified, so that it can send commands for controlling the magnet power supply. One application that we have been studying is ^{195}Pt NMR in bulk platinum particles and platinum nanoparticles, which show informative structure in the resonance lines; the ^{195}Pt Knight shift reflects the local structure of the electronic state, and the resonance line depends heavily on the particle size and the surface environment.

Figure 15B shows a screenshot displaying the spin echoes of ^{195}Pt in platinum powder acquired by the CPMG sequence. The experiments were performed at a carrier frequency of 50.74 MHz. The ^{195}Pt signal

was found in the magnetic fields ranging from 5.53 to 5.78 T, and field dependence of the echo intensities is plotted in Figure 15C.

3.3.2. An NMR setup based on a high-temperature superconducting materials

A superconducting magnet using bulk high-temperature superconducting materials[19–22] is a promising candidate for a complement or an alternative to the current superconducting magnet in the future, because of the following attractive reasons:

(1) The size of the superconducting magnet is as small as a wide-bore NMR probe.
(2) The magnetic field is stable over months.
(3) Operation requires neither liquid helium nor liquid nitrogen; only electricity suffices.
(4) A standard UPS battery system is capable of running the cooler, allowing us to prepare unexpected electric power failure or to carry the system to a place without power supply.
(5) Stray fields are weak at the fringe of the magnet.

The bulk high-temperature superconducting magnet can be magnetized by the field-cooling method. First, the bulk magnet is kept above the transition temperature, and is immersed in the magnetic field. This is done by placing it into a superconducting magnet that is used in the conventional NMR system. It is then cooled below the transition into the superconducting phase. Efforts have been made by Nakamura et al.[22] to improve the field homogeneity, and the magnet is now of practical use for MRI of small animals/plants. Presumably, high-resolution liquid-state NMR would also be feasible in near future. The bore size of the magnet (24 mm) may appear rather small for application to high-resolution solid-state NMR using MAS. Nevertheless, the latest sample-spinning modules for very fast MAS use a thin rotor with a diameter of as small as $\sim$1 mm, and the module itself is compact enough to fit in the bore of the bulk magnet. For these reasons, the bulk high-temperature superconducting magnet suggests one direction for the standard NMR magnet in the future.

Figure 16 shows an NMR system based on the bulk high-temperature superconducting magnet and the OPENCORE NMR spectrometer, in which ^{1}H NMR in water was performed in 4.7 T.

3.3.3. A DNP system

Using the OPENCORE spectrometer, a research group led by M. Kitagawa in Osaka have developed an experimental setup for dynamic nuclear polarization (DNP) using electron spins in the photo-excited triplet state. This nuclear hyperpolarization technique, called hereafter triplet DNP,

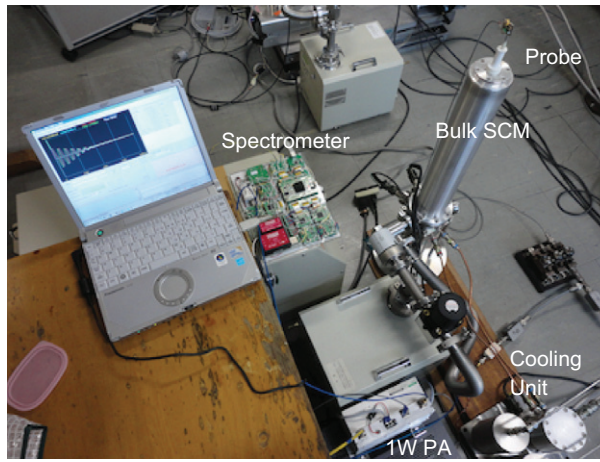

Figure 16 An NMR system using a bulk high-temperature superconducting magnet and the OPENCORE NMR spectrometer. The temperature of the bulk SCM was 40 K, while the sample space with a diameter of 24 mm was at room temperature. On the computer screen displayed is a ^{1}H FID of water taken on this system. The resonance frequency was 200.045 MHz.

can be applied to a class of molecules in which, upon photo-excitation to the excited singlet state, undergoes intersystem crossing into the metastable triplet state. Depending on the symmetric properties of the spin-orbit coupling that drives the intersystem crossing and the wave functions of the singlet state and the individual triplet sub-states, the population distribution over the triplet sub-levels can be highly biased. The non-equilibrium electron spin polarization thus created can be transferred to the nuclear spins during the lifetime of the triplet state. The cycle of photo-excitation, intersystem crossing, polarization transfer, and decay to the ground state can be repeated, so that the polarization of the nuclear spins can be pumped up one after another. When the non-equilibrium electron spin polarization in the triplet state is larger than the thermal polarization, the expected gain in the nuclear spin polarization can exceed that expected in the case of DNP using free radicals.[23,24]

The issues raised recently with regard to triplet DNP is to reveal the fundamental processes behind the buildup behaviour of the macroscopic nuclear magnetization,[26–28] and to transport the enhanced nuclear polarization to systems of physical/chemical/biological interest. Figure 17A schematically shows an experimental system developed to perform triplet DNP in a relatively low field, and to carry out NMR measurements in a high field.[25] The magnet providing the lower field is a field-variable electromagnet, and the field value is adjusted according to the resonance

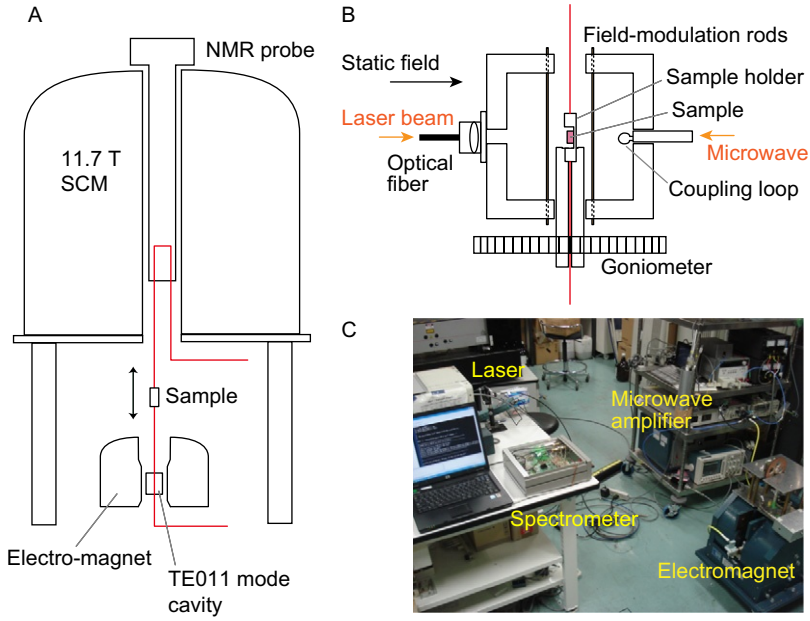

Figure 17 (A) A diagram describing the experimental setup for a magnetic-field cycling system with DNP using electron spins in the photo-excited triplet state.[25] In this design, nuclear hyperpolarization is performed in an electromagnet providing variable magnetic fields up to ~0.5 T. The electromagnet is placed below a vertical superconducting magnet, and a stepping motor enables sample shuttling between the magnets. The system is capable of applying laser irradiation, microwave irradiation, and magnetic-field modulation in the electromagnet, while ^{1}H–^{13}C–^{2}H triple resonance NMR experiments can be performed in the superconducting magnet. (B) A schematic view of a home-built X-band microwave cavity placed inside the electromagnet. (C) A snapshot of the experimental setup for the field-cycling triplet-DNP system, showing a flashlamp-pumped dye laser, a travelling-wave-tube X-band microwave amplifier, and the electromagnet together with the OPENCORE NMR spectrometer.

frequency of the microwave cavity that is used for resonant microwave irradiation to the electron spins in the photo-excited triplet state. The structure of the cavity is depicted in Figure 17B. For photo-excitation, a laser beam can be irradiated at the sample inside the cavity. The orientation of a single crystal sample with respect to the static field can be adjusted using a uniaxial goniometer, in order to optimize the orientation-dependent electron spin polarization in the triplet state. After polarizing the nuclear spins, the sample can be shuttled into the high-field superconducting magnet, where NMR experiments are performed.

In this experimental system, it was necessary to trigger the laser pulse, the microwave pulse, and field modulation at the right timing, then to

trigger the stepping motor for shuttling the sample between the high and low fields. In this setup, the OPENCORE NMR has been used to serve for this function, in addition to the NMR experiments in the high field. Figure 17C shows a scene of the triplet DNP experiment, and a few examples of the triplet-DNP experiments are demonstrated in Figure 18. A single crystal sample of pentacene-doped naphthalene was grown by the Bridgmann method, and triplet-DNP experiments were carried out by photo-exciting the guest pentacene molecule using a flashlamp-pumped dye laser with a wavelength of 590 nm and a pulse width of 1 μs. By utilizing an efficient polarization transfer technique proposed by Henstra et al.,[23] the ^{1}H polarization of the host naphthalene molecules was built up. Figure 18A shows a ^{1}H magic-sandwich echo spectrum obtained in 11.7 T after building up the ^{1}H polarization in 0.2958 T. For comparison, the ^{1}H spectrum measured with the same experimental condition except that the DNP was not performed is also shown in the figure.

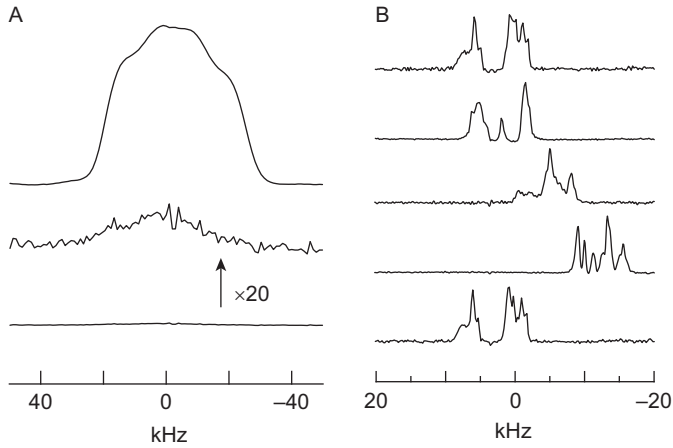

Figure 18 (A) (top) A single-scan ^{1}H NMR spectrum in a single crystal sample of pentacene-doped naphthalene measured in 11.7 T. The ^{1}H polarization was built up by performing triplet-DNP in the electromagnet (0.2958 T) described in Figure 17A, and then by shuttling the sample into the superconducting magnet. The magic-sandwich echo sequence was used to obtain the spectrum. The sample size was 1.2 × 1.4 × 1.6 mm, and its temperature was kept at 203 K. (bottom) A ^{1}H NMR spectrum of the same crystal measured in thermal equilibrium in 11.7 T. Its magnified view is shown in the middle. (B) Single-scan, natural abundance ^{13}C spectra of the same single crystal sample of pentacene-doped naphthalene measured for various crystal orientations. After polarizing the ^{1}H spins by triplet DNP, the sample was shuttled into the high field, where the crystal orientation was adjusted using a goniometer. Then, ^{1}H–^{13}C CP was performed to transport the enhanced ^{1}H polarization to the ^{13}C spins. The ^{13}C NMR signal was measured under ^{1}H decoupling.

A number of attempts to transfer the spin polarization directly from the triplet electrons to the ^{13}C spins that are present in the sample have been unsuccessful. Nevertheless, it is possible to polarize the ^{13}C spins indirectly, by polarizing the ^{1}H spins first, and then transporting the enhanced ^{1}H polarization to the ^{13}C spins by the conventional cross-polarization technique. Figure 18B shows the enhanced ^{13}C spectra obtained in this way using the same crystal of pentacene-doped naphthalene.

The fact that dynamic ^{13}C polarization is only possible through the indirect way via the ^{1}H spins suggests the mechanism of polarization transfer. Since the polarization transfer between the electrons and nuclei are driven by the dipolar interactions between them, and the fraction of the guest triplet molecules was small, it would be natural to assume that the polarization of the electron spins in the photo-excited triplet state is given to those ^{1}H spins which happen to be close to the electron spins, and then the ^{1}H polarization would be transported away over the whole volume of the sample by spin diffusion among the ^{1}H spins.

Even though this model appears to be rather logical, experimental evidence supporting it have not been reported until very recently, when Negoro et al. carried out the following experiments using the OPENCORE NMR spectrometer-based triplet-DNP system.[27] They have grown a crystal of heavily-deuterated naphthalene doped with undeuterated pentacene, and tried to polarize the residual ^{1}H spins in the deuterated sample. Figure 19A shows a ^{1}H magic-sandwich echo spectrum obtained 100 μs after applying a single-shot triplet-DNP operation. That is, the NMR signal was acquired without repeating the operation of laser pulsing followed by microwave irradiation. The multiplet structure of the ^{1}H magic-echo spectrum indicates the presence of ^{1}H homonuclear dipolar interactions, and the signal was assigned to be the polarized ^{1}H spins in the undeuterated, guest pentacene molecules.

As increasing the time interval between the single-shot DNP operation and the ^{1}H NMR measurement, the intensity of the magic echo was found to decrease. Instead, the intensity of the ^{1}H Hahn echo grew up, as demonstrated in Figure 19B–D). The fact that the inhomogeneous character in the ^{1}H spectra increased with time shows that the spin polarization had been transferred to the place where the ^{1}H spins were dilute, that is surrounded by the ^{2}H spins in the heavily deuterated host material.

For the dilute ^{1}H spins surrounded by a large number of the ^{2}H spins, the heteronuclear ^{1}H–^{2}H dipolar interaction is dominant, lifting the spectral overlap between the ^{1}H packets. ^{1}H spin diffusion is driven by the flip-flop term of the ^{1}H–^{1}H dipolar interaction, which becomes secular in the presence of spectral overlap. Thus, ^{1}H spin diffusion would be accelerated if it had not been for the ^{1}H–^{2}H dipolar interaction. In order to confirm this prediction, they used another RF channel of the OPENCORE

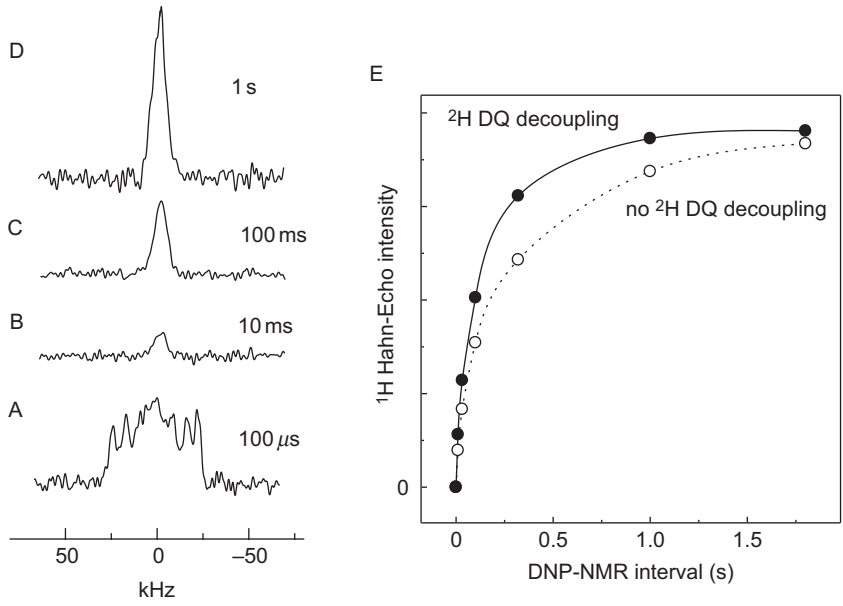

Figure 19 (A) A ^{1}H magic-sandwich echo spectrum of a single crystal sample of 98.3%-deuterated *p*-terphenly doped with undeuterated pentacene with a concentration of 0.05 mol%. The spectrum was measured 100 μs after a single-shot triplet-DNP sequence. (B–D) ^{1}H Hahn echo spectra of the same sample after 10 ms, 100 ms, and 1 s of the single-shot triplet DNP. (e) Hahn echo intensity dependence on the time interval between the single-shot triplet-DNP and NMR measurement with (filled circles) and without (open circles) ^{2}H DQ decoupling.

spectrometer to apply ^{2}H double-quantum (DQ) decoupling[29,30] during the interval of the single-shot triplet-DNP and NMR measurement. Figure 19E shows the time-interval dependence of the ^{1}H Hahn echo intensity with and without ^{2}H DQ decoupling. The faster buildup of the Hahn echo in the former case supports the proposed model.

3.4. The role of nuclear magnetization in a levitating body by the magneto-Archimedes effect

In this section, we describe an attempt to study the role of nuclear magnetization in a levitating body by the magneto-Archimedes effect, and how the OPENCORE NMR spectrometer was utilized for this purpose.

A diamagnetic body such as a droplet of water has, by its very definition, negative magnetic susceptibility. In the presence of a magnetic field, a force acts on the body when the scale of the magnetic-field

inhomogeneity is larger than the size of the body. This effect of the diamagnetic force is to push the body out of the magnet. In the upper region of the bore of a vertical superconducting magnet, the diamagnetic force is against the gravitational force. The forces balance when the magnetic field times the magnetic-field gradient equals to $\sim 1400\ \mathrm{T^2\ m^{-1}}$. Then the water droplet is known to stay floating in the air,[32] forming a spherical shape like that in a zero gravity spacecraft. Diamagnetic levitation of a frog[33] and an apple[34] have also been demonstrated.

Unfortunately, the condition $1400\ \mathrm{T^2\ m^{-1}}$ is so demanding that only a few institutes in the world having very strong magnets can demonstrate diamagnetic levitation. Nevertheless, levitation is also possible in more popularly used, less-strong magnets by introducing a paramagnetic medium like oxygen gas,[35] which has a tendency of, in contrast to the diamagnetic material, being attracted toward inside the magnet. As the oxygen molecules are dragged into the magnet, the density gradient of the oxygen gas becomes so strong that the buoyant force is significantly enhanced according to the Archimedes' principle, which states that the buoyancy is given by the weight of the medium pushed away by the body. In this case, when the condition

$$[(\chi_\mathrm{w} - \chi_\mathrm{a})/\mu_0]B(z_0)\frac{\mathrm{d}B(z_0)}{\mathrm{d}z} = (\rho_\mathrm{w} - \rho_\mathrm{a})g \sim \rho_\mathrm{w} g \tag{1}$$

is satisfied, the body, for example a water droplet, stays floating in the air at the position z_0 that fulfills Equation (1). Here, χ_w and χ_a are the susceptibilities of water and oxygen gas, and ρ_w and ρ_a are their densities. $\mu_0 = 4\pi \times 10^{-7}\ \mathrm{H\ m^{-1}}$ and $g \sim 9.8\ \mathrm{m\ s^{-2}}$ are the permeability of vacuum and the acceleration of gravity. The static magnetic field B is assumed to be axially symmetric about the z-axis. For example, $\chi_\mathrm{w} \sim -9.0 \times 10^{-6}$ and $\chi_\mathrm{a} \sim 1.8 \times 10^{-6}$ at room temperature and atmospheric pressure. Then, according to Equation (1), the levitation condition is obtained as $B(\mathrm{d}B/\mathrm{d}z) \sim 1140\ \mathrm{T^2\ m^{-1}}$. The requirement on the magnetic field becomes less demanding as increasing the pressure of the oxygen gas. At 10 atm, χ_a is 10 times that at 1 atm, so that the levitation condition reduces to $B(\mathrm{d}B/\mathrm{d}z) \sim 455\ \mathrm{T^2\ m^{-1}}$. Magnetic enhancement of the buoyant force in the paramagnetic media is known as the magneto-Archimedes effect.[35]

The issue we address is the *previously unconsidered* contribution of the nuclear magnetization in the levitating bodies.[36, 37] To be specific, let us consider the proton magnetization in water levitating by the magneto-Archimedes effect. Assuming that the proton spin system is in thermal equilibrium at room temperature, its susceptibility χ_p is given by

$$\chi_\mathrm{p} = \frac{\mu_0 \rho \gamma^2 \hbar^2 I(I+1)}{3kT} = \sim 4 \times 10^{-9}, \tag{2}$$

where $\rho \sim 6.7 \times 10^{28}$ m^{-3} is the density of the protons in water, $\gamma \sim 2\pi \cdot 4.26 \times 10^{7}$ rad s^{-1} T^{-1} is the gyromagnetic ratio, and $I = 1/2$. Taking account of the nuclear paramagnetism, we propose to correct Equation (1) as

$$\left[\left(\chi_w - \chi_a + \chi_p\right)/\mu_0\right] B(z_0) \frac{dB(z_0)}{dz} \sim \rho_w g. \tag{3}$$

That is, in the floating body, there should be a balance of forces due to the nuclear paramagnetic force as well as the gravity, the diamagnetic force, and the buoyancy (Figure 20A).

In order to verify whether the nuclear paramagnetism does really have a discernible effect on the balance of forces, we carried out an experiment exploiting the unique feature of the nuclear magnetism; the nuclear magnetization can be *manipulated* by the established NMR technology. The idea is to invert the ^{1}H magnetization of the levitating object. Then, in order to take the balance, the body should shift its position, as depicted in Figure 20B.

Figure 21A is a snapshot of the probe developed for this purpose. Inside a sealed container, a saddle coil was placed. The coil was connected to a tuning circuit placed outside the container through a sealed port. Impedance matching at frequencies ranging from 400 to 500 MHz was possible. Using a CCD camera, the sample can be monitored through a transparent window on one side of the wall. This probe was inserted from the top of a wide-bore 14 T superconducting magnet (JASTEC), and placed ~270 mm above the field centre, where the diamagnetic force and the buoyant force was the maximum. At this position, the ^{1}H resonance frequency was expected to spread due to the strong field gradient over several MHz around ~450 MHz. Figure 21B shows how the spectrometer is used to examine the nuclear paramagnetic force in the levitating body.

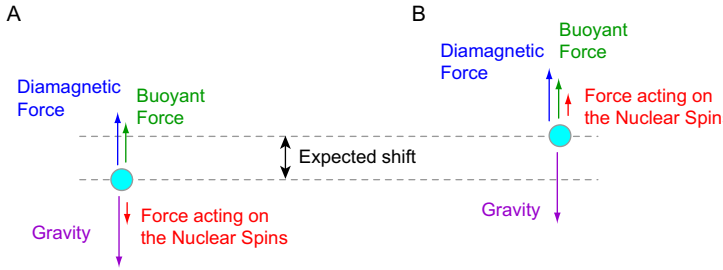

Figure 20 (A) Forces acting on a body levitating by the magneto-Archimedes effect. The gravitational pull toward the earth is balanced by the diamagnetic force and the buoyant force. In addition, the nuclear paramagnetic force ought to act on the body. (B) Upon inversion of the nuclear magnetization, the body should move to take the balance of the forces.

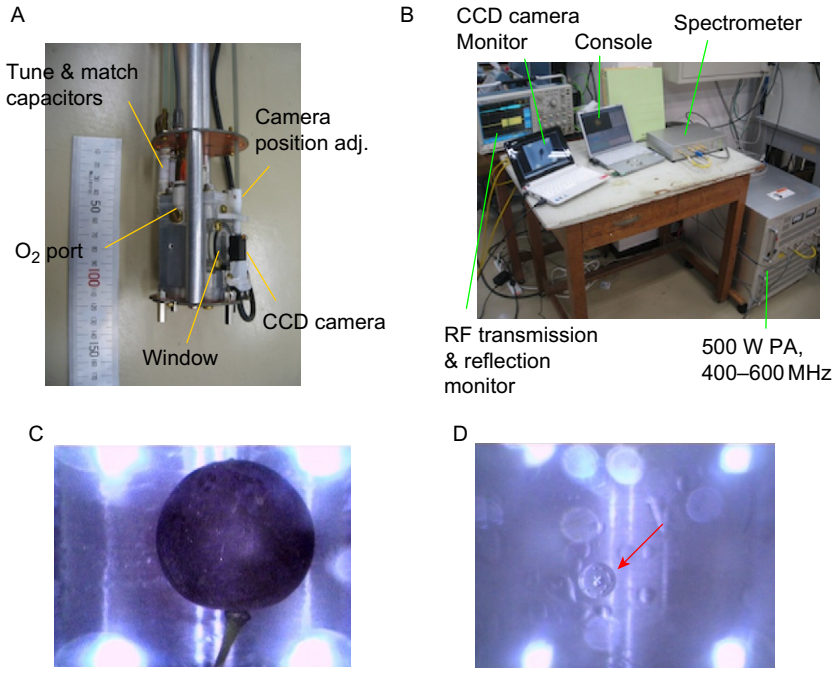

Figure 21 (A) A probe developed to examine the role of nuclear magnetization in the levitating body by the magneto-Archimedes effect. In a sealed aluminium container, oxygen gas can be filled with pressures of up to 1 MPa. A saddle coil is embedded inside the container, so that RF irradiation can be applied to the sample. The coil can be impedance matched at frequencies ranging from 400 to 500 MHz. An acrylic window is made on one side of the container, so that a CCD camera can monitor what happens inside the container. (B) An experimental setup composed of the OPENCORE spectrometer, a power amplifier, an oscilloscope, and a CCD camera monitor. (C) A piece of Delaware grape levitating inside a 14-T superconducting magnet. The container was filled with oxygen gas with a pressure of 0.72 MPa. (D) A levitating water drop (red arrow). The bright spots in (C) and (D) are due to the illumination lights reflected on the acrylic window.

Upon inversion, the point z'_0 of the balanced forces would be such that

$$\left[\left(\chi_w - \chi_a - \chi_p\right)/\mu_0\right] B(z'_0)\frac{dB(z'_0)}{dz} \sim \rho_w g. \tag{4}$$

Thus, the effect of the spin inversion would be to shift the balanced point by $\delta z = z'_0 - z_0$. In order to estimate the shift δz, we note that the field times the field gradient $B(dB/dz)$ should shift by

$$B(z'_0)\frac{dB(z'_0)}{dz} - B(z_0)\frac{dB(z_0)}{dz} \sim \mu_0 \rho_w g \frac{2\chi_p}{(\chi_w - \chi_a)^2}, \tag{5}$$

which is, when the oxygen pressure is 10 atm, $\sim 0.14\ T^2\ m^{-1}$. The shift δz one would expect depends on the field profile of the magnet in use. For the superconducting magnet that we used, δz is estimated to be on the order of 10 μm, which is rather small but still discernible. Moreover, the kinetic motion of the body could be enhanced by mechanical resonance by applying successive spin inversions in synchronous with the characteristic oscillation of the levitating body around the balanced point.

Examination of what happens when the ^1H spins in the levitating objects are inverted is in progress. This work potentially provides another one of few examples in which the nuclear magnetization causes a macroscopic kinetic effect.[38]

3.5. Active compensation of RF pulse transients

Here we describe the idea of active compensation of RF pulse transients.[39,40] Even though the idea itself is simple, its practical aspect is somewhat complicated and tedious. In the following, we show how the home-built spectrometer and software can be flexibly adopted toward its implementation.

In NMR experiments, probe tuning is important, because otherwise the irradiation efficiency and the sensitivity would be very poor. The price to pay is that the shape of the pulse that the nuclear spins feel deviates from what we expect, in particular, at the leading and the trailing edges of the pulse. The deviation becomes significant as increasing the Q factor of the probe and as decreasing the frequency. This problem is well known as the transient effect, and has been studied extensively, in the context of reducing the receiver dead time that sets the limit on how soon data sampling can be started after the pulse. The transient effect has also been of interest in multiple-pulse experiments. For example, in FSLG or PMLG, it is known that the sequence works better by slightly de-tuning the probe, and explanation was given in terms of the transient effect.[41]

In order to suppress the transient effect, a phase-inverted pulse following the main pulse has been employed.[42] Q-switching of the circuit at the edges can also be a solution.[43–47] Recently, it was shown that RF pulses can be applied in a more controlled way by utilizing the idea of active compensation.[39,40] Figure 22A shows a quadrature representation of the response to a rectangular RF pulse measured using a pickup coil, which was placed inside the probe. While the transmitter of the OPENCORE spectrometer irradiated an RF pulse, the receiver monitored the RF field produced by the sample coil through the pickup coil. At the leading edge and the trailing edge of the pulse, the transient effect was observed in both the amplitude and phase of the pulse. By the procedure described below,

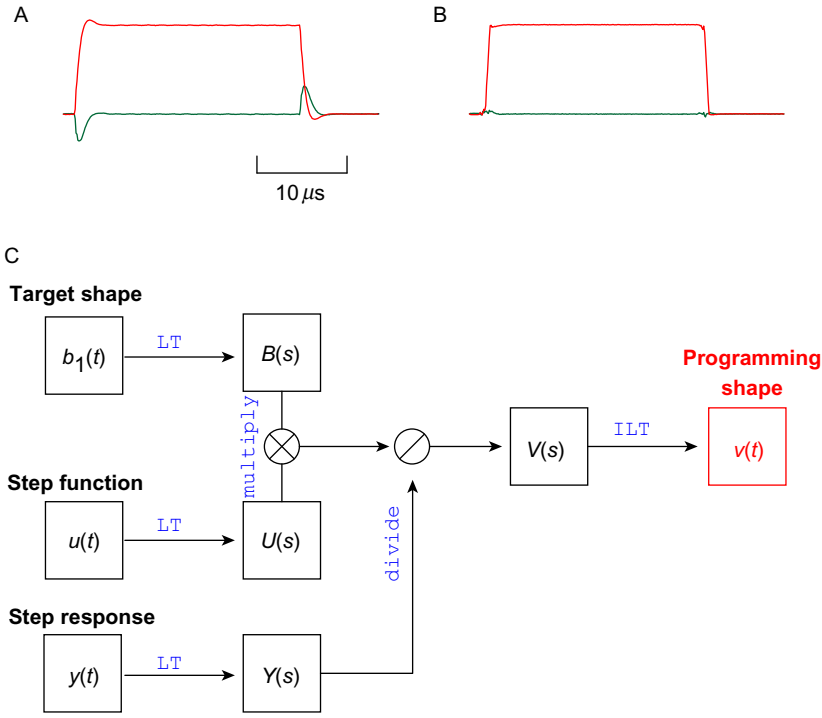

Figure 22 (A) The in-phase (red line) and quadrature (green line) components of the response of a tuned probe to a rectangular RF pulse. The X channel of a Varian 3.2 mm T3 probe was tuned at 100.645 MHz. The Q factor of the circuit was ~100. The RF field created at the sample coil was monitored using a pickup coil placed near the coil. The pickup coil was connected to the receiver input of the OPENCORE NMR spectrometer, and the signal was digitally demodulated into the in-phase and quadrature components. (B) The response of the same circuit to an actively compensated pulse, which was designed to result in linear leading and trailing edges with a width of 500 ns. (C) A flow chart describing the procedure to calculate the shape of the programming RF pulse ($v(t)$) that results in the intended RF pulse shape ($b_1(t)$). In advance of the calculation, it is necessary to measure the response $y(t)$ of the probe circuit to a step excitation. LT and ILT stand for Laplace transformation and inverse Laplace transformation, respectively.

the actively compensated pulse can be designed on the software of the spectrometer, so that the response results in the signal shown in Figure 22B.

Active compensation relies on the fact that, to a good approximation, the causal relation between the programmed pulse shape and the resultant pulse shape is linear. Then, it is possible to calculate the pulse shape

that we should program, *back from* the target pulse shape that we want to apply to the spin system. Here we briefly overview its procedure proposed by Tabuchi et al.[40]

For a linear system like a probe circuit, the response $b_1(t)$ (RF *field* created by the coil) to the excitation $v(t)$ (RF *voltage* produced by the spectrometer) is expressed by a convolution relation

$$b_1(t) = \int \mathrm{d}t' h(t - t') v(t) = h * v. \tag{6}$$

Here, $h(t)$ characterize the behaviour of the system, and is called the response function, or the impulse response, because it is identical to the response to a unit impulse excitation.

Now, the goal here is to solve Equation (6), so that we can calculate the programming pulse shape $v(t)$ from the target pulse shape $b_1(t)$. For this purpose, we perform Laplace transformation:

$$\begin{aligned} B(s) &= \int \mathrm{d}t \mathrm{e}^{st} b_1(t), \\ H(s) &= \int \mathrm{d}t \mathrm{e}^{st} h(t), \\ V(s) &= \int \mathrm{d}t \mathrm{e}^{et} u(t), \end{aligned} \tag{7}$$

Then, the convolution turns into a product

$$B(s) = H(s)V(s). \tag{8}$$

In this way we obtain $V(s) = B(s)/H(s)$, and its inverse Laplace transformation gives the solution $v(t)$.

For the design of the actively compensated RF pulse, experimental and numerical determination of the response function $h(t)$ of the circuit is necessary. We should also keep in mind that modification to the circuit, such as probe tuning, insertion or removal of RF filters, and so on, can alter $h(t)$. In practice, it is convenient to measure the response $y(t)$ to a step excitation $u(t)$ instead of that to the impulse excitation. By performing Laplace transformation to

$$y(t) = \int \mathrm{d}t' h(t - t') u(t) = h * u, \tag{9}$$

we obtain

$$Y(s) = H(s)U(s). \tag{10}$$

Using Equations (8) and (10),

$$V(s) = \frac{B(s)U(s)}{Y(s)}. \tag{11}$$

Figure 22C summarizes the procedure for calculating the programming pulse shape $v(t)$ from the target pulse shape $b_1(t)$ and the step response $u(t)$. In addition to the measurement of $y(t)$, we need to perform a number of data operations such as multiplication, division, Laplace and inverse Laplace transformations. All of these functions can be performed on the software.

Figure 23 shows screenshots of the data processing at various stages performed in order to design the actively compensated pulse that results in the RF field profile displayed in Figure 23A. Here, the leading and trailing edges have a cosine shape[40] with a transition time of 1.25 μs. This interval was divided into 50 steps, so that each step has a width of 25 ns,

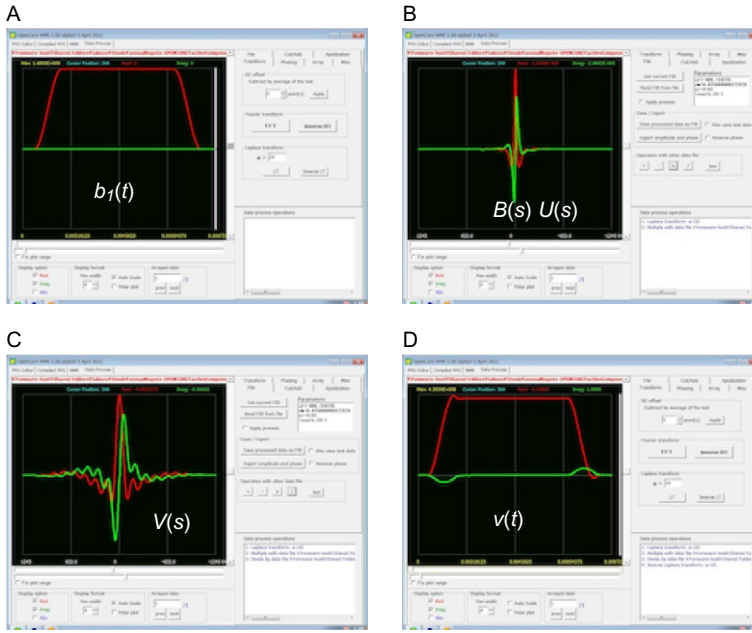

Figure 23 Calculation of the shape of the actively compensated pulse can be carried out on the software. (A) shows the real (red line) and the imaginary (green line) component of an example of the target pulse shape $b_1(t)$. Its leading and the trailing edges have a cosine shape with a transition time of 1.25 μs in 50 steps, and the width of the plateau is 5 μs. (B) Laplace transformation $B(s)$ multiplied by the Laplace transformed step function $U(s)$. (C) It was then divided by the Laplace transformation $Y(s)$ of the measured step response $y(t)$ of the proton channel of a 3.2-mm Varian T3 probe tuned at 400.244 MHz to obtain $V(s)$. (D) Finally, inverse Laplace transformation was performed on $V(s)$ to obtain the compensated pulse that results in the RF pulse with the target shape. Time resolution was 25 ns, and $a = 20$ was used for the Laplace and inverse Laplace transformations.

corresponding to the minimum data sampling interval and minimum width of the RF pulse supported by the current design of the OPENCORE spectrometer. The target function $b_1(t)$ is in general a complex function, with its real and imaginary parts shown in the figure. In the present example of the cosine pulse, the imaginary part of the target was zero.

Next, $b_1(t)$ was Laplace transformed into $B(s)$, and then multiplied by the Laplace transformation $U(s)$ of the step function $u(t)$. The result $B(s)U(s)$ is displayed in Figure 23B. In this example, the step response $y(t)$ was measured for the ^{1}H channel of a Varian 3.2 mm T3 probe tuned at 400.244 MHz with a time resolution of 25 ns, and Laplace transformed into $Y(s)$. By dividing $B(s)U(s)$ by $Y(s)$, the function plotted in Figure 23C was obtained, from which, by performing inverse Laplace transformation, the programming pulse shape $v(t)$ was finally obtained, as shown in Figure 23D. The amplitude and the phase of the complex function $v(t)$ give the intensity and the phase of the transient-compensated shaped pulse.

4. SUMMARY

In this work, an open-resource, integrated, FPGA-based NMR spectrometer, named the OPENCORE NMR spectrometer, was described together with its applications to the various scenes. Currently, the transmitter is capable of modulating amplitude, phase, and frequency of the RF pulses at up to 600 MHz. The minimum width and increment of the pulse are 25 and 6.25 ns, respectively. The spectrometer has three independent RF transmitters, which can operate in either synchronous or asynchronous ways. In the signal acquisition part, the receiver is equipped with a 14-bit ADC operating at the sampling frequency of 80 MHz, thus providing the maximum spectral bandwidth of 40 MHz given by half the sampling frequency. Since the spectrometer has the trigger output and input ports, more than two spectrometers can be synchronized with each other to realize more than four transmitter channels and/or dual receiver signal acquisition.

The unique design concept of the spectrometer is to let a single FPGA chip undertake all the digital jobs required for the NMR spectrometer. Modification to the digital functions of the spectrometers can be made merely by updating the hardware description codes. The system can thus be updated without replacing the electric parts or physical wire connections. Recent progress in the FPGA devices is remarkable, and in the near future, significant improvement can be expected in terms of the memory size, operation speed, and elaborate digital signal processing.

In the architecture of the current spectrometer, one of the two DDS modules in an RF channel is operating at 160 MHz, which is twice the

ADC sampling rate, and is producing the fundamental wave at a quarter (20 MHz) of the ADC sampling rate. In this very configuration can one extend the intermediate frequency in the simple way that was described above, by utilizing the DDS-image frequency and the super-Nyquist sampling scheme.

The spectrometer supports phase cycling, asynchronous sequence implementation, and parameter-array experiments. Thus, most standard solid-state NMR experiments are feasible, including CPMAS, multiple-pulse ^{1}H decoupling such as TPPM, 2D experiments, multiple-quantum NMR, and so on. In addition, the focus of development is on its extension of, or modification to, the hardware and/or the software, in the spirit of enabling the users to put their own new ideas into practice. In this paper, several examples of such have been described. They include the compact NMR and MRI systems, active compensation of RF pulse transients, implementation of a network analyzer, dynamic receiver-gain increment,[31] and so on.

The OPENCORE NMR project is not going to follow up what the modern commercial systems offer. Since the developer has been trying to keep the system at the root of evolution of the NMR spectrometer, efforts have been paid to keep the system simple, or even to make the system simpler. In this sense, it would be fair to mention that the commercial spectrometers would be much more convenient for many practical circumstances. Nevertheless, the author believes that there is room for making contributions in scientific researches through the OPENCORE NMR project, which is looking at the different direction of development from that of the other spectrometers.

ACKNOWLEDGEMENT

This work has its origin in my student days, when I used to use a home-built NMR spectrometer developed by my supervisors, Takehiko Terao and K. Takegoshi. It was old, but had worked well. I used the spectrometer for solid-state NMR experiments, including dipolar recoupling experiments under magic angle spinning, and DNP using the high polarization of the electron spins in the photo-excited triplet state. Quite often it went out of order, and I had to open the chassis of the spectrometer and repair the hardware. This experience helped me to understand what happens inside the spectrometer, and eventually, to decide to develop another spectrometer using the latest available technologies.

My colleagues who are brave enough to try on using the spectrometer reported a number of problems. Without their helpful cooperation, the project would have ended up with much fewer attractive outcomes. In particular, a number of sensitivity-demanding experiments have given me opportunities to improve the system. They include ^{195}Pt NMR of Pt nanoparticles done with Tetsu Yonezawa and Hirokazu Kobayashi, microcoil MAS experiments by Munehiro Inukai. In these works, the intensities of the NMR signals were quite weak, and careful tune up of the system was required. If the spectrometer were used only for the demonstrative purpose without application to such demanding chemical analyses, its performance would have remained much less. In the cryo-coil MAS experiments, on the other

hand, the sensitivity was dramatically enhanced as the sample coil and preamplifier were cooled to cryogenic temperatures. In order to evaluate the signal to noise ratio attained with such a sophisticated detection system, the unexpected noise arising in the spectrometer was distracting. Takashi Mizuno, the principal developer of the cryo-coil MAS probe, contributed a lot to suppress the spurious noise in the system and thus enabled Yasuto Noda to obtain a high quality ^{6}Li 2D spectrum using a combination of the cryo-coil MAS probe and the OPENCORE NMR spectrometer.

A number of researchers, Takayuki Suzuki, Matthias Ernst, Marcin Krajewski, Michael Batel, Makoto Negoro, Akinori Kagawa, Weng Kung Peng, Masahiro Kitagawa, Takashi Nakamura, Takahiro Iijima, Daiki Tamada, Shinya Handa, Tomoyuki Haishi, Katsumi Kose, Li Xiaonan, Zhang Xiao Ling, Naoki Ichijo, Yusuke Nishiyama, Ryo Yamada, Shinya Otsuka, and Daiki Shimizu, have been positive and serious about using the spectrometer, albeit realizing that the system has been in the stage of development, and still has many potential problems. The project owes a lot to them, as the spirit of development is not the development itself but to use it to push the NMR spectroscopy and science forward in various scenes.

The ^{13}C labelled amyloid beta sample was synthesized and provided by Yuichi Masuda.

The development of the OPENCORE NMR spectrometer has been supported by the CREST program, SENTAN program of Japan Science and Technology Agency, and Grant-in-Aid for Young Scientists (A) by the Ministry of Education, Culture, Sports, Science and Technology (MEXT).

REFERENCES

1. K. Takeda, *Rev. Sci. Instrum.*, 2007, **78,** 033103.
2. K. Takeda, *J. Magn. Reson.*, 2008, **192,** 218.
3. http://kuchem.kyoto-u.ac.jp/bun/indiv/takezo/opencorenmr/index.html.
4. M. H. Levitt, *J. Magn. Reson.*, 1997, **126,** 164.
5. M. H. Levitt and O. G. Johannessen, *J. Magn. Reson.*, 2000, **142,** 190.
6. A. E. Bennett, C. M. Rienstra, M. Auger, K. V. Lakshmi and R. G. Griffin, *J. Chem. Phys.*, 1995, **103,** 6951.
7. Z. Gan and R. R. Ernst, *Solid State Nucl. Magn. Reson.*, 1997, **8,** 153.
8. AD9858 datasheet, Analog Devices..
9. A technical tutorial on digital signal synthesis, Analog Devices, 1999.
10. K. Takeda, 49th ENC, PAcific Grove, CA, USA, 2008.
11. H. Janssen, A. Brinkmann, E. R. H. van Eck, P. J. M. van Bentum and A. P. M. Kentgens, *J. Am. Chem. Soc.*, 2006, **128,** 8722.
12. K. Yamauchi and T. Asakura, *Chem. Lett.*, 2006, **35,** 426.
13. M. Inukai and K. Takeda, *Concepts Magn. Reson.*, 2008, **33B,** 115.
14. A. P. M. Kentgens, J. Bart, P. J. M. van Bentum, A. Brinkmann, E. R. H. van Eck, J. G. E. Gardeniers, J. W. G. Janssen, P. Knijn, S. Vasa and M. H. W. Verkuijlen, *J. Chem. Phys.*, 2008, **128,** 052202.
15. A. Brinkmann, S. K. Vasa, H. Janssen and A. P. M. Kentgens, *Chem. Phys. Lett.*, 2010, **485,** 275.
16. D. Sakellariou, G. le Goff and J.-F. Jacquinot, *Nature*, 2007, **447,** 694.
17. M. Inukai and K. Takeda, *J. Magn. Reson.*, 2010, **202,** 274.
18. T. Mizuno, K. Hioka, K. Fujioka and K. Takegoshi, *Rev. Sci. Instrum.*, 2008, **79,** 044706.
19. T. Nakamura, Y. Itoh, M. Yoshikawa, T. Oka and J. Uzawa, *Concepts Magn. Reson. B Magn. Reson. Eng.*, 2007, **31,** 65.
20. S. Nariki, N. Sakai, I. Hirabayashi, M. Yoshikawa, Y. Itoh, T. Nakamura and H. Utumi, *Physica C*, 2008, **468,** 1451.

21. N. Sakai, S. Nariki, E. Teshima, M. Morita, I. Hirabayashi, T. Nakamura, Y. Itoh, M. Yoshikawa and H. Utsumi, *TEION KOGAKU*, 2011, **48,** 131.
22. T. Nakamura, Y. Itoh, M. Yoshikawa, N. Sakai, S. Nariki, I. Hirabayashi and H. Utsumi, *TEION KOGAKU*, 2011, **48,** 139.
23. A. Henstra, T.-S. Lin, J. Schmidt and W. Th. Wenckebach, *Chem. Phys. Lett.*, 1990, **165,** 6.
24. M. Iinuma, Y. Takahashi, I. Shaké, M. Oda, A. Masaike and T. Yabuzaki, *Phys. Rev. Lett*., 2000, **84,** 171–174.
25. A. Kagawa, M. Negoro, K. Takeda and M. Kitagawa, *Rev. Sci. Instrum.*, 2009, **80,** 044705.
26. A. Kagawa, Y. Murokawa, K. Takeda and M. Kitagawa, *J. Magn. Reson.*, 2009, **197,** 9.
27. M. Negoro, K. Nakayama, K. Tateishi, A. Kagawa, K. Takeda and M. Kitagawa, *J. Chem. Phys.*, 2010, **133,** 154504.
28. K. Takeda, Triplet State Dynamic Nuclear Polarization. VDM Verlag, 2009.
29. A. Pines, D. J. Ruben, S. Vega and M. Mehring, *Phys. Rev. Lett.*, 1976, **36,** 110.
30. A. Pines, S. Vega and M. Mehring, *Phys. Rev. Lett*., 1978, **B18,** 112.
31. K. Takeda and K. Takegoshi, *J. Magn. Reson.*, 2011, **208,** 305.
32. M. Tagami, M. Hamai, I. Mori, K. Watanabe and M. Motokawa, *J. Cryst. Growth*, 1999, **203,** 594.
33. M. V. Berry and A. K. Geim, *Eur. J. Phys.*, 1997, **18,** 307.
34. I. Mogi, K. Takahashi, S. Awaji, K. Watanabe and M. Motokawa, *J. Phys. Conf. Ser.*, 2006, **51,** 431.
35. Y. Ikezoe, N. Hirota, J. Nakagawa and K. Kitazawa, *Nature*, 1998, **393,** 749.
36. K. Takeda, 50th ENC, Pacific Grove, CA, USA, 2009.
37. K. Takeda, ISMAR Conference, Florence, Italy, , 2010.
38. C. F. Evans, *Philos. Mag.*, 1956, **1,** 370.
39. K. Takeda, Y. Tabuchi, M. Negoro and M. Kitagawa, *J. Magn. Reson.*, 2009, **197,** 242.
40. Y. Tabuchi, M. Negoro, K. Takeda and M. Kitagawa, *J. Magn. Reson.*, 2010, **204,** 327.
41. A. J. Vega, *J. Magn. Reson.*, 2004, **170,** 22.
42. D. I. Hoult, *Rev. Sci. Instrum.*, 1979, **50,** 193.
43. G.-Y. Li, X.-J. Xia and H.-B. Xie, *Rev. Sci. Instrum.*, 1996, **67,** 704.
44. E. R. Andrew and K. Jurga, *J. Magn. Reson.*, 1987, **73,** 268.
45. T. N. Rudakov, V. V. Fedotov, A. V. Belyakov and V. T. Mikhal'tsevich, *Instrum. Exp. Tech.*, 2000, **47,** 87.
46. A. S. Peshkovsky, J. Forguez, L. Cerioni and D. J. Pusiol, *J. Magn. Reson.*, 2005, **177,** 67.
47. V. A. Zabrodin, V. P. Tarasov, B. A. Shumm and L. N. Erofeev, *Instruments and Experimental Techniques*, 2007, **50,** 86.

SUBJECT INDEX

A

Accord adequate and 1,1-ADEQUATE experiments
  2[1-(4-chlorobenzyl)-1*H*-indol-3-yl]-2-oxo-*N*-pyridin-4-yl acetamide
    correlation structure, 235–236
    treatment, oxalyl chloride, 235–236
  cytosporacin, 238–239
  4,5-dibromopyrrol-2-carboxylic acid, 234–235
  5,6-dihydrolamellarin
    molecule, 234
    n,1-and *m*,*n*-ADEQUATE, 232–233
  3,4-dihydroxy-2-quinolin-2-ylpyrido [3,2,1-jk]carbazol-6-ones, 242–243
  3,4-epoxynephthenol acetate, 247
  HMBC/GHMBC, 230–232
  jamaicamide, 236
  leucanthoside-A
    acid hydrolysis, 240–241
    ^{1}H and ^{13}C NMR assignment, 240
  medermycin/lactoquinomycin-A structure
    antibiotic structure, 237–238
    molecule structure, 2D NMR methods, 238
  phakellin and isophakellin, 243–244
  phormidolide, 236–237
  piperidylrifamycins, 239–240
  retrorsine and declosine
    HSQC-1,1-ADEQUATE and HSQC-1, *n*-ADEQUATE, 247
    structure elucidator CASE program, 245–246
    strychnine, 245–246
  rhodoptilometrin, 245
  S-(2-pyrrole)cysteine S-oxide *vs.* S-(3-pyrrole)cysteine S-oxide
    AMX proton spin systems, 247–248
    t_1 increments, 248
  withanolides, 242
ACCORD-HMBC, 219
1,1-ADEQUATE and accord adequate, application
  2[1-(4-chlorobenzyl)-1*H*-indol-3-yl]-2-oxo-*N*-pyridin-4-yl acetamide, 235–236
  cytosporacin, 238–239
  4,5-dibromopyrrol-2-carboxylic acid, 234
  5,6-dihydrolamellarin, 232–234
  3,4-dihydroxy-2-quinolin-2-ylpyrido [3,2,1-jk]carbazol-6-ones, 242–243
  3,4-epoxynephthenol acetate, 247
  HMBC/GHMBC, 230–232
  jamaicamide, 236
  leucanthoside-A, 240–241
  medermycin/lactoquinomycin-A structure, 237–238
  phakellin and isophakellin, 243–244
  phormidolide, 236–237
  piperidylrifamycins, 239–240
  retrorsine and declosine, 245–247
  rhodoptilometrin, 245
  S-(2-pyrrole)cysteine S-oxide *vs.* S-(3-pyrrole)cysteine S-oxide, 247
  withanolides, 242
correlation information
  carbon-carbon connectivity, 225
  ^{13}C chemical shift, 225
  GHSQC, 225
  multiplicity-edited GHSQC, 225–227
  strychnine, 226, 228
data acquisition and processing
  delay optimization, 224
  $^{1}J_{CC}$ homonuclear, 224
  phase cycle, 224
drawbacks, 219–220
$^{1}J_{CH}$ and $^{1}J_{CC}$, 220
pulse sequence, 220, 222
response modulation
  $^{1}J_{CC}$ optimization, 229, 231, 232
  marine natural product, 228
  retrorsine, C15-C17 correlation, 229
sample requirement
  alkaloids, 221–223
  multiplicity-edited HSQC, 221–223

1,1-ADEQUATE (*cont.*)
strychnine, 220–221

B

Bacteriorhodopsin (BR)
amino-acid sequence, 45
^{13}C NMR
assignment, 51
CPMAS and DDMAS methods, 48, 49, 50
2D crystalline preparation, 46–47
α-helix and loops, 48
membrane proteins, 46
random coil peak, 48, 48
site-directed mutagenesis, 46–47
partially disorganized 2D lattice
^{13}C CPMAS NMR spectra, 61, 62
dynamic structures, 61
trimeric structure, 57–59
Trp residues, 57–59
PM, 2D crystal
bacterio-opsin (bO), 55
^{13}C chemical shifts, 51–52, 54
characteristic conformational changes, 55–57
conformation and dynamics, 53–55
CP α-helices, 51–52
^{15}CPMAS NMR spectra, 56
DIPSHIFT experiment, 52–53
interhelical loops, 53
X-ray diffraction method, 52
Biological active schiff bases, NMR
proteorhodopsin/bacteriorhodopsin
^{13}C CP MAS, 158–159
description, 158
^{15}N CP MAS, 159–160
pyridoxal phosphate
A-and B-isozymes, 155
chemical shift and line width, 154
description, 153–154
H152A mutant enzyme, 155
O-acetylserine sulf-hydrylase, 154
role, as intermediate products, 153
rhodopsin
description and β-cyclodextrin role, 155–156
^{1}H and ^{13}C CP MAS, 156–158
^{15}N CP MAS, 158
BIRD experiment
H^r magnetization
double-difference principle, 311
long-range evolution period, 311
low-pass J filter, 311
multiple quantum coherence, 311
$^{1}J_{CH}$ signals suppression, 309–310
properties, 310
timing diagram, 309–310

C

Carbon-13 heteronuclear longitudinal spin relaxation
Bloch equations, 93
chemical shift anisotropy (CSA)
isotropic shielding coefficient, 95–96
molecular re-orientational motion, 96
parameters, 96
quantum mechanical point, 96
screening, static magnetic field, 95
shielding tensor, 95–96
spectral density, 96
correlation function, 92–93
cross-relaxation/cross-correlation
extended Solomon equations, 100–102
simple Solomon equations, 97–100
description and relaxation parameters, 90–91
dipolar interaction
Fourier transform, 94
gyromagnetic constants, 94
magnetic field, 93–94
molecular reorientation, 94
relaxation rate, 94
experimental procedures
HOESY, 111–114
NOE factor measurement, 109–111
principle, proton decoupling, 107–108
relaxation time measurement, 108–109
geometrical determinations
agreement, techniques, 120
AMX spin system, 118
C–H distances, 118
''cryosolvent'', 121–122
hexamethylenetetramine, 121–122
inverse approach, 120–121
''*J*-separated'' mode, 119–120
molecular reorientation, 118–119
molecule uses, HOESY possibilities, 118–119
quantum chemical calculations, 119–120
quantum mechanical calculations, 119–120
α,α,2,6-tetrachlorotoluene, principal axis system, 120–121

NOE, 91–92
significance, CSA, 93
Solomon equations, 91–92
spectral densities
anisotropic tumbling, 104–105
description, 102
isotropic tumbling, 102–103
local motions, 105–107
spectral density, 92–93
stereo and conformational studies
aqueous micellized sodium octanoate, 116–117
build-up curves, 116–117
^{13}C responses, 114, 115
discrimination, E and Z isomers, 114, 115
flexibility, 117–118
inter-molecular dipolar interactions, 117–118
oligosaccharide sequencing and conformational distribution, 115
proton spin system, 117
remote correlations, 117
uridine, preferential conformation, 115
thermal equilibrium, 92–93
Carbon-13 longitudinal relaxation time measurement
experimental data, 109
inversion-recovery, 107, 108
saturation-recovery, 108–109
Charge polarized magic angle spinning nuclear magnetic resonance (CP MAS NMR)
^{13}C, proteorhodopsin/bacteriorhodopsin
chemical shifts analysis, 158
H-C14–C15-H dihedral angles analysis, 158–159
solid state NMR signal intensities (SRI), 159
^{1}H and ^{13}C, rhodopsin
description, 156
DQ-filtered signal, 157
estimation, dipole-dipole couplings, 157
measurement, relaxation time, 157–158
pertubation and photoisomerisation, 157
stabilisation, 156
^{15}N, proteorhodopsin/bacteriorhodopsin
chemical shifts, Schiff bases, 159, 160
dynamic nuclear polarisation (DNP), 159
green variants, 160
K and L intermediate state, 160
^{15}N-^{1}H HETCOR MAS technique, 159
^{15}N, rhodopsin, 158
Chemical shift anisotropy (CSA). *See* Carbon-13 heteronuclear longitudinal spin relaxation, 89–121
Complexes, optically active schiff bases
Co(II, III)
Jocabsen's Schiff base, 167
reaction, 166
signals, paramagnetic, 166
spectra analysis, paramagnetic, 167
titration and *cis* and *trans* isomers, 166–167
description, 160
Fe(II), 165
lanthanide
assignment, signals, 174
^{1}H NMR spectra, 174
NOESY spectra, 173–174
Mn(III), 164
Mo(VI)
description, 163
differences, Mo-N bonding, 164
spectral data, ligands and complexes, 164
Ni(II)
anisotropy, chemical shift, 168–169
derivatives, 169
differences, chemical shift, 168
temperature measurements, 169
Pt
chemical shifts and coupling constants, 170
description, 169
formation, chiral pocket, 169–170
proton signals, 170
series, 170
Re(VII)
chemical shifts, coordinated and uncoordinated MTO signals, 165
description, 164–165
Rh(III) and Ir(III)
diastereoselectivity, 168
epimerisation, 167
integration, signals, 168
Ru(II), 166
Sn(II)
analysis, NMR spectra, 172
chemical shifts, 173

Complexes, optically active schiff bases (*cont.*)
coordination plane, 173
fluorine substituent, 173
pentacoordinated/hexacoordinated tin atom, 173
Ti(IV)
comparison, 161
formation, homo-and bimetallic, 161
interactions, 160–161
perturbation, equilibrium, 162
ratio, 161
U(IV)
20-and 40-membered UO_2 complexes, 174–175
binding constants, 174–175
splitting, *N*-methylene proton signals, 174–175
stereochemistry, 175
T-ROESY data, 175–176
V(V)
domination, *S*-diastereomers, 162–163
signals, DMSO solution, 163
Zn(II) and Cd(II)
derivatives, 172
description, 171
1,4-diazobicyclo-[2,2,2]octane (DABCO), 171
racemic and enantiopure camphoric unit, 171–172
sandwich conformation, 171
Zr(IV), 162
Covariance NMR methods
ADEQUATE data
2D, 271
indirect, 271
UIC and GIC method, 271–272
$C_{indirect}$, 271
COSY, TOCSY, NOESY and ROESY, 269
heteronuclear 2D, 269–271
HSQC-1,1-ADEQUATE
CDK-2 inhibitor dinaciclib, 282
C12 methine resonance, 276–277
cyclin-dependant kinase inhibitor dinaciclib, 279–283
GIC processing, 281
HSQC-1,*n*-ADEQUATE, retrorsine, 283
HSQC-1,*n*-ADEQUATE, strychnine, 283–285
multiplicity-edited GHSQC, 275
posaconazole, 277–279
retrorsine, 283
signal-to-noise measurement, 276
strychnine, 274
UIC/GIC processing, 272–275
CP MAS NMR. *See* Charge polarized magic angle spinning nuclear magnetic resonance, 158–190
Cryogen-free superconducting magnet. *See* OPENCORE NMR applications, 368–390
Customized NMR systems, OPENCORE
analog-to-digital converter (ADC) sampling rate, 390–391
applications
active compensation, RF pulse transients, 386–390
DNP system, 377–382
field-variable, cryogen-free superconducting magnet, 374–377
high-temperature superconducting materials, 377
measurements, conventional, 368–372
and MRI systems, 372–374
nuclear magnetization role, magneto-Archimedes effect, 382–386
characterisation, 391
customized systems, 356
description, 356
design
architecture, 359
FPGA, 357–359
higher intermediate frequency, 363–366
polar plot option, software, 367–368
RF transmitter, 359–362
signal acquisition, 362–363
modification, digital functions, 390
receiver, signal acquisition part, 390
significance, 391
structure, 356, 357

D

DANTE-Z technique, 113–114
DENA element
10-and 9.9-ppm spectra, 339–340
DENA-HSQC (HMBC), 339–340
sensitivity-enhanced HSQC experiment, 339–340
Deuterium isotope effects, chemical shifts ^{13}C NMR
correlation, DC-2(D) values and proton mole fraction, 148–149

dihodium tetracarboxylate adducts, 150–151
2-hydroxynaphthaldehyde and lithium salts, 150
proton transfer equilibrium, 148–149
racemic gossypol, 149
trans-1,2-diaminocyclohexane, 149
unsymmetrical di-Schiff bases, 149
definition, 148
^{15}N NMR
CDCl3 solution and solid state, 151–152
mole fraction, proton, 151
position, proton transfer equilibrium, 152
proton transfer, 151–152
types, 148
Diacylglycerol kinase (DGK)
gel phase lipids, 74–75
liquid crystalline phase, 74–75
Diffusion NMR
applications
DOSY experiment, 199
DPPC and DPPG, 200
gelatine–SDS model system, 198
HA, 199–200
L-tryptophan and ibuprofen, 197–198
molecules, 195–196
PFG, 196–197
protein, 196
two state mobility model, 198–199
theory
DOSY, 195
Fick's second law, 192–195
molecular species, 192
PFG-NMR spectroscopy, 192
Dynamic nuclear polarization (DNP)
system. *See* OPENCORE NMR
applications, 368–390

E

Enantiomeric purity
BINOL derivatives
amino acids and 1,2-aminoalcohols, 130
proton signals splitting, 129–130
myrtenal derivatives
β-aminoalcohols and α-amino acids 1*R* (-)-myrtenal, 127–128
derivatisation procedure, 128
imines and *R:S* ratio, 128–129
primary amines derivatives, 129
three-component derivatives
advantages, 131
chiral diols, 130–131
4-fluoro-2-formylphenylboronic acid use, 131
imino-boronate esters, 131–132
Equilibria, optically active schiff bases
anomeric
D-2-glucosamine, 152
positions, 153
proton transfer
description and OH-tautomer, 144
deuterium isotope effects, 148–152
^{1}H and ^{13}C NMR spectroscopy, 144–146
^{15}N NMR spectroscopy, 146–148
racemisation/epimerisation, imines
amino acids and *R*(-)-myrtenal, 140
atropisomerisation, gossypol, 141
formation, chiral receptor, 141
(S)-2-hydroxy-2¢-(3-phenyl-uryl-benzyl)-1,1¢-binaphthyl-3-carboxaldehyde, 140–141
photoepimerization, gossypol, 141–142
S(+)-2-aminobutane-gossy-polone-imine, 141
stereomutations, non-symmetrical di-schif bases, 142
ring-chain tautomerism
composition, 143–144
C-substituted serinols, 143
ferrocenyl derivative and methylthienyl unit, 142–143
norephedrine derivatives, 142
types, 140

F

Fibrillation and amyloid proteins
nuclear pore proteins
collagen molecules, 34
dehydration-induced structural changes, 35
dipolar couplings, 34
helical chains, 34
molecular process, 34
nuclear pore complexes (NPCs), 35
process
acidic and neutral conditions, 39
agitation and partial dehydration, 42–44
Alzheimer's disease, 42–44
amylin striated ribbons, 44
^{13}C DDMAS, 39, 40
description, 39

Fibrillation and amyloid proteins (*cont.*)
detergent-bound structures, 44
hCT molecules, 39
homogeneous nucleation process, 43
kinetic equation, 39
two-step reaction mechanism, 41, 42
PrP^cs
bovine spongiform encephalopathy, 36–38
Aβ (1–40) protofilaments, 37
chemical shifts and interatomic distances, 35–36
fibrils/plaques, 35–36
helical windings, 36–38
high-resolution magic angle spinning (HRMAS) conditions, 36–38
Parkinson's disease, 36
Field-programmable gate array (FPGA). *See* OPENCORE NMR design, 368–390

G

G-BIRD-HMBC experiment
adiabatic clean
chemical shifts, 317
pulse miscalibration, 317
residual dipolar couplings, 317
strong coupling, 316
timing diagram, 317
leaking intensity
heteronuclear coupling, 314
imperfect pulses and offset effects, 315–316
one-bond constants, 315–316
residual $^1J_{CH}$ signals, 315
residual one-bond couplings, 313–315
stringent test, 315
low-pass J filters, 311–312
nominal flip angles, 313
timing diagram, 312

H

^{1}H and ^{13}C NMR spectroscopy
(R)-1-(9-anthryl)-ethylamine and 2-(2¢-pyridyl/quinolyl)acetophenone, 146
C-7 chemical shifts, 145
2-hydronaphthaldehyde and threonine, 146
^3J(NH,H) coupling constant, 144–146
lithium and tetrabutylammonium salts, 146
trans-1,2-diaminocyclohexane and *ortho*-hydroxyaldehydes, 145
values, ^3J(NH,H), 145
HAT-HMBC experiment
multiplet components, 335
phase difference, 334–335
pulse sequence, 335
two-bond correlations, 334–335
H2BC experiment
experimental verification, 329–332
^{13}C nuclei, 330
cyclosporine, 331
INADEQUATE-type connectivity, 332
pulse sequence, 331
two-and three-bond correlations, 329–330
principles, 329
Hetero and homonuclear dipolar recoupling
dipole–dipole interactions, 202–203
REDOR, 203
techniques, 203–204
Heterogeneous systems
biological functions, 7–8
carbon spin–lattice relaxation time, 7
cross-linked synthetic polymers, 5
3D structure, 7–8
dynamically, membrane proteins
bacteriorhodopsin, 45–62
integral monotopic, 77
membrane enzymes, 74–75
motional fluctuations, 44–45
multidrug transporters, 74
peripheral, 77–79
phospholamban, 75–77
proteorhodopsin, 73–74
sensory rhodopsin, 62–73
transmembrane (TM) moieties, 44–45
dynamic parameters, solution and solid-state NMR
chemical exchange, 15–16
longitudinal/transverse relaxation times, 8–15
time domain, 16–19
flexible and rigid portions, 5
hydrogels network structures and dynamics
fibrillation and amyloid proteins, 34–44
polysaccharide gels, 28–34
synthetic polymer gels, 19–28
liquid-like portions, 5
MAS, 5–6
proton decoupling, 5–6
spin–lattice relaxation times, 5

structurally, 19–44
Heteronuclear multiple bond correlation (HMBC)
analytical laboratories, 295
direct $^{1}J_{CH}$ responses, 307–309
direct $^{1}J_{CH}$ suppression
low-pass J filters, 302–309
one-bond correlations, 301–302
transverse proton magnetization, 301–302
fast experiments
experimental verification, 341
principles and theory, 341
F^{1} resolution improvement
10 and 9.9 ppm experiments, 338–339
constant-time experiments, 335
DENA element, 339–340
10-ppm experiments, 335–338
impact experiments
experimental verification, 343–345
longitudinal proton magnetization, 341–342
principles, 342–343
relaxation delay, 341–342
$^{2}J_{CH}$ and $^{3,4}J_{CH}$suppression
H2BC experiment, 329–332
^{1}H–^{1}H homonuclear couplings, 325
HMBC–RELAY experiment, 326–329
STAR element, 324–326
$^{1}J_{CH}$ suppression
BIRD experiment, 309–311
G-BIRD experiment, 311–316
long-range coupling constants
CBC-HSQMBC experiment, 347
dipole-dipole cross-correlation, 348
extraction procedure, 348
1H-1H couplings, 347
HMQC scheme, 347
IP and AP data, 348
NMR spectroscopy, 348
quantitative measurements, 347
measurements
projection-reconstruction techniques, 345–346
SMAll Recovery Times (SMART) method, 345–346
SOFAST experiments, 345–346
missing $^{1}J_{CH}$ corrections
accordion optimized experiments, 317–318
broadband, 318–321
J-compensated, 321–323
organic molecular structures, 294–295
pulsed field gradients (PFGs), 295
pulse sequence
acquisition and processing parameters, 301
and application, 296
cyclosporine A, 301
dashed circle displays, 300
H^{d} magnetization, 298–299
H^{r} magnetization, 296–298
missing and weak long-range correlations, 299–300
spectra editing
description, 332
experimental verification, 334
HAT-HMBC experiment, 334–335
principles, 332–333
time sharing (TS), ^{1}H-^{13}C and ^{1}H-^{15}N
concept, 348–349
organic and organometallic compounds, 349
Heteronuclear Overhauser effect spectroscopy (HOESY)
advantages, 111–112
amplitude modulation, 112
build-up curves, 111, 112
cross-relaxation rates, 112
DANTE-Z technique, 113–114
description, 111–112
2D mode, 112
^{1}H–^{13}C cross-relaxation rate, 112–113
INEPT sequence, 112–113
inter-molecular dipolar interactions, 111–112
phase cycling, 110, 112–113
proton chemical shift labelling, 113–114
pulse sequences, 111–112
HMBC/GHMBC
ACCORD-HMBC, 219
description, 218
drawback, 218–219
heteronuclear shift correlation, 219
HMBC–RELAY experiment
evaluation, 328–329
principles, 328
pulse sequence, 326–327, 328
HOESY. *See* Heteronuclear Overhauser effect spectroscopy, 110–113
Hyaluronic acid (HA) derivatives, 200

I

Integral monotopic membrane proteins
  membrane-bound enzyme, 77
  microsomal heamoproteins, 77
  ^{15}N–H dipolar coupling, 77
  NMR measurements, 77

J

Jacobsen catalysts, 126

L

Ligand–receptor interactions
  affinity, 204
  binding affinities, 206
  CP-MAS, 205–206
  magnetic orientation, 204–205
  MAOSS, 205
  molecules, 207
Lipari–Szabo model, 105–107
Longitudinal/transverse relaxation times
  fast fluctuation motions
    isotropic molecular motions, 9
    polymers, 9–10
    probability density function, 9–10
    simple isotropic motions, 9–10
  gyromagnetic ratios, 8–9
  interatomic contact/strong interactions
    anhydrous paramylon, 14
    glycine and serine, 13
    hindered CH_3 rotation, 14
    hydrogen bonding, 14
    internal fluctuations, 13
    metalcomplexed ionophores, 13–14
    methyl/hydroxymethyl groups, 15
    tetranactin and nonactin, 14
  intermediate frequency motions
    CPMAS and DDMAS spectra, 12
    dipolar and chemical shift interactions, 11–12
    fluctuation frequency, 10–11
    Gly-Gly residues, 12
    ^{1}H-decoupling field, 12–13
    polymer dynamics, 12
    spin diffusion process, 12–13
    spinner rotation rate, 12
  NMR measurements, 8
Low-pass J filters
  experimental verification
    HMBC experiments, 307, 309
    $^1J_{CH}$ artefact's intensity, 307, 308
    structure and carbon atoms, 307
  general scheme, 302–303
  HMBC, 303–304
  long-range magnetization attenuation
    chemical functionalities, 306–307
    couplings, 305–306
    single experimental parameter, 307
  maximal residual transverse proton magnetization, 306
  molecules possessing, 303–304
  one-bond heteronuclear coupling constants, 302
  pulse element, 302
  steps, 303
  theoretical residual transverse proton magnetization, 305
  transverse magnetization, 302

M

Magic angle spinning (MAS), 5–6
Magneto-Archimedes effect. *See* OPENCORE NMR applications, 368–390
Missing $^1J_{CH}$ corrections
  accordion optimized experiments, 317–318
  broadband HMBC
    practical applications, 320–321
    principles and theory, 318–320
  J-compensated
    adiabatic pulses, 321–322
    constant-time construction, 323
    definition, 321–322
    drawbacks, 321–322
    long-range coupling constants, 323
    pulse sequences, 323
m,n-ADEQUATE experiments
  1,1-ADEQUATE
    bromo-and dibromophakellins, 268
    COCON CASE program, 268–269
    COCON computation, 267, 268
    HMBC and COSY spectral data, 269
  5,6-dihydrolamellarin, 266–267
  strychnine
    ^{13}C-^{13}C DQ coherence, 264
    correlation, 264
    GHMBC spectrum, 264–265
    $^mJ_{CH}$ and $^nJ_{CH}$ magnetization transfer, 263
    $^mJ_{CH}$long-range magnetization transfer, 266
    $^mJ_{CH}$ transfer step, 263–264

N

1,*n*-ADEQUATE experiment
aromatic compounds
euglobal-G1 and euglobal-G2, 252
methine resonance, 252–253
5,6-dihydrolamellarin correlation, 248
$^{1}J_{CC}$, $^{2}J_{CC\ and\ 3}J_{CC}$ coupling constants, 253
phakellin and isophakellin alkaloids, 253–255
retrorsine
and 1,1-ADEQUATE correlation, 255–256
covariance processing, 256
$^{2}J_{CC}$ correlations, 256
strychnine spectrum
correlations, 250–251
5,6-dihydrolamellarin, 251
5 Hz, 249–250
600 MHz, 249–250
n,1-ADEQUATE experiments
application, 5,6-dihydrolamellarin
heteronuclear couplings, long-range, 262
$^{n}J_{CH}$correlations, 262
vs. 1,*n*-ADEQUATE, 263
$^{n}J_{CC}$ coupling, 256–257
strychnine
carbon-carbon correlations, 259
C14-C21 correlation, 259–260
C14-C13 DQ correlation frequency, 259, 260–261
^{13}C chemical shifts, 259
H23a/b protons, 257–259
$^{1}J_{CC}$ coupled resonances, 259
$^{n}J_{CH}$ correlation, 261
$^{n}J_{CH}$ delay, 257, 258
positive double quantum frequency range, 260
transmitter, 257
NMR techniques, liquid state
2D, 187
diffusion, 192–200
lead generation approach, 182–184
NOE experiment and pumping, 184–185, 187
relaxation time measurement
data, 191
food chemistry, 188–189
^{1}H and ^{13}C, 191
Hill equation, 189–190
^{1}H times values and signal percentages, 188–189, 190
polymeric hydrogels, 188
spin–lattice, 190–191
water/polymers interactions, 187–188
screening methods, 182
selectins and ligands, 185
STD, 185–186
^{15}N NMR spectroscopy
adduct formation, 147
CDCl3, δN values, 146–147
chemical shift, crown Schiff base, 147–148
gossypol and L-phenylalanine methyl ester, 147–148
range, δN values, 147
use, δN chemical shift, 146
NOE. *See* Nuclear Overhauser effect, 91–92, 108–110
Nuclear magnetic resonance (NMR). *See* Optically active schiff bases, NMR, 125–177
Nuclear Overhauser effect (NOE)
description, 91–92
factor, 98
measurement, factor
description, 109–110
proton-decoupled ^{13}C spectrum, 109–110
simulations, 109–110
spin state and polarization, proton, 109–110
use, high power decoupling, 110–111
proton–electron dipolar interactions, 97

O

OPENCORE NMR applications
active compensation, RF pulse transients
calculation, programming pulse shape, 387, 389
compensated pulse, 386–387
convolution relation, 388
data processing, 389–390
experimental setup, home-built spectrometer, 386
Laplace transformation, 388, 390
measurement, pickup coil, 385, 386–387
phase-inverted pulse, 386–387
probe tuning and transient effect, 386
programmed and resultant pulse shape, 387–388
target function, 389–390
cryogen-free superconducting magnet, field-variable
array experiments, 376

OPENCORE NMR applications (*cont.*)
carrier frequency, 375
description, 374–375
desktop NMR system, 374–375, 376
^{195}Pt Knight shift, 376
spin echoes, ^{195}Pt, 376–377
DNP system
crystal, heavily-deuterated naphthalene, 381
experimental setup, triplet, 379–380
^{2}H double-quantum (DQ) decoupling, 381–382
^{1}H magic-sandwich echo spectrum, 379–380, 381, 382
laser, microwave pulse, and field modulation, 379–380
magnetic-field cycling system, 378–379
nuclear hyperpolarization technique, 377–378
nuclear magnetization, 378–379
nuclear spins, 377–378
pentacene-doped naphthalene, 379–380
photo-excitation, 377–378
polarization transfer, 381
spin diffusion and dipolar interaction, ^{1}H, 381–382
spin polarization, 381
time interval and magic echo intensity, 381
high-temperature superconducting materials
description and significance, 377
experimental setup, 377, 378
field-cooling method, 377
magneto-Archimedes effect, nuclear magnetization role
balanced forces, inversion, 385–386
balance, paramagnetic force, 384
buoyancy, principle, 383
definition, 383
description, 382
diamagnetic force, 382–383
diamagnetic levitation, 383
^{1}H magnetization, 384
paramagnetism, 383–384
probe development and CCD camera, 384
shift, 385–386
susceptibility, proton spin system, 383–384
measurements, conventional
^{13}C CPMAS spectrum, 368, 369
cryo-coil MAS probe, 368–370
experimental setup, 370
^{1}H-^{13}C CPMAS, 368
^{6}Li 2D exchange, 369–370
MACS, 368
magnitude, reflecting signal, 369, 372
microcoil MAS, 368
network analyzer, 370
parametric plot, 369, 372
probe tuning, 370–372
S_{11} parameter, 370
Varian T3-probe, 370–372
and MRI systems
demonstration, ^{1}H, 373, 374
experimental setup, 374, 375
NEOMAX 1 T permanent magnet, 372–373
RF power level, 373
spectrometer, 374
superconducting magnet and power amplifier, 372
OPENCORE NMR design
architecture
block diagram, 359
observation channel, 357, 359
RF transmission and signal acquisition, 359
trigger signals, 359
FPGA
characteristics, 358
core module and open-resource, 358
customized device, 357–358
description, 357–358
NOT gate and circuit, 357–358
performance, core modules, 359
higher intermediate frequency
band-pass filter, 365
circuit diagram and snapshot, band-pass filter, 365, 366
clock-jitter tolerance, 365–366
digital signal sampling, 363–364
line width and PTS synthesizer, 365–366
liquid-state ^{1}H spectra, 365
phase-tunable signal wave, 363
slight hardware modification, 363
spectral decomposition, DDS, 361, 363
super-Nyquist sampling, 363–364
up-conversion, 363
polar plot option, software

^{79}Br Larmor frequency, 367–368
conventional data plotting scheme, 367
generic graph-plotting software, 368
screenshots, console software, 367–368
RF transmitter
DDS, 359
DDS-dedicated LSI AD9858, 362
description, DDS, 361–362
frequency mixing scheme, 360
gyromagnetic ratio, 360
operation, pulse programmers, 361
phase modulation and phase cycling, 362
phase wheel, DDS, 361–362
pulse programmers, 361
signal, analog multiplier, 361
signal, DDS(I) and (II), 359–360
signal acquisition
bandwidth and finite impulse response (FIR) filters, 362
digital quadrature demodulation, 362
receiver circuit, 362
Open-resource, home-built NMR spectrometer. *See* Customized NMR systems, OPENCORE, 355–392
Open-resource, integrated, FPGA-based NMR spectrometer (OPENCORE NMR) spectrometer. *See* Customized NMR systems, OPENCORE, 355–392
Optically active schiff bases, NMR
absolute configuration
α-amino acids, 132
α-chiral primary, 132
diamagnetic effect, naphthalene ring, 132–133
spectra, ^{1}H, 133
^{27}AL, 176
^{9}BE, 176
and biological, conformation and molecular interaction
proteorhodopsin/bacteriorhodopsin, 158–160
pyridoxal phosphate, 153–155
rhodopsin, 155–158
chiral recognition
dirhodium method, 133
parameters, 133–134
racemic gossypol and L-phenylalanine amino acid methyl ester, 134
complexes
Co(II, III), 166–167
description, 160
Fe(II), 165
lanthanide, 173–174
Mn(III), 164
Mo(VI), 163–164
Ni(II), 168–169
Pt, 169–170
Re(VII), 164–165
Rh(III) and Ir(III), 167–168
Ru(II), 166
Sn(II), 172–173
Ti(IV), 160–162
U(IV), 174–176
V(V), 162–163
Zn(II) and Cd(II), 171–172
Zr(IV), 162
description, 126, 127
enantiomeric purity
BINOL derivatives, 129–130
myrtenal derivatives, 127–129
primary amines derivatives, 129
three-component derivatives, 130–132
equilibria
anomeric, 152–153
proton transfer, 144–152
racemisation/epimerisation, imines, 140–142
ring-chain tautomerism, 142–144
types, 140
identification and conformation
chiral calixsalen-type macrocycles, 135
chitosan resin, 139
degree of substitution (DS), chitosan, 138–139
description, 134
dialkylzinc addition, 138
di-and tetra-, macrocyclic, 137
2D NOESY spectrum, 135
L-phenylalanine and 2-hydroxynaphthaldehyde, 139–140
macrocycle formation, 136
macrocyclic, ^{1}H, 135
macrocyclisation process, 136
N-deacetylated oligomers synthesis, 139
peptidomimetic macrocycles synthesis, 136
ROESY spectrum, 136–137
simplification, 136
structure, poly-schiff bases, 138

Optically active schiff bases, NMR (*cont.*)
trans-1,2-diaminocyclohexane, 135
UV-vis, ^{1}H and ^{13}C, 134–135
Jacobsen catalysts, 126
^{29}SI MAS, 176–177
tool, enantiomeric excess/absolute configuration, 127

P

Peripheral membrane proteins
hydrophobic layer, 77–79
lipid bilayer surface, 77–79
myelin basic protein (MBP), 79
PIP2 and IP3, 78
pleckstrin homology (PH) domain, 77–79
water-hydrophobic layer, 77–79
Phospholamban (PLB)
AFA-PLN and WT-PLN bound, 76–77
backbone dynamics, 75–76
NMR restraints, 76–77
pentamer, 76
sarcoplasmic reticulum (SR), 75–76
Polysaccharide gels
amylose, agarose and carrageenan gels
^{13}C NMR signals, 33
DDMAS NMR technique, 33–34
helical junction zones, 33–34
κ-carrageenan, 33–34
liquid-like domain, 33
(1→3)–β-d-glucans
^{13}C NMR spectra, 30
crystalline sample, 30–32
curdlan, 29
helix forms, 29–30
heterogeneous portions, 32
hydrate powders, 29–30
hydrophobic association, 32
linear glucans, 30–32
network structure and gelation mechanism, 32
physical properties, 28
physical treatments, 31
slow cooling, 31
triple helical structure, 28
water molecules, 28–29
Probing interactions between molecules and polymers
NMR techniques, liquid state, 182–200
solid state NMR
atoms and molecules, 201
cross polarization, 202
decoupling, 201
hetero and homonuclear dipolar recoupling, 202–204
ligand–receptor interactions, 204–207
magic-angle spinning, 201
role, 200–201
supramolecular chemistry
HB interactions, 208–209
IR, 208
^{15}N chemical shift, 208
technique, 207–208
Proteorhodopsin/bacteriorhodopsin
^{13}C CP MAS NMR, 158–159
description, 158
^{15}N CP MAS NMR, 159–160
Proteorhodopsins
GPR ion-transporting function, 73–74
heptahelical architecture, 73–74
ring-shaped oligomeric assembly, 73–74
Pulsed field gradient NMR (PFG-NMR)
measurement, 196–197
signals, 200
spectroscopy, 192
technical development, 195

R

Rhodopsin
^{1}H and ^{13}C CP MAS NMR, 156–158
^{15}N CP MAS NMR, 158
Rotational-echo, double-resonance (REDOR), 203

S

Sensory rhodopsin
^{13}C NMR signals, 62–63, 72
C-terminal α-helix, 65–68
dominant residue types, 73
egg PC bilayer, 64, 65, 66, 69
hydrogen bonding, 68
photochemical reactions, 62–63
ppR, 68
switch model, 68–73
transmembrane and cytoplasmic ahelices, 70
Solomon equations
extended/longitudinal spin order
creation, 101
cross-correlation rate, 100
description, equations, 100
dipolar and CSA contributions, 100–101

dipolar–dipolar cross-correlation rate, 101–102
product operator, 100
significance, CSA mechanism, 101
simple
coefficients, 99
cross-and auto-relaxation rate, 97
definition, 97
description, cross-relaxation rate, 97
dipolar interaction, relaxation rate, 98
expression, cross-relaxation rate, 97
global information spanning, 98
NOE factor, 98
proton–carbon-13 cross-relaxation rate, 98
proton longitudinal relaxation rate, 99–100
solution, 99
steady state carbon polarization, 98
Spectral densities, carbon-13 heteronuclear longitudinal spin relaxation
anisotropic tumbling
diffusion rotation, 105
formulae, 104–105
notations, correlation times, 105
polar angles, relaxation vector, 104
principal axes, rotational diffusion tensor, 104
description, 102
isotropic tumbling
correlation time, 102–103
extreme narrowing and relaxometry, 102–103
normalized, 102–103
relaxation vectors, 103
small-step rotational diffusion, 102
Stokes–Einstein equation, 102
local motions
empirical parameter, 105–107
homologous CSA spectral density, 105–107
Lipari–Szabo model, 105–107
overall tumbling, 105–107
rotational diffusion anisotropy, 105–107
STAR element
CIGAR-HMBC, 324
evaluation
^{1}H–^{1}H homonuclear couplings, 325
$^{2}J_{CH}$ and $^{3}J_{CH}$ couplings, 325
^{2}J,^{3}J-HMBC experiment, 309
timing diagram, 326
Stokes–Einstein equation, 102
Structure elucidator CASE program, 245–246
Synthetic polymer gels
biocompatible hydrogels
blend-type copolymer, 25
^{13}C DDMAS NMR spectra, 23
^{13}C NMR signals, 19–20
CPMAS and DDMAS spectra, 22–24
cross-linked synthetic polymers, 20
cross-linking agent, 20–22
network structure and dynamics, 19–20
PHEMA gel, 24–25
resilient opaque gel, 20–22
surface-coating materials, 22
PVA and MMA gels
diffusional behaviours, 27–28
fibrillar network, 25–26
freeze-thaw cycle, 25
hydrogen bond networks, 25–26
PMMA gel samples, 27–28
probe molecule (PS), 27–28
pulse sequence, 25–26
solid phase reaction field, 27–28

T

Time domain NMR measurements
diffusometry
cross-linked hydrogels, 19
PDMAA gel, 19
FCR and residual dipolar couplings
cross-linked elastomers, 16
cross-linked systems, 17–19
dipolar correlation effect (DCE), 17
DQ buildup, 18
free induction decay (FID), 17
^{1}H dipolar couplings, 17
segmental orientation, 17–19
separation-of-time-scale approximation, 17–19
styrene-butadiene rubbers (SBR), 16